Lars Larsson and Hoyte C. Raven

Principles of Naval Architecture Series

Ship Resistance and Flow

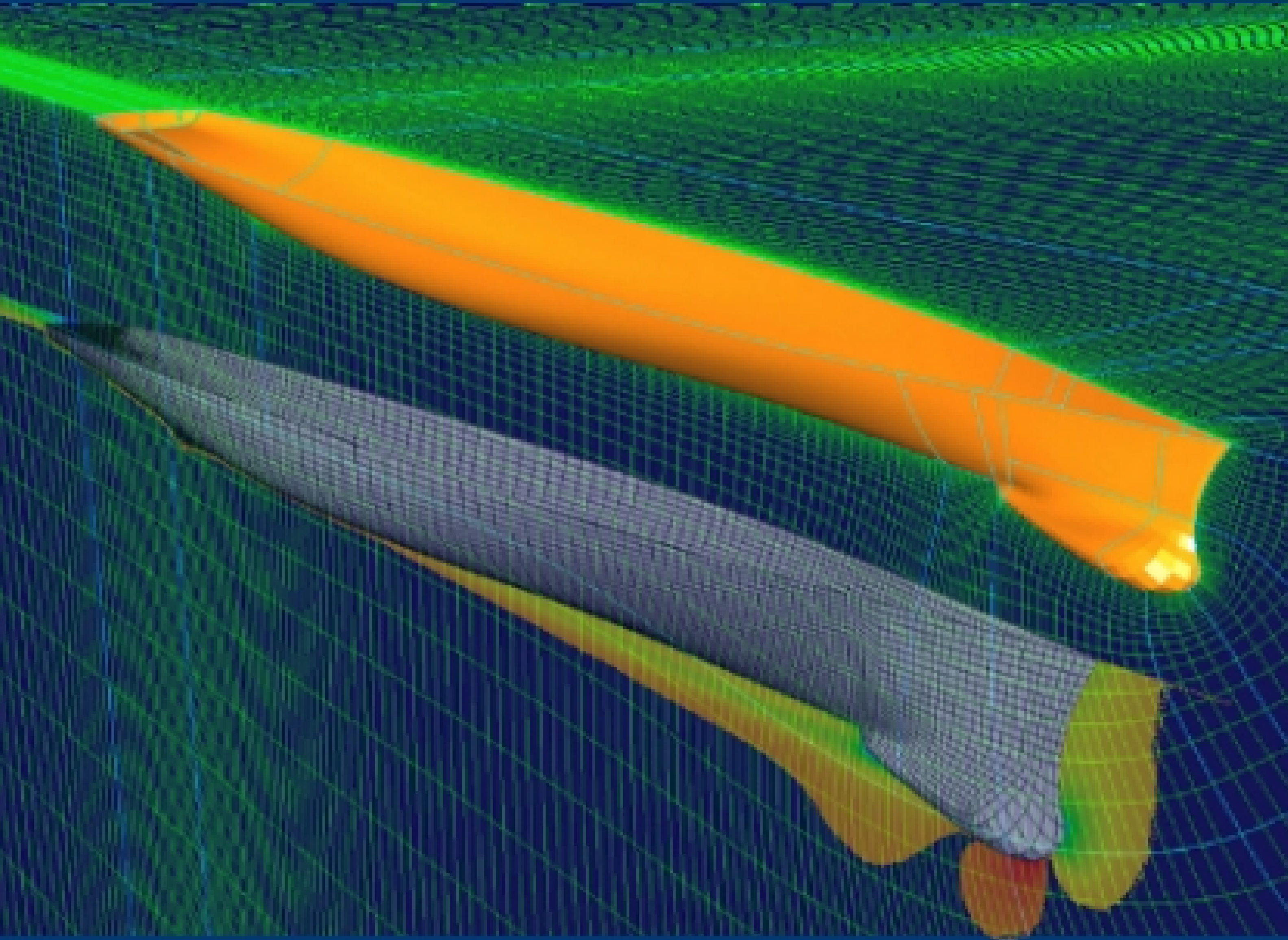

J. Randolph Paulling, Editor

The Principles of
Naval Architecture Series

Ship Resistance and Flow

Lars Larsson and Hoyte C. Raven

J. Randolph Paulling, Editor

2010

Published by
The Society of Naval Architects
and Marine Engineers
601 Pavonia Avenue
Jersey City, New Jersey 07306

Library of Congress Cataloging-in-Publication Data
Larsson, Lars.
Ship resistance and flow / Lars Larsson and Hoyte C. Raven; J. Randolph Paulling, editor.
p. cm. — (Principles of naval architecture)
Includes bibliographical references and index.
ISBN 978-0-939773-76-3 (alk. paper)
1. Ship resistance—Mathematics. 2. Inviscid flow—Mathematics. 3. Viscous flow—Mathematics.
4. Hulls (Naval architecture)—Mathematics. 5. Ships—Hydrodynamics—Mathematics.
I. Raven, Hoyte C. II. Paulling, J. Randolph. III. Title.
VM751.L37 2010
623.8'12—dc22
2010020298

ISBN 978-0-939773-76-3

Printed in the United States of America

First Printing, 2010

An Introduction to the Series

The Society of Naval Architects and Marine Engineers is experiencing remarkable changes in the Maritime Industry as we enter our 115th year of service. Our mission, however, has not changed over the years . . . "an internationally recognized . . . technical society . . . serving the maritime industry, dedicated to advancing the art, science and practice of naval architecture, shipbuilding, ocean engineering, and marine engineering . . . encouraging the exchange and recording of information, sponsoring applied research . . . supporting education and enhancing the professional status and integrity of its membership."

In the spirit of being faithful to our mission, we have written and published significant treatises on the subject of naval architecture, marine engineering, and shipbuilding. Our most well known publication is the "Principles of Naval Architecture." First published in 1939, it has been revised and updated three times – in 1967, 1988, and now in 2008. During this time, remarkable changes in the industry have taken place, especially in technology, and these changes have accelerated. The result has had a dramatic impact on size, speed, capacity, safety, quality, and environmental protection.

The professions of naval architecture and marine engineering have realized great technical advances. They include structural design, hydrodynamics, resistance and propulsion, vibrations, materials, strength analysis using finite element analysis, dynamic loading and fatigue analysis, computer-aided ship design, controllability, stability, and the use of simulation, risk analysis, and virtual reality.

However, with this in view, nothing remains more important than a comprehensive knowledge of "first principles." Using this knowledge, the Naval Architect is able to intelligently utilize the exceptional technology available to its fullest extent in today's global maritime industry. It is with this in mind that this entirely new 2008 treatise was developed – "The Principles of Naval Architecture: The Series." Recognizing the challenge of remaining relevant and current as technology changes, each major topical area will be published as a separate volume. This will facilitate timely revisions as technology continues to change and provide for more practical use by those who teach, learn or utilize the tools of our profession.

It is noteworthy that it took a decade to prepare this monumental work of nine volumes by sixteen authors and by a distinguished steering committee that was brought together from several countries, universities, companies, and laboratories. We are all especially indebted to the editor, Professor J. Randolph (Randy) Paulling for providing the leadership, knowledge, and organizational ability to manage this seminal work. His dedication to this arduous task embodies the very essence of our mission . . . "to serve the maritime industry."

It is with this introduction that we recognize and honor all of our colleagues who contributed to this work.

Authors:

Dr. John S. Letcher	Hull Geometry
Dr. Colin S. Moore	Intact Stability
Robert D. Tagg	Subdivision and Damaged Stability
Professor Alaa Mansour and Dr. Donald Liu	Strength of Ships and Ocean Structures
Professor Lars Larsson and Dr. Hoyte C. Raven	Ship Resistance and Flow
Professors Justin E. Kerwin and Jacques B. Hadler	Propulsion
Professor William S. Vorus	Vibration and Noise
Prof. Robert S. Beck, Dr. John Dalzell (Deceased), Prof. Odd Faltinsen and Dr. Arthur M. Reed	Motions in Waves
Professor W. C. Webster and Dr. Rod Barr	Controllability

Control Committee Members are:
Professor Bruce Johnson, Robert G. Keane, Jr., Justin H. McCarthy, David M. Maurer, Dr. William B. Morgan, Professor J. Nicholas Newman and Dr. Owen H. Oakley, Jr.

I would also like to recognize the support staff and members who helped bring this project to fruition, especially Susan Evans Grove, Publications Director, Phil Kimball, Executive Director, and Dr. Roger Compton, Past President.

In the new world's global maritime industry, we must maintain leadership in our profession if we are to continue to be true to our mission. The "Principles of Naval Architecture: The Series," is another example of the many ways our Society is meeting that challenge.

Admiral Robert E. Kramek
Past President (2007–2008)

Nomenclature

A	wave amplitude
A_L	lateral area of topsides and superstructure
A_M	area of midship section
AR	aspect ratio
AR_e	effective aspect ratio
A_T	frontal (transverse) area of topsides and superstructure
A_{tr}	transom area
$A(\theta), B(\theta)$	wave amplitude functions
a	coefficient in discretized equations
$\vec{a}$	acceleration vector
B	ship beam
b	width of channel or plate, wing span
c	wave speed, volume fraction
C_B	block coefficient of ship
C_D	drag coefficient
C_{Di}	induced drag coefficient
C_f	local skin friction coefficient
C_F	total skin friction
C_{F0}	total skin friction for a flat plate
c_g	wave group velocity
C_K, C_M, C_N	moment coefficients about x, y, z-axes
C_P	prismatic coefficient of ship hull, pressure resistance coefficient
C_p	pressure coefficient
$C_{p\ \mathrm{hd}}$	hydrodynamic pressure coefficient
$C_{p\ \mathrm{hs}}$	hydrostatic pressure coefficient
C_R	residuary resistance coefficient
C_T	total resistance coefficient
C_V	viscous resistance coefficient
C_X, C_Y, C_Z	force coefficients in x, y, z-directions
C_W	wave resistance coefficient
©	"circular C": ship resistance coefficient
D	drag, diffusion conductance
D_i	induced drag
E_{wave}	wave energy
E_{kin}	kinetic energy in wave
En	Euler number
E_{pot}	potential energy in wave
$\dot{E}$	wave energy flux
F	volume flux per unit area
$\vec{F}$	force vector
$\vec{F}_b$, $\vec{F}_p$, $\vec{F}_v$	body force, pressure force, and viscous force, respectively
Fn, Fn_L	Froude number based on ship length
Fn_B	Froude number based on ship beam
Fn_h	Froude number based on water depth
Fn_{tr}	Froude number based on $-\zeta_{tr}$
g	acceleration of gravity
h	water depth
H	approximate wave elevation in linearization
H_M	mean height of lateral projection of topsides and superstructure
K, M, N	moments about x, y, z-axes
k	wave number, form factor, turbulent kinetic energy
K_0,k_0	fundamental wave number
k_{MAA}	roughness (Mean Apparent Amplitude)
k_s	equivalent sand roughness
Ⓚ	"circular K": nondimensional speed
L	lift
L, L_{pp}	ship length (between perpendiculars)
L_p	length scale of pressure variation
m	mass
$\dot{m}$	mass flux
$\vec{m}$	dipole moment
n	wall-normal coordinate, inverse of exponent in velocity profile formula
P_D	delivered power
P_E	effective power
Pe	Peclet number
p	pressure
p^*	approximate pressure in SIMPLE algorithm
p'	pressure correction in SIMPLE algorithm
p_{hd}	hydrodynamic contribution to pressure
p_{hs}	hydrostatic pressure
p_{max}	stagnation pressure
p_∞	undisturbed pressure
Q	source strength
q	dynamic head
R	distance
r	radius of (streamline) curvature
r_1, r_2	principal radii of curvature of a surface
R_F	frictional resistance
R_H	hydraulic radius of channel
R_{ij}	Reynolds stress
Rn	Reynolds number
R_R	residuary resistance
R_T	total resistance
R_V	viscous resistance
R_W	wave resistance
S	wetted surface, source term
s, t, n	coordinates of local system on free surface
S_{ij}	rate of strain tensor
T	ship draught, wave period, turbulence level
t	time, thrust deduction fraction
U_∞	inflow velocity
$\vec{u}$	velocity vector
u, v, w	flow velocity components in x, y, z-directions
u_τ	friction velocity
u^+	non-dimensional velocity in wall functions
u^*	approximate velocity in SIMPLE algorithm
u'	velocity correction in SIMPLE algorithm
V	ship speed
$\vec{v}$	velocity vector
V_A	propeller advance velocity
$\vec{V}_{TW}$, $\vec{V}_{AW}$	true and apparent wind velocity, respectively
W	weight of ship, Coles' wake function

Wn	Weber number
w	wake fraction
X, Y, Z	forces in x, y, z-directions
x, y, z	coordinates of global system
y^+	non-dimensional wall distance in wall functions
z_v	dynamic sinkage
$\overline{z}_{tr}$	z-coordinate of transom centroid
α	angle of attack
β	blockage ratio, boundary layer cross-flow angle
β_{TW}, β_{AW}	true and apparent wind angle, respectively
β_w	wall cross-flow angle
γ	surface tension, overspeed ratio in channel
Γ	vortex strength, generalized diffusion coefficient
Δp_γ	pressure jump due to surface tension
Δ	weight of ship
δ	boundary layer thickness
δ_1	boundary layer displacement thickness
δ_{ij}	Kronecker delta
ε	rate of dissipation of turbulent kinetic energy
ζ	wave elevation
ζ'	perturbation of wave elevation
ζ_r	wave height deduced from double-body pressure
ζ_{tr}	height of transom edge above still-watersurface
η_D	propulsive efficiency
η_H	hull efficiency
η_R	relative rotative efficiency
η_0	open-water efficiency of propeller
θ	wave divergence angle, boundary layer momentum thickness
κ	von Kàrmàn constant
λ	wave length
λ_0	length of transverse wave, fundamental wave length
λ_x	length of wave, measured in longitudinal section
μ	dynamic viscosity, doublet density
μ_{eff}	effective dynamic viscosity
μ_t	turbulent dynamic viscosity
ν	kinematic viscosity
ν_{eff}	effective kinematic viscosity
ν_t	turbulent kinematic viscosity
ρ	density
σ	cavitation number, source density
σ_{ij}	stress tensor
τ	trim angle
τ_w	wall shear stress
ϕ	general dependent variable in finite volume theory
φ	velocity potential
φ'	perturbation of potential, in linearization
Φ	base flow potential in linearization
Ω_{ij}	rotation tensor
ω	radial frequency, specific rate of dissipation of turbulent energy
$\vec{\omega}$	vorticity vector
∇	displacement

Indices

a, w	air and water, respectively
M, S	model and ship, respectively
P	central point in a discretization stencil
W, E, N, S, T, B	neighboring points in a discretization stencil
w, e, n, s, t, b	cell faces
x, y, z	components of a vector in the x-, y-, or z-directions
$1, 2, 3$	components of a vector in the x-, y-, or z-directions (alternative representation)

Preface
Ship Resistance and Flow

During the 20 plus years that have elapsed since publication of the previous edition of *Principles of Naval Architecture*, there have been remarkable advances in the art, science and practice of the design and construction of ships and other floating structures. In that edition, the increasing use of high speed computers was recognized and computational methods were incorporated or acknowledged in the individual chapters rather than being presented in a separate chapter. Today, the electronic computer is one of the most important tools in any engineering environment and the laptop computer has taken the place of the ubiquitous slide rule of an earlier generation of engineers.

Advanced concepts and methods that were only being developed or introduced then are a part of common engineering practice today. These include finite element analysis, computational fluid dynamics, random process methods, numerical modeling of the hull form and components, with some or all of these merged into integrated design and manufacturing systems. Collectively, these give the naval architect unprecedented power and flexibility to explore innovation in concept and design of marine systems. In order to fully utilize these tools, the modern naval architect must possess a sound knowledge of mathematics and the other fundamental sciences that form a basic part of a modern engineering education.

In 1997, planning for the new edition of *Principles of Naval Architecture* was initiated by the SNAME publications manager who convened a meeting of a number of interested individuals including the editors of PNA and the new edition of *Ship Design and Construction* on which work had already begun. At this meeting it was agreed that PNA would present the basis for the modern practice of naval architecture and the focus would be *principles* in preference to *applications*. The book should contain appropriate reference material but it was not a handbook with extensive numerical tables and graphs. Neither was it to be an elementary or advanced textbook although it was expected to be used as regular reading material in advanced undergraduate and elementary graduate courses. It would contain the background and principles necessary to understand and to use intelligently the modern analytical, numerical, experimental, and computational tools available to the naval architect and also the fundamentals needed for the development of new tools. In essence, it would contain the material necessary to develop the understanding, insight, intuition, experience, and judgment needed for the successful practice of the profession. Following this initial meeting, a PNA Control Committee, consisting of individuals having the expertise deemed necessary to oversee and guide the writing of the new edition of PNA, was appointed. This committee, after participating in the selection of authors for the various chapters, has continued to contribute by critically reviewing the various component parts as they are written.

In an effort of this magnitude, involving contributions from numerous widely separated authors, progress has not been uniform and it became obvious before the halfway mark that some chapters would be completed before others. In order to make the material available to the profession in a timely manner it was decided to publish each major subdivision as a separate volume in the *Principles of Naval Architecture Series* rather than treating each as a separate chapter of a single book.

Although the United States committed in 1975 to adopt SI units as the primary system of measurement the transition is not yet complete. In shipbuilding as well as other fields we still find usage of three systems of units: English or foot-pound-seconds, SI or meter-newton-seconds, and the meter-kilogram(force)-second system common in engineering work on the European continent and most of the non-English speaking world prior to the adoption of the SI system. In the present work, we have tried to adhere to SI units as the primary system but other units may be found, particularly in illustrations taken from other, older publications. The symbols and notation follow, in general, the standards developed by the International Towing Tank Conference.

A major goal in the design of virtually all vessels as varied as commercial cargo and passenger ships, naval vessels, fishing boats, and racing yachts, is to obtain a hull form having favorable resistance and speed characteristics. In order to achieve this goal the prediction of resistance for a given hull geometry is of critical importance. Since the time of publication of the previous edition of PNA important advances have been made in theoretical and computational fluid dynamics and there has been a steady increase in the use of the results of such work in ship and offshore structure design. The present volume contains a completely new presentation of the subject of ship resistance embodying these developments. The first section of the book provides basic understanding of the flow phenomena that give rise to the resistance encountered by a ship moving in water. The second section contains an introduction to the methods in common use today by which that knowledge is applied to the prediction of the resistance. A third and final section provides guidance to the naval architect to aid in designing a hull form having favorable resistance characteristics.

William Froude in the 1870s proposed the separation of total resistance into frictional and residual parts, the former equal to that of a flat plate of the same length, speed, area, and roughness as the ship wetted surface, and the latter principally due to ship generated waves. Since Froude's time, much research has been conducted to obtain better formulations of the flat plate resistance with refinements to account for the three dimensional nature of the flow over the curved shape of the hull. Simultaneously, other research effort has been directed to obtaining a better understanding of the basic nature of the flow of water about the ship hull and how this flow affects the total resistance.

The three methods currently in general use for determining ship resistance are model tests, empirical methods, and theory. In model testing, refinements in Froude's method of extrapolation from model to full scale are described. Other experimental topics include wave profile measurements, wake surveys, and boundary layer measurements. Empirical methods are described that make use of data from previous ships or model experiments. Results for several "standard series" representing merchant ships, naval vessels, fishing vessels, and yachts are mentioned and statistical analyses of accumulated data are reviewed.

The theoretical formulation of ship resistance began with the linear thin ship theory of Michell in 1898. The present volume develops the equations of inviscid and viscous flow in two and three dimensions, including free surface effects and boundary conditions. From this basis are derived numerical and computational methods for characterizing the flow about a ship hull. Modern computing power allows these methods to be implemented in practical codes and procedures suitable for engineering application. Today, it is probable that many, if not most, large ships are designed using computational fluid dynamics, or CFD, in some form either for the design of the entire hull or for components of the hull and appendages.

Concluding sections describe design considerations and procedures for achieving favorable flow and resistance characteristics of the hull and appendages. Examples are covered for ships designed for high, medium, and low speed ranges. Design considerations affecting both wave and viscous effects are included. A final section discusses flow in the stern wake that has important implications for both resistance and propeller performance.

J. RANDOLPH PAULLING
Editor

Table of Contents

1

Introduction

1.1 The Importance of Accurate Resistance Predictions A central problem for the practicing naval architect is the prediction of the resistance of a new design already at an early stage in the project. When a new ship is ordered, a contract containing a specification of the ship is signed between the owner and the shipyard. One of the more strict specifications is the so-called contract speed, which is the speed attained at a specified power consumption in a trial run before delivery. This trial is supposed to take place under ideal conditions (i.e., with no wind or seaway and with no influence from restricted water and currents). In reality, corrections most often have to be applied for the influence of these factors. Should the corrected speed be lower than the contract speed, the yard will have to pay a penalty to the owner, depending on the difference between the achieved speed and the contract speed. If the difference is too large, the owner might even refuse to accept the ship.

The dilemma for the designer and the yard is:

- Because of the fierce competition between shipyards on the global market, the offer must be as least as good as that of the competitors. A few percent higher power for a given speed may result in a lost order.
- If the prediction has been too optimistic, and the ship does not meet the specification, it could be a very expensive affair for the yard.

The engine power required to drive the ship at a certain speed is not only dependent on the resistance; an important factor is also the propulsive efficiency (i.e., the performance of the propeller and its interaction with the hull). Losses in the power train must also be considered. However, the resistance is the single most important factor determining the required power.

Because the resistance, as well as other forces acting on the hull, are the result of shear and normal stresses (pressures) exerted on the hull surface by the water flow, knowledge of the flow around the ship is essential for the understanding of the different resistance components and for the proper design of the hull from a resistance point of view. Further, the flow around the stern determines the operating conditions for the propeller, so in this book a large emphasis is placed on describing the flow around the hull.

As in all design projects, a number of conflicting demands have to be satisfied. The hydrodynamic qualities, representing only one of many important aspects, include the ship's seakeeping and manoeuvring capabilities. These, and the propulsive efficiency, will be considered in other volumes of the *Principles of Naval Architecture.*

1.2 Different Ways to Predict Resistance

1.2.1 Model Testing. Because of the complicated nature of ship resistance, it is natural that early recourse was made to experiments, and it is recorded that Leonardo da Vinci (1452–1519) carried out tests on three models of ships having different fore-and-aft distributions of displacement (Tursini, 1953). The next known use of models to investigate ship resistance were qualitative experiments made by Samuel Fortrey (1622–1681), who used small wooden models towed in a tank by falling weights (Baker, 1937). After this, there was a steady growth of interest in model experiment work (Todd, 1951). Colonel Beaufoy, under the auspices of the Society for the Improvement of Naval Architecture founded in London in 1791, carried out between 9000 and 10,000 towing experiments between 1791 and 1798 in the Greenland Dock, using models of geometrical shape and flat planks (Beaufoy, 1834). In Sweden, Fredrik af Chapman carried out a large number of resistance tests with bodies of simple geometrical shape, presented in a thesis in 1795 (af Chapman, 1795). In 1764, Benjamin Franklin was probably the first American to make model experiments to verify observations he had made in Holland that resistance to motion increased in shallow water (Rumble, 1955).

The major problem encountered by the early investigators was the scaling of the model results to full scale. In what way should the measured towing force be extrapolated, and at which speed should the model be towed to correspond to a given speed at full scale? This problem was first solved by the French scientist Ferdinand Reech (1844), but he never pursued his ideas or used them for practical purposes. Therefore, the solution to the problem is attributed to the Englishman William Froude, who proposed his law of comparison in 1868 (Froude, 1955). In Froude's own words: "The (residuary) resistance of geometrically similar ships is in the ratio of the cube of their linear dimensions if their speeds are in the ratio of the square roots of their linear dimensions." The residuary resistance referred to is the total resistance minus that of an equivalent flat plate, or plank, defined as a rectangular plate with the same area and length, and moving at the same speed as the hull.

The idea was thus to divide the total resistance in two parts: one because of the friction between the hull and the water, and the other (the residuary resistance) because of the waves generated. The friction should be obtained from tests with planks (which do not produce waves) both at model- and full-scale, whereas the residuary resistance should be found from the model test by subtraction of the friction. This residuary resistance should then be scaled in proportion to the hull displacement from the model to the ship and added to the plank friction at full scale. A prerequisite for this scaling was that the ratio of the speeds at the two scales was equal to the square root of the length ratios, or, in other words, the speed divided by the square root of the length should be the same at both scales.

William Froude made his first model experiments in 1863 in a large rainwater tank using a falling weight to tow the hull. This was the technique used by most earlier investigators, but he soon became dissatisfied with the limitations of these experiments and turned his mind to the use of a larger tank. He made proposals to the British Admiralty in 1868, which were accepted, and a new tank was completed near his home in Torquay in 1871 (Froude, 1955). This tank had a length of 85 m, a width at the water surface of 11 m, and a depth of water along the centerline of 3 m. It was equipped with a mechanically propelled towing carriage to tow the models, in place of the gravitational device, and because of this and its size may be considered as the forerunner of the tanks so common today.

Froude's hypothesis paved the way for modern resistance prediction techniques, but a major weakness was the formula suggested for the friction of the equivalent plate. The correct way of scaling friction was not known until Reynolds (1883) found that the scaling parameter is a dimensionless number, which later became known as the Reynolds number. The Reynolds number was introduced in model testing by Schoenherr (1932), who proposed a plank friction formula, but it was not until 1957 that the International Towing Tank Conference (ITTC) recommended the use of Reynolds number scaling of the friction, then by a different formula.

The modified procedure, where the "ITTC-57" friction line replaces Froude's original formula for the friction, is known as "Froude scaling" and is still used by some towing tanks. However, it was realized in the early 1960s when ships with very high block coefficients became more common, that a more detailed division of the resistance into components is required. All effects of viscosity will not be included in the plank friction, so another component of the viscous resistance, related to the three-dimensional (3D) shape of the hull, had to be introduced. The new technique is known as "3D extrapolation" and was proposed for general use by the ITTC in 1978. It is therefore named the "ITTC-78" procedure and is presently used by most tanks for scaling resistance, at least for normal displacement hulls.

1.2.2 Empirical Methods. Model tests are rather time-consuming, particularly if a large number of alternative designs are to be evaluated at a very early design stage. There is thus a need for very fast, but not necessarily as accurate, methods for resistance estimates. Such methods are of two different types: systematic series and statistical formulas based on unsystematic data.

The first comprehensive series of systematic tests was carried out in the Experimental Model Basin in Washington during the first years of the 20th century, but they were not reported in full until the 1933 edition of the Speed and Power of Ships, by Admiral Taylor. The series is known as the Taylor standard series and has been used extensively over the years. Unfortunately, the first evaluations of the residuary resistance were made using less well-established friction coefficients from measurements in the same tank, and no corrections were made for variation in the water temperature and the blockage effect of the tank walls and bottom. Further, the tests were made without turbulence stimulation. To adopt the results to the more modern procedure using Schoenherr's skin friction formula, Gertler reanalyzed the original data and applied corrections for the effects mentioned (Gertler, 1954).

Although the corrected Taylor series was not presented until the 1950s, it was based on a very old ship, the *Leviathan*, designed in 1900. All models of the series were obtained by systematic variation of the offsets of this parent model. To obtain results for more modern ships, the Society of Naval Architects, in cooperation with the American Towing Tank Conference (ATTC), initiated a new series in 1948. Unlike the Taylor series, this new series had several parent models, one for each block coefficient tested. In this way, realistic hull shapes could be obtained for all variations. The results of the tests were presented by Todd (1963) in a comprehensive report, which could be used for estimating the resistance of existing ships. In addition, using the design charts, new hulls could be developed with the presumably good resistance characteristics of the new series. Further, results were also presented for the self-propelled condition, which enables the designer to estimate the delivered power of his/her design. The new series was named the Series 60.

A large number of systematic tests were carried out in the 1950s and 1960s at various organizations. Several of them will be mentioned in Section 10. In more recent years, very few systematic tests have been carried out because of the very large expenses in model testing. A notable exception is, however, the extensive series of tests with sailing yacht models carried out in Delft from the mid-1970s. The series is continously extended and covers at present more than 50 models (Keuning & Sonnenberg, 1998).

The first attempt to develop a statistical formula for resistance based on unsystematic data was made by Doust and O'Brien (1959). They used results from tests of 150 fishing vessels and tried to express the total resistance at a given speed-length ratio as a function of six different shape parameters. The function chosen was a polynomial, with no terms of higher degree than two. An important result of the work is that optimization can be made with respect to the parameters tested. A similar approach has been taken by the Delft series experimentalists, who have developed regression formulas for sailing yacht resistance (Keuning & Sonnenberg, 1998). Their data were however obtained from systematic tests.

A disadvantage of the Doust and O'Brien approach is that the regression formula does not involve any physics, it is merely a polynomial in the tested parameters. A more scientific approach was proposed by Holtrop and Mennen (1978), who used a theoretical expression for the wave resistance of two travelling pressure disturbances (the bow and stern) in their regression formula, where the coefficients were determined from tests with 334 hulls. Further, the resistance was divided according to the 3D model-ship extrapolation procedure mentioned previously. The Holtrop-Mennen method is the most widely used technique for rapid estimates of ship resistance available today.

1.2.3 Computational Techniques. Thanks to the rapid development of computer technology during the past 50 years, computational techniques in ship hydrodynamics have developed over a shorter time span than the experimental ones. However, the first method which may be considered as computational hydrodynamics was presented in a landmark paper by the Australian mathematician Michell more than a century ago (Michell, 1898). Like all other early researchers in the field, he neglected the viscosity of the fluid, which considerably simplifies the theory. The mathematical expression for the inviscid flow around a "slender" ship of narrow beam placed in a uniform stream was obtained. By integrating the fore-and-aft components of the pressure computed on the hull, an expression could be derived for the total wave resistance. To make the problem amenable to existing mathematical methods, Michell had to linearize the boundary conditions of the computational domain. The hull boundary condition was applied to the centerplane rather than to the actual hull surface, so that the results applied strictly to a vanishingly thin ship, and the condition on the free surface was applied to the original flat, free surface of the water, the distortion of the surface resulting from the wave pattern being neglected.

An alternative method was developed by Havelock and his coworkers during the first decades of the 20th century (see, for instance, Havelock, 1951) in which the wave-making resistance was measured by the energy in the wave system. Havelock also introduced the idea of sources and sinks, which he distributed on the centerplane of the hull. Each source was assumed proportional to the local waterline angle, positive on the forebody and negative aft. Summing the wave making effect of the sources, the farfield waves could be determined, and thereby the wave resistance.

Important work on wave resistance was also carried out in Japan during the 1960s and 1970s by Inui and his coworkers. This work, which is summarized in Inui (1980), included among other things theories for optimizing the hull from a wave resistance point of view. In the same period, methods for experimentally determining the wave resistance from wave cuts on the surface near the hull were developed. A landmark paper on these techniques was presented by Eggers, Sharma, and Ward (1967).

All methods referred to so far were developed for inviscid flows, and to a large extent based on analytical techniques. However, with the introduction of the computers in the 1960s another technique, based on numerical methods* started to develop. A typical example is the method developed at the Douglas Aircraft Company by Hess and Smith (1962). This is an inviscid method where the velocity is obtained from a boundary condition on the body surface, discretized by flat quadrilateral panels. Because the method was applicable to arbitrary 3D bodies, it immediately became useful in aerodynamic design. In hydrodynamics, the method also turned out to be of fundamental importance. It was later improved in several papers by Hess who, among other things, introduced circulation and lift. Of more importance to ship hydrodynamics was, however, the introduction of the free surface into a similar panel method by Dawson (1977). Dawson imposed a free surface boundary condition linearized about a "double model" solution, obtained by assuming the surface to be a plane of symmetry. This is a different linearization as compared to Michell's, which was made about the undisturbed flow. Because for a bluff hull, the double model flow must be considerably closer to the real one, Dawson's approach may be considered less approximate. Further, as in all panel methods, the exact hull boundary condition was satisfied on the hull surface. As we have seen previously, in Michell's method, a linearized condition was applied at the hull centerplane.

One drawback of Dawson's method is the inconsistency of boundary conditions: exact on the hull and linearized on the free surface. This drawback was removed in research during the 1980s. Larsson, Kim, and Zhang (1989) presented a method based on Dawson's approach, but with an (at least in some sense) exact free-surface boundary condition. This method was further refined and validated by Janson (1997). A similar development was carried out in Germany by Jensen (1988) and in Holland by Raven (1996). Panel methods are now used extensively in ship design, but there is an inherent weakness in the assumption of zero viscosity, so it is unlikely that the correspondence with measured data will improve substantially in the future. To improve the accuracy further, viscosity must be taken into account.

Computational techniques for viscous flows† also started to appear with the introduction of the computer. During the 1960s several new methods for two-dimensional (2D) boundary layer prediction were presented (Kline, Coles, & Hirst, 1968). Research on 3D boundary layers had just begun, and it continued for the larger part of the 1970s. In 1980, a workshop was organized in Gothenburg to evaluate the performance of existing methods in the prediction of ship boundary layers (Larsson, 1981). The general conclusion of the workshop was that the boundary layer was well computed over the forward and middle parts of the hull, but that the stern flow could not be predicted at all using the boundary layer approximation. For such a prediction to be successful,

---

*The difference between the "analytical" and "numerical" techniques will be explained in Section 9.

†Although regions of the flow independent of viscosity may be called inviscid, there is a semantic problem finding a general name for regions where viscosity does play a part. As is most common, such regions will hereinafter be called viscous. However, some fluid dynamicists reserve the label "viscous" for flows at very low Reynolds numbers (i.e., with very large viscosity). See the previous discussion.

methods of the Reynolds-Averaged Navier-Stokes* (RANS) type would be needed. Such a method had just been applied for the first time to ship flows by Spalding and his coworkers at Imperial College (Abdelmeguid et al., 1978), and the international research during the 1980s was directed toward this approach. In 1990, a second workshop was held in Gothenburg (Larsson, Patel, & Dyne, 1991). Seventeen out of 19 participating methods were now of the RANS type, and considerably better stern flow predictions had become possible. One problem was, however, the prediction of the wake contours in the propeller plane. Because of an underprediction of the strength of a vortex intersecting the propeller disk, the computed wake contours became too smooth. Therefore, a main target of the research in the 1990s was to improve the prediction of the detailed wake distribution.

To resolve the problem of free-surface/boundary layer interaction, free-surface boundary conditions are needed in RANS methods, and during the first half of the 1990s, the research in this area accelerated. At a third workshop held in Tokyo in 1994 (Kodama et al., 1994), no less than 10 methods featured this capability. However, computer power was still too limited to enable sufficient resolution on the free surface, so the potential flow panel methods still produced better waves. Limited computer power was also blamed for some of the problems still encountered at the fourth workshop in 2000 (Larsson, Stern, & Bertram, 2003). Considerable improvements in accuracy, with respect to the wake, as well as the waves, were noted, but there was still room for improvements when it came to the details of the flow. By better resolution of the RANS solutions, such improvement can be expected, but the inherent problem of modeling the turbulence cannot be avoided. To overcome this difficulty, the much more computer-demanding methods of Large Eddy Simulation* (LES) or Direct Numerical Simulation* (DNS) type must be employed, and this will call for very substantial enhancements in computer power.

1.2.4 Use of the Methods. The three different methods for determining resistance are used at different stages of the ship design process. At the very early basic design stage, the main parameters of the hull are often varied and the design space explored with respect to length, beam, draft, block coefficient, and longitudinal position of the center of buoyancy. Because the entire design of the ship depends on these parameters, time is often short, and a reasonable estimate is required rapidly. Then the empirical methods come into play. A large design space may be explored with little effort and the main particulars of the ship determined at least approximately. Because the shape variation is very much linked to computer-aided design (CAD), most CAD packages for ship design contain a module for predicting ship resistance, in most cases based on the Holtrop-Mennen method.

During the past couple of decades, the numerical methods have made their way into design offices. Thus, having a good idea of the hull main dimensions, they may be further optimized using these methods. More important, however, is the possibility of optimizing the local shape of the hull, not only the main parameters. Forebody optimization using potential flow methods is now a standard procedure used by most ship designers. Particular features to look at are the size and shape of the bulb and the radius of the fore shoulder. The purpose is normally to minimize wave resistance (Valdenazzi et al., 2003).

Very recently, afterbody optimization has started to appear in ship design offices. Because the effect of the boundary layer is much larger at the stern than at the bow, viscous flow methods are required. Boundary layer theory is too approximate for computing the wake behind the hull, so more advanced methods are required. At present, the only alternative is the RANS technique. Even though the computational effort is considerably larger than for potential flow methods, several alternatives may be evaluated in one day, which is good enough. Typical features to optimize are the stern sections (V-, U-, or bulb-shaped) and the local bilge radius. Recently, the effect of the rudder has also been included. Normally, the purpose is not to minimize resistance, but delivered power, and this calls for some method to estimate the interaction between the hull and the propeller. Some designers do that by experience, but methods are available for computing the effect, either approximately by representing the propeller by forces applied to the flow (Han, 2008), or by actually running the real rotating propeller behind the hull (Abdel-Maksoud, Rieck, & Menter, 2002). Note that it is not only delivered power that is of interest; noise and vibrations caused by the propeller in the uneven wake should also be considered.

Although most optimizations so far are carried out manually by systematically varying the hull shape, formal optimization methods may be applied as well. The optimizer is then linked to a computational fluid dynamics (CFD) code and a program for changing the hull shape, often a CAD tool. Given certain constraints, one or several objective functions may be optimized, starting from an initial shape. In a typical single-objective optimization, delivered power may be minimized; in a multiobjective optimization, pressure fluctuations may be considered as well, or completely different capabilities such as seakeeping qualities. For a survey of optimization techniques in ship hydrodynamics, see Birk and Harries (2003).

To obtain a very accurate prediction of resistance and power, model testing is still used for the majority of new ships. Typically, optimization is first carried out using numerical methods, whereas the final decision about the hull shape is taken only after model tests of a few of the best candidates have been carried out. This is so because numerical predictions have not yet reached the reliability of model test results. There is no question, however, that the regular testing of ship models will

---

*The difference between methods for viscous flow computation (RANS, Large Eddy Simulation, and Direct Numerical Simulation) will be explained in Section 9.

be replaced by numerical predictions, sooner or later. Towing tanks and other test facilities will then be used more for more advanced investigations and for validation of new computational techniques.

1.3 The Structure of this Book. The objective of the present volume of the *Principles of Naval Architecture* is to provide:

- A basic understanding of the resistance problem for ships and other marine vehicles
- Insight into the three different methods for predicting resistance
- Practical guidelines for the designer.

The next six sections cover the first objective. In Section 2, the equations governing the flows of interest are derived and discussed together with their boundary conditions. These equations are used in Section 3 to prove the similarity laws governing the extrapolation of model-scale data to full scale. Thereafter, in Section 4, the total resistance of four widely different ships is divided into components, which are briefly described. These components are then discussed in detail in subsequent Sections 5 to 7, dealing with the wave resistance, the viscous resistance, and "other components," respectively. The three prediction techniques are described in Sections 8 to 10, covering experimental techniques, numerical methods, and empirical predictions, respectively. Finally, in Section 11, practical guidelines for designing a ship with good resistance properties are presented.

2

Governing Equations

In this section, we will derive the equations governing the viscous flow around a ship and discuss the appropriate boundary conditions. We will start by defining the global Cartesian coordinate system x, y, z used throughout the book. Thereafter, the continuity equation will be derived, followed by Navier-Stokes equations (three components). Together, these equations constitute a closed system for the pressure, p, and the three velocity components u, v, and w. Boundary conditions are discussed next, and the section is concluded by notes on surface tension and pressure decomposition. Note that we consider water to be an incompressible fluid (i.e., the density, ρ, is assumed constant).

2.1 Global Coordinate System. As explained previously, this book deals with the flow around ships at steady forward speed, denoted V in the following. Unsteadiness resulting from motions and waves as well as manoeuvring are neglected. The nomenclature used is the one recommended by the ITTC. Fig. 2.1 displays the global Cartesian coordinate system adopted. x is directed sternward, y to starboard, and z vertically upward. The origin is at midship and the undisturbed water level. The coordinate system thus moves with the ship, so we consider a ship at a fixed position in a uniform inflow from ahead. In this coordinate system, the entire flow field is steady in a time-averaged sense (turbulent fluctuations filtered out, see Section 9.7); in other words, the mean velocity and pressure fields and the wave pattern are functions of the spatial coordinates but not of time. Turbulent fluctuations may occur, however, so the equations are derived in their unsteady form for later use in Section 9.7.

2.2 The Continuity Equation. The continuity equation may be derived easily by considering the infinitesimal fluid element $dxdydz$ in Fig. 2.2, where the mass flows through the faces with normals in the x-direction are shown. It is only the u-component which can transport any mass through these surfaces. The mass inflow is $\rho\, udydz$ and the outflow $\left[\rho u + \frac{\partial}{\partial x}\rho udx\right]dydz$ (i.e., the net outflow in this direction is $\frac{\partial}{\partial x}\rho udxdydz$. Correspondingly, in the other two directions, the net outflows are $\frac{\partial}{\partial y}\rho vdydz$ and $\frac{\partial}{\partial z}\rho wdxdz$, respectively.

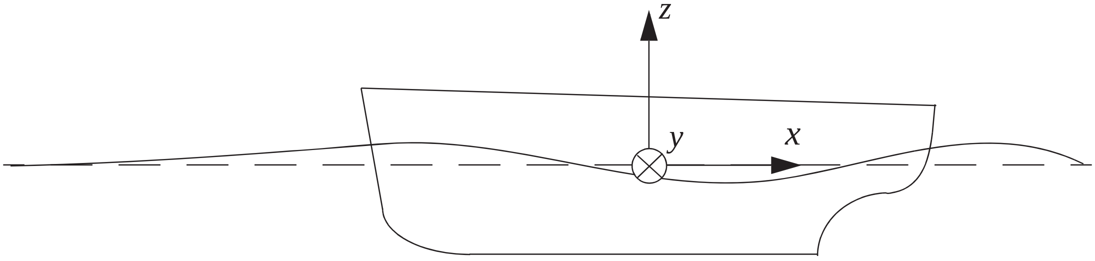

Figure 2.1 Global coordinate system.

be replaced by numerical predictions, sooner or later. Towing tanks and other test facilities will then be used more for more advanced investigations and for validation of new computational techniques.

1.3 The Structure of this Book. The objective of the present volume of the *Principles of Naval Architecture* is to provide:

- A basic understanding of the resistance problem for ships and other marine vehicles
- Insight into the three different methods for predicting resistance
- Practical guidelines for the designer.

The next six sections cover the first objective. In Section 2, the equations governing the flows of interest are derived and discussed together with their boundary conditions. These equations are used in Section 3 to prove the similarity laws governing the extrapolation of model-scale data to full scale. Thereafter, in Section 4, the total resistance of four widely different ships is divided into components, which are briefly described. These components are then discussed in detail in subsequent Sections 5 to 7, dealing with the wave resistance, the viscous resistance, and "other components," respectively. The three prediction techniques are described in Sections 8 to 10, covering experimental techniques, numerical methods, and empirical predictions, respectively. Finally, in Section 11, practical guidelines for designing a ship with good resistance properties are presented.

2
Governing Equations

In this section, we will derive the equations governing the viscous flow around a ship and discuss the appropriate boundary conditions. We will start by defining the global Cartesian coordinate system x, y, z used throughout the book. Thereafter, the continuity equation will be derived, followed by Navier-Stokes equations (three components). Together, these equations constitute a closed system for the pressure, p, and the three velocity components u, v, and w. Boundary conditions are discussed next, and the section is concluded by notes on surface tension and pressure decomposition. Note that we consider water to be an incompressible fluid (i.e., the density, ρ, is assumed constant).

2.1 Global Coordinate System. As explained previously, this book deals with the flow around ships at steady forward speed, denoted V in the following. Unsteadiness resulting from motions and waves as well as manoeuvring are neglected. The nomenclature used is the one recommended by the ITTC. Fig. 2.1 displays the global Cartesian coordinate system adopted. x is directed sternward, y to starboard, and z vertically upward. The origin is at midship and the undisturbed water level. The coordinate system thus moves with the ship, so we consider a ship at a fixed position in a uniform inflow from ahead. In this coordinate system, the entire flow field is steady in a time-averaged sense (turbulent fluctuations filtered out, see Section 9.7); in other words, the mean velocity and pressure fields and the wave pattern are functions of the spatial coordinates but not of time. Turbulent fluctuations may occur, however, so the equations are derived in their unsteady form for later use in Section 9.7.

2.2 The Continuity Equation. The continuity equation may be derived easily by considering the infinitesimal fluid element $dxdydz$ in Fig. 2.2, where the mass flows through the faces with normals in the x-direction are shown. It is only the u-component which can transport any mass through these surfaces. The mass inflow is $\rho\, udydz$ and the outflow $\left[\rho u + \frac{\partial}{\partial x}\rho u dx\right]dydz$ (i.e., the net outflow in this direction is $\frac{\partial}{\partial x}\rho u dxdydz$. Correspondingly, in the other two directions, the net outflows are $\frac{\partial}{\partial y}\rho v dydz$ and $\frac{\partial}{\partial z}\rho w dxdz$, respectively.

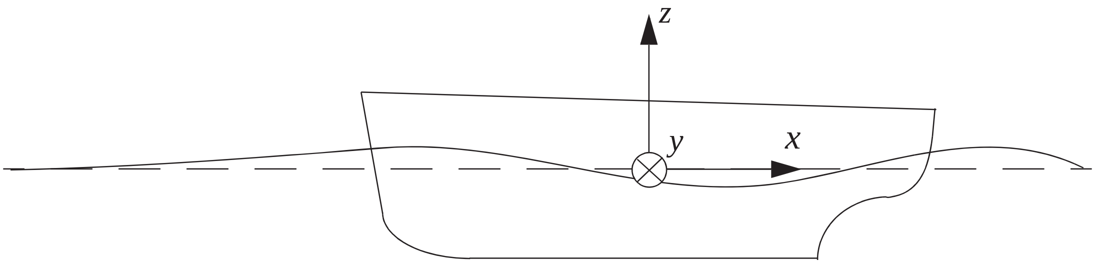

Figure 2.1 Global coordinate system.

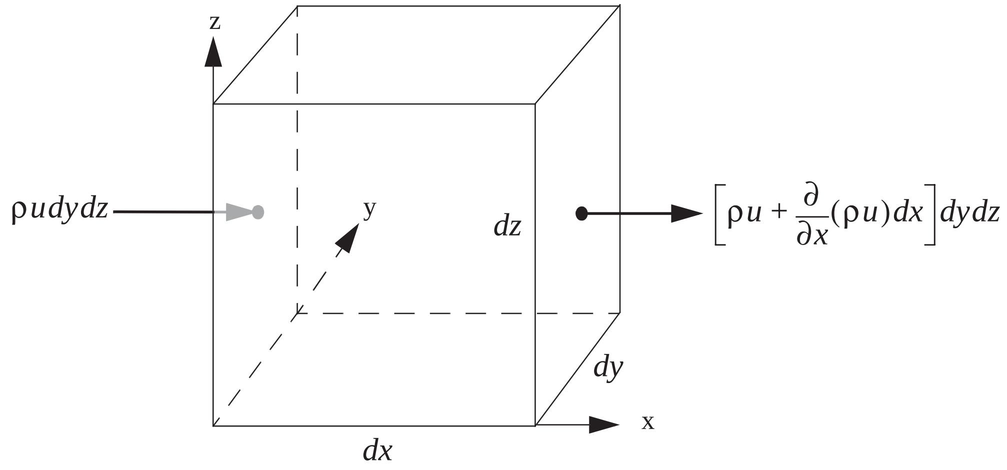

Figure 2.2 Mass flow in the *x*-direction through the fluid element.

Because the total net transport of mass out of the element must be zero in the absence of mass sources, the following equation is obtained

$$\frac{\partial}{\partial x}\rho u dxdydz + \frac{\partial}{\partial y}\rho v dxdydz + \frac{\partial}{\partial z}\rho w dxdydz = 0$$

With ρ constant, the equation may be written

$$\frac{\partial u}{\partial x} + \frac{\partial v}{\partial y} + \frac{\partial w}{\partial z} = 0 \tag{2.1}$$

This is the continuity equation for incompressible flows.

2.3 The Navier-Stokes Equations. The Navier-Stokes equations require a rather lengthy derivation, which is good to know to understand the origin of the different terms. A reader not interested in the details may, however, jump directly to the final result: equations (2.13a) to (2.13c).

We start by by applying Newton's second law to the infinitesimal fluid element *dxdydz* of Fig. 2.3

$$d\vec{F} = dm \cdot \vec{a} \tag{2.2}$$

where $d\vec{F}$* is the total force on the element, dm is its mass, and $\vec{a}$ is its acceleration.

In fluid mechanics, three different types of forces need to be considered: pressure forces $d\vec{F}_p$, body forces $d\vec{F}_b$, and viscous forces $d\vec{F}_v$. Inserting these into equation (2.2) divided by dm yields

$$\vec{a} = \frac{d\vec{F}_p}{dm} + \frac{d\vec{F}_b}{dm} + \frac{d\vec{F}_v}{dm} \tag{2.3}$$

But

$$\vec{a} = \frac{d\vec{u}}{dt} \tag{2.4}$$

where $\vec{u}$ is the velocity vector with the components $u = u(x,y,z,t)$, $v = v(x,y,z,t)$, and $w = w(x,y,z,t)$. Applying the chain rule, the three components of the acceleration may thus be written

$$a_x = \frac{du}{dt} = \frac{\partial u}{\partial t} + u\frac{\partial u}{\partial x} + v\frac{\partial u}{\partial y} + w\frac{\partial u}{\partial z} \tag{2.5a}$$

$$a_y = \frac{dv}{dt} = \frac{\partial v}{\partial t} + u\frac{\partial v}{\partial x} + v\frac{\partial v}{\partial y} + w\frac{\partial v}{\partial z} \tag{2.5b}$$

$$a_z = \frac{dw}{dt} = \frac{\partial w}{\partial t} + u\frac{\partial w}{\partial x} + v\frac{\partial w}{\partial y} + w\frac{\partial w}{\partial z} \tag{2.5c}$$

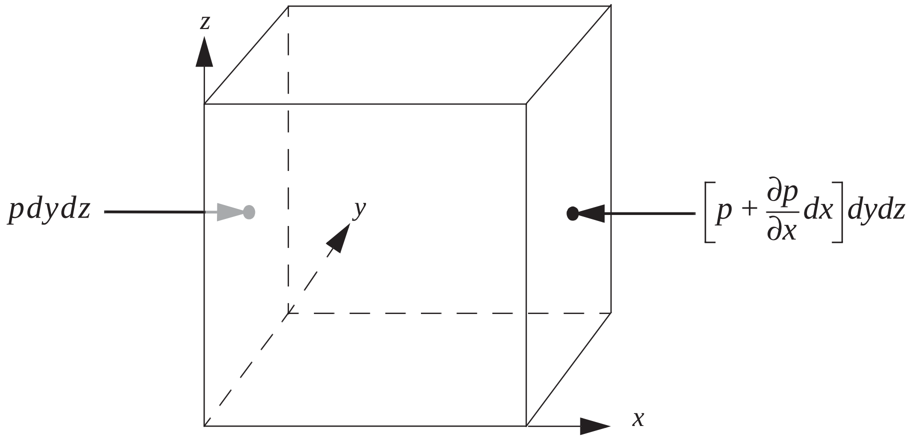

Figure 2.3 Pressure acting on the *x*-faces of the fluid element.

---

*Vectors are denoted by arrows.

It now remains to determine the three forces. Let us start with the pressure force and consider its x-component dF_{px}. As appears from Fig. 2.3, the pressure force on the left surface is $pdydz$, while the force has changed to $\left(p+\frac{\partial p}{\partial x}dx\right)dydz$ on the right surface because of the pressure gradient. The resulting force thus points in the negative x-direction. It may now be written

$$dF_{px} = -\frac{\partial p}{\partial x}dxdydz$$

Division by the mass $dm = \rho\, dxdydz$ yields for the first term on the right-hand side of the x-equation

$$\frac{dF_{px}}{dm} = -\frac{1}{\rho}\frac{\partial p}{\partial x} \tag{2.6a}$$

Similarly, for the other two directions

$$\frac{dF_{py}}{dm} = -\frac{1}{\rho}\frac{\partial p}{\partial y} \tag{2.6b}$$

$$\frac{dF_{pz}}{dm} = -\frac{1}{\rho}\frac{\partial p}{\partial z} \tag{2.6c}$$

The only body force we will consider in the following is gravity. In the coordinate system adopted (see Fig. 2.1), the z-direction is vertically upward, so gravity has no component in the x- and y-directions. In the z-direction, it will be equal to $-gdm$, where g is the acceleration of gravity. We thus have

$$\frac{dF_{bx}}{dm} = 0 \tag{2.7a}$$

$$\frac{dF_{by}}{dm} = 0 \tag{2.7b}$$

$$\frac{dF_{bz}}{dm} = -g \tag{2.7c}$$

The final force is that due to viscosity, $d\vec{F}_v$. For several reasons, this is considerably more difficult to obtain than the other two. First, we note that the viscous force is because of stresses acting on the sides of the fluid element, both in the normal and tangential directions. This is shown in Fig. 2.4. Each stress is identified by two indices, where the first one represents the surface on which the stress acts and the second one its own direction. The surface is identified by the direction of its normal. Because both indices may attain three values, the viscous stress tensor σ_{ij} has nine components.

In Fig. 2.4, the stresses acting in the x-direction on all six faces of the element are shown. By adding the contributions (with sign!) from opposing sides, in the same way as for the pressure, the total viscous force in the x-direction is obtained.

$$dF_{vx} = \left[\frac{\partial \sigma_{xx}}{\partial x} + \frac{\partial \sigma_{yx}}{\partial y} + \frac{\partial \sigma_{zx}}{\partial z}\right]dxdydz \tag{2.8}$$

so the viscous term in equation (2.6a) becomes

$$\frac{dF_{vx}}{dm} = \frac{1}{\rho}\left[\frac{\partial \sigma_{xx}}{\partial x} + \frac{\partial \sigma_{yx}}{\partial y} + \frac{\partial \sigma_{zx}}{\partial z}\right] \tag{2.9a}$$

Similarly, for the other two components

$$\frac{dF_{vy}}{dm} = \frac{1}{\rho}\left[\frac{\partial \sigma_{xy}}{\partial x} + \frac{\partial \sigma_{yy}}{\partial y} + \frac{\partial \sigma_{zy}}{\partial z}\right] \tag{2.9b}$$

$$\frac{dF_{vz}}{dm} = \frac{1}{\rho}\left[\frac{\partial \sigma_{xz}}{\partial x} + \frac{\partial \sigma_{yz}}{\partial y} + \frac{\partial \sigma_{zz}}{\partial z}\right] \tag{2.9c}$$

It now remains to determine the stresses, and here we have to rely on a hypothesis, however very well proven over the years. In his work *Principia*, Newton postulated in 1687 a linear relationship between the shear stress and the normal velocity gradient in the flow around a rotating cylinder. It was not until 1845,

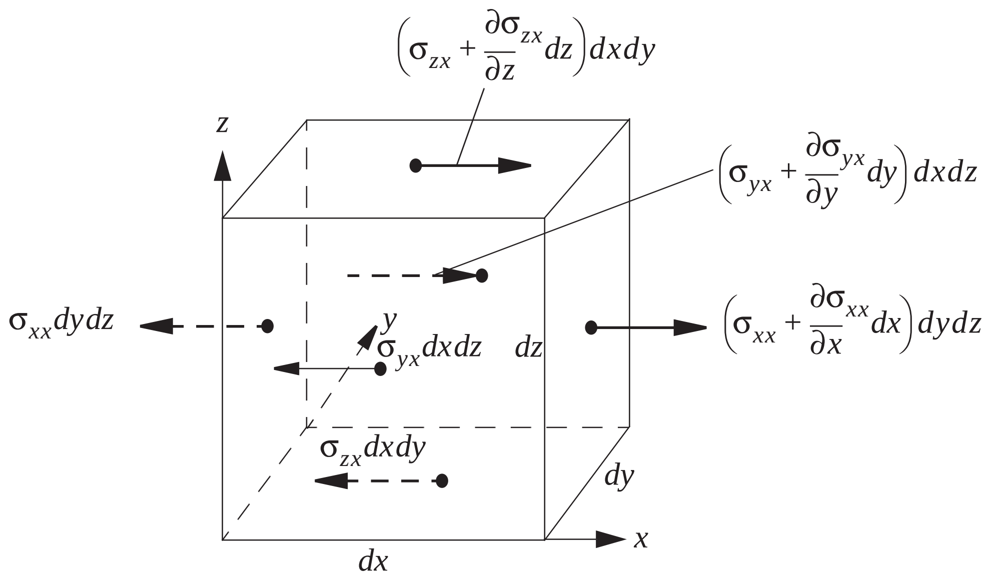

Figure 2.4 Viscous stresses in the x-direction on the fluid element.

however, that this hypothesis was generalized to general 3D flows by Stokes. For most flows of engineering interest, the viscous stress tensor σ_{ij} is proportional to a rate of strain tensor S_{ij}, defined as

$$S_{ij} = \frac{\partial u_i}{\partial x_j} + \frac{\partial u_j}{\partial x_i}$$

where i and j may attain any one of the values 1, 2, or 3. u_1, u_2, and u_3 are then to be interpreted as u, v, w. The constant of proportionality is the dynamic viscosity μ.

$$\sigma_{ij} = \mu S_{ij} \tag{2.10}$$

For a discussion of the theoretical background of this hypothesis, the reader is referred to Schlichting (1987), Panton (1984), or Acheson (1990). See also Section 9. We note that the rate of strain tensor is symmetric (i.e., swapping i and j does not change the value of the component). There are thus six independent components, which may be written as follows

$$\sigma_{xx} = 2\mu \frac{\partial u}{\partial x} \tag{2.11a}$$

$$\sigma_{xy} = \sigma_{yx} = \mu \left(\frac{\partial u}{\partial y} + \frac{\partial v}{\partial x}\right) \tag{2.11b}$$

$$\sigma_{zx} = \sigma_{xz} = \mu \left(\frac{\partial w}{\partial x} + \frac{\partial u}{\partial z}\right) \tag{2.11c}$$

$$\sigma_{yy} = 2\mu \frac{\partial v}{\partial y} \tag{2.11d}$$

$$\sigma_{yz} = \sigma_{zy} = \mu \left(\frac{\partial v}{\partial z} + \frac{\partial w}{\partial y}\right) \tag{2.11e}$$

$$\sigma_{zz} = 2\mu \frac{\partial w}{\partial z} \tag{2.11f}$$

Introducing the x-components of equations (2.11a), (2.11b), and (2.11c) into the x-component equation (2.9a) yields, after some rearrangement of the terms,

$$\frac{dF_{vx}}{dm} = \frac{\mu}{\rho}\left[\frac{\partial^2 u}{\partial x^2} + \frac{\partial^2 u}{\partial y^2} + \frac{\partial^2 u}{\partial z^2} + \frac{\partial^2 u}{\partial x^2} + \frac{\partial^2 v}{\partial x \partial y} + \frac{\partial^2 w}{\partial x \partial z}\right]$$

Here, the last three terms disappear because

$$\frac{\partial^2 u}{\partial x^2} + \frac{\partial^2 v}{\partial x \partial y} + \frac{\partial^2 w}{\partial x \partial z} = \frac{\partial}{\partial x}\left[\frac{\partial u}{\partial x} + \frac{\partial v}{\partial y} + \frac{\partial w}{\partial z}\right] = 0$$

due to continuity, as seen previously. Defining the kinematic viscosity as $\nu = \frac{\mu}{\rho}$, the final expression for the viscous x-component is thus

$$\frac{dF_{vx}}{dm} = \nu\left[\frac{\partial^2 u}{\partial x^2} + \frac{\partial^2 u}{\partial y^2} + \frac{\partial^2 u}{\partial z^2}\right] \tag{2.12a}$$

Correspondingly, for the other two components

$$\frac{dF_{vy}}{dm} = \nu\left[\frac{\partial^2 v}{\partial x^2} + \frac{\partial^2 v}{\partial y^2} + \frac{\partial^2 v}{\partial z^2}\right] \tag{2.12b}$$

$$\frac{dF_{vz}}{dm} = \nu\left[\frac{\partial^2 w}{\partial x^2} + \frac{\partial^2 w}{\partial y^2} + \frac{\partial^2 w}{\partial z^2}\right] \tag{2.12c}$$

Introducing the acceleration in equations (2.5a) to (2.5c), the pressure force in equations (2.6a) to (2.6c), the body force in equations (2.7a) to (2.7c), and the viscous force in equations (2.12a) to (2.12c) into the components of equation (2.3), the following three equations are obtained

$$\frac{\partial u}{\partial t} + u\frac{\partial u}{\partial x} + v\frac{\partial u}{\partial y} + w\frac{\partial u}{\partial z} = -\frac{1}{\rho}\frac{\partial p}{\partial x} + \nu\left(\frac{\partial^2 u}{\partial x^2} + \frac{\partial^2 u}{\partial y^2} + \frac{\partial^2 u}{\partial z^2}\right) \tag{2.13a}$$

$$\frac{\partial v}{\partial t} + u\frac{\partial v}{\partial x} + v\frac{\partial v}{\partial y} + w\frac{\partial v}{\partial z} = -\frac{1}{\rho}\frac{\partial p}{\partial y} + \nu\left(\frac{\partial^2 v}{\partial x^2} + \frac{\partial^2 v}{\partial y^2} + \frac{\partial^2 v}{\partial z^2}\right) \tag{2.13b}$$

$$\frac{\partial w}{\partial t} + u\frac{\partial w}{\partial x} + v\frac{\partial w}{\partial y} + w\frac{\partial w}{\partial z} = -\frac{1}{\rho}\frac{\partial p}{\partial z} - g + \nu\left(\frac{\partial^2 w}{\partial x^2} + \frac{\partial^2 w}{\partial y^2} + \frac{\partial^2 w}{\partial z^2}\right) \tag{2.13c}$$

These are the Navier-Stokes equations for incompressible flow,* assuming that gravity is the only body force and that it is directed along the negative z-axis. The equations are written in component form. Other forms of the equations will be considered in later sections.

2.4 Boundary Conditions. The Navier-Stokes equations may be mathematically classified as second order, elliptical partial differential equations. Elliptical equations require conditions on all boundaries of the computational domain, and we will now specify the boundary conditions for the unknowns u, v, w, and p in the Navier-Stokes and continuity equations. The boundaries are of three kinds: solid surfaces, water surfaces, and "infinity." We will consider them one by one.

2.4.1 Solid Surfaces. At the intersection between a solid surface and a liquid, interaction occurs at a molecular level. Molecules from one phase move over to another phase, thereby colliding with the molecules of the other phase. The phases are thus mixed in a very thin layer, and the tangential velocity of the molecules from one side of the interface is transferred to the other side. Velocity differences between the two phases are thus smoothed out, and practically all experience in fluid mechanics suggests that the difference is zero (i.e., the liquid sticks to the submerged solid surface). This is the so called "no-slip" condition. Recent research (see, for example, Watanabe, Udagawa, & Udagawa, 1999) suggests that for extremely hydrophobic (water repellant) surfaces, the no-slip conditions do not apply, but so far this hypothesis is not well proven and we will assume in the following that the no-slip condition holds.

As the coordinate system (see Fig. 2.1) moves with the hull, the no-slip condition on the hull surface is simply

$$u = v = w = 0 \tag{2.14}$$

On other solid surfaces, fixed to the earth, such as the seabed, beaches, and canal banks, the corresponding equation reads

$$u = V, \qquad v = w = 0 \tag{2.15}$$

---

*The reader who has skipped the derivation should note that the left-hand sides of the three equations represent the acceleration of a fluid particle in the x, y, and z directions, respectively. The right-hand sides represent forces on the particle per unit of mass. The first term appears because of pressure gradients and the last one because of viscous forces. There is an intermediate term only in the z-equation. This represents the effect of gravity.

because these surfaces will move backward at the speed V relative to the hull.

2.4.2 Water Surface. The previous discussion on the solid–liquid interface applies equally well to a liquid–gas interface, such as the water surface (and certainly also to solid–gas interfaces). In the following, the water surface will be called the free surface, as is common in numerical hydrodynamics. Because of molecular interchange between the water and the air, both will attain the same speed at the interface. Further, there must be an equilibrium of forces across the interface. Tangentially, this means that

$$\sigma_{(ns)w} = \sigma_{(ns)a} \qquad \sigma_{(nt)w} = \sigma_{(nt)a} \tag{2.16}$$

where the indices w and a refer to water and air, respectively, and s,t,n is a local Cartesian coordinate system with n normal to the surface. If Δp_γ is the effect of surface tension (positive for a concave surface), the normal force equilibrium may be written

$$(\sigma_{nn} - p)_w = (\sigma_{nn} - p)_a + \Delta p_\gamma \tag{2.17}$$

These are the dynamic boundary conditions on the surface. However, the viscous stresses are normally very small and are mostly neglected. The inviscid dynamic boundary condition is then obtained. It reads as follows

$$p = p_a - \Delta p_\gamma \tag{2.18}$$

where the index has been dropped for the water pressure.

The pressure jump because of surface tension can be obtained from (see White, 1994, p. 28)

$$\Delta p_\gamma = \gamma\left(\frac{1}{r_1} + \frac{1}{r_2}\right) \tag{2.19}$$

where γ is the surface tension and r_1 and r_2 are the principal radii of curvature* of the water surface.

There is also a kinematic condition on the surface expressing the fact that there is no flow through the surface. Note that this is in the macroscopic sense. In our model, we assume that the interface is sharp and without through flow. The molecular effects discussed previously are taken into account by the continuity of stresses and velocities.

If there is to be no flow across the boundary, the vertical velocity of a water particle moving along the surface must be equal to the total derivative of the wave height with respect to time (i.e., both the temporal and spatial wave height changes must be considered).

$$w = \frac{d\zeta}{dt} \tag{2.20}$$

where $\zeta = \zeta(x, y)$ is the equation for the free surface.

2.4.3 Infinity. Even though the water always has a limited extension, it may be advantageous to consider the flow domain to be infinite in some directions. Then, the boundary condition to be applied simply states that all disturbaces must go to zero at infinity:

$$u = V \qquad v = w = 0 \qquad p = p_\infty \tag{2.21}$$

where p_∞ is the undisturbed pressure. Note that these are the mathematical boundary conditions. As will be seen in Section 9, the computational domain will always have to be restricted in numerical methods. Therefore, artificial numerical boundaries are introduced. At such boundaries, the pressure and velocities, or alternatively their derivatives in one direction, will have to be specified.

2.5 Hydrodynamic and Hydrostatic Pressure. In a liquid at rest, the pressure increases linearly in the vertical direction. Each liquid element at a certain depth has to carry the weight of all other elements above it. This hydrostatic pressure p_{hs} may be computed as

$$p_{hs} = -\rho gz \tag{2.22}$$

in the coordinate system adopted here.

Once the liquid is disturbed, pressure forces related to the motion are created. These pressures may be called hydrodynamic, p_{hd}. In general, the pressure which can be measured in a fluid in motion is thus

$$p = p_{hs} + p_{hd} \tag{2.23}$$

Thus,

$$p_{hd} = p - p_{hs} = p + \rho gz \tag{2.24}$$

Consider the pressure and gravity terms in the z-component of the Navier-Stokes equation (2.13c)!

$$\frac{dF_p}{dm} + \frac{dF_b}{dm} = -\frac{1}{\rho}\frac{\partial p}{\partial z} - g$$

This may be written

$$\frac{dF_p}{dm} + \frac{dF_b}{dm} = -\frac{1}{\rho}\frac{\partial(p + \rho gz)}{\partial z} = -\frac{1}{\rho}\frac{\partial p_{hd}}{\partial z}$$

Thus, if the pressure p in the z-component is replaced by p_{hd}, the gravity term may be dropped. Because $\frac{\partial p_{hd}}{\partial x} = \frac{\partial p}{\partial x}$ and $\frac{\partial p_{hd}}{\partial y} = \frac{\partial p}{\partial y}$, as can be easily seen from equation (2.24), p may be replaced by p_{hd} in the x- and y-components of the Navier-Stokes equations. We have now arrived at a very important conclusion: *If the pressure in the Navier-Stokes equations is replaced by the hydrodynamic pressure, no gravity terms shall be included.*

Another way of looking at this is that the hydrostatic pressure has been removed from the equations. The motions of the flow, which as we know are governed by the Navier-Stokes equations, are thus independent of the hydrostatic pressure. This is in fact obvious because the hydrostatic pressure is just large enough to balance the weight of each fluid element. Therefore, it does not give rise to any motions. Note that this division of the pressure into hydrodynamic and hydrostatic components is normally not considered in general fluid dynamics. For air, it is irrelevant because the aerostatic pressure is very small and liquids are often considered in small systems, where the hydrodynamic effects are much larger than the hydrostatic effects.

---

*On all sufficiently smooth surfaces, which are not flat, there is one direction in which the normal curvature is maximum and one at right angles thereto, in which the normal curvature is minimum. These are the directions of principal curvature and the radii of curvature in these directions are the principal radii of curvature.

3
Similarity

Most experiments in ship hydrodynamics are carried out with scale models. Small replicas of ships are tested in water basins, and forces and motions are measured. In the present section, we are mainly interested in the towing tank experiment where the model is towed by a carriage and the force, and perhaps the flow around the hull, is measured at different speeds. It is fairly obvious that the model shall be geometrically similar to the ship (a geosim), but it is not as straightforward to determine the speed at which the model shall be run. Nor is it obvious how to scale the forces and velocities measured for the model. These issues will be dealt with in the present section.

3.1 Types of Similarity. *Geometric similarity* means that the ship and the model shall have the same shape. This is necessary, in principle, but not down to the smallest details. Consider for instance the surface of the hull! It is virtually impossible to scale the roughness exactly, but, as will be discussed in Section 6, the roughness has no effect if it is sufficiently small. The requirement is rather easily met for the model, but not for the ship. Here, roughness has an important effect, but this is taken into account in an empirical way (see Section 8).

Kinematic similarity means that all velocities in the flow (including components!) are scaled by the same factor. This means that the streamlines around the hull will be geometrically similar at model and full scale.

Dynamic similarity means that all forces of the flow (including components!) are scaled by the same factor. Force vectors thus have the same direction at both scales.

3.2 Proof of Similarity. In order to derive the similarity laws, the quantities in the governing equations and their boundary conditions are made dimensionless. The general idea is to see under which conditions, if any, the equations are rendered independent of scale. If that can be achieved, the solution, in nondimensional variables, is unique, which means that both kinematic and dynamic similarity has been achieved between any scales. Dimensional solutions can then easily be obtained by converting nondimensional values back to dimensional ones.

The following nondimensional quantities are introduced:

$$\overline{x}=\frac{x}{L},\ \overline{y}=\frac{y}{L},\ \overline{z}=\frac{z}{L},\ \overline{\zeta}=\frac{\zeta}{L},\ \overline{r_1}=\frac{r_1}{L},\ \overline{r_2}=\frac{r_2}{L}$$

$$\overline{u}=\frac{u}{U_\infty},\ \overline{v}=\frac{v}{U_\infty},\ \overline{w}=\frac{w}{U_\infty},\ \overline{p}=\frac{p_{hd}}{\rho U_\infty^2},\ t=\frac{t\cdot U_\infty}{L}$$

where L is a reference length, usually taken as the length between perpendiculars, L_{pp}, and U_∞ is a reference velocity, normally the ship speed V.

These are introduced into the governing equations and their boundary conditions. Note that the hydrodynamic pressure has been used in defining $\overline{p}$! For the x-component of the Navier-Stokes equations, this yields

$$\frac{\partial(\overline{u}U_\infty)}{\delta\left(\bar{t}\frac{L}{U_\infty}\right)}+\overline{u}U_\infty\frac{\partial(\overline{u}U_\infty)}{\partial(\overline{x}L)}+\overline{v}U_\infty\frac{\partial(\overline{u}U_\infty)}{\partial(\overline{y}L)}+$$
$$\overline{w}U_\infty\frac{\partial(\overline{u}U_\infty)}{\partial(\overline{z}L)}=-\frac{1}{\rho}\frac{\partial(\overline{p}\rho U_\infty^2)}{\partial(\overline{x}L)}+$$
$$\nu\left(\frac{\partial^2}{\partial(\overline{x}L)^2}(\overline{u}U_\infty)+\frac{\partial^2}{\partial(\overline{y}L)^2}(\overline{u}U_\infty)+\frac{\partial^2}{\partial(\overline{z}L)^2}(\overline{u}U_\infty)\right)$$

If this is divided by $\frac{U_\infty^2}{L}$, the following x-component equation is obtained

$$\frac{\partial\overline{u}}{\partial\bar{t}}+\overline{u}\frac{\partial\overline{u}}{\partial\overline{x}}+\overline{v}\frac{\partial\overline{u}}{\partial\overline{y}}+\overline{w}\frac{\partial\overline{u}}{\partial\overline{z}}=-\frac{\partial\overline{p}}{\partial\overline{x}}+$$
$$\enclose{circle}{\frac{\nu}{U_\infty L}}\left(\frac{\partial^2\overline{u}}{\partial\overline{x}^2}+\frac{\partial^2\overline{u}}{\partial\overline{y}^2}+\frac{\partial^2\overline{u}}{\partial\overline{z}^2}\right)\tag{3.1a}$$

and, correspondingly, in the other two directions

$$\frac{\partial\overline{v}}{\partial\bar{t}}+\overline{u}\frac{\partial\overline{v}}{\partial\overline{x}}+\bar{\nu}\frac{\partial\overline{v}}{\partial\overline{y}}+\overline{w}\frac{\partial\overline{v}}{\partial\overline{z}}=-\frac{\partial\overline{p}}{\partial\overline{y}}+$$
$$\enclose{circle}{\frac{\nu}{U_\infty L}}\left(\frac{\partial^2\overline{v}}{\partial\overline{x}^2}+\frac{\partial^2\overline{v}}{\partial\overline{y}^2}+\frac{\partial^2\overline{v}}{\partial\overline{z}^2}\right)\tag{3.1b}$$

$$\frac{\partial\overline{w}}{\partial\bar{t}}+\overline{u}\frac{\partial\overline{w}}{\partial\overline{x}}+\overline{v}\frac{\partial\overline{w}}{\partial\overline{y}}+\overline{w}\frac{\partial\overline{w}}{\partial\overline{z}}=-\frac{\partial\overline{p}}{\partial\overline{x}}+$$
$$\enclose{circle}{\frac{\nu}{U_\infty L}}\left(\frac{\partial^2\overline{w}}{\partial\overline{x}^2}+\frac{\partial^2\overline{w}}{\partial\overline{y}^2}+\frac{\partial^2\overline{w}}{\partial\overline{z}^2}\right)\tag{3.1c}$$

Introduction of the nondimensional quantities in the continuity equation yields

$$\frac{\partial(\overline{u}U_\infty)}{\partial\overline{x}L}+\frac{\partial(\overline{v}U_\infty)}{\partial\overline{y}L}+\frac{\partial(\overline{w}U_\infty)}{\partial\overline{z}L}=0$$

and, after division by $\frac{U_\infty}{L}$

$$\frac{\partial\overline{u}}{\partial\overline{x}}+\frac{\partial\overline{v}}{\partial\overline{y}}+\frac{\partial\overline{w}}{\partial\overline{z}}=0\tag{3.2}$$

For the boundary conditions, the following is obtained

Hull surface, equation (2.14)

$$\overline{u}=\overline{v}=\overline{w}=0\tag{3.3}$$

Earth-fixed boundaries, equation (2.15)

$$\overline{u}=1\qquad\overline{v}=\overline{w}=0\tag{3.4}$$

Free surface, *kinematic condition*, equation (2.20)

$$\overline{w}U_\infty=\frac{d(\overline{\zeta}L)}{d\left(\bar{t}\frac{L}{U_\infty}\right)}\Rightarrow\overline{w}=\frac{d\overline{\zeta}}{d\bar{t}}\tag{3.5}$$

Free surface, *dynamic condition* [neglecting the viscous stresses, equation (2.18)]. Note that p in equation (2.18) includes both the hydrodynamic and the hydrostatic pressures

$$p_{hd} + p_{hs} = p_a - \Delta p_\gamma \tag{3.6}$$

or

$$\bar{p}\rho U_\infty^2 - \rho g \bar{\zeta} L = p_a - \frac{\gamma}{L}\left(\frac{1}{\bar{r}_1} + \frac{1}{\bar{r}_2}\right) \tag{3.7}$$

where the hydrostatic pressure at the surface $\bar{\zeta}$ of equation (2.22) has been introduced, as well as expression (2.19) for the surface tension.

Resolving for $\bar{p}$

$$\bar{p} = \enclose{circle}{\frac{p_a}{\rho U_\infty^2}} + \enclose{circle}{\frac{gL}{U_\infty^2}}\,\bar{\zeta} - \enclose{circle}{\frac{\gamma}{\rho U_\infty^2 L}}\left(\frac{1}{\bar{r}_1} + \frac{1}{\bar{r}_2}\right) \tag{3.8}$$

Infinity, equation (2.21)

$$\bar{u} = 1 \qquad \bar{v} = \bar{w} = 0 \qquad \bar{p} = 0 \tag{3.9}$$

Geometrically similar bodies and boundaries may be represented by the functions

$$f_i\,(\bar{x}, \bar{y}, \bar{z}) = 0) \tag{3.10}$$

where the f_i are independent of scale.

Summarizing, the problem is defined by the governing equations (3.1a) to (3.1c) and (3.2), the boundary conditions (3.3) and (3.4) for the solid surfaces, the free-surface boundary conditions (3.5) and (3.8), and the infinity condition (3.9). It turns out that the only parameters appearing in these equations are the circled ones, i.e., the Reynolds number Rn [rather $\frac{1}{Rn}$] in equations (3.1a) to (3.1c), where

$$Rn = \frac{U_\infty L}{\nu} \tag{3.11}$$

and the Euler number En, the Froude number Fn(rather $\frac{1}{Fn^2}$), and the Weber number Wn (rather $\frac{1}{Wn}$) in equation (3.8), where

$$En = \frac{p_a}{\rho U_\infty^2} \tag{3.12}$$

$$Fn = \frac{U_\infty}{\sqrt{gL}} \tag{3.13}$$

$$Wn = \frac{\rho U_\infty^2 L}{\gamma} \tag{3.14}$$

The Euler number is of importance because p_a determines the absolute pressure level in the fluid. An increase in the atmospheric pressure at the water surface will increase the pressure everywhere in the water by the same amount. If the pressure anywhere goes below the vapor pressure p_v, cavitation will occur. A measure of the "margin" to cavitation is $p_a - p_v$, which is mostly used in the numerator. We then obtain the cavitation number σ

$$\sigma = \frac{p_a - p_v}{\frac{1}{2} \cdot \rho U_\infty^2} \tag{3.15}$$

Because the Euler and cavitation numbers differ only by a constant, they are exchangeable as similarity parameters.

We have now achieved the objectives specified in the introduction to this section. Parameters have been defined such that if these parameters are unchanged between two scales, all equations and boundary conditions are also unchanged, which means that the solution in nondimensional form is unchanged. Using the definition, dimensional values may then be easily obtained at each scale from the dimensionless values. All velocities are thus scaled by the same factor (U_∞), which means kinematic similarity, and all forces are scaled by another factor ($\rho U_\infty^2 L^2$), which means dynamic similarity. Geometric similarity is achieved by the linear scaling by L of all solid bodies and boundaries. *The constancy of the Reynolds number, the Euler (cavitation) number, the Froude number, and the Weber number is a necessary and sufficient condition for flow similarity between geosim bodies at different scales.*

In the present analysis, we have used the governing equations and their boundary conditions to obtain the similarity requirements. An alternative approach is to use dimensional analysis, based on a theorem by Buckingham (1914), known as the Π-theorem. For references on this approach, see White (1994).

3.3 Consequences of the Similarity Requirements

3.3.1 Summary of Requirements. In theory, the following requirements should be satisfied in towing tank testing of ship models:

- With the exception of the surface roughness, the model and the ship must be geometrically similar.
- Because the contract conditions specified for the ship are normally for unrestricted waters, the tank must be suffiently wide and deep to avoid blockage effects (this will be further discussed in Section 5).
- The Reynolds number

$$Rn = \frac{U_\infty L}{\nu}$$

must be the same at both scales if the effect of viscosity shall be correct. Because the Reynolds number appears in the Navier-Stokes equations, it has an effect on all flows governed by these equations. This means, in practice, all flows of interest in hydrodynamics. There is, however, an approximation known as the "inviscid flow," where the effect of viscosity is neglected. Under certain circumstances, this is a good approximation, and many useful results may be obtained from this theory, as will be seen in Section 5. In this approximation, the Reynolds number is insignificant.

- The Froude number

$$Fn = \frac{U_\infty}{\sqrt{gL}}$$

must be the same at both scales if the effect of gravity on the free surface shall be correct. Note that this parameter, as well as the remaining two, Wn and σ, only appear in the dynamic free-surface boundary condition.

This means that if there is no free surface, as in most water tunnels (without cavitation), none of these parameters is significant. In most hydrodynamic cases of interest there is, however, a free water surface, and gravity is then the driving force for the waves. A correct Froude number is thus a requirement for correctly scaled waves, and if the waves are correctly scaled, so is the resistance component caused by the wave generation (see Section 5).

- The Weber number

$$Wn = \frac{\rho U_\infty^2 L}{\gamma}$$

must be the same to achieve the correct effect of the surface tension. This means that spray and wave breaking, which contain water drops and air bubbles with small radii, are correctly scaled. This holds also for surface waves of very small length, where the radius of curvature of the surface may be very small.

- The cavitation number

$$\sigma = \frac{p_a - p_v}{\frac{1}{2} \cdot \rho U_\infty^2}$$

must be unchanged to obtain the same cavitation pattern. Note that cavitation means vapor bubbles with a free surface between vapor and water. Because cavitation hardly ever occurs in the flow around the hull, it is not normally considered in towing tank testing, and it will not be further considered in this volume of the *Principles of Naval Architecture.* It may be very important in propeller design, however, and is dealt with at some length in the propulsion volume.

3.3.2 The Dilemma in Model Testing. Unfortunately, it is impossible to simultaneously satisfy all requirements in practice. In a model test, the length of the model is by definition smaller than that of the ship, so the model speed should be adjusted to yield the correct Reynolds, Froude, and Weber numbers. As is easily realized, this is not possible. To obtain the correct Froude number, the model speed has to be smaller than that of the ship; whereas, for correct Reynolds and Weber numbers, the speed has to be higher. In principle, it would be possible to satisfy the requirements by changing the physical properties of the model test fluid (i.e., ν, g, ρ, or γ), but no suitable fluid has been found, and the tests are normally carried out in fresh water, with very similar constants as the salt water at full scale. In reality, it is only possible to satisfy one of the three similarity requirements in model testing. The other two requirements have to be sacrificed.

Considering the effects of incorrect scaling, it turns out that a wrong Weber number has the smallest effect on the flow around the hull and the resistance. As will be seen, models are tested at a smaller speed than that at full-scale, which means that the Weber number is too small. This has to be accepted, but it means that the effect of surface tension is too large, which causes the following problems in model-scale experiments:

- A different appearance of breaking waves compared to full scale with much less "white water"
- A different appearance of spray at high speed with more coherent water films than at full scale being ejected sideward
- Occurrence of capillary waves at low speeds, with no counterpart at full scale
- Deviations in the wave pattern of the model, if the model speed is around 0.23 m/s, so there is a need to stay away from this speed if wave making is of interest.

The remaining two parameters (i.e., the Reynolds number and the Froude number) are both very important for the resistance and for the flow around the hull. Model testers are thus faced with a real dilemma: which parameter to keep constant and which one to sacrifice.

The practical solution to the dilemma is to satisfy the Froude number requirement, correcting for the main errors introduced by the wrong Reynolds number. Note that this is exactly what William Froude suggested in 1868 (see Section 1.2.1). By testing at the right Froude number, the major driving force for the waves, namely the gravity, is correctly scaled. The resistance component caused by the wave making (called wave resistance in the following) is then also scaled with high accuracy as $\rho V^2 L^2$, as explained previously. Because ρ is assumed constant and the speed scales as $\sqrt{L}$ for constant Froude number, this means the wave resistance scales as L^3 (i.e., in proportion to the displacement). This is also what Froude had found. The lesson to learn from this discussion is thus: *the model shall be tested at the same Froude number as the ship.* Note that there is indeed a small effect also of the Reynolds number on the waves because the governing equations contain this number, but this effect is normally much smaller than the main effect of the Froude number.

As will be seen in the next section, the other main resistance component is the viscous resistance caused by the fluid viscosity. From the discussion in Section 3.3.1, it is clear that this is mainly governed by the Reynolds number. Froude suggested to compute this resistance component from an empirical formula based on plank tests, and even if a somewhat more sophisticated method is used today (see Section 8), empirical formulas are still used. All modern formulas are functions of one parameter only: the Reynolds number (see Section 6.3.4). However, the viscous resistance depends to a large extent on the wetted surface of the hull and appendages, and this surface is slightly influenced by the Froude number, as the wave profile along the hull changes with speed. There is thus a small influence of the Froude number on the viscous resistance.

In the practical application of the similarity theory, the wave resistance is thus considered dependent only on the Froude number, whereas the viscous resistance is dependent only on the Reynolds number. In reality, both resistance components depend on both numbers, but the approximation adopted has proven to be sufficiently accurate for scaling model test data to full scale in most cases.

Knowing the scaling rules, advantages are often taken of the different possibilities of water tank and wind tunnel testing. Thus, rudders and other appendages are often tested in wind tunnels. Detailed boundary layer measurements are also often carried out there, even for ship models. This is because of the easier access to equipment inside the wind tunnel. Requirements on robustness of the equipment are also often smaller in air.

On the other hand, there are situations where aerodynamic problems are best solved in water. One example is the testing of automobiles in water tanks (Larsson et al., 1989). The great advantage here is that the car may be towed along the bottom of the tank thus creating the correct flow around the rotating wheels and under the car. In a wind tunnel, there is always a boundary layer in the approaching flow, which does not exist when the car moves through still air. This boundary layer has to be removed, and this cannot be done without problems. It is also very difficult to model the effect of the rotating wheels, which must not touch the wind tunnel floor.

4

Decomposition of Resistance

Having derived the equations governing the flow around the hull and the subsequent similarity laws, we will now turn to a physical discussion of the flow and the various resistance components. Knowledge of the physics is required for understanding hull shape optimization and experimental techniques. In Section 3, we introduced the two main resistance components: wave resistance and viscous resistance. Here, we will make a subdivision of these components. More detailed discussions of all components will then be given in the subsequent Sections 5, 6, and 7.

4.1 Resistance on a Straight Course in Calm, Unrestricted Water

4.1.1 Vessel Types. In the present section, we will discuss the resistance decomposition of four different vessels operating at Froude numbers from 0.15 to 1.4. The first three operate in the displacement speed range, below 0.5, whereas the fastest hull is of the fully planing type. Main dimensions, Froude number, and total resistance coefficient for all hulls are given in Table 4.1. Here and in the following, force coefficients are defined by dividing the force by the dynamic head times the wetted surface S, in other words

$$C_{TS} = \frac{R_{TS}}{\frac{1}{2}\rho V_S^2 S_S} \tag{4.1}$$

where R_T is the total resistance and the index S stands for "ship" (full scale), as before. Note that large variations in dimensions and resistance components occur in each class of vessels. The values given may be considered typical in each class.

4.1.2 Detailed Decomposition of the Resistance. In Fig. 4.1, the total resistance of each of the four ships is represented by a bar, whose length corresponds to 100% of the resistance. This bar is split into components, given in percent of the total. To emphasize that the total resistance varies between the ships, the total resistance coefficient is given at the top of each bar. It is seen in Fig. 4.1 that the viscous resistance is now subdivided into four components: flat plate friction, roughness effects, form effect on friction, and form effect on pressure. The wave resistance is split into two components: wave pattern resistance and wave breaking resistance. These components will now be introduced.

Ever since William Froude's days, naval architects have used the frictional resistance of an "equivalent" flat plate as a measure of the frictional resistance of the hull. In this context, "equivalent" means a plate having the same wetted surface, run in water of the same density at the same Reynolds number and speed as the ship. Although more advanced scaling procedures are used

Table 4.1 Typical Data of Four Different Vessels

Quantity	Tanker	Containership	Fishing Vessel	Planing Boat
Length L_{WL} (m)	316	248	23	22.5
Beam B (m)	56	30	7	—
Draft T (m)	20	9.5	2.5	—
Speed V_S (knots)	16	23	10	40
Froude number Fn	0.15	0.24	0.34	1.4
Reynolds number $Rn \times 10^{-9}$	2.6	2.9	0.12	0.46
Total resistance coefficient $C_{TS} \times 10^3$	2.2	2.3	8.1	5.4

both resistance components depend on both numbers, but the approximation adopted has proven to be sufficiently accurate for scaling model test data to full scale in most cases.

Knowing the scaling rules, advantages are often taken of the different possibilities of water tank and wind tunnel testing. Thus, rudders and other appendages are often tested in wind tunnels. Detailed boundary layer measurements are also often carried out there, even for ship models. This is because of the easier access to equipment inside the wind tunnel. Requirements on robustness of the equipment are also often smaller in air.

On the other hand, there are situations where aerodynamic problems are best solved in water. One example is the testing of automobiles in water tanks (Larsson et al., 1989). The great advantage here is that the car may be towed along the bottom of the tank thus creating the correct flow around the rotating wheels and under the car. In a wind tunnel, there is always a boundary layer in the approaching flow, which does not exist when the car moves through still air. This boundary layer has to be removed, and this cannot be done without problems. It is also very difficult to model the effect of the rotating wheels, which must not touch the wind tunnel floor.

4
Decomposition of Resistance

Having derived the equations governing the flow around the hull and the subsequent similarity laws, we will now turn to a physical discussion of the flow and the various resistance components. Knowledge of the physics is required for understanding hull shape optimization and experimental techniques. In Section 3, we introduced the two main resistance components: wave resistance and viscous resistance. Here, we will make a subdivision of these components. More detailed discussions of all components will then be given in the subsequent Sections 5, 6, and 7.

4.1 Resistance on a Straight Course in Calm, Unrestricted Water

4.1.1 Vessel Types. In the present section, we will discuss the resistance decomposition of four different vessels operating at Froude numbers from 0.15 to 1.4. The first three operate in the displacement speed range, below 0.5, whereas the fastest hull is of the fully planing type. Main dimensions, Froude number, and total resistance coefficient for all hulls are given in Table 4.1. Here and in the following, force coefficients are defined by dividing the force by the dynamic head times the wetted surface S, in other words

$$C_{TS} = \frac{R_{TS}}{\frac{1}{2}\rho V_S^2 S_S} \tag{4.1}$$

where R_T is the total resistance and the index S stands for "ship" (full scale), as before. Note that large variations in dimensions and resistance components occur in each class of vessels. The values given may be considered typical in each class.

4.1.2 Detailed Decomposition of the Resistance. In Fig. 4.1, the total resistance of each of the four ships is represented by a bar, whose length corresponds to 100% of the resistance. This bar is split into components, given in percent of the total. To emphasize that the total resistance varies between the ships, the total resistance coefficient is given at the top of each bar. It is seen in Fig. 4.1 that the viscous resistance is now subdivided into four components: flat plate friction, roughness effects, form effect on friction, and form effect on pressure. The wave resistance is split into two components: wave pattern resistance and wave breaking resistance. These components will now be introduced.

Ever since William Froude's days, naval architects have used the frictional resistance of an "equivalent" flat plate as a measure of the frictional resistance of the hull. In this context, "equivalent" means a plate having the same wetted surface, run in water of the same density at the same Reynolds number and speed as the ship. Although more advanced scaling procedures are used

Table 4.1 Typical Data of Four Different Vessels

Quantity	Tanker	Containership	Fishing Vessel	Planing Boat
Length L_{WL} (m)	316	248	23	22.5
Beam B (m)	56	30	7	—
Draft T (m)	20	9.5	2.5	—
Speed V_S (knots)	16	23	10	40
Froude number Fn	0.15	0.24	0.34	1.4
Reynolds number $Rn \times 10^{-9}$	2.6	2.9	0.12	0.46
Total resistance coefficient $C_{TS} \times 10^3$	2.2	2.3	8.1	5.4

Figure 4.1 Resistance components for four vessels (%).

today, the flat plate friction is still used for the extrapolation of model-scale data to full scale. The flat plate friction is exclusively due to tangential forces between the solid surface and the water (i.e., the skin friction).

If the surface roughness exceeds a certain limit, it will influence skin friction. Normally, ship models are smooth enough for this component to be insignificant, but full-scale ships always have a surface roughness causing a resistance increase. The roughness allowance shown in Fig. 4.1 is for a ship without fouling; for fouled surfaces, this component is much larger. In the extrapolation of model test data to full scale, the roughness allowance is computed using a simple formula.

The fact that the hull has a 3D shape causes several resistance components, two of which are of viscous origin. As the flow approaching a vessel has to go around the hull, the local velocity of the water (outside the boundary layer) is different from that of the undisturbed flow ahead of the vessel. This is not the case for a flat plate parallel to the flow, where the velocity outside the boundary layer is practically undisturbed. (There is a small increase in speed caused by the displacement effect of the boundary layer, but this is mostly neglected.) At the bow and stern of the ship, the velocity is reduced, but over the main part of the hull there is a velocity increase, causing an increase in friction as compared to the plate. This is the form effect on friction.

The second form effect of viscous origin is caused by a pressure imbalance between the forebody and the afterbody. According to d'Alembert's paradox (Newman, 1977), there is zero resistance for a body without lift in an inviscid fluid without a free surface (i.e., the longitudinal component of the pressure forces acting on all parts of the body cancel each other exactly). In a viscous fluid, a boundary layer will develop along the surface, and this will cause a displacement outward of the streamlines at the stern. The pressure at the aft end of the hull is then reduced and the integrated pressure forces will not cancel. There is thus a form effect on pressure caused by viscous forces. Note that this resistance component is because of normal forces (pressures) as opposed to all other viscous resistance components which result from tangential forces (friction).

When the vessel moves along the surface water, particles are removed from their equilibrium position and waves are generated. If the disturbances are large, the waves may be steep enough to break down into eddies and foam. The energy thus removed from the wave system is found in the wake of the ship and the corresponding resistance component is called wave breaking resistance. The remaining wave energy is radiated away from the ship through the wave system and gives rise to the wave pattern resistance.

The grouping of the resistance components into viscous and wave resistance is the one normally used in ship hydrodynamics and adopted in this text. However, Froude's division into flat plate friction (with roughness) and residuary resistance is still used at some experimental establishments, and is indicated in Fig. 4.1. A third possibility would be to group the resistance components into those that act through tangential forces (friction) and through normal forces (pressure). In order not to complicate the figure, this division is not shown, but it differs from the viscous/wave resistance decomposition only with respect to the form effect on pressure, which is obviously a pressure component, as the two wave resistance components. The first three components from the bottom in the figure act through friction.

4.1.3 Comparison of the Four Vessel Types. The flat plate friction is the dominating component for the two slowest ships, which have a very small wave resistance. Note that the sum of the two wave resistance components is only 7.5% for the tanker. Roughness resistance increases with speed and is therefore a larger part of the viscous resistance for the high-speed hulls than for the slower ones. Of the two viscous form effects, that due to pressure is considerably larger than that due to friction. For the two bluntest hulls, the tanker and the fishing vessel, the total viscous form effect is about 30% of the flat plate friction, whereas it is about 20% for the containership and practically zero for the planing hull. There is normally a very small displacement effect of the relatively thin boundary layer near the stern of planing hulls with a submerged transom.

The wave breaking resistance is the largest component of the wave resistance for the tanker, but considerably smaller than the wave pattern resistance for the containership and the fishing vessel. For the planing hull, the wave breaking is replaced by spray. Note that the planing hull has a resistance component missing for the others: appendage resistance from propeller shaft, brackets, etc. This component, which is of viscous origin, is discussed later.

4.2 Other Resistance Components. If a vessel moves with a leeway, as in a turn or when there is a wind force component sideward, a lift force (directed sideward) is developed. Associated with the lift is an induced resistance, which can be considerable, especially for sailing yachts and vessels. When the hull moves slightly sideward, a high pressure is developed on one side (leeward) and a low pressure on the other (windward). The pressure difference gives rise to a flow from the high to the low pressure, normally under the bottom or tip of the keel and rudder, and longitudinal vortices are generated. These vortices contain energy left behind and are thus associated with a resistance component: the *induced resistance.*

The *appendage resistance* is mainly of viscous origin and could well be included in the viscous resistance. There are reasons, however, to treat this component separately. First, the Reynolds number, based on the chord length of brackets, struts, etc., is considerably smaller than that of the hull itself and therefore a separate scaling is required. Second, the appendages are normally streamlined sections, for which separate empirical relations apply. For sailing yachts, the correct shape of the appendages is of utmost importance for good performance, particularly because these appendages normally operate at an angle of attack.

A resistance component which may be considerable, for instance for fully loaded containerships, is the *wind resistance*. The frontal area facing the relative wind on board the ship can be large and the containers do not have an aerodynamic shape, so large forces may be generated in strong winds. Even in still air, there is a resistance component, however small. This component, the *air resistance*, is considered in the model-ship extrapolation procedure described in Section 8.

In restricted waters, the flow around the hull and the wave making are influenced by the presence of the confining surface. This could be the seabed in shallow water or the banks of a canal. All resistance components may be influenced. Often, the effect is modeled as an additional resistance component because of the *blockage effect* of the confining walls. See Section 5.

Finally, a seaway will cause an additional resistance of the vessel. This is due mainly to the generation of waves by the hull when set in motion by the sea waves, but is also due to wave reflection in short sea waves. *Added resistance in waves* is discussed in the seakeeping volume of the *Principles of Naval Architecture*.

5

Inviscid Flow Around the Hull, Wave Making, and Wave Resistance

5.1 Introduction. In Section 4, some different decompositions of the total resistance of a ship were discussed. We shall now consider in more detail the principal physical phenomena determining a ship's resistance. Here we shall use the decomposition into a wave resistance and a viscous resistance, the decomposition most directly related with separate physical phenomena. The wave making of a ship, which leads to its wave resistance, and the viscous flow around the hull (causing its viscous resistance) will be dealt with separately in Sections 5 and 6, respectively.

Physically, these phenomena occur simultaneously and various interactions occur; therefore, dealing with wave making and viscous flow separately may seem artificial. On the other hand, their separation is a most useful approach in practice. Moreover, there is a close relation with two perhaps more familiar distinctions.

The first is the way in which ship model tests are conducted. In Section 3.3.2, we saw that a dilemma arises as it is impossible to make both the Reynolds number *Rn* and the Froude number *Fn* equal for model and ship. The practical and well-proven approximation then is to test a ship model at a Froude number equal to that of the ship because in that case the wave pattern is geometrically (nearly) similar to that of the ship and the wave resistance can be scaled up easily. Apparently, the wave making is rather insensitive to viscous effects: the difference in *Rn* of a factor of 100 or so makes little difference to the wave making. Regarding the resistance coefficient, this is approximated by

$$C_T(Fn, Rn) \approx C_W(Fn) + C_V(Rn)$$

which again excludes a viscous effect on the wave resistance (and also, a wave effect on the viscous resistance).

The other related separation of physical phenomena is found in boundary layer theory. As will be discussed in Section 6.2, for high Reynolds numbers viscous effects on the flow around a body are mostly confined to a thin *boundary layer* close to the body surface and a narrow wake aft of it. In thin boundary layer theory it is derived that the pressure field inside the boundary layer is equal to that just outside it, and to a first approximation the boundary layer does not affect that pressure distribution. Therefore, the pressure field around the body, and its wave making, to a first approximation are independent of viscosity.

The relation with both these accepted approximations provides a justification to consider wave making as unaffected by viscosity. This approximation has been found to be extremely useful in ship hydrodynamics, and will form the basis of our further considerations. In other words, in the following we consider the wave making and wave pattern of a ship as an inviscid phenomenon. In Section 5.7 we briefly mention some of the limitations of the approximation.

This section is set up as follows. We first consider the principal equations governing the inviscid flow around a body and introduce the concept of potential flows. We study the physical behavior of potential flow around a body. Section 5.3 then derives the main properties of surface waves. Section 5.4 derives and discusses various aspects of ship wave patterns, after which wave resistance and its behavior in practice is considered.

Whereas in these sections the water depth is assumed to be unlimited, Sections 5.8 to 5.10 address the effect of limited water depth on the properties of water waves, ship wave patterns, and ship resistance. In Section 5.11 we discuss "wash effects" (i.e., ship wave effects causing nuisance or damage for others) as this is a topic of current interest for fast ferries in coastal areas. Finally, channel effects, caused by limited width and depth of the waterway, are dealt with in Section 5.12.

5.2 Inviscid Flow Around a Body

5.2.1 Governing Equations. As an introduction to the wave resistance aspects, we shall first consider inviscid flow around a body in case there is no free water surface present (e.g., a body deeply submerged in a fluid). We use a coordinate system attached to the ship, as that in Fig. 2.1. There is an incoming flow in positive x-direction with velocity U_∞, equal and opposite to the ship speed. The flow is undisturbed far ahead of the ship.

A resistance component which may be considerable, for instance for fully loaded containerships, is the *wind resistance*. The frontal area facing the relative wind on board the ship can be large and the containers do not have an aerodynamic shape, so large forces may be generated in strong winds. Even in still air, there is a resistance component, however small. This component, the *air resistance*, is considered in the model-ship extrapolation procedure described in Section 8.

In restricted waters, the flow around the hull and the wave making are influenced by the presence of the confining surface. This could be the seabed in shallow water or the banks of a canal. All resistance components may be influenced. Often, the effect is modeled as an additional resistance component because of the *blockage effect* of the confining walls. See Section 5.

Finally, a seaway will cause an additional resistance of the vessel. This is due mainly to the generation of waves by the hull when set in motion by the sea waves, but is also due to wave reflection in short sea waves. *Added resistance in waves* is discussed in the seakeeping volume of the *Principles of Naval Architecture*.

5

Inviscid Flow Around the Hull, Wave Making, and Wave Resistance

5.1 Introduction. In Section 4, some different decompositions of the total resistance of a ship were discussed. We shall now consider in more detail the principal physical phenomena determining a ship's resistance. Here we shall use the decomposition into a wave resistance and a viscous resistance, the decomposition most directly related with separate physical phenomena. The wave making of a ship, which leads to its wave resistance, and the viscous flow around the hull (causing its viscous resistance) will be dealt with separately in Sections 5 and 6, respectively.

Physically, these phenomena occur simultaneously and various interactions occur; therefore, dealing with wave making and viscous flow separately may seem artificial. On the other hand, their separation is a most useful approach in practice. Moreover, there is a close relation with two perhaps more familiar distinctions.

The first is the way in which ship model tests are conducted. In Section 3.3.2, we saw that a dilemma arises as it is impossible to make both the Reynolds number *Rn* and the Froude number *Fn* equal for model and ship. The practical and well-proven approximation then is to test a ship model at a Froude number equal to that of the ship because in that case the wave pattern is geometrically (nearly) similar to that of the ship and the wave resistance can be scaled up easily. Apparently, the wave making is rather insensitive to viscous effects: the difference in *Rn* of a factor of 100 or so makes little difference to the wave making. Regarding the resistance coefficient, this is approximated by

$$C_T\,(Fn, Rn) \approx C_W\,(Fn) + C_V\,(Rn)$$

which again excludes a viscous effect on the wave resistance (and also, a wave effect on the viscous resistance).

The other related separation of physical phenomena is found in boundary layer theory. As will be discussed in Section 6.2, for high Reynolds numbers viscous effects on the flow around a body are mostly confined to a thin *boundary layer* close to the body surface and a narrow wake aft of it. In thin boundary layer theory it is derived that the pressure field inside the boundary layer is equal to that just outside it, and to a first approximation the boundary layer does not affect that pressure distribution. Therefore, the pressure field around the body, and its wave making, to a first approximation are independent of viscosity.

The relation with both these accepted approximations provides a justification to consider wave making as unaffected by viscosity. This approximation has been found to be extremely useful in ship hydrodynamics, and will form the basis of our further considerations. In other words, in the following we consider the wave making and wave pattern of a ship as an inviscid phenomenon. In Section 5.7 we briefly mention some of the limitations of the approximation.

This section is set up as follows. We first consider the principal equations governing the inviscid flow around a body and introduce the concept of potential flows. We study the physical behavior of potential flow around a body. Section 5.3 then derives the main properties of surface waves. Section 5.4 derives and discusses various aspects of ship wave patterns, after which wave resistance and its behavior in practice is considered.

Whereas in these sections the water depth is assumed to be unlimited, Sections 5.8 to 5.10 address the effect of limited water depth on the properties of water waves, ship wave patterns, and ship resistance. In Section 5.11 we discuss "wash effects" (i.e., ship wave effects causing nuisance or damage for others) as this is a topic of current interest for fast ferries in coastal areas. Finally, channel effects, caused by limited width and depth of the waterway, are dealt with in Section 5.12.

5.2 Inviscid Flow Around a Body

5.2.1 Governing Equations. As an introduction to the wave resistance aspects, we shall first consider inviscid flow around a body in case there is no free water surface present (e.g., a body deeply submerged in a fluid). We use a coordinate system attached to the ship, as that in Fig. 2.1. There is an incoming flow in positive x-direction with velocity U_∞, equal and opposite to the ship speed. The flow is undisturbed far ahead of the ship.

The flow around the body is well described by the Navier-Stokes equations (2.13) and continuity equation (2.1). However, for inviscid flow we can drop all viscous terms in equation (2.13) and retain just the balance of convective and pressure gradient terms. This set of equations is called *Euler equations.*

We write the Euler equations as

$$\left(\frac{\partial}{\partial t} + u\frac{\partial}{\partial x} + v\frac{\partial}{\partial y} + w\frac{\partial}{\partial z}\right)\vec{v} = \nabla\left(-\frac{p}{\rho} - gz\right) \qquad (5.1)$$

where $\nabla = \left(\frac{\partial}{\partial x}\frac{\partial}{\partial y}\frac{\partial}{\partial z}\right)^T$ is the gradient operator. If then we take the inner product of both sides with $\vec{v}$, we can derive

$$\vec{v}\frac{\partial\vec{v}}{\partial t} + \left(u\frac{\partial}{\partial x} + v\frac{\partial}{\partial y} + w\frac{\partial}{\partial z}\right)\left[\frac{1}{2}(u^2 + v^2 + w^2) + \frac{p}{\rho} + gz\right] = 0 \qquad (5.2)$$

For steady flows the first term is zero, so this means that the material derivative of the expression in square brackets must also be zero, so

$$\frac{1}{2}(u^2 + v^2 + w^2) + \frac{p}{\rho} + gz = \begin{array}{l}\text{constant along}\\ \text{a streamline}\end{array} \qquad (5.3)$$

This is the *Bernoulli equation.* It indicates that in an inviscid flow, total head ($1/g$ times the left-hand side) is constant along a streamline. Without further conditions, the constant may differ from one streamline to another. But for the particular case considered here, all streamlines originate from an undisturbed field upstream where $\vec{v} = \vec{U}_\infty$ and $p = p_a - \rho gz$ so the constant is equal for the whole field.

The next simplification we introduce is to suppose that the flow is *irrotational.* This means that the vorticity, the curl of the velocity vector, is zero throughout the flow field

$$\vec{\omega} = \nabla \times \vec{v} = 0$$

or

$$\frac{\partial w}{\partial y} - \frac{\partial v}{\partial z} = 0 \qquad \frac{\partial u}{\partial z} - \frac{\partial w}{\partial x} = 0 \qquad \frac{\partial v}{\partial x} - \frac{\partial u}{\partial y} = 0 \qquad (5.4)$$

This is an acceptable assumption as we are considering an inviscid flow that is uniform far upstream. Whereas in a viscous flow vorticity is being generated at solid boundaries due to wall friction, in an incompressible inviscid flow this does not happen—and according to Kelvin's theorem, vorticity is only being convected with the flow. Far upstream, the inflow is uniform so it is irrotational, and consequently the flow will remain irrotational everywhere.

For irrotational flows, a most useful simplification is to introduce a scalar function, the velocity potential $\phi(x, y, z)$, such that

$$\vec{v}(x, y, z) = \nabla\phi \qquad (5.5)$$

As the curl of a gradient always vanishes, this simplification guarantees that the flow is irrotational [as is also easily checked by substituting equation (5.5) into equation (5.4)]. Thus, because of the neglect of viscosity and the irrotationality of the inflow, we consider *potential flows* in this section [i.e., flows that satisfy equation (5.5) for some scalar field ϕ].

Potential flows are determined by two main equations. The first, the Bernoulli equation, derives from the Euler equations; the second is the Laplace equation derived from the continuity equation. For potential flows in general, Bernoulli's equation can be further simplified. We use the expression (5.5) to express all velocity terms in the Euler equations:

$$\frac{\partial}{\partial t}(\nabla\phi) + \nabla\phi \cdot \nabla(\nabla\phi) + \nabla\left(\frac{p}{\rho} + gz\right) = 0 \qquad (5.6)$$

to be recast in

$$\nabla\left(\frac{\partial\phi}{\partial t} + \frac{1}{2}\nabla\phi \cdot \nabla\phi + \frac{p}{\rho} + gz\right) = 0 \qquad (5.7)$$

showing that

$$\frac{\partial\phi}{\partial t} + \frac{1}{2}\nabla\phi \cdot \nabla\phi + \frac{p}{\rho} + gz = C(t) \qquad (5.8)$$

as the constant can still depend on time but not on the position in the field.

For steady potential flow, this means that the Bernoulli equation holds with a constant that now is the same for the entire field, not just along a streamline

$$\frac{1}{2}\nabla\phi \cdot \nabla\phi + \frac{p}{\rho} + gz = \text{constant} \qquad (5.9)$$

At the undisturbed water surface far upstream of the ship, the pressure is atmospheric (and we put $p_a = 0$ for simplicity), $z = 0$, and $\nabla\phi = \vec{U}_\infty$. We use this to evaluate the constant and obtain the pressure directly from

$$p = -\rho gz + \frac{1}{2}\rho(U_\infty^2 - \nabla\phi \cdot \nabla\phi) \qquad (5.10)$$

where the first part is the hydrostatic pressure and the second is the hydrodynamic contribution [see Section 2.5, equation (2.24)].

As stated, the second equation is the continuity equation (2.1), which on substitution of equation (5.5) becomes

$$\frac{\partial^2\phi}{\partial x^2} + \frac{\partial^2\phi}{\partial y^2} + \frac{\partial^2\phi}{\partial z^2} = 0 \qquad \text{or} \qquad \nabla^2\phi = 0 \qquad (5.11)$$

which is the *Laplace equation* for the velocity potential.

Summing up, we find that for inviscid, irrotational, and incompressible flows:

- We have been able to replace the complicated set of the continuity equation plus the Navier-Stokes equations for the three velocity components, by the Bernoulli equation plus the Laplace equation for a scalar, the velocity potential.
- Because the Laplace equation does not contain the pressure, the equations are uncoupled: usually the potential (and thereby the velocity field) can be solved

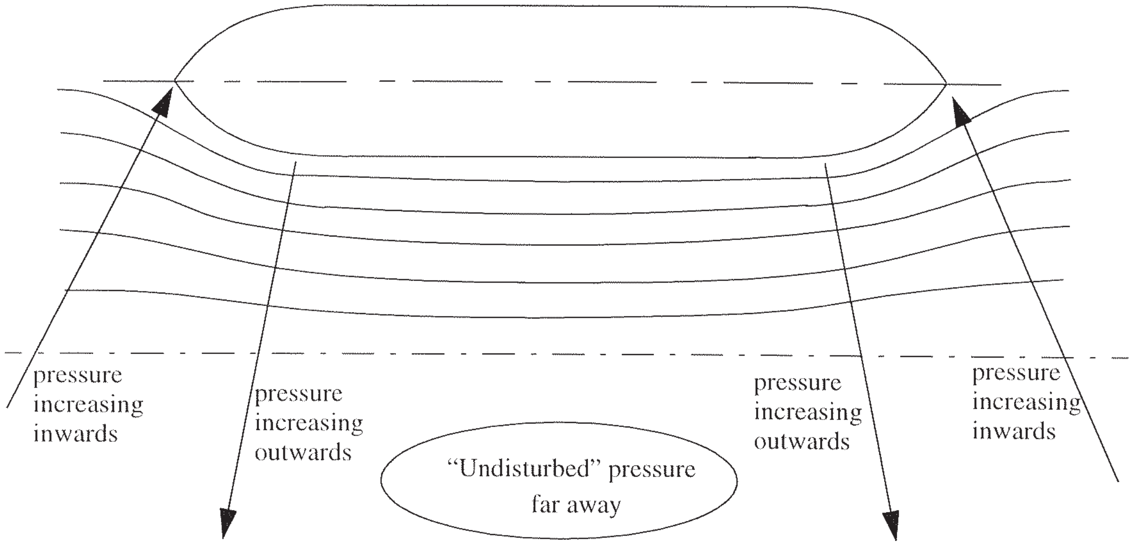

Figure 5.1 Pressure variation due to streamline curvature.

for first, and after that the pressure can be found from the Bernoulli equation.

- Moreover, the Laplace equation is a linear and homogeneous equation, and thus admits superposition of solutions for the potential or velocity field; a property that we shall exploit both in Section 5.4 (for superposition of linear waves) and in Section 9 (superposition of elementary potential fields).

This makes potential flows far easier to study or compute than viscous flows for which these simplifications are not allowed.

5.2.2 Inviscid Flow Around a Two-Dimensional Body. In the first place, let us consider the potential flow around a body in a parallel flow without viscosity, as sketched in Fig. 5.1. For the moment we suppose the body to be 2D, so the sketch may represent the waterplane for an infinite-draft ship. Again we disregard the water surface and wave making.

Upon approaching the body, the straight streamlines have to bend sideward to pass it. At the fore shoulder they turn back to follow the middle part of the body; at the aft shoulder they bend inward, and thereafter outward again to adjust to the parallel flow behind the body. For this rather bluff body there are thus four regions where the streamlines have significant curvature: at the front end, the fore shoulder, the aft shoulder, and the aft end.

There is a simple relation between the curvature of a streamline and the component of the pressure gradient normal to it. This relation is easily understood from a simple balance of forces acting on a fluid volume $dx.dy.dz$ that travels along a streamline with a local radius of curvature r (Fig. 5.2). To make the mass in the fluid volume ($\rho dx.dy.dz$) follow the curvature, a centripetal force must act on it: a net lateral force on the volume in the direction of the centre of the curvature. From basic mechanics, this force is $\rho dx.dy.dz.u^2/r$, if u is the local velocity. In inviscid flow, this force can only be provided by a pressure gradient. The pressure force is equal to the pressure difference between the inner and outer surfaces of the volume, $\partial p/\partial y.dy$, times the area $dx.dz$. Equating both expressions, we find that

$$\frac{\partial p}{\partial r} = \rho u^2/r$$

so the pressure increases in the direction away from the center of the curvature.

Returning to the 2D body, at the bow and stern the streamline curvature is away from the body; at the fore and aft shoulder, the surface is convex, and the curvature is toward the body. We may thus infer that the pressure must rise toward the body at the front and aft ends, but it must decrease toward the body at the shoulders. The streamlines have the same type of curvature also further away from the body; sufficiently far from

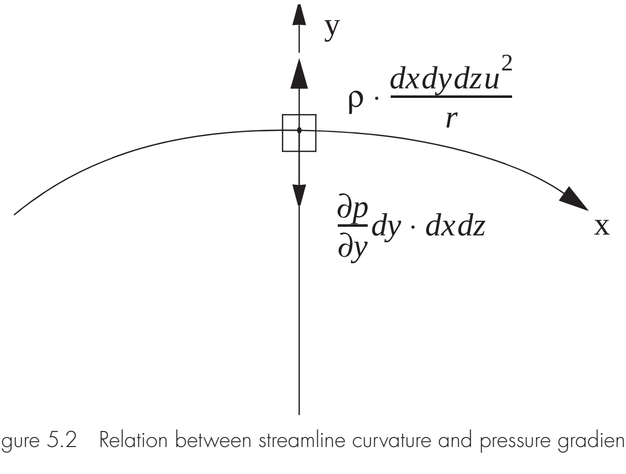

Figure 5.2 Relation between streamline curvature and pressure gradient.

the body, all streamlines will have straightened out, the flow may be considered undisturbed, and $p = 0$. Starting from this region (far sideward of the body) and moving toward the body either at the front end or the aft end, the pressure will rise so the pressure on the body surface will be higher than the undisturbed pressure level (positive) at the ends; it will drop if moving toward the shoulders, so the surface pressure is negative at the shoulders. Fig. 5.3 illustrates this.

In inviscid flow, the velocity distribution along the body is linked with the pressure distribution via Bernoulli's law. A high pressure, such as around the bow and stern stagnation points, means a low velocity, and a low pressure, such as at the shoulders, means a high velocity, exceeding the ship speed. The lower part of Fig. 5.4 reflects this. The changes indicated for a real, viscous flow will be discussed in Section 6.

If we consider the streamline that approaches the body precisely along the symmetry line, symmetry considerations prevent it to curve to port or starboard and it will end right at the bow. If subsequently it would follow the hull surface at one side, that would mean the streamline would have infinite curvature at the bow (it has a kink), requiring an infinite pressure gradient. Instead, in such a point, the velocity drops to zero, and the pressure remains finite (but high): From equation (5.10) with $\nabla\phi = 0$, we find that the hydrodynamic pressure at such a *stagnation point* is equal to

$$p_{\max} = \frac{1}{2}\rho U_\infty^2$$

the so-called *stagnation pressure*. This is the highest value that the hydrodynamic pressure can reach in a steady flow. It is customary to define a (hydrodynamic) pressure coefficient as

$$C_p = \frac{p + \rho g z}{\frac{1}{2}\rho U_\infty^2} = 1 - \frac{\nabla\phi \cdot \nabla\phi}{U_\infty^2} \tag{5.12}$$

At the stagnation points, C_p is thus equal to unity, and its distribution is plotted in Fig. 5.3.

5.2.3 Inviscid Flow Around a Three-Dimensional Body. Next we consider a 3D body, such as a ship. For now, we again disregard the effect of the water surface, which we assume to remain flat; the meaning of this will be discussed in Section 9.5.5. The relation pointed out before between streamline curvature and pressure gradients is still valid. However, we make a distinction between two types of curvature: streamline curvature in planes normal to the surface, which as in the 2D example causes a normal pressure gradient and a deviation from the undisturbed pressure; and streamline curvature in planes parallel to the surface, which is connected with pressure variation along the girth.

Fig. 5.5 shows the distribution of inviscid streamlines over a tanker hull, the so-called KVLCC2 tanker, a standard test case in numerical ship hydrodynamics. Also the hydrodynamic pressure distribution is shown in the form of isobars; lines for negative C_p values are dotted. These lines have been obtained from potential flow calculations (see Section 9.5.5).

Again there must be at least one stagnation point at the bow, where a streamline impinges and the velocity drops to zero. This is true in general in a finite number of bow points, one of them at the tip of the bulb.

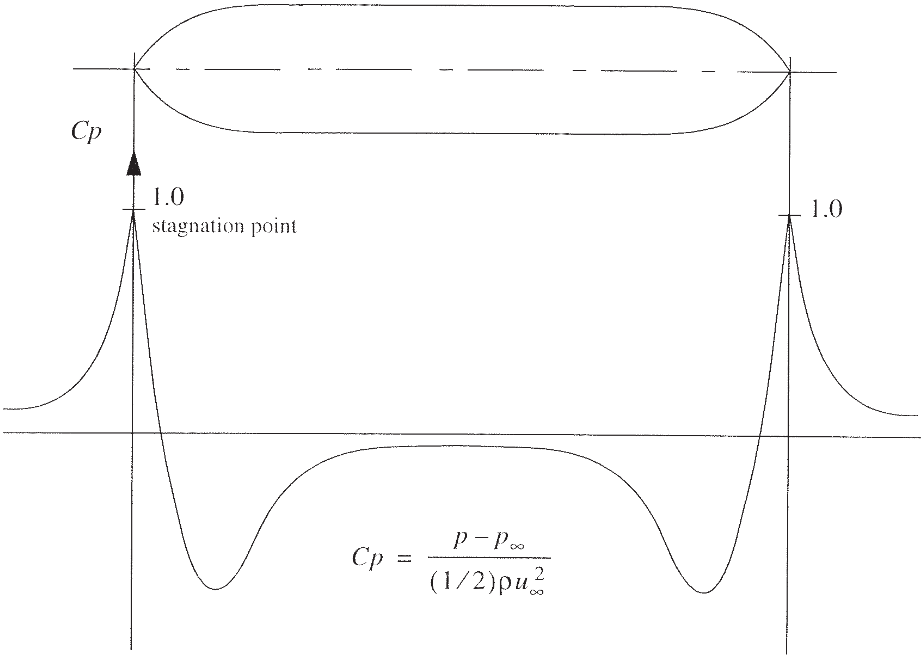

Figure 5.3 Pressure distribution along a 2D body in inviscid flow.

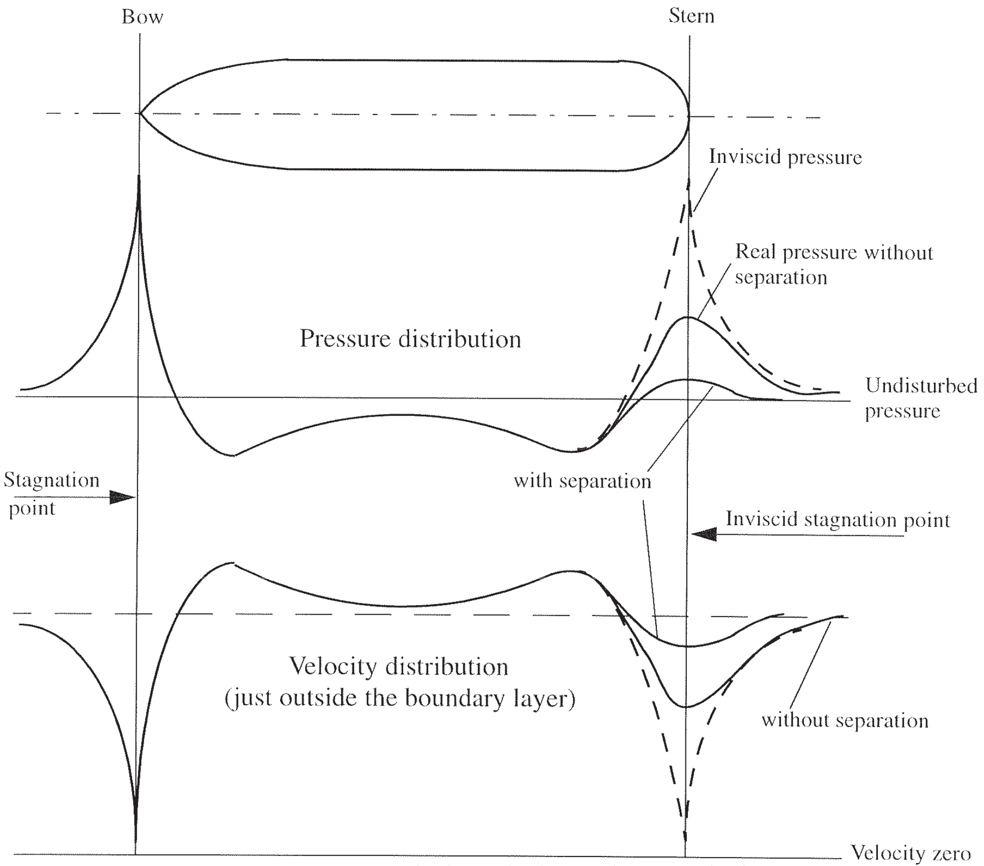

Figure 5.4 Pressure and velocity distribution along a 2D body.

The upper streamlines run aft essentially horizontally, and in this region the normal curvature causes the same kind of pressure distribution as for the 2D body shown in Fig. 5.3. On the forebody, where the approaching streamlines bend outward, there is a high pressure. At the fore shoulder where they bend back to follow the parallel part of the hull, the convex curvature causes a low pressure. At the aft shoulder the curvature is convex again and the pressure must be low. Then towards the stern, the flow bends back to parallel and the pressure is high. The distribution of the hydrodynamic pressure coefficient shown in Fig. 5.5 confirms that there is a high pressure at the bow and stern ends of the hull and low pressures at the shoulders, particularly the forward one which is sharpest. Again, the Bernoulli equation links the velocity along the hull with the pressure.

Further down on the forebody, the streamlines will move down to the bottom. In doing so they pass over a region of higher normal curvature: the bilge on the forebody. There the curvature of the streamlines in the normal direction is large, so a large pressure gradient outward will be created, and the pressure at the hull is low ($C_p < -0.3$).

On the parallel middle body there is no normal curvature of the surface, so pressure gradients must be small. There is, however, a slight curvature of the streamlines a little bit outside of the hull, as away from the hull the streamlines tend to even out the variation in curvature along the hull. Thus there is still a small pressure gradient outward, giving rise to a slightly negative pressure on the parallel middle body. (The same is also observed in Fig. 5.3.) At the stern the flow from the bottom moves upward, and again it has to pass the bilge region, causing a low pressure. Ultimately the streamlines will end up in one or more stagnation points at the stern.

Evidently, a pressure distribution like this exerts a force on the hull surface. It would seem interesting to integrate the longitudinal component of the pressure force over the hull in order to find a resistance component. However, because in this case we are considering a closed body in an infinite fluid domain in inviscid flow, and we are disregarding the free surface, *d'Alembert's paradox* applies: the total force is exactly zero (see e.g., Prandtl & Tietjens, 1957). Nevertheless, the pressure distribution is still valuable, as we shall see in Section 11 (Figs. 11.34 and 11.35).

5.3 Free-Surface Waves. Although the consideration of the inviscid flow around a body without a free surface gives useful insights, it does not give a wave pattern or wave resistance. Therefore, a next step is required, the explicit consideration of free-surface waves.

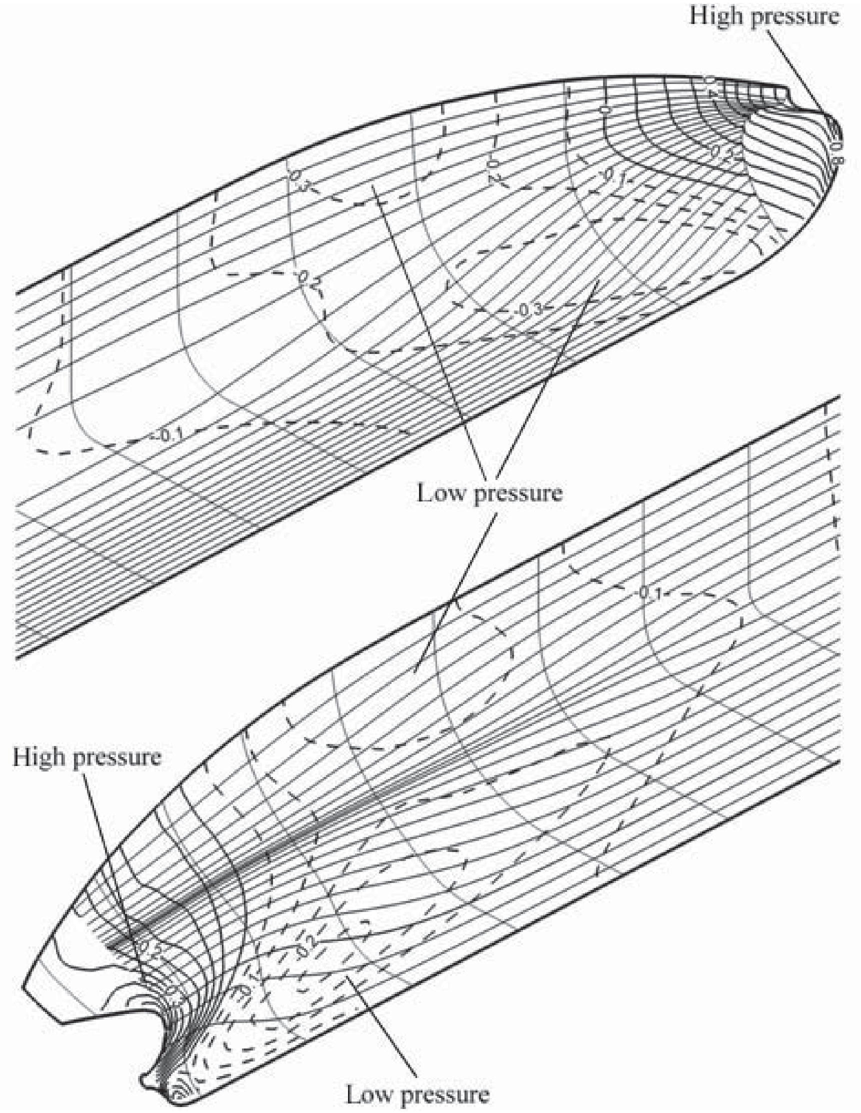

Figure 5.5 Pressure distribution and streamlines around a ship hull in inviscid flow. Contours labeled by Cp.

Fig. 5.6 shows an example of a ship wave pattern. The pattern has a clear and regular structure that suggests a mathematical background. Understanding that background will help to explain the wave pattern and its relation with the hull form, and thereby, will help to design for minimum wave resistance. The present section provides the main physics and mathematics of ship waves; in Section 11.5, this will be practically applied in hull form design.

It will appear later that a ship wave pattern is made up of a near-field disturbance, which has several aspects in common with the inviscid flow without free surface described previously, plus a system of waves that, at a sufficient distance from the ship, can be considered as a superposition of sinusoidal wave components, generated by different parts of the hull and propagating in various directions. These sinusoidal waves are essential for understanding ship wave making; in this subsection, we first focus on sinusoidal waves in general and derive some of their important properties.

An important question is whether that superposition of sinusoidal waves is permitted. We previously derived that inviscid irrotational flows are governed by the Laplace equation for the velocity potential, which is a linear equation that therefore admits superposition of solutions. However, surface waves not only satisfy the Laplace equation, but also the boundary conditions at the water surface. To allow superposition, those boundary conditions must also be (nearly) linear. Here, the following steps will be made.

- From the general form of the free-surface boundary conditions, a linear and homogeneous form is derived, the so-called Kelvin condition. This is an appropriate

Figure 5.6 A ship wave pattern.

free-surface boundary condition for waves of small amplitude; and as it is linear, any superposition of such waves again satisfies this condition.

- From the Laplace equation and the Kelvin condition, the potential and velocity field of sinusoidal surface waves is derived. This provides general relations between wave length and wave speed.
- Expressions are derived for the energy in a surface wave, and for the energy flux that accompanies a propagating wave; the derivation gives rise to the group velocity concept.

These derivations are incorporated for completeness but can be skipped by readers just interested in the phenomenology. The results will be summarized and discussed in Section 5.3.2.

5.3.1 Derivation of Sinusoidal Waves. We shall first derive some main properties of a free-surface wave propagating in still water of unlimited depth. For this general case we consider an earth-fixed coordinate system. In this system the wave moves so the flow is unsteady. Fig. 5.7 defines some quantities to be used. The free-surface boundary conditions have been briefly introduced in Section 2.4.2. The dynamic free-surface condition (2.18) is further simplified because we disregard the surface tension, so $p = p_a$. We need to use the unsteady form of the Bernoulli equation [equation (5.8)]. The constant is deduced from the undisturbed wave elevation far upstream, and we find an expression for the wave elevation ζ,

$$\zeta = -\frac{1}{g}\frac{\partial \phi}{\partial t} - \frac{1}{2g}\nabla\phi \cdot \nabla\phi \tag{5.13}$$

to be evaluated at $z = \zeta$.

The kinematic free-surface condition demands that the flow goes along the wave surface. In the general form $w = d\zeta/dt$ (2.20), we substitute the velocity potential and obtain:

$$\frac{\partial \zeta}{\partial t} + \phi_x \frac{\partial \zeta}{\partial x} + \phi_y \frac{\partial \zeta}{\partial y} - \phi_z = 0 \text{ at } z = \zeta \tag{5.14}$$

These free-surface boundary conditions are nonlinear and would not admit superposition of simple waves. However, if we consider the case of waves of small amplitude propagating through still water, we can linearize these conditions as follows. We suppose that the wave steepness (ratio between wave height and wave length) is small of $\mathbb{O}(\varepsilon)$, $\varepsilon << 1$. In the kinematic boundary condition (5.14), all derivatives of ζ thus become of $\mathbb{O}(\varepsilon)$ as well, which shows that also $\nabla\phi = \mathbb{O}(\varepsilon)$. Substitution in the dynamic and kinematic condition and dropping terms of $\mathbb{O}(\varepsilon^2)$ yields

$$\zeta = -\frac{1}{g}\frac{\partial \phi}{\partial t} \qquad \frac{\partial \zeta}{\partial t} - \phi_z = 0 \tag{5.15}$$

Eliminating ζ produces a simple, linear, and homogeneous condition for the potential,

$$\frac{\partial^2 \phi}{\partial t^2} + g\phi_z = 0 \tag{5.16}$$

This is the well-known *Kelvin free-surface condition* for unsteady flow. It is consistent to apply it simply at $z = 0$, the undisturbed free-surface level, instead of at $z = \zeta$.

Here we have completed the first step: we have found that for waves of sufficiently small amplitude, a linear form of the free-surface boundary conditions applies, and such waves may simply be linearly superimposed. (As found in practice, this still works well for waves that are not so small at all.) No assumption has been made on the direction of propagation, so waves running in different directions may be superimposed.

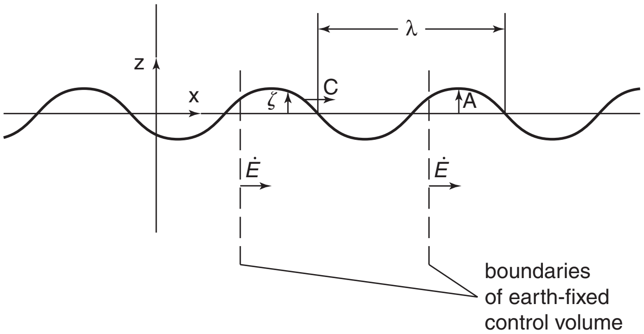

Figure 5.7 Definitions used for derivation of wave properties.

The second step is to determine a potential field that represents such a surface wave and that satisfies both the Laplace equation and the Kelvin condition. We suppose a simple sinusoidal wave of small amplitude, wave length λ, wave propagation speed c, and a shape that does not change in time and is invariable in the direction along the crest. The water depth is supposed to be unlimited. Without loss of generality we suppose the wave propagates in the x-direction. A suitable form of the potential then is

$$\phi(x, z, t) = F(z) \cdot \sin(kx - \omega t) \tag{5.17}$$

where the wave number $k = 2\pi/\lambda$, the radial frequency $\omega = 2\pi/T$, in which T is the wave period, and $F(z)$ is an unknown function describing the vertical distribution of the potential.

This potential must satisfy the Laplace equation. Substitution yields the condition

$$\frac{d^2F}{dz^2} - k^2F(z) = 0 \tag{5.18}$$

for all z, x, and t. The solution for $F(z)$ is any sum of e^{kz} and e^{-kz} contributions. However, in deep water the effect of the wave must vanish far beneath the water surface, for $z \to -\infty$, so only the first contribution is admissible. Therefore, the form of the potential becomes

$$\phi(x, z, t) = C \cdot e^{kz} \cdot \sin(kx - \omega t) \tag{5.19}$$

Finally, the potential must also satisfy the Kelvin condition. Substitution leads to

$$\omega^2 = gk \tag{5.20}$$

For practical reasons we recast this expression into one for wave length as a function of wave speed. Since the wave speed is such that one wavelength passes in one period, $c = \lambda/T = \omega/k$. Using this to express ω in equation (5.20) in c and k, we find

$$k = \frac{g}{c^2} \qquad \text{or} \qquad \lambda = \frac{2\pi c^2}{g} \tag{5.21}$$

Collecting all results and evaluating the wave elevation, we can then write the potential of a wave propagating in x direction with velocity c, in the earth-fixed coordinate system, as

$$\phi = c \cdot A \cdot e^{gz/c^2} \cdot \sin(gx/c^2 - gt/c) \tag{5.22}$$

where A is the wave amplitude.

The final derivation we make is for the energy in the waves and the energy flux. We consider regular 2D waves with length λ and phase velocity c, in the same earth-fixed frame of reference with x in the direction of the wave propagation velocity. We assume a control volume with length λ and extending down to $-\infty$(see Fig. 5.7). The kinetic energy in that volume is easily found from the gradient of the wave potential

$$\begin{aligned} E_{kin} &= \frac{1}{2}\rho\int_0^\lambda dx \cdot \int_{-\infty}^{\zeta} \left(\left(\frac{\partial\phi}{\partial x}\right)^2 + \left(\frac{\partial\phi}{\partial z}\right)^2\right) dz \\ &= \frac{1}{2}\rho\int_0^\lambda dx \cdot \int_{-\infty}^{\zeta} A^2\,\frac{g^2}{c^2} \cdot \exp(2gz/c^2)\,dz = \frac{1}{4}\rho g A^2\lambda \end{aligned}$$

The excess potential energy (relative to still water) in the same volume is

$$E_{pot} = \int_0^\lambda dx \cdot \int_{-\infty}^{\zeta} \rho g z\,dz = \int_0^\lambda \frac{1}{2}\rho g\zeta^2\,dx = \frac{1}{4}\rho g A^2\lambda$$

Therefore, the total amount of wave energy in the control volume is

$$E_{wave} = \frac{1}{2}\rho g A^2\lambda \tag{5.23}$$

As the control volume is bounded by two vertical planes a distance λ apart, at which the velocity distribution is always identical, the energy flux through both planes is the same and the energy in the control volume is conserved. This energy flux to leading order is the rate of work done by the hydrodynamic pressure p_{hd}, which is

$$\begin{aligned} \dot{E} &= \int_{-\infty}^{\zeta} p_{hd} \cdot \phi_x\,dz = -\rho\int_{-\infty}^{\zeta} \frac{\partial\phi}{\partial t} \cdot \frac{\partial\phi}{\partial x}\,dz \\ &= \rho A^2\,gc\cos^2\left(\frac{gx}{c^2} - \frac{gt}{c}\right) \cdot \exp\left(\frac{2g\zeta}{c^2}\right) \end{aligned}$$

This energy flux depends on x and t, but its average is

$$|\dot{E}| = \frac{1}{4}\rho g A^2 \cdot c \tag{5.24}$$

5.3.2 Properties of Sinusoidal Waves. The expressions derived in the last subsection have several important implications.

Linearity Provided the wave amplitude is sufficiently small, the free-surface boundary conditions can be approximated and a simple, linear expression is obtained. Sinusoidal waves have been derived that satisfy this condition and the Laplace equation, and these waves may therefore be superimposed to obtain new solutions.

Dispersion Relation The propagation velocity of water waves depends on the wave length (but not on wave amplitude, as long as that amplitude is small enough to make linear theory applicable) according to a simple expression:

$$c = \sqrt{\frac{g\lambda}{2\pi}} \qquad \text{or} \qquad \lambda = \frac{2\pi c^2}{g} \tag{5.25}$$

This is a difference with, for example, electromagnetic or sound waves that have a fixed wave speed. Water waves are thus *dispersive*: if an initial disturbance of the still water surface is present at some location, it can be regarded as a superposition of sinusoidal (Fourier) components, which will move with different speeds. Therefore, a general disturbance will not keep its shape but will get dispersed and disintegrate into separate sinusoidal components, which at a later time are found at different locations.

Vertical Distribution The disturbance caused by a surface wave decays exponentially with the depth beneath the surface, according to the function $F(z) = exp(2\pi z/\lambda)$. Therefore, at one half of a wave length beneath the water surface, the disturbance has decreased to just 4% of the magnitude it has at the surface. Short waves in particular are thus confined to a thin layer along the water surface.

Velocity Field The disturbance velocity components in the x and z directions oscillate sinusoidally with equal amplitude and a 90-degree phase difference. Therefore, in an earth-fixed frame of reference, fluid particles describe circular paths with a radius $A.exp(gz/c^2)$, which at the surface is equal to the wave amplitude and decreases exponentially with depth (Fig. 5.8). The fluid particles travel along that circular path with velocity $A\frac{g}{c}exp(gz/c^2)$ with the same period as the wave. Therefore, although the wave propagation speed is c, the average velocity of the fluid is zero, in linear theory; and the instantaneous velocity differs from c as well, depending on wave amplitude and period rather than wave velocity.

Group Velocity The average amount of (kinetic plus potential) wave energy per unit of surface area is

$$E_{wave} = \frac{1}{2}\rho g A^2 \tag{5.26}$$

But according to equation (5.24), the average flux of energy through a vertical plane extending down from the water surface is

$$|\dot{E}| = \frac{1}{4}\rho g A^2 \cdot c$$

Therefore, contrary to what one would expect, the wave energy does not travel with the same speed as the wave crest, but at half that speed: the energy transport velocity, or *group velocity*, is

$$c_g = |\dot{E}|/E = \frac{1}{2}c \tag{5.27}$$

In deep water, the group velocity is just one half of the phase velocity! In a regular system of plane waves this is not noticed, but it is in other cases. For example, when one throws a stone in a pond, a pattern of circular waves results, usually in the form of a group of a few waves moving outward through water that otherwise is hardly disturbed. One might expect this wave group to move with a radial velocity c in agreement with the length of the waves. However, on close observation one notices that individual waves successively arise at the inner edge of the wave group and move forward until they reach the outer edge and disappear. The wave propagation velocity (or *phase velocity*) therefore is significantly larger than the "group velocity." Because the wave energy evidently is linked with the group of waves, the group velocity is equal to the energy transport velocity, which is half the phase velocity. In the next subsection we shall see some of the important consequences of this fact.

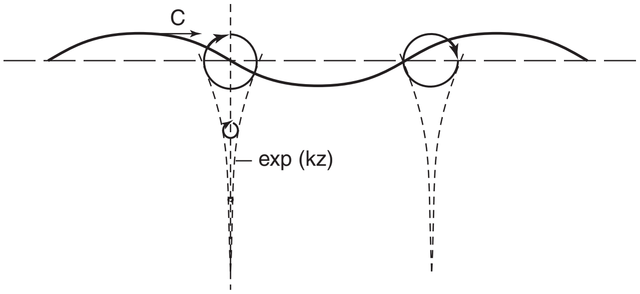

Figure 5.8 Orbital motion in a deep-water wave.

These and other properties of water waves are all described much more extensively and completely in various textbooks, such as Lighthill (1980) and Newman (1977). We have here only indicated the main line of the derivations, and pointed out some of the properties that will play a role in the following.

5.4 Ship Waves

5.4.1 Two-Dimensional Waves. After the preparatory work in the last subsection, we are now in a position to understand ship waves and their properties. Let us consider in the first place a 2D situation, such as an object with infinite width (e.g., a submerged cylinder at right angles to the flow) moving with constant speed V through still water [Fig. 5.9]). For a steady situation,

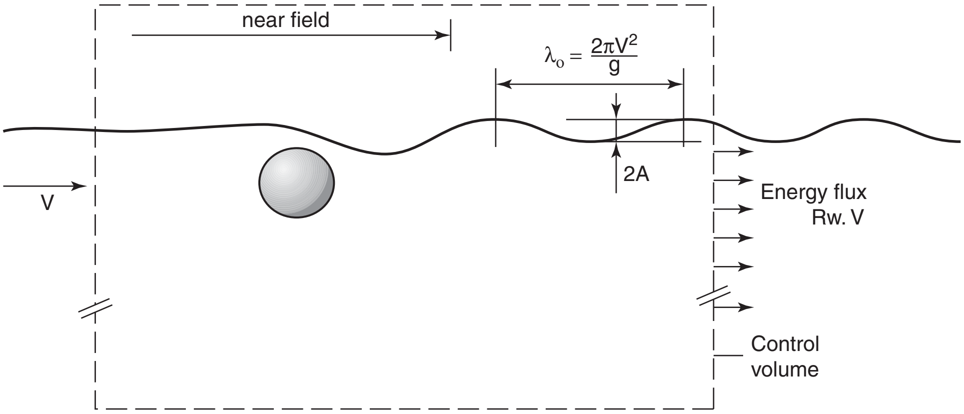

Figure 5.9 Steady waves of a 2D body.

as achieved after a sufficient time of constant motion, we expect a wave pattern that is steady in a coordinate system that moves with the body: all waves follow the body and remain at a fixed position relative to it. Therefore, the phase velocity of the waves in the wave pattern must be equal to V and the dispersion relation (5.25) immediately tells that the wave length must be equal to $\lambda = 2\pi V^2/g = 2\pi Fn^2 L$. So, far enough aft of the body, there is just a single wave component present. We know its wave length but not its amplitude and phase, unless we use other methods.

Close to the body, there must be a local disturbance of this simple wave field: evidently the simple potential field (5.22) does not satisfy the boundary condition on the body surface, and other potential fields must be present. However, at some distance downstream the simple sinusoidal wave is recovered (provided its amplitude is small).

The fact that waves only occur downstream of the body is a consequence of the group velocity being less than the phase velocity. The trailing wave system contains wave energy, as derived previously. This wave energy does not travel with the phase speed V but with the group velocity $c_g = \frac{1}{2}V$. Therefore, a control volume around the body and moving with it loses wave energy through its downstream boundary at a rate equal to $E.V - \dot{E}$, where $\dot{E}$ is the energy flux through an earth-fixed vertical plane as previously derived. In a steady situation, this energy loss needs to be compensated by a continuous supply of energy by the body, which is wave resistance × speed. Consequently, the wave resistance R_W (per unit span, in this 2D case) is

$$R_W = (E.V - \dot{E})/V = \frac{1}{4}\rho g A^2 \qquad (5.28)$$

The only unknown here is the wave amplitude A.

5.4.2 Three-Dimensional Waves. In 3D cases such as ships, there is an additional degree of freedom which is the wave propagation direction, indicated as θ in Fig. 5.10. A local disturbance, such as the bow of a ship, can generate a continuous set of wave components propagating in various directions $-\pi/2 < \theta < +\pi/2$. Waves with small values of θ and their crests more or less at right angles to the path of the ship are called *transverse waves*; those with large values of θ are called *diverging waves*. The limit is often chosen at $\theta = 35$ degrees, for reasons that will become clear later. "The transverse wave" denotes the wave component with $\theta \approx 0$. In actual ship wave patterns, components with angles up to $\theta = 60 - 70$ degrees can often be observed.

The wave lengths and phase velocities follow from equation (5.25) and Fig. 5.10. The waves with $\theta = 0$ essentially correspond to the waves in the 2D case. The requirement of their being steady in the coordinate system moving with the ship means that again their phase speed is equal to the speed of the ship V, so their length is $\lambda = 2\pi V^2/g = 2\pi Fn^2 L$. However, for wave components at larger angles, the crests and troughs are still stationary relative to the ship if their phase velocity is $c = V\cos\theta$, as indicated in Fig. 5.10. Consequently, the dispersion relation (5.25) tells that they have a length

$$\lambda(\theta) = 2\pi c^2/g = 2\pi\, Fn^2\, L\cos^2\theta \qquad (5.29)$$

(As measured in a longitudinal cut through the wave pattern, the length found is $\lambda_x = \lambda/\cos\theta = 2\pi\, Fn^2\, L\cos\theta$.)

The longest waves in the pattern therefore are the transverse waves which have a length $\lambda_0 = 2\pi Fn^2 L$, the fundamental wave length. All other steady waves are shorter than that by a factor $\cos^2\theta$. As long as the wave amplitudes are small, the resulting far-field wave pattern is just the sum of all these components. (For larger amplitudes, this is still qualitatively correct.)

For later reference we derive here a general expression for the far-field wave pattern. Referring to Fig. 5.10, for a point *(x,y)* in the ship-fixed coordinate system (here taken with origin at the bow), we define a function p as the distance of this point to the first

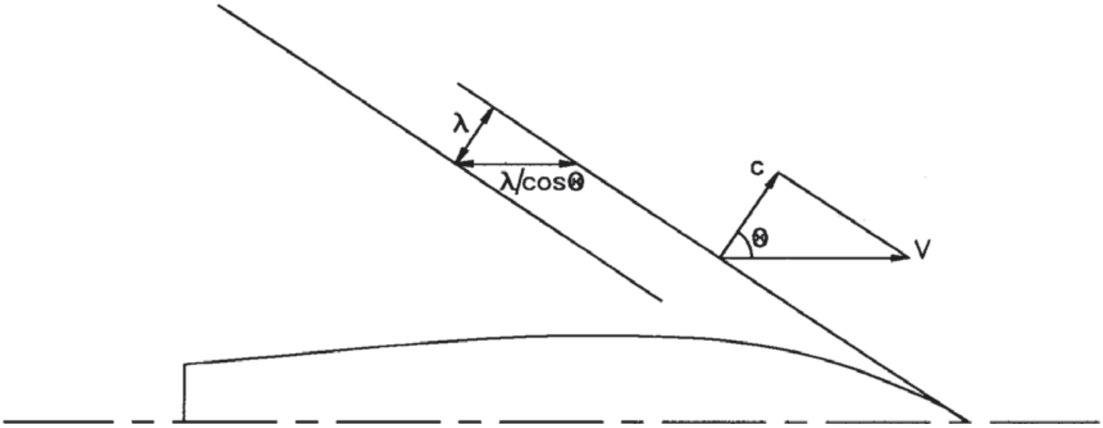

Figure 5.10 Direction, phase speed, and length of wave components in 3D cases.

crest line at angle θ passing through the bow; measured normal to that crest and positive aft. Noting that y is negative for positive θ, as indicated in the figure, we then find:

$$p = x \cos\theta + y \sin\theta$$

The wave component at angle θ in this coordinate system is just a 2D wave, and can be written as

$$\zeta = A\cos\frac{2\pi p}{\lambda} + B\sin\frac{2\pi p}{\lambda} =$$

$$A\cos\frac{2\pi(x\cos\theta + y\sin\theta)}{\lambda} + B\sin\frac{2\pi(x\cos\theta + y\sin\theta)}{\lambda}$$

Now, we substitute for λ from equation (5.29), and we superimpose all wave components, which in the continuous case is an integration. Thus we get

$$\zeta(x,y) = \int_{-\frac{\pi}{2}}^{+\frac{\pi}{2}}\left[A(\theta)\cos\frac{g(x\cos\theta + y\sin\theta)}{V^2\cos^2\theta} + B(\theta)\sin\frac{g(x\cos\theta + y\sin\theta)}{V^2\cos^2\theta}\right]\cdot d\theta \tag{5.30}$$

5.4.3 The Kelvin Pattern. A simple-minded construction of the ship wave pattern would be to draw continuous crests such as those in Fig. 5.10, extending to infinity, for all θ. The wave pattern would then fill the entire area behind the first transverse wave crest, which would extend transversely from the bow. However, here the group velocity causes a drastic change of the appearance. Consider the first wave crest drawn in Fig. 5.10. It is generated at the bow, and energy is supplied to it there. This energy travels in the direction of propagation; it therefore leaves the bow and at later times is found at a transverse distance. However, as the group velocity is just half the wave phase velocity, the wave energy does not stay with the crest but lags behind—just as it does for waves caused by a stone thrown in a pond. Consequently, the first wave crest dies out, and a second one emerges behind it, which dies out again and generates the next wave. Therefore, the fact that the group velocity is less than the phase velocity is responsible for the fact that wave crests do not extend indefinitely, but are short and are arranged in a fan-shaped pattern, as seen in Fig. 5.6.

Let us consider the location of the wave energy that was generated by the bow when it was at the point P indicated in Fig. 5.11. At that moment, a part of the wave crest was generated, which has traveled outward with a velocity $\vec{c} = (-c.\cos\theta,\ c.\sin\theta) = (-V\cos^2\theta,\ V\sin\theta\cos\theta)$ and a time t later is found at point C. Relative to the origin at the ship bow, which moves with velocity V in the$-x$-direction, the position of the crest at a time t therefore is

$$x_C = Vt(1 - \cos^2\theta) \qquad y_C = Vt\sin\theta\cos\theta$$

But the wave energy travels with the group velocity $\vec{c}_g = \frac{1}{2}c = \left(-\frac{1}{2}V\cos^2\theta, \frac{1}{2}V\sin\theta\cos\theta\right)$, and thus is found at the point E

$$x_E = V\cdot t\cdot\left(1 - \frac{1}{2}\cos^2\theta\right) \qquad y_E = \frac{1}{2}V\cdot t\cdot\sin\theta\cos\theta$$

The collection of all points x_E, y_E forms a "ray" along which the wave energy of wave component θ travels relative to the bow of the ship. The direction of this ray is

$$y_E/x_E = \frac{\sin\theta\cos\theta}{2 - \cos^2\theta}$$

which is graphically represented in Fig. 5.12.

Clearly, the rays of transverse waves stay close to the path of the ship, like those of the most sharply diverging waves. At an intermediate θ the function has a maximum. This means that for all θ between 0 and $\pi/2$, the rays cover a sector behind the bow, bounded by those rays for which y_E/x_E is maximum. By simple calculus, this is found to be for $\sin\theta = \sqrt{1/3}$, so $\theta = 35$ degrees, for which the ray direction is $\tan^{-1}y_E/x_E = 19°28'$.

Therefore, all wave energy generated by the ship is contained in a sector originating at the bow and with a half top angle of 19°28′. There are no waves aligned with the edge of this sector, it is just the envelope of the fan-shaped pattern mentioned before. Fig. 5.12 also indicates that there is a range of θ–values for which the ray direction is close to its maximum value, and for which

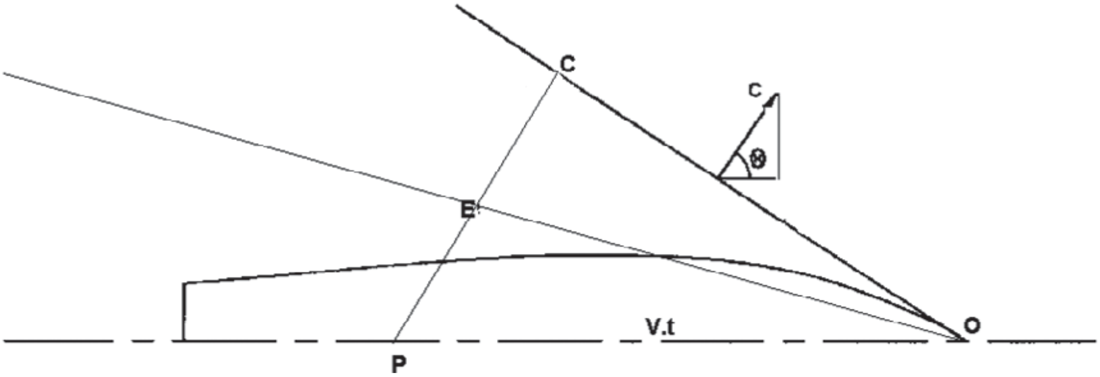

Figure 5.11 Construction of ray direction.

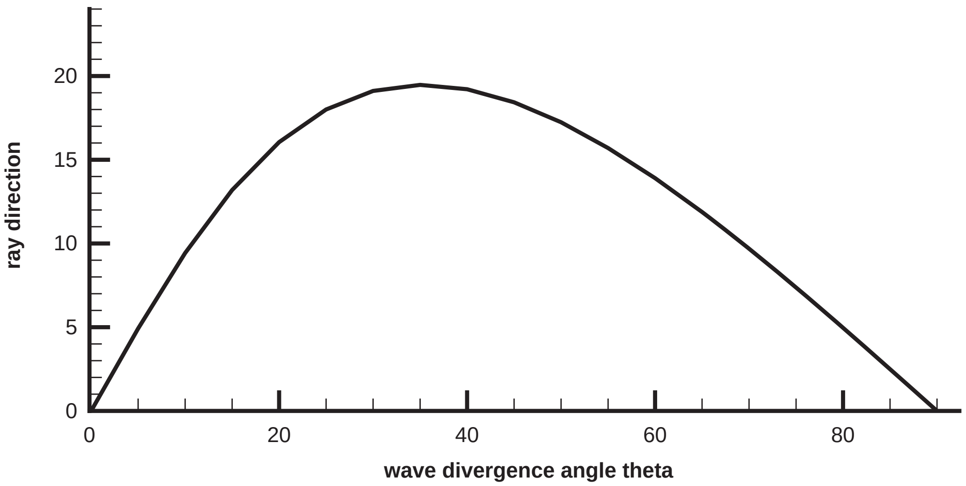

Figure 5.12 Ray direction $\tan^{-1} y_E/x_E$ as a function of wave angle θ.

consequently the wave energy is found close to the outer edge of the sector. This explains why in practice the outer edge is often more conspicuous than the wave components that occur inside the sector.

The sector that contains the wave pattern is called the *Kelvin wedge*, after Lord Kelvin, one of the earliest researchers who, around 1900, studied ship waves (Thompson, 1887, 1904). He considered a single pressure point travelling in a straight line over the surface of the water, thereby sending out wave components in all directions. These combine to form a characteristic interference pattern, now called the *Kelvin pattern*, sketched in Fig. 5.13. A system of transverse waves is observed following behind the point, together with a series of divergent waves, the whole pattern being contained within the Kelvin wedge. The transverse waves are curved back some distance out from the centerline and meet the diverging waves in cusps at the edge of the Kelvin wedge.

We previously derived the locus of wave components with a certain direction and originating from a certain point (e.g., the bow) as a ray with a direction dependent on the wave direction. Fig. 5.14 illustrates how this can be a well-defined line in practice, extending to large distances from the ship. Consequently, the wave energy of waves within a certain range of θ–values is contained in a sector bounded by the rays associated with the limiting θ–values of that range. Because the separation between those rays increases linearly with distance from the ship, the wave energy density decreases as the inverse distance to the origin of the waves. As the energy is quadratic in the wave amplitude, the amplitude of wave components inside the Kelvin wedge must decay as distance$^{-1/2}$. This applies to both transverse and diverging components. However, the mathematical analysis of the Kelvin pattern shows that the waves right at the Kelvin wedge (those with $\theta \approx 35$ degrees) decay with distance$^{-1/3}$ (Lighthill, 1980). Therefore these particular wave components decrease less rapidly than those of the transverse waves, and eventually at a large distance they tend to dominate the wave system.

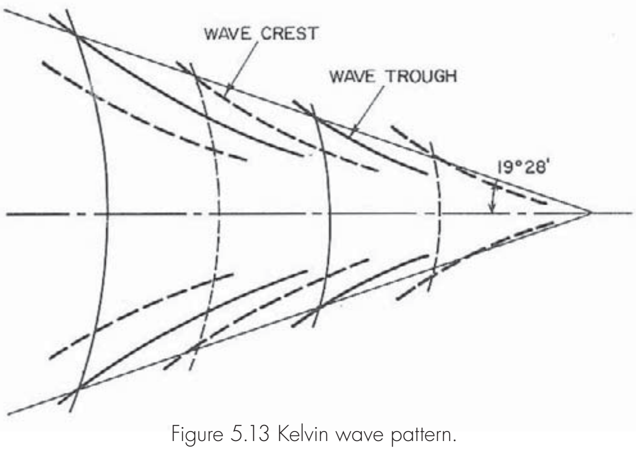

Figure 5.13 Kelvin wave pattern.

5.4.4 Ship Wave Patterns. The Kelvin wave pattern illustrates and explains many of the features of the ship wave system. In particular, for a ship the entire wave pattern is also contained in a sector bounded by lines that, at a sufficient distance from the ship, make an angle of 19°28′ with the longitudinal axis. Even if nonlinear effects occur in the near field, at a sufficient distance the wave amplitude always decreases enough to make the waves behave as linear waves, and the properties derived previously apply. Also, the wave amplitude decay rate with distance is as mentioned, following a $-\frac{1}{2}$ or $-\frac{1}{3}$ power.

Like the Kelvin pattern, a ship wave pattern is determined by interference between wave components in various directions. Again, transverse and diverging waves occur in general. The properties of the Kelvin pattern are often best recognized in the wave pattern generated by the bow, which usually comes closest to an isolated pressure point. Between the divergent waves on each side of the ship, transverse waves are formed which are most easily seen along the middle portion of a ship or model with parallel body or just behind the ship.

Figure 5.14 A ship wave pattern displaying some clearly defined rays at the outside of the Kelvin wedges from bow, shoulder, and stern.

However, there are also several differences between Kelvin and ship wave patterns. A ship is not a single isolated pressure point, but has a number of features that generate waves (e.g., bow, stern, shoulders). These generate their own wave systems, contained in separate Kelvin wedges that overlap and interfere, with separate divergent and transverse components; however, not all of these are always so clearly distinguishable because of the general disturbance already present from the bow wave system.

As the wave-making features of a ship have a finite dimension and a finite spacing, some wave components are being generated more strongly, others less strongly. Therefore, as will be described later, the *ship wave spectrum* differs from that of the Kelvin pattern. Consequently, the interference pattern differs in detail and depends on ship form and speed. Although transverse and diverging waves are present, the typical concave shape of the diverging wave crests seen in Fig. 5.13 often does not occur, and crests are short and straight rather than long and concave as a result of prevalence of certain components in the spectrum. Fig. 5.15, from William Froude's publication (Froude, 1877), illustrates this.

We have derived before that a system of sinusoidal waves propagating in still water satisfies the boundary conditions on the water surface, for limited wave amplitudes. However, this is only a valid representation of the wave pattern far from the ship. The velocity field corresponding with just these waves does not satisfy the condition that the flow must pass around the hull. Therefore, as in the 2D example of Section 5.4.1, there must be a near-field disturbance in addition to the Kelvin wave pattern. In the near field the flow is deflected, accelerated, and decelerated. Its characteristics are similar to those described in Section 5.2.3, although changes occur as a result of the presence of the water surface; some of these are discussed in Section 11.5.

Waves generated by the hull first have to propagate over this curved and nonuniform flow in the near field, leading to various changes of the wave direction, amplitude, and position (Raven, 1997). Therefore, the direction, length, amplitude, and phase of the waves generated are only observed precisely once they have left the near field and are at some distance away from the hull. One consequence is the fact that the top of the Kelvin wedge of the bow wave system seems displaced forward (the cusp lines outward). In Fig. 5.11, the need for such an outward displacement can be understood from the fact that the ray drawn based on simple far-field considerations would pass through the hull, which is impossible.

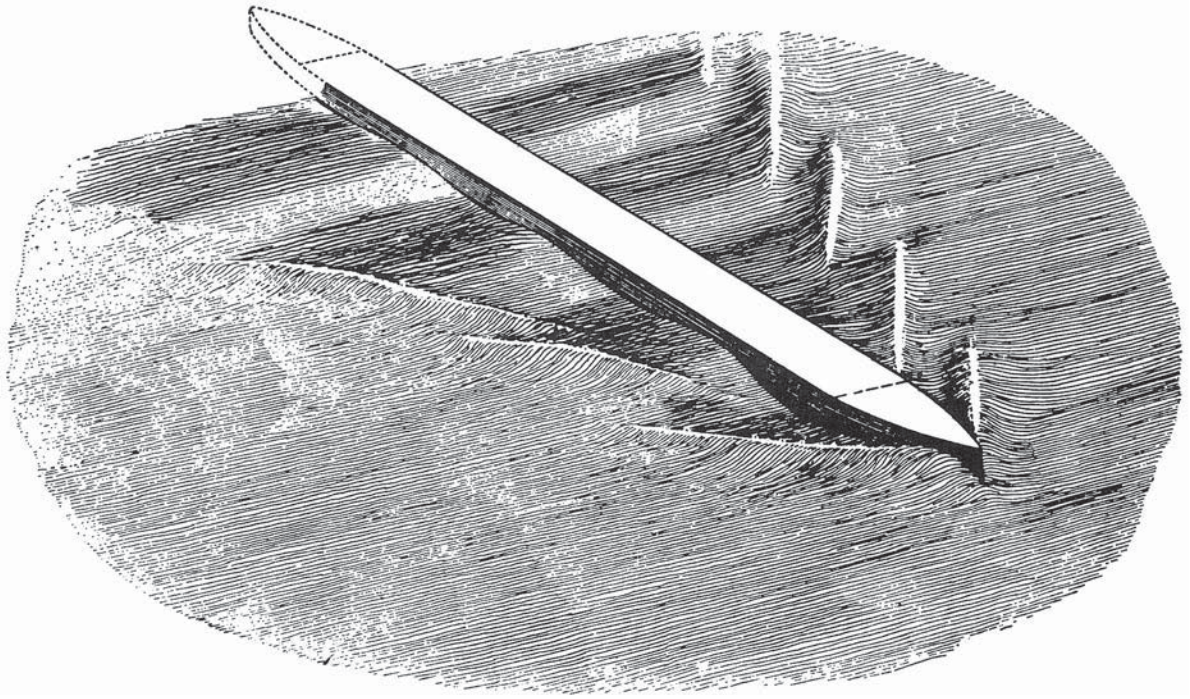

Figure 5.15 W. Froude's sketch of characteristic bow wave train (Froude, W., 1877).

5.4.5 Interference Effects. The pressure distribution around a ship was discussed in Section 5.2.3. We recollect that at the bow the pressure is high; C_p attains its maximum value of 1.0 at the stagnation points (there may be more than one), and is positive along most of the bow contour. Dependent on the type of stern a high pressure is often also attained there. Between the high-pressure regions at the bow and stern, there are normally two minima related to the fore and aft shoulders. For a hull without shoulders, such as a sailing yacht, there is only one minimum, and it is usually very shallow.

Since the surface waves can be considered to be generated by pressure disturbances, the most prominent wave systems around a ship will be generated by the high pressures at the bow and stern and the low pressures at the shoulders. The first two will produce waves starting with a crest, whereas the latter two will generate waves starting with a trough. In a classical paper by Wigley (1931), the waves around a generic body were calculated using the "thin ship theory," which will be described in Section 9.6.3. The body (Fig. 5.16) had waterlines defined by a double wedge with a parallel part inserted in the middle. Wigley's results display in a very clear way the interference between the different systems and the effect on the wave resistance, and will therefore be described in some detail.

The wave systems originating from different parts of the hull may well contain transverse and diverging components in their different, partly overlapping Kelvin wedges. However, for the moment we just consider the wave profile along the hull and centerline, which is dominated by the transverse waves. As seen in Fig. 5.16, the wave profile along the hull contains five contributions:

1. A near-field disturbance of the surface, with positive peaks at the bow and stern and negative peaks at the shoulders. In this example it has fore-and-aft symmetry because the hull form is symmetrical. This disturbance dies out quickly ahead and astern of the hull. No waves are thus left behind, and consequently no energy is radiated. This disturbance is also called the local disturbance, or the Bernoulli wave.
2. The bow wave system, beginning with a crest
3. The fore shoulder wave, starting with a trough
4. The aft shoulder wave, also starting with a trough
5. The stern wave system, here starting with a crest.

The wave profile along the model was then approximated by the sum of these five systems. The measured profile was found to be in general agreement with it and confirmed the basic idea.

Because of the distinct sharp corners at bow, stern, and shoulders, the four wave systems have their origins fixed at points along the hull and the primary crests and troughs are more or less fixed in position. As speed increases, the wave length of each of the four systems increases so the second crest/trough shifts downstream. The total wave profile thus will continuously change in shape with increasing speed as the crests and troughs of the different systems pass through one another. At speeds at which wave crests of two or more systems coincide, high waves result; if a crest and a trough coincide, they cancel.

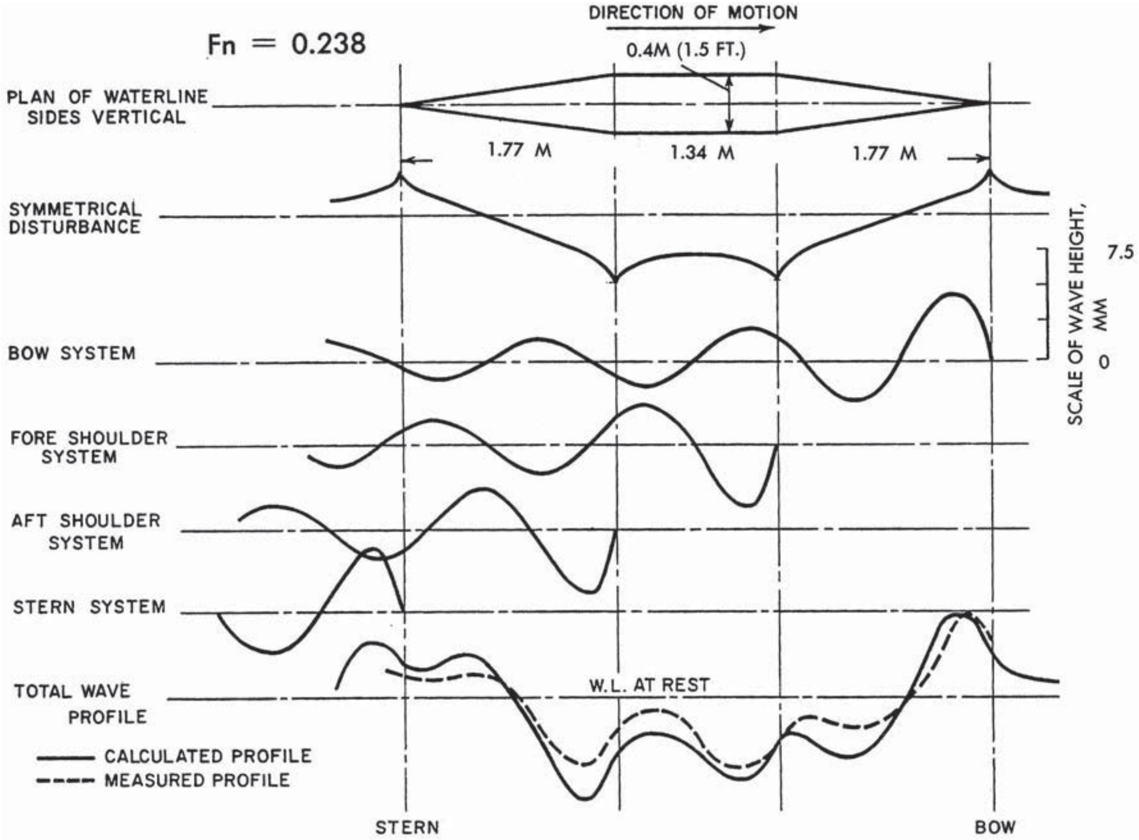

Figure 5.16 The near-field disturbance and the free wave systems for the wedge hull.

For this model, the positive and negative interference effects are uniquely defined by the ratio of the wave length to the hull length (i.e., $\lambda_0/L = 2\pi Fn^2$). For instance, the bow and stern waves will interact positively when this ratio is equal to one and the crests of the two systems coincide. We have to note here that this only applies strictly to the transverse waves of the different wave systems; waves for larger θ have a smaller length and interfere differently. However, interference effects are often most prominent for nearly transverse waves, as other wave components quickly move away from the hull. Therefore, Wigley's considerations for transverse waves only are still relevant.

For more ship-shaped forms with smooth waterlines without sharp discontinuities, the wave pattern often still can be considered to consist of five components—a near-field disturbance and four free-wave systems (Wigley, 1934). The occurrence of recognizable shoulder waves and the type of stern waves depends on the hull form. The shoulder systems are no longer tied to definite points because the change of slope is now gradual and spread over the whole entrance and run. Even so, for a given hull shape the interference is uniquely defined by the Froude number.

It deserves mention that the existence of interference effects of this kind was known to naval architects long before this analysis had been developed. The Froudes demonstrated them in a striking way by testing a number of models consisting of the same bow and stern separated by different lengths of parallel body (Froude, R. E., 1881; Froude, W., 1877).

5.4.6 The Ship Wave Spectrum. As we have seen, far enough aft of the ship the wave pattern can be considered as a superposition of sinusoidal wave components propagating in various directions, each satisfying the dispersion relation that links wave length and wave speed. Moreover, the requirement of the wave being steady in a coordinate system moving with the ship means a unique relation between the wave direction and the wave speed: $c = V \cos \theta$. Therefore, for a wave component in a certain direction θ, we know its length and speed, and the only unknowns are its amplitude and phase.

This is borne out by the expression for the free-wave pattern, equation (5.30). The functions $A(\theta)$, $B(\theta)$ represent the free-wave spectrum, which by virtue of this fixed relation between wave length, speed, and direction is a one-dimensional spectrum. This is a quite compact representation of the far-field wave pattern that the ship generates. Fig. 5.17 shows an example for the amplitude $\sqrt{A(\theta)^2 + B(\theta)^2}$ against θ. This ship is found to generate a significant transverse wave, substantial waves around $\theta = 36$ degrees, and a variety of less pronounced other wave components. The spectrum is continuous, but

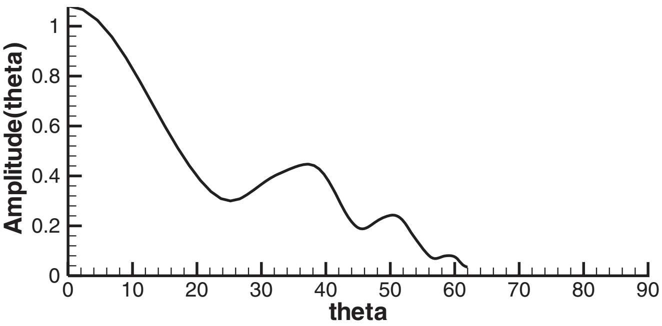

Figure 5.17 Example of a ship wave spectrum.

shows the particular preference for generation of certain wave components by a given hull form at a certain speed. For reference, we mention that the Kelvin pattern, for an isolated pressure point, has a spectrum of amplitude (θ) = $C/\cos^2\theta$ which has a large contribution from diverging waves.

To determine a ship wave spectrum experimentally, several different methods have been proposed. The general representation of the far field, equation (5.30), allows to solve the unknown $A(\theta)$, $B(\theta)$ from measured wave elevations at a sufficient number of points. The most usual approaches are *wave pattern analysis* techniques based on measured longitudinal or transverse cuts through the wave pattern. Longitudinal cuts are particularly easy to measure by recording the wave elevation at a fixed location in a towing tank against time, during passage of a model. Transverse cut techniques do the same for a set of wave-height gauges on a transverse subcarriage mounted to the towing carriage. The measurements are discussed in Section 8.4.6. Eggers, Sharma, and Ward (1967) give a comprehensive survey of the various wave pattern analysis formulations.

Once the spectrum functions $A(\theta)$, $B(\theta)$ have been determined, in principle the entire potential field and velocity and pressure field far from the ship are known as a superposition of the corresponding fields for all wave components. From this, it is possible to derive the energy flux through a vertical, transverse plane far aft of the ship. We come back to this in the next section.

5.5 Wave Resistance. In Section 5.2 we considered the inviscid flow without free surface around a body and studied the pressure distribution and its relation with the hull form. It was pointed out that integrating the longitudinal pressure forces exerted on the hull by this pressure distribution would not yield a resistance because of d'Alemberts paradox. If the body is traveling on or near the surface, however, a wave pattern is generated, and the pressure distribution over the hull is altered, even though the main features discussed before are mostly conserved. The resultant net longitudinal force is the wave-making resistance:

$$R_W = -\iint_s p \cdot n_x \cdot dS \qquad (5.31)$$

in which S is the wetted area of the hull up to the actual wavy waterline, n_x is the longitudinal component of the outward normal on the hull surface, and p is the pressure, including both the hydrostatic and hydrodynamic parts. (We suppose an inviscid flow here because a change of the pressure caused by viscous effects should be included in the viscous pressure resistance, not the wave resistance.)

This pressure resistance must be of such magnitude that the energy expended in moving the body against it is equal to the energy necessary to maintain the wave system. The wave pattern generated by the ship contains wave energy that radiates out and aft of the hull. Therefore, in a steady case, the same energy flux needs to be supplied by the ship, as wave resistance × speed. We can derive this energy flux from the free-wave representation of the far field, as is inherent to the ship wave spectrum. From this, we find the following expression for the wave resistance (or "wave pattern resistance") (Havelock, 1934):

$$R_W = \frac{1}{2}\pi\rho V^2 \int_{-\frac{\pi}{2}}^{+\frac{\pi}{2}} \left(A(\theta)^2 + B(\theta)^2\right)\cos^3\theta\, d\theta \qquad (5.32)$$

This expression as a simple integration over the free-wave spectrum shows clearly that the wave resistance depends again quadratically on the wave amplitude, and that the phase of the waves in the far field has no effect on the resistance. Also, there is a weighting factor $\cos^3\theta$, which means that transverse waves are far more important for wave resistance than divergent waves, a significant finding for ship hull form design. Reducing the far-field amplitude of transverse waves (e.g., by optimizing the wave interference) has a direct benefit for the resistance.

It is important to realize that a far-field consideration of the wave pattern and radiated wave energy, and an integration of the pressure (in inviscid flow) over the hull, are two ways to look at the same quantity, not two resistance components.

As we have seen [e.g., in equation (5.23)], the wave energy is proportional to the square of the wave amplitude, and so is the wave resistance. Owing to this quadratic dependence, evidently the superposition of wave components does not apply to their resistance contributions! Therefore, interference between wave components plays an important role: "constructive interference" in which wave systems amplify each other leads to a high wave resistance, whereas the opposite situation of "destructive interference" in which waves cancel each other corresponds to a low wave resistance. The dependence of the wave interference on the Froude number therefore causes an oscillatory variation of the wave resistance with Fn. The resulting peaks in the resistance coefficient curve are called *humps* and the valleys are called *hollows*.

As long as interference between different systems plays a role, when the speed is varied there will be a succession of speeds when the crests of the two systems reinforce each other, separated by other speeds at which crests and troughs tend to cancel each other. The Froude number at which a certain interference will take place depends significantly on the hull form. It is good design practice to ensure whenever possible that in service conditions the ship is running at a favorable speed. The dependence of these humps and hollows on the Froude number accounts for the close relationship between economic speed and ship length.

To obtain some information on the location of humps and hollows, we first consider the wedge hull again. For this, the wave resistance coefficient was found to be of the form

$$C_W \equiv \frac{R_W}{\frac{1}{2}\rho V^2 S} = V^4 \times \begin{array}{l}(\text{constant term } + \\ \text{four oscillating terms})\end{array} \qquad (5.33)$$

The oscillating terms are caused by the interference between different wave systems, as indicated in Fig. 5.18. For Fn increasing beyond about 0.48 most wave systems ultimately cancel each other, which compensates the steady increase in C_W. At still higher speeds the transverse wave length is substantially larger than the ship length, and the interference effect for transverse waves vanishes. The higher the Froude number in this regime, the lower the value of C_W.

Wigley also made calculations to show the separate contributions to the wave-making resistance of the transverse and divergent systems (Wigley, 1942). Up to a Froude number of 0.4, the transverse waves are mainly responsible for the positions of the humps and hollows (Fig. 5.19), as we assumed before. Above this speed, the contribution from the divergent waves becomes more and more important, and the interference of the transverse waves alone will not correctly determine the position of the higher humps, particularly the last one at $Fn = 0.5$.

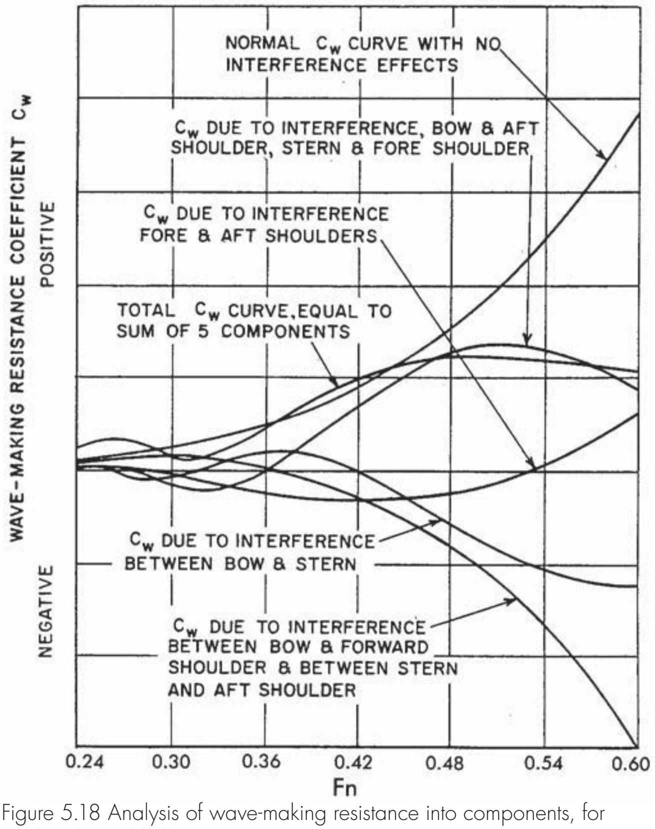

Figure 5.18 Analysis of wave-making resistance into components, for wedge-shaped hull.

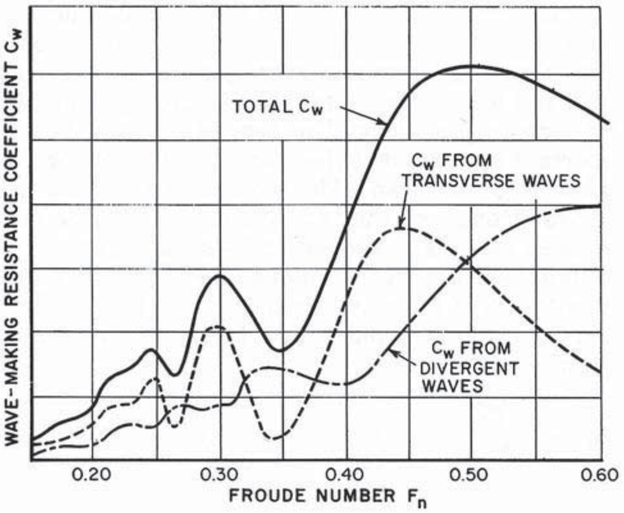

Figure 5.19 Contributions of transverse and divergent waves to wave resistance.

Wigley's study was quite simplified by the choice of the hull form, by the main focus on interference of transverse waves, and by the simplifications in the theoretical method used. For an arbitrary ship, an empirical way to determine the position of the humps and hollows is to use the so-called *z-method*. It considers only two of the wave systems: the bow wave system (starting with a crest) and the aft shoulder wave system (starting with a trough). The distance between these two was named the *wave-making length*, z. A wave-making maximum occurs when $z = (2k + 1) \cdot \frac{\lambda}{2}$ and a minimum when $z = k.\lambda$, where λ is the transverse wave length and $k = 0, 1, 2, \ldots.$ Based on experiments, Baker and Kent (1919) proposed a formula for z, appropriate for $k = 1, 2,$ and 3 (but not for $k = 0$):

$$z = C_P \cdot L + \frac{1}{4}\lambda$$

where C_P is the hull prismatic coefficient. Using the dispersion relation for the transverse waves, the Froude numbers corresponding to a hump thus become:

$$Fn = \sqrt{\frac{C_P}{2\pi(k + 1/4)}}$$

If we take Wigley's wedge model, with $C_P = 0.637$, as an example, humps would occur at $Fn = 0.177$, 0.212, and 0.285. This agrees fairly well with Wigley's result of hump speeds at $Fn = 0.173$, 0.205, 0.269, and 0.476.

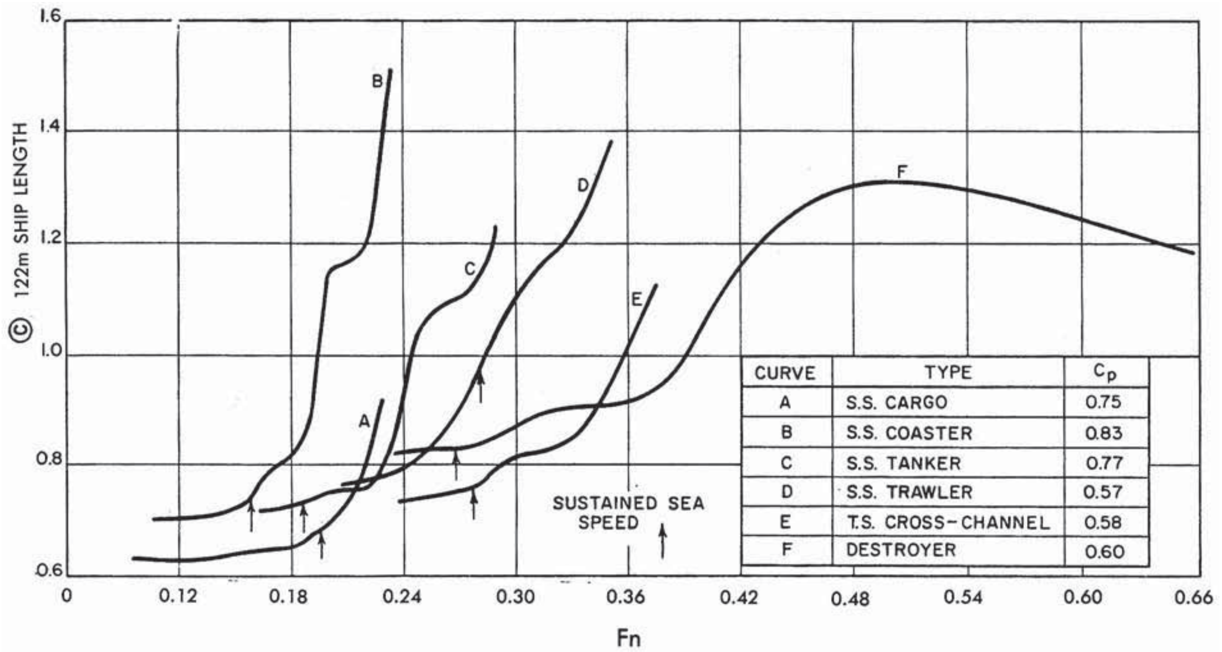

Figure 5.20 Typical curves of resistance coefficient ©.

This slightly more refined estimate, which is based on empirical data and takes into account one aspect of the hull fullness, still cannot provide quite precise results because there is a substantial variability in hull forms and the position of their main wave systems, even for a given C_P. The particulars of the hull shape determine whether and where significant shoulder wave systems occur, what the type and location of the stern wave system is, what wave components prevail, etc. These complicated dependencies are the very reason for model testing and adhering to the concept of “corresponding speeds,” implying equal Froude numbers on the model and the actual ship.

Fig. 5.20 shows typical resistance curves for different types of ships (Todd, 1963). Although this figure is for old hull forms and proportions, it illustrates well that for different ship types, the humps are very different in magnitude and occur at slightly different speeds; it also indicates the large variation in overall slope of the resistance curve between ship types. The ordinate here is the coefficient

$$\copyright \equiv \frac{125\, R_T}{\frac{1}{2}\pi\rho\nabla^{2/3}\, V^2}$$

which is another form of resistance coefficient used in the past (see the discussion in Section 10.1.1). The different graphs give a nice illustration of the humps and hollows in the curves (e.g., humps at $Fn \approx 0.24$, 0.30, and 0.48), which can be more or less pronounced dependent on the fullness of the ship. When going from left to right in this diagram, we shall now indicate how the wave pattern changes.

At very low speeds, the waves made by the ship are very small; some diverging waves around the shoulders and at the bow can be noticed only on extremely full forms. The wave resistance is almost negligible, and the total resistance is almost entirely viscous in character. As the frictional resistance varies at a power of the speed a little less than two, below $Fn = 0.10$ the total resistance coefficient is nearly constant, slightly decreasing, as seen for curves A and B.

If the speed is increased to about $Fn = 0.15$, a clear rise of the bow wave and a depression at the forward shoulder will be seen on fuller ships. Between the diverging waves and the hull and also behind the ship, a system of transverse waves has developed. (In addition, for all ships a bulbous bow that is not fully submerged will generate waves already at low speeds; at higher speeds these can disappear owing to the increased submergence caused by the bow wave.) A Froude number of 0.15 corresponds to the service speed of many large high-block ships such as very large crude carriers (VLCCs), and for these the magnitude of the wave resistance is quite small and of the same order as the still-air resistance. Above this Froude number, for fuller ships the resistance coefficient starts increasing more noticeably. The coaster of curve B, with a prismatic coefficient $C_P = 0.83$, cannot be driven above $Fn = 0.16$ without a large increase in resistance.

At a Froude number of about 0.2, which is the service speed of many coastal vessels and other merchant ships of moderate fullness, the wave pattern is more fully developed. These ships are more slender than those operating at a Froude number of 0.15, to reduce the magnitude of the wave resistance. The energy radiated by the transverse waves, in particular the stern wave, is becoming relatively more important in this speed range. Attention should be paid to the interference of bow and fore-shoulder wave systems.

At speeds corresponding to a Froude number of 0.25, the wave resistance can be important. A Froude number of 0.25 is typical for a sea-going ferry, a cruise liner, or a containership. For the trawler of curve D, with a fine hull form of $C_P = 0.57$, the lower humps are not very marked, and an Fn value of 0.24 can be reached before the rise in the ©-curve begins. However, speed has great significance in these ships, to get to the fishing grounds quickly and to get home to market afterwards, and they are usually overdriven up to values of $Fn = 0.30$.

Around $Fn = 0.30$, interference of bow and stern waves becomes important. At this speed, a significant and unwanted interference hump on the resistance curve is often found. The transverse waves carry a large part of the energy away. Froude numbers of 0.3 are typical for fishing vessels, tugs in free running condition, and the cruising speed of naval vessels such as frigates. The cross-channel ship of curve E, of $C_P = 0.58$, can be driven to $Fn = 0.33$ without excessive resistance, for although the prismatic coefficient is the same as in the trawler, the L/B ratio is perhaps twice as great, showing the advantage of length in delaying the onset of heavy wave-making. The same goes for modern fast car ferries that frequently run at $Fn = 0.32$ and still have limited wave resistance owing to a sophisticated hull form design.

At $Fn = 0.4$, the wave length of the transverse wave system becomes equal to the length of the ship. This results in a sharp increase of the wave resistance until the main hump is reached at a Froude number around 0.5. Ships of moderate fullness generate a pronounced wave system. A slight increase of the length of these ships and a corresponding fullness reduction to preserve displacement and capacity is extremely beneficial from a powering point of view. The loosely defined term “hull speed” is sometimes used for this Froude number range, in which the fast increase of resistance for most displacement ships can prevent a further speed increase even with large power. At the hump speed of $Fn = 0.5$, the ship sails in her own wave and only transom-type ships designed with a flat afterbody are able to pass the main hump. Ships with V-type sections in the afterbody, however, will meet a progressively higher wave resistance in this range of Froude numbers.

At speeds above the main hump at a Froude number of 0.5, the dynamic lift acting on the (flat) afterbody becomes more and more important. This is the mechanism through which the ship is lifted and the resistance curve flattens off. The range of speeds $Fn > 0.5$ is often referred to as the semi-planing range. The transverse waves become relatively unimportant at speeds well beyond the main hump. The destroyer of curve F, for which economy in the commercial sense is not paramount, normally has a top speed of $Fn = 0.6$ or more.

At a Froude number of about 1.0, the planing speed range is entered. It is to be noted that $Fn = 1$ is no precise limit or critical speed at all, unlike, for example, a Mach number 1! The dynamic lift is fully developed here and carries the weight of the ship to a great extent. Here, the wave resistance is gradually becoming less important in a relative sense. The wave pattern is reduced to a narrow V-pattern. The angle of the V-pattern decreases as the speed is increased. Actually, the extent of the Kelvin wedge is unchanged, only the wave components with $\theta \leq 35$ degrees are not generated at these high speeds, and the cusp line is invisible.

5.6 Wave Breaking and Spray. In Section 5.4, the far-field wave motion has been considered to be made up of sinusoidal waves, and much of the theory presented only applies to such waves with relatively small amplitude. However, at least closer to the ship the wave steepness can be substantial, and nonlinear effects occur that slightly modify the relation between wave length and wave speed. Moreover, as mentioned, the propagation of waves over a curved and variable flow field around the hull affects the wave properties. Still these changes are rather mild and qualitative.

A completely different type of wave behavior is wave breaking, which may occur if the wave steepness is large, therefore mostly close to the hull. Steep wave slopes will collapse in the direction of wave propagation, and a breaker is formed. Two types of wave breaking are usually distinguished. The first is a “plunging” breaker, in which a high wave crest steepens and forms a forward-directed jet at its tip, which falls down in forward direction onto the wave surface (Tulin & Landrini, 2000). The other type is a “spilling” breaker, which can be regarded as a patch of aerated water riding on top of a less disturbed underlying flow, virtually sliding down the forward face of a wave (Cointe & Tulin, 1994). The distinction is not always very clear, and a plunging breaker often becomes spilling in its later stage.

Typical wave breaking occurrences in steady ship wave patterns are:

- At a sharp bow, where the bow wave at higher speeds can climb up along the hull surface, then falls over and forms a breaker of the plunging type, the crest overturning sidewards;
- Around a blunt ship bow, where a spilling breaker may form at the front of the wide bow wave crest;
- At a pronounced fore or aft shoulder, where a spilling breaker can occur at the aft side of the wave trough; and
- Aft of the stern, as a spilling breaker on the first wave crest aft of the transom, and sometimes breaking of the diverging waves from the corners of the transom.

A completely satisfactory explanation of the inception of the breaking process has not yet been found, but a few hypotheses have been put forward. For bow-wave breaking, it has been suggested that a thin boundary layer is formed on the free surface in front of the ship and that viscous effects in this layer cause the flow to separate in front of the hull. This idea is substantiated by test results where the boundary layer has been artificially thickened by towing a plastic sheet on the surface. When thickening the boundary layer in this way, the breaking increased. In another hypothesis, the bow wave gets unstable and falls over in the forward direction. A vortex in the form of a “necklace” is then formed, as shown in Fig. 5.21. A notable vorticity has been measured in this region, supporting the hypothesis, but it is also possible that the vorticity could come from the other process mentioned. In some occurrences of ship wave breaking there is an evident effect of the viscous flow around the hull, in particular on the stern and aft shoulder waves. For aft shoulders, the occurrence of wave breaking seems accompanied by viscous flow separation just beneath the wave surface.

In the steady flows we are considering, a breaking wave still is steady in a time-averaged sense. In the breaking, the well-ordered orbital motions in the waves are converted to a turbulent flow with irregular eddies; in addition, the forward motion in the breaker generates a wake with a recognizable momentum loss, which, for bow wave breaking, flows along the hull and may be found in the wake of the ship. This phenomenon was first measured by Baba (1969), who carried out wake surveys of the flow behind bluff hulls. Fig. 5.21 is a sketch of his findings. There are two wake lobes, one on each side, outside of the main wake.

The relevance of wave breaking for hull form design is primarily that it indicates that steep waves are generated; this may be a reason to modify the design. In principle, wave breaking converts wave energy into turbulent energy and other kinetic energy contributions, and that energy loss is related with a wave breaking resistance (as opposed to the wave pattern resistance representing the contribution of the radiated waves). By measuring the momentum loss in the wake lobes, the wave breaking resistance has been determined by Baba and others, showing that this resistance component could amount to 15% of the total resistance for a full hull form. On the other hand, the energy conversion also means that the amplitude of the trailing wave system is reduced, so simultaneously less wave energy is left behind by the ship, and the sum of both is not necessarily much different from when no wave breaking would occur. An aspect for which the occurrence of wave breaking is important indeed is the generation of flow noise, relevant for naval vessels.

When scaling model tests to full scale, both wave resistance components (wave pattern resistance and wave breaking resistance) are scaled up directly. This is reasonable because both are related to the wave generation. However, the distribution of resistance between these two components may not be right because the Weber number is much smaller at model-scale, making the surface tension forces more important. There is thus considerably less breaking at model-scale, and the appearance of wave breaking is different with less white water, but this does not seem to have a noticeable effect on the extrapolation of the total wave resistance. Today, it is therefore not customary to make a distinction between the two parts of wave resistance, as this would give little advantage.

At high speeds, an additional resistance component can arise in connection with the water surface: spray drag. A sharp bow at high speeds can give rise to a thin sheet of water following the hull surface, then detaching and breaking up into spray. The resistance consequences can be reduced by mounting spray rails deflecting the sheet away from the hull.

For high-speed planing craft, a low deadrise angle and an aft trim can cause a blunt entrance of the waterline at speed. The occurrence of spray is an essential element in the attachment of the water surface to the bottom of the hull. Savitsky, DeLorme, and Datia (2007) discuss the phenomena, propose a simple estimation method, and give indications on spray rail location.

5.7 Viscous Effects on Ship Wave Patterns. The distinction between wave making and viscous flow, and the consideration of ship wave making as an entirely inviscid phenomenon as proposed in Section 5.1, is an approximation. Viscous effects on the wave pattern do

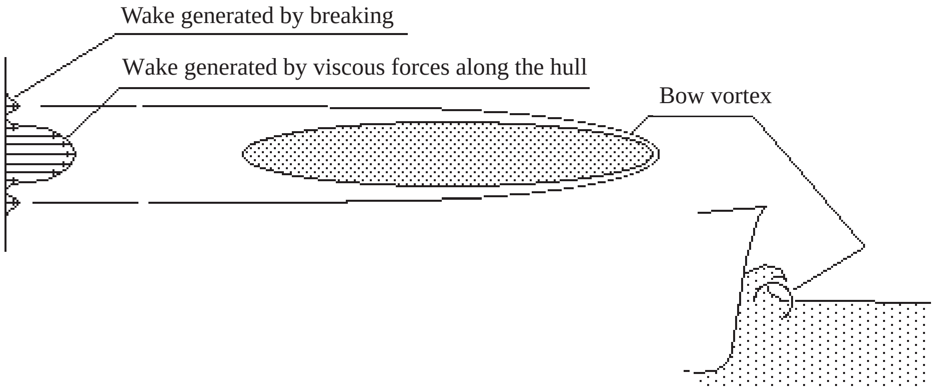

Figure 5.21 Wave breaking and the resulting necklace vortex.

exist, but they are usually rather small. Only recently, with the advent of accurate free-surface viscous flow calculation methods as discussed in Section 9.8, is it possible to quantify these effects and to see the scale effect on the wave pattern that results from the difference in Reynolds number.

A first point to be made is that viscous effects on the *propagation* of water waves in deep water, in the form of viscous wave attenuation, is entirely negligible on a ship scale. The only effects on the wave pattern are due to viscous effects on the wave *generation*, and in certain cases an effect of the wave propagating through the viscous wake of the ship leading to changes in wave length and wave direction.

The principal effect observed is a rather pronounced reduction of the stern wave system caused by the presence of the boundary layer and wake which change the pressure field around the stern. An example from computations is shown in Fig. 9.11. This reduction is usually larger at model-scale than at full scale as a result of the thicker boundary layer. More examples from computations are shown in Raven et al. (2008). In general, the importance of these viscous effects has been found to increase with the fullness of the hull form, but to depend significantly on hull form details.

Besides, viscous effects play a crucial role in the flow off an immersed transom stern that causes a recirculation area aft of it (wetted-transom flow), and affect the transitions between transom-flow regimes. Substantial changes of the wave pattern can also be caused by flow separation at the waterline, such as at a sharp aft shoulder or a bulbous bow at a too low draft. Nevertheless, in most cases these are secondary effects that do not change the considerations in the previous sections.

5.8 Shallow-Water Effects on Wave Properties. In the previous sections, we assumed that the depth and width of the waterway are unlimited. In many coastal regions, however, the water is rather shallow, which can substantially affect the flow and the wave and viscous resistance. We shall first discuss the effect of limited water depth on wave properties; the following sections then address the consequences for a ship's wave pattern and its resistance.

In Section 5.3.1 we have derived the potential of a sinusoidal wave propagating in deep water. Introducing an unknown vertical distribution $F(z)$ of the potential and substituting it into the Laplace equation yielded

$$\frac{d^2F}{dz^2} - k^2F(z) = 0$$

In deep water, the wave disturbance must vanish at infinite depth; this then led to the solution $F(z) = C.e^{kz}$. However, in a finite water depth h, the boundary condition must hold that there is no velocity normal to the bottom of the waterway, or $dF/dz = 0$ at $z = -h$. The solution then takes the form $C.\cosh k(z + h)$, so the potential becomes

$$\phi(x, z, t) = C.\cosh k\,(z + h).\sin\,(kx - \omega t) \qquad (5.34)$$

From this form of the potential we derive the wave amplitude A using the dynamic free-surface boundary condition, and thus can express the unknown constant C in that amplitude. We then obtain the expression for the velocity potential of a wave with amplitude A propagating in x-direction with wave number k and radial frequency ω, in water of finite depth h, in an earth-fixed coordinate system, as

$$\phi = \frac{gA}{\omega}\,\frac{\cosh k(z + h)}{\cosh kh}\,\sin(kx - \omega t) \qquad (5.35)$$

Furthermore, we substitute this form of the potential into the Kelvin free-surface condition

$$\frac{\partial^2\phi}{\partial t^2} + g\phi_z = 0 \qquad (5.36)$$

which yields

$$-\omega^2 + gk\tanh kh = 0 \qquad (5.37)$$

or, using $k = 2\pi/\lambda$ and $\omega = 2\pi c/\lambda$, we obtain the dispersion relation for finite water depth

$$c = \sqrt{\frac{g\lambda}{2\pi}\tanh\left(\frac{2\pi h}{\lambda}\right)} \qquad (5.38)$$

From this form of the potential and the dispersion relation valid for small-amplitude waves in shallow water, we derive the following main properties:

Dispersion Relation Equation (5.38) differs from the corresponding deep-water relation equation (5.25) by the $\tanh\frac{2\pi h}{\lambda}$ factor. Evidently, for water depth tending to infinity that factor goes to unity, and the dispersion relation assumes the form for deep water. However, for larger λ/h the factor introduces a dependence on the ratio of wave length to water depth. Fig. 5.22 shows this dependence. Here,

$$\frac{c}{\sqrt{gh}} = \sqrt{\frac{\lambda}{2\pi h}\tanh\frac{2\pi h}{\lambda}} \qquad (5.39)$$

is plotted, which is a function of λ/h only. In the left part of the graph, the curve coincides with the deep-water relation, as indicated. Once the wave length is more than two to three times the water depth, it starts deviating from this line, in the sense that waves of equal length are slower in shallow than in deep water; or, for the same propagation speed, they must be longer. When the depth h decreases more and more and the ratio λ/h becomes large, $\tanh(2\pi h/\lambda)$ approaches the value $2\pi h/\lambda$; formula (5.38) shows that then the wave velocity approaches a limiting value of

$$c = \sqrt{gh} \qquad (5.40)$$

Therefore, in shallow water there is an upper limit to the wave propagation speed!

This range of constant wave speed is essentially reached when the water depth is less than about 7% of the wave length. It is also significant that in this range of shallow-water waves, the unique relation

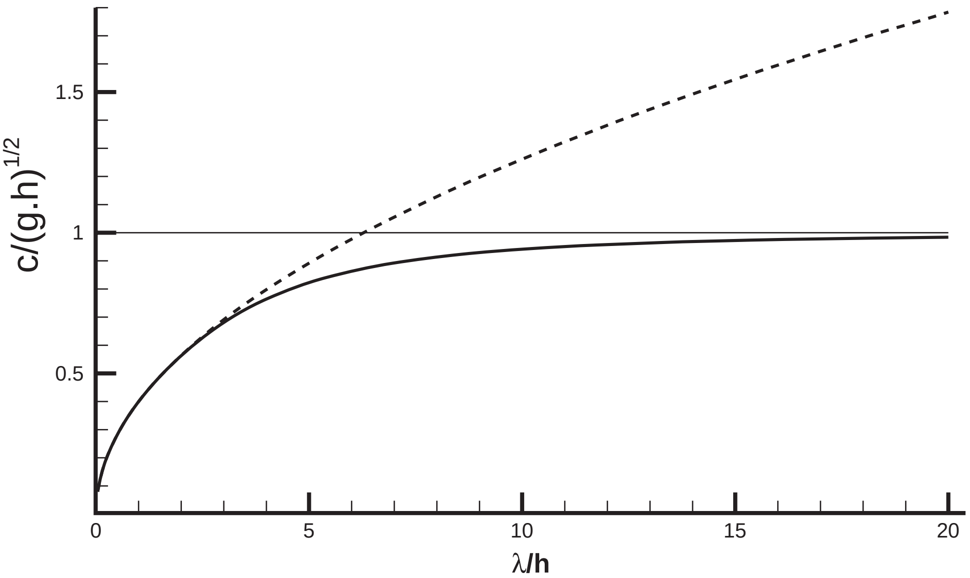

Figure 5.22 Wave propagation speed for sinusoidal wave on shallow water (*solid line*) and the corresponding deep-water relation (*dashed line*).

between wave length and wave speed is lost: all waves that are longer than about $14h$ run at essentially the same speed. Thus, as far as wave properties are concerned, "shallow" means a small ratio of water depth to wave length; the same waterway can be shallow for long waves and deep for short waves.

Velocity Field From the expression for the potential, it is easy to derive the velocity field induced by the wave. As Fig. 5.23 indicates, the circular paths of fluid particles in a deep-water wave become elliptical paths in shallow water, with an increased horizontal component and decreased vertical component. At the bottom the latter actually vanishes and the fluid motion is a purely horizontal oscillation.

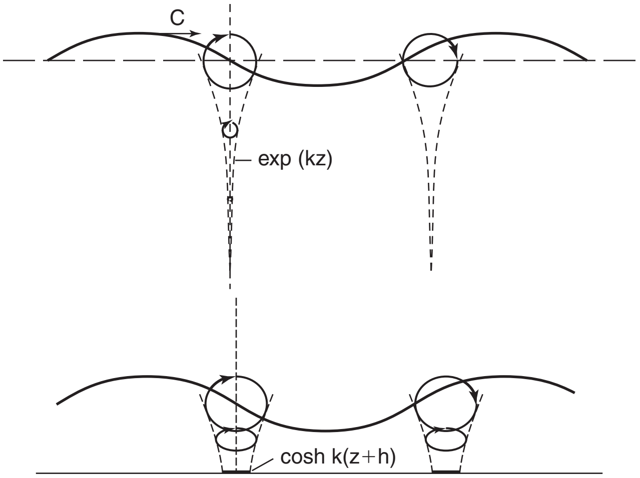

Figure 5.23 Paths of fluid particles due to propagating sinusoidal wave, in deep water (*top figure*) and shallow water (*bottom figure*).

Vertical Distribution Fig. 5.24 illustrates the variation of the length of the horizontal axis of these elliptical paths with distance beneath the surface. It thus compares the amplitude of ϕ_x for a wave of equal length and amplitude in deep water and in shallow water for an arbitrarily chosen water depth $h = \lambda/2\pi$. It is noteworthy that for the same wave amplitude and wave length, the horizontal velocity components are substantially larger in shallow than in deep water.

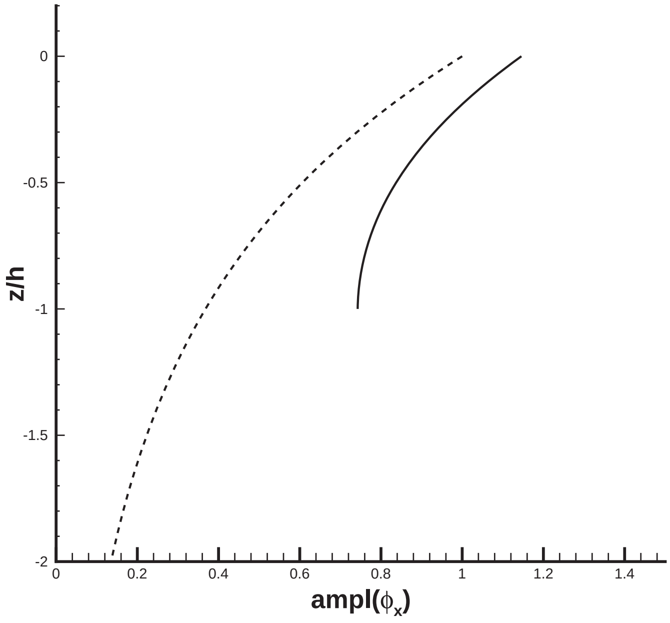

Figure 5.24 Comparison of vertical distribution of horizontal velocity amplitude in deep and shallow water (dashed and solid line, respectively), for same wave amplitude and wave length $\lambda = 2\pi h$.

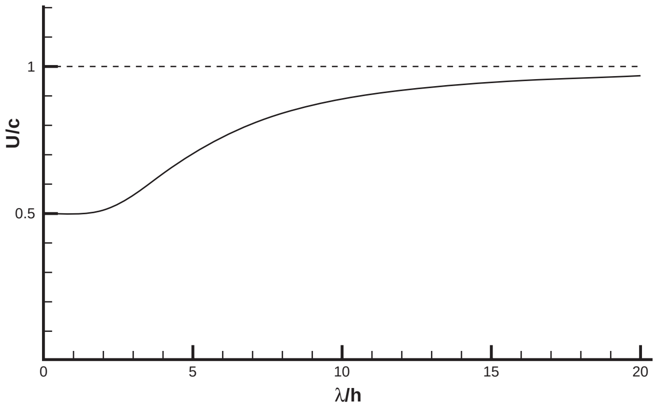

Figure 5.25 Ratio of group velocity and wave velocity, as a function of wave length/water depth ratio.

Group Velocity In Section 5.3.2, we have seen that in deep water, the group velocity of a wave is just half the wave propagation speed. As is derived in Lighthill (1980), in water of depth h the ratio of group velocity c_g to wave propagation speed c is given by

$$c_g/c = \frac{1}{2}\left(1 + \frac{4\pi h/\lambda}{\sinh\,(4\pi h/\lambda)}\right) \tag{5.41}$$

dependent on the water depth/wave length ratio. Fig. 5.25 illustrates its behavior. As further evidence of the completely different character of shallow-water waves, we notice that for $\lambda/h \to \infty$, the group velocity becomes equal to the wave speed. As will appear, this has some important consequences.

With these wave properties, we have collected enough material to consider ship wave making in shallow water, which will be done in the next section.

5.9 Shallow-Water Effects on Ship Wave Patterns. In Section 5.4.2 we discussed how a ship's wave pattern consists of wave components traveling in various directions, having propagation speeds $c = V\cos\theta$, dependent on the divergence angle θ, the angle between the direction of wave propagation and the ship's longitudinal direction. Of course this relation still holds in shallow water, as all wave components must be steady in a coordinate frame moving with the ship. However, the relation between wave speed and wave length does change in shallow water.

We saw that in shallow water there is an upper limit to wave speed. The ratio between ship speed and this maximum wave speed will appear to be an important parameter. This is the Froude number based on water depth:

$$Fn_h \equiv \frac{V}{\sqrt{gh}}$$

Evidently, the geometry of a ship's wave pattern in shallow water not only depends on its length Froude number but also on its depth Froude number, which modifies the wave lengths and thus the interference of wave components. Based on the value of Fn_h various flow regimes can be distinguished, which will be discussed in the following subsections.

5.9.1 Low Subcritical: $Fn_h < 0.7$. As long as the water depth is large compared with even the longest waves in the ship wave pattern, no change of the shape of the wave pattern is noticed. This holds as long as the water depth is more than one-third of the transverse wave length, so

$$h > \frac{2}{3}\,\pi Fn^2 L \qquad \text{or} \qquad Fn_{\mathrm{h}} < 0.7$$

approximately. In this depth-Froude number range, the wave lengths and directions will be essentially unaffected.

However, this does not mean there are no shallow-water effects yet. Even for a small depth Froude number the ratio h/T (where T is ship draft) can be rather small, meaning the vessel sails with little keel clearance. The bottom of the waterway then restricts the flow under the ship and forces it to pass along the sides of the hull rather than under its bottom. As a result, the flow will follow a more horizontal path, along waterlines rather than buttocks. This path will often have larger curvature and, together with the mirroring effect of the bottom, this causes larger pressure gradients. Simultaneously, the increased flow speed past the vessel due to the proximity of the bottom means a lower pressure, causing an increased dynamic sinkage of the vessel. Both factors contribute to an increase of the wave *amplitudes* in shallow water, even in the regime $Fn_h < 0.7$ where the wave *lengths* are still unaffected. This effect depends on geometric parameters such as h/T, h/B, etc.

A further effect noticed in this regime is the fact that the primary wave disturbance, the area of overspeed next to the hull, extends to larger distances in shallow water. This is noticed as a stronger "suction" caused by a ship in shallow water or a channel.

Fig. 5.26 shows the computed potential flow past the hull of a tanker (the same KVLCC2 case as in Fig. 5.5) in deep and shallow water, illustrating the strongly increased pressure gradients, the much larger extension of the primary disturbance (the area of water level depression around the hull), and the increased wave amplitudes (mostly the transverse wave next to the hull). For this particular case with $h/T = 1.20$, the calculated sinkage increased by a factor of 4 and the bow-down trim by a factor of 3.

Besides these changes in the potential flow and wave making, the viscous flow is also affected. The increased overspeed next to the hull increases the frictional resistance. Moreover, the boundary layer along the hull is driven by the outer inviscid flow, and thus will also follow a more horizontal path and is subjected to larger pressure gradients. Near the stern, this may lead to an increased thickening of the boundary layer,

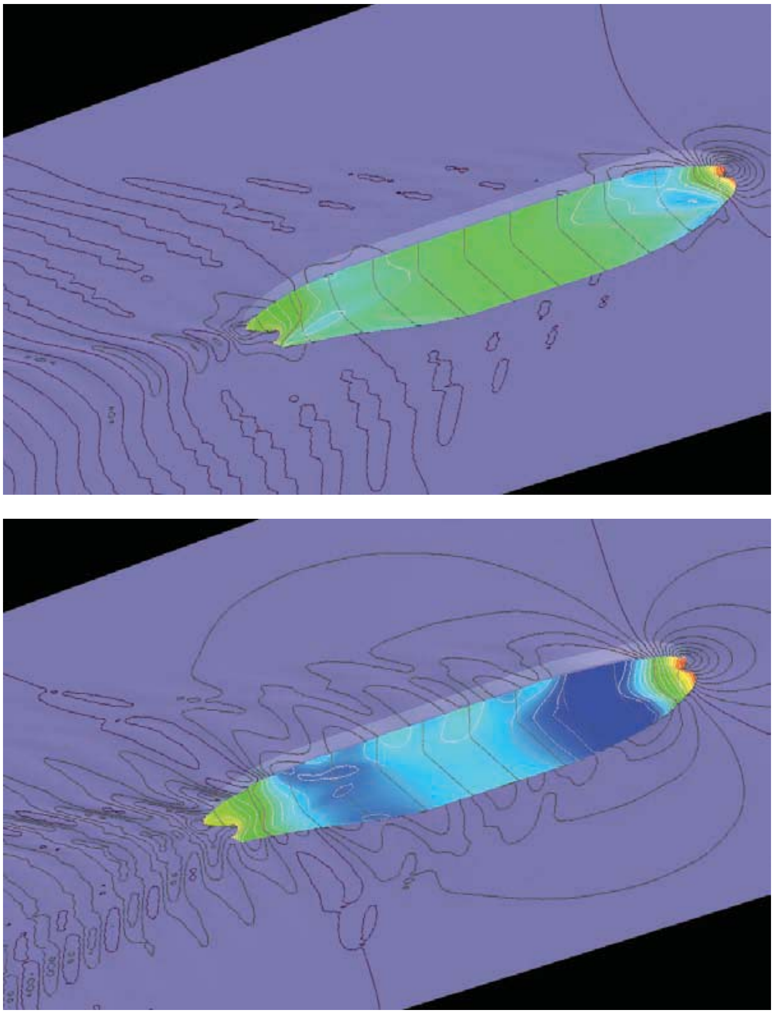

Figure 5.26 Hull pressure distribution and wave pattern for a tanker at $Fn_L = 0.142$. *Top*: deep water; *bottom*: shallow water ($h/T = 1.20$).

possibly leading to flow separation. Thus also the viscous resistance can be increased substantially due to a limited water depth, as expressed by h/T, h/B, and similar parameters. The modified flow direction may lead to additional effects resulting from an imperfect appendage alignment, causing further resistance consequences.

5.9.2 High Subcritical: $0.7 < Fn_h < 0.9$. For a further decreasing water depth or increasing speed, the shape of the wave pattern will start to change. Historically, these changes have been studied by Havelock (1908) for a point pressure impulse traveling over a free-water surface; Fig. 5.27 shows a graph of his results.

Upon a decrease of the water depth, the limit $h < \lambda/3$ will be passed first for the longest wave components, the transverse waves. As their speed must be equal to the ship speed, their length is increased by the limited depth, as can be read from Fig. 5.22. At the same time, diverging components in the ship's wave pattern can still be unaffected. For further increasing Fn_h, more and more components will start changing.

The increase of wave lengths is accompanied by another remarkable change. In Section 5.4.3 it was demonstrated that the wave pattern of a ship is contained within the Kelvin wedge, the top angle of which is determined by the ratio of group velocity to wave propagation velocity. This ratio, 0.5 in deep water, is increased in shallow water. Reconsidering Fig. 5.11 in Section 5.4.3, in shallow water the ray *OE* will thereby be further outward. The location where waves with a given divergence angle θ are found moves outward, and the width of the Kelvin wedge increases with increasing Fn_h until, as we will see, its half top angle is 90 degrees at $Fn_h = 1$.

Simultaneously with these changes in the shape of the wave pattern, the proximity of the bottom still increases

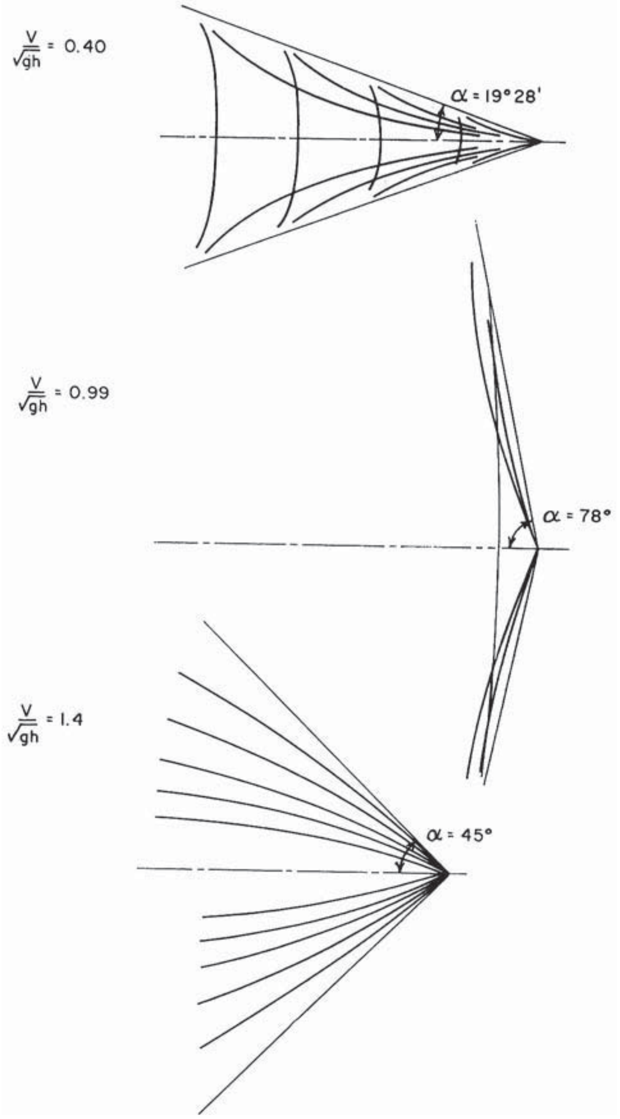

Figure 5.27 Change of wave pattern of a pressure patch with varying Fn_h, according to Havelock (1908).

the wave amplitudes and the wave and viscous resistance by the mechanisms mentioned before, as determined by h/T, h/B, and similar parameters. Therefore, two different physical shallow water effects occur simultaneously, each dependent on its own parameters.

5.9.3 (Trans)critical: $0.9 < Fn_h < 1.1$. In a (not precisely bounded) transcritical range around $Fn_h = 1$, shallow water effects can be dramatic. As the transverse waves move as fast as the ship itself, if the depth Froude number $Fn_h = 1$ they move at the maximum wave speed $\sqrt{gh}$ and become pure shallow-water waves. This means that their length is not determined by the ship speed. According to linear theory, these waves are nondispersive and a regular trailing wave pattern consisting of transverse waves with constant length is not necessarily present. In practice, strong transverse crests at bow and (in particular) stern are often observed.

For these critical waves, the group velocity is equal to the wave speed. Consequently, the wave energy does not lag behind and is not spent in a trailing wave system, but is kept in the wave itself where it is generated. The pressure field (and resistance) of the ship continuously feeds energy into this wave, which can grow quite strongly. The whole transverse wave system might not become steady—at least, differences in the critical wave pattern dependent on the time spent at that speed have been measured (Doyle, Whittaker, & Elsaesser, 2001). Actually, the growth of the wave height will be limited by energy loss or dispersion caused by nonlinearities, wave breaking, and the growth of the lateral extent of the wave crests.

From the fact that the group velocity approaches the wave propagation velocity for $Fn_h \rightarrow 1$, it can be understood that the Kelvin wedge as such has ceased to exist. The transverse waves extend further and further in lateral direction during a prolonged critical-speed operation.

If these critical waves are substantial, a large amount of water is pushed ahead, and a very large increase of the resistance occurs, accompanied by a large trim and sinkage. Most displacement ships will be unable to pass critical speed just by lack of power or because of hitting the bottom.

It is, however, important to realize that the only waves that are critical at critical speed are the transverse waves. At the same time, divergent waves which are shorter and slower are still subcritical, and some may even be hardly affected by water depth. For a ship, therefore, sharply diverging waves forming the familiar sequence of short crests and troughs arranged around the ray direction may well be observed simultaneously with critical transverse waves (see the middle graph of Fig. 5.28).

Critical speed effects can be quite dramatic for some ships, causing a large wave buildup and a drastic increase of resistance, but may be hardly noticeable for other ships. An important insight is that this depends on the strength of the transverse waves the ship generates. Very slender ships tend to generate diverging rather than transverse waves. Also, fast ships operating at length Froude numbers well beyond the primary hump ($Fn_L >> 0.5$) hardly generate transverse waves. When such vessels pass critical speed, the theoretical effects on those transverse waves may be unnoticeable (although a prolonged operation at critical speed might change this). Such an experience is reported in Stumbo, Elliot, and Fox (2000). Conversely, if critical speed coincides with a speed at which the strongest transverse waves are generated, for instance at $Fn_L = 0.4$ (taking into account the longer waves

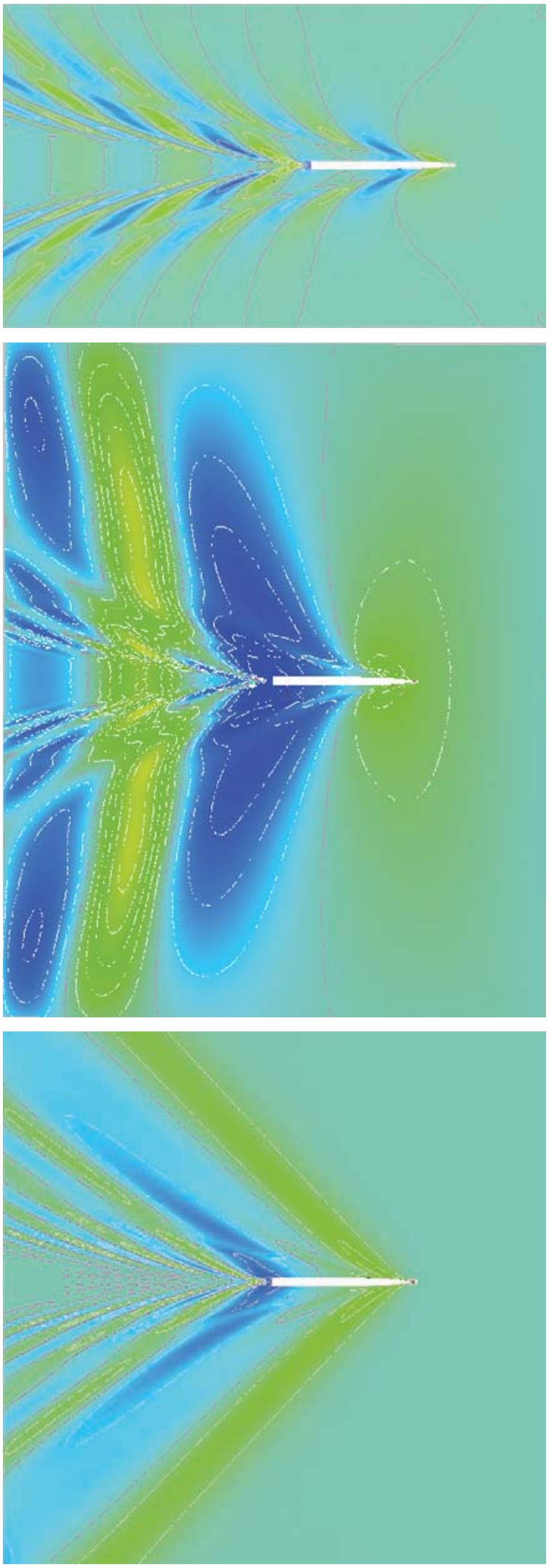

Figure 5.28 Effect of water depth on wave pattern for a ship at $Fn_L = 0.35$, as computed. Top to bottom: $Fn_H = 0.40$, 0.99, and 1.40.

in shallow water), critical speed effects will be very large. This would be the case for $L/h = 6.25$ and in a wide range around it.

If the waterway is laterally restricted as well, such as in a channel, but also in a towing tank, some peculiar effects can be observed in the transcritical speed range. The lateral restriction means that the transverse waves can build up and start moving ahead of the vessel, forming a series of solitary waves preceding the vessel (or model). In a model basin, this causes periodic variations in all measured flow quantities, which would not be present in the corresponding unlimited-width situation. For full-scale ships this phenomenon is rarely of importance.

5.9.4 Supercritical: $Fn_h > 1$. If the speed increases or the depth decreases further, the ship enters the supercritical range. The ship speed now is larger than the maximum wave propagation speed; therefore, transverse waves cannot exist and are left behind at passage of the critical speed. However, diverging waves can still be present. Because $c = V.\cos\theta$ for all steady wave components, the wave speed limit $c \leq \sqrt{gh}$ means that $\theta \geq \cos^{-1}(1/Fn_h)$.

The wave with this limiting value of θ is a shallow-water wave, it is nondispersive, the group velocity equals the phase velocity, and it forms a single continuous crest and trough without a trailing system of parallel wave crests. This wave forms the outer boundary of the entire wave system at supercritical speeds. The higher the depth Froude number, the narrower the area in which the wave system is found. Although the wave pattern is again confined within a triangular area, this is not a Kelvin wedge: its top angle is determined by the ratio of ship speed and maximum wave speed, not by the ratio of wave speed and group velocity.

The outer waves have similar properties as the transverse waves at critical speed, but usually have less build-up. Because the wave energy moves outward from the vessel along the crest, it does not accumulate in the way it does at critical speed. In practical cases, for ships that are able to reach supercritical speeds the outer waves may be hardly visible, but they still can have important consequences, as discussed in Section 5.11. Inside the pattern there are still subcritical waves as well, moving at larger divergence angles. The radical changes in the wave pattern are usually accompanied by a substantial decrease of the trim and sinkage and the resistance when critical speed is passed.

Figs. 5.27 and 5.28 illustrate the wave pattern in the various speed regimes for a pressure patch (Havelock, 1908), and for a ship (as computed with a free-surface panel code). In the latter case, the computations are for a constant speed of the ship ($Fn_L = 0.35$) and varying water depth, again yielding $Fn_h = 0.40$, 0.99, and 1.40. The change of wave properties in shallow water appears to bring about dramatic changes of the shape and amplitude of the wave pattern.

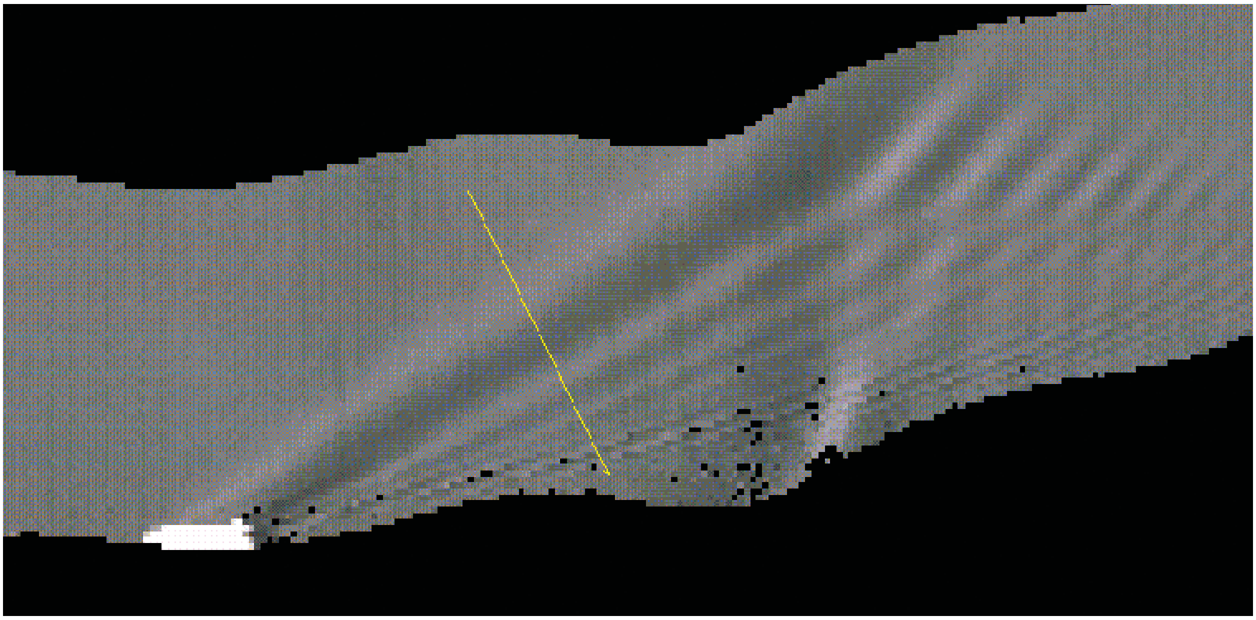

Figure 5.29 Supercritical wave pattern at Fn_h = 1.5, as measured from an airplane. (Picture courtesy of E. Bolt, Transport Research Centre, Ministry of Public Works and Water Management, Netherlands.)

Fig. 5.29 is a visualization of a wash pattern of a catamaran ferry running at $Fn_L = 0.41$, $Fn_h = 1.5$. Remarkably, this is a full-scale measurement carried out on a lake! A laser altimetry system has been used, operated from an airplane, to provide a unique mapping of the overall wash pattern in a large domain (Bolt, 2001). Fig. 5.29 shows the scanned part of the pattern. Clearly, the leading wave of the supercritical pattern is a very long wave with a continuous crest and is followed by a second crest diverging away from it at a small angle. Inside this pattern, waves at larger divergence angles are seen, in particular a set of subcritical, dispersive waves forming the familiar fan-shaped pattern, probably originating from the transom sterns. Along the top edge of the scanned area, the waves reach a deeper part of the waterway and change their direction and length.

5.10 Shallow-Water Effects on Resistance. The effect on resistance caused by these changes in wave pattern in shallow water has already been investigated by Havelock (1908) for a pressure disturbance of linear dimension l travelling over water of depth h. The resistance curves are reproduced in Fig. 5.30. Each curve is marked with the value of the ratio of depth of water h to the characteristic length of the disturbance l, that marked ∞ being for deep water. When the ratio h/l is 0.75, there is a marked peak at a speed corresponding to a value of $V/\sqrt{gh} = 0.86$. Because $\sqrt{h/l} = 0.866$, this corresponds to $Fn_h = 1$, the critical speed. The same goes for the peaks in the other curves. At this speed, the resistance is much greater than in deep water, in particular for small h/l. Beyond the peak, in the supercritical range, the resistance falls below the deep water value.

The characteristic behavior of the resistance of a high-speed ship in shallow water is illustrated in Fig. 5.31, which shows resistance and trim curves for a model of a destroyer run in different depths of water (Rota, 1900). Fig. 5.32 shows the same data as a percentage increase in resistance relative to deep water, plotted against Fn_h. On each curve in Fig. 5.31, the critical speed $Fn_h = 1$ for that particular depth is marked by an arrow. Considering the curves for the shallowest depth, $h/T = 3.08$, it will be seen that as

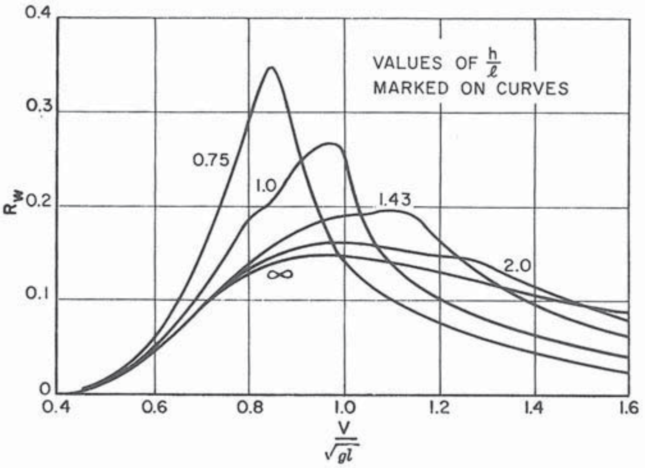

Figure 5.30 Effect of shallow water on wave resistance, according to Havelock (1908).

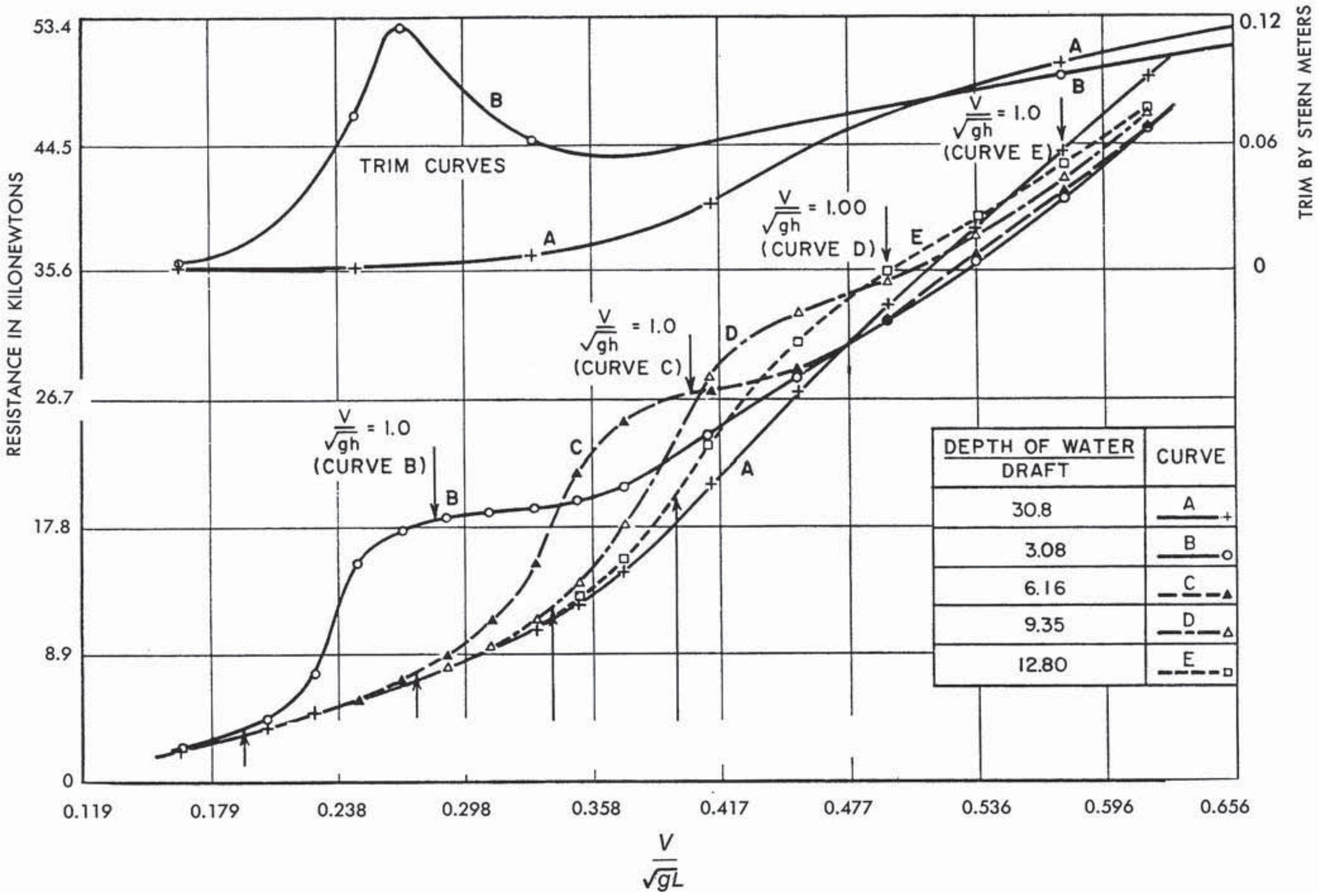

Figure 5.31 Resistance of destroyer in shallow water.

the speed of the model approaches the critical speed, the trim by the stern and the resistance both begin to increase very rapidly. Fig. 5.32 shows that the peaks occur at values of $V/\sqrt{gh}$ somewhat less than unity. The percentage increase at the peak is greater for a smaller ratio of draft to water depth, and for the smallest depth an almost threefold resistance is found!

When the critical speed is passed, the trim falls off very quickly. In addition, the resistance increase caused by shallow water decreases quickly above the critical speed. Well above critical speed the resistance is somewhat less than in deep water, and the same generally applies to the wave amplitudes, trim, and sinkage.

The large resistance peak at critical speed is the cause of the fact that nearly all displacement ships operate in the subcritical zone; faster ship types like planing craft, multihulls, and similar ship types frequently operate in the supercritical range. Just as for the wave amplitudes, the magnitude of the resistance peak at critical speed also depends on the strength of transverse waves generated by the vessel at that speed.

For practical purposes it is important to be able to estimate how the resistance of a given ship will be increased by limited water depth, and we will now describe some simplified approaches to make such estimates. These are applicable to the subcritical regime only.

In Section 5.4.5, we considered a simple theory on wave interference effects, based on only the transverse wave lengths and the distance between locations on the hull where such waves are generated. In shallow water, a wave of a given length will move more slowly than in deep water; correspondingly, for a ship wave pattern, the same interference will occur at a lower speed. Thereby, the shape of the wave resistance curve and its humps and hollows will be shifted to lower speeds.

This insight underlies an approximate method to estimate the effect of shallow water on resistance. Schlichting (1934) analyzed shallow-water effects for subcritical speeds, based on theoretical considerations and on model experiments carried out in the Hamburg and Vienna towing tanks. His method is schematically illustrated in Fig. 5.33. Suppose we know the frictional and total resistance curves for deep water. At any particular speed V_∞ in deep water, they are R_F and R_T respectively, indicated by the points E and A in the

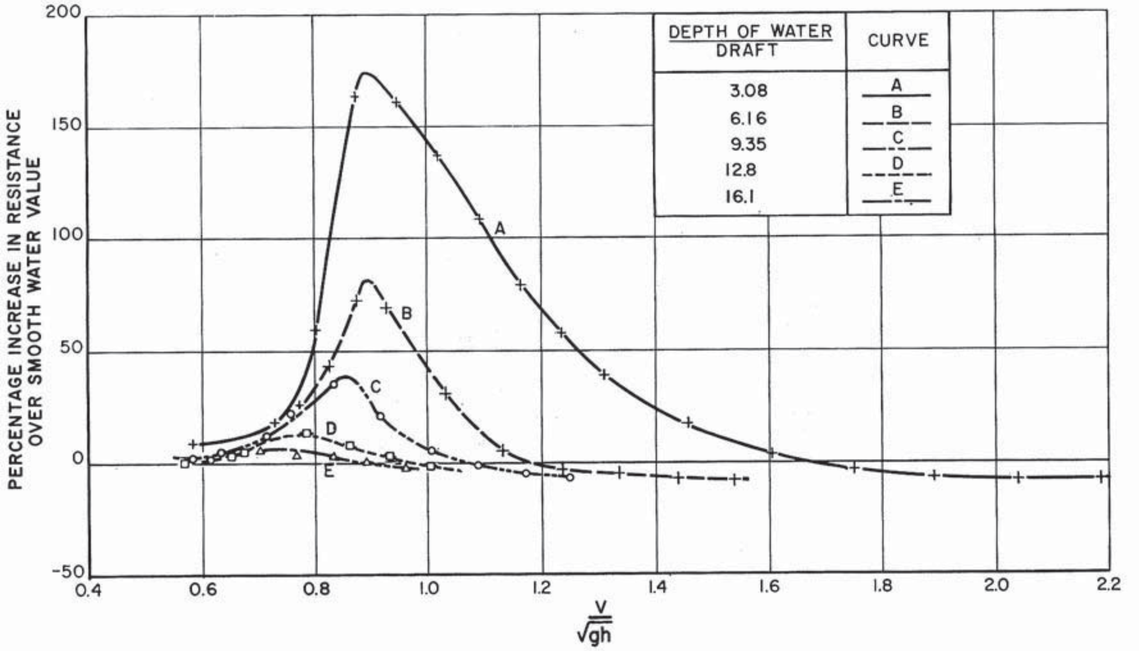

Figure 5.32 Percentage increase in resistance in shallow water. Same model as Figure 5.31.

graph. At this speed, the transverse waves generated by the ship have a wave length λ_0 such that

$$V_\infty = \sqrt{\frac{g\lambda_0}{2\pi}} \tag{5.42}$$

In water of depth h, the same wave length λ_0 would be generated at some lower speed V_I where

$$V_I = \sqrt{\frac{g\lambda_0}{2\pi}\tanh\frac{2\pi h}{\lambda_0}} \tag{5.43}$$

and the ratio of the two speeds is

$$V_I/V_\infty = (\tanh 2\pi h/\lambda_0)^{1/2} = (\tanh gh/V_\infty^2)^{1/2} \tag{5.44}$$

A curve of V_I/V_∞ is shown to a base of $V_\infty/\sqrt{gh}$ in Fig. 5.34. Schlichting then assumed that the wave-making resistance in shallow water at speed V_I would be the same as that at speed V_∞ in deep water, in view of the effect of interference between transverse wave components from, for example, the bow and stern or bow and fore shoulder. The total resistance at speed V_I would then be found by adding the wave-making resistance $R_{W\infty}$ to the appropriate frictional resistance at this speed, R_{Fh}. In Fig. 5.34, we thus construct point B of a curve corrected for shallow water effects on the wave resistance, such that the line AB is parallel to EF in Fig. 5.33.

As already stated for the low-subcritical range, the reduced water depth will also affect the viscous resistance. The increased flow speed past the hull caused by the proximity of the bottom increases the frictional resistance, and the increased pressure gradients may increase the viscous pressure resistance. Schlichting also provides estimates for this resistance increase, again expressed as a speed reduction δV_P, based on model tests in deep and shallow water. As indicated in Fig. 5.33, this second speed correction δV_P is now set out horizontally from B, and the resulting point C will be a point on the curve of total resistance in

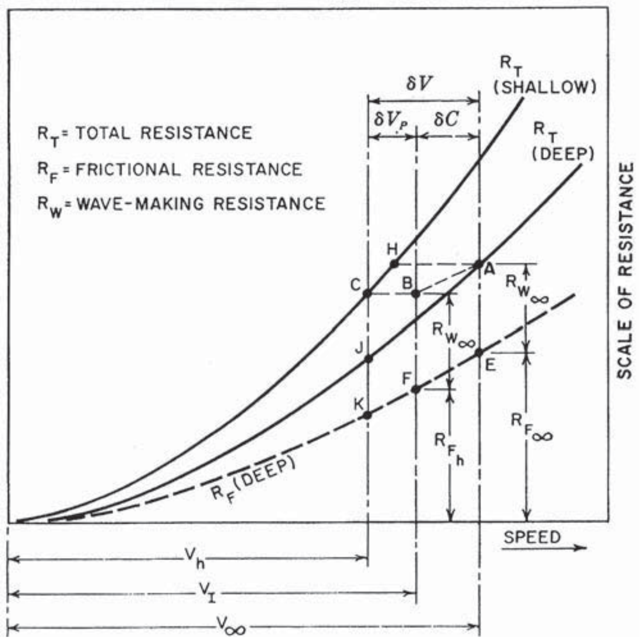

Figure 5.33 Determination of shallow water resistance by method of Schlichting (1934).

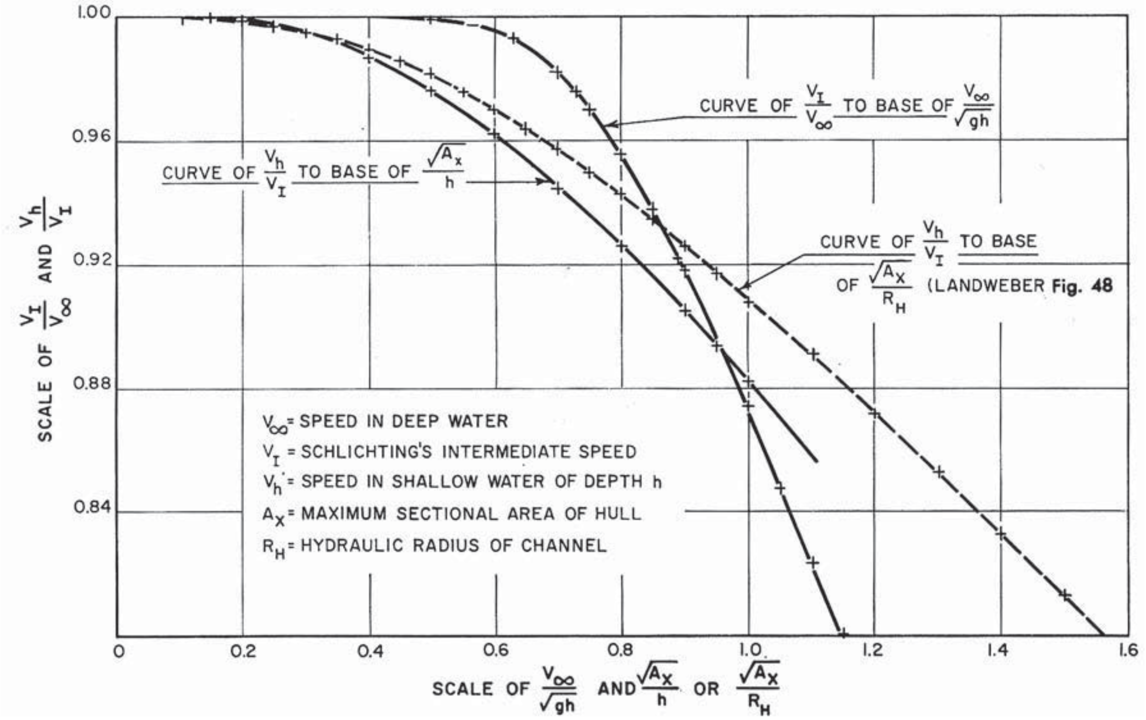

Figure 5.34 Curves of velocity ratios for calculating resistance in shallow water (Schlichting, 1934).

shallow water. The corresponding speed is V_h. This construction can be made for a number of points to obtain the whole curve.

Schlichting found that the principal factor controlling δV_P was the ratio $\sqrt{A_M}/h$, where A_M is the maximum cross-sectional area of the hull (marked A_X in Figs 5.34 and 5.35) and h is the water depth. Fig. 5.34 shows the curve of V_h/V_I, which represents the second speed correction, against this parameter, as derived by Schlichting from his model tests. Also, the ratio V_I/V_∞ (the wave resistance correction) is shown for different water depths.

The total speed loss $\delta V = \delta C + \delta V_P$ is shown as a percentage of the deep-water speed in the contour diagram Fig. 5.35. It should be noted that at point C in Fig. 5.33, the total resistance in shallow water at speed V_h is less than that in deep water at speed V_∞ (point A).

Schlichting's method is not theoretically rigorous, and several objections can be made. In particular, the assumption of equal wave resistance in deep and shallow water when the lengths of the ship-generated transverse waves are equal is a simplification, as it disregards both the contribution from diverging waves and the increase of wave amplitudes due to the proximity of the bottom; probably both effects partly cancel in Schlichting's data. Also, the effect on viscous resistance is clearly dependent on hull form. However, Schlichting's method may be looked at as an engineering solution of a complicated problem and is useful for a first estimate of limited shallow-water effects on the resistance of a ship.

A simpler method was developed by Lackenby (1963). Its purpose is just to correct the results of speed trials carried out in a somewhat limited water depth, and it is unlikely to be precise for more severe shallow-water effects. The speed correction again depends on the two parameters: $\sqrt{A_M}/h$ representing the effect on viscous resistance due to the proximity of the bottom, and Fn_h representing the effect on wave resistance. The speed correction is available in a diagram (Fig. 5.36), which largely matches that of Schlichting but details the area of small shallow-water effects, and as the expression

$$\frac{\Delta V_s}{V_s} = 0.1242\left(\frac{A_M}{h^2} - 0.05\right) + 1.0 - \left(\tanh\left(\frac{gh}{V_s^2}\right)\right)^{\frac{1}{2}} \quad (5.45)$$

More recently, Jiang (2001) showed for some cases that the water depth effect on resistance curves could be represented by a speed correction based on the mean dynamic sinkage of the model, z_v. Plotting resistance data measured at different water depths against the effective speed

$$V_e = \sqrt{\frac{V_s^2 + 2gz_v}{1 - z_v/h}} \quad (5.46)$$

the curves essentially coincided. The mean sinkage is to be measured, estimated, or computed using, for example, a panel code.

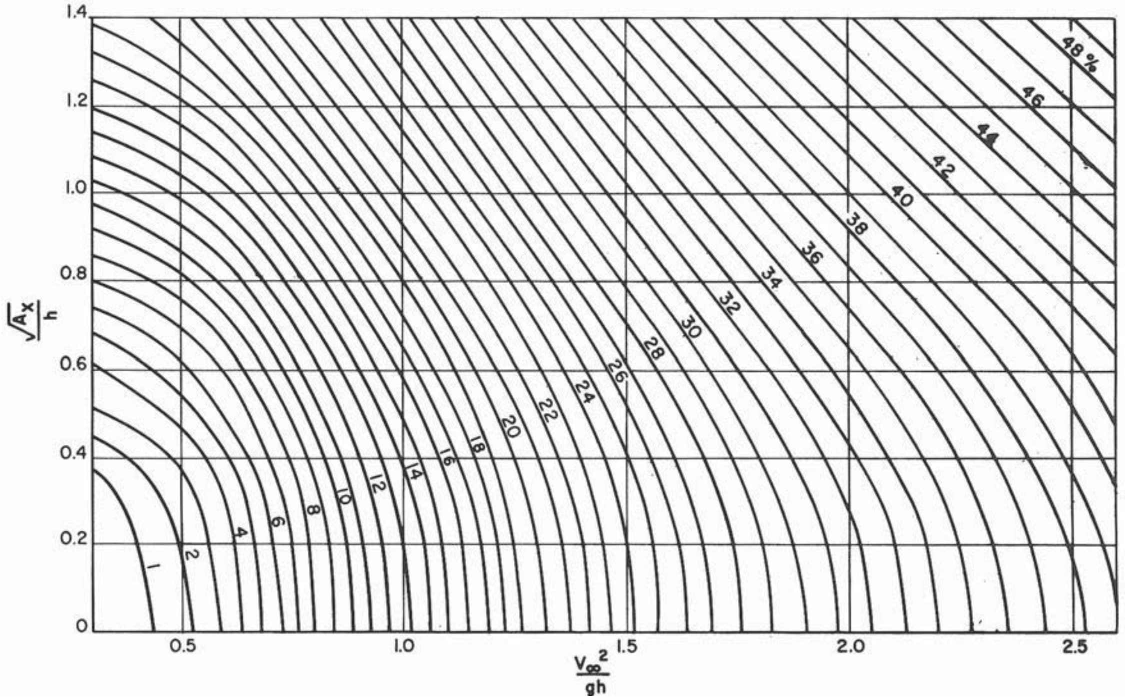

Figure 5.35 Schlichting's (1934) chart for calculating reduction in speed in shallow water.

All these semi-empirical correction methods can be useful to provide indications of shallow-water effects in the subcritical regime. However, physically the effects are complicated and hull-form dependent, and precise estimates cannot be expected based on one or two parameters.

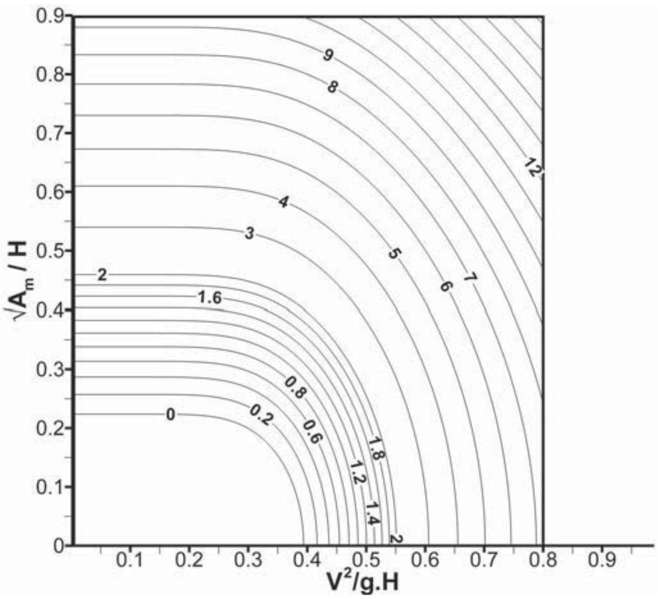

Figure 5.36 Lackenby's (1963) diagram for calculating reduction in speed in shallow water. The labels indicate the percentage change of the speed.

5.11 Far-Field Waves and Wash

5.11.1 Introduction. Since 1990 there has been increasing attention to detrimental effects of ship waves, in that context often called "wave wash." Ship waves impinging on shores incidentally have been found to cause bank or bottom erosion, damage or nuisance to moored vessels or small craft, endangerment of people bathing or walking along the coast, or harm to natural environments. Such effects often are caused by operation of fast ferry services, sometimes also by conventional ships as a result of increasing traffic, the use of larger vessels, or higher propulsion power.

In the early years of introduction of fast ferry services, the wash problems came quite unexpectedly, as the waves generated by these vessels in the open sea are often quite low. Problems that occurred were often caused by operation in shallow water or by propagation of the ship waves into shallow water.

As is now understood, there are several different categories of wash-related problems:

- A basic difference with slower ships is the fact that fast vessels generate waves with longer wave periods; typical periods of 7–10 seconds are quoted. It thus has happened that the operation of fast ships caused problems for vessels moored along the waterway, as they simply responded more strongly to the longer wave periods.
- Some of the problems have been caused by operation near critical speed. As is evident from the previous description, at critical speed wave generation can be

strongly amplified, dependent on the ship type. Moreover, the critical waves are nondispersive according to linear theory, and after a sufficient duration of the critical-speed operation, they will have rather little decrease of amplitude with distance from the track of the vessel. Therefore, at large distances they can be quite pronounced. These shallow-water waves contain much energy and can cause serious problems.

- Most unexpected have been the problems caused by supercritical speed operation. In view of the decrease of resistance in the supercritical regime and the modest steepness of the outer waves in the wave pattern, those problems initially were not well understood. To current understanding, the principal problems originate from the very large apparent wave periods at large distances and the slow amplitude decay, as will be discussed subsequently.
- "Shoaling" effects (i.e., the increase of wave amplitudes and wave steepness when waves approach a coast with gradually decreasing water depth) can be most pronounced for the long waves generated by fast ferries. Consequently, even when their amplitudes seem innocent at sea, these waves can cause increased erosion of coast and bottom, cause large run-up on a beach, endanger bathers, or lead to other problems.
- In addition to the aspects mentioned previously, in some situations the precise bathymetry of the waterway, the bank outlines, or the curved path sailed by the vessel have played a crucial role. As a result of refraction, wave focusing, and shoaling effects, large wave heights can occur locally. Thus it is often the combination of characteristics of the vessel and the waterway that determines the occurrence of wash effects.

5.11.2 Far-Field Wave Amplitudes. In case the waves propagate in water of constant depth, it is possible to estimate the far-field wave amplitudes directly from those closer to the vessel. This estimate must be based on a wave pattern already at a sufficient distance from the vessel to be outside near-field effects and interference from wave systems originating from different parts of the hull.

Subcritical Regime Theoretically, for most wave components the amplitude decays with the distance y to the path of the vessel as

$$A(y) \sim y^{-1/2}$$

However, for waves near the Kelvin wedge boundary (i.e., with divergence angle $\theta \approx 35°$), the decay is as

$$A(y) \sim y^{-1/3}$$

There has been some discussion whether this holds precisely for ship wave patterns (Doctors & Day, 2001) but in practice it is usually close to this.

Mathematically, it will always be the waves on the Kelvin wedge that will dominate in the limit to infinite distance; however, for vessels that have the largest wave generation in other wave components this may be irrelevant: if the waves inside the Kelvin wedge have an a times larger amplitude at a distance y than those on the Kelvin wedge, the latter would only start dominating at distances greater than $a^6 \cdot y$. This insight may resolve some of the controversy regarding subcritical decay rates, as it explains that an inverse-square root decay may well be observed in practice even at large distances.

Although these decay rates indicate how the maximum wave amplitudes in the wave pattern depend on distance to the vessel, it is important to note that the shape of a distant wave cut cannot be estimated by simple scaling of a nearby wave cut using the theoretical decay. The shape of a longitudinal wave cut changes substantially with distance from the path of the vessel, and to actually predict this, more elaborate methods are needed such as using a spectral representation (Raven, 2000).

Critical Speed Regime Here the decay rate cannot be determined from simple theory, and just some observations are available. Doyle, Whittaker, and Elsaesser (2001a) indicated that from some model tests, rather large decay rates have been found because of a more local wave build-up. However, far-field amplitudes appeared to increase, and wave decay rate to decrease, with the time spent at critical speed. Simply extrapolating wave amplitudes from a model experiment or computation disregarding the time-dependence might be misleading. For prolonged critical-speed operation, a conservative estimate would be to assume no decay of the critical waves. The more divergent waves occurring simultaneously, which are still subcritical, can be extrapolated using the normal subcritical decay rates.

Supercritical Regime The leading waves in the pattern are again nondispersive, but steady. In special model tests, decay rates have been found varying between $y^{-0.2}$ in very shallow water to $y^{-0.33}$ at somewhat larger depth/draft ratios (Doyle, Whittaker, & Elsaesser, 2001a). Although these data may not yet be sufficiently complete to use them for an actual wave extrapolation, clearly the decay of the leading waves is very slow; for smaller h/L, the wave decay becomes slower and the wave energy at a large distance increases substantially (Doyle, Whittaker, & Elsaesser, 2001). Here again, the more diverging waves further inside the pattern are more dispersive and will have a larger decay with distance.

While these data on wave decay rates are for constant water depths, variations of the water depth can have complicated effects on the wave evolution. To predict or estimate the amplitudes, lengths, and directions of ship waves after propagation over a bottom topography, special methods are needed. The physical phenomena playing a role in this can cause a large increase of wave amplitudes, so the importance of this needs to be acknowledged.

5.11.3 Far-Field Wave Periods. The relevance of the far-field wave periods has mostly to do with the behavior of waves when propagating into shallower water. Very long waves usually increase much more in height and steepness. Moreover, unlike the waves from conventional ships that approach the coast as spilling breakers, the long waves from fast vessels have been reported to cause large plunging breakers and to cause a larger wave run-up on a beach. The fact that this happens unexpectedly when the fast ship may already be out of sight adds to the problems.

In the subcritical regime, the far-field periods are easy to derive, being completely determined by the near-field wave spectrum. For the critical regime, little information is available.

The supercritical regime has provided some surprises, as described in Doyle, Whittaker, and Elsaesser (2001, 2001a). Full-scale measurements at large distances from the path of a fast ferry running at supercritical speed have displayed some extremely large wave periods at the start of the passage of the wave system; up to 20–40 sec at 3 km distance, with associated wave heights of 0.4–0.7 m. A careful examination has shown that the leading, critical wave and the second wave behind it diverge from each other at a small angle, around 10–12 degrees near the vessel, diminishing to some 2 degrees at large distances. Consequently, the separation between these wave crests, and thereby the apparent wave period, increases with distance. The resulting long-period waves undergo a large magnification by shoaling, and this has likely been the cause of some of the reported incidents caused by wash.

From the experiences with fast vessels, it can be concluded that problems have resulted from wave properties not evident at first sight; in particular in the supercritical regime, a careful consideration of the possible consequences of very large wave periods is necessary. To eliminate problems, precise consideration of the track of the vessel, the speed sailed, and the location where critical speed is passed has been successful in several instances, but this may have consequences for the viability of a fast ferry service. In the design of fast ships, it is important to pay attention to the generation of the longer waves in the first place.

Limitations for the wash generated by ships are being imposed in some countries. From the previous text, it is clear that such limitations should not just be based on wave heights, but also involve wave periods or wave energy. As this subject is currently still evolving, we will not discuss it further.

5.12 Channel Effects. If the waterway is not only shallow, but also has restricted width, such as in a canal or a river, some additional effects occur. The wave propagation speeds are not affected by the width, so the effects governed by Fn_h will in a first approximation be unchanged. However, the effect of the proximity of the bottom is magnified by the "blockage" (i.e., the ratio of the midship sectional area of the ship to the cross-section of the waterway). This increases the overspeed next to the hull, thus it increases the sinkage, the pressure gradients, the wave amplitudes, and the viscous resistance.

For moderate channel effects, a correction method similar to Schlichting's is possible. For the wavemaking part of the resistance, it is reasonable to assume that Schlichting's correction method (which depends on Fn_h) can still be applied. The speed correction to correct for the increased viscous resistance (δV_P), however, has to be modified. Landweber (1939) published the results of experiments on the resistance of a merchant ship model in a number of different-sized rectangular channels at subcritical speed. In shallow water of unlimited width, this second speed reduction is a function of $\sqrt{A_M}/h$, and Landweber sought a similar parameter which would also introduce the width of the channel, b. He found this in terms of the *hydraulic radius* of the channel, R_H.

This ratio is in common use in hydraulics, and is defined as

$$R_H = \frac{\text{area of cross-section of channel}}{\text{wetted perimeter}} \tag{5.47}$$

For a rectangular channel of width b and depth h, $R_H = bh/(b + 2h)$. When b becomes very large, $R_H = h$; this corresponds to the case of shallow water of unlimited width.

When a ship or model is in a rectangular channel, the hydraulic radius is

$$R_H = (bh - A_M)/(b + 2h + p) \tag{5.48}$$

where A_M is again the maximum cross-sectional area of the hull and p is the wetted girth of the hull at this section.

From the model results, Landweber was able to deduce a single curve giving the ratio V_h/V_I, in terms of $\sqrt{A_\mathrm{M}}/R_\mathrm{H}$ for use in restricted, shallow channels. This curve is also shown in Fig. 5.34, and it does not quite agree with that derived by Schlichting, a fact that can be accounted for by Schlichting's neglect of the effect of the width of the tank in which his experimental data were obtained.

However, channel effects can be much more severe than this, as is best explained using Kreitner's theory (Kreitner, 1934). Kreitner considered the case of a ship sailing at a small length Froude number and having a long parallel midbody, such that in unrestricted water, the flow along the hull would be essentially undisturbed and have no overspeed. In a waterway with restricted width and depth, an overspeed along the hull must then be present, such that all the inflow from ahead (with a volume flow rate $V_s.b.h$, in which b is the width of the channel) passes through the area next to the ship. Kreitner assumed this overspeed to be uniformly distributed over the cross-section of the waterway. If we define the *blockage* as $\beta \equiv \mathrm{A}_M/(b.h)$ and the overspeed ratio as

$\gamma \equiv (V_S + v)/V_S$, then for low ship speed, the overspeed ratio would simply be

$$\gamma = 1/(1 - \beta) \tag{5.49}$$

However, the overspeed is accompanied by a depression of the water surface next to the ship (again assumed uniformly distributed), according to Bernoulli's law; this depression will also cause an equal sinkage of the ship. Therefore, the cross-section next to the ship is reduced by an amount

$$b \cdot \Delta h = \frac{bV_s^2}{2g}(1 - \gamma^2) = \frac{1}{2} hbFn_h^2(1 - \gamma^2) \tag{5.50}$$

Therefore, the depression of the water level introduces an Fn_h influence on the overspeed.

Taking into account this further reduction of the cross-section and requiring that all flow passes through this reduced area, we find

$$\gamma\left(1 - \beta - \frac{1}{2}Fn_h^2[\gamma^2 - 1]\right) = 1 \tag{5.51}$$

a third-degree equation from which the overspeed ratio γ can be solved for given blockage and Fn_h.

The solution has some very interesting properties. Fig. 5.37 shows how, for increasing depth Froude number, the overspeed $\gamma\ V_s$ first increases linearly, but then starts increasing more quickly because of the water level depression. At a certain Fn_h value, the overspeed increases indefinitely, indicating it is impossible to let all fluid pass along the ship. This is the lower limit of an "inaccessible region" (marked with II in Fig. 5.37) around $Fn_h = 1$ in which no steady solution exists. The higher the blockage, the wider that region. Beyond this range, there is the opposite phenomenon of an underspeed along the hull, causing an increase of the water level and a negative sinkage that again lets all fluid pass the ship. As Kreitner derived, in the intermediate region the solution is unsteady and takes the form of a wave of translation moving ahead of the ship and a wave trough propagating aft that compensate for the excess fluid that cannot pass the ship.

Therefore, in a waterway (or towing tank) of restricted width, phenomena similar to critical speed set in at a depth Froude number significantly below 1: a large increase of the sinkage, a very large resistance increase, and various violent flow phenomena. The resulting shift of the steep rise of the resistance curve toward lower Fn_h is something to be aware of in model testing

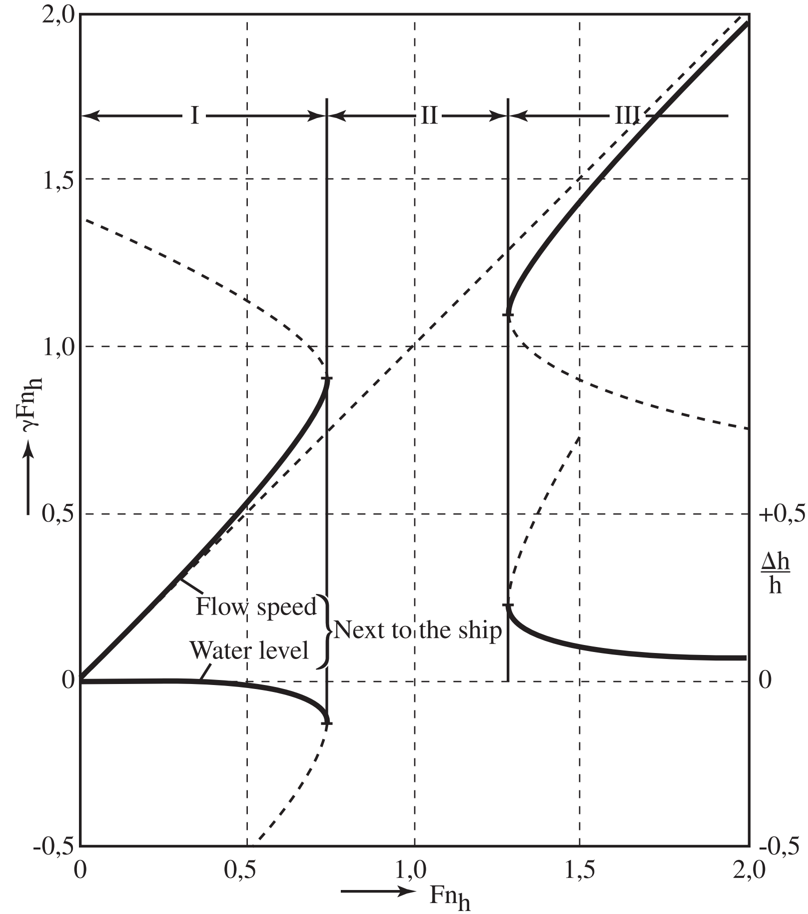

Figure 5.37 Overspeed next to ship (as a fraction of $\sqrt{gh}$) against Fn_h, for a blockage $\beta = 0.05$. (Graph from Kreitner [1934].)

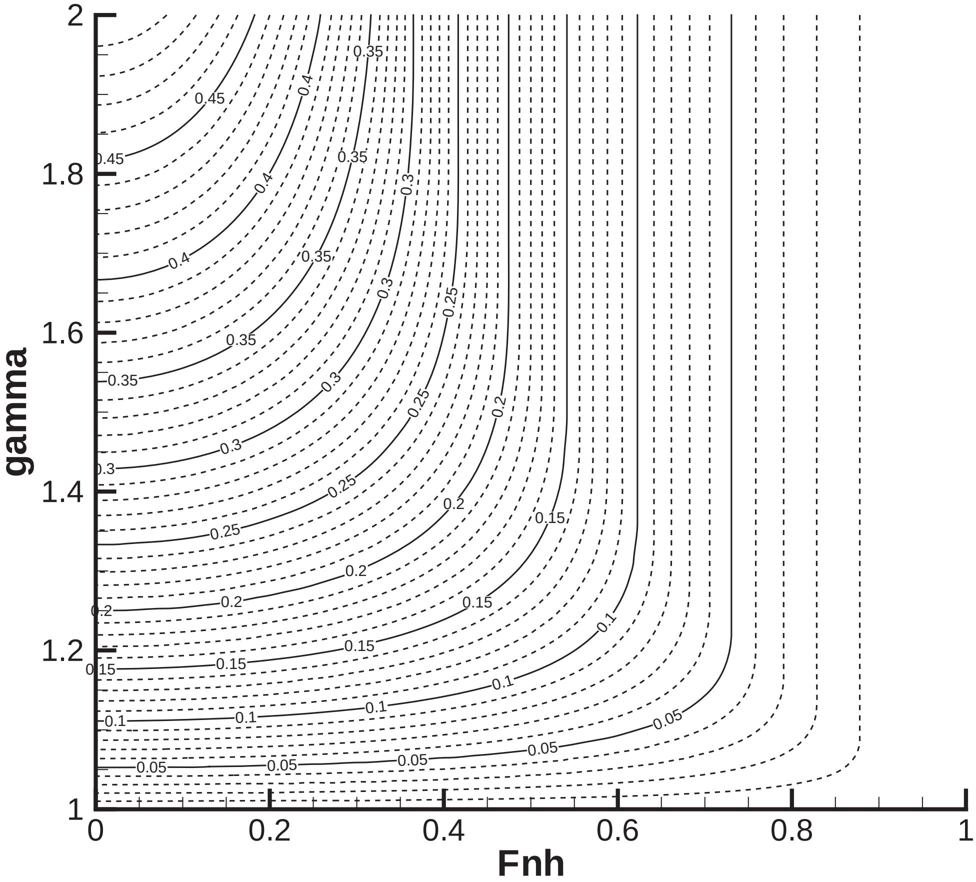

Figure 5.38 Overspeed ratio γ next to ship as a function of Fn_h, for blockage $\beta = 0.0\ (0.01)\ 0.50$.

at high Fn_h as it may cause gross errors if the resistance curve in a waterway of unlimited width is predicted based on such tests.

Fig. 5.38 shows the overspeed ratio as a function of Fn_h for blockage values from 0.01 to 0.49 for the subcritical range. The critical channel speed for a given blockage ratio can be read from the position of the vertical asymptotes.

On the other hand, the assumptions underlying Kreitner's theory, in particular that of a uniform overspeed over the entire channel cross-section, are limited to ships with long parallel midbody in relatively narrow channels, and lead to a less realistic estimation in other cases. Therefore, the quantitative results of Kreitner's method need to be used with caution.

6

The Flow Around the Hull and the Viscous Resistance

Having dealt with the wave resistance in Section 5, we will now turn to the other major resistance component: the viscous resistance. As explained in Section 5, the two components are linked, but there are good reasons to treat them separately. Therefore, the waves and all other effects of the free surface are neglected in the present section. This means that the Froude number is irrelevant and that the only similarity parameter to consider is the Reynolds number. Another effect of neglecting the free surface is that the hydrostatic pressure, which enters the equations through the free-surface boundary condition, will disappear. Thus, only the hydrodynamic pressure remains, and for simplicity the index "hd" will be dropped. Also the word "hydrodynamic" will be dropped when referring to the pressure in this section.

All viscous resistance components described in Section 4 are related to the boundary layer around the hull. For a 3D body, such as a ship hull, the boundary layer is complex and no simple solutions of the governing equations exist. However, many of the features of the 3D case are also present for simpler cases, where analytical and empirical results are available. So, in the present section boundary layers are considered for increasingly more complex bodies. The flat plate is the simplest case, followed by general 2D bodies, axisymmetric bodies, and finally the fully 3D case. Note that many relations obtained for the simpler cases may also be used as a first estimate in the more complicated cases. We will start this section with a general description of the boundary layer concept, but first a comment will be given on the coordinate system adopted in this section.

6.1 Body-Fitted Coordinate System. For solving boundary layer equations, it is considerably more convenient to use a coordinate system fitted to the hull than the global Cartesian system specified in Fig. 2.1. Body-fitted coordinate systems are curvilinear and in general nonorthogonal. However, for reasons explained later, orthogonal systems may be used in boundary layers. The ITTC nomenclature recommends the use of the coordinates x, y, z for such systems. We will adopt this convention here, although it conflicts with the definition of x, y, z as a global Cartesian system (see Fig. 2.1), also recommended by the ITTC. The risk of confusion is small, however. In connection with boundary layer equations, x is thus along the surface, in the direction of the flow at the edge of the boundary layer, y is normal to the surface, and z is directed to form a right-handed orthogonal system (i.e., along the surface at right angles to x). In the following, the three coordinate directions will also be referred to as "longitudinal," "normal," and "lateral" for the x-, y-, and z-directions, respectively.

6.2 The Boundary Layer

6.2.1 Physical Description of the Boundary Layer. The no-slip boundary condition, discussed in Section 2.4.1, states that the relative velocity between a solid surface and a fluid is zero. The fluid "sticks" to the surface because of molecular action at the interface. Moving away from the surface, the relative velocity, at least in a time-averaged sense, increases within a region of small thickness relative to the body dimensions.* This is the boundary layer, which covers the entire surface and generally grows in thickness downstream (Fig. 6.1). In the forwardmost part of the boundary layer, the flow is laminar, and the velocity increases monotonically without fluctuations toward the edge of the boundary layer. Thanks to the molecular motions in the direction normal to the surface, momentum parallel to the surface is transferred between adjacent layers of the fluid. A molecule from one level that jumps out to a higher level will have a lower momentum than the others at that level, and when it interacts with the others it will tend to reduce the speed at that level. Conversely, when a particle jumps inward, it will tend to increase the speed at the new level. The molecular motions, responsible for the jumps, thus tend to equalize the speed between the different layers of the fluid. In fluid mechanics, the fluid is assumed a continuum and the effect of the molecular motion

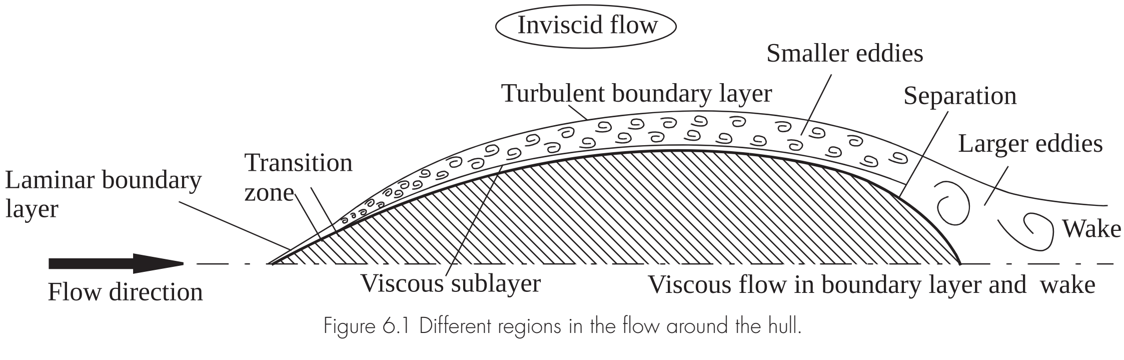

Figure 6.1 Different regions in the flow around the hull.

---

*The most common dimension to refer to is the body length. For a flat plate this is an obvious choice, but for curved surfaces the radius of normal curvature may be a more relevant measure.

is modelled as a stress determined by equation (2.10). The concept of viscosity is thus introduced through this equation, which for a 2D boundary layer is simplified to

$$\sigma_{yx} = \mu \frac{\partial u}{\partial y} \tag{6.1}$$

The longitudinal shear stress is thus proportional to the normal gradient* of velocity, and the constant of proportionality is the dynamic viscosity.

In the laminar boundary layer, fluctuations are damped because of viscosity, but if the body is sufficiently long the flow will eventually become unstable. This occurs at the point of neutral stability. The region that follows thereafter is called transitional. It is characterized by bursts of turbulence which eventually become so frequent that the boundary layer may be considered turbulent. In the innermost part of the turbulent boundary layer, known as the viscous sublayer, the flow is still essentially laminar, but interrupted by turbulent bursts.

Outside of the viscous sublayer, the turbulent boundary layer contains eddies of varying sizes, the smallest ones (Kolmogoroff scale) being of the order of 0.1 mm at Reynolds numbers relevant to ships and ship models (note that the order of magnitude is the same at both scales). The largest ones are of the same order of magnitude as the boundary layer thickness: 0.1 m at model-scale Reynolds numbers and 1–10 m at full scale.

The (macroscopic) effect of the eddies may be interpreted in a way similar to the (microscopic) effect of the molecular motions. When a fluid package due to fluctuations is moved away from the surface, it will tend to reduce the speed of the fluid at the new position and conversely when the package is moved toward the surface. This effect is normally much stronger than the effect of the molecular motions, but it may be described in a similar way, namely by introduction of a new concept: the turbulent (or eddy) viscosity μ_t. In a turbulent 2D boundary layer, the shear stress may thus be computed using the effective viscosity μ_{eff}

$$\sigma_{yx} = \mu_{eff} \frac{\partial u}{\partial y} \tag{6.2}$$

where

$$\mu_{eff} = \mu + \mu_t \tag{6.3}$$

Equation (6.2) may be generalized to the same form as equation (2.10). Note that μ_t is not a fluid property, like μ, which in hydrodynamics mostly may be considered a constant. The turbulent viscosity depends on the fluctuating velocities and varies in the flow domain. For a further discussion of the turbulent viscosity, see Section 9.

6.2.2 Approximations of First Order Boundary Layer Theory. The boundary layer concept, introduced by Prandtl (1904), enables a very convenient division of the flow into a region near the hull and in the wake where viscosity is dominating the flow, and an outer region, where viscosity may be neglected (see Fig. 6.1). Note that the reason why viscosity may be neglected in the outer region is that the velocity gradients (i.e., the rates of strain) are negligible. Although the viscosity μ is the same everywhere, its effect disappears if the velocity gradients can be neglected. The outer flow is therefore, somewhat inconsistently, called inviscid.

Boundary layer theory is based on the fact that the boundary layer thickness δ is small relative to some relevant dimension, say L, of the body on which it has developed. By evaluating the order of magnitude of each term in the Navier-Stokes equations in terms of δ/L, first or higher order boundary layer equations my be derived (see e.g., Schlichting [1987] for 2D equations or Nash & Patel [1972] for 3D ones). It turns out that the first order equations yield a constant pressure across the boundary layer.

Another consequence of the thinness of the boundary layer is that the pressure distribution on the body can be obtained to first order from an inviscid solution, neglecting the boundary layer entirely. Together, the two approximations for the pressure make it possible to develop a very efficient computational procedure for the boundary layer. The pressure distribution on the body is computed first, using inviscid theory, as presented in Section 5. Thereafter, the boundary layer equations are solved with the pressure at every point in the boundary layer taken from the point on the surface on the same normal. In this way, the pressure is prescribed and only velocities (and turbulence quantities) need to be computed. The tricky coupling between velocity and pressure, needed in more advanced viscous methods (see Section 9.7), is avoided, and a solution can be obtained in a small fraction of the time needed for the more advanced methods.

6.2.3 Local Boundary Layer Quantities. Perhaps the most important local boundary layer quantity is its *thickness*, δ. There is not a very sharp edge of the boundary layer, however. The velocity within the boundary layer merges smoothly with the outer inviscid flow. Therefore, the thickness is normally defined by the position where the velocity u has reached a certain percentage of that just outside the layer, U_e. Both 99% and 99.5% are used. When specifying the thickness, the corresponding percentage should be given.

Another important thickness measure is the *displacement thickness*, δ_1, defined as

$$\delta_1 = \int_0^\delta (1 - \frac{u}{U_e}) dy \tag{6.4}$$

A physical interpretation of this quantity is shown in Fig. 6.2. The volume flux within the boundary layer (per unit of width at right angles to the plane of the paper) is represented by the area within the velocity profile. The profile to the right has the same area, and thus the same volume flux, but with a constant velocity $u = U_e$ from the boundary layer edge down to a distance δ_1 from the surface. Within the distance δ_1 from the surface, the velocity is zero. If

---

*The gradient of a scalar function is a vector whose component in any direction is the derivative of the function in that direction. In fluid mechanics the component of the gradient vector in a certain direction is often, inconsistently, referred to as the gradient in that direction (longitudinal pressure gradient, etc.). This convention is adopted here.

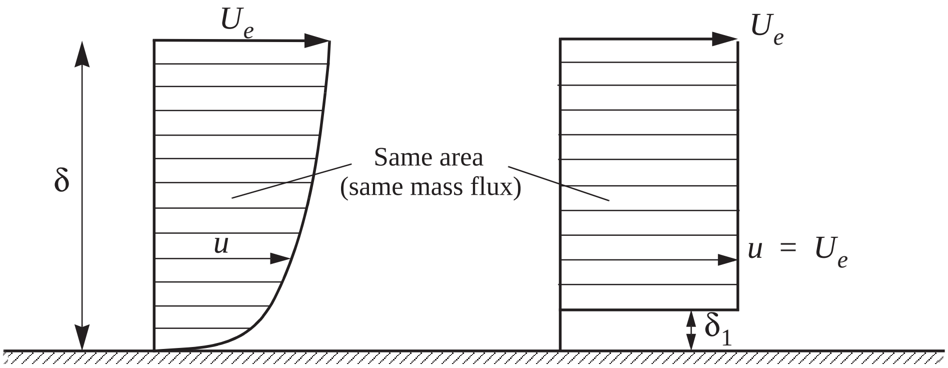

Figure 6.2 Interpretation of the displacement thickness concept.

the body is locally thickened by δ_1 and the velocity at the boundary layer edge (U_e) is used all the way down to the thickened body, the correct volume flux is thus obtained. In practice, this is used in procedures where the first order boundary layer approximation, as described previously, is improved by iterations with the inviscid solution. The pressure distribution from the first inviscid flow solution is then used for computing the boundary layer and its displacement thickness, which is added to the body, after which a new inviscid flow solution is obtained for the thickened body, the boundary layer recomputed, etc.

There is also a third thickness measure, often used for estimating resistance. This is the momentum thickness θ, obtained from

$$\theta = \int_0^\delta \frac{u}{U_e}\left(1 - \frac{u}{U_e}\right) dy \qquad (6.5)$$

The relation between momentum thickness and resistance may be derived with respect to Fig. 6.3, which shows the derivation for a flat plate. A control volume *ABCDA* is defined by a vertical line *AB* at the leading edge of the plate, a streamline *BC* just outside the boundary layer, a vertical line *CD* at a distance *L* from the leading edge, and the surface of the plate *AD* between $x = 0$ and $x = L$. According to the momentum theorem, the reduction in x-momentum (mass flux times velocity in the x-direction) when the fluid passes the control volume is equal to the force in the negative x-direction on the volume. This force is equal but opposite to the frictional force on the plate, R_F. Because the pressure is considered constant, no pressure forces are involved.

There is no velocity through the sides *BC* and *AD* because the former is a streamline and the latter is the surface of the plate. All momentum entering the control volume must pass the side *AB* and that leaving the volume must pass *CD*. With b as the plate width the following relation thus holds

$$R_F = \int_0^h (\rho U_e) U_e b dy - \int_0^\delta (\rho u) u b dy$$

which may be written

$$R_F = \rho U_e^2 b h - \rho b \int_0^\delta u^2 dy$$

But continuity requires that the mass flux entering through *AB* must be the same as that leaving through *CD*, in other words

$$\int_0^h \rho U_e b dy = \int_0^\delta \rho u b dy$$

or

$$U_e h = \int_0^\delta u dy$$

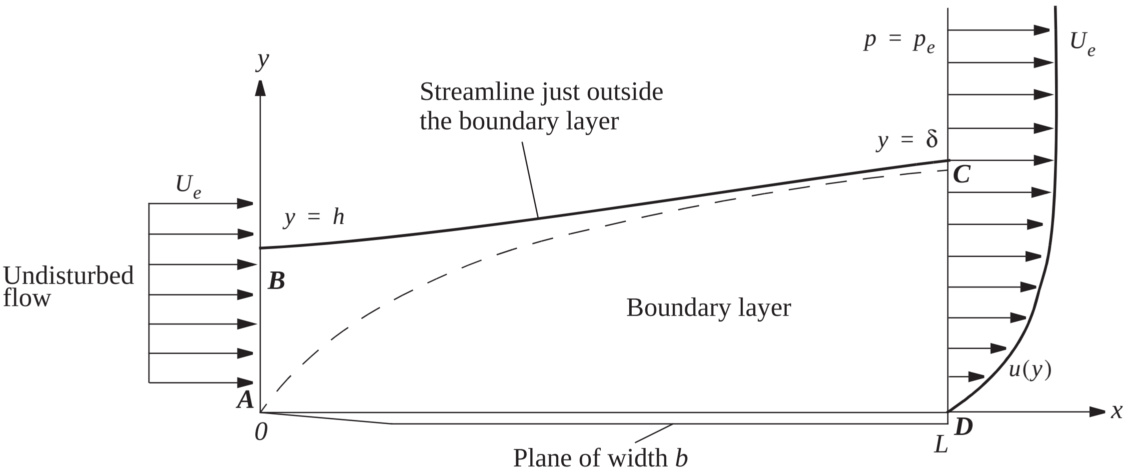

Figure 6.3 Control volume for the derivation of the relation between resistance and momentum thickness.

Inserting this into the formula for R_F yields

$$R_F = \rho b U_e \int_0^\delta u dy - \rho b \int_0^\delta u^2 dy$$

or, finally

$$R_F = \rho b U_e^2 \int_0^\delta \frac{u}{U_\infty}\left(1 - \frac{u}{U_\infty}\right) dy = \rho b U_e^2 \theta \qquad (6.6)$$

The total frictional resistance back to a certain point on the plate is thus proportional to the momentum thickness at that point. If the control volume is extended behind the plate, the momentum thickness will be constant aft of the trailing edge, so measuring the velocity profile at any position behind the plate will yield the frictional resistance of the plate. (The velocity profile will change, but not the momentum thickness.)

In fact, equation (6.6) holds for all 2D bodies, provided the velocity profile is measured far enough behind the body for the pressure to have become undisturbed. Note that in this case it is not only friction that is computed; the total viscous resistance is obtained (i.e., both form effects and roughness effects are included). It is the total force on the control volume that must balance the momentum loss. The momentum thickness thus forms the basis for resistance measuring techniques based on wake surveys.

Apart from the boundary layer thicknesses the ***local*** *skin friction coefficient* C_f is often of interest. It is defined as

$$C_f = \frac{\tau_w}{\frac{1}{2}\rho U_e^2} \qquad (6.7)$$

where τ_w is the local wall shear stress.

The ***total*** *skin friction coefficient* C_F defined like other force coefficients

$$C_F = \frac{R_F}{\frac{1}{2}\rho U_\infty^2 S} \qquad (6.8)$$

may be obtained by integrating the longitudinal component of the local friction over the body surface.

Note that all local quantities given here are for 2D cases. In three dimensions, other displacement and momentum thicknesses appear. The skin friction then has two components (Nash & Patel, 1972). In the viscous resistance relation, corresponding to equation (6.6), the momentum thickness is replaced by a momentum area (Schlichting, 1987).

6.3 The Flat Plate. The simplest boundary layer is that developing on a flat plate, assumed infinitely thin, parallel to the approaching flow and with its leading edge (and trailing edge, if any) at right angles to the flow. Many of the features of more general boundary layers are found in this simple case, which will be described first. The major reason why the flat plate boundary layer is simpler than the more general ones is that the pressure may be considered constant and undisturbed along the plate. This is in accordance with first order boundary layer theory: the plate itself will not disturb the pressure, and the effect of the displacement thickness is neglected. The velocity at the boundary layer edge is thus considered undisturbed (i.e., $U_e = U_\infty$ for this case).

6.3.1 Laminar Boundary Layer. The laminar boundary layer along a flat plate is one of the few viscous flow cases for which an analytical solution exists. This solution was obtained for the first time by Blasius (see Schlichting, 1987), who showed that all *velocity profiles* in the growing boundary layer along the plate could be made to coincide if scaled properly in the normal direction. More specifically, this type of "similar" solution was obtained in the form

$$\frac{u}{U_\infty} = f\left(\frac{y}{x}\sqrt{Rn_x}\right) \qquad (6.9)$$

where x is the distance from the leading edge and Rn_x is defined as

$$Rn_x = \frac{U_\infty x}{\nu} \qquad (6.10)$$

The velocity profile (6.9) will be shown in Fig. 6.5.

Other important results of the Blasius solution are the boundary layer thicknesses and the skin friction. The 99% *boundary layer thickness* is given by

$$\delta = 5.0 \frac{x}{\sqrt{Rn_x}} \qquad (6.11)$$

wheras the *displacement thickness* is obtained from

$$\delta_1 = 1.72 \frac{x}{\sqrt{Rn_x}} \qquad (6.12)$$

and the momentum thickness from

$$\theta = 0.664 \frac{x}{\sqrt{Rn_x}} \qquad (6.13)$$

The displacement and momentum thicknesses for a laminar boundary layer are thus about one-third and one-eighth, respectively, of the boundary layer thickness.

The formulas for the *local* and *total skin friction coefficients* are

$$C_f = \frac{0.664}{\sqrt{Rn_x}} \qquad (6.14)$$

and

$$C_F = \frac{1.328}{\sqrt{Rn_x}} \qquad (6.15)$$

respectively.

Note that the coefficient for the total friction is exactly twice that of the local friction at any distance from the leading edge.

6.3.2 Transition From Laminar to Turbulent Flow. The transition process is complex and not completely understood, but some useful insight may be obtained from boundary layer stability theory (see, for example, Schlichting, 1987). Here, only a few purely empirical relations for the flat plate will be given, serving relatively well as a first approximation.

Data for ideal conditions suggest that the transition on a flat plate is completed at a critical Reynolds number Rn_{crit} equal to about $3 \cdot 10^6$, where

$$Rn_{crit} = \frac{U_\infty x_{crit}}{\nu} \qquad (6.16)$$

and x_{crit} is the distance from the leading edge at which transition is completed. However, this high value of Rn_{crit} is seldom found in practice because it requires a very low turbulence level in the upstream flow. Defining the turbulence level T as

$$T = \frac{\sqrt{u'^2 + v'^2 + w'^2}}{\bar{u}} \tag{6.17}$$

where the primed quantities are root-mean-square-(RMS)-values of fluctuations and the barred quantity the mean flow, the requirement on T for Rn_{crit} to be equal to $3 \cdot 10^6$, is about 0.1%, which is only found in high-quality wind tunnels and in towing tanks that have not been used for several hours. Much higher levels are normally noted both in the atmospheric boundary layer and in the upper part of the ocean. A more realistic value of Rn_{crit} often given in the literature is $5 \cdot 10^5$. There is thus a relatively large span of possibilities depending on the quality of the approaching flow.

Transition also depends to some extent on surface roughness. According to measurements by Feindt (see Schlichting, 1987), the critical roughness height can be computed from the formula

$$\frac{U_\infty k_s}{\nu} = 120 \tag{6.18}$$

where k_s is the so-called equivalent sand roughness to be explained in Section 6.8.2. This requirement is about the same as for a hydraulically smooth surface in turbulent flow, as described in the same section.

In model testing, roughness is also of interest in another connection. Because models are tested at a considerably smaller Reynolds number than at full scale, transition occurs much further aft on the model. This complicates the extrapolation of the data to full scale, so in practically all testing, the laminar boundary layer is stimulated to achieve premature transition closer to the bow. Turbulence stimulation is described in Section 8.

For shapes other than the flat plate, pressure gradients, particularly in the longitudinal direction, will have a profound influence on the location of transition. This fact is utilized for generating low drag foil sections, as will be shown. There is also some effect of the normal curvature of nonflat surfaces.

6.3.3 Turbulent Boundary Layer. An assumption well validated over the years is that the *velocity profile* in the inner part of the turbulent boundary layer must be independent of the thickness of the layer and dependent only on the shear stress at the wall, τ_w, and the two fluid properties ρ and μ. By dimensional reasoning this relation may be written

$$\frac{u}{u_\tau} = f\left(\frac{y u_\tau}{\nu}\right) \tag{6.19}$$

where u_τ is a scaling parameter, known as the friction velocity, and defined as

$$u_\tau = \sqrt{\frac{\tau_w}{\rho}} \tag{6.20}$$

Using the definition of C_f, equation (6.7), u_τ may also be written

$$u_\tau = U_\infty \sqrt{\frac{C_f}{2}} \tag{6.21}$$

Defining a nondimensional velocity u^+ as

$$u^+ = \frac{u}{u_\tau} \tag{6.22}$$

and a nondimensional distance from the surface y^+ as

$$y^+ = \frac{y u_\tau}{\nu} \tag{6.23}$$

the generic equation (6.19) takes the simple form

$$u^+ = f(y^+) \tag{6.24}$$

Another well validated assumption is that the velocity profile in the outer part of the boundary layer must be independent of viscosity. The deviation from the external flow velocity U_∞ must, on the other hand, depend on the boundary layer thickness, apart from the wall shear stress and the density. Dimensional analysis thus yields

$$\frac{U_\infty - u}{u_\tau} = f_1\left(\frac{y}{\delta}\right) \tag{6.25}$$

An important contribution to the theory of 2D boundary layers is due to Millikan (see White, 2005), who showed that the only way for equation (6.24) to merge smoothly into equation (6.25) is for the intermediate region to be logarithmic in y.

The practical result of these more generic discussions is the profile shown in Fig. 6.4, where the boundary layer is divided into four regions with different expressions for the velocity. This profile is very well substantiated by experiments and has, at least until recently, been undisputed. The four regions are:

I. The viscous sublayer, $0 \leq y^+ \leq 5$

$$u^+ = y^+ \tag{6.26}$$

The profile is thus linear in this region.

II. The buffer layer, $5 < y^+ \leq 30$

Here the profile changes smoothly from linear in region I to logarithmic in region III.

III. The logarithmic region, $30 < y^+ < 500\text{–}10{,}000$

$$u^+ = \frac{1}{\kappa} \log y^+ + C \tag{6.27}$$

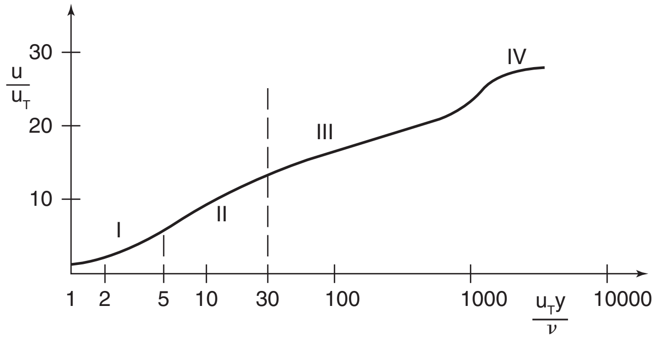

Figure 6.4 The wall–wake law.

The two constants, κ, known as the von Kármán constant, and C usually attain the values 0.41 and 5.0, respectively, but some variation is reported in the literature. Note that the outer edge of this region varies considerably, depending on the Reynolds number. The lower value is typical for the model scale, whereas the higher value is for the full scale.

IV. The wake region, between the logarithmic region and the boundary layer edge (the largest of the four regions)

Here a special function, the law of the wake $W\left(\frac{y}{\delta}\right)$ is added to the logarithmic law

$$u^+ = \frac{1}{\kappa}\log y^+ + \frac{\Pi}{\kappa}W\left(\frac{y}{\delta}\right) + C \tag{6.28}$$

where the constant Π is equal to 0.55 for a flat plate. The wake function is normally approximated as

$$W\left(\frac{y}{\delta}\right) = \left[\sin\left(\frac{\pi}{2}\frac{y}{\delta}\right)\right]^2 \tag{6.29}$$

Knowing the friction velocity u_τ and the boundary layer thickness δ the velocity profile in regions I, III, and IV may be computed from the formulas given. In region II, the same expression as in region III, but with constants that make the profile continuous (not the derivatives!) at $y^+ = 5$ and 30, respectively, is often used. Note that the wake strength parameter Π depends on the pressure distribution and is equal to the value given previously only for constant pressure, as on a flat plate.

The four region velocity profile is based on sound physical reasoning, as we have seen, and should be used for accurate prediction of the velocity, at least in the inner parts of the boundary layer. However, the equations are a bit complex, so an alternative, more approximate representation of the profile is very often used. This representation is entirely empirical, and it is not very accurate close to the surface, but it serves well for estimates of the flow velocity if the near wall region is avoided. It reads

$$\frac{u}{U_e} = \left(\frac{y}{\delta}\right)^{\frac{1}{n}} \tag{6.30}$$

where n depends on the pressure gradient and to some extent also on the Reynolds number. For flat plates at $Rn = 10^7$ (model-scale) $n \approx 7$ and at $Rn = 10^9$ (full scale) $n \approx 9$. In Fig. 6.5, the two profiles corresponding to $n = 7$ and $n = 9$ are compared with the more exact four region wall–wake law at the model Reynolds number. For comparison, the laminar Blasius velocity profile is also given. The most striking feature of Fig. 6.5 is the large difference between the laminar profile and the turbulent profiles. The differences between the latter are small, particularly between the two at the same Reynolds number. To really see the differences, the region close to the surface has to be magnified.

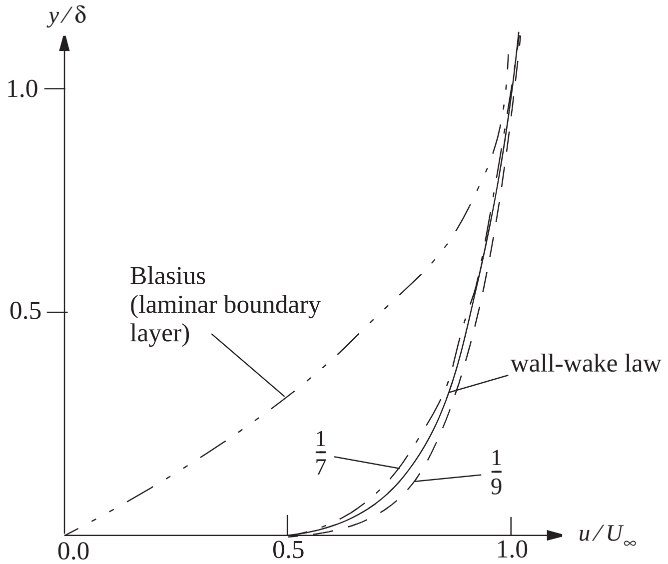

Figure 6.5 Different velocity profiles.

Relations for the boundary layer thicknesses and the skin friction may be obtained based on either the wall–wake law or the power law. In practice, only the latter is used (see Schlichting, 1987). The formula for the *boundary layer thickness* is then

$$\delta = \frac{0.37x}{\sqrt[5]{Rn_x}} \tag{6.31}$$

and for the *displacement thickness*

$$\delta_1 = \frac{0.046x}{\sqrt[5]{Rn_x}} \tag{6.32}$$

whereas the *momentum thickness* may be computed from

$$\theta = \frac{0.036x}{\sqrt[5]{Rn_x}} \tag{6.33}$$

For the turbulent boundary layer, the differences between the various thicknesses are larger than for the laminar boundary layer. The displacement thickness is one-eighth and the momentum thickness about one-tenth of the boundary layer thickness. These ratios are for $n = 7$. Somewhat different ratios are obtained for other powers.

The *local skin friction coefficient* is obtained from the following formula

$$C_f = \frac{0.058}{\sqrt[5]{Rn_x}} \tag{6.34}$$

The total skin friction coefficient will be discussed in the next section.

Note that the turbulent boundary layer thicknesses are proportional to $x^{4/5}$, but the laminar ones are proportional to $x^{1/2}$. The turbulent boundary layer grows faster than the laminar one. Equations (6.31) to (6.34) are very useful relations for rapid estimates of boundary layer thickness and local skin friction even for more complex cases than the flat plate.

6.3.4 Flat Plate Friction and Extrapolation Lines. The total skin friction on a plate covered by a turbulent boundary layer may be obtained by integrating equation (6.34) along the plate. However, rather than giving the integrated relation directly, a historical survey will be made of skin friction relations for flat plates, or planks, as they are often called. The reason is that the friction of an "equivalent flat plate" (see Section 4) has played a fundamental role in model test procedures, ever since William Froude's days, and some relations, which have been in use until recently, were derived long before the theory described was developed.

William Froude himself undertook a basic investigation into the frictional resistance of smooth planks in his tank at Torquay, England, the results of which he gave to the British Association (Froude, W., 1872, 1874). The planks varied in length from 0.6 to 15 m and the speed range covered was from 0.5 to 4 m/s. Froude found that at any given speed, the resistance per unit of surface area was less for a long plank than for a shorter one, which he attributed to the fact that toward the after end of the long plank, the water had acquired a forward motion and so had a lower relative velocity. He thus anticipated the existence of the boundary layer many years before Prandtl's time.

Based on his plank tests, Froude gave an empirical formula for the resistance R_F in the form

$$R_F = fSV^n \tag{6.35}$$

where S is the total wetted area and V the speed. f and n depend on the length and nature of the surface. For a smooth varnished surface, the value of the exponent n decreases from 2.0 for the short plank to 1.83 for the 15 m plank. For the planks roughened by sand, the exponent has a constant value of 2.0.

William Froude's values of friction coefficients were stated to apply to new, clean, freshly painted steel surfaces, but they lie considerably above those now generally accepted for smooth surfaces. The original curves were modified and extended by R. E. Froude (1888), up to a length of 366 m, but these extended curves had no experimental basis beyond the 15 m plank tests made in 1872. Nevertheless, they have been used until recently in some towing tanks.

During the early years of the 20th century, many tests were carried out with flat plates. In 1932, Schoenherr collected most of the results of plank tests then available. He included the results of experiments on 6 m and 9 m planks towed at the Experimental Model Basin in Washington, DC, and some original work at the lower Reynolds numbers on 1.8 m catamarans with artificially induced turbulent flow. At the higher Reynolds numbers, he was guided largely by the results given by Kempf (1929) for smooth varnished plates. Kempf's measurements were made on small plates inserted at intervals along a 76.8 m pontoon, towed in the Hamburg tank. The local resistances so measured were integrated by Schoenherr to obtain the total resistance for surfaces of different lengths. In order to present his results in conformity with rational physical principles, Schoenherr fitted the following formula to his data

$$\frac{0.242}{\sqrt{C_F}} = \log(RnC_F) \tag{6.36}$$

where Rn is the Reynolds number based on the plank length and the total friction coefficient C_F is defined as in equation (6.8). The introduction of the Reynolds number as the independent variable represents a considerable improvement relative to Froude's formula, but the Reynolds number was not known at the time of William Froude. Reynolds presented his revolutionary work on pipe flows, where Reynolds scaling was proposed, in the 1880s (Reynolds, 1883).

Schoenherr's formula was adopted by the ATTC in 1947, and it is therefore also known as the "ATTC line." To account for the roughness found even on clean new vessels, an allowance of 0.0004 was recommended. The Schoenherr line has been used extensively over the years, especially in the United States, and it is shown in Fig. 6.6.

One problem with the Schoenherr line, identified at a very early stage, is that the slope is not sufficiently steep at the low Reynolds numbers appropriate to small models. This means that it does not give a good correlation between the results of small and large models. Schoenherr had used data from many sources, and the planks were in no sense geosims, so the experimental figures included aspect ratio* and edge effects (the same applied to Froude's results). To obtain a better data base, Hughes (1952, 1954) carried out many resistance experiments on planks and pontoons, in the latter case up to 78 m in length, and so attained Reynolds numbers as high as $3 \cdot 10^8$. These plane surfaces covered a wide range of aspect ratios, and Hughes extrapolated the

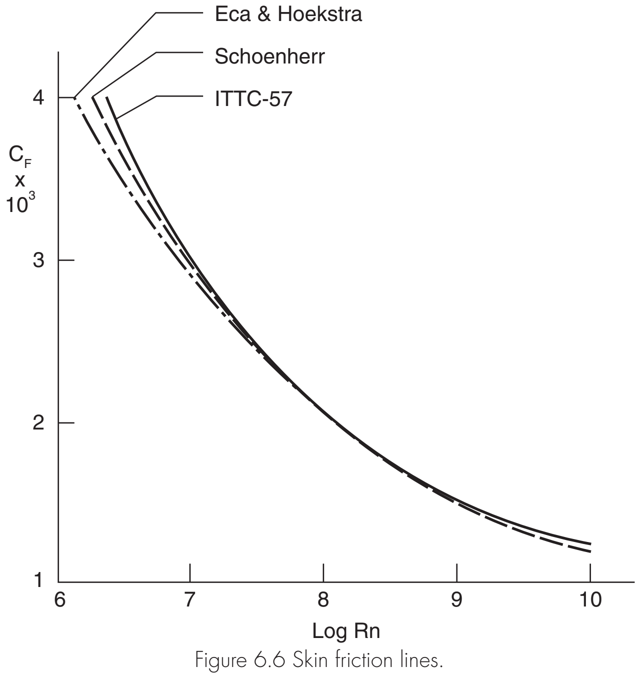

Figure 6.6 Skin friction lines.

---

*The aspect ratio is the breadth of the plank divided by its length. An infinite aspect ratio plank is a plank with no sides.

resistance coefficients to infinite aspect ratio, obtaining what he considered to be a curve of minimum turbulent resistance for plane, smooth surfaces in 2D flow. This curve had the equation

$$C_{FO} = \frac{0.066}{(\log Rn - 2.03)^2} \tag{6.37}$$

where C_{FO} denotes the frictional resistance coefficient in 2D flow.

Although Hughes' formula may be considered a true flat plate resistance relation, it could not be used for estimating the total viscous resistance of ships, so in 1957, the ITTC in Madrid decided to make some corrections, which would take the form effect of contemporary ships into account. The new formula, known as the ITTC-57 model-ship correlation line, has since been used in the work of most towing tanks of the world. It reads

$$C_F = \frac{0.075}{(\log Rn - 2)^2} \tag{6.38}$$

This line is also shown in Fig. 6.6. Note that this line was not proposed as a true flat plate friction line. It includes some effect of the 3D shape of the ship. For typical ships of the 1950s, all such effects on the viscous resistance were supposed to be included. Comparing with Hughes' formula, it turns out that the ITTC friction is about 12% higher over the whole range of Reynolds numbers. A form effect of 12% may thus be considered added to the flat plate line. By this addition, the total resistance (C_T) could be obtained as the sum of only two components, the friction (C_F) and the residuary resistance (C_R) (plus some roughness allowance). Model test data could then be extrapolated to full scale using Froude's original hypothesis. This type of extrapolation, called "Froude scaling," is still used at some towing tanks. However, as became apparent with the introduction of very bluff ships during the 1960s, a more exact treatment of the effect of the three-dimensionality is required (i.e., the two form effects specified in Fig. 4.1 need to be considered individually for each ship). The procedure for taking this into account is known as "3D extrapolation" and will be discussed in Section 8. It was proposed by the ITTC in 1978.

In recent years, several attempts have been made to derive a formula for the flat plate resistance using numerical methods. Grigson (1993) used the momentum integral equation for the flat plate together with the wall–wake law, equation (6.28) for the velocity profile, to compute the skin friction as a function of Reynolds number. The same approach was used by Katsui et al. (2005), but with slightly different constants κ and Π. The most comprehensive investigation was carried out by Eca and Hoekstra (2008), who used a method based on the Reynolds-Averaged Navier-Stokes (RANS) equations to compute the local friction on the plate. Through systematic grid refinement, the numerical error could be kept below 1%. The influence of the modeling error was studied by carrying out the calculations using seven different turbulence models (see Section 9.7.3). Comparing the integrated friction with the ITTC and Schoenherr formulas, as well as with the two numerical procedures just mentioned, the difference between the results from the various turbulence models was smaller. The total error in the computations must therefore be considered very small.

Results for one of the turbulence models (SST $k - \omega$) is shown in Fig. 6.6. It is seen that the slope of this curve is smaller at the lower Reynolds number. This is because the first part of the flow on the plate was assumed laminar, whereas the two other lines assume turbulent flow from the beginning. The usefulness of the numerical approach, even though it produces an accurate result for a real flat plate boundary layer, is somewhat limited at small Reynolds numbers because ship models are normally fitted with turbulence stimulators to promote early transition (see Section 8.2.3). At higher Reynolds numbers, the influence of the laminar flow becomes smaller, and it is interesting to note that the numerical friction line gets very close to the ITTC line (in the figure the lines coincide) above a Reynolds number of 10^8. This is somewhat surprising because the ITTC line includes a form effect, as explained.

6.4 Two-Dimensional Bodies. Flat plates serve well for describing the basics of boundary layer theory. However, as compared with the fully 3D case, there are three important effects missing: longitudinal pressure gradients, lateral streamline convergence, and lateral pressure gradients. We will introduce these additional complexities one by one in this section and in Sections 6.5 and 6.6. In the present section, which deals with general 2D cases, the longitudinal pressure gradient appears. Remember that the pressure distribution in the normal direction is always constant in first order boundary layer theory!

The interpretation of the word "2D" in this context is that the body is infinitely long in one direction, z, say, with a constant cross-section and that the flow is in the x,y-plane. All dependent variables can then be expressed as functions of x and y. Orienting the body in such a way that the z-axis is at right angles to the plane of a sheet of paper, the body and the flow may be drawn in two dimensions on the paper. There is no possibility for the streamlines to bend in the z-direction; they are all parallel, viewed at right angles to this axis.*

6.4.1 Pressure Distribution. Figure 5.3 shows the pressure distribution in inviscid flow. In reality, the boundary layer will disturb the pressure, as explained in connection with the explanation of the displacement thickness. In Fig. 6.7 , a sketch of the streamlines near the stern in an inviscid flow are compared with the corresponding ones in

---

*If the approaching flow is not at right angles to the infinitely long body of constant cross-section, a cross-flow will develop inside the boundary layer, as explained in the subsequent section. However, both the longitudinal and cross-flow velocity profiles will be independent of the spanwise position on the body. All flow quantities can then be expressed in two independent coordinates. The case is mathematically 2D, but physically 3D. It was a neat test case for 3D boundary layer methods in the 1970s (Larsson, 1975).

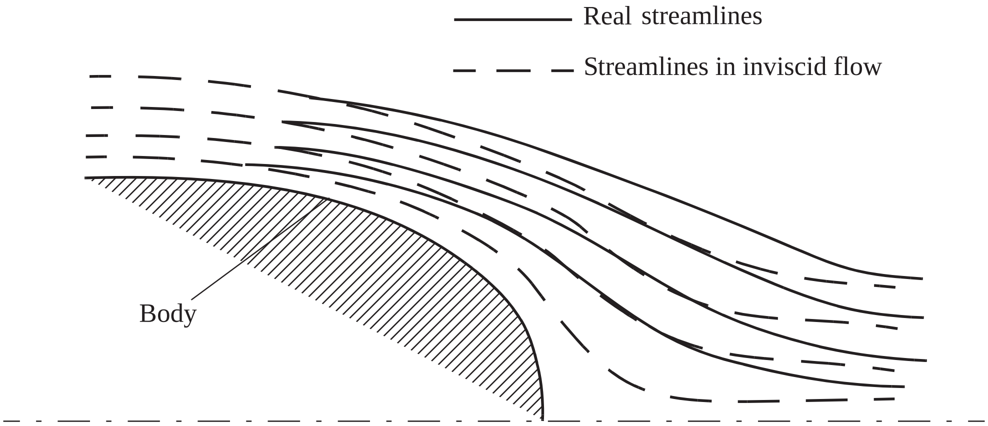

Figure 6.7 Displacement of streamlines in inviscid flow due to the boundary layer.

a flow with viscosity. Because the velocity is lower inside the boundary layer, the viscous streamlines have to be displaced outward.

Figure 6.8 shows how the displacement thickness is added to the hull, to represent the displacement effect of the boundary layer on the inviscid flow. Using this thickened body in an inviscid calculation, the pressure along the real body in a viscous fluid may be obtained.* Because the thickened body has no aft end (the wake extends in principle to infinity), there will be no stagnation pressure there. The straighter streamlines will cause a smaller pressure variation across the streamlines and thus a smaller pressure at the stern than in an inviscid flow. The change is shown in Fig. 6.9., which is the same as Fig. 5.4. As a result of the lower pressure, the *form effect on the pressure* (*viscous pressure resistance*), shown in Fig. 4.1, occurs.

6.4.2 General Effects of the Longitudinal Variation in Pressure. The velocity distribution around the body *in an inviscid flow* is linked to the pressure distribution via Bernoulli's law, as explained in Section 5. A high pressure means a low velocity, and vice versa. The velocity goes to zero at the stagnation points and is highest at the pressure minima near the shoulders. Fig. 6.9 shows the velocity distribution in a flow with viscosity, but here it is the velocity U_e at the edge of the boundary layer where pressure and velocity may be linked by Bernoulli's law.

A fluid element moving longitudinally in the boundary layer on a flat plate is restrained only by viscous forces (i.e., its acceleration or deceleration is determined by the sum of the viscous forces in this direction). This is when the pressure is constant. If the pressure is not constant, as in the general 2D case, there are also pressure forces acting in the longitudinal direction. In regions where the pressure is diminishing along the body the pressure forces will tend to accelerate the fluid element, but in regions of increasing pressure the element is decelerated. This has several important implications.

Because negative pressure derivatives tend to accelerate the flow within the boundary layer, the latter grows more slowly than on a flat plate, and conversely, positive pressure derivatives give rise to a more rapid increase in thickness. There is also a tendency for the velocity profile to become "fuller" in regions of diminishing pressure and "thinner" in increasing pressure. Fuller means that the velocity is relatively more rapid in the

---

*According to the theory (Lighthill, 1958), the pressure will be correct at the location of the boundary layer edge. In practice, the pressure is computed at the displacement body and transferred at right angles down to the body surface. See also the discussion of the pressure variation across the boundary layer later in the text.

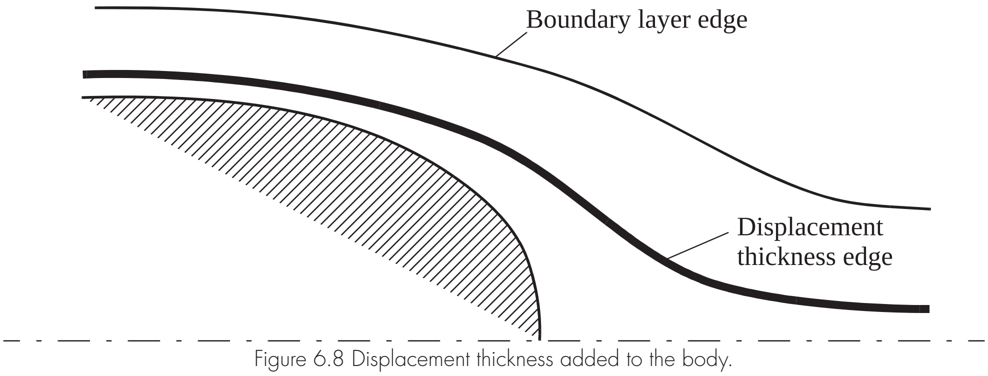

Figure 6.8 Displacement thickness added to the body.

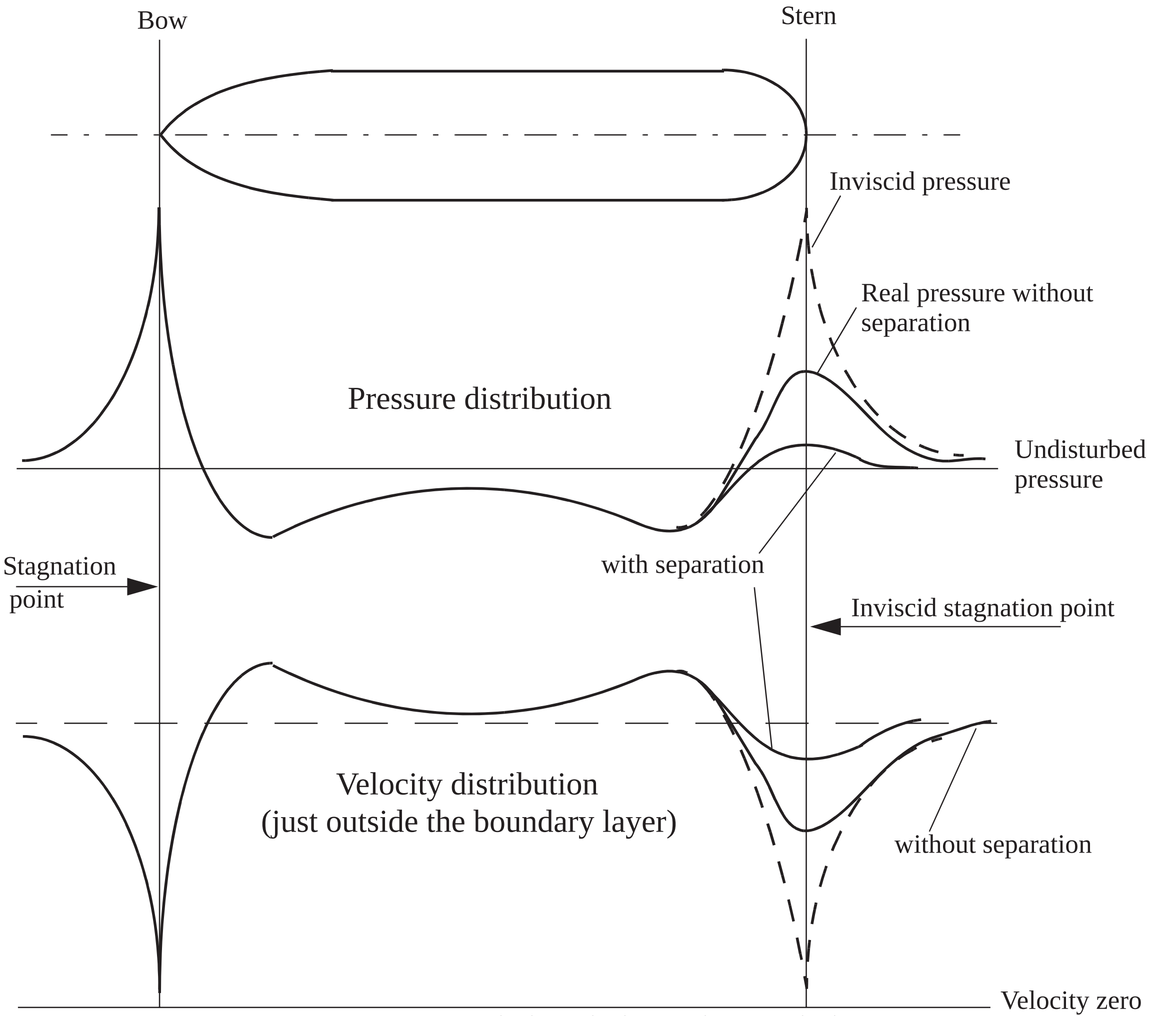

Figure 6.9 Pressure and velocity distributions along a 2D body.

inner parts of the layer (i.e., the velocity profile looks more square). To quantify these effects of pressure gradients, the boundary layer equations have to be solved, and this is out of the scope of this more phenomenological discussion. There are no simple relations, like those on a flat plate, for general pressure gradients. On the other hand, if the gradients are not too large, reasonable estimates of boundary layer thicknesses, skin friction, and velocity profiles may be made using the relations for a flat plate.

6.4.3 Transition. There are, however, a couple of effects of pressure gradients that do need to be considered. The first one is the effect on transition from laminar to turbulent flow. This is an instability phenomenon causing lateral and normal fluctuations of the flow. In regions where the flow is accelerated longitudinally by the pressure, these fluctuations are reduced, but in regions where the flow is decelerated they are increased. Thus, a negative pressure derivative tends to stabilize the flow, thereby delaying transition, whereas the opposite is true for a positive derivative. Negative pressure derivatives are utilized to create low-drag laminar airfoil sections, as will be seen in Section 7. In fact, the pressure gradient effect is normally stronger than the Reynolds number effect on transition, so for a range of Reynolds numbers the transition process takes place near the first pressure minimum on a body. This is where the pressure starts rising, often quite sharply. If the location of transition is to be estimated, the first pressure minimum is a good choice, at least at model-scale.

6.4.4 Separation. The second effect of pressure gradient is related to the increase in pressure at the aft end of bodies. If this increase is too rapid, the decelerating force on the fluid elements very close to the surface may be so large that their longitudinal motion stops. The streamlines then have to leave the surface, creating a zone of reversed flow. This phenomenon is called *separation* and is sketched in Fig. 6.10 (see also Fig. 6.1). The separation zone is characterized by

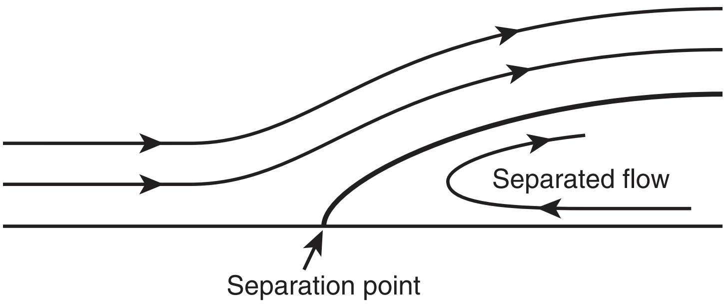

Figure 6.10 Flow near the separation point (S).

very small axial mean velocity, but large velocity fluctuations. This is in contrast to the attached turbulent boundary layer, where the fluctuations are small relative to the mean longitudinal velocity. Although it is the pressure increase at the stern that may create separation, the separation itself will cause a reduction in the pressure gradient. Because the streamlines outside of the separation zone now move even more straight backward than those shown in Fig. 6.7 for the unseparated boundary layer, the pressure build-up at the stern will be even smaller, as seen in Fig. 6.9.

6.4.5 Form Effects and Form Factor. Because of the effect of the pressure gradient, which causes the variation of the velocity at the boundary layer edge, the friction on the body will not be the same as on a flat plate. In fact, the integrated friction is normally larger because the body displaces the streamlines, which will then be closer together over the body than at infinity. This means that the velocity at the boundary layer edge in general is larger than for a flat plate, thereby increasing the friction on the body. This effect is the *form effect on the friction* in Fig. 4.1.

The two form effects (i.e., the one on pressure and the one on friction) are normally lumped together in a total form effect represented by a form factor, r, which is often written as $1 + k$. This factor is defined as the ratio of the total viscous resistance C_V for the body and the friction on the equivalent flat plate C_{F0}

$$1 + k = \frac{C_V}{C_{F0}} = \frac{C_F + C_P}{C_{F0}} \tag{6.39}$$

where C_F and C_P are the skin friction and pressure resistance coefficients, respectively, for the body. This definition is used also for general 3D cases. The form factor is very important in the ITTC-78 extrapolation procedure to obtain full-scale data from model tests. This will be further explained in Section 8.

6.5 Axisymmetric Bodies. From a boundary layer point of view, the fundamental difference between an axisymmetric and a 2D body is the fact that the width of the surface along which the boundary layer develops varies along the body.

The interpretation of the word "axisymmetric" is that the body is generated by a plane curve, rotating around an axis in the same plane as the curve. For an axisymmetric body, the streamlines closest to the surface (on the surface in inviscid flow, just outside the surface in viscous flow) will diverge out from the forward stagnation point and they will be most spread at the section with the largest diameter. They will converge at the tail toward the aft stagnation point (Fig. 6.11).

The lateral distance between the streamlines will be proportional to the local circumference of the body (i.e., proportional to the local radius). This has to have an effect on the boundary layer development. In regions where the lateral distance between streamlines increases (i.e., where the radius of the body increases), continuity demands that the boundary layer growth will be reduced, whereas the opposite is true for regions where the streamlines converge. The initial growth of the thickness is thus smaller than for a 2D body at the fore end, but it is larger at the tail.

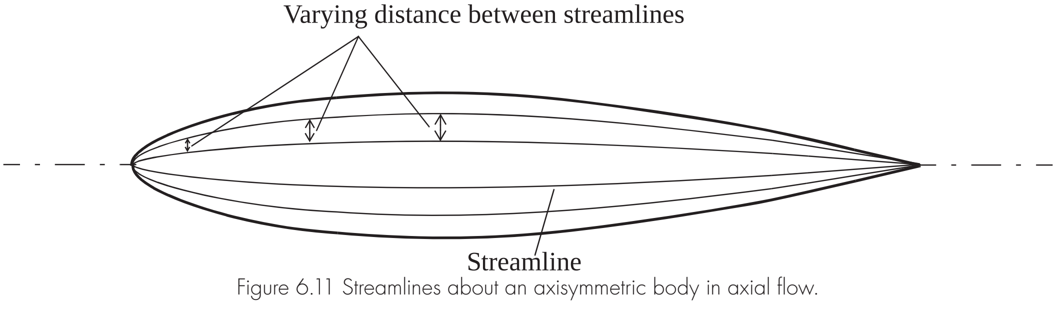

Figure 6.11 Streamlines about an axisymmetric body in axial flow.

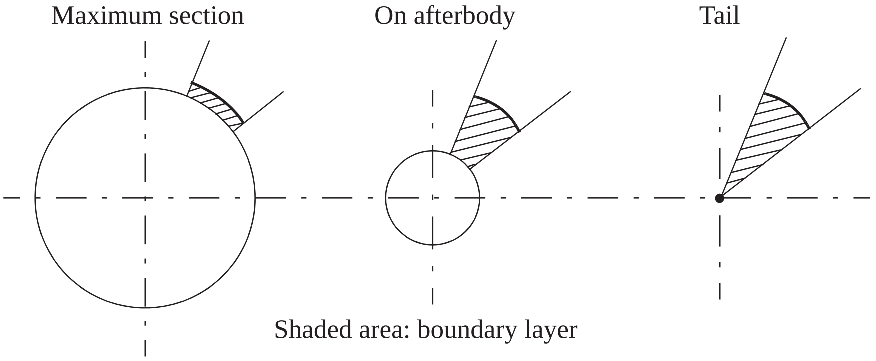

Figure 6.12 Cross-section of the axisymmetric body and a segment of the boundary layer. Thickness influenced by both the shrinking circumference and the diverging normals.

Because the streamlines close to the surface converge toward a point, the lateral distance goes to zero, which would have caused the boundary layer thickness to go to infinity had it not been for the radial spreading of the normals to the surface (Fig. 6.12). The lateral distance between two meridian planes is proportional to the radial distance from the axis, so away from the surface there is still some space for the boundary layer, even with finite thickness. In other words, the effect of the strong divergence and convergence of the streamlines close to the surface is reduced further away from the surface, but it is still significant.

The equations governing the flow around an axisymmetric body differ somewhat from those in two dimensions because the radius of the body must be introduced. For a derivation, see for example Schlichting (1987). It is thus not possible to use the equations presented in Section 2 based on Cartesian coordinates. We will not consider the equations further, but restrict ourselves to the physical reasoning previously discussed. When applying the simple flat plate formulas for estimating boundary layer quantities, the general effects of the streamline convergence/divergence should be kept in mind.

6.6 Three-Dimensional Bodies. Starting from the flat plate boundary layer, we have now introduced two complicating factors: the longitudinal pressure variation for the 2D body and the laterally diverging/converging streamlines of the axisymmetric body. We will now take the final step toward a general case and introduce pressure gradients also in the lateral direction (i.e., in a plane parallel to the surface but at right angles to the flow at the boundary layer edge).

6.6.1 Cross-flow. The resulting flow is seen in Fig. 6.13. To clearly illustrate the principle, a 2D boundary layer velocity profile is assumed at one position on the surface (to the right in Fig. 6.13). Because of a pressure gradient $\frac{\partial p}{\partial z}$ in the plane of the surface, but at right angles to the flow in the profile, the external flow bends to the left (i.e., in the negative z-direction) and the radius of curvature of the streamlines at the edge of the boundary

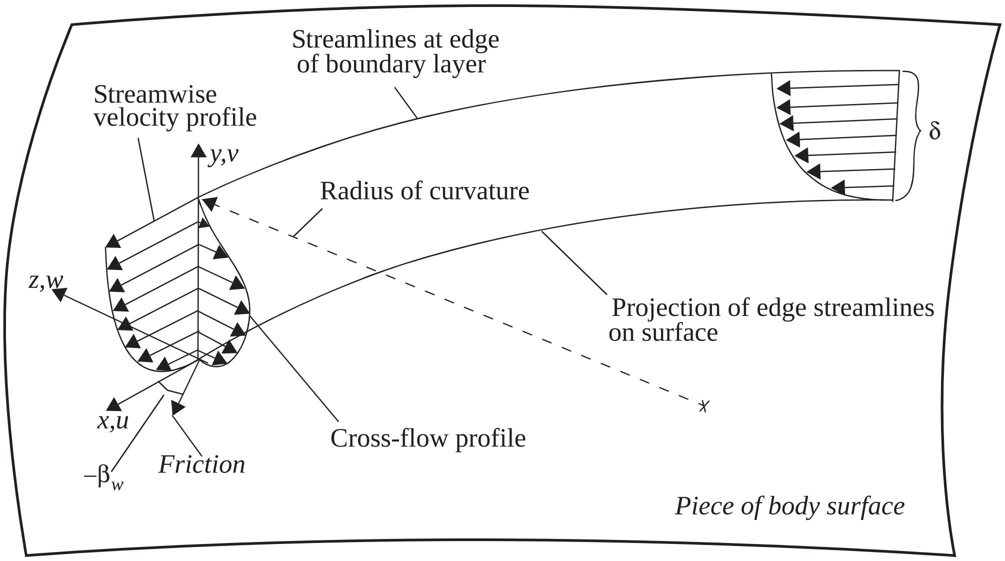

Figure 6.13 Cross-flow development due to lateral curvature of streamline.

layer is determined by the magnitude of the pressure gradient, as seen in Section 5.2.1 As the pressure may be assumed constant in the y-direction across the boundary layer,* the pressure gradient $\frac{\partial p}{\partial z}$ may also be assumed constant with respect to y. At every distance from the surface on a certain normal to the surface, we thus have the same $\frac{\partial p}{\partial z}$. This means that $\frac{\rho u^2}{r}$ has to be the same at all y. But the local velocity u varies with y, which means that the local radius r will also vary (in proportion to u^2). The smaller the velocity, the smaller the transverse radius of curvature (i.e., the closer to the surface the sharper the turn toward the left for the local streamline). Thus, the flow will not be parallel to that at the edge: a cross-flow will develop to the left, as seen in the Fig. 6.13. This is not surprising; the reduced momentum inside the boundary layer relative to the edge will make it easier for a given lateral pressure gradient to bend the flow. Note that the cross-flow profile (in the yz-plane) must go to zero at the surface due to the no-slip condition.

Should $\frac{\partial p}{\partial z}$ change sign further to the left along the external streamline (i.e., if there is an inflexion point and it starts to bend to the right), the innermost streamlines will react immediately, and a cross-flow to the right will develop. However, because of the higher momentum at the outer streamlines, it will take some time for the cross-flow in the outer part of the boundary layer to change sign. An S-shaped cross-flow profile thus develops over a certain distance along the streamline, before all cross-flow has turned to the right.

The cross-flow angle β is defined as

$$\beta = \operatorname{atan}\frac{w}{u} \tag{6.40}$$

At the surface there is no flow because of the no-slip condition, so equation (6.40) cannot be applied. However, according to l'Hospital's rule, a limiting value β_w may be computed as

$$\beta_w = \lim_{y\to 0}\operatorname{atan}\frac{w}{u} = \lim_{y\to 0}\operatorname{atan}\frac{\frac{\partial w}{\partial y}}{\frac{\partial u}{\partial y}}$$

But the velocity gradients are related to the shear stress, in general according to equation (2.10) and for a 2D boundary layer according to equation (6.1). The 3D analog to equation (6.1) is

$$\sigma_{yx} = \mu\frac{\partial u}{\partial y} \qquad \sigma_{yz} = \mu\frac{\partial w}{\partial y}$$

where the limiting value of the shear stress (σ_{yz},σ_{yx}) at the wall is (τ_{wz},τ_{wx}). Thus

$$\beta_w = \operatorname{atan}\frac{\tau_{wz}}{\tau_{wx}} \tag{6.41}$$

We have now shown that the limiting value of the flow direction on the surface is the direction of the shear stress on the surface. If a set of lines is traced along the surface, based on the direction of the friction, these lines represent the limit on the surface of the streamlines in the boundary layer. They are therefore called *limiting streamlines*. In towing tank testing, the limiting streamlines are obtained by a technique where strips of dark paint are applied girthwise at several stations on the hull. Towing the hull when the paint is still wet, paint particles will be dragged along the surface by the friction, thus creating fine lines of paint on the surface. These show the direction of the friction and may be used for tracing the limiting streamlines. See Fig. 8.10.

6.6.2 Three-Dimensional Separation. Three-dimensional flow may separate in two different ways, both shown in Fig. 6.14. The bubble type, shown to the left, is the one most similar to that described for 2D boundary layers in Section 6.4.4 (the same type occurs for axisymmetric bodies). In the bubble separation, the flow leaves the surface along a line (dividing line in Fig. 6.14) on the surface. A bubble is created, where the flow on the outside is directed backward and on the inside forward. The top view to the left shows a cut through the bubble and is very similar to the 2D picture of Fig. 6.10. Here the flow leaves the surface at a non-zero angle and the friction is zero, just as in the 2D case. At all other points on the dividing line, the friction is different from zero and the flow leaves the surface tangentially.

The vortex sheet separation, shown to the right, occurs when the streamlines near the surface converge. For continuity reasons, the flow then has to leave the surface, whereby the boundary layer is swept out. Two different boundary layers will then meet, and relatively strong vortices appear in the intermediate layer. This vortex sheet is unstable and will ultimately break down into a longitudinal vortex in the flow direction. An in-depth discussion of 3D separation is found in Maskell (1955).

6.7 The Boundary Layer Around Ships. In Table 6.1, the result of the discussions so far in Section 6 are summarized. Based on the knowledge thus acquired of 3D boundary layers, we will now turn to the boundary layer on a ship hull. It should be pointed out again that all effects of the waves are neglected in this section. The undisturbed free surface is treated as a symmetry plane. The case considered is thus the real underwater part of the hull plus its mirror image in the undisturbed free surface, a so-called double model. As an example, we will use a VLCC which has been used extensively for CFD validation in recent years, for instance at the CFD Workshops in 2000 (Larsson, Stern, & Bertram, 2002, 2003) and in 2005 (Hino, 2005). A double model of this hull was tested in a wind tunnel, but there are also towing tank data with the real hull available (see Kim, Van, & Kim, 2001; Lee et al., 2003; Van et al., 1998a,b). The hull was originally designed

---

*For this statement to be true, the normals to the surface need to be parallel. According to the boundary layer assumption that $\frac{\delta}{r}$ is negligible, the variation in distance between two normals is also negligible within the boundary layer.

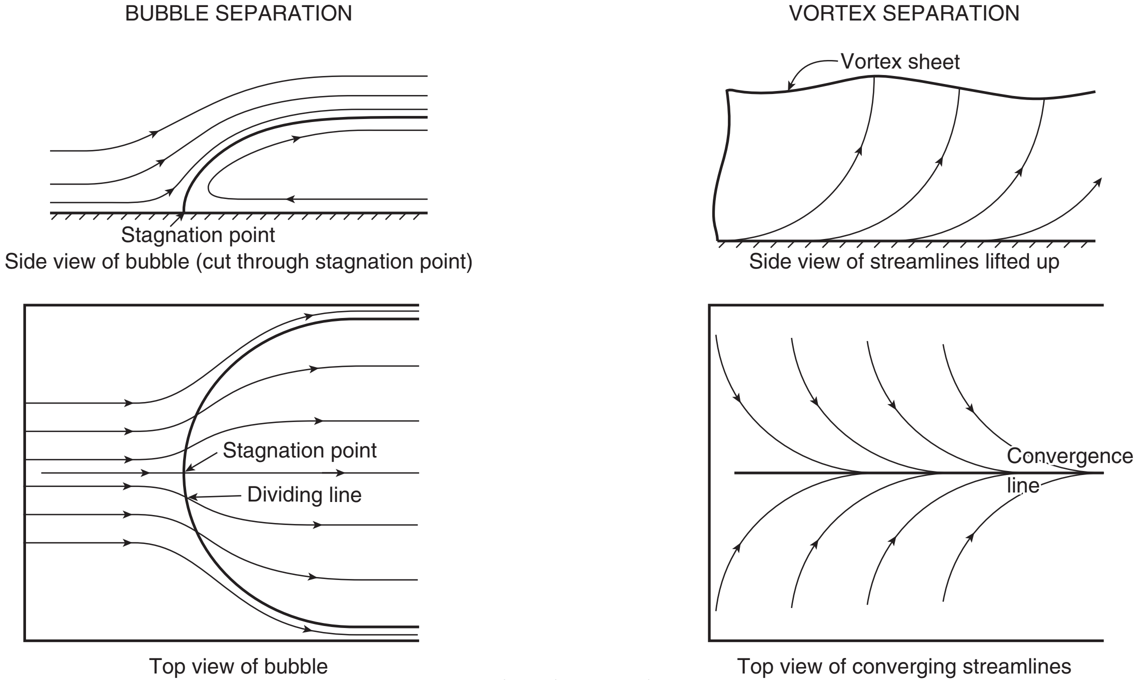

Figure 6.14 Three-dimensional separation.

at the Korea Research Institute of Ships and Ocean Engineering and is the second variant of a VLCC design. It is known as the KVLCC2. The block coefficient is 0.85, so it is a very bluff hull. This means that the effects of three-dimensionality are relatively strong and easily seen. For more slender displacement hulls, the effects are weaker, but they are present in most cases. For planing hulls with a submerged transom, the flow is normally somewhat simpler. Streamlines leave the edge of the transom without converging very much and often without lateral curvature, so in the stern region, where the boundary layer on displacement ships is most complicated, the boundary layer is relatively 2D.

The discussion in Section 6.7 will be based on computed results, rather than measured data. A more complete flow picture may be obtained in this way because some experimental data are not available, such as the detailed pressure distribution and the local friction on the hull. Full-scale flow data of all kinds are also very rare, and not at all available for the hull selected here. Very detailed validation studies for the viscous method used to obtain the present results have been made in several projects, like the different international workshops described, or VIRTUE, a project sponsored by the European Commission (see Marzi, 2008), and the authors are convinced that the accuracy of the results is high enough for the present purposes, at least at model-scale. The accuracy at full scale is more difficult to assess because data are rare, but validation studies [e.g., in another European project, EFFORT (see Regnström & Bathfield, 2006)] indicate that the results are at least qualitatively correct.

Table 6.1 Boundary Layer Features

Boundary Layer Type	Main Flow Features
Flat plate	No-slip
Two-dimensional	No-slip, longitudinal pressure gradient
Axisymmetric	No-slip, longitudinal pressure gradient, lateral streamline convergence/ divergence
Three-dimensional	No-slip, longitudinal pressure gradient, lateral streamline convergence/ divergence, lateral pressure gradient

6.7.1 Pressure Distribution and Boundary Layer Development. The boundary layer development is driven by the pressure distribution around the hull. In Fig. 5.5, the pressure around the KVLCC2 hull was given, assuming the flow to be inviscid. For convenience, the pressure distribution is repeated as Fig. 6.15.* The lines represent contours of constant pressure (isobars) and the value of the pressure coefficient C_p is given on most of the lines. Positive pressure coefficients are repre-

---

*All figures of Section 6.7 were produced by Michal Orych at FLOWTECH International AB and are published with his permission. The inviscid results were obtained by a potential flow panel method whereas the viscous ones are from a method based on the RANS equations. See Section 9 for a description of the different methods.

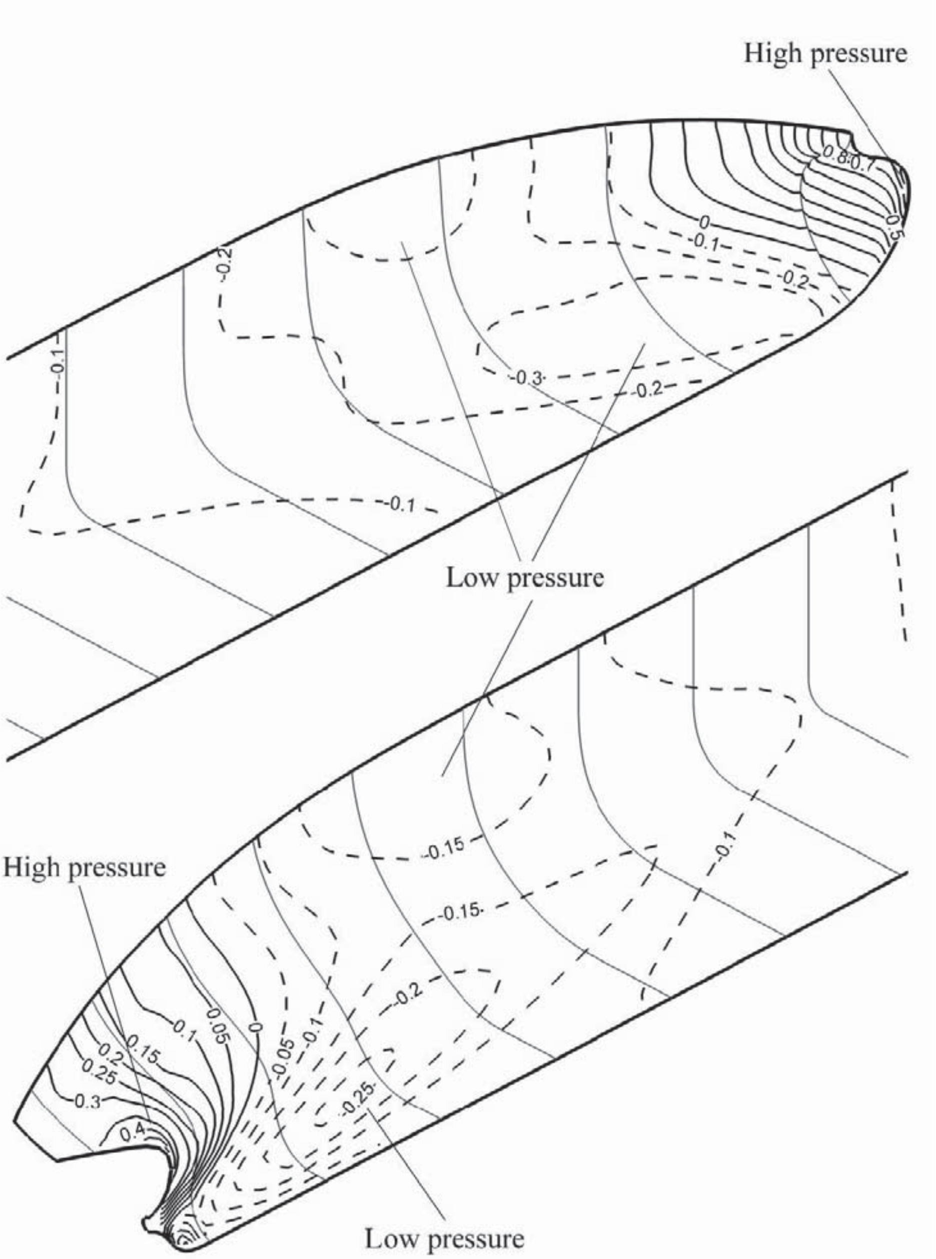

Figure 6.15 Pressure distribution around the KVLCC2 hull in inviscid flow. Contours labeled by C_p.

sented by full lines whereas negative ones have broken lines. There are two high-pressure zones, one at the bow and one at the stern. Low-pressure zones are found at the two shoulders and at the bilges near the bow and stern. The reasons for this variation in pressure were explained in Section 5.2.

In reality, the pressure will be influenced by the boundary layer because of the displacement effect, but this effect is very small on the forebody. On the afterbody, the differences are larger, as can be seen in Fig. 6.16, where the pressure distribution at model-scale in a real, viscous flow is shown. The Reynolds number at model-scale is $4.6 \cdot 10^6$.

Comparing Figs. 6.15 and 6.16, it is seen that the -0.1 contours, located just behind the parallel middle body, are almost identical. Further aft, the differences increase, and at the very end, close to the transom, the high inviscid pressure is reduced by 0.1–0.2 in C_p in the viscous flow. The pressure minimum at the bilge is about 0.05 higher in the real case. In general, the distribution of pressure is very similar in the two cases, but the variations are somewhat smoothed out in the real flow, compared to the inviscid one.

When explaining the pressure distribution in Fig. 5.5, use was made of the normal curvature of the hull and its relation with pressure gradients in the normal direction. Now we will direct our interest toward the lateral

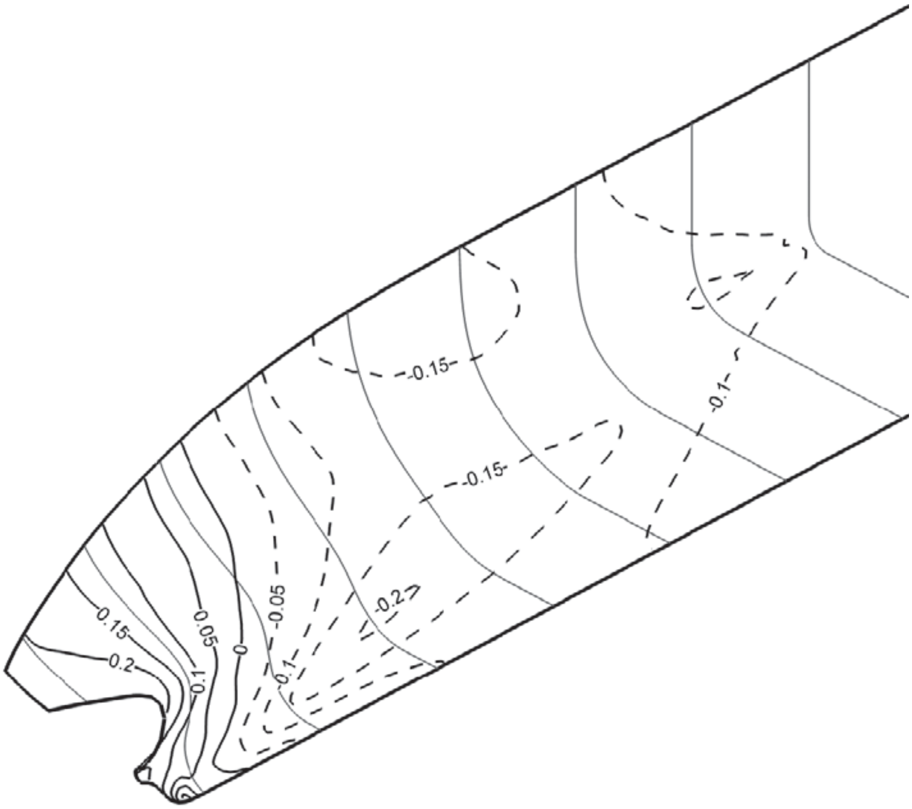

Figure 6.16 Pressure distribution at model scale in a real, viscous flow. Contours labeled by C_p.

pressure gradients, which are linked to the lateral* curvature of the streamlines. The streamlines of interest are those at the edge of the boundary layer, as seen in Fig. 6.13. In first order boundary layer theory, these are assumed the same as those traced on the hull in the inviscid flow (i.e., those shown in Fig. 5.4). The streamline distribution is shown again in Fig. 6.17.

The lines along the upper part of the hull move more or less horizontally and have very little lateral curvature. Little cross-flow is thus developed in this region. The streamlines in the bilge region on the forebody start relatively horizontally at the bow, thereafter curving downward to pass under the bottom. Having reached the bottom, they turn back to the original direction. There is thus an inflexion point located on the bilge; first the line turns left, thereafter right. At the inflexion point the lateral pressure gradient changes sign; from positive upward to positive downward. The location of the inflexion point varies in the longitudinal direction on the hull, as seen in Fig. 6.17. Above the line connecting the inflexion points, cross-flow is developed downward(toward a lower pressure) whereas it develops upward (also toward a lower pressure) below the line. As explained in Section 6.6.1, it takes some time for the cross-flow to change from one direction to the other, so immediately after the inflexion the cross-flow profile will be S-shaped, but the cross-flows *in the inner part* of the boundary layer will have opposite directions above and below the inflexion line. In both areas, the flow will be toward the line, which means that the flow will converge along the line.

We thus have the situation described in Fig. 6.14 for the vortex type separation: because of streamline convergence in the inner parts of the boundary layer, a vortex sheet leaving the surface is created, and this sheet rolls up into a vortex essentially aligned with the external flow. The *bilge vortex* thus created is not very strong on most forebodies, but it may be significant on hulls which have a small bilge radius forward. It is an important task for the ship designer to avoid the forward bilge vortex to the largest possible extent because it increases the viscous resistance of the hull. One way to reduce the effect is to increase the bilge radius, but it is also possible to avoid the problems by fitting a bow bulb to the hull. The bulb creates a much more horizontal flow along the hull, even at the deeper levels, so the streamlines do not have to go over the sharp bilge, thus avoiding the low pressure in the region.

Although the bilge vortex on the forebody is normally weak, the corresponding one on the afterbody is much stronger. Looking at the streamline distribution aft, we see that the situation is the same as on the forebody: there

---

*In differential geometry, this is known as geodesic curvature.

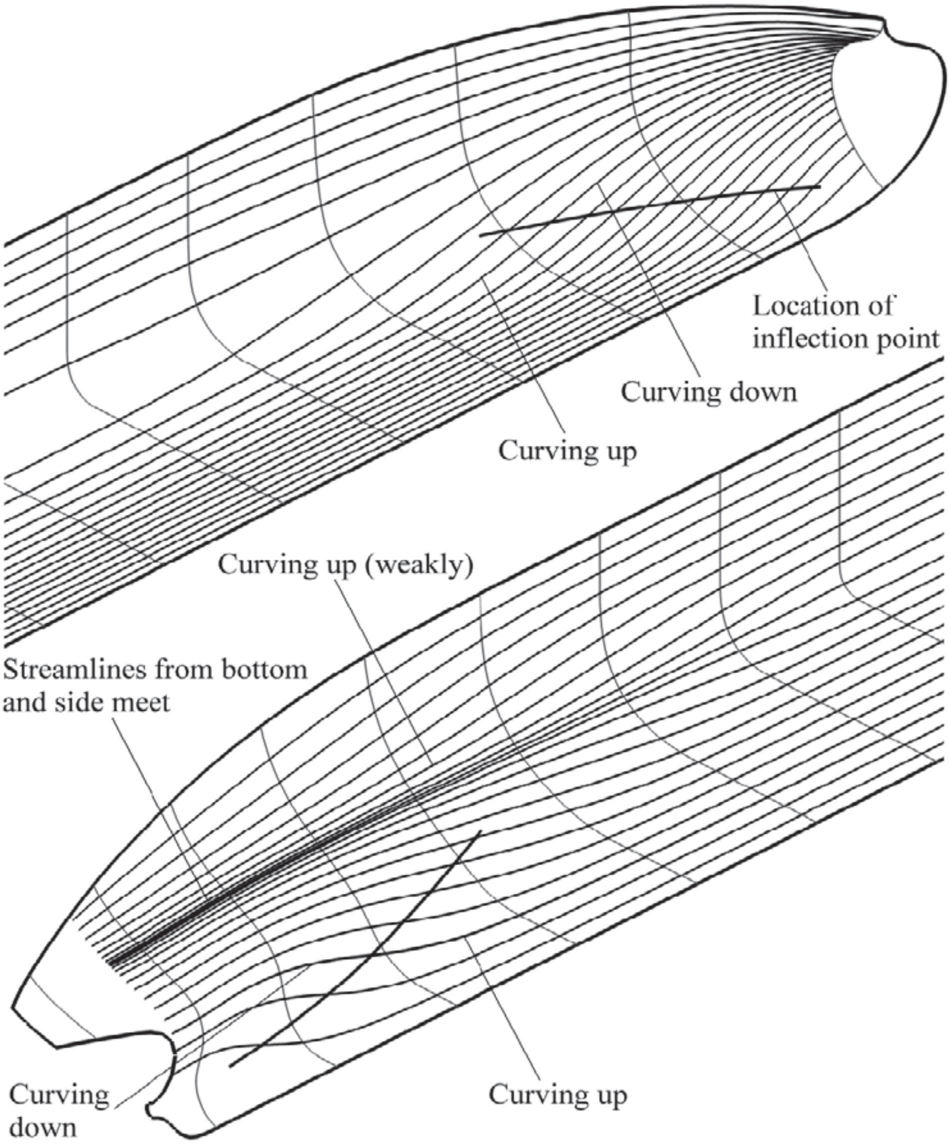

Figure 6.17 Inviscid streamlines on the KVLCC2 hull.

is a line connecting the inflexion points and the cross-flow developed will meet near this line. The reason why the stern bilge vortex is stronger is that the boundary layer is much thicker over the stern than over the bow. Related to this is a much smaller friction, which means that u_τ is smaller and so are the velocities in the wall law region. The momentum in the inner parts of the boundary layer is thus much smaller than on the forebody, so the flow will react much more easily to a lateral pressure gradient. The stern bilge vortex has a fundamental influence on the flow into the propeller, as will be seen shortly.

Another region of interest on the afterbody is that at about half draft. If we again look at the potential flow streamlines of Fig. 6.17, we see that they tend to converge along an essentially horizontal line. In order for the streamlines to converge along this line, and become more or less parallel there, the lateral curving of the flow is slightly upward above the line and, more strongly, downward below. The associated cross-flows thus go in the directions away from the line; the situation is opposite to that at the bilges. In Fig. 6.18, the computed limiting streamlines around the stern of the tanker are shown. The lines are traced based on the flow computed at the innermost points in the computational grid, very close to the surface ($y^+ < 1$). The conjectures from our discussion based on the lateral inviscid streamline curvature are here confirmed. At about half draft, the limiting streamlines diverge, but at the bilge they converge. The diverging flow turns almost vertical close to the aft contour, but there is no sign of bubble separation except at a very small region at the aft end of the keel. This hull is well designed; other very bluff hulls may encounter a

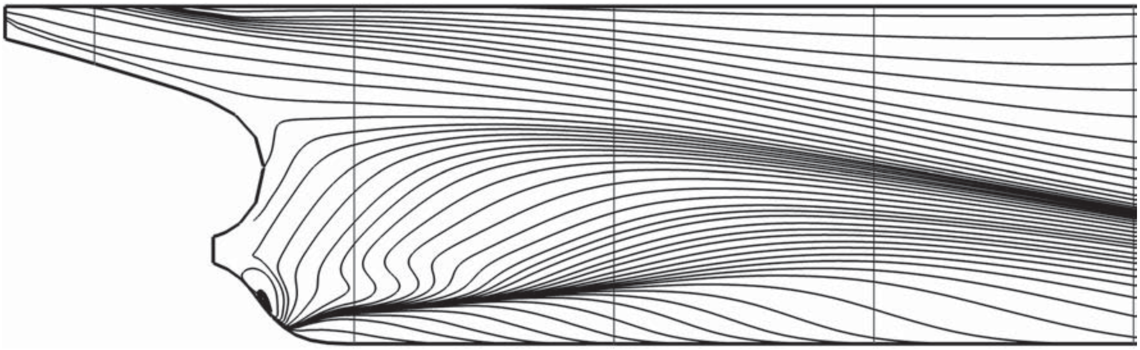

Figure 6.18 Limiting streamlines at the stern, model scale.

larger bubble separation in the region above the propeller shaft. As a result of the strong convergence of the limiting streamlines at the bilge, a strong bilge vortex is created and has an important effect on the flow into the propeller, as will be seen subsequently.

6.7.2 Cross-sections Through the Boundary Layer. We are now in a position to show the velocity distribution in several cross-planes on the afterbody. First, we note again that in the region at about half draft, the potential flow streamlines are convergent whereas the limiting streamlines are divergent. Thus, the flow in the outer part of the boundary layer, which is close to the external flow, is convergent but it is divergent close to the surface. This gives rise to a distinct two-layer structure of the boundary layer, with a stepwise change in velocity, as noted by Löfdahl and Larsson (1984).

Fig. 6.19 shows isovelocity contours at three stations along the hull, including the propeller plane. Contours are given for the axial velocity component u, made dimensionless by the undisturbed flow velocity U_∞. At the foremost station, the contours 0.7–1.0 are given, at the next station contours 0.4–0.9, and at the propeller plane contours 0.3–0.9. The reason why 1.0 is not given at the last stations is that the flow at the boundary layer edge does not reach this value. U_e is smaller than U_∞ in the stern region.

At the first station, the boundary layer is rather evenly distributed around the girth. This station is close to the parallel middle body. A considerable redistribution of the boundary layer thickness has however occured at the second station, which is in the region where the external streamlines (assumed equal to the inviscid streamlines) converge at half draft. Because of this convergence, the outer part of the boundary layer has increased considerably in thickness. Note the bulge of the 0.9 contour! However, the inner part of the boundary layer has become thinner because of the divergence of the inner (limiting) streamlines. This is reflected in the shape of the 0.4 and 0.5 contours just above half draft.

At the last station, the same features can be seen, but the most striking feature at this plane is the shape of the contours in the propeller disk. There is an “island” of low-velocity fluid, represented by the 0.3 and 0.4 contours in the central part of the propeller disk. On closer inspection, it turns out that this island is created by the bilge vortex from the stern, which hits the propeller plane in this region. Fig. 6.20 shows a projection of the velocity vectors in the plane. As seen in Fig. 6.19, the vortex tends to move low-speed fluid outward from the region near the propeller center and inward further up. The prediction of the bilge vortex and the associated “hooks” in the velocity contours was a major challenge to the CFD community for two decades (see Section 1.2.3), but at present very accurate predictions can be made. Obviously, the detailed shape of the velocity contours has an important effect on the operation of the propeller. This topic will be further discussed in Section 11.4.1.

The first order boundary layer theory, introduced in Section 6.2.2, is adequate for predicting the boundary layer development over the major part of the ship hull, see Larsson (1981), and can be used for rapid estimates of the flow. However, the theory fails close to the stern, where the boundary layer is too thick for the basic assumption to hold. Terms neglected in the first order equations become important, and the inviscid pressure distribution is modified by the boundary layer displacement effect, as seen in Fig. 6.16. For ship stern flows the less approximate methods of Sections 9.7 and 9.8 are required.

6.7.3 Effects on Viscous Resistance. The drag increase due to the bow bilge vortex was mentioned previously. A similar increase occurs for the stern vortex. However, in this case, there are advantages that might outweigh the disadvantage of a larger resistance. Because the velocity contours in the propeller plane get a rounder shape caused by the vortex, better conditions for the propeller are created. If the axial velocity at a given radius is kept as constant as possible, variations in the angle of attack of the rotating propeller blades are minimized and so are the load variations. This has a favorable effect on noise and vibrations, and the propulsive efficiciency may be increased. A more thorough discussion on these effects will be given in Section 11.

Although there is practically no bubble type separation for this hull, bluffer or less well designed afterbodies may experience this problem, which is associated with a large momentum loss, and thus with a considerable drag increase. Therefore, bubble separation should be avoided.

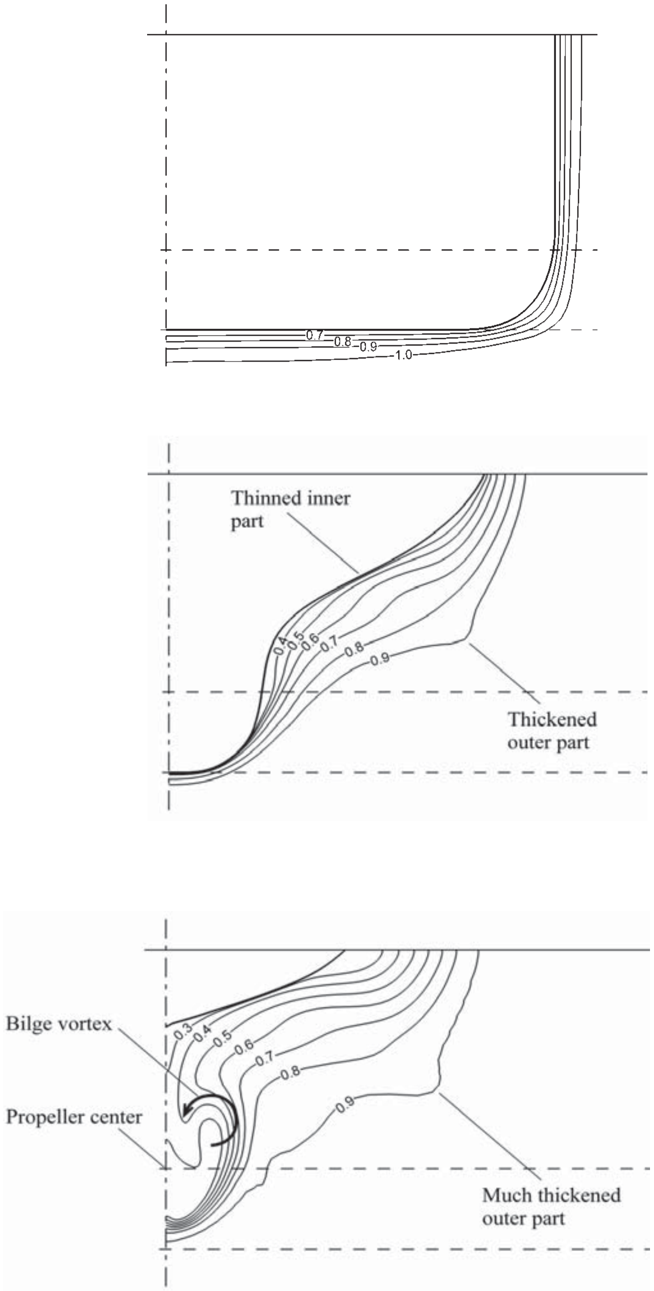

Figure 6.19 Contours of constant axial velocity at three stations, 82.5%, 95.5%, and 99.125% of L_{pp} from the FP. The latter station is the propeller plane. Velocities are nondimensionalized by the undisturbed velocity; model scale.

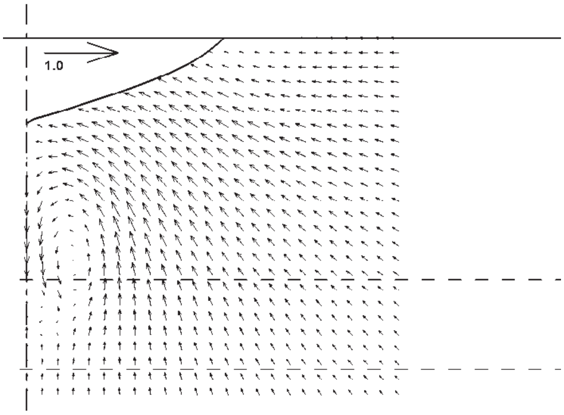

Figure 6.20 Projection of velocity vectors at the propeller plane; model scale.

For both types of separation, the resistance increase is caused by a loss of pressure on the hull, but there is also a small compensating effect in a loss of friction. More important boundary layer effects on the friction are, however, the larger shear stresses in regions where the boundary layer is thin. This is seen in Fig. 6.21. Along the keel where the boundary layer is thin because of divergence of the external streamlines, the friction is very high. There is also a much higher friction on the forebody than on the afterbody, as expected, because of the thinner boundary layer.

6.7.4 Scale Effects. As appears from the flat plate equations in Section 6.3, the boundary layer depends on the Reynolds number. The flat plate boundary layer thickness, for instance, is inversely proportional to the Reynolds number to the one-fifth power. Because the Reynolds number for a ship is normally at least two orders of magnitude larger than that of a model, there should be a considerable difference in the relative boundary layer thickness between the model and the ship. In fact, all quantities presented in Sections 6.7.1 and 6.7.2 for the model are different for the ship, except the inviscid flow results, which are independent of scale.

Fig. 6.22 shows the pressure distribution around the stern of the full-scale KVLCC2 hull at a Reynolds number of $2.0 \cdot 10^{10}$. Looking at the pressure minimum at the bilge and the maximum at the aft end, it is obvious that the full-scale pressure is closer to the inviscid results of Fig. 6.15, as compared with that of the model in Fig. 6.16 (Reynolds number $4.6 \cdot 10^6$). The thinner boundary layer causes a smaller displacement effect (i.e., a reduced smoothing of the pressure variations).

The limiting streamlines for the full-scale hull are presented in Fig. 6.23. As compared with the model streamlines in Fig. 6.18, the full-scale ones do not diverge as much on the afterbody and the convergence in the bilge region is not so strong. The vortex separation is weaker and the bilge vortex less pronounced. This is well reflected in the shape of the wake contours seen in Fig. 6.24. The hook-like shape of the innermost contours for the model in Fig. 6.19 has now disappeared. Much smoother contours are obtained because of the reduced stirring effect of the bilge vortex. Comparing contours 0.3–0.8 at model- and full-scale also reveals the expected thinning of the boundary layer at the high Reynolds number. The outermost contour, 0.9, has not moved much because it is likely to be outside the boundary layer, at least at full scale.

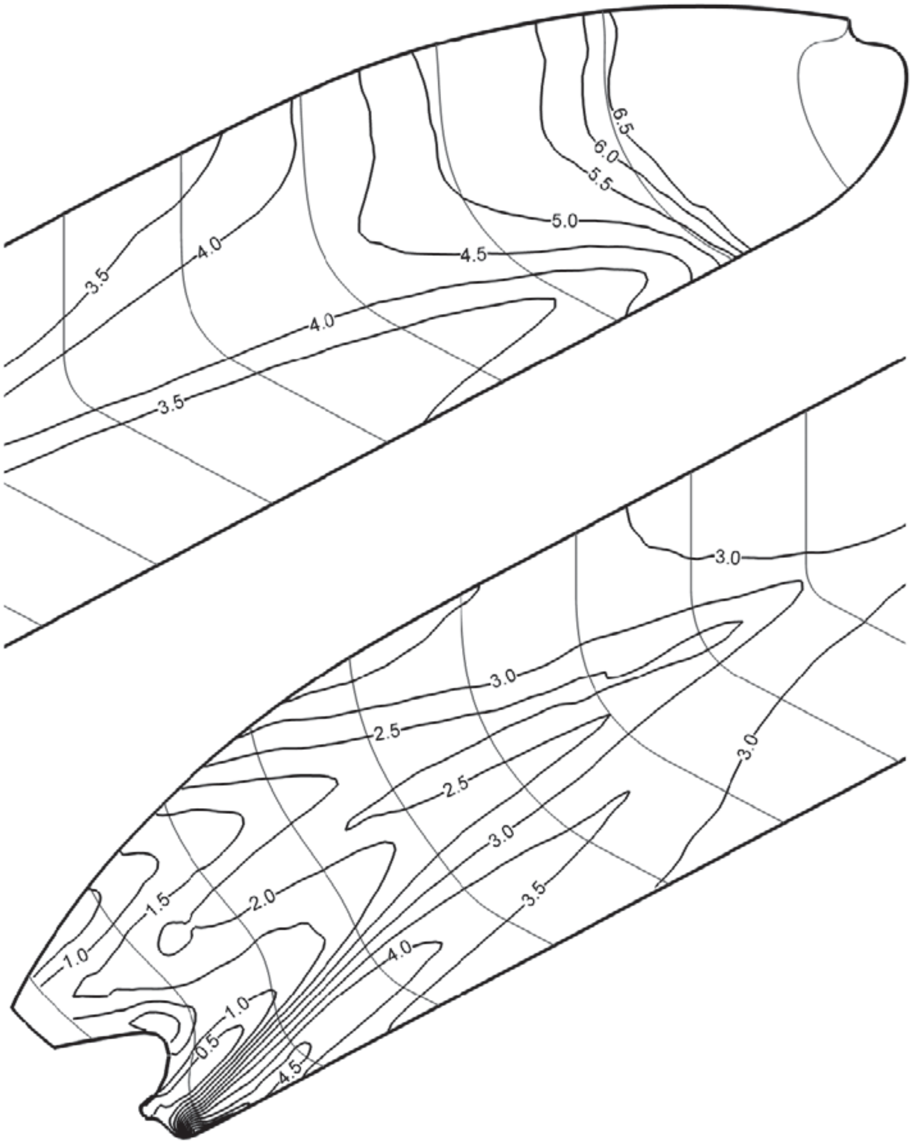

Figure 6.21 Distribution of friction on the hull at model scale. Contours labeled by the local skin friction coefficient multiplied by 1000.

The smaller boundary layer displacement effect at full scale, and the correspondingly smaller modification of the inviscid pressure distribution at the stern, also has an effect on resistance. The viscous pressure resistance becomes smaller. Although there is a very small increase in the form effect on friction (see Section 4.1), the total form effect is reduced, and the general assumption in model testing it is that the form factor is constant. The viscous resistance is thus proportional to the flat plate friction, according to equation (6.39). The validity of this assumption is discussed in Section 8.3.4.

6.8 Roughness Allowance. The boundary layer development around increasingly complex bodies has now been described. We have assumed that the flow is not influenced by imperfections in the surface (i.e., that the surface is hydraulically smooth). This is most often true for well manufactured ship models, but not for full-scale ships. As appears from Fig. 4.1, the roughness resistance, or allowance, may be considerable. In this section, we will first discuss the characterization of roughness and thereafter its influence on the boundary layer and the resistance.

6.8.1 Roughness and Fouling on Ships. There are different kinds of roughness on the hull surface of a ship. The new plates used for the hull skin are normally shot blasted and relatively smooth, but still not hydraulically smooth at the speed of the ship. Welding joints cause additional roughness. On the plate, there are several layers of paint which are not smooth, and over time both the steel surface and the paint deteriorate. Further, a considerable increase in roughness may be caused by fouling.

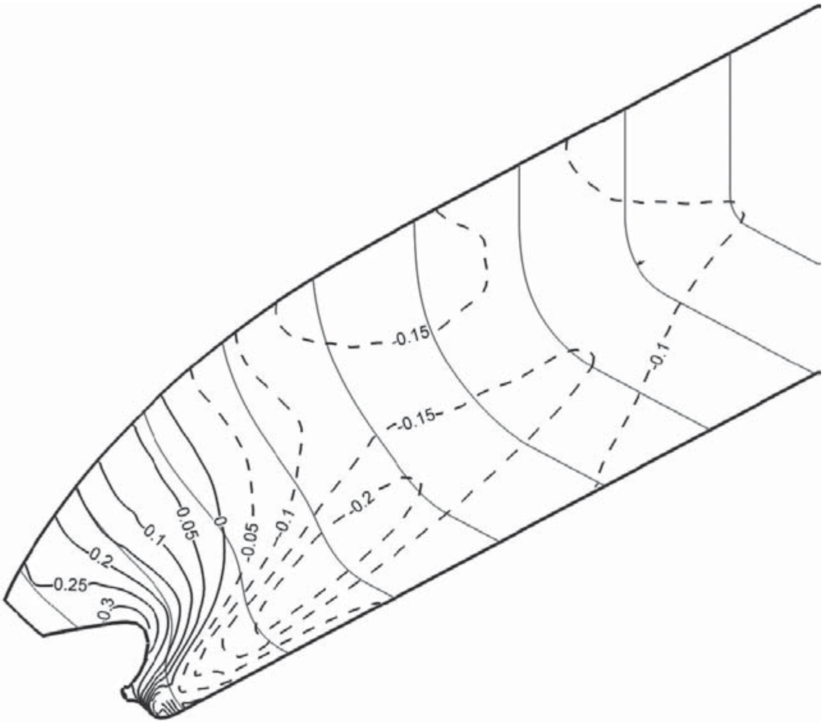

Figure 6.22 Pressure distribution around the stern at full scale. Contours labeled by C_p.

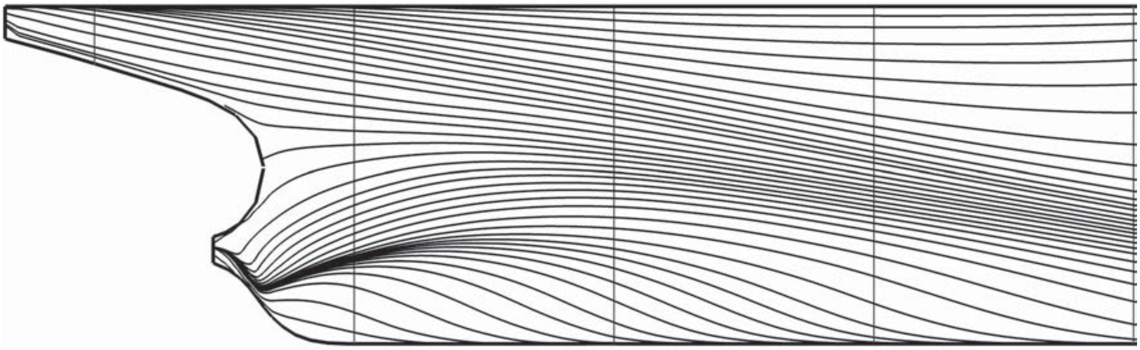

Figure 6.23 Limiting streamlines at full scale.

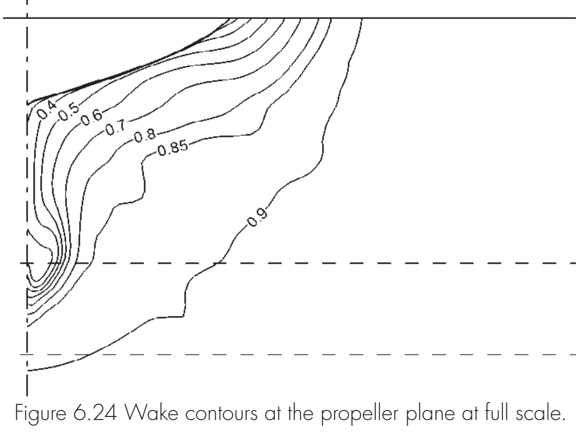

Figure 6.24 Wake contours at the propeller plane at full scale.

During the past decades, a new type of antifouling paint has been introduced, which eliminates some of the problems. The new self-polishing copolymer (SPC) paint becomes smoother and smoother with time, due to abrasion of the peaks of the roughness elements in the paint. Because the speed of the flow is higher over the peaks than over the valleys, the friction is larger and so is the abrasive effect. Thanks to the abrasion, fouling is also reduced. Through the introduction of the SPC paints, the docking period has been increased from typically 1.5 years to about 5. The hull may stay in service as long as there is still enough paint left to cover the surface. According to Almeida, Diamantino, and de Sousa (2007), the SPC-active antifouling agent tributyltin (TBT) accounted for close to 70% of all commercial ship coatings in 1999.

The introduction of the SPC paints has greatly reduced the roughness problem for ships, but there is another trend that may again increase the problem. Thanks to the greater awareness of environmental problems, the toxicity of the antifouling paints will have to be reduced. The use of toxic paints in lakes is already banned for pleasure craft in some countries, and for such craft the use of the most harmful paints like TBT has been banned for a long time. For commercial ships, tin-based paints were phased out over a period from 2003 to 2008 according to an agreement within the International Maritime Organization.

Because of the ban of TBT coatings, a wide array of substitutes have emerged on the market. Biocide coatings are available within three groups: controlled depletion paint, tin free-SPC, and hybrid systems. They all release biocides, but with less toxic antifouling agents, such as copper oxide and cobiocides, compared to TBT coatings.

Fully biocide-free alternatives are also available, working in a different way. Instead of killing the fouling, these coatings create a surface for which adhesion of marine organisms becomes difficult or impossible. One approach within this category is silicone or fluoropolymer coated surfaces, which usually require ship speeds of at least 15 knots to keep the surface clean of biofouling. Another approach is to give the surface a special structure preventing barnacles from attaching (Berntsson et al., 2000; Dahlström et al., 2000). An excellent overview of antifouling paints is found in Almeida, Diamantino, and de Sousa (2007).

6.8.2 Characterization of Roughness. Attempts have been made in the past to characterize roughness by several parameters and to link these parameters to an increase in skin friction. However, these attempts have not been successful. In most techniques for computing the roughness resistance, some measure of the roughness height is the only geometrical quantity, but in more advanced methods height is also combined with some measure of the roughness efficiency.

The classical way to compute roughness resistance is to refer to surfaces covered by densely packed sand. For such surfaces, the roughness allowance is well known. The so-called *equivalent sand roughness*, k_s, for different types of surfaces can be found in standard text books on mechanical design. Some examples are given in Table 6.2.

Table 6.2 Equivalent Sand Roughness for Different Surfaces

Type of Surface	Equivalent Sand Roughness, $k_s(\mu)$
Glass	0.3
New tubes (brass or copper)	1.5
Cast iron	250
Concrete	30–300
Wood	20–1000

In ship hydrodynamics, the generally accepted way to quantify roughness is to use the Mean Apparent Amplitude (MAA) method. The roughness of the surface is registered using a needle at right angles to the surface, supported by a small carriage. When the carriage is moved along the surface on a special rail, the needle is allowed to move up and down and tracks the contour of the surface, which is registered. Normally, the contour is measured in this way along a straight line 750 mm long. This line is then divided into 50 mm intervals and within each interval the distance, measured normal to the surface, from the highest peak to the lowest valley is recorded. The roughness height k is obtained as the mean of the 15 values. The MAA value is thus a kind of mean wave height based on a 50 mm wave length.

Fig. 6.25 shows the increase in roughness with time for a large number of ships before the SPC-era (Townsin et al., 1980). For newer ships, k (MAA) was about 100 μ, but for older ships heights of 600–700 μ were common. Note that this was for cleaned, but not shot-blasted hulls. As explained, the roughness does not increase with time for SPC-coated hulls, rather the opposite.

6.8.3 Hydraulically Smooth Surfaces. Experience shows that a surface may be considered hydraulically smooth if the roughness elements are embedded in the viscous sublayer, defined by equation (6.26). The requirement is thus that the roughness should be within $y^+ = 5$. With k as the roughness height

$$\frac{u_\tau k}{\nu} \leq 5$$

or

$$k \leq \frac{5\nu}{u_\tau} \tag{6.42}$$

The friction velocity u_τ may be obtained from the definition (6.21) using a skin friction formula such as equation (6.34). Because the skin friction is generally reduced with the distance from the bow, u_τ will also decrease, which will cause an increase in permissible roughness aftward.

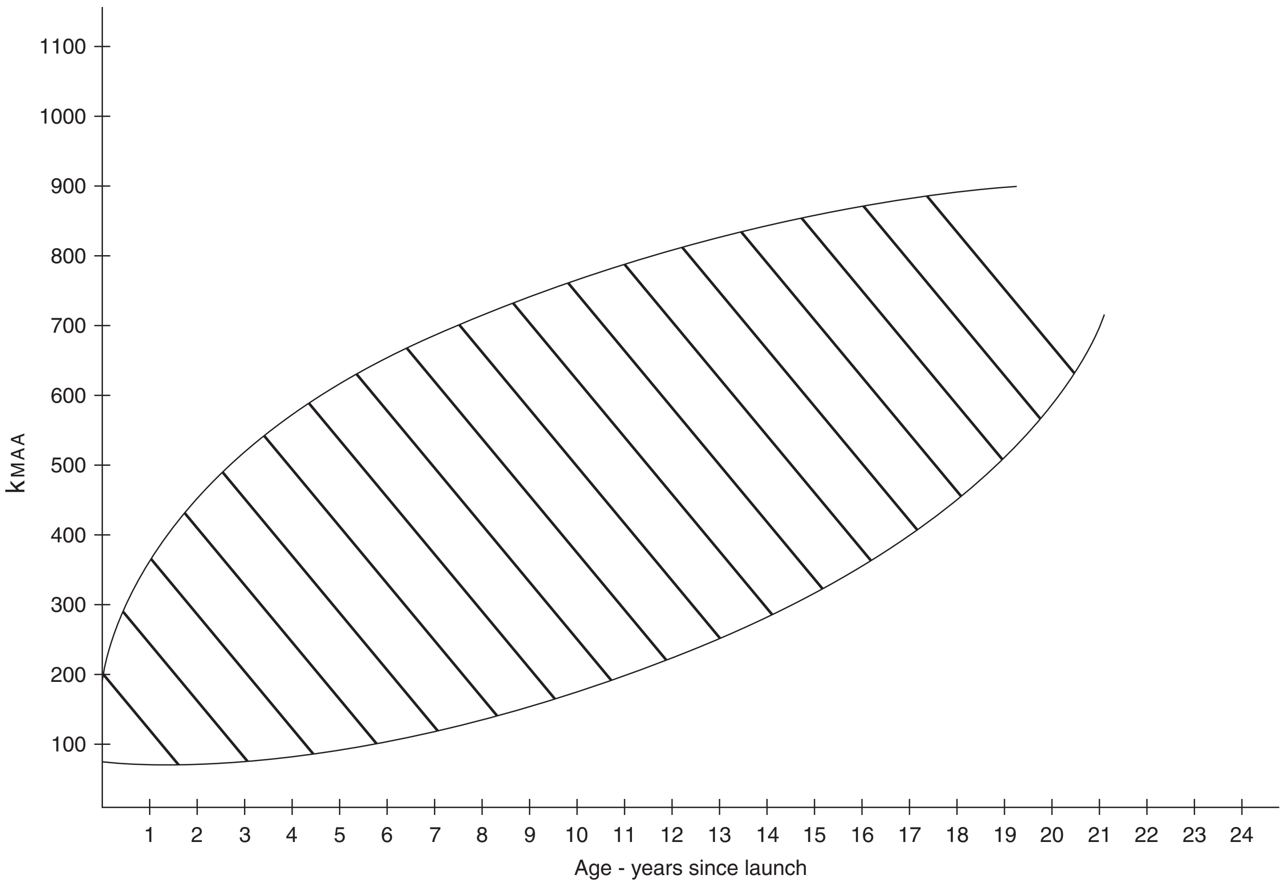

Figure 6.25 Roughness measured on ships before the SPC-era (excluding shot-blasted hulls).

If a very rough estimate of the permissible roughness is required, a very simple and easy to remember formula is the following

$$k = \frac{100}{V} \tag{6.43}$$

where k is the roughness height *in microns* and V is the speed in m/s. The maximum speed of pleasure craft of the displacement type is typically 4 m/s (8 knots), which yields a permissible roughness of 25 μ. For large ships, a typical speed is 10 m/s (20 knots), which yields a height of 10 μ. This is a conservative estimate giving the permissible roughness over the forebody.

6.8.4 Roughness Allowance Prediction. If the equivalent sand roughness is known, the Prandtl-Schlichting diagram (Schlichting, 1987) may be used for determining the roughness allowance, ΔC_F. However, the equivalent sand roughness is rarely known for ship hulls. Experiments are needed to obtain data based on the MAA roughness. A device (*floating element balance*) used for such tests is shown in Fig. 6.26 (Johansson, 1984). The surface to be

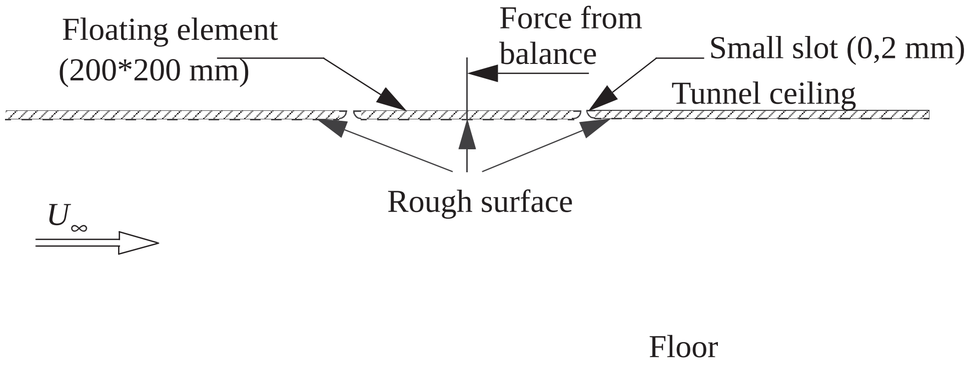

Figure 6.26 The floating element balance (principle).

tested is mounted on the ceiling of a water or wind tunnel. A small piece of the surface (the *element*, typically 200 × 200 mm for a water tunnel) is cut out and separated from the surrounding plate by small slots (typically 0.2 mm). The element is held flush with the surface by a balance mounted outside the tunnel and the shear force is measured by the balance.

On the basis of floating element measurements for plates treated in the same way as a newly built ship, the diagram shown in Fig. 6.27 has been produced (Johansson, 1984). This diagram should be more accurate than the Prandtl-Schlichting diagram, and might be used for ship surfaces also after a certain time in service. Note that the roughness height is denoted h in this diagram. h is measured using the MAA method.

An alternative way of measuring friction is to use pipes where the pressure drop is registered. This technique is considerably less expensive than the one just described, which requires a water or wind tunnel, but the disadvantage is that the roughness of interest has to be applied to the inside of the tubes. The method is less accurate for measuring small skin friction increases, and requires some assumptions and corrections to be applicable for flat plates and ship flows. But for large skin friction increases (i.e., from biofouling) and high Reynolds numbers, it is a very efficient method (Leer-Andersen & Larsson, 2003). Other skin friction measurement methods used are flow cells or flat plate towing in a tank .

6.8.5 Bowden's Formula. There are still relatively few data available for rough surfaces in hydrodynamics, so rather than using the existing data, the ITTC decided in 1978 to use an empirical formula for the roughness allowance in the model-ship extrapolation procedure. This formula, attributed to Bowden, reads

$$\Delta C_F = \left[105\left(\frac{k}{L}\right)^{1/3} - (0.64)\right]10^{-3} \tag{6.44}$$

where k is the MAA roughness height.

Bowden derived this formula in a very interesting way. He compared the results of a large number of ship trials with the corresponding extrapolated values from model tests without including any correction for the roughness of the ship surface. The gap thus found between "reality" and extrapolated values was attributed to roughness, and the roughness allowance was expressed as an equation (6.44). This ΔC_F must contain other effects, not accounted for in the model-ship extrapolation procedure, but as

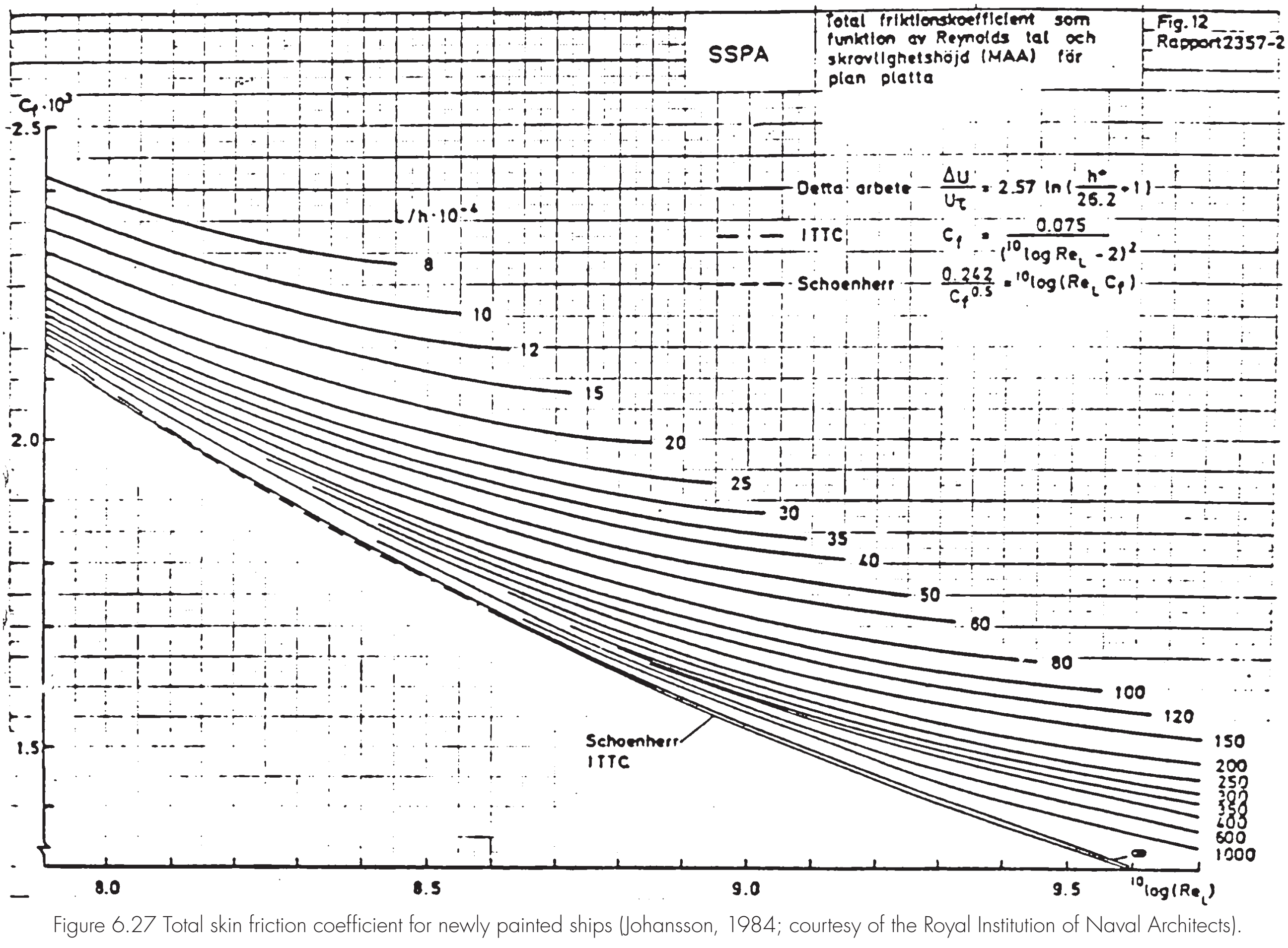

Figure 6.27 Total skin friction coefficient for newly painted ships (Johansson, 1984; courtesy of the Royal Institution of Naval Architects).

a means for correcting model-scale data, it is probably better than using data from measurements with rough surfaces. If, on the other hand, the true effect of roughness is requested, Bowden's formula should not be used.

We will return to the roughness allowance in Section 8 in connection with the ITTC-78 procedure for extrapolating model test data to full scale. It may be of interest to note that before the introduction of Bowden's formula, a constant ΔC_F equal to 0.0004 was used by towing tanks.

6.8.6 Fouling The roughness discussed so far arises from imperfections in the surface of the hull plates or coating. If the surface is covered by fouling, considerably larger increases in resistance may be seen. Because the geometry of such roughness elements may differ widely, it is hard to give any general guidelines for their effect on friction. However, the diagram of Fig. 6.28 may be used for surfaces covered with densely packed barnacles. It was derived from measurements using a floating element balance and a surface with barnacles 5 mm high, covering almost 100% of the surface (Johansson, 1984). The diagram may be used for other heights of the barnacles, but they need to be densely packed. In a study using the pipe flow technique, a large number of surfaces covered with barnacles of different density were tested and the results may be found in Leer-Andersen and Larsson (2003).

6.9 Drag Reduction. During the past 60 years, the possibilities of reducing the friction to a level below that of a hydraulically smooth surface have been known. Toms (1948) noted in experiments with dilute polymer solutions in tubes that the friction coefficient in the tube was very much affected by the polymers. Very large reductions in resistance turned out to be possible and in systematic experiments by Paterson and Abernathy (1970), drag reductions of 75% were noted for a concentration of 50 parts per million (PPM) of long-chain molecule polymers. More recently, even larger reductions, up to 90%, have been measured for concentrations of 100 PPM and with more efficient polymers. Even for concentrations as low as 1 PPM, effects are noted.

The physical mechanism behind the drag reduction has not been fully explained, but there is an obvious effect on the turbulence. It has been suggested (see Marchaj, 1979) that the long and flexible molecules, which align themselves with the flow, will have a damping effect on transverse oscillations, thereby delaying transition of a laminar flow and reducing the growth of the turbulent spots in the viscous sublayer in turbulent flow. Note that all polymers are not equally effective. They need to have a high molecular weight and good solubility. The most popular one for drag reduction is Polyethylene-oxide. Other substances have also turned out to have a similar effect, for instance polysaccarides, which have been proposed for drag reduction of sailing yachts.

An unwanted drag reducing effect has also been found in towing tanks polluted by some algae. In experiments at the towing tank at Haslar, England, with the vessel *Iris* the resistance, seemingly without reason, dropped more than 10%. This phenomenon, which could be explained later as an effect of algae in the water, has become known as "Iris storms" (Marchaj, 1979) and is very much dreaded by towing tank experimentalists. To avoid the problem, most towing tanks are built to avoid direct exposure to the sun of the water surface. Many tanks are without windows, and where there are windows they normally face north (on the northern hemisphere).

Another drag reduction technique is to introduce air (or another gas) in the innermost part of the boundary layer. The most promising results have been achieved with microbubbles covering the surface, and as much as 80% drag reduction has been demonstrated (see Merkle & Deutsch [1989] for a survey of the early work in this area). An explanation of the effect has been proposed by Ferrante and Elghobashi (2004). The presence of the bubbles induces a velocity away from the wall and this influences the structure of the flow near the surface. Longitudinal vortices are "lifted up," and the streaky pattern of alternating low- and high-speed flow near the surface is changed such that the high-speed regions are reduced and the low-speed regions increased. The microbubbles should be quite small, typically 50 μ in diameter, and it seems to be necessary to keep them at this level to get a large resistance reduction. Tests by the author (Larsson) have shown that there are several practical problems involved in applying this technique. It is virtually impossible to create an even layer of bubbles beneath the horizontal surface, and once the bubbles are created, they tend to cohere, forming larger bubbles with a much larger buoyancy. If the hull surface is not perfectly horizontal (which it seldom is in reality), the bubbles will then move rapidly toward the water surface.

More recently, there has also been an interest in a related technique where a thick layer of air is introduced in a cavity at the flat bottom of the ship. The cavity is designed such that only a little air escapes downstream, and an air–water interface is created over a considerable part of the bottom. Very little friction is created at this interface.

Dolphins are believed to have a very high swimming efficiency. Estimates by biologists (Gray, 1936) of the available power suggest that the resistance of the animal must be considerably lower than for a rigid body of the same shape and size. One explanation offered is that the flexible skin of the dolphins may have a damping effect on the turbulence in the boundary layer, thereby making it more laminar and thus with less friction. Inspired by this idea, Kramer (1961) carried out a large number of tests with bodies having flexible skins. The idea was also investigated by several others and drag reductions of some 10% were measured using compliant coatings on a surface. However, in similar tests at the American National Aeronautics and Space Administration (NASA) (Bushnell, Hefner, & Ash, 1977), no

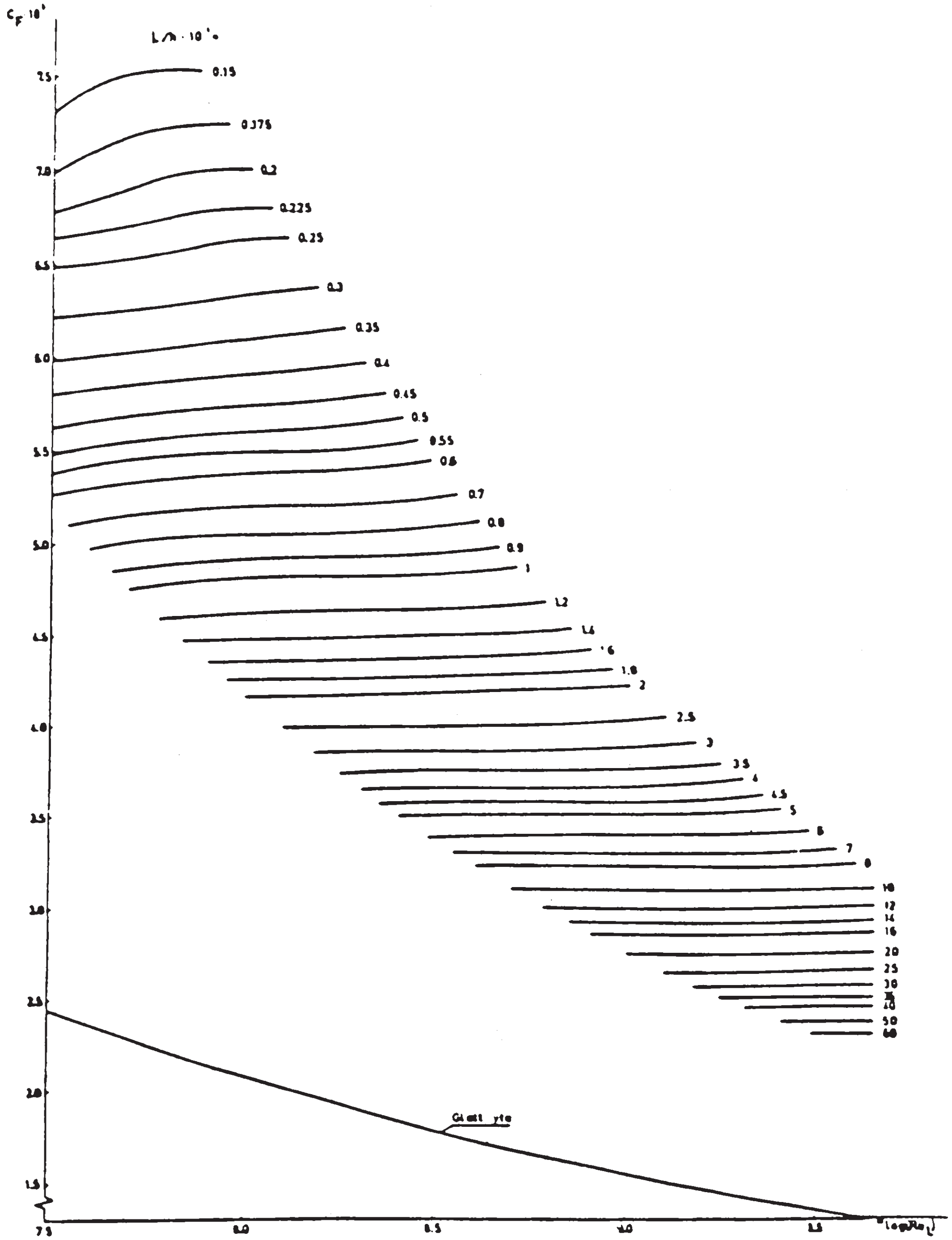

Figure 6.28 Total skin friction coefficient for surfaces covered with densely packed barnacles (Johansson, 1984; courtesy of the Royal Institution of Naval Architects).

reductions were noted, and the positive results previously reported were attributed to other reasons, such as inadequate measuring equipment. The high swimming efficiency of the dolphins is likely because of other effects, possibly an active turbulence control through vibrations in the skin. It has also been suggested that the efficiency is simply because the dolphins jump out of the water regularly to breathe, and the resistance in the air is about three orders of magnitude smaller than in the water.

The skin of sharks has also been studied with interest by experimentalists interested in drag reduction (see e.g., Bechert et al., 1986). The dermal denticles of the skin form a ridge-like texture, which may affect the

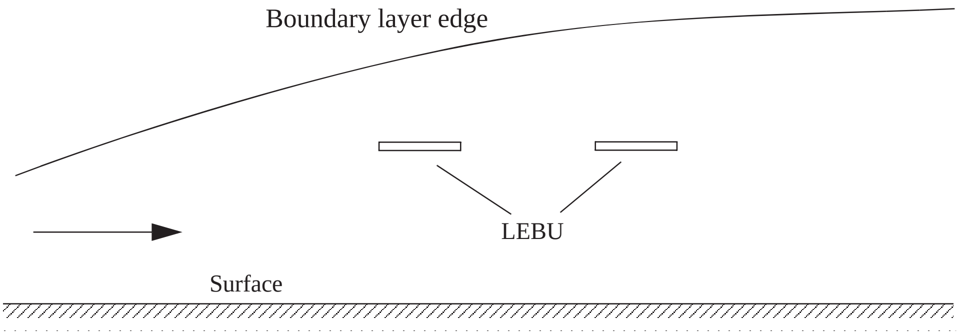

Figure 6.29 LEBU.

growth of the turbulent bursts in the viscous sublayer, thereby making the flow more laminar. This idea was adopted by a group of NASA scientists (Walsh & Lindemann, 1984), who tested the effect of small riblets on the surface, aligned with the flow. The height and spacing of the riblets was quite small, typically about 0.1 mm, but the effect on the friction was significant, around 10%. To put the idea to practical use, the American company 3M (St. Paul, MN) developed a plastic adhesive film, with an exterior structured in the way suggested by the NASA specialists. The film was used in the 1987 America's Cup races by several teams, but the effect was questioned, most likely because of the difficulties of sticking the film to the nondevelopable hull surface without wrinkles and gaps between film patches. The film was not a success, and it is no longer produced by 3M. However, some scientists in Sweden observed that a structure, much like the 3M riblets, prevented barnacles from settling on a surface (Berntsson et al., 2000). They also obtained a patent of the idea of combining the antifouling effect with drag reduction and are presently developing an alternative plastic film technique for application on pleasure craft.

Another drag reduction technique which was much tested during the 1980s is based on the idea of breaking up the large eddies in the boundary layer. As explained in Section 6.2, eddies of a range of sizes are present in this layer. Although the smallest eddies are of the order of 0.1 mm for ship models and full-size ships, the largest ones are of the order of the boundary layer thickness. If the latter are disturbed, the entrainment of external fluid into the boundary layer is affected, which could have an effect on the friction. To obtain a suitable disturbance, "wings" or steel ribbons (large eddy break-up devices [LEBUs]) are placed in tandem parallel to the surface at a distance of about 0.75δ from the surface. The principle is shown in Fig. 6.29.

Earlier low Reynolds number tests indicated a net drag reduction (considering the extra drag of the LEBUs) of some 20%, but later experiments at more interesting Reynolds numbers showed very disappointing results. The drag of the LEBUs was almost exactly as large as the reduction in friction on the plate tested. See Walsh and Anders (1989) for a survey. The present interest in this technique is low.

7

Other Resistance Components

In Section 4, the two main resistance components (i.e., the wave and viscous resistance) were discussed first (in Section 4.1), and additional components were introduced thereafter (in Section 4.2). Having completed a more thorough discussion of the two main components in Sections 5 and 6, we will now turn to the additional resistance components. Note that the blockage effects were covered already in Sections 5.9 to 5.12. According to Section 4.2, the remaining effects are:

1. Induced resistance
2. Appendage resistance
3. Air and wind resistance
4. Added resistance in a seaway

The latter is very closely linked to the theory of seakeeping and the reader is referred to the Seakeeping volume for an introduction. In the present section, we will concentrate on the first three components, which may be of importance for a wide variety of vessels, from sailing yachts to slender high-speed ships and bluff tankers.

7.1 Induced Resistance. The induced resistance is a component which appears because of lift generation in an asymmetric flow. It is of importance for wing-like bodies such as keels and rudders, but also for hulls under certain circumstances. Typical examples from hydrodynamics are:

- Sailing yachts at non-zero leeway
- Ships at non-zero leeway
- Rudders at non-zero angle of attack
- Hydrofoils
- Bilge keels and stabilizers
- Twin skeg sterns
- Catamaran hulls
- Trimaran outriggers

It should be noted that the induced resistance is an inviscid phenomenon, governed by the equations of Section 5.

7.1.1 Lift Generation. Because the induced resistance is closely linked to lift, a short explanation of the physics of lift generation will be given in this paragraph. Note that "lift" is an expression borrowed from aerodynamics, where the lift force is normally directed upward, balancing the weight of an aircraft. In hydrodynamics, the lift is mostly horizontal,* acting to move the body sideward, relative to the direction of motion. The theory of lift and induced resistance was developed in aerodynamics more than 100 years ago and is well described in the aerodynamics literature (see e.g., Kuethe & Chow [1986] or Anderson [1991]).

Consider the wing in Fig. 7.1. The wing is an obstacle for the flow approaching from the left. Because the fluid cannot penetrate the wing, it has to follow its contour,* which means it will leave the trailing edge in a direction different from that of the undisturbed flow far ahead. The major effect of the wing on the fluid is thus to change the flow direction. The wing exerts a force on the flow to make it turn. This force is equal, but opposite to the force exerted on the wing by the flow (i.e., the lift). In general, the streamlines around the wing will turn downward. The center of curvature is thus below the wing. Referring to the relation between streamline curvature and lateral pressure gradients introduced in Section 5.2, it may be concluded that the pressure on the lower side must be higher than the undisturbed pressure whereas the opposite is true on the upper side, where a suction is developed (see the discussion of Fig. 5.2).

For the flow deflection, and hence lift generation, to be effective, the trailing edge should be sharp. The flow should leave the trailing edge smoothly on both sides. This is called the Kutta condition and is a key element in inviscid flow theory. It may be applied either as an equal pressure condition, where the pressure is set equal on the two sides of the trailing edge, or as a flow direction condition, where the flow is specified to be in the bisector plane immediately after the trailing edge.

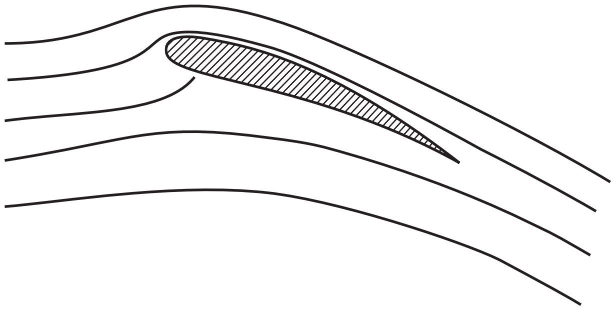

Figure 7.1 Lift generation.

---

*For sailing yachts, the lift may be inclined relative to the horizontal plane. It is assumed to heel with the yacht.

*In a viscous fluid, the flow may separate on the upper side of the wing. The flow may then be directed forward on the surface in the separated region. For wings operating properly, the separated region is small, however, and does not disturb the turning of the main flow significantly.

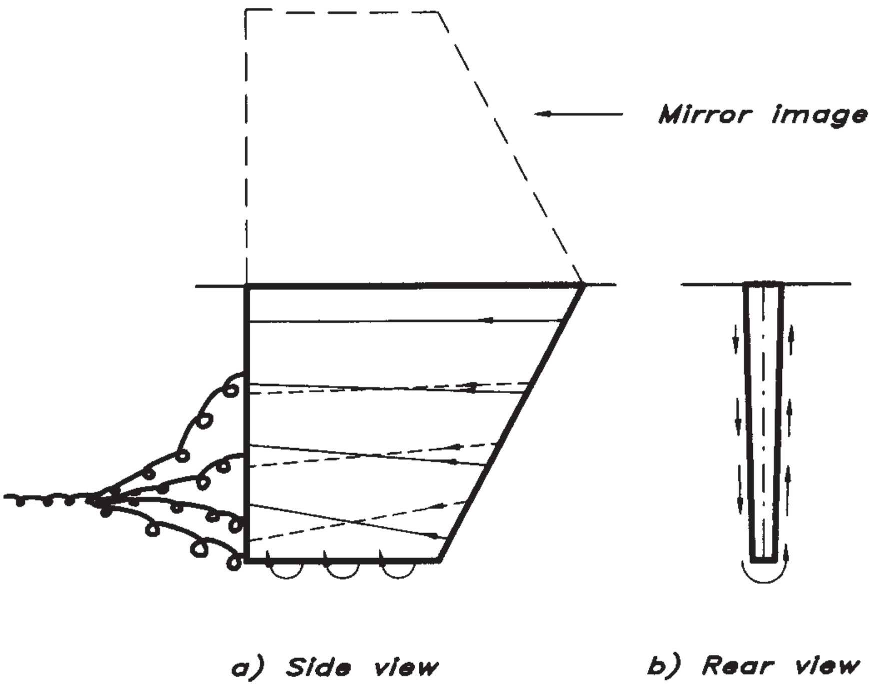

Figure 7.2 Vortex generation around a keel.

7.1.2 Vortices and Induced Resistance. Fig. 7.2[†] shows a sailing yacht keel moving at an angle of attack equal to the leeway angle of the hull. Because there is nothing preventing the flow on the pressure (leeward) side of the keel in Fig. 7.2 to escape below the tip to the low pressure on the other side, a cross-flow around the tip is generated. This means that the flow on the entire pressure side will have a downward velocity component superimposed on the main flow backward. On the suction side, the opposite is true, and the effect increases toward the tip on both sides. Thus, the flows from the two sides will move in slightly different directions when they meet at the trailing edge. Fluid elements just behind the trailing edge will experience a downward stress component on one side and an upward stress on the other. As a result, they will start rotating around a horizontal axis. Longitudinal trailing vortices are generated. At the keel root, the flow is along the hull bottom on both sides, so there is no vortex generation,* but the closer the tip, the stronger the vortices. The vortex sheet leaving the trailing edge is unstable, and it ultimately rolls up into one concentrated vortex behind the keel. Because the trailing vortex system contains rotational energy, it corresponds to an increase in resistance, which, multiplied by the speed, will yield a work per time unit equal to that required for generating the vortices.

Note that a prerequisite for the trailing vortex system to appear is a free end of the keel (or wing, in general). If there is no free end, no trailing vortices will develop, and there will be no induced resistance. An example is a wing mounted between the walls of a wind tunnel. This is a set-up used for testing different cross-sections. There is no free end, so the flow cannot escape from the pressure side to the suction side, and hence no trailing vortices of this kind are generated.* A wing of constant section spanning a wind tunnel is an example of a 2D case. For such cases, the induced resistance is zero.

In Fig. 7.3, a 3D wing is represented by its vortex system. The wing may be seen as the keel tilted 90 degrees and with the hull bottom as the plane of symmetry (x-z plane) shown in the figure. In this mathematical representation, the wing itself is replaced by a bound vortex (along the y-axis). Free trailing vortices in the local flow direction are shown behind the wing. In fact, the vortex system may be considered a superposition of a bunch of horseshoe vortex filaments with different span. Along each filament, from the trailing part on one side through the bound part on the wing and back to the trailing part on the other side, the vortex strength is constant. At every spanwise position on the wing, the total bound

---

[†] Fig. 7.2 is reproduced from Larsson and Eliasson (2007). Courtesy of Adlard Coles Nautical.

*A local vortex may, in fact, appear in the junction between the keel and the hull (or the wing and the tunnel wall), but this is a completely different effect caused by interference between the boundary layers on the hull and the keel (or the wing and the tunnel wall).

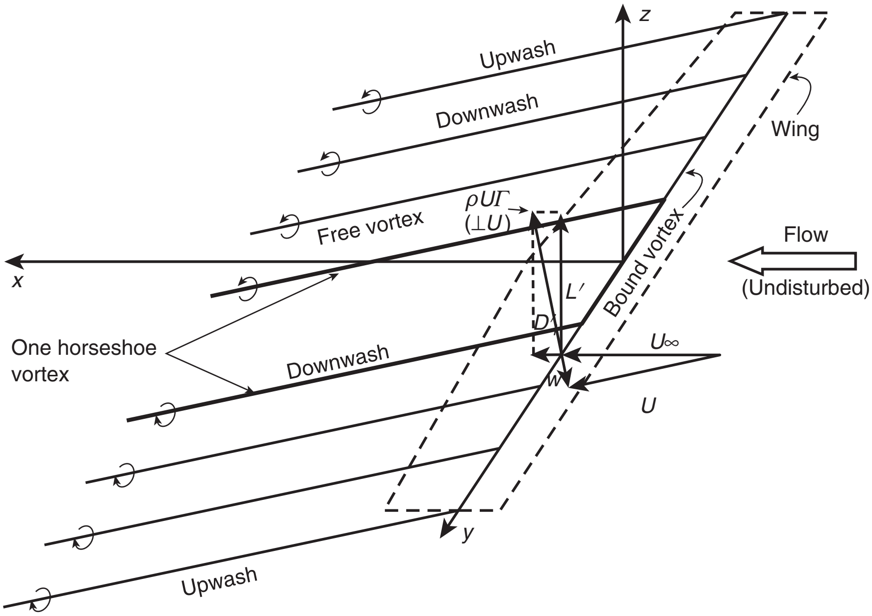

Figure 7.3 Mathematical representation of the vortex system.

vorticity strength is the sum of that of the horseshoe vortices at that position. At the wing center ($y = 0$) all horseshoe vortices are present, but as the tip is approached more and more vortices have left the wing and turned backward. The bound vorticity thus has its maximum at the centerplane and drops to zero at the two tips.

The constancy of the vortex strength along a filament is according to Helmholz's first vortex theorem (See Acheson, 1990). In his second theorem, Helmholz states that a vortex cannot end in the fluid, so the trailing vortices have to be closed downstream. This is in the form of the starting vortex, which is equivalent to the bound part in the wing, but rotating in the other direction. The horseshoe vortices are therefore in theory ring vortices, but in steady flow the effect of the starting vortex is mostly neglected because it is convected with the flow and assumed to be far away.*

The trailing vortex system has a very important effect on the flow. As can be seen in Fig. 7.3, all vortices on one side tend to generate a downward flow on the other side. They also tend to generate an upward flow outside the sheet on their own side. The result of all this is a downflow in the entire sheet, but an upflow outside the sheet. These flows are called downwash and upwash, respectively.

Of particular interest is the downwash generated at the wing (y-axis in Fig. 7.3). In Fig. 7.3, the downwash velocity is denoted w, which, superimposed on the undisturbed velocity U_∞ yields the total velocity U and the induced angle of attack α_i

$$\alpha_i = \operatorname{atan} \frac{w}{U} \tag{7.1}$$

or, because w is always small

$$\alpha_i \approx \frac{w}{U_\infty} \tag{7.2}$$

where α_i is given in radians.

According to the Kutta-Joukowski theorem, the lift force on a bound vortex of strength Γ is at right angles to the approaching flow (i.e., at right angles to U, *not* U_∞) and its magnitude is $\rho U\Gamma$. The lift is thus tilted backward an angle α_i relative to the z-axis. But according to the normal definitions, the lift and drag shall be computed at right angles to, and parallel with, the undisturbed flow U_∞. This yields the following.

$$L' = \rho U\Gamma \cos \alpha_i \approx \rho U\Gamma \tag{7.3}$$

$$D_i' = -\rho U\Gamma \sin \alpha_i \approx -\rho U\Gamma_i \tag{7.4}$$

where L' and D_i' are the lift and induced resistance (mostly called drag in connection with wings) components, the prime denoting force per unit span.

7.1.3 The Elliptical Load Distribution. According to equation (7.4), the induced drag is proportional to the induced angle of attack, which in turn is caused by the trailing vortices. This is another way of relating trailing vorticity and drag, as compared to the energy explanation. Although equations (7.1) to (7.4) are important to

---

*In unsteady flow, a starting vortex is generated whenever the velocity or angle of attack is changed. This vortex is initially close to the wing and cannot be neglected.

explain the physics behind the lift and drag generation of a 3D wing, they are not very useful for practical calculations because the circulation and induced angle of attack are not easily obtained. A particular case of great importance is the elliptical load distribution (i.e., where Γ is an elliptical function of the spanwise coordinate y). Then the integrated effect of the trailing vortices may be obtained analytically and very useful formulas for lift and drag obtained. With the definitions

$$C_L = \frac{L}{\frac{1}{2}\rho U_\infty^2 S_p} \qquad C_{Di} = \frac{D_i}{\frac{1}{2}\rho U_\infty^2 S_p} \tag{7.5}$$

where L and D_i are the total lift and induced drag forces and S_p the projected wing area, the following simple expressions are obtained (see Kuethe & Chow [1986] or Anderson [1991]).

$$C_L = \frac{2\pi}{1 + \frac{2}{AR}}\,\alpha \tag{7.6}$$

$$C_i = \frac{C_L^2}{\pi AR} \tag{7.7}$$

The numerator 2π in equation (7.6) is for symmetric wings in inviscid flow, and with α in radians. For α in degrees, the constant becomes 0.11. A more realistic value is however 0.10, considering the small viscous effect on lift. AR is the *aspect ratio* of the wing, defined for an arbitrary planform as

$$AR = \frac{b^2}{S_p} \tag{7.8}$$

where b is the span. For a trapezoidal wing, the aspect ratio is the span divided by the mean chord. The projection of the area shall be taken in a direction at right angles to the plane of the wing. Note the difference between S_p and S, where the latter is the total wetted surface used for most coefficients in the present text.

In Fig. 7.2, the mirror image of the keel in the bottom of the hull is indicated. This image shall be considered in the computation of the aspect ratio (but not in the computation of the area). If the keel were attached to an infinitely large horizontal flat plate, the span would be exactly doubled thanks to the mirror image. For a modern flat-bottom hull this is a good approximation.

Finite wing theory also shows that the elliptical circulation distribution gives minimum induced drag and that it may be obtained with a wing of elliptical planform (untwisted). Such a shape is thus preferable from a resistance point of view. For wings with other planforms (most wings), the spanwise circulation distribution will not be elliptic. In fact, Schrenk (1940) showed empirically that for unswept and untwisted wings, the lift at every spanwise position is halfway between the elliptical and the actual chord distribution for the same total area and span. This approximation is exemplified in Fig. 7.4, where the upper figures show the planform (triangular and rectangular) and the lower ones the way to obtain the lift distribution as the average of the actual planform shape and an ellipse.

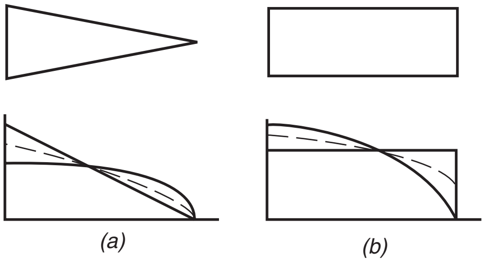

Figure 7.4 Schrenk's (1940) approximation of the lift distribution. *Top figures*: planform. *Bottom figures*: chord distribution, elliptical distribution, and real lift distribution (*dashed line*).

Schrenk's approximation applies to unswept wings. At non-zero sweep angle, the circulation distribution is influenced in such a way that the centroid of the distribution is moved outward for positive sweep and inward when the sweep is negative. The definition of the sweep angle is given in Fig. 7.5.[*] It is seen that the angle is measured relative to the "quarter chord" line connecting points 25% of the distance from the leading to the trailing edges at all spanwise stations.

Fig. 7.5 also includes a definition of the taper ratio. For a rectangular wing, this ratio is 1, and for a triangular one it is zero. It turns out that the taper ratio of a trapezoidal wing that best corresponds to an elliptical shape is approximately 0.45. For larger ratios, the circulation will be too large in the outer parts of the wing whereas the opposite is true for smaller ratios. However, an unfavorable planform distribution may be compensated at least partly by the sweep angle. If the tip chord is too small, the circulation may be increased in the outer parts of the wing by positive sweep and an almost elliptical lift distribution is obtained. The relation between taper ratio and sweep angle for optimum circulation distribution (minimum induced resistance) is given in Fig. 7.6. The larger the angle, the smaller the taper for best performance.

The computation of the lift and induced drag for arbitrary lift distributions is complicated and no simple expressions like (7.6) and (7.7) exist. Instead, the concept of an effective aspect ratio, AR_e, is introduced. This is always smaller than the geometrical one defined in equation (7.8), and may be defined using equation (7.7) as

$$AR_e = \frac{C_L^2}{\pi C_{Di}} \tag{7.9}$$

where C_L and C_D are now the lift and induced drag coefficients for the nonelliptical distribution. It should be noted that the sensitivity for deviations from the elliptical shape is relatively small. For most shapes, AR_e differs from AR by only a few percent. In Fig. 7.7, the very large influence of the aspect ratio on the lift coefficient is shown. These curves correspond very well with equation

---

[*] Figs. 7.5–7.17 are reproduced from Larsson and Eliasson (2007). Courtesy of Adlard Coles Nautical.

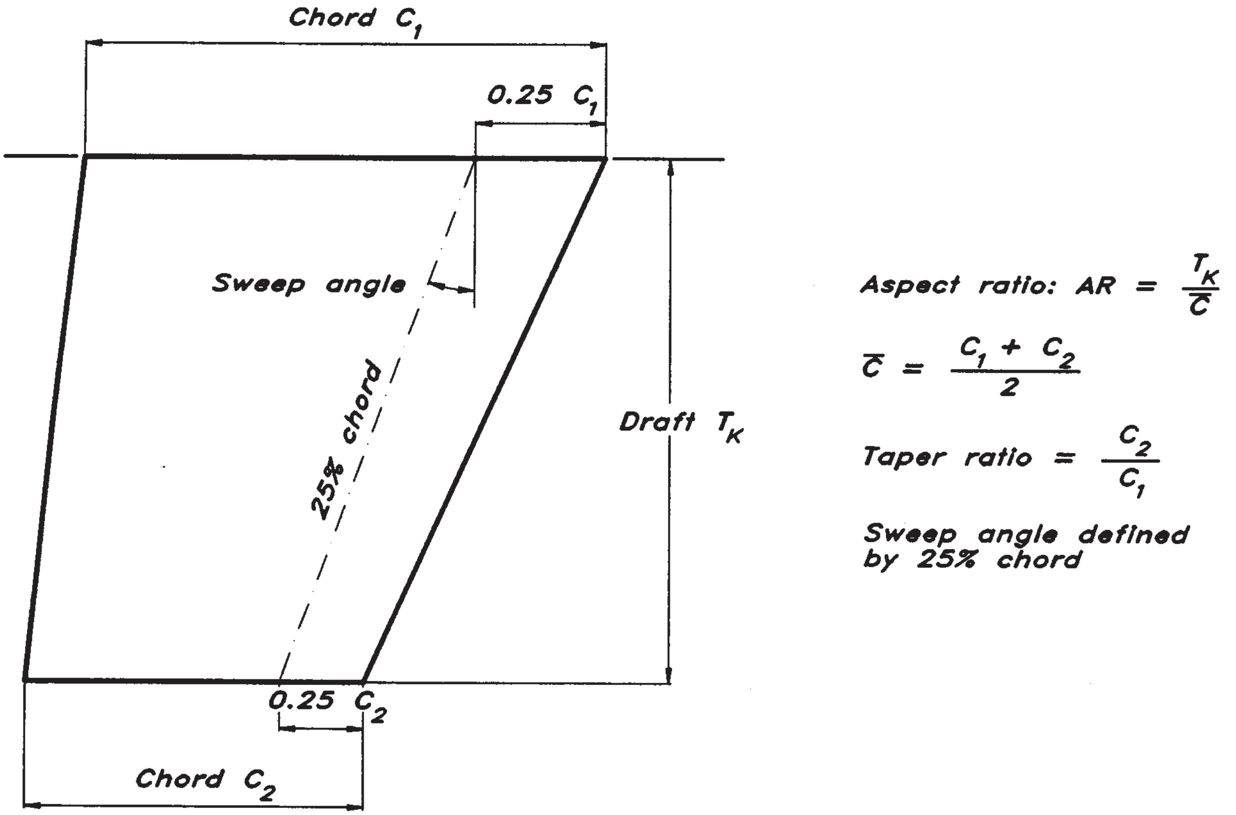

Figure 7.5 Definition of planform parameters for trapezoidal wings.

(7.6). For more detailed discussions on lift and induced drag, see Kuethe and Chow (1986), Anderson (1991), Newman (1977), or Larsson and Eliasson (2007). The latter deals with sailing yachts and, as stated in the footnotes, several figures in the present section are from this book.

7.2 Appendage Resistance. In Fig. 4.1, showing the resistance components for different hulls, no appendage resistance was specified for the displacement hulls. This is an approximation because all hulls with exposed shafts will have some additional resistance arising from the shaft and its support. As appears from Fig. 4.1, this resistance component may be considerable for a planing hull. Although the dynamic forces lift the hull and reduce its wetted surface, the appendages remain submerged, thus taking over more and more of the viscous resistance with increasing speed. Another type of vessel where the appendage drag is considerable is the sailing yacht. In the following, the properties of foil sections useful for sailing yacht keels and rudders, as well as shaft brackets and fins of propeller-driven ships, will be presented. A section on bluff bodies, such as propeller shafts and sailing yacht masts, follows thereafter. Note that appendage resistance is of viscous origin; it is caused by frictional and viscous pressure losses around the appendage, and the flow and resistance is governed by the Reynolds number.

7.2.1 Streamlined Bodies. Streamlined sections are used frequently in fluid mechanics, often for creating lift forces, but also to reduce resistance (more often called drag in this connection). The most prominent example of lifting sections is the aircraft wing, whose counterpart in hydrodynamics is the hydrofoil. Other important hydrodynamic lifting sections are rudders and keels. The possibility to reduce resistance by streamlining, without lift generation, is also of major importance whenever bodies of any kind are immersed in a flowing fluid. Typical examples in hydrodynamics are struts and brackets. Fig. 7.8 shows the huge effect of streamlining a 2D body. The two bodies shown have approximately the same drag, although the upper one has a frontal area which is about 30 times that of the lower one, which is a circular cylinder. Through streamlining, the flow along the upper body is attached all the way to the trailing edge whereas, for the cylinder, massive separation is found. The pressure recovery around the aft end, shown in Fig. 6.9, is practically absent, and the low pressure behind the cylinder causes a very large pressure resistance. In this case, friction is almost negligible. The streamlined body, on the other hand, has very little pressure resistance. It is not zero because of the displacement effect of the boundary layer, but it is considerably smaller than the friction. Section 7.2.1 deals with friction dominated flows on streamlined sections and the massively separated flow around bluff bodies will be dealt with thereafter.

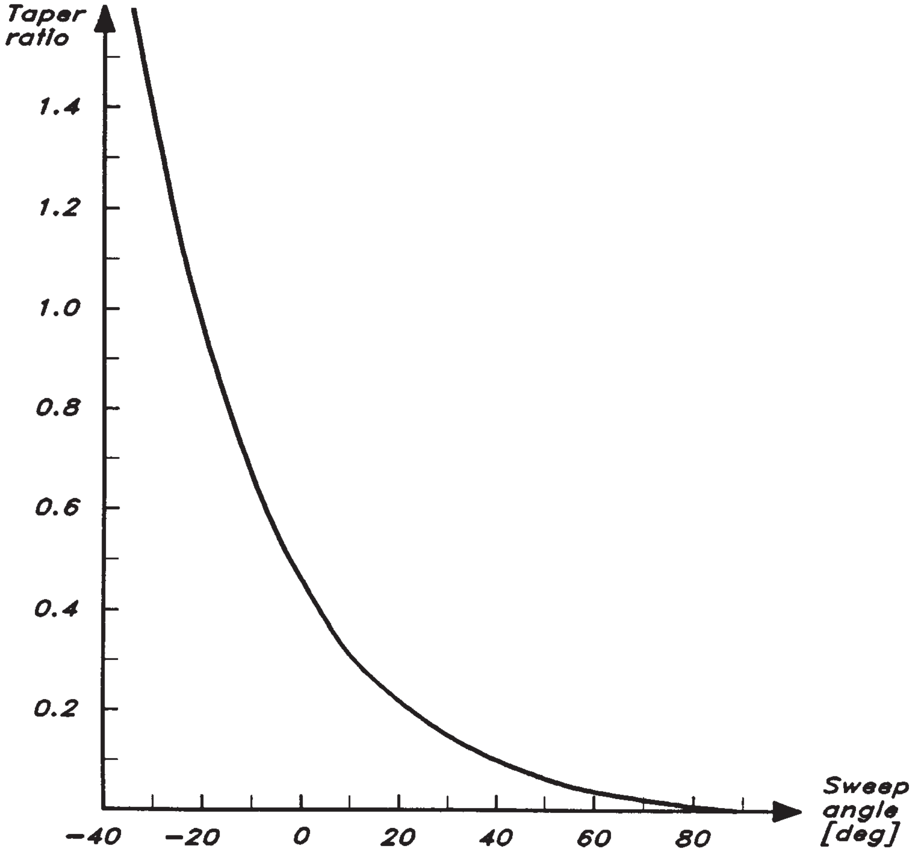

Figure 7.6 Relation between taper and sweep for minimum induced resistance.

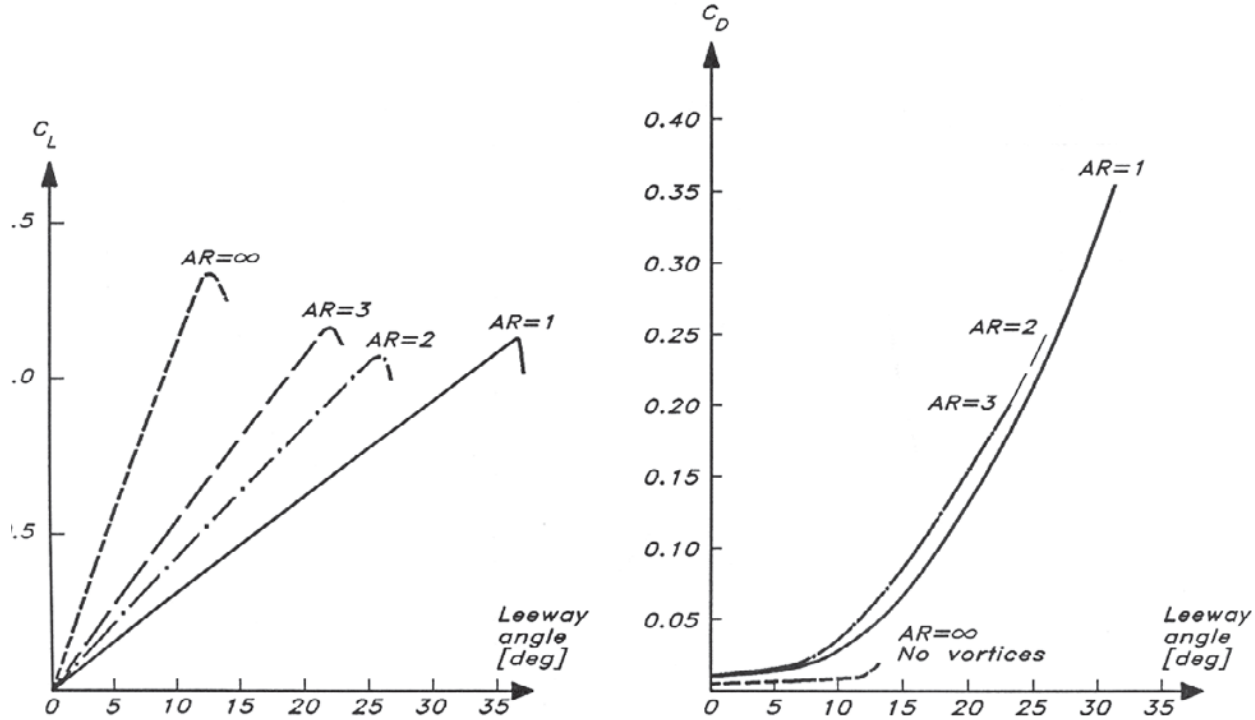

Figure 7.7 Influence of aspect ratio on lift and drag.

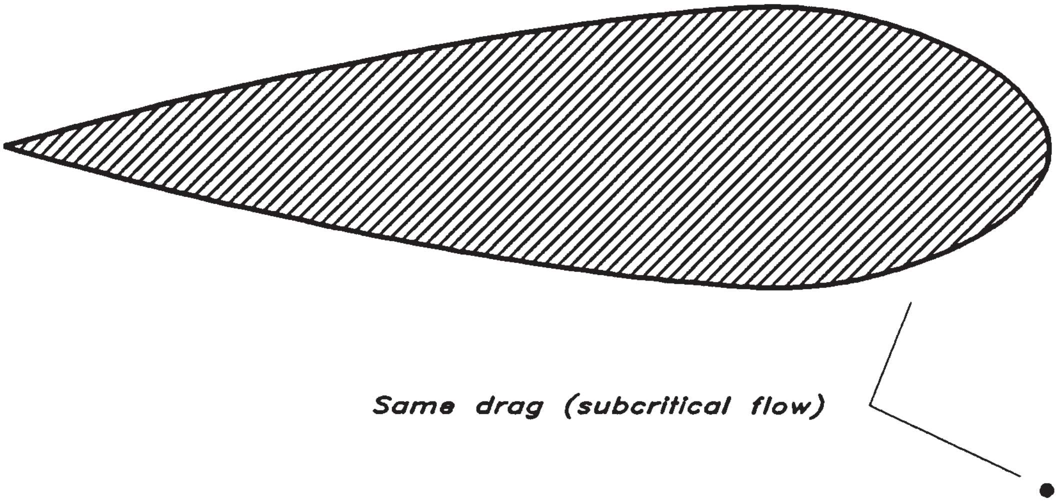

Figure 7.8 The effect of streamlining.

Although many foils of hydrodynamic interest are symmetric (keels, rudders, struts, and brackets), foil sections are generally asymmetric. Important parameters describing an asymmetric foil are shown in Fig. 7.9. The mean line is midway between the upper and lower surfaces, and the chord length C is the distance between the intersections of the mean line and the nose and trailing edge, respectively. The local thickness t is measured at right angles to the mean line and its maximum value t_{max} (or t_{max}/C, rather) is often used for classification of the section. The nose radius is defined as the radius of curvature of the section at the nose (the intersection with the mean line). In practice, the most forward part of the section may be represented by a circular arc. This approximation is usually good enough back to about 45 degrees on either side of the intersection.

Most foils used in fluid mechanics have a section shape from the NACA series. NACA is the precursor of NASA. During the 1930s and 1940s, extensive tests with systematically varied wing sections were carried out in wind tunnels and the results presented in the form of pressure distributions, forces, and moments at varying angles of attack. The most interesting series

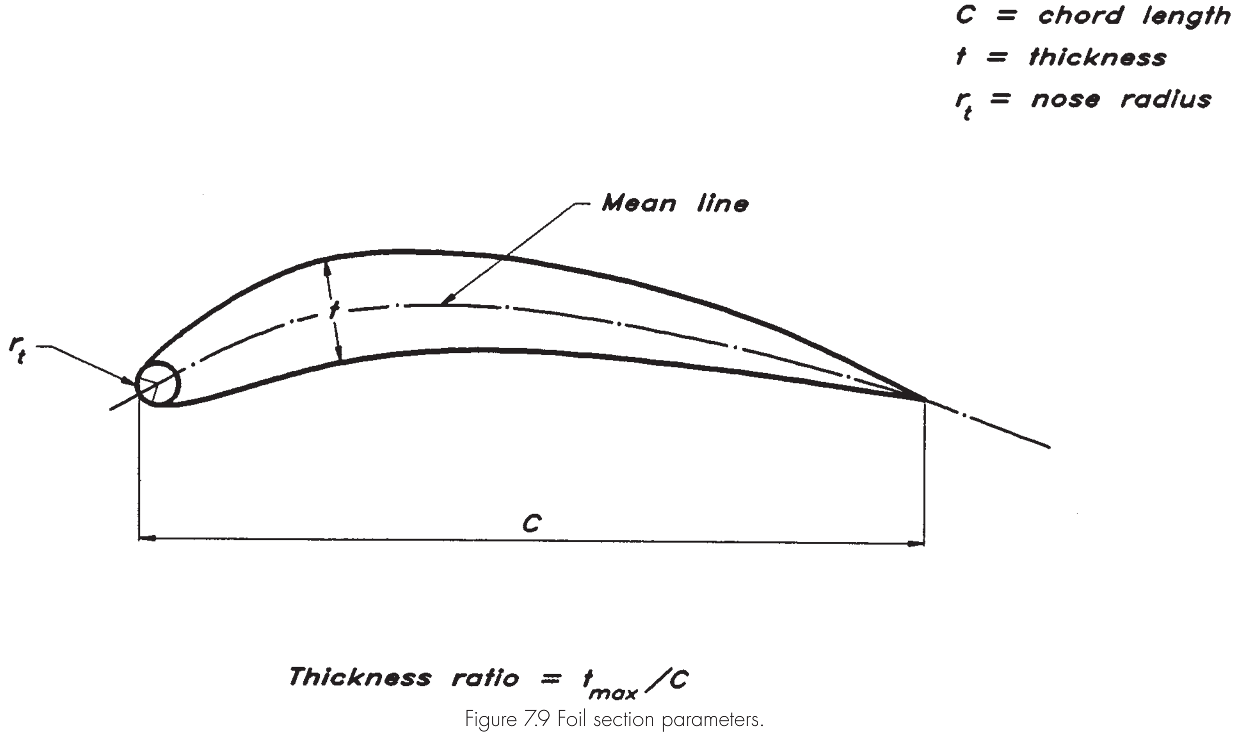

Figure 7.9 Foil section parameters.

from a hydrodynamic point of view are the four-digit and six-series (for propellers, other series may be of interest). Three examples are presented in Table 7.1, where half the thickness t is given versus distance x from the leading edge. Both variables are given in percent of the chord length C. All three sections are symmetrical and should be useful for struts, brackets, rudders, and keels.

NACA 0010 belongs to the four-digit series and the last two digits represent the thickness ratio t_{max}/C. The first two digits define the camber for an asymmetric section and are zero for a symmetric section. The two other sections belong to the six-series, indicated by the first digit. In this case, the second digit represents the position of minimum pressure of the foil. When multiplied by 10, this digit gives the axial position of the pressure minimum in percent of the chord length. After the dash, the first digit represents the camber, which is zero in this case, and the last two show the thickness ratio. A very extensive treatment of wing theory, including a large number of experimental results for NACA sections, is presented in Abbot and van Doenhoff (1949).

Table 7.1 Three NACA Sections (Values in Percent)

x/C	*t/2C*	*t/2C*	*t/2C*
	0010	**63–010**	**65–010**
0	0	0	0
0.5		0.829	0.772
0.75		1.004	0.932
1.25	1.578	1.275	1.169
2.5	2.178	1.756	1.574
5.0	2.178	1.756	1.574
7.5	3.500	2.950	2.647
10	3.902	3.362	3.040
15	4.455	3.994	3.666
20	4.782	4.445	4.143
25	4.952	4.753	4.503
30	5.002	4.938	4.760
35		5.000	4.924
40	4.837	4.938	4.996
45		4.766	4.963
50	4.412	4.496	4.812
55		4.140	4.530
60	3.803	3.715	4.146
65		3.234	3.682
70	3.053	2.712	3.156
75		2.166	2.584
80	2.187	1.618	1.987
85		1.088	1.385
90	1.207	0.604	0.810
95	0.672	0.214	0.306
100	0.105	0	0

The nose radii for the two series versus thickness ratio is presented in Fig. 7.10, which also gives the radius of curvature for an elliptic section. Note that the four-digit series has twice as large a radius as the ellipse and the six-series is somewhere in between. As a general rule, the larger the nose radius, the less sensitive the section to separation at the leading edge at an angle of attack. The four-digit series is thus the most robust one in this respect. Other differences in performance between the sections will now be explained.

Fig. 7.11 shows the pressure distribution for three sections: 0009, 65–009, and 65–021. A comparison between the first two will reveal the differences between a four-digit section and a relatively advanced six-series section. The meaning of advanced will be explained shortly. Comparing the latter two, the differences between a thin and a fat section will be shown.

In Fig. 7.11, the pressure coefficient C_p is given along the chord *with the positive axis downward*. This unusual coordinate system is frequently used for wings because the upper side normally has a negative pressure whereas the opposite is true for the lower side. It is seen that the pressure on the 0009 section has its minimum very far forward, around 10% of the chord from the nose. This is in contrast to the two six-series sections, which have their minima close to midchord, as expected from their designation. For these two foils, three curves are given, and a lift coefficient is given for each curve. $C_L = 0$ corresponds to zero lift (i.e., zero angle of attack), and the two other curves correspond to the maximum lift for which the pressure still has its minimum at midchord. For larger lift, the minimum will rapidly move to a position much closer to the leading edge.

Why this focus on the minimum pressure? As explained in Section 6.4.3, the location of transition is very much dictated by the pressure distribution, a negative pressure gradient stabilizing the flow and delaying transition. In fact, over a large range of Reynolds numbers, transition tends to occur at the pressure minimum. Delaying this as much as possible means a larger area of laminar flow in the boundary layer and a correspondingly lower friction. This fact is exploited in the six-series whose sections are often called laminar. The 63-series is modest with 30% of laminar flow whereas the most extreme one, the 67-series, has 70% laminar flow for angles of attack below the critical lift. This series does, however, have several disadvantages which makes it less used; in practice, the most extreme series is the 65-series, which is displayed in Fig. 7.11.

We will now turn to the forces generated by the foils in the four-digit and six-series. A comparison between the drag curves of two 9% thick profiles is made in Fig. 7.12. The drag coefficient is given versus angle

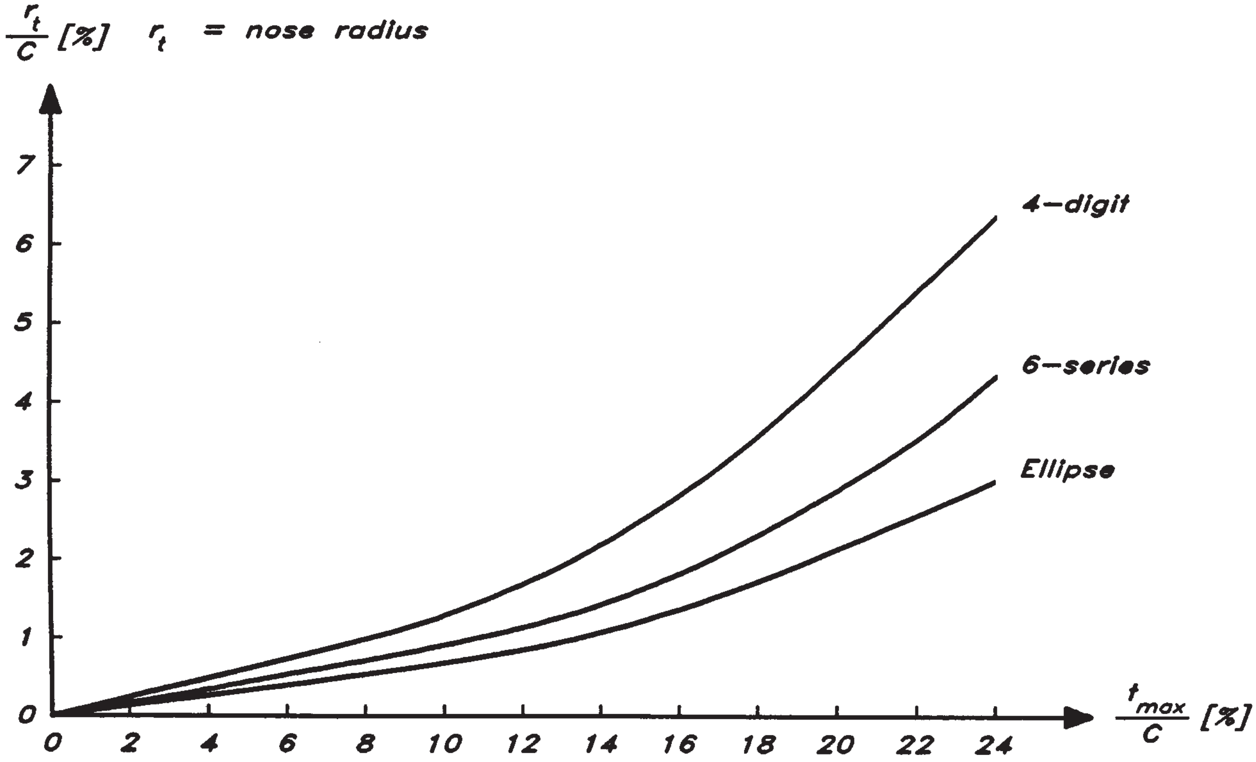

Figure 7.10 Nose radius for two sections and an ellipse.

of attack for a Reynolds number of $3 \cdot 10^6$. It is seen that the 0009 has a higher drag at small angles, but a smooth increase in drag with angle of attack. The 63–009 has a low drag below about 2 degrees, but a rapid increase in the interval up to about 3 degrees, thereafter increasing the drag smoothly, but at a higher level than the 0009. This may now be explained by the fact that the six-series profile has a larger area of laminar flow up to the point where the pressure minimum moves forward. Once this has happened, this section is worse than the 0009.

In Fig. 7.13, the effects of thickness ratio and position of minimum pressure are presented for the six-series. Two profiles are 9% thick and two are 21% thick. Two are of the 63 type and two of the 65 type. The two thin profiles have the lowest drag at small angles, but have the rapid increase noted above between 2 degrees and 3 degrees. The profile with the largest area of laminar flow (i.e., the 65-009) is the best at small angles, but the increase is faster for this profile than for the 63-009, which becomes the best of the two at higher angles. The differences between these profiles are similar to those between the two in Fig. 7.12: the section with the smallest area of laminar flow at small angles has a smoother drag curve than the other.

The drag curves of the two thick profiles differ considerably from those of the thinner ones. As seen in Fig. 7.11, the pressure minimum stays at midchord until the lift coefficient is quite high, corresponding to an angle of attack of around 5 degrees. This is reflected in Fig. 7.13, where the sharp increase in drag occurs around 5–6 degrees. The most extreme profile, 65-009, has the lowest drag below the critical angle, but the highest drag above this limit. Note that there is a region ($\alpha \cong 3$–7 degrees) where the thick profiles have lower drag than the thin ones. The drag at zero angle of attack for the four-digit, 63-, and 65-series is shown versus thickness ratio in Fig. 7.14. It appears, as expected, that the drag increases with thickness for all profiles, and that the more extreme the profile (i.e., the further back the pressure minimum), the lower the drag at this angle.

Although the drag differs considerably between the four-digit and six-series sections, the lift is quite similar, at least below about 7 degrees (Fig. 7.15). In fact, the theoretical lift slope $\left(\frac{\partial C_L}{\partial \alpha}\right)$ is the same for all symmetric sections, namely 2π per radian. This is seen from equation (7.6), introducing an infinite aspect ratio, relevant for 2D sections. As mentioned in connection with this formula, 2π per radian corresponds to about 0.11 per degree, but a more realistic value in a viscous fluid is 0.10. The slight differences between the sections are because of different boundary layer developments.

Above the linear part of the lift curves, there is a considerable difference between the thin and the thick profiles. For the thick ones, the lift levels off to a more or less constant value whereas the thin ones exhibit a

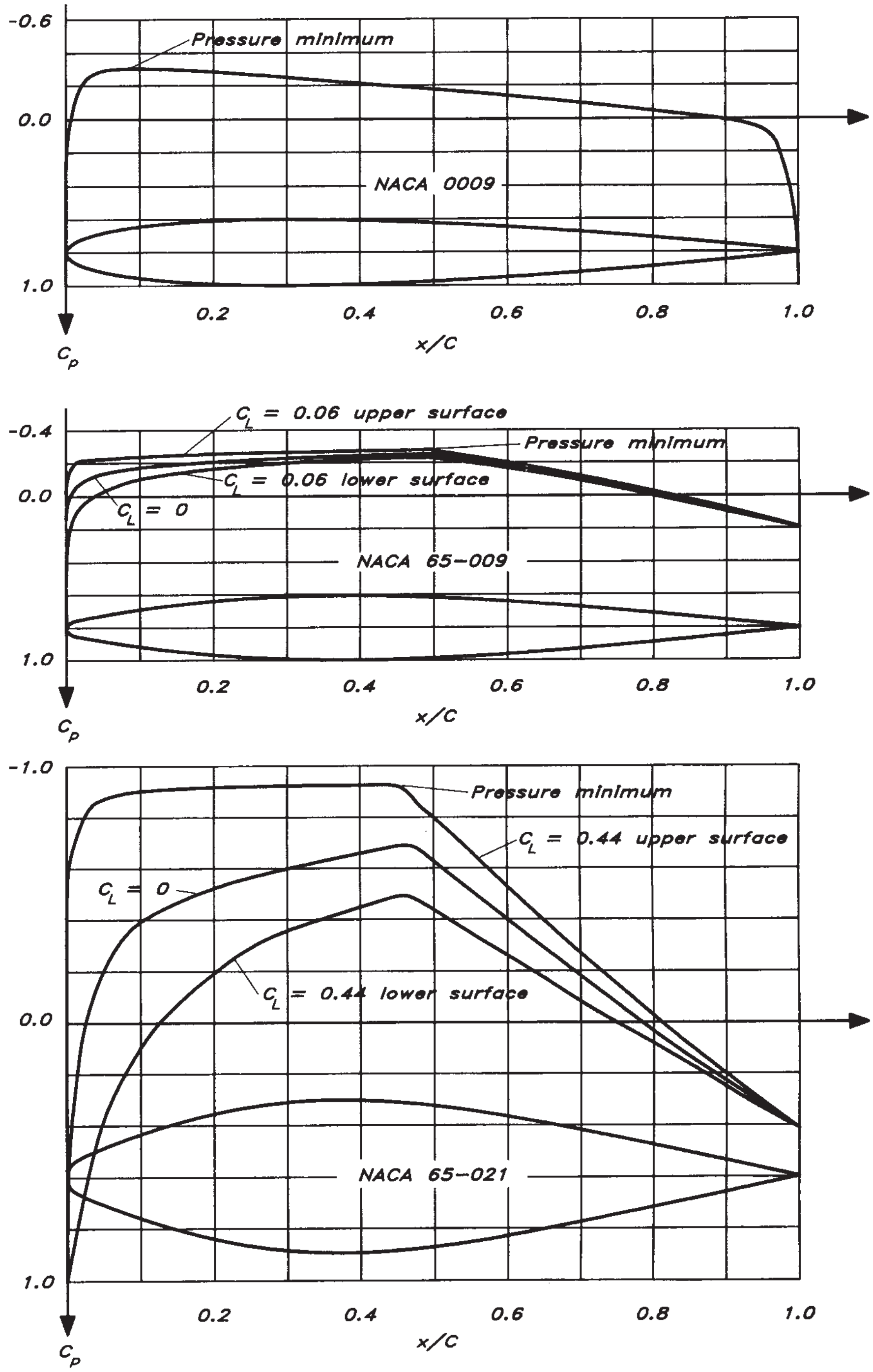

Figure 7.11 Pressure distribution around three sections.

rapid drop in lift above a certain angle. The reason why the lift ceases to follow the straight line is flow separation on the suction side. The wing stalls. Depending on the thickness of the profile, the separation may occur in different ways. Fig. 7.16 shows three principally different stall patterns. The thick profile of Fig. 7.16a stalls by trailing edge separation, which starts to occur at relatively small angles of attack. However, the increase of the separation region is gradual, and the lift slope is reduced until the whole suction side has become separated.

A completely different separation occurs for the very thin wing in Fig. 7.16b. Here, the flow around the sharp leading edge from the stagnation point just be-

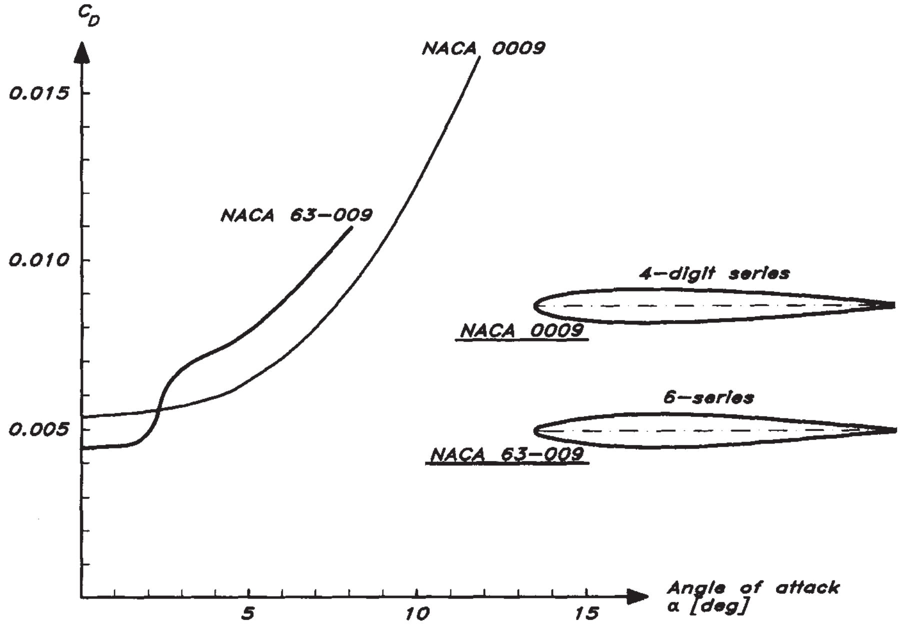

Figure 7.12 Comparison between the drag of two sections from different series.

low separates immediately, creating a bubble with an attachment point further back on the wing. At small angles, the separation bubble is small, but it increases with angle of attack until it covers the whole suction side. Profiles this thin have not been discussed, but they exhibit a similar type of lift curve as the thick ones: the lift slope is gradually reduced when the separation bubble increases. The section of Fig. 7.16c with moderate thickness, 9% to 12%, say, stalls by separation from both ends. This starts to occur at relatively high angles of attack, but the separation is developed rapidly, and the drastic drop in lift occurs when the two separation bubbles meet. Note that this is the type of section most used in hydrodynamics.

Although the lift/drag ratio is important in many applications, such as sailing yacht keels, the maximum lift is a key parameter in others. The rudder, for example, has to be designed to generate a certain

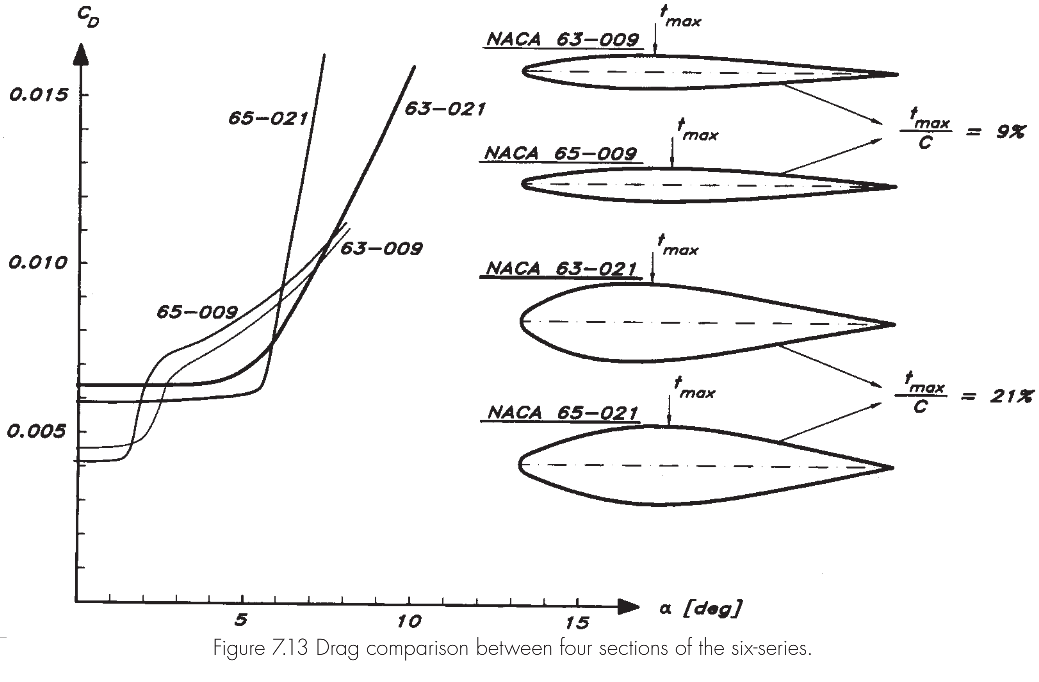

Figure 7.13 Drag comparison between four sections of the six-series.

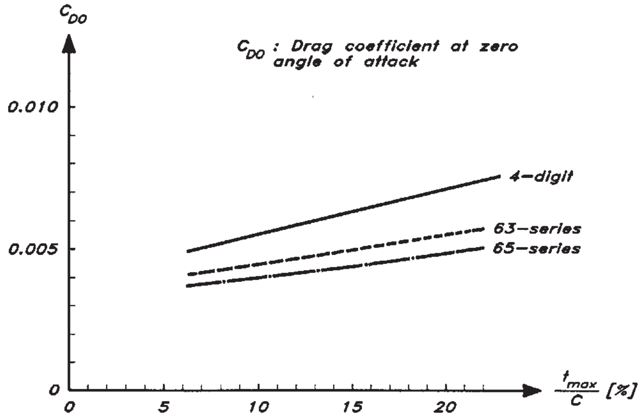

Figure 7.14 Drag at zero angle of attack versus thickness ratio.

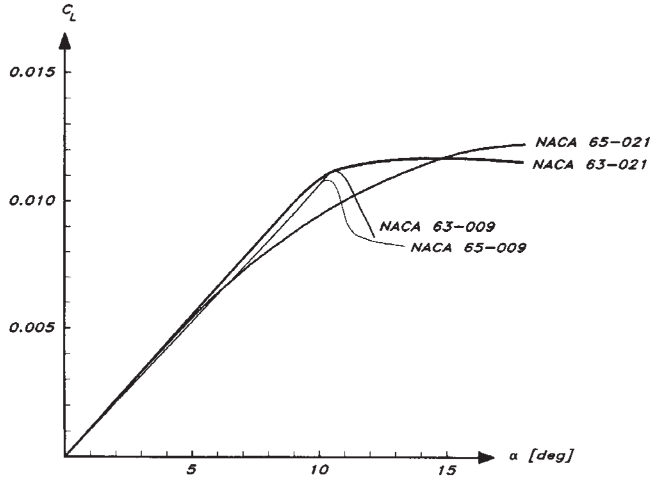

Figure 7.15 Lift comparison between four sections of the six-series.

turning moment on the hull and its value at a given speed is determined by the lift coefficient times the rudder area. For safety reasons, the maximum turning moment has to be above a certain minimum value, and the larger the lift coefficient, the smaller the area to generate the required moment. Sections with a high maximum lift before stall thus require a smaller wetted surface.

Fig. 7.17 shows the maximum lift coefficient for the four-digit, 63-, and 65-series. The thickness ratio is given on the horizontal axis, and on the curves the stall angle is given for a range of thickness ratios. It is seen that the four-digit series has the largest maximum lift. For a 9% thick profile, for instance, the four-digit series has a C_{Lmax} of 1.32 whereas the 63- and 65-series have a maximum of 1.12 and 1.05, respectively. A rudder with a 65-series section thus needs about 25% larger area than a four-digit section to generate the required maximum lift. This means increased friction over a large range of angles of attack. However, within the drag bucket, the lower drag coefficient of the more modern profile (see Fig. 7.14) approximately compensates for the larger area. Because rudders, as opposed to keels, often operate over a relatively wide range of angles, the four-digit series is preferable. Note that the 12% profile is the best profile for this purpose. As presented

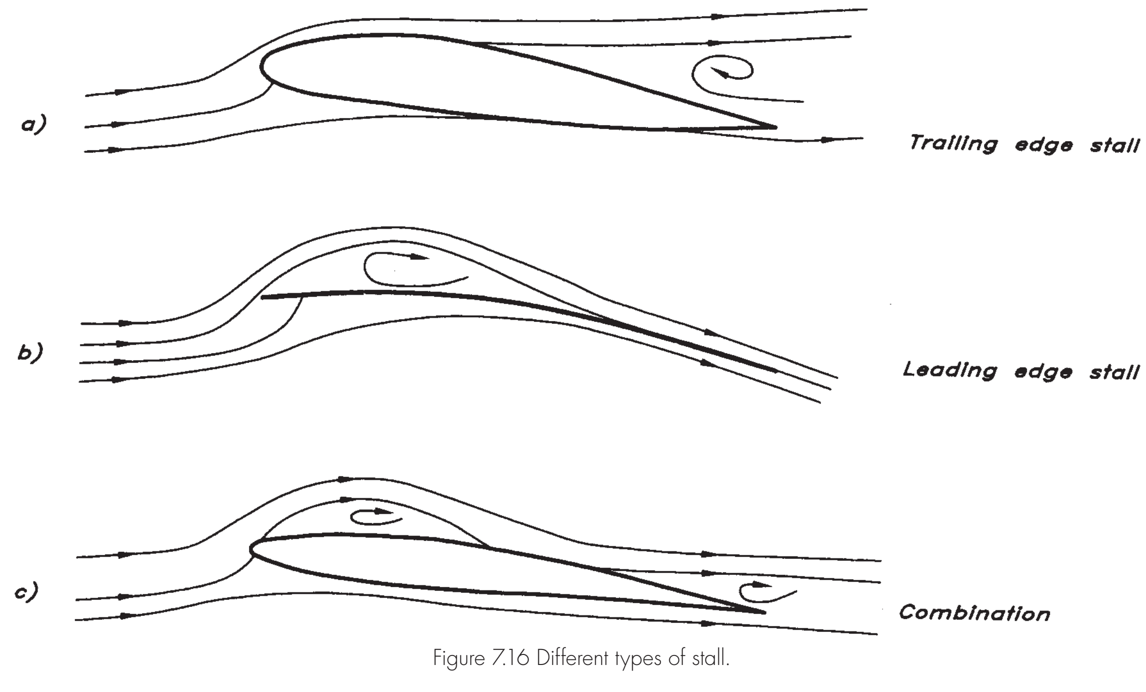

Figure 7.16 Different types of stall.

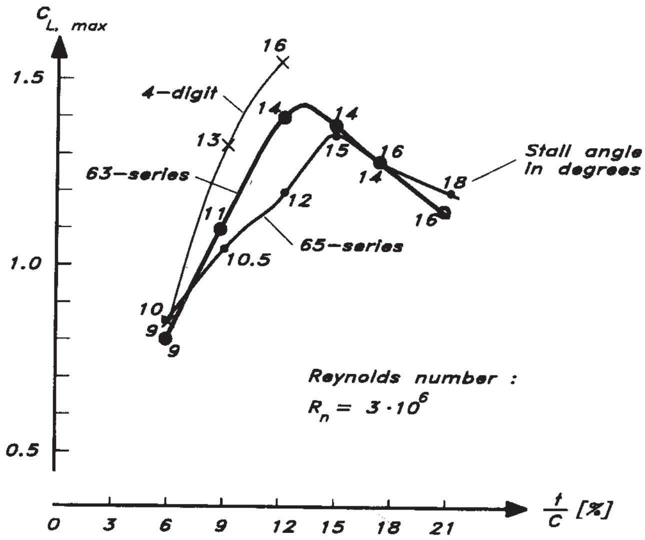

Figure 7.17 Maximum lift coefficient for three sections.

in the Manoeuvring volume of the *Principes of Naval Architecture*, other sections especially for rudders have been developed.

The NACA profiles were tested at three different Reynolds numbers: 3, 6, and $9 \cdot 10^6$ based on the chord. This is a range typical for keels and rudders of pleasure craft. Full-scale ships, however, have considerably larger appendage Reynolds numbers and ship models normally have much smaller. This creates a problem in model testing because the scale effects of the appendages are often quite different from those of the hull. Fig. 7.18 shows the variation in drag with Reynolds number at zero lift of sections of three different thicknesses: 6%, 12%, and 25%. The figure is based on a collection of data by Hoerner (1965) and each line represents an average of data from several measurements for the particular thickness. For comparison, laminar and turbulent flat plate lines are also included, as well as the drag of a smooth circular cylinder.

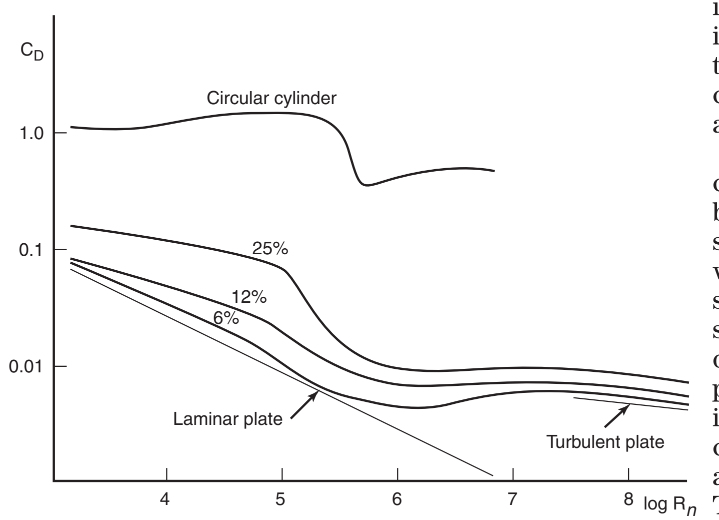

Figure 7.18 Reynolds number dependence of section drag.

It is seen that there is a gradual reduction in drag below a critical Reynolds number around 10^5, after which there is an abrupt drop, followed by a more or less constant region in the range 10^6–10^7, above which the slope follows the turbulent friction. The reasons for the different behavior will now be explained.

Below the critical Reynolds number, the boundary layer is laminar and separation occurs before transition (i.e., there is no turbulent boundary layer). For increasingly thick profiles, the pressure drag arising from separation increases, and the most extreme case is the circular cylinder (note the logarithmic scales!). The cylinder drag is entirely dominated by the pressure deficiency, which does not change with Reynolds number, so its drag coefficient is constant in this region. The 6% profile has very little separation drag, so the curve more or less follows the flat plate curve and the two other profiles are between the two extremes.

Above the critical Reynolds number, transition occurs before separation (i.e., the boundary layer turns turbulent before it separates). Because the eddies of the turbulent boundary layer stir the flow and transfer high speed flow into the layer, separation is delayed and thereby the pressure resistance is reduced. For the cylinder, the separation moves from a position in front of maximum thickness, around 80 degrees measured from the symmetry line, back to about 120 degrees. This has a dramatic effect on the wake width and the pressure in the wake, and the drag is reduced by about 75%. For the profiles the effect is less pronounced, but clearly visible, at least in case of the thicker profiles.

The more or less constant level of the drag coefficient in the range 10^6–10^7 indicates that transition moves forward with increasing Reynolds number, thus extending the turbulent part of the boundary layer. This would increase the drag, but this effect is just about offset by the normal drop in drag with Reynolds number, which can be clearly seen above 10^7, where transition seems almost fixed.

7.2.2 Bluff Bodies. The large drop in drag at the critical Reynolds number for the circular cylinder may be explained with reference to Fig. 7.19. Here, the pressure distribution is shown versus angular position, with zero at the forward stagnation point. For comparison, the inviscid distribution is also given. From the stagnation pressure $C_p = 1.0$, there is a continuous drop down to -3.0 in the inviscid distribution. This happens at 90 degrees, and thereafter there is a symmetric increase up to $+1.0$ at 180 degrees. The supercritical curve shows similarities with the inviscid one, but has a minimum of about 2.5 at approximately 90 degrees. The largest difference is the plateau-like distribution aft of 120 degrees, where the pressure coefficient is

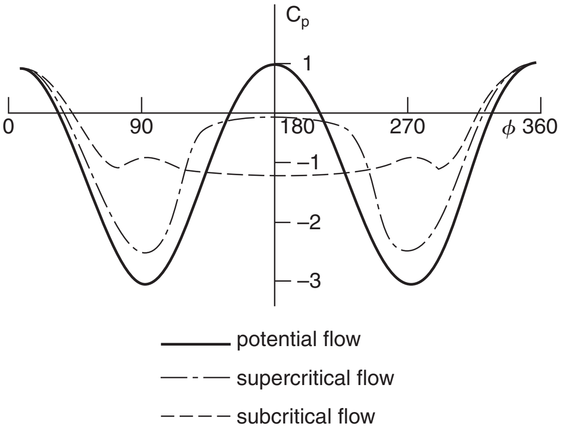

Figure 7.19 Pressure variation around a circular cylinder.

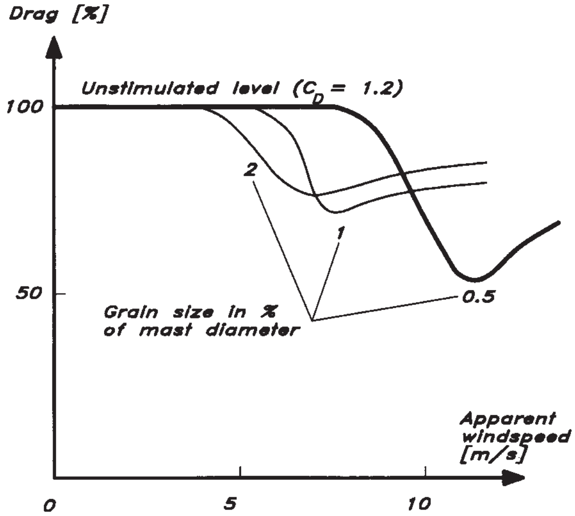

Figure 7.20 Effect of roughness on drag.

slightly negative all the way to 180 degrees. Unlike the inviscid case, there is no balancing of the positive pressure around the stagnation point, so a pressure drag occurs. This drag is, however, small compared to the one caused by the pressure distribution of the subcritical case. Here, the pressure exhibits a minimum at about 70 degrees, thereafter becoming more or less constant at a C_P around −1.0. This large negative pressure on the entire back side causes the large drag. Note that the curves shown are mean values. In reality, the flow fluctuates periodically, generating lift forces fluctuating from side to side.

An interesting possibility to reduce the drag at Reynolds numbers below the critical value is offered by disturbing the boundary layer in some way. One possibility is to generate disturbances in the flow approaching the cylinder, but a more practical way is to introduce roughness on the surface. The roughness elements will disturb the laminar flow in the boundary layer and cause premature transition. The critical Reynolds number is thus lowered and in the region up to the undisturbed critical value the drag is reduced. Fig. 7.20*, shows the drag of a circular mast section covered with sand grains of different sizes. As expected, the larger the disturbance, the larger the effect on the critical Rn. However, the minimum drag increases when the roughness gets higher. The possibility to reduce drag, at the same time reducing the wake width, is of particular interest for sailing yacht masts, where the additional advantage of an improved flow around the sail cannot be neglected.

A complicating factor when it comes to propeller shafts is that they are not at right angles to the flow. Unfortunately, the effect of the flow component parallel to the axis is very much dependent on the Reynolds number, so no simple formula has been devised. A procedure for calculating the effect is however proposed by Kirkman and Kloetzli (1980). When computing the drag of appendages, it should be noted that some of them, notably the rudder, are in the propeller race, where the speed is higher than the ship speed. The excess velocity depends on the propeller loading, but 10% is a reasonable value. On the other hand, many appendages are more or less immersed in the hull boundary layer, where the speed is reduced. Estimations of this effect may be made using the flat plate boundary layer formulas of Section 6.3.3

7.3 Air and Wind Resistance. A ship moving on a smooth sea and in still air experiences a resistance arising from the movement of the above-water part of the hull through the air. This resistance depends on the speed of the ship and on the area and shape of the upper structure.

When a wind is blowing, the resistance depends also on the wind speed and its relative direction. In addition, the wind generates waves which normally cause a further increase in resistance. The effect of waves is dealt with in the Seakeeping volume of the *Principles of Naval Architecture* and the effect of the air will be discussed here.

7.3.1 True and Apparent Wind. The true wind,* $\vec{V}_{TW}$, is termed to be the wind which is due to natural causes and would exist at any point above the sea, had the ship been absent. Zero true wind is still air. The relative or apparent wind, $\vec{V}_{AW}$, is the vector sum of the true wind and the wind generated in still air due to the movement of the ship through the air (i.e., $-\vec{V}$, where $\vec{V}$ is the ship velocity)

$$\vec{V}_{AW} = \vec{V}_{TW} - \vec{V} \tag{7.10}$$

---

*Fig. 7.20 is reproduced from Larsson and Eliasson (2007), courtesy of Adlard Coles Nautical.

*According to normal standard in the yachting literature, the word "wind" is to be interpreted as "wind velocity."

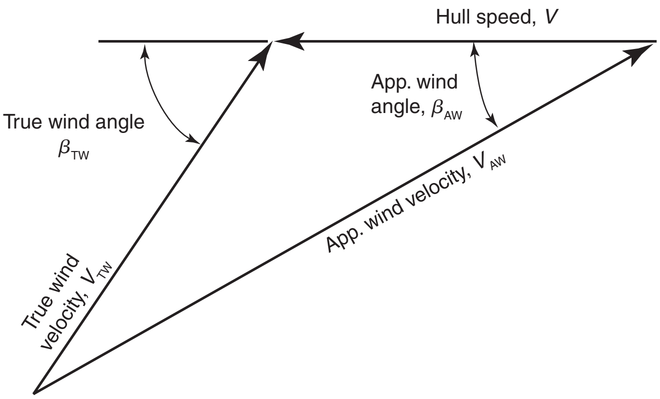

Figure 7.21 Relation between true and apparent wind.

Because both components may be assumed parallel to the water surface, the magnitude of the apparent wind, V_{AW}, may be obtained as

$$V_{AW} = (V_{TW}^2 + V^2 + 2VV_{TW}\cos\beta_{TW})^{\frac{1}{2}} \tag{7.11}$$

where V_{TW} and V are the magnitudes of the true wind and ship velocity, respectively, and β_{TW} is the angle between the true wind and the x-axis (Fig. 7.21).

The angle β_{AW} between the apparent wind and the x-axis may be obtained as

$$\beta_{AW} = \operatorname{atan}\frac{V_{TW}\sin\beta_{TW}}{V + V_{TW}\cos\beta_{TW}} \tag{7.12}$$

The true wind varies with the distance z from the water surface because of the atmospheric boundary layer and, as seen in Blendermann (1990), a reasonable approximation for the variation is [cf. equation (6.30)]

$$V_{TW}(z) = V_{TW}(10)\left(\frac{z}{10}\right)^{\frac{1}{n}} \tag{7.13}$$

The reference value for the wind speed is usually given at 10 m height, as assumed in the equation. This wind velocity is related to the Beaufort (Bft) scale through the equation

$$V_{TW}(10) = 0.836(Bft)^{\frac{3}{2}} \tag{7.14}$$

Different values of n should be used for strong and light winds. In stronger winds, stable atmospheric conditions are met and a relatively full velocity profile should be used. A suitable value of n is 10. In lighter airs, the boundary layer is generally unstable and the velocity profile less full. The value of n should then be about 5.

In equation (7.12), V is independent of z, but V_{TW} varies according to equation (7.13), which means that β_{AW} will also depend on z. The apparent wind profile is thus twisted. Close to the water surface, the true wind speed is small and the effect of the ship speed dominates, but the effect of the true wind becomes larger and larger with distance from the surface. The flow is thus directed more along the hull at lower levels. This effect is important for sailing yachts, where the sails have to be twisted to accommodate the wind twist. For ships, the effect is mostly neglected, however, and the direction of the flow is taken as the one at the mean height of the lateral projection of the above-water part of the hull.

7.3.2 Forces and Moments. For most ships, the force developed by the airflow is considered horizontal. Exceptions are some high-speed hulls where the lifting effect of the airflow is utilized. The force components normally considered are thus X and Y in the x- and y-directions, respectively. Two moments are of interest: K and N around the x- and z-axis (roll and yaw moment), respectively.

Like other forces, X and Y are nondimensionalized by a dynamic pressure and a representative area. In this case, the dynamic pressure is defined as

$$q_a = \frac{1}{2}\rho_a V_{AW}^2 \tag{7.15}$$

where the index a stands for air.

The two force coefficients may be nondimensionalized by the same area, often the projected area A_L in the lateral direction of the above-water part of the ship. Sometimes, the longitudinal force X is made dimensionless by the (transverse) projected area A_T in the longitudinal direction. This convention is adopted here.

$$C_X = \frac{W}{q_a A_T} \quad C_Y = \frac{Y}{q_a A_L} \tag{7.16}$$

Coefficients for the moments are defined as follows

$$C_K = \frac{W}{q_a A_L H_M} \quad C_N = \frac{N}{q_a A_L L} \tag{7.17}$$

where H_M is the mean height of the lateral projection and L is the length overall of the ship

$$H_M = \frac{A_L}{L} \tag{7.18}$$

The force and moment coefficients are functions of the apparent wind direction. At zero apparent wind angle, the projection of the area in the wind direction is rather small (A_T), but the force is along the hull. For non-zero angles, the projected area is larger but the resulting force is not along the hull.* A maximum in the resistance force X is therefore often found in the range

---

*The force is neither along the hull nor in the main flow direction. The flow is deflected by the hull and the resulting force is somewhere between these two directions (see Blendermann, 1990).

20 degrees $< \beta_{AW} <$ 30 degrees and a corresponding minimum (maximum in the opposite direction) in the range 150 degrees $< \beta_{AW} <$ 160 degrees.

Wind effects on ships are most often measured in wind tunnels, where the atmospheric boundary layer may or may not be modeled. It should be noted that neither case is correct because the apparent wind is an effect of both the true wind and the velocity generated when moving through still air, as explained. The correct, twisted apparent wind profile can be modeled, but this is complicated and very rarely done. At the University of Auckland, a special wind tunnel with a twisted inflow is available (see e.g., Hansen, 2007). This tunnel is mainly used for sail testing, where the twist effect is important. Note that the inflow profile in this case depends on the speed of the hull relative to the wind speed, so there is one more parameter to consider compared to other wind tunnel tests.

The forces generated by the wind are almost exclusively caused by the pressure deficiency in separated regions on the leeward side of the ship. Frictional forces are very small. Because separation is caused by sharp edges around the profile of the hull and its superstructure, the location of separation lines is independent of the Reynolds number. This means that all force and moment coefficients are independent of the Reynolds number, so the wind tunnel coefficients may be used with good accuracy at full scale.

In a very comprehensive wind-tunnel investigation, Blendermann (1990) measured the aerodynamic coefficients for a number of different ship types under various loading conditions. These results may be used for computing the aerodynamic loads of most ships with a reasonable accuracy. In Fig. 7.22, measured results are presented. Data for the ships are listed in Table 7.2.

The coefficients of Fig. 7.22 may be converted to include the boundary layer effect in an approximate way using the mean dynamic pressure over the ship's height. For the special case of a ship at rest, V_{AW} is equal to $\underline{V_{TW}}$, and equation (7.13) inserted into equation (7.15) yields

$$q_a = \frac{1}{2}\rho_a V_{TW}^2(10)\left(\frac{z}{10}\right)^{\frac{2}{n}} \tag{7.19}$$

Integrating this expression up to the ship's mean height H_M yields (after division by the mean height) an average dynamic pressure $\overline{q}_a$, which is related to the dynamic pressure at the reference height q_{10} through the equation

$$\frac{\overline{q}_a}{q_{10}} = \frac{n}{n+2}\left(\frac{H_M}{10}\right)^{\frac{2}{n}} \tag{7.20}$$

Table 7.2. Data for the Ships of Fig. 7.22

Hull/Main Data	L_{OA} (m)	L_{PP} (m)	B (m)	T (m)	AL (m^2)	AF (m^2)	SL (m)	SH (m)
Car carrier	190.7	179.6	23.0	9.9	4257	654	−6.2	11.9
Container vessel I	210.8	194.5	30.5	11.6	3751	802	−3.9	10.1
Container vessel II	210.8	194.5	30.5	9.6	3774	857	−4.9	10.2
Container vessel III	210.8	194.5	30.5	9.6	2947	857	−2.1	8.7
Cargo/container vessel	198.2	187.3	32.2	12.2	3690	826	−4.9	11.1
Ferry	143.9	139.6	17.4	5.9	2126	325	−1.4	8.2
Tanker, loaded	351.4	336.0	55.4	23.5	3402	1132	−24.5	6.8
Tanker, ballast	351.4	336.0	55.4	8.3/13.0	7840	1804	−8.3	12.34
Offshore supply vessel I	62.0	58.3	13.0	4.9	337	137	8.0	4.1
Offshore supply vessel II	61.00	58.35	13.0	4.9	260	110	7.1	3.1
Deep sea drilling ship	150.1	137.0	21.4	7.0	1872	556	1.2	9.6

AF, front area; AL, lateral area; B, breadth; LOA, length overall; LPP, length between perpendiculars; SH, center of lateral area (vertical position relative to water line); SL, center of lateral area (longitudinal position relative to midship, positive forward); T, draft

All three coefficients C_X, C_Y, and C_N measured without the boundary layer may be converted to the boundary layer case by multiplication by the factor

$$\frac{\overline{q}_a}{q_{10}}$$

Because the center of pressure changes vertically in the boundary layer, the lever arm for the rolling moment changes as well, and it is straightforward to show that C_K should be multiplied by the factor

$$\frac{n+1}{n+2}\frac{\overline{q}_a}{q_{10}}$$

Assuming a mean height H_M of 10 m, which is a reasonable value for many ships, C_X, C_Y, and C_N will be reduced by 17% with $n = 10$ (i.e., in strong winds) and by 29% in light winds with $n = 5$. The reduction in C_K is smaller: 11% and 17%, respectively.

For the somewhat more general case with a ship moving in a headwind or a sternwind (i.e., $\beta_{TW} = \beta_{AW} = 0$ degrees or $\beta_{TW} = \beta_{AW} = 180$ degrees), the mean dynamic pressure may be obtained by numerical integration of the velocity profile containing the effects of both the ship movement and the wind [equation (7.11)]. Because the resulting velocity profile will not go to zero at the water level, this will yield larger values of the coefficients than equation (7.20) (with the velocity at the reference height equal to the sum of the wind and ship speeds). On the other hand, the coefficients will be smaller than the original values assuming a constant velocity over the ship's height.

For the most general case with the wind in an arbitrary direction and the ship moving, it is very difficult to include the boundary layer effect because the apparent velocity profile is skewed. The different directions of the aerodynamic force at different levels will have to be considered when integrating over the mean height of the ship. The uncorrected coefficients obtained without the boundary layer effect are likely to be too high and the corrected ones according to equation (7.20) too small. Because the twisting of the profile gives a more longitudinal flow below the reference height, the reduction in dynamic pressure because of the boundary layer is somewhat compensated when it comes to the axial force component C_X. For the transverse component C_Y, the twisting somewhat exaggerates the correction needed. As in the special case described previously, both corrections should be smaller than for the ship at rest. In practice, it may therefore be sufficient to only consider the uncorrected coefficients.

The mean value of C_X at zero apparent wind angle for all hulls in Fig. 7.22 (except the drilling ship) is 0.6. In still air, this yields a resistance force, often called R_{AA}, which may be obtained from

$$R_{AA} = \mathrm{C}_X \cdot \frac{1}{2}\rho_a V^2 A_T = 0.6 \cdot \frac{1}{2}\rho_a V^2 A_T \qquad (7.21)$$

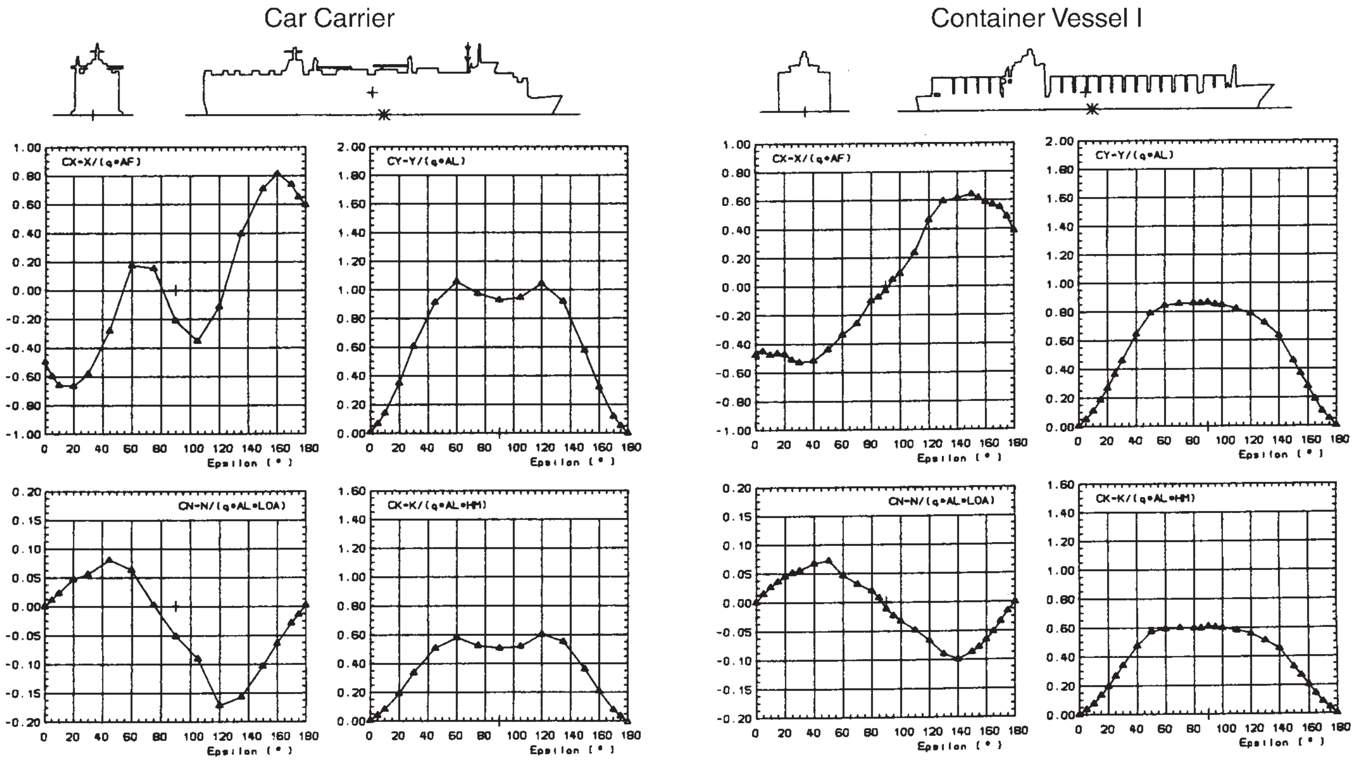

Figure 7.22 Wind forces on a series of ships according to Blendermann (1990). Note that the longitudinal force in the figure is positive forward. The apparent wind angle is denoted ε. Upper left figure, CX; upper right, CY; lower left, CN; lower right, CK. *(continued)*

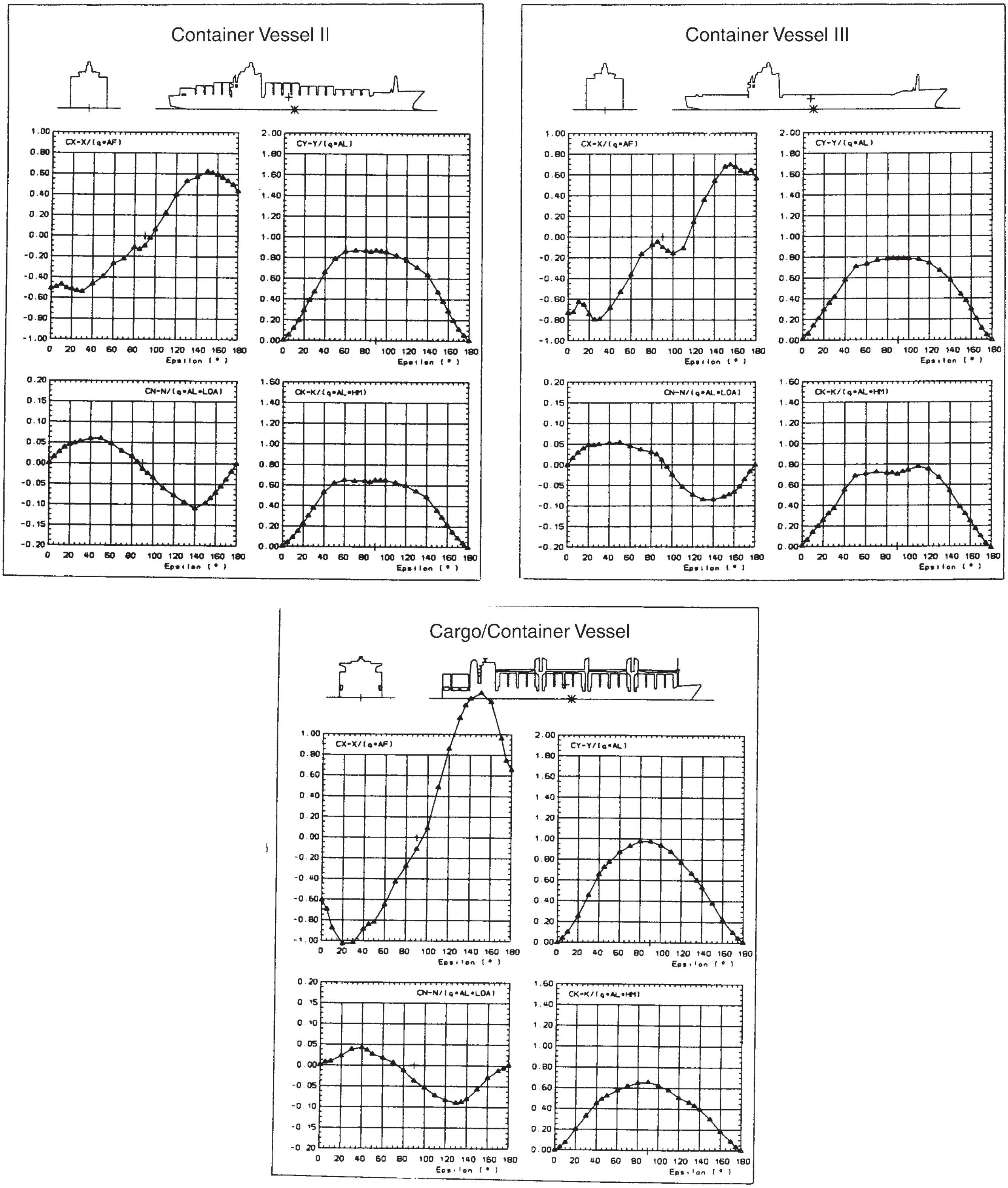

Figure 7.22b *(continued)*

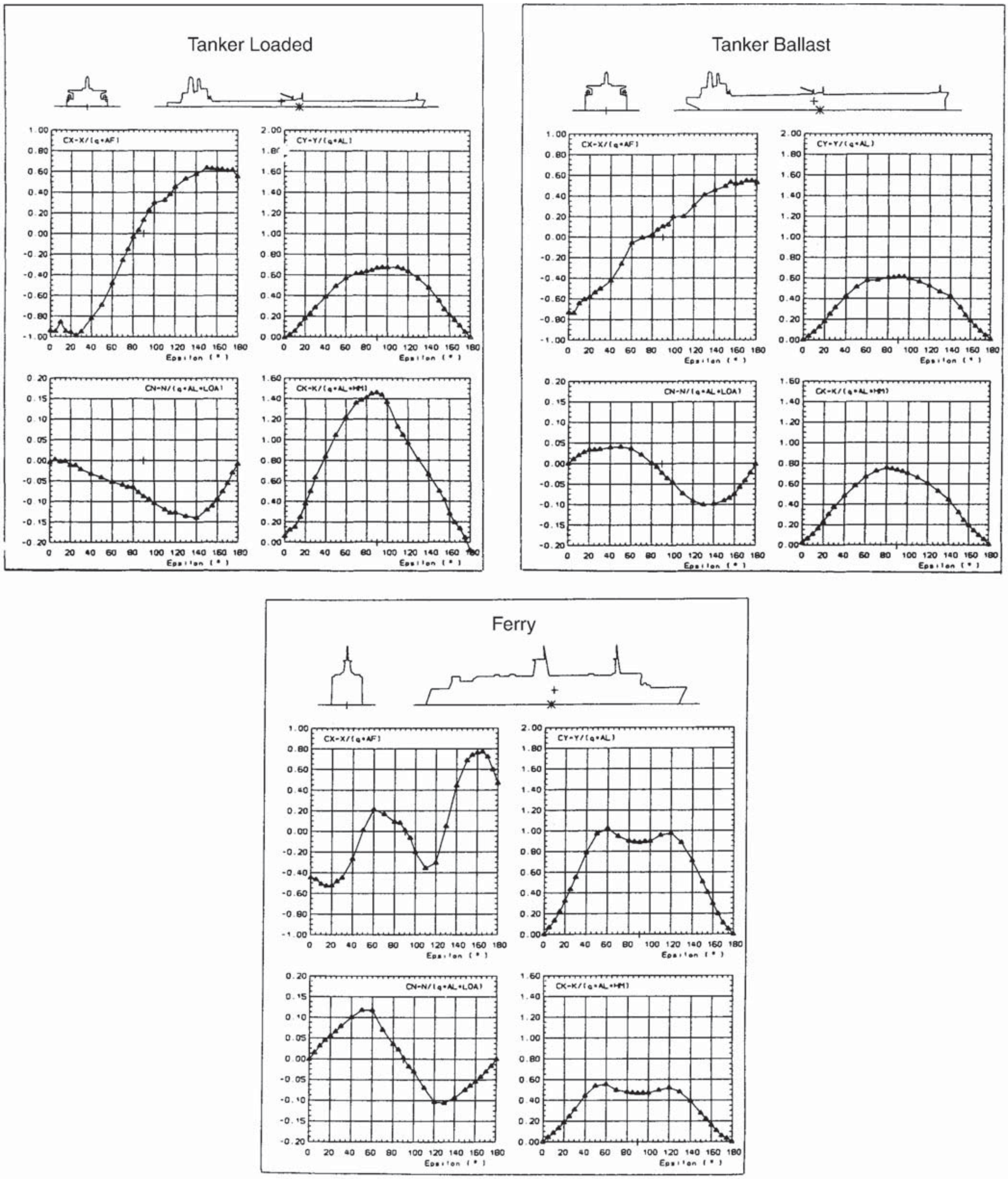

Figure 7.22c *(continued)*

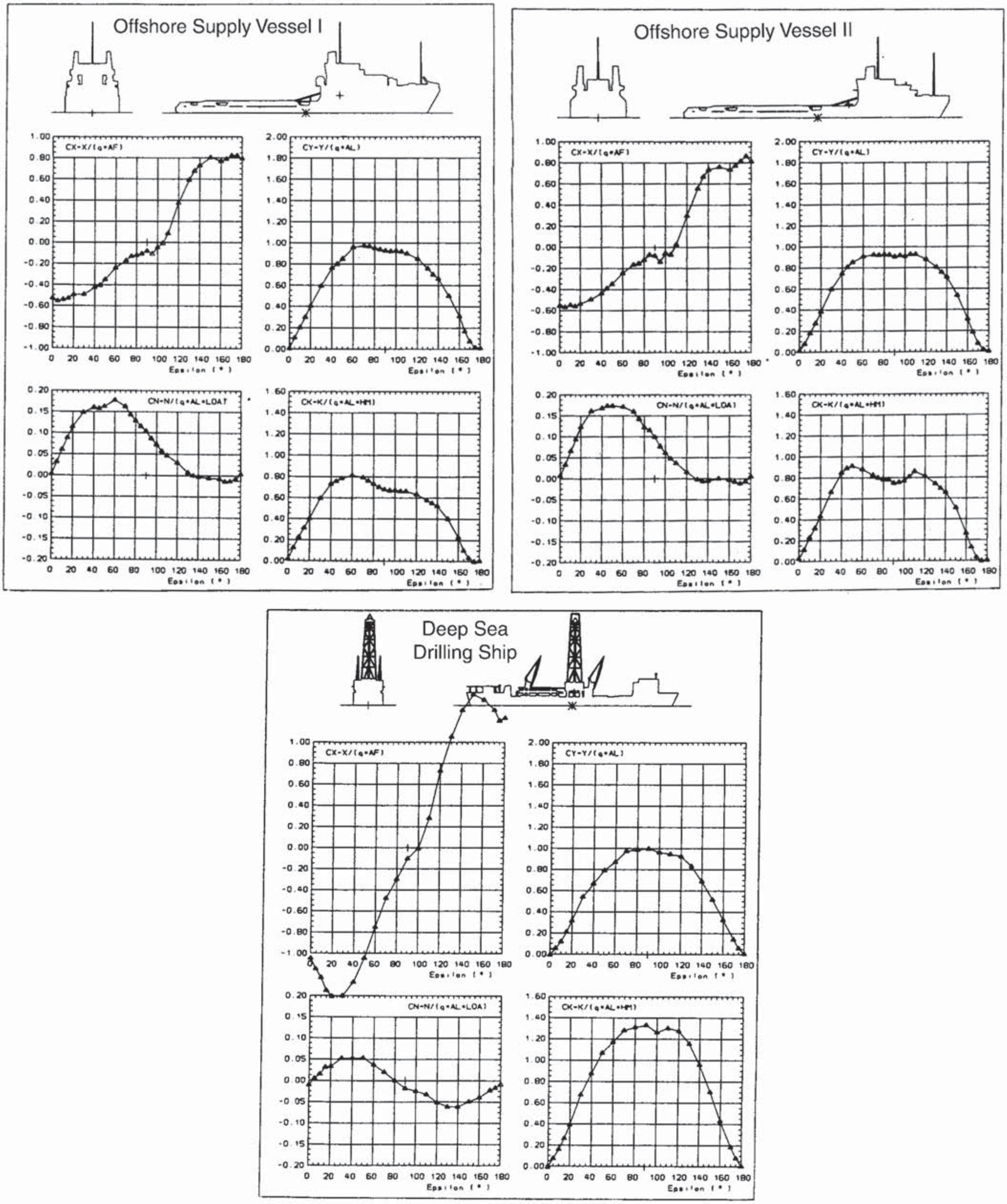

Figure 7.22d *(continued)*

Because all hydrodynamic coefficients are nondimensionalized by the water density ρ and the wetted area of the ship S, it is convenient to use the same quantities here. This yields

$$C_{AA} = \frac{R_{AA}}{\frac{1}{2}\rho V^2 A_S} = \frac{0.6 \cdot \frac{1}{2}\rho_a V^2 A_T}{\frac{1}{2}\rho_a V^2 A_S} = 0.72 \cdot 10^{-3} \cdot \frac{A_T}{A_S} \quad (7.22)$$

where the densities of the air and water are assumed to be 1.2 and 10^3 kg/m^3, respectively. The coefficient C_{AA} is used in the extrapolation from model tests to full scale, as will be seen in Section 8. It is normally assumed that the models are towed without a superstructure and that the air resistance of the hull itself can be neglected because of its streamlined shape. C_{AA} is thus neglected for the model but is added to the hydrodynamic coefficients for the ship. The coefficient is however considered a small correction and is computed with only one significant digit in the constant, which then becomes 0.001.

7.3.3 Indirect Effects of the Wind. When the wind is not along the hull, the side force generated will cause the hull to slide sideward such that the aerodynamic force is balanced by a corresponding hydrodynamic side force. The hull will move with a leeway angle. Normally, the two side forces will not act along the same line, so a yawing moment is developed. This has to be balanced by the rudder, so the ship will move with nonzero rudder angle.

Because of the lift generation, both the hull and the rudder will cause an induced drag. In the latter case, equations (7.6) and (7.7) can be used for accurate computations of the required lift and the corresponding induced drag. For the hull, the accuracy of the equations is smaller because of the very small aspect ratio of the underwater part of the hull, but they should be useful for a rough estimate. Note that the mirror image of the hull in the water surface has to be included when computing the aspect ratio (the effective aspect ratio is twice the geometrical one if the free surface may be considered a symmetry plane).

In a thorough analysis of the effects of wind forces on ships, van Berlekom (1981) concluded that the order of magnitude of the direct wind force on the above-water structure of the ship is the same as that of the added resistance due to waves. The effect of the leeway and rudder is less important according to this study.

8

Experimental Resistance Prediction and Flow Measurement

Testing of ship models to determine the resistance has a very long history, as shown in Section 1.2. Ever since William Froude's days in the middle of the 19th century, the basic testing techniques have been the same, although improvements have been made both on the procedures for scaling of the model data to full scale and on the measuring equipment. Most of the world's leading towing tanks have been in operation for many years and have acquired a wealth of knowledge on testing techniques and interpretation of results. Even though the numerical methods to be presented in Section 9 have now acquired a level of accuracy good enough for replacing some of the systematic model tests in the ship design optimization procedure, the towing tank still provides the most accurate predictions of resistance and power for the majority of ships.

8.1 Experimental Facilities. In towing tank testing, a model is towed at constant speed in still water. Commercial towing tanks employ mechanically or electrically driven towing carriages, running on rails along the model basin. They use models 4 to 10 or more meters in length and conduct resistance tests, propulsion tests, and various other experiments on ship models and other bodies. The carriage is equipped with computer systems for data processing, permitting direct inspection and first analysis of the measurement data. Platforms on the carriage permit close observation of the test and of the flow features. During the tests, photographs and video recordings are usually taken for later inspection.

Typical dimensions of these larger tanks are 250 m long, 10 m wide, and 5 m deep. For investigations in shallow water, some establishments have adopted a basin in excess of 20 m wide and a (variable) depth of up to about 3 m. High-speed craft need extra long tanks. In that case, often relatively narrow basins are employed, typically 4 m wide and 4 m deep, and the speed of the towing carriages needs to be well in excess of the maximum speed of about 10 m/sec normally employed in other tanks. Some towing tanks are equipped with wave makers for seakeeping tests. Fig. 8.1 shows a typical model basin and towing carriage.

Besides these tanks for commercial operation, there is a considerable number of small tanks generally associated with educational and research establishments, using models 1 to 3 m in length.

Water tunnels are not used for measuring resistance, but they are very suitable for measuring and visualizing

Because all hydrodynamic coefficients are nondimensionalized by the water density ρ and the wetted area of the ship S, it is convenient to use the same quantities here. This yields

$$C_{AA} = \frac{R_{AA}}{\frac{1}{2}\rho V^2 A_S} = \frac{0.6 \cdot \frac{1}{2}\rho_a V^2 A_T}{\frac{1}{2}\rho_a V^2 A_S} = 0.72 \cdot 10^{-3} \cdot \frac{A_T}{A_S} \quad (7.22)$$

where the densities of the air and water are assumed to be 1.2 and 10^3 kg/m^3, respectively. The coefficient C_{AA} is used in the extrapolation from model tests to full scale, as will be seen in Section 8. It is normally assumed that the models are towed without a superstructure and that the air resistance of the hull itself can be neglected because of its streamlined shape. C_{AA} is thus neglected for the model but is added to the hydrodynamic coefficients for the ship. The coefficient is however considered a small correction and is computed with only one significant digit in the constant, which then becomes 0.001.

7.3.3 Indirect Effects of the Wind. When the wind is not along the hull, the side force generated will cause the hull to slide sideward such that the aerodynamic force is balanced by a corresponding hydrodynamic side force. The hull will move with a leeway angle. Normally, the two side forces will not act along the same line, so a yawing moment is developed. This has to be balanced by the rudder, so the ship will move with nonzero rudder angle.

Because of the lift generation, both the hull and the rudder will cause an induced drag. In the latter case, equations (7.6) and (7.7) can be used for accurate computations of the required lift and the corresponding induced drag. For the hull, the accuracy of the equations is smaller because of the very small aspect ratio of the underwater part of the hull, but they should be useful for a rough estimate. Note that the mirror image of the hull in the water surface has to be included when computing the aspect ratio (the effective aspect ratio is twice the geometrical one if the free surface may be considered a symmetry plane).

In a thorough analysis of the effects of wind forces on ships, van Berlekom (1981) concluded that the order of magnitude of the direct wind force on the above-water structure of the ship is the same as that of the added resistance due to waves. The effect of the leeway and rudder is less important according to this study.

8

Experimental Resistance Prediction and Flow Measurement

Testing of ship models to determine the resistance has a very long history, as shown in Section 1.2. Ever since William Froude's days in the middle of the 19th century, the basic testing techniques have been the same, although improvements have been made both on the procedures for scaling of the model data to full scale and on the measuring equipment. Most of the world's leading towing tanks have been in operation for many years and have acquired a wealth of knowledge on testing techniques and interpretation of results. Even though the numerical methods to be presented in Section 9 have now acquired a level of accuracy good enough for replacing some of the systematic model tests in the ship design optimization procedure, the towing tank still provides the most accurate predictions of resistance and power for the majority of ships.

8.1 Experimental Facilities. In towing tank testing, a model is towed at constant speed in still water. Commercial towing tanks employ mechanically or electrically driven towing carriages, running on rails along the model basin. They use models 4 to 10 or more meters in length and conduct resistance tests, propulsion tests, and various other experiments on ship models and other bodies. The carriage is equipped with computer systems for data processing, permitting direct inspection and first analysis of the measurement data. Platforms on the carriage permit close observation of the test and of the flow features. During the tests, photographs and video recordings are usually taken for later inspection.

Typical dimensions of these larger tanks are 250 m long, 10 m wide, and 5 m deep. For investigations in shallow water, some establishments have adopted a basin in excess of 20 m wide and a (variable) depth of up to about 3 m. High-speed craft need extra long tanks. In that case, often relatively narrow basins are employed, typically 4 m wide and 4 m deep, and the speed of the towing carriages needs to be well in excess of the maximum speed of about 10 m/sec normally employed in other tanks. Some towing tanks are equipped with wave makers for seakeeping tests. Fig. 8.1 shows a typical model basin and towing carriage.

Besides these tanks for commercial operation, there is a considerable number of small tanks generally associated with educational and research establishments, using models 1 to 3 m in length.

Water tunnels are not used for measuring resistance, but they are very suitable for measuring and visualizing

Figure 8.1 Model basin and towing carriage. (Photo: Sven Wessling. Courtesy of SSPA.)

the flow around the hull. A special type of water tunnel is the circulating water channel, where the measuring section has a free water surface. Resistance and wave tests may then be carried out. Normally, these facilities allow only small models to be tested, but there are larger circulating water channels as well, such as the one at the Technical University of Berlin, with a length of 11 m and a width of 5 m.

In the normal towing tank resistance tests, measurement of the carriage speed and the resistance force are often combined with sinkage and trim measurements. For flow measurements or observation, towing tanks usually have available pitot tubes for wake measurements, and underwater observation possibilities for tuft tests. Some tanks have laser-Doppler velocimetry (LDV) systems for flow measurements but, today, particle-image velocimetry (PIV) systems are in increasing use. These additional experiments are briefly described in Section 8.4.

8.2 Model Resistance Tests

8.2.1 General. The resistance test is usually the first test done with a model. It serves to predict the resistance of the full-scale vessel, is a part of the prediction procedure of the full-scale required power, and, by comparing with available resistance data for comparable vessels or empirical/statistical methods, provides a measure of the quality of the design from a resistance point of view.

Resistance tests are carried out with the model attached to the carriage. The model is ballasted and trimmed to the required displacement and waterline, and attached to the resistance dynamometer of the towing carriage. A clear statement as to whether molded or total displacement is meant should be included. The model is free to take up any sinkage or trim dictated by the water forces, but any yawing motion is prevented by guides.

On a test run, the carriage is driven at the desired constant speed and records are taken of speed and resistance. Besides measuring the so-called towing force, the sinkage of the model at the forward and aft perpendicular is measured and observations and photo and video recordings of the waves close to the model are often made, as an aid to subsequent understanding of the results.

For any given displacement and trim condition, a number of test runs are made at different speeds and a curve of resistance against speed is obtained. It is important that sufficient time is taken between the test runs to make sure that the waves and current in the basin generated by the towing of the model have died out, as otherwise these would disturb the measurements.

Before proceeding to propulsion tests, a number of other experiments are often made, such as flow measurements; wake field measurements; measurements to determine the best line for bilge keels; experiments to determine the flow around the afterbody to settle the best alignment for bossings, shaft brackets, and rudders; and in some cases, to determine the flow over the whole form by paint tests. Sometimes models are modified if there is reason to do so, and tests are repeated.

The "jump" in Reynolds number going from model to ship is very large; in the case of a 125-m ship and a 5-m model, the speeds of the ship and model are, for example, 25 and 5 knots, respectively, so that the values of Reynolds number, proportional to the product VL, would be in the ratio of 1 to 125. (This is not always realized in looking at experiment plots because it is general to use a base of log Rn, which greatly reduces the apparent degree of extrapolation.) The measurement of the model resistance must therefore be extremely accurate to minimize errors in the extension to the ship. Constancy of speed of the towing carriage is a most important basic requirement, as is the accuracy of the towing dynamometer. Also, the models must be made to close tolerances, the surface correctly finished, and the models properly ballasted and trimmed.

8.2.2 Model Size. The choice of model size is governed by several considerations. The larger the model, the more accurately it can be made and the larger the forces to be measured, both features leading to greater accuracy in the measurement of resistance. However, the bigger the model, the more expensive it is to build and handle, and the larger are the facilities and instruments necessary, so a compromise in size must be reached.

If the model is too large for a particular basin, interference from the walls and bottom will increase the resistance. There is still no real agreement on the proper assessment of this interference effect. Broadly speaking, the model length should not be much in excess of the water depth or half the width of the basin in order to avoid interference with the wave resistance. The midship cross-sectional area of the model should not exceed about 1/200 of that of the basin in order to avoid setting up appreciable return flow in the water around the model, the so-called blockage effect. However, in cases where wave making is small, larger models can be used and corrections made for the remaining blockage effect (Comstock & Hancock, 1942; Emerson, 1959; Hughes, 1957, 1961; Kim, 1962; Telfer, 1953). For high-speed models, care must also be taken to avoid the critical depth Froude number $V/(\sqrt{gh}) = 1$. A model run at any speed above about 0.7 of this value will give a resistance different from that appropriate to deep water.

If self-propelled model experiments are to follow the resistance tests, as is usual, the size of the model propellers has also to be considered when choosing the scale for the hull model. Finally, an important consideration in choosing the model size is the need to avoid presence of significant regions of laminar flow on the model (see following discussion).

8.2.3 Turbulence Stimulation. In all model testing, it is important to ensure that the flow over the model is fully turbulent because the flow around the full-scale ship is turbulent. The presence of laminar flow can usually be detected from the shape of the resistance curve (Fig. 8.2). At low values of the Froude number, where the wave resistance is vanishingly small, the C_T curve should run more or less parallel to the curve of skin friction coefficient C_F, as *ABC*. A curve which falls away in this region or even becomes horizontal, such as *ABD* or *ABE*, is at once suspect as being subject to partial laminar flow, which will yield too small a resistance.

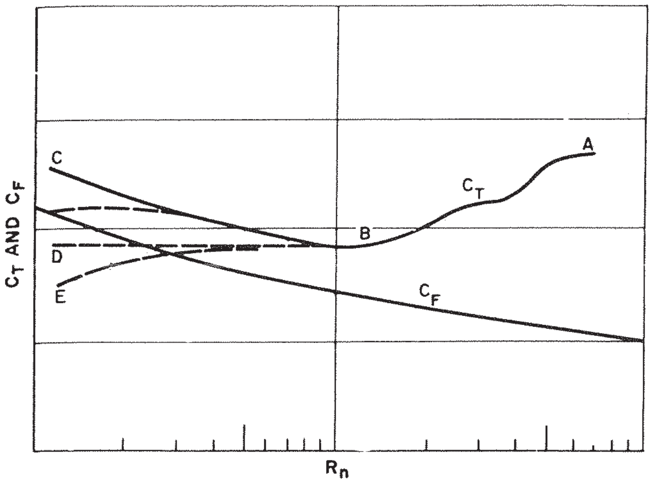

Figure 8.2 Effects of laminar flow on the resistance at low speed.

The practical answer to the laminar flow problem is to deliberately "trip" the laminar flow by some kind of roughness near the bow. Trip-wires about 1 mm diameter placed around the hull at a station 5% of the length from the forward perpendicular are now standard practice. Other devices, used particularly for stimulating the flow around appendages (but also for the hull itself), are sandstrips or studs. A typical stud height is 2.5 mm, and the diameter is normally about 3 mm. The studs are placed in a row parallel to the leading edge of the appendage or the stem of the ship. The stimulating device increases the resistance because of its own parasitic drag. If it is placed too close to the stem, there is a danger of the laminar flow reestablishing itself if the pressure gradient is favorable, but when placed in the usual position (5% Lpp aft of the stem) it leaves the laminar flow (if it exists) undisturbed over the first part of the length up to the stimulator. In this case, the resistance of this portion of the surface will be less than the turbulent resistance desired. It is usual to assume that this defect in resistance balances the additional parasitic drag of the wire or studs.

8.3 Prediction of Effective Power. The effective power P_E of the ship is the power required to drive the ship at a certain speed without any propulsive losses (i.e., it is the resistance times the speed of the ship, $R_T \cdot V$). To determine the full-scale (index *S*) resistance from the model (index *M*) test, essentially only two methods have been in use: Froude's method and the method recommended by the ITTC in 1978. The latter is presently used by most tanks, but there are still cases where Froude's method is employed. Both will be described in the following.

Ship model resistance tests are generally based on the following principles, which have been described in more detail Section 3.3.

1. Froude's hypothesis that the resistance of a model or ship can be split in two independent parts: a viscous or frictional resistance, and a pressure-related, wave, or "residuary" resistance (such decompositions are discussed in Section 4.1)

2. In Section 3.3, it has been pointed out that these two parts are essentially governed by two different nondimensional parameters: the Froude number $F_n = V/(\sqrt{gL})$ and the Reynolds number $R_n = (VL)/\nu$. It is not possible to make both parameters equal for model and ship, and a choice needs to be made (see Section 3.3.2).

3. The practical solution is to test the model at the same Froude number as the ship, which is done by choosing $V_M = V_S\sqrt{L_M/L_S}$. In that case, the wave (or residuary) resistance coefficient of ship and model, $C_R = R_R/(0.5\rho V^2S)$, are equal (see Section 3.3.2).

4. Then the viscous or frictional resistance cannot be scaled up directly, and an approximation needs to be made for its Rn-dependence. In Froude's method, the Rn-dependence is supposed *equal* to that of the frictional resistance of a flat plate, whereas in the ITTC-78 method, the viscous resistance is supposed to be *proportional* to the frictional resistance of a flat plate. The constant of proportionality is the form factor.

The two basic extrapolation methods will be described. Because the major difference between the two methods is the form factor, a description will be given of the determination of this factor in Section 8.3.3. As before, all force coefficients are obtained from the forces by division by $0.5\rho V^2S$, where V is the speed and S the wetted surface.

8.3.1 Froude's Method. In Froude's method, the decomposition of the resistance is in a frictional resistance that is supposed equal to that of an equivalent flat plate (i.e., a flat plate with equal wetted surface and equal length towed at equal speed [so, equal Rn]) and a residuary resistance, which is everything else. Therefore, the residuary resistance not only incorporates the wave resistance, but also the form effect on friction and the form effect on pressure (see Section 4.1). In modern terminology,

$$C_T(Rn, Fn) = C_{F0}(Rn) + C_R(Fn) \tag{8.1}$$

in which C_{F0} is the plate friction coefficient and C_R the residuary resistance coefficient. In practice, the flat plate friction C_{F0} is now replaced by C_F from the ITTC-57 line, equation (6.38). Because this contains 12% form effect, which in the original procedure should have been included in C_R, the procedure is not quite as proposed by Froude.

The following steps are taken when extrapolating the measured model resistance R_{TM} to the full-scale resistance R_{TS}.

1. Perform resistance tests with the model at the same Froude number as the ship (i.e., $V_M = V_S\sqrt{L_M/L_S}$). Measure the total resistance coefficient C_{TM}

2. Compute the friction coefficient of the model using the ITTC-57 formula

$$C_{FM} = \frac{0.075}{({}^{10}\log Rn_M - 2)^2} \tag{8.2}$$

where the Reynolds number Rn_M is for the model; or use another extrapolation line (see Section 6.3.4)

3. Compute the residuary resistance C_{RM} for the model

$$C_{RM} = C_{TM} - C_{FM} \tag{8.3}$$

4. Because the Froude number is the same, the residuary resistance coefficient is also the same at the two scales

$$C_{RS} = C_{RM} \tag{8.4}$$

5. Compute the friction coefficient of the ship

$$C_{FS} = \frac{0.075}{({}^{10}\log Rn_S - 2)^2} \tag{8.5}$$

where the Reynolds number Rn_S is for the ship

6. Compute the total resistance coefficient for the ship

$$C_{TS} = C_{FS} + C_{RS} + \Delta C_F \tag{8.6}$$

where the roughness allowance coefficient is set as a constant $\Delta C_F = 0.0004$

7. The full-scale resistance R_S is finally computed as

$$R_S = C_{TS}\cdot\frac{1}{2}\rho_S V_S^2 S_S \qquad \text{(N)} \tag{8.7}$$

and the effective power P_E as

$$P_E = R_S\cdot V_S \tag{8.8}$$

A graphical representation of the method is shown in Fig. 8.3.

8.3.2 ITTC-78. We will now describe the method most widely used by towing tanks today, the ITTC-78 method. In this method, the decomposition is in a viscous resistance, which includes the form effect on friction and pressure, and a wave resistance. The form factor is the ratio of the viscous resistance of the ship, and the frictional resistance of an equivalent flat plate. Through the introduction of the form factor, a better division of the total resistance is obtained, and the components can be better scaled. Therefore, the assumption is

$$C_T(Rn, Fn) = (1 + k)C_{F0}(Rn) = C_W(F_n) \tag{8.9}$$

in which C_{F0} is the plate friction coefficient, $1 + k$ the form factor, and C_W the wave resistance coefficient. How the form factor is determined in practice is described in Section 8.3.3. Again, the flat plate friction C_{F0} is replaced by C_F from the ITTC-57 line, equation (6.38). This will be discussed later. The following steps are taken.

1. Perform resistance tests with the model at the same Froude number as the ship (i.e., $V_M = V_S\sqrt{L_M/L_S}$). Measure the total resistance coefficient C_{TM}

2. Compute the friction coefficient of the model according to ITTC-57

$$C_{FM} = \frac{0.075}{({}^{10}\log Rn_M - 2)^2} \tag{8.10}$$

where the Reynolds number Rn_M is for the model

3. Determine the form factor k (usually by the Prohaska method, Section 8.3.3)

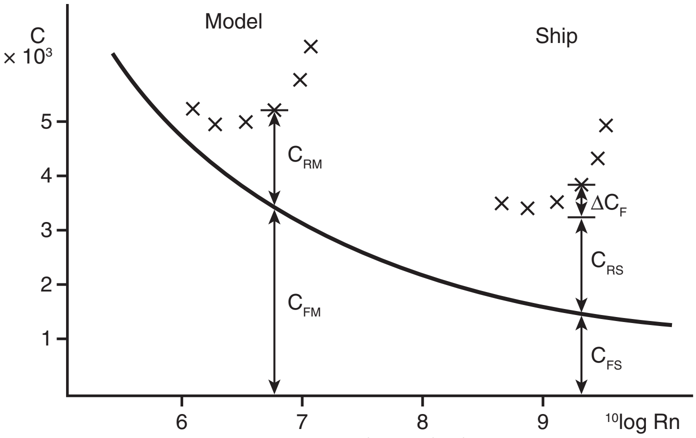

Figure 8.3 Froude's method.

4. Compute the wave resistance C_{WM} of the model

$$C_{WM} = C_{TM} - (1 + k) \cdot C_{FM} \tag{8.11}$$

5. Assume that $C_{WS} = C_{WM}$. Note that this wave resistance is smaller than the residuary resistance for the Froude method!

6. Compute the friction coefficient C_{FS} of the ship

$$C_{FS} = \frac{0.075}{({}^{10}\log Rn_S - 2)^2} \tag{8.12}$$

where the Reynolds number Rn_S is for the ship

7. Compute the roughness allowance ΔC_F according to Bowden

$$\Delta C_f = \left(105 \cdot \left(\frac{k_{MAA}}{L}\right)^{\frac{1}{3}} - 0.64\right) \cdot 10^{-3} \tag{8.13}$$

where k_{MAA} is the roughness in microns(10^{-6} m), measured according to the MAA method (Section 6.8.2). ITTC recommends $k_{MAA} = 150$ microns as a typical value.

8. Determine the air resistance coefficient

$$C_{AA} = 0.001 \cdot \frac{A_T}{S} \tag{8.14}$$

where A_T is the frontal area of the ship above the water

9. Compute the total resistance coefficient of the ship

$$C_{TS} = (1 + k) \cdot C_{FS} + C_{WS} + \Delta C_F + C_{AA} \tag{8.15}$$

10. The total resistance R_S may now be obtained as

$$R_S = C_{TS} \cdot \frac{1}{2} \rho_S V_S^2 S_S \tag{8.16}$$

and the effective power as

$$P_E = R_S \cdot V_S \tag{8.17}$$

A graphical representation of the method is shown in Fig. 8.4.

These are the steps taken when extrapolating a resistance test to full scale. Considerably more steps are

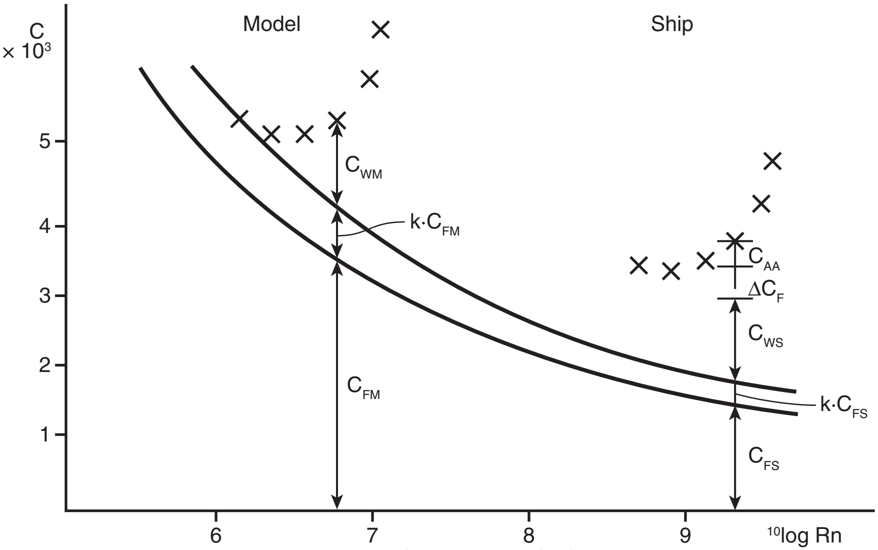

Figure 8.4 The ITTC-78 method.

required for extrapolating self-propulsion tests, as described in the Propulsion volume of the *Principles of Naval Architecture.*

8.3.3 Determination of the Form Factor. The form factor $1 + k$ was defined in equation (6.39) and it represents the ratio of the (smooth) viscous resistance and the resistance of the equivalent flat plate. It thus incorporates the form effect on the viscous resistance: the increased flow speed and pressure gradients due to the thickness of the body (Section 4.1), the effect of the boundary layer and wake displacement on the pressure at the stern (Sections 4.1 and 6.4.1), and possible flow separation. The formula was given for 2D flows, but it holds also for 3D flows.

In the strict definition, the real friction for the plate, CF0, appears, and one of the plate friction lines discussed in Section 6.3.4 should be used, but as seen, the ITTC-57 formula (6.38) is mostly used. Recall that this formula already includes about 12% form effect, so the approach is not logical, but it will lead to correct results provided the form factor is used together with the friction formula it is intended for (and with a consistent roughness allowance). Three different ways of determining the form factor will now be described.

Empirical Formula The most popular empirical formula for determining the form factor is attributed to Watanabe

$$k = -0.095 + 25.6 \cdot \frac{C_B}{\left(\frac{L}{B}\right)^2 \sqrt{\frac{B}{T}}} \tag{8.18}$$

In this formula, C_B is the block coefficient, L the length between perpendiculars, B the beam, and T the draft. Note that equation (8.18) can be used only in combination with the ITTC-57 formula.

Determination at Low Speed An apparently very simple way of determining the form factor is to run the model at low speed (e.g., $Fn < 0.15$) where the wave resistance is negligible. The form factor k can then be determined from equation (8.9) with $C_W = 0$ and C_{F0} approximated by the ITTC-57 formula. Unfortunately, problems with laminar flow may occur, as explained, and the forces at these low speeds are normally very small, making accurate measurements difficult. The procedure is explained in Fig 8.5.

Prohaska's Method The most widely used method for determining the form factor is attributed to Prohaska (1966). The method is based on the assumption that the wave resistance coefficient is proportional to the Froude number to the fourth power, which is supported by the calculations by Wigley described in Section 5.4.5. The total resistance coefficient, C_T, may the be written

$$C_T = (1 + k)\, C_F + k_1 Fn^4 \tag{8.19}$$

Division by C_F yields

$$\frac{C_T}{C_F} = (1 + k) + k_1 \frac{Fn^4}{C_F} \tag{8.20}$$

which is a straight line in Fig. 8.6.

If the assumption on the wave resistance is correct, the measurement points will fall on the straight line with $(1 + k)$ as the intercept on the vertical axis. Normally, this is true for the points in the lower Froude number range. The line is thus adjusted to go through these points as well as possible, and the form factor is read on the intersection with the vertical axis. Dependent on the hull form, Prohaska's method can be applied to model tests at a somewhat higher speed than a simple low-speed test.

8.3.4 Discussion. The two extrapolation methods discussed would, without further corrections, give substantially different full-scale resistance predictions (e.g., for a ship with a form factor $1 + k = 1.2$, the total form effect amounts to 20% of the plate friction resistance). As the plate friction coefficient for the ship is of the order of one-half of that for a model, that form effect is supposed also to decrease by about one-half in the ITTC-78 method, but to remain equal in Froude's method, in which it is included in the residuary resistance. This

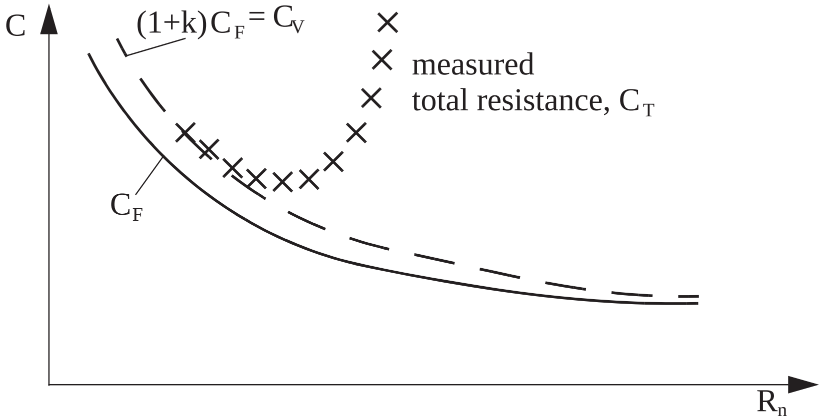

Figure 8.5 Determination of the form factor at low speed.

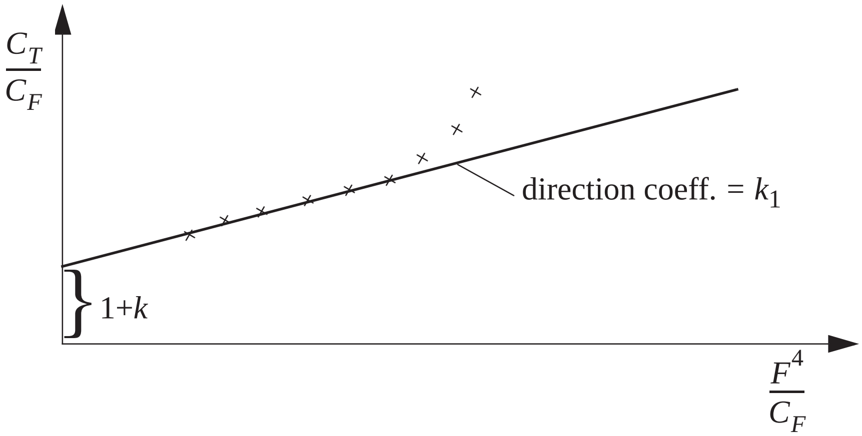

Figure 8.6 Prohaska's method.

gives a difference in full-scale resistance of 10% of the plate friction drag, so perhaps some 5% of the total resistance. However, the "correlation allowances" or "roughness allowances" for Froude's method are different, and generally smaller, than those for the ITTC-78 method. On average, this compensates for the difference in extrapolated resistance level. Therefore, the true measure of the validity of an extrapolation method is the variability of the correlation allowances that are needed to get the correct trial predictions.

Although the ITTC-78 method is generally preferred and considered more physically correct, it is not always easy to determine the form factor. Prohaska's method supposes that the wave resistance is a sixth-order function of the speed; other orders may be tried as well, but in any case the condition is that in the low-speed regime considered there are no clear wave interference effects playing a role. However, a bulbous bow close to the water surface can produce local waves already at low speed (as the local Froude number is high), sometimes causing a nonsmooth behavior of the resistance, and preventing an accurate determination of the form factor. Also, an immersed transom that is only dry at higher speeds can cause inaccuracies. In case an experimental determination of the form factor fails, empirical formulas can be used, but still the accuracy is limited. On the other hand, a less accurate form factor does not immediately cause gross errors in the extrapolated resistance.

The form factor approach, or the assumption that the viscous resistance is proportional to the frictional resistance of an equivalent flat plate, is also of limited validity. It probably holds well for rather slender ships without flow separation. But for full hull forms having a bubble-type flow separation at model-scale that is perhaps absent at full scale, there is little reason to believe in this proportionality. For vessels with sharp edges from which flow separation takes place, the extent of the separation is independent of Rn and it may be better to apply a direct scaling of the associated resistance contribution. The problems with the scaling of appendage resistance were discussed in Section 7.2.1, in connection with Fig. 7.18. In order not to introduce unnecessary errors when the appendage resistance is large, this component should be scaled separately.

Another approximation inherent to the extrapolation methods is the basic assumption of independence of the wave making and the viscous flow, governed by Fn and Rn, respectively. In reality, the stern wave system is generally reduced by viscous effects, and less so at full scale than at model-scale; therefore, some increase of the wave resistance coefficient from model- to full scale can be expected. Moreover, the viscous resistance can well be Fn-dependent: the wavy water surface along the hull, and the change of the pressure distribution because of the wave making, also affect the viscous flow and the wetted surface and can even lead to flow separation. Therefore, the form factor determined in a low-speed test may not be entirely appropriate for higher speeds. For a computational study of scale effects on form factors and wave resistance, see Raven et al. (2008).

Nevertheless, the methods to predict the power from model test results presented here, or variants thereof, still are the best established approaches. But the shortcomings discussed mean that the correlation allowances, which have been determined by regression of trial data, contain a variety of unknown corrections, not only roughness effects. In practice, the predictions and intermediate results of extrapolation procedures are usually compared with results for similar vessels, and further corrections are applied when needed. Therefore, experience is still important to predict the full-scale effective power accurately from model test results.

8.4 Model Flow Measurements. Besides resistance tests, a variety of other tests are carried out in towing tanks to determine the properties of the flow around the hull. We will first briefly describe the principal techniques used for measuring velocities and wave elevations. Then, we will review the usual tests carried out in model basins that are relevant to resistance and flow.

8.4.1 Measurement Techniques for Flow Velocities and Wave Elevations. For measurement of the velocity field around the hull, the following devices are used in towing tanks.

- A *five-hole pitot tube* (Fig. 8.7) measures the pressure differences between the five holes in the spherical head of the tube. The flow velocity magnitude and direction can then be determined from a relation found by calibration. Larger incidence angles, proximity of a wall, and large velocity gradients or turbulent fluctuations reduce the accuracy of the measurement.
- For Laser-Doppler Velocimetry (*LDV*), monochromatic light from a laser is split in two beams that by optical systems are made to intersect, in a small "measurement volume" in the flow at a distance from the optical devices. Particles in the flow (naturally present in the towing tank, or introduced by "seeding") pass through the volume and reflect or scatter the light. Owing to the particle velocity, the light from the two beams is reflected by the particle with a different Doppler shift of the frequency, resulting in interference. A photodetector detects this interference frequency, which is used to derive the local flow speed and direction in the measurement volume. Based on records of a sufficient number of particles, the average flow speed and turbulence quantities can be deduced.
- Particle-Image Velocimetry (*PIV*) is a more recent technique for flow speed measurement. A laser system casts a thin sheet of light into the flow. Particles in the flow pass that sheet and are briefly illuminated. Two photographs are taken of the measurement plane, at a very small time interval (typically some milliseconds). In the two photographs, the same particles will be found at slighty different positions, and their shift over the known time interval is a measure of their speed tangential to the measurement plane. To recognize the same groups of particles in the two photographs, pattern recognition methods are applied. The result is a distribution of the instantaneous tangential flow velocity distribution in the measurement plane. By using stereo photography in the same set-up, the velocity component normal to the laser sheet can also be determined.

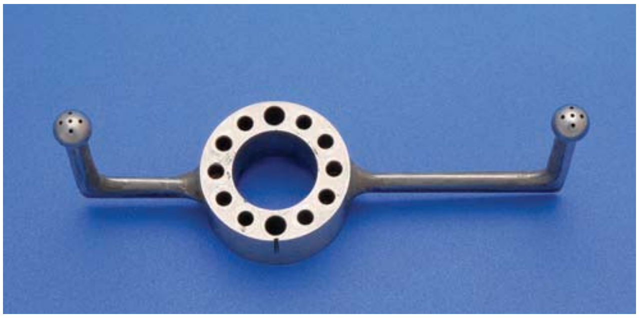

Figure 8.7 Rake for wake measurements containing two five-hole pitot tubes. (Photo: Sven Wessling. Courtesy of SSPA.)

For measuring wave elevations, the most widely used devices are *capacitance* or *conductance probes*. These produce an electric signal dependent on their immersion, which is read out at a given scanning frequency, thus providing a record of wave elevation against time. Such probes are available as (twin) wires mounted to a support rod, but also incorporated in flexible tape that can be attached to the model surface.

This type of probe is less suited for measurement of the wave elevation if there is a substantial flow speed relative to the wave probe. For that purpose, servo-driven probes touching the water surface and following its motion have been used, sometimes called "finger probes." Alternative measurement techniques have also been used (e.g., based on stereo photography, giving a height map of the water surface, or based on pictures taken of a vertical laser sheet that intersects and illuminates the wave surface).

These techniques are used in towing tanks, mainly for the following measurements.

8.4.2 Wake Field/Flow Field Measurement. A conventional wake field measurement specifically determines the velocity field at the location of the propeller. This is done for a model without propeller and is called the "nominal wake field" to distinguish it from the field with the operating propeller. It is normally measured using a pitot tube rake that can be rotated around the propeller shaft center and is set at various angles and radii to scan the propeller plane. All three velocity components (axial, radial, and tangential) are measured. Usually, it takes several runs through the basin to complete this test. The nominal wake field gives important first indications on the propeller inflow and thus on the risk of cavitation.

A wake field can also be measured using LDV or PIV methods. LDV systems have been used successfully in model basins, enabling precise measurements of the flow and turbulence around the hull, but also the inflow to a working propeller. For these applications, the entire LDV system must be attached to the carriage, and the measurements require a large number of runs. Therefore, their use in towing tanks has never become popular. LDV is much more easily operated in circulating water channels.

A particular application of LDV systems is for measurements of the boundary layer and wake of full-scale ships; in this case, the equipment is positioned inside the ship hull and operated through Plexiglas windows in the underwater hull surface.

PIV is used in model basins for determining the flow field around a ship model, using either an earth-fixed or a carriage-fixed system. The method is quite fast, as a whole measurement plane is measured at once, but several measurements are needed to get the proper average velocity field in a turbulent flow. The optical accessibility of the measurement plane (requiring proper camera angles) can be problematic in practice, and often requires the use of streamlined underwater housings attached to

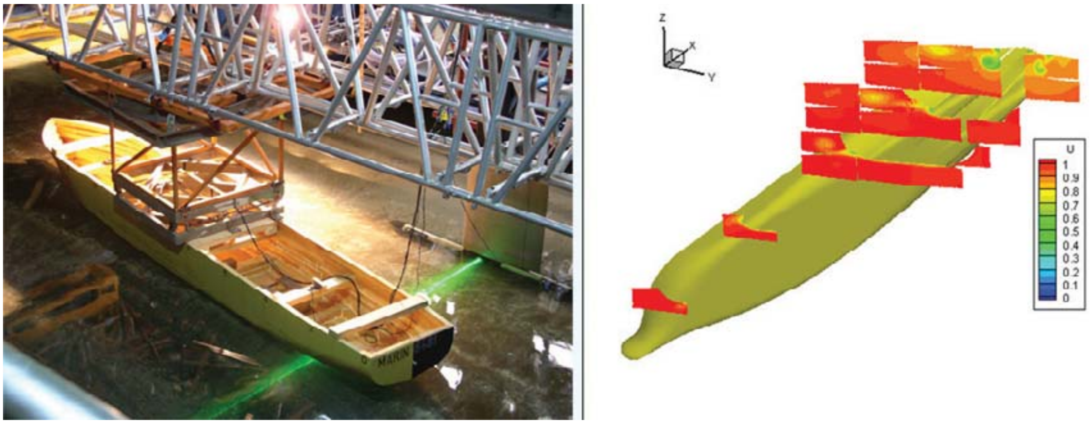

Figure 8.8 PIV measurements. *Left*: photo from a towing tank test; *right*: velocity distribution at some measurement planes.

the carriage. Fig. 8.8 shows an example of the set-up for measurements in shallow water.

It is believed that PIV can become an alternative to the conventional pitot tube measurements of wake fields for routine use in towing tanks, and may already well be more practical if several planes need to be measured.

Besides these quantitative flow measurements, more qualitative information on the flow is often collected in towing tanks, as an aid to understanding and improving the model's performance:

8.4.3 Tuft Test. In a tuft test, the model is fitted with short pieces of yarn mounted on the surface and at the tip of pins of about 50 mm height. The tufts will align themselves with the flow, and observing them with an underwater video camera gives an idea of the local flow direction and the skewing of the flow within the first 50 mm from the surface. The local unsteadiness of the flow is seen and the possible occurrence of flow separation may also be displayed. The result is a rather qualitative indication of the flow properties in the area in which tufts are mounted. Fig. 8.9 shows an example.

8.4.4 Paint Test. A paint test is a more detailed and quantitative flow measurement. Special paint is applied in girthwise strips on the model, which then is run through the tank at the desired speed. Because of the precisely tuned paint properties, it is smeared out by the flow, forming traces in the direction of the surface shear stress (skin friction). This indicates the so-called limiting streamlines (see Section 6.6.1). The paint flow traces are used to construct a set of "streamlines" which will indicate the skin friction direction, separation regions, etc. However, in the stern area, the low skin friction makes it hard to get good paint traces. Fig. 8.10 shows an example of a paint test.

8.4.5 Appendage Alignment Test. Although a paint test provides the shear stress direction on the hull surface, the flow direction at a distance from the hull is needed for aligning shaft support struts. To determine this experimentally, either pitot tubes are used, or various other devices such as small vanes on a rod mounted at the position of the strut, or plates to which paint is applied that gives paint traces indicating the local flow.

8.4.6 Wave Pattern Measurement. Wave pattern measurements are most easily done using a wave gauge at a fixed position in the tank. The probes are read out at a set frequency and thus provide a record of wave elevation against time during the passage of the model at constant speed. This registration can easily be converted to wave elevation against position relative to the model using the model speed, scanning frequency, and a starting signal given when the model is at a known position. The result is a longitudinal cut through the steady wave pattern of the model. The useful part of the registration is from the arrival of the wave disturbance of the model, until the moment that waves reflected from the tank wall reach the wave probes.

Such measured longitudinal wave cuts are used for comparison between model variations; for comparison with computational predictions; for generating far-field wave (wash) predictions (see Section 5.11); or for wave pattern analysis, a technique to deduce the wave spectrum (Section 5.4.6) and from it, the wave

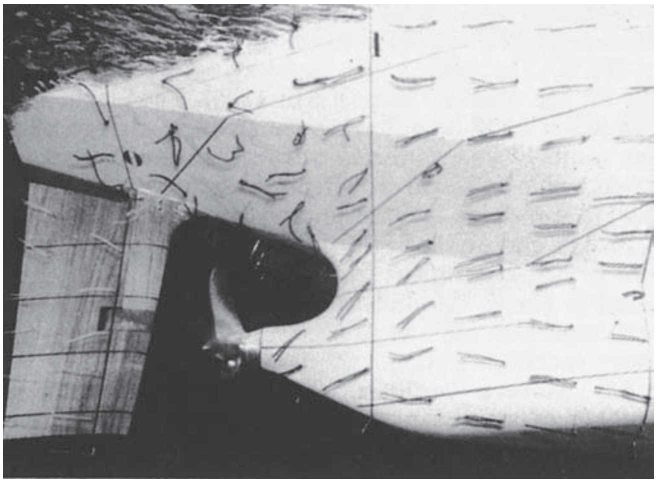

Figure 8.9 Tuft test on the afterbody of a ship model.

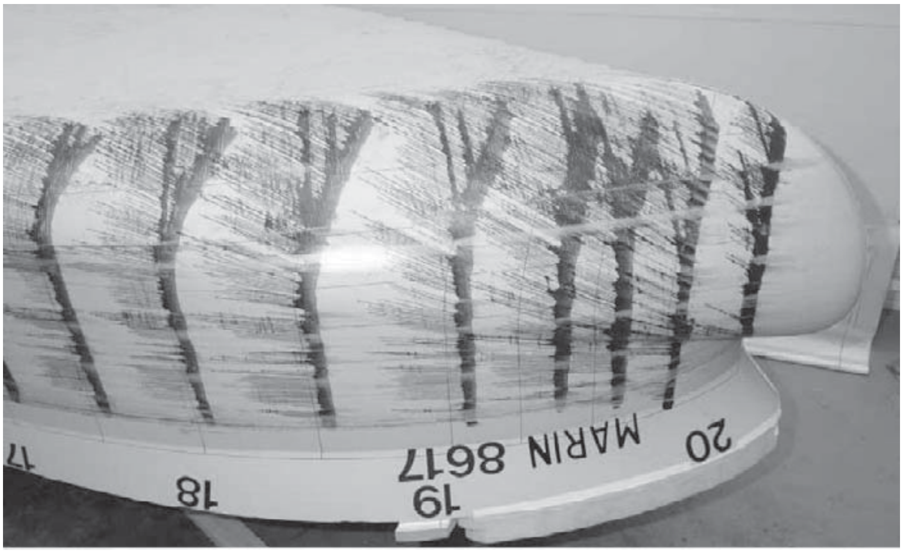

Figure 8.10 Paint test on the forebody of a ship model.

resistance directly. Although, in the 1960s, much work was done on wave pattern analysis (Eggers, Sharma, & Ward, 1967) with the hope to use the resulting wave resistance directly to improve extrapolation methods, this seems to be hardly used in practice today.

Such measurements can provide longitudinal cuts at a minimum distance of half the beam of the model, and alternative techniques are needed to measure wave elevations in the path of the vessel (e.g., aft of the stern). Finger probes mounted to a subcarriage running along a rail attached to the carriage, photographs taken of the water surface illuminated by a laser sheet, or stereo photography from the ceiling of the towing tank building have been used.

Simpler but less meaningful is a determination of the wave profile along the hull. Although the flexible wave gauge strips could be used for this, a steady wave profile is usually just determined by taking a photograph of the model and measuring the wave profile relative to a grid of waterlines and sections painted on the model surface.

9

Numerical Prediction of Resistance and Flow Around the Hull

9.1 Introduction. After having considered the main physical phenomena in the flow around a ship hull in steady motion in still water in Sections 5 and 6, and after having discussed experimental techniques in Section 8, we shall now consider the principal techniques used to predict flow and resistance by purely theoretical means.

Theoretical predictions of resistance and flow play an important role in ship design today. Since about 1980, a revolutionary growth of the possibilities for theoretical prediction and optimization of ship performance has taken place. Major contributing factors to this have been the availability of fast computers, the development of improved numerical techniques, growing insight in an adequate modeling of the principal phenomena, and the development of specialized computation methods for ship hydrodynamic problems.

Today computations of wave pattern and wave resistance are routinely used in ship hull form design, not just by specialized ship hydrodynamic institutes but also by many shipyards. Such computations have given increased insight in favorable hull form characteristics and have reduced the need for extensive model testing because much of the hull form refinement is done in a computational preoptimization. Also viscous flow computations play an increasing role in practical ship design and a more routine use is developing. In principle, these techniques can bring a level of completeness of the analysis and refinement of the hull form design that in several respects is higher than what a towing tank can offer; on the other hand, ship performance predictions based on CFD do not yet reach the same level of accuracy as model tests.

Consequently, a consideration of theoretical predictions of resistance and flow is indispensable in this book; even though it should be noted that a fast development is taking place and some of the assessments of capabilities

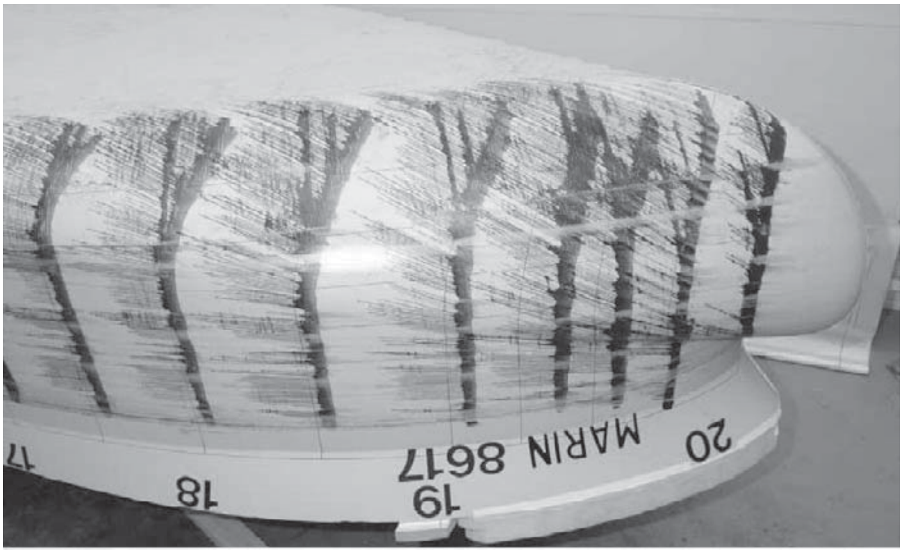

Figure 8.10 Paint test on the forebody of a ship model.

resistance directly. Although, in the 1960s, much work was done on wave pattern analysis (Eggers, Sharma, & Ward, 1967) with the hope to use the resulting wave resistance directly to improve extrapolation methods, this seems to be hardly used in practice today.

Such measurements can provide longitudinal cuts at a minimum distance of half the beam of the model, and alternative techniques are needed to measure wave elevations in the path of the vessel (e.g., aft of the stern). Finger probes mounted to a subcarriage running along a rail attached to the carriage, photographs taken of the water surface illuminated by a laser sheet, or stereo photography from the ceiling of the towing tank building have been used.

Simpler but less meaningful is a determination of the wave profile along the hull. Although the flexible wave gauge strips could be used for this, a steady wave profile is usually just determined by taking a photograph of the model and measuring the wave profile relative to a grid of waterlines and sections painted on the model surface.

9

Numerical Prediction of Resistance and Flow Around the Hull

9.1 Introduction. After having considered the main physical phenomena in the flow around a ship hull in steady motion in still water in Sections 5 and 6, and after having discussed experimental techniques in Section 8, we shall now consider the principal techniques used to predict flow and resistance by purely theoretical means.

Theoretical predictions of resistance and flow play an important role in ship design today. Since about 1980, a revolutionary growth of the possibilities for theoretical prediction and optimization of ship performance has taken place. Major contributing factors to this have been the availability of fast computers, the development of improved numerical techniques, growing insight in an adequate modeling of the principal phenomena, and the development of specialized computation methods for ship hydrodynamic problems.

Today computations of wave pattern and wave resistance are routinely used in ship hull form design, not just by specialized ship hydrodynamic institutes but also by many shipyards. Such computations have given increased insight in favorable hull form characteristics and have reduced the need for extensive model testing because much of the hull form refinement is done in a computational preoptimization. Also viscous flow computations play an increasing role in practical ship design and a more routine use is developing. In principle, these techniques can bring a level of completeness of the analysis and refinement of the hull form design that in several respects is higher than what a towing tank can offer; on the other hand, ship performance predictions based on CFD do not yet reach the same level of accuracy as model tests.

Consequently, a consideration of theoretical predictions of resistance and flow is indispensable in this book; even though it should be noted that a fast development is taking place and some of the assessments of capabilities and practical use may need to be adjusted over time. We start our discussion by considering the general approach used to develop a method to compute fluid flow phenomena and the approximations made in this. This is followed by a brief discussion of the general process to establish the adequacy of a computational method. Then we shall review and explain the main classes of computational methods and their possibilities.

9.2 Sources of Error in Numerical Methods. In general it is important to be aware of the steps taken in developing a numerical method to predict a physical phenomenon and the approximations made in the process. An understanding of these approximations allows an assessment of the value of a numerical prediction and judgement of the validity of a method.

Fig. 9.1 shows in principle how the physical reality is modeled when carrying out computations using a computer code in science and engineering. The first step in the development is to establish a *conceptual model*. Here, the problem is specified, principal physical phenomena are identified, and effects that may be assumed less important are sorted out. For instance, it is often assumed that the flow around the above-water part of a ship is unimportant for the water flow, a very good approximation in most cases.

Having formed a conceptual model, this is translated into a *continuous mathematical model*. In physics, this model often contains a set of differential or integral equations. For these to be solvable with reasonable effort, various approximations of the full model are often introduced. Examples are linearizations or introduction of empirical data, such as in turbulence models.

To be able to solve the continuous equations numerically, they have to be discretized. Derivatives are replaced by differences, integrals by sums, etc. Various numerical methods are used, such as finite-difference methods, finite-volume methods, finite-element methods, boundary element methods. The discretization means an approximation of the actual values and thus introduces *discretization errors*.

There may be other steps introducing errors, such as choosing a finite domain size for an effectively unbounded flow problem and imposing far-field boundary conditions at the outer boundaries.

The discretized mathematical model needs to be solved by numerical algorithms. Most numerical methods for technical computations use some kind of iterative approach to reach a solution, either because a direct solution is not possible because of nonlinearities in the equations, or because an iterative solution is faster. If the iterative solution converges, the difference between two successive iterations becomes smaller and smaller and the equations more and more precise. Once a given *convergence criterion* is met, the iterative procedure is terminated and the solution is supposed to have been reached. However, because of imperfect convergence, it still contains *convergence errors*.

Finally, *roundoff errors* caused by the internal representation of numbers in the computer may affect the result. For certain problems, these round-off errors can accumulate and can affect the results more seriously than one might expect, therefore double precision is often recommended.

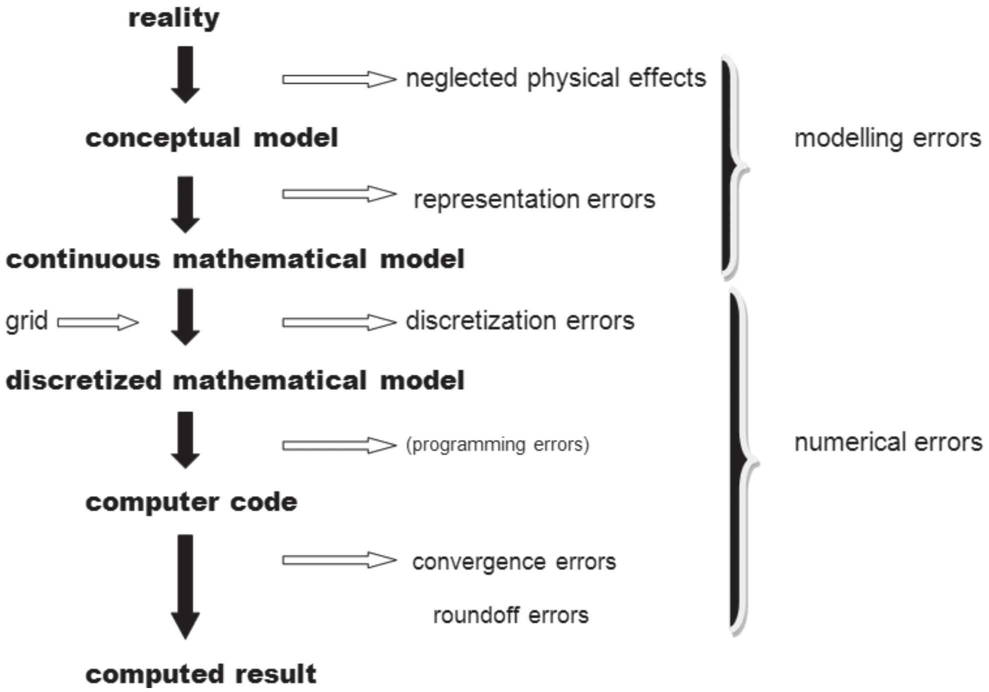

Figure 9.1 Sources of errors in computed results.

We have left out of account programming errors here, considering that these are supposed to have been removed prior to any error quantification or validation, otherwise leading to unpredictable results. Careful code verification, for which techniques have been proposed, can help detect such mistakes.

Clearly there are several sources of errors that may affect the computed results. A common distinction is between *numerical errors* (discretization errors, convergence errors, roundoff errors) and *modeling errors* (due to approximations in the conceptual and continuous mathematical model). In addition there can be errors due to a finite computational domain size, less adequate far-field boundary conditions, etc. These can either be classified as modeling errors or as belonging to a different category, *input parameter errors*. Different error taxonomies have been proposed and are discussed in Roache (2009). Whatever the classification, a good understanding of the possible error sources and a good control of their magnitude are essential for achieving a sound computational result and assessing its validity. Some of the errors are the responsibility of a code developer, some of the code user, and some errors depend on both developer and user. In particular, the discretization errors and convergence errors can be rather variable in practice and cause that experienced users can often achieve better results with a given method.

Discretization errors depend on the type of numerical scheme used and on the discretization spacing, the step length between two successive discretization points. For a sound numerical method, the effect of the discretization errors on the result must vanish when the step size is reduced so the numerical solution must approach the solution of the continuous problem. In other words, on refinement of the grid, the result should *converge* toward a *grid-independent* result.

How fast the numerical solution approaches the continuous one when the step size is reduced theoretically depends on the order of accuracy of the method: In a first order method the error is proportional to the step size, in a second order method it is proportional to the step size squared, etc. In practice, however, for complicated problems on realistic grids, the actual behavior can be different and the theoretical order of the error might only be found on impractically dense grids. First-order discretization methods tend to make the numerical method more stable; however, they are too inaccurate in many cases. The order of accuracy is therefore often a compromise between stability and accuracy of the solution. In many commercial CFD codes, stability is prioritized at the expense of accuracy and the user should be aware of this.

The user of a code may have options available to select a type of discretization, but in any case he or she has the responsibility to keep the discretization errors at a low level by selecting a sufficiently dense grid with a good quality. What is considered good quality depends on the problem and the code, but it includes aspects like small deviation from orthogonality, limited cell aspect ratio, smooth distribution of cell sizes, refinement in regions of high gradients, alignment of grid lines with flow directions, etc.

The level of iterative convergence reached is also a responsibility of the person making a computation. Different criteria can be used to judge convergence. The difference in the solution between two successive iterations is one possibility, but this criterion is dangerous because small differences may occur also due to slow or stagnating convergence. A convergence criterion based on the residuals (i.e., the difference between the left- and right-hand side of the discretized equations when the solution is substituted) is usually better. Iterative convergence can be determined as some kind of average over all grid points (e.g., an *L2*–norm) or as the maximum absolute values occurring anywhere. It is not possible to say in general what level of convergence is required for accurate results, as this depends on many details. Monitoring an integral value only and stopping the computation whenever this does not change anymore, without considering other flow properties, is a dangerous practice.

9.3 Verification and Validation. As described, different classes of errors are introduced in a computational method. Therefore, it is not evident that the result of a computation will agree with physical reality, and careful testing of the quality of a method is necessary to ascertain this.

One might suppose that the best way to do this is to simply compare the result of a computation with an experimental result. However, if the comparison is favorable, that might be due to a fortuitous canceling of modeling errors and numerical errors for the particular case considered. But these errors in general follow entirely different rules, and for another case the modeling and numerical errors might add up rather than cancel. Therefore, without further information, that favorable conclusion cannot be generalized to other cases. To have any certainty on the quality of a computational method, we must have a good idea of the *separate* effects of modeling errors and numerical errors.

The proper approach in most cases is therefore, first to determine the numerical errors. As stated previously, provided the iterative convergence errors have been made negligible, these errors should ultimately vanish when the discretization is refined. If we make successive grid refinements until we obtain a grid-independent result (which is not always feasible, see below), we thus obtain the actual solution of the continuous mathematical model. A solution on a coarser grid can be compared with that fine-grid solution, so we can determine what is the effect of numerical errors on that coarse grid. This first step is called solution *verification*. Verification thus means checking that the solution accurately agrees with that of the continuous mathematical model. Experimental results play no role in this stage; it is a purely numerical exercise. (It is noted that verification can also address the effects of finite domain size and perhaps other artificial parameters used in the computation, by systematically varying these.)

Having done the verification, the next step is *validation*. The computed results have to be validated against data in which one has more confidence, usually experimental data. Here the (ideally) grid-independent result is compared with experimental data. Any disagreement must now be a shortcoming of the continuous mathematical model. Carrying out this verification and validation process for more cases, we learn about the validity of the mathematical model, which permits us to increase our understanding or improve the model, and we find out what is the required discretization to control the numerical errors.

In practice a true grid-independent result may not be achievable, and we may have to live with the numerical uncertainty resulting from the discretization errors that have been estimated in the verification phase. Also the experimental data will contain an experimental uncertainty. In comparing the computed results for a given discretization with experimental data, we need to take into account both uncertainty bands and may need to be more cautious in stating the validity of the method considered. A standard procedure for doing this is described in American Society of Mechanical Engineers (2008). In any case, only by making both the verification and the validation step can we come to sound conclusions on the applicability of a computational method and largely rule out false conclusions based on fortuitous error cancellation.

The process to estimate the numerical errors is known as *CFD uncertainty analysis*, and it has been a hot topic in hydrodynamics over the past 10 years. The main problem with the procedure described is how to quantify the numerical uncertainty based on results on different grids, if a true grid-independent result cannot be achieved. Several verification procedures have therefore been proposed (e.g., Eça & Hoekstra, 2006; Roache, 1998; Stern et al., 2001) and workshops have been held to test various methods (e.g. Eça and Hoekstra, 2008a). Roache (2009) is a recent, comprehensive book on the subject of verification and validation.

However, the main point to be made here is that any comparison of a computed result with experimental data can only demonstrate a method's applicability if a solid indication of the effect of discretization errors on the computed result is available.

9.4 Separation of Physical Phenomena—The Zonal Approach. After these general words on numerical methods, we shall start considering the conceptual model for the flows of interest. Fig. 9.2 sketches the situation we are addressing. As before, we consider the flow around a ship moving with constant velocity on a straight course in still water, described in a coordinate system

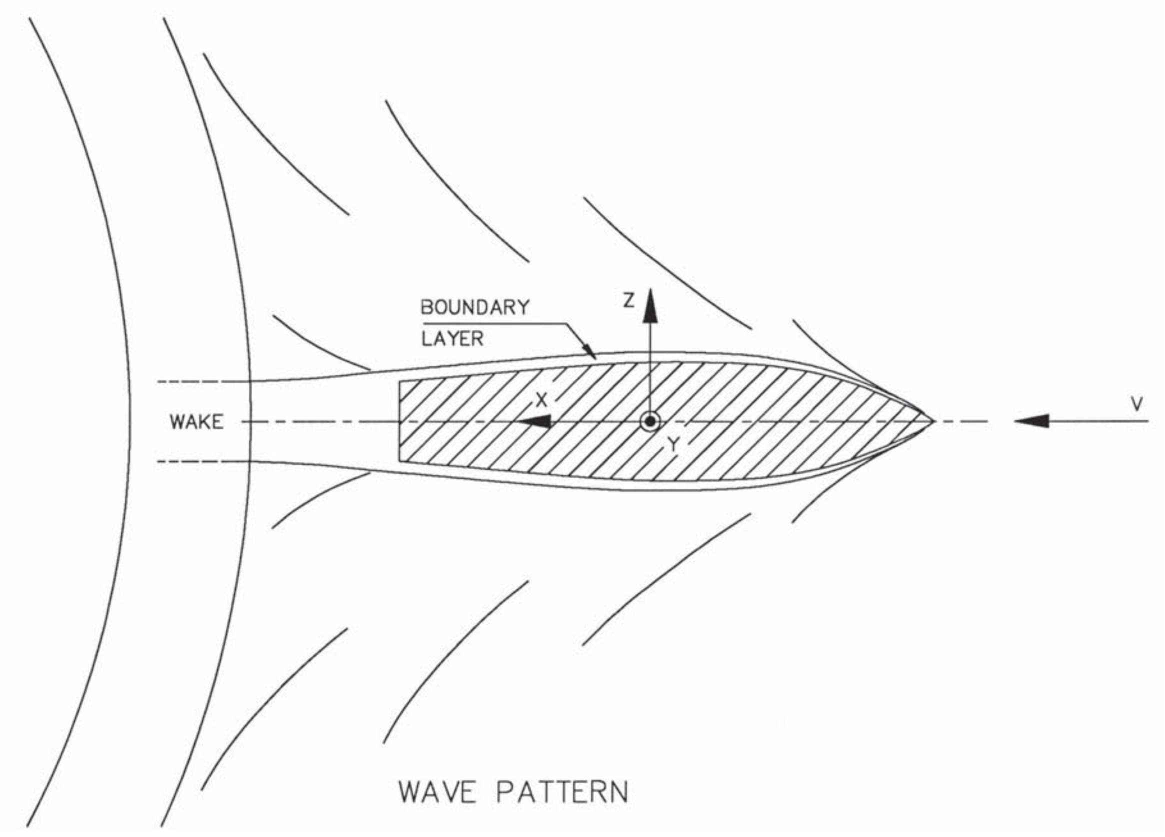

Figure 9.2 The flow phenomena to be modeled.

fixed to the hull. In this system, there is a uniform incoming flow with velocity U_∞ from ahead, and the flow field is (assumed to be) steady, at least in an average sense (not considering the time-dependent turbulent motion).

In this situation, the two main physical phenomena that have been considered in Sections 5 and 6 occur simultaneously:

- The generation of a wave pattern, which extends to large distances from the hull
- A viscous flow in a region quite close to the hull, with a turbulent, vortical motion, extending aft into a wake field.

(In addition, wave breaking and spray may occur, but these will here be disregarded because their impact is usually limited and satisfactory computational methods for these phenomena are lacking.) As in the physical considerations and in model testing, in setting up computational methods we shall have to answer the question of how to deal with these different but simultaneous phenomena.

The appropriate mathematical model for viscous fluid flows in the regimes of interest consists of the continuity and Navier-Stokes equations derived in Section 2. Together with suitable boundary conditions on the hull and on the water surface these adequately describe the viscous flow field and the wave pattern generated by the ship. The practical impossibility to solve these equations for a ship flow is discussed in Section 9.7.1, and as shown there a more feasible problem is defined by the Reynolds-Averaged Navier-Stokes (RANS) equations, which are obtained by time-averaging. To solve this mathematical model for the flow around the hull with free surface, one could discretize the equations on a 3D grid surrounding the hull and fitted to (or extending through) the wavy water surface; and make small time steps for the transient form of the equations, updating the wave surface until a steady state solution is reached. A flow-field prediction is thus obtained that incorporates the wave pattern, the viscous flow around the hull and in the wake, and all interactions between both.

Although, today, several methods exist that do solve the complete viscous free-surface flow problem (see Section 9.8), this was unusual until about 1995. Part of the difficulty of this problem comes from combining phenomena with quite disparate spatial and temporal scales in a single mathematical model. The boundary layer is relatively thin, has large velocity gradients, and small-scale structures are important for the flow behavior, so in any viscous flow computation a very dense distribution of points (a dense grid) is needed in order to resolve the small-scale phenomena. But the wave making is a large-scale process, with wave lengths comparable to the ship length and a rather slow adjustment in time. Therefore, the dense grid should also cover a larger region to include the relevant wave pattern, and the time stepping must continue over a longer period until all transient wave phenomena have died out. Thus methods for computing viscous flow with free surface are usually much more time-consuming than other viscous-flow computations, and definitely much less practical than the methods to be described in Section 9.6.

A reasonable simplification, and until around 2003 the only practical approach for predicting the flow field around a ship, is a separation of the two different physical aspects. In Section 5.1 we have motivated that the main phenomena contributing to the resistance, viz. the wave making and the viscous flow, to a large extent can be regarded as independent. This assumption can be founded in boundary layer theory, which states that the pressure field around a body is only slightly affected by the presence of a boundary layer, and it is consistent with the principle underlying ship model testing and resistance extrapolation. A similar decomposition is often made in computational methods:

- The wave generation is considered as an inviscid process in the whole domain around the ship.
- The viscous flow is considered as unaffected by wave making and occurring in a relatively narrow region around the hull and in a wake.

The separate treatment of the viscous flow and the wave making simplifies the methods and makes the computation more efficient and more practical; in particular for the wave making which can then be calculated with a much coarser discretization and (as will appear) simpler methods. Obviously, viscous effects on the wave making, and wave effects on the viscous flow, do occur in reality (see Section 5.7), but they are considered as "interaction effects" of secondary importance.

Correspondingly, this section will be set up as follows. Section 9.5 describes the prediction of inviscid flow around arbitrary closed bodies. Section 9.6 considers the prediction of wave pattern and wave resistance based on the assumption of inviscid flow. Section 9.7 considers the computation of the viscous flow around the hull, in which the wave making is left out of account. Section 9.8 reviews methods in which the wave making and the viscous flow are combined in a single computational model.

9.5 Prediction of Inviscid Flow Around a Body

9.5.1 Introduction. In this subsection, we introduce and discuss some methods to compute inviscid flow around a body. We limit ourselves here to nonlifting bodies in an unbounded domain, without a free surface.

In Section 5.2.1 it was described how, from the assumption of inviscid flow, the mathematical model of the flow could be substantially simplified. We recall some of the main steps taken:

- For inviscid, irrotational flow, the velocity field can be represented by the gradient of a scalar velocity potential: $\vec{v} = \nabla\phi$
- For incompressible flow, this potential must satisfy the Laplace equation

$$\frac{\partial^2\phi}{\partial x^2} + \frac{\partial^2\phi}{\partial y^2} + \frac{\partial^2\phi}{\partial z^2} = 0 \qquad (9.1)$$

- The pressure follows from the Bernoulli equation

$$\frac{1}{2}\nabla\phi \cdot \nabla\phi + \frac{p}{\rho} + gz = \text{constant} \tag{9.2}$$

where the constant is equal in the entire flow field.

- The Laplace equation is linear and homogeneous, so it admits superposition of solutions for ϕ and $\vec{v}$ (but not for p)

As pointed out in Section 5.2, the original set of four coupled equations has thus been reduced to a single equation for the potential and an equation for the pressure. Because the pressure does not occur in the Laplace equation, the potential field can be computed first, and then the pressure can be determined afterwards from equation (9.2). The main task in computing a potential flow is therefore finding a solution of the Laplace equation in the fluid domain, satisfying the boundary conditions imposed.

The main classes of methods to do this are Boundary Integral Methods or Panel Methods. Here, we shall first give a simple explanation of their principle, followed by a more formal and general derivation for flow around a nonlifting body in an unbounded domain.

9.5.2 Use of Singularities. As in the consideration of ship wave patterns in Section 5, we exploit the linearity of the Laplace equation to compose the solution of the potential flow problem from a superposition of elementary potential flows. We shall select the superposition in such a way as to obtain the desired flow field: one representing flow around a solid body.

As elementary potential flows, we first consider the flow fields induced by so-called singularities: sources, vortices, and dipoles.

- A *source* is a point from which fluid emerges at a rate Q and spreads evenly in all directions. The potential and velocity field induced in point $\vec{x}$ by a source at the point $\vec{x}_0$, in a 3D space, are

$$\phi(\vec{x}) = -\frac{Q}{4\pi R} \qquad v_R(\vec{x}) = \frac{Q}{4\pi R^2} \tag{9.3}$$

in which $R = |\vec{x} - \vec{x}_0|$ and v_R is the velocity in radial direction away from the source. The radial velocity falls off inversely with the square of the distance from the source, such that a constant flow rate Q passes through each sphere centered at the source point. A negative source, which absorbs fluid that streams toward it from all sides, is called a *sink*.

- A *dipole* is a pair of a source and a sink of equal strength, in the limit of their strength tending to infinity and their distance vanishing, such that the product of distance and strength (the dipole moment $\vec{m}$ pointing from sink to source) is constant. The potential and velocity field are given by

$$\phi(\vec{x}) = -\frac{\vec{m}\cdot(\vec{x}-\vec{x}_0)}{4\pi R^3}$$

$$\vec{v}(\vec{x}) = -\frac{\vec{m}}{4\pi R^3} + \frac{3\vec{m}\cdot(\vec{x}-\vec{x}_0)}{4\pi R^5}\cdot(\vec{x}-\vec{x}_0) \tag{9.4}$$

- A *vortex* is an isolated line in a 3D field (or a point in 2D) around which the flow circulates. For an infinite straight line vortex, the velocity decreases proportionally with the inverse distance from the vortex. In general, the induced velocity field in 3D is given by the Biot-Savart law:

$$\vec{v}(\vec{x}) = \frac{\Gamma}{4\pi}\int \frac{\vec{ds}\times\vec{R}}{R^3} \tag{9.5}$$

where the integral is along the length of the (possibly curved) vortex.

It can be checked that, regardless of the position $\vec{x}_0$, each of these potentials satisfies the Laplace equation, except at $\vec{x} = \vec{x}_0$, the location of the singularity itself, where the velocity is infinite and its direction indeterminate.

As a first illustration of the use of singularities in constructing potential flows, let us consider a uniform flow which meets a single source of strength Q. The velocity field is the superposition of the uniform flow and the source-induced flow:

$$\vec{v} = \vec{U}_\infty + \frac{Q}{4\pi R^3}\cdot(\vec{x}-\vec{x}_0) \tag{9.6}$$

and because both satisfy the Laplace equation, that is also the case for the composed field which is, therefore, an incompressible potential flow. Fig. 9.3 shows the streamline pattern found from equation (9.6). The incoming flow from the right is retarded and deflected on approaching the source point. There is a stagnation point on the x-axis (at a distance $\sqrt{Q/(4\pi U_\infty)}$ upstream of the source) where the velocity vanishes as the two

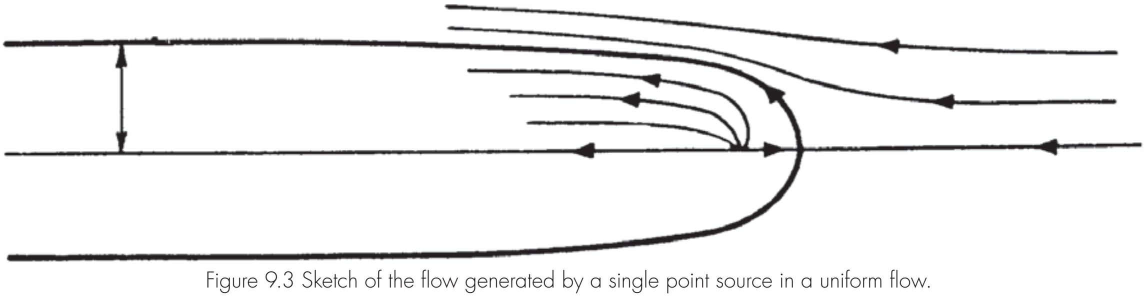

Figure 9.3 Sketch of the flow generated by a single point source in a uniform flow.

contributions from uniform flow and source flow cancel. It can be observed that the streamlines coming from the stagnation point form a stream surface that separates the flow originating from the source and the flow coming from infinity.

If we superimpose more source flows, we can construct other flow fields. For example, if we add a sink $-Q$ at a point on the x-axis downstream of the source, the fluid emerging from the source is absorbed by the sink, and the stream surface coming from the forward stagnation point closes again in a rear stagnation point, making the streamline pattern fore-and-aft symmetric. (In the limiting case, a dipole in a uniform flow generates a spherical stream surface.)

There is now a single closed stream surface in the flow. The flow originating from upstream never crosses that surface, just as it would never cross a solid body, and actually the potential flow field outside the stream surface is identical to that around a body with the shape of that stream surface. (On the other hand, the flow inside the stream surface is meaningless in the context of flow around a body.) We can thus determine the inviscid flow around such a body from a sum of simple source potentials.

A variety of axisymmetric bodies can thus be "generated" using an arrangement of sources and sinks on the axis. Other 3D bodies can be generated using spatial arrangements of singularities. However, usually we want to compute the flow around a given body, rather than determining the body corresponding with a given source distribution. It then appears that a small number of point sources cannot always generate the desired shape. A generalization is necessary to make it work in practice.

9.5.3 Panel Methods. This generalization is a *source distribution* (or similarly, a dipole or vortex distribution). The flow now does not emerge from a single point, but from a surface—for which usually the surface of the body itself is chosen. This surface has a *source density* σ (flow rate per unit of surface area) which may vary from point to point. The potential and velocity fields induced by a source distribution on a surface S in a uniform inflow are a generalization of those induced by a point source

$$\phi(\vec{x}) = U_\infty \cdot x - \frac{1}{4\pi}\iint_S \frac{\sigma(\vec{\xi})}{R}\,dS$$

$$\vec{v}(\vec{x}) = \vec{U}_\infty + \iint_S \frac{\sigma(\vec{\xi})}{4\pi R^3}\cdot(\vec{x} - \vec{\xi})dS \tag{9.7}$$

in which $R = \left|\vec{x} - \vec{\xi}\right|$. Similarly, dipole and vortex distributions can be used, but these will not be specifically addressed here.

For using these expressions in a numerical solution method, they are discretized. Conventionally, the surface on which the source distribution is located is subdivided in *source panels*, usually triangular or quadrilateral, which together approximate the surface S. Each of them carries a source density with a certain distribution. The simplest (and most popular) panels are quadrilaterals having a constant source density. Like a point source, each panel induces a potential and velocity field in the entire space. These simple quadrilateral source panels were used in the method of Hess and Smith (1962), probably the first practical method to compute inviscid flow over an arbitrary body.

Spreading out a point source over a panel has an important advantage: whereas the velocity near a point source tends to infinity, near a source distribution it tends to a constant velocity $\sigma/2$, normal to both sides of the surface; so there is a jump in the normal velocity of magnitude σ. Whereas point sources should not be put at the boundary of a flow domain, source distributions can. On the other hand, at larger distances the induced velocity field of a source panel approaches that of a point source with equal total strength $\sigma \cdot A$ (i.e., radially outward from the panel with a velocity inversely proportional to the square of the distance). The potential field induced by a source panel located anywhere in the domain satisfies the Laplace equation everywhere except at the panel itself; the same therefore goes for the potential field induced by any arbitrary combination of source panels.

Suppose we want to compute the potential flow around a given closed body in an infinite fluid domain, in an inflow with velocity U_∞. The following steps (illustrated in Fig. 9.4) are then taken.

First we subdivide the surface of the body in N source panels. The geometric properties of the panels are thereby fixed. Each panel j is here supposed to have a uniform source density σ_j. The induced potential and velocity can be found from equation (9.7), where S now is the entire paneled area. This then takes the form

$$\begin{aligned}\vec{v}(\vec{x}) &= \vec{U}_\infty + \sum_{j=1}^{N}\sigma_j \iint_{Sj} \frac{(\vec{x}-\vec{\xi})}{4\pi R^3}\cdot dS \\ &= \vec{U}_\infty + \sum_{j=1}^{N}\sigma_j \cdot V_j(\vec{x})\end{aligned} \tag{9.8}$$

therefore a summation of the uniform inflow and contributions from all panels; each consisting of the product of the actual source density of the panel and the induced velocity of the panel if it would have a unit source density. These panel inductions V_j depend only on the panel geometry and the position of the point $\vec{x}$ relative to the panel center.

For flat panels with constant source density, and several more complicated ones, analytical expressions are known for the induced potential and velocity field in terms of basic geometric properties of the panel.

The panel source densities σ_j are then the only unknowns in the problem. These must be selected so as to satisfy the boundary conditions. For flow around a body we require again that a closed stream surface coincides with the body surface; so in all points of the body surface, the velocity component normal to the body must be zero

$$\vec{v}\cdot\vec{n} = \frac{\partial\phi}{\partial n} = 0$$

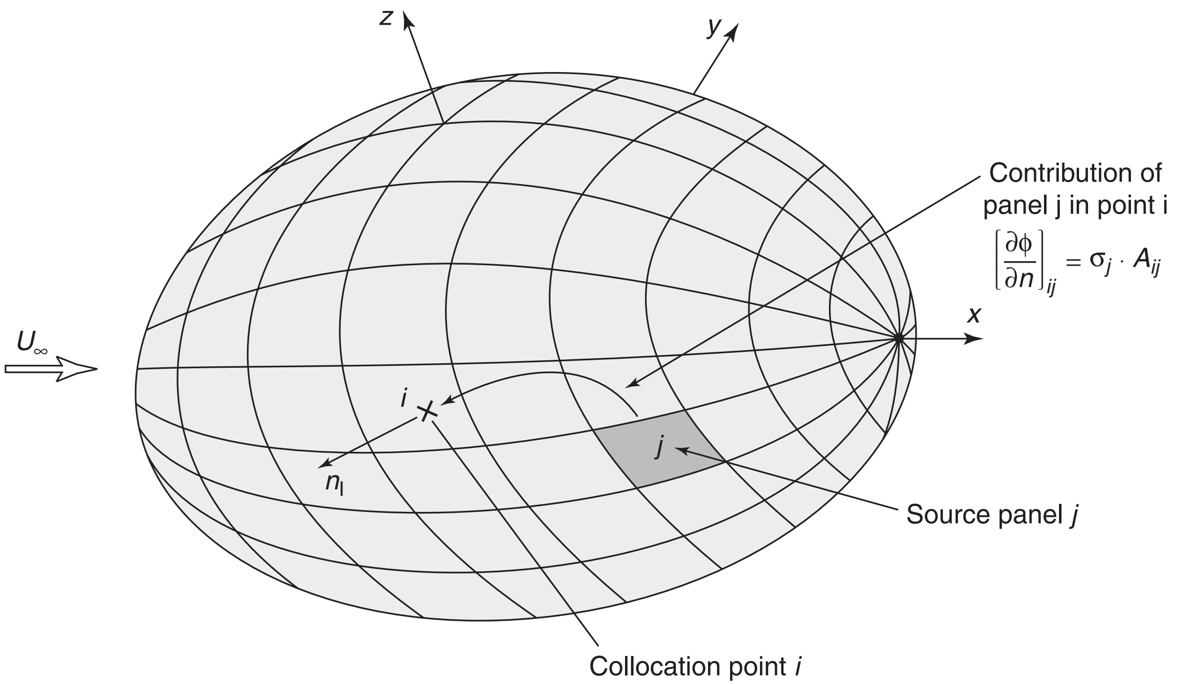

Figure 9.4 A panel method for flow around a closed body.

In a numerical method this condition can only be imposed in a somewhat approximate form. A usual way is to impose it in a discrete set of *collocation points*, rather than all over the surface. On each panel we choose one particular collocation point (usually the panel center). We demand that the normal component of the velocity vanishes, which from equation (9.8) yields the expression

$$\sum_{j=1}^{N} \sigma_j \cdot \vec{n}_i \cdot \vec{V}_j\,(\vec{x}_i) = -\vec{U}_\infty \cdot \vec{n}_i \tag{9.9}$$

This equation, written out for all *N* collocation points, has the form

$$\sum_{j=1}^{N} A_{ij} \cdot \sigma_j = RHS \qquad i = 1,N \tag{9.10}$$

in which the matrix elements A_{ij} are the "influence coefficients," in this case the contribution to the normal velocity in collocation point i, of the velocity field induced by a unit source density on panel *j*. These coefficients can be easily derived from the analytical expressions for V_j mentioned previously.

The boundary conditions imposed at all *N* collocation points thus form a closed set of *N* algebraic equations with *N* unknowns. Because each condition contains all *N* source strengths, the matrix *A* is full. Solving this system of equations yields the source strengths σ_j. With these, we can compute the velocity at every desired point in the flow by evaluating the expression (9.7), and we have got the potential flow around the given body. Using Bernoulli's equation, we can find the pressure.

The explanation given here applies to the method of Hess and Smith (1962), which is widely used and fairly accurate. However, there are other ways of casting the boundary value problem for the Laplace equation into the form of a boundary integral equation (Hess, 1990; Hunt, 1980). The principle of panel methods will now be derived more formally, in order to provide a more general framework. This piece of theory could be skipped by those just interested in the overall ideas.

9.5.4 General Derivation of Panel Methods. Suppose we have an internal fluid domain Ω_I within a closed boundary *S* (Fig. 9.5). Green's second identity then states that, for two arbitrary, C^2−continuous functions ϕ_I and *G*

$$\iiint_{\Omega_I} [\phi_I \nabla^2 G - G \nabla^2 \phi_I]\, d\Omega$$
$$= \iint_S \left[\frac{\partial \phi_I}{\partial n} \cdot G - \phi_I \cdot \frac{\partial G}{\partial n}\right] dS \tag{9.11}$$

in which ∇^2 is the Laplace operator and *n* is a direction normal to *S* into the fluid domain. For *G* we take the *Green's function*

$$G\left(\vec{\xi}; \vec{x}\right) \equiv -\frac{1}{4\pi \left|\vec{x} - \vec{\xi}\right|}$$

in which $\vec{x}$ is a fixed point and $\vec{\xi}$ is the variable point in the integration. For ϕ_I we take a potential in the internal domain that satisfies the Laplace equation. So both $\nabla^2 \phi_I = 0$ and $\nabla^2 G = 0$, with the exception of the singular point of *G* at $\vec{x} = \vec{\xi}$. We except this point from the domain

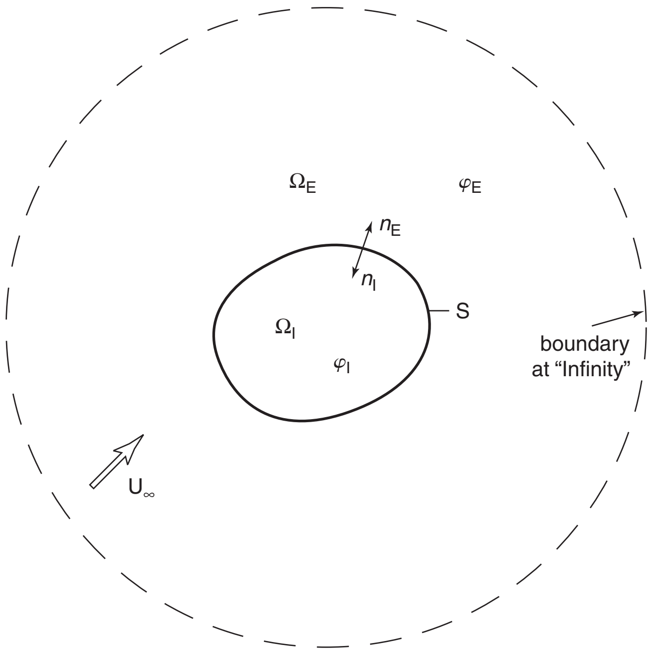

Figure 9.5 Definition sketch for derivation of panel method.

Ω_I by adding a sphere of vanishing radius around it and carrying out the surface integration also over the sphere. This produces an expression for the potential as an integral over the domain boundary only

$$T \cdot \phi_I(\vec{x}) = \iint_S \left[\frac{\partial \phi_I(\vec{\xi})}{\partial n} \cdot G(\vec{\xi};\vec{x}) - \phi_I(\vec{\xi}) \cdot \frac{\partial G(\vec{\xi};\vec{x})}{\partial n} \right] dS \quad (9.12)$$

and a corresponding equation for $\nabla \phi_I$. The integral is to be taken in a principal value sense. The left-hand side originates from the integration over the small sphere, and T is the fraction of the sphere that is inside the domain Ω_I: for points $\vec{x}$ in the interior of the domain $T = 1$, for points on a smooth part of the boundary $T = 1/2$, and for points outside the domain $T = 0$.

However, in the applications considered in this section we have to deal with a fluid domain Ω_E *external* to a (supposedly nonlifting) body. We first add a spherical outer boundary surrounding the body at an "infinite" distance (see Fig. 9.5), and apply the same expressions to the "internal" domain enclosed between the body and the far boundary. This results in an expression identical to equation (9.12) but with the integral running over the body and over the far boundary. In the limit of infinite radius of the far boundary, the latter contributes just the undisturbed potential $\phi_\infty = U_\infty \cdot x$, which would prevail in the absence of the body. The resulting boundary integral expression for the potential ϕ_E in the external domain is then

$$T \cdot \phi_E(\vec{x}) = \phi_\infty + \iint_S \left[\frac{\partial \phi_E(\vec{\xi})}{\partial n} \cdot G(\vec{\xi};\vec{x}) - \phi_E(\vec{\xi}) \cdot \frac{\partial G(\vec{\xi};\vec{x})}{\partial n} \right] dS \quad (9.13)$$

This expression in itself is a useful basis for a Boundary Integral Method. For points on a smooth part of the boundary ($T = 1/2$), it expresses the potential on the boundary as an integral over the boundary; the integrand containing the potential and its normal derivative. For example, in case Neumann boundary conditions are given prescribing $\partial\phi/\partial n$ all over the boundary, the first term in the integrand is known and we have obtained an integral equation involving only the unknown potential on the boundary. After discretization this is easily transformed to a set of algebraic equations for the potential in collocation points on the boundary. This class of methods, in which the original integral equation is used without any assumption on the potential field inside the body, is often called *Green's identity methods*.

The source-only method described in simple terms in Section 9.5.3 is derived more formally by adding the expressions (9.12) and (9.13), taking into account the change of sign due to the opposite orientation of the inward normals, and the different definition of T. This yields

$$T \cdot \phi_E + (1 - T)\phi_I = \phi_\infty + \iint_S \left[\left(\frac{\partial \phi_E}{\partial n} - \frac{\partial \phi_I}{\partial n} \right) \cdot G(\vec{\xi};\vec{x}) - (\phi_E - \phi_1) \cdot \frac{\partial G}{\partial n} \right] dS \quad (9.14)$$

and a similar expression for the velocity field. Here n now is the outward normal direction on the body surface, and T is the coefficient relevant for the outer domain.

This expression in itself cannot be used for determining the external potential yet. However, for a surface source distribution as used in the previous section, we have already mentioned the result that there is a discontinuity in the normal velocity across the surface

$$\frac{\partial \phi_E}{\partial n} - \frac{\partial \phi_I}{\partial n} = \sigma$$

In addition, it can be derived that the potential is continuous across a surface source distribution: $\phi_E - \phi_I = 0$. Substituting this in equation (9.14) and in a corresponding equation for the velocity field yields

$$\phi_E(\vec{x}) = \phi_\infty + \int_S \int \sigma(\vec{\xi}) G(\vec{\xi};\vec{x}) dS \quad (9.15)$$

$$\nabla\phi_E(\vec{x}) = \nabla\phi_\infty(\vec{x}) + (1 - T)\sigma(\vec{x})\vec{n} + \int_S \int \sigma(\vec{\xi}) \nabla_{\vec{x}} G(\vec{\xi};\vec{x}) dS \quad (9.16)$$

which corresponds with equation (9.7). This is a general expression valid for points inside the outer domain Ω_E ($T = 1$) or on the surface S ($T = 1/2$).

It is to be noted that the use of a source-only distribution thus implies an assumption on the internal potential ϕ_I inside the body. In this case, that potential is fixed by the Dirichlet condition $\phi_I = \phi_E$ over the entire boundary. Although ϕ_I is physically meaningless, it is important that the implied problem that defines it is well-posed; some less sound formulations lead to a nonexistent or nonunique solution for ϕ_I.

Similarly, for a distribution of normal dipoles, the normal derivative of the potential is continuous across the surface but there is a jump in the potential itself, equal to the local dipole density:

$$\frac{\partial \phi_E}{\partial n} - \frac{\partial \phi_I}{\partial n} = 0 \qquad \phi_E - \phi_I = -\mu$$

and on substitution now the other part of the integrand vanishes. The internal potential is fixed by an internal Neumann condition now.

Moreover, various mixes of source and dipole distributions can be used, provided that care is taken for the well-posedness of the implied problem for ϕ_I. The general expression valid for any mixed distribution of sources σ and normal dipoles μ is

$$\phi_E(\vec{x}) = \phi_\infty(\vec{x}) - (1-T)\mu(\vec{x}) + \iint_S \left[\sigma(\vec{\xi})G(\vec{\xi};\vec{x}) + \mu(\vec{\xi})\,\frac{\partial G(\vec{\xi};\vec{x})}{\partial n}\right] dS \qquad (9.17)$$

and a somewhat more intricate equation for the velocity field, for which we refer to Hunt (1980).

Whatever the precise singularity type used, an integral expression is thus obtained for the potential or velocity on the boundaries of the domain. The boundary conditions, which prescribe either ϕ or $\partial\phi/\partial n$ or any combination of both, are then substituted. The boundaries are discretized into panels on which certain modes of the unknowns are assumed. Writing out the discretized integral equation in collocation points leads to a set of algebraic equations for the unknowns: the potential, its normal derivative, or the source or dipole strength on the panels, depending on the formulation. After solution, all other quantities can be computed.

The framework presented here accommodates a variety of methods. For familiar types of boundary conditions, the properties of these methods are well known and discussed at length elsewhere (e.g., Hess, 1990; Hunt, 1980). The particular choice of a Green's identity method or any source and/or dipole distribution has various consequences, such as:

- Numerical accuracy: boundary conditions are only imposed at discrete points, and will in general not be precisely satisfied between those points. This "leakage" generally is minimized by choosing a singularity distribution that is as weak and smooth as possible (i.e., has limited magnitude and small gradients). Different types of problems may ask for different choices.
- Existence, uniqueness, well-posedness: some singularity distribution types, combined with certain boundary conditions, may lead to nonexistent or nonunique solutions for the singularity strength, which is to be avoided (e.g., by reformulation of the boundary conditions).
- Type of integral equation: this depends on the type of singularity and the boundary conditions. Some of the resulting integral equations, after discretization, lead to a system of equations that lends itself well to iterative solution, others do not.
- Computational effort: the number of panel-to-collocation-point inductions (a few times N^2) to be computed differs between methods. This affects computation time and storage.
- Computation of physical quantities: often the velocity distribution is needed. In methods in which the potential is the unknown that is solved for, the velocity may need to be found by finite differencing over the body surface, which can be complicated.

In addition, methods differ in the order of the discretization. For example, the singularity strengths may be assumed to be constant over each panel, or have a linear or higher-order distribution over the panels. The representation of the geometry must be of a corresponding level: flat, parabolic, or more general panel shapes. Higher-order methods are more accurate for a given number of panels or require fewer panels to reach a certain accuracy, but the expressions for the induced velocities are more complicated, so the advantage in computation time often is small.

9.5.5 Application to a Ship: Double-Body Flow. The general methods described here addressed the potential flow around closed nonlifting bodies of arbitrary form in a fluid domain of infinite extent. This may be appropriate for a submarine far beneath the water surface, but not for a surface ship, for which the flow domain is also bounded by the water surface where wave making occurs. This requires extended methods described in the next section.

However, the basic panel methods described may still be a useful approximation for surface ships in case the wave making is limited. Section 5 derived that the perturbation caused by a surface wave decays with depth under the water surface, and that the short waves occurring at low Froude numbers are confined to a region close to the surface. Below that region, the velocity field is essentially equal to that without waves. Therefore, in the limit for low Froude numbers the flow field with waves can be supposed to approach that with a flat water surface, except in a region of thickness $d/L=O(Fn^2)$ along that surface. Therefore, knowledge of the potential flow around the hull under a flat, undisturbed water surface is often practically useful.

The potential flow around the ship hull with a flat water surface could be computed using an additional panel distribution on the water surface and imposing the boundary condition $\partial\phi/\partial n = 0$ there. However, it is more accurate and efficient to represent the water surface by a symmetry plane in the calculation. As Fig. 9.6 illustrates, the flow field of interest is identical to the lower half of the flow around a double model of the underwater body, symmetrical with respect to the undisturbed waterplane. The double body is again a closed body in an infinite fluid, and the *double-body flow* can thus be computed using any of the Boundary Integral Methods described.

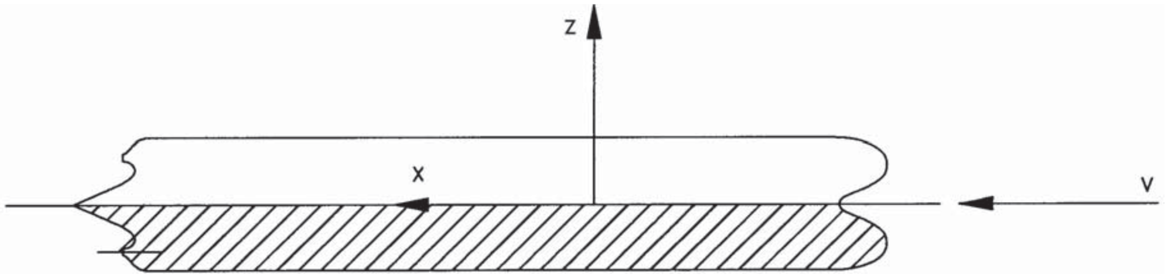

Figure 9.6 Double-body flow, representing the flow with a flat water surface.

Results of such a double-body potential flow computation already can be useful in assessing properties of the hull form, as the discussion in Section 5.2.3 and Fig. 5.5 illustrated. Specifically, the magnitude of streamline curvature along the hull, flow directions, and pressure maxima and minima can be observed. On the other hand, in the vicinity of the water surface the accuracy will be limited because of the neglect of the wave pattern. Moreover, mirroring of the underwater part of the hull introduces a sharp knuckle at the waterline for flared sections, or a narrow area between a bulbous bow and its mirror image, which locally further invalidate the double-body flow.

For all nonlifting potential flows around closed bodies in an infinite fluid, including double body flow, d'Alembert's Paradox applies: no resistance acts on the hull. To compute the wave resistance, wave pattern, and the flow around the hull including the wave-making effect, a further step is needed.

9.6 Prediction of Inviscid Flow with Free Surface

9.6.1 The Free-Surface Potential Flow Problem. We have seen how a panel method can be used to compute the flow around a body immersed in a flow without free surface, or the flow around a ship hull if the effect of the free surface is disregarded. In such a double-body flow, the pressure at the still water surface in general is not constant and not equal to the atmospheric pressure, so this cannot be a valid solution of the true problem with free surface. The pressure imbalance will cause an adjustment of the flow near the water surface, leading to surface waves radiating out and trailing downstream.

As in Section 5.4, to compute the flow with wave making we make the assumptions that the flow and wave pattern are steady in the coordinate system fixed to the hull (shown in Fig. 2.1); that viscous effects can be disregarded and a potential flow model used; and that wave breaking and spray will not be modeled. In addition, surface tension is not modeled, being of little importance for the larger-scale flow behavior.

Another assumption is that the wave surface can be described as a single-valued function of the horizontal coordinates, $z = \zeta(x, y)$; this excludes a description of overturning waves.

The problem again is described by the Laplace equation for the velocity potential φ, but some of the boundary conditions are substantially more complicated than in the preceding section:

Body Boundary Condition As in Section 9.5, this simply states that the flow passes along the hull surface:

$$\partial\phi/\partial n = 0$$

Dynamic Free-Surface Condition Because we disregard viscous stresses, surface tension, and the dynamics of the air flow above the water surface, the pressure in the water at the surface must be constant and equal to the atmospheric pressure p_a. The Bernoulli equation then yields

$$p_a + \rho g z + \frac{1}{2}\rho\,(\nabla\phi \cdot \nabla\phi) = C \text{ at } z = \zeta$$

We evaluate the constant by considering the situation far upstream, where $z = 0$ and $\nabla\phi = \vec{U}_\infty$ at the still water surface. We can then derive an expression for the wave elevation

$$\zeta = \frac{1}{2g}\left(U_\infty^2 - \nabla\phi \cdot \nabla\phi\right) \qquad (9.18)$$

The difference with the similar expression derived in Section 5.3.1 comes from the fact that now we consider a steady flow in a coordinate system moving with the ship, rather than a time-dependent flow in an earth-fixed system.

It is useful to express this in nondimensional quantities, obtained by dividing lengths by the ship length L and velocities by the ship speed U_∞, yielding

$$\overline{\zeta} = \frac{1}{2}Fn^2(1 - \nabla\overline{\phi} \cdot \nabla\overline{\phi}) \text{ at } \overline{z} = \overline{\zeta} \qquad (9.19)$$

Kinematic Free-Surface Condition The flow goes along the wave surface. As derived in Section 2, the general form is

$$w = \frac{D\zeta}{Dt}$$

If the time dependence is omitted and a velocity potential is substituted, this becomes equal to the expression derived in Section 5.3.1

$$\phi_x\frac{\partial\zeta}{\partial x} + \phi_y\frac{\partial\zeta}{\partial y} - \phi_z = 0 \text{ at } z = \zeta \qquad (9.20)$$

in which the subscripts indicate partial derivatives: $\phi_x \equiv \partial\phi/\partial x$. The nondimensional form is an identical expression in $\overline{\zeta}$, $\overline{\phi}$, etc.

Bottom Boundary Condition In most cases, the depth of the water is assumed infinite, and the associated far-field condition is

$$\phi \rightarrow U_\infty x \quad \text{or, in nondimensional form,} \quad \overline{\phi} \rightarrow \overline{x} \quad \text{for } z \rightarrow -\infty \tag{9.21}$$

Instead, for shallow water with depth h, a boundary condition is to be imposed on the bottom

$$\phi_z = 0 \text{ at } z = -h \tag{9.22}$$

Radiation Condition As to the behavior at infinity, simply requiring decay of the disturbance with distance from the body, such as in Section 2.4.3, is often not appropriate for wave-making problems. For instance, for 2D cases the trailing wave system persists downstream with constant amplitude, and the flow never returns to an unperturbed state. A (decaying) wave-like behavior must be admitted downstream, but special formulations may be needed to exclude any waves upstream of the bow, where a nonwavy disturbance decaying as

$$\phi = x + O\left(\frac{1}{\sqrt{x^2 + y^2}}\right) \text{ for } x \rightarrow -\infty \tag{9.23}$$

is present. The precise form of this "radiation condition" depends on the particular method to solve the problem.

Transom Conditions Besides these general conditions applying to all surface-piercing bodies, special conditions may be required to model the flow behavior at the edge of a transom stern (see the part on "Transom Sterns" in Section 9.6.5).

Trim and Sinkage Equilibrium Usually, the case of interest is that in which the ship changes attitude freely under the action of the hydrodynamic pressure distribution. This dynamic sinkage and trim are found from a balance between the hydrodynamic and hydrostatic pressure forces on the hull and the ship's weight distribution.

This completes the statement of the steady wave resistance problem. From here on, the overbars will be omitted and nondimensional quantities will be used.

An important alternative form of the free-surface boundary conditions is obtained by using the dynamic free-surface condition (9.19) to eliminate the wave elevation ζ from the kinematic boundary condition (9.20):

$$\frac{1}{2} Fn^2 \left(\phi_x \frac{\partial}{\partial x} + \phi_y \frac{\partial}{\partial y} + \phi_z \frac{\partial}{\partial z}\right)(\nabla\phi \cdot \nabla\phi) + \phi_z = 0 \quad \text{at } z = \zeta \tag{9.24}$$

This *combined free-surface boundary condition* can replace either the kinematic or the dynamic condition (but not both at the same time). Although it defines exactly the same problem, it has different properties in numerical solution methods.

In the previous section, the problem of potential flow around a body was solved by covering the boundaries of the flow domain with source panels, imposing the boundary condition in the panel centers, and solving the resulting system of algebraic equations. A similar approach will be applied to the free-surface potential flow problem defined now, but we shall meet additional difficulties. In the first place the free-surface conditions are nonlinear, as they contain squares and cross products of unknowns. Therefore, if the term $\nabla\phi \cdot \nabla\phi$ in the dynamic free-surface condition is expressed in the velocities induced by N panels, this leads to an expression containing $\frac{1}{2}N \cdot (N + 1)$ products $\sigma_m \cdot \sigma_n$, not to a form (9.10). Secondly, boundary conditions are to be imposed on the free surface, the shape of which is still unknown. Similarly, the free trim and sinkage of the hull make the location of the collocation points on the hull unknown. Therefore, we have to solve a "nonlinear free-surface problem," where the nonlinearity comes from the boundary conditions, not from the field equation (the Laplace equation) which is still linear.

Generally, there are two possible approaches: either the problem is simplified by linearization and the solution of the linearized problem is used, or the fully nonlinear problem is solved by an iterative procedure. Both approaches will be discussed.

9.6.2 Linearization of the Free-Surface Potential-Flow Problem. Until about 1990, it was not practically possible to solve the full nonlinear problem, and the only practical option was to solve an approximate, linearized problem. Today, linearized methods are disappearing, having been superseded by solution of the nonlinear problem, but they will be described here for completeness, historical interest, and understanding.

The principle of linearization is to replace an unknown quantity by the sum of a known estimate and an unknown perturbation. If the estimate is good, the perturbation is small, and any quadratic or higher-order terms in the perturbation can be neglected, such that only linear terms are retained.

In our problem, linearization is used to solve both the problem of the nonlinearity of the free-surface boundary conditions and the problem of the unknown location where those conditions are to be imposed. We introduce estimates for the potential field and the wave elevation

$$\nabla\phi = \nabla\Phi + \nabla\varphi' \qquad \text{and} \qquad \zeta = \mathrm{H} + \zeta'$$

in which the "base flow" $\nabla\Phi(x, y, H)$ and the approximate wave surface $H(x, y)$ must be known.

The kinematic and dynamic boundary conditions, linearized in these perturbations, then read

$$\Phi_x\zeta_x + \Phi_y\zeta_y + \varphi'_x H_x + \varphi'_y H_y - \Phi_z - \varphi'_z = 0 \tag{9.25}$$

(with neglected terms $\varphi'_x\zeta'_x + \varphi'_y\zeta'_y$);

$$\zeta = \tfrac{1}{2}Fn^2(1 - \Phi_x^2 - \Phi_y^2 - \Phi_z^2 - 2\Phi_x\varphi_x' - 2\Phi_y\varphi_y' - 2\Phi_z\varphi_z') \tag{9.26}$$

(with neglected terms $-\frac{1}{2}Fn^2\left[(\varphi_x{}')^2+(\varphi_y{}')^2+(\varphi_z{}')^2\right]$). Squares and cross products in the perturbations have here been dropped, and the resulting conditions are linear in the unknown perturbation φ'. However, they still are to be satisfied on the unknown free surface $z = \zeta$. To allow a solution, they must be transfered to the known estimated surface $z = H$, which can be done by a Taylor expansion from $z = H$. For example, for the velocity at the free surface this would be

$$\nabla\phi_{(z=\zeta(x,y))} \approx \nabla\Phi_{(z=H(x,y))} + \nabla\varphi'_{(z=H(x,y))} + \zeta'\cdot\frac{\partial\nabla\Phi}{\partial z}$$

where again nonlinear terms have been dropped.

In several methods, such additional "transfer terms" either disappear, being of higher order, or are disregarded. If we disregard them here and simply impose the linearized free-surface boundary conditions on the known surface $z = H$, we find for the combined free-surface boundary condition

$$\begin{aligned}&-\frac{1}{2}Fn^2\left(\Phi_x\frac{\partial}{\partial x}+\Phi_y\frac{\partial}{\partial y}+\Phi_z\frac{\partial}{\partial z}\right)\\&[\Phi_x^2+\Phi_y^2+\Phi_z^2+2\Phi_x\varphi'_x+2\Phi_y\varphi'_y+2\Phi_z\varphi'_z]\\&+\varphi'_xH_x+\varphi'_yH_y-\Phi_z-\varphi'_z=0\end{aligned}\tag{9.27}$$

(Note that, in contrast with the original kinematic condition, z-derivatives are needed here as well because the term in square brackets is a function of three coordinates, whereas ζ is a function of x and y only.)

The next steps differ depending on the type of linearization used. We shall consider three options:

Linearization Relative to a Uniform Flow giving rise to the Kelvin free-surface boundary conditions, methods based on the use of Kelvin or Havelock sources, Neumann-Kelvin theory, and the further simplifications to thin ship, flat ship, and slender-body theories;

Linearization Relative to Double-Body Flow, leading to slow-ship linearized methods, among which is Dawson's method;

Linearization Relative to the Result of a Previous Iteration, which is the usual solution method for the nonlinear problem.

9.6.3 Uniform-Flow Linearization. The simplest kind of linearization is that with respect to the undisturbed, uniform flow. This supposes that at the free surface, the entire disturbance caused by the presence of the ship is small. Therefore,

$$\Phi = x \qquad H = 0 \quad \phi(x,y,z) = x + \varphi'(x,y,z) \tag{9.28}$$

where the perturbation potential is supposed to be $\varphi' = \mathcal{O}(\varepsilon)$, $\varepsilon \ll 1$. Substituting this into the dynamic free-surface condition (9.26) and in the combined condition (9.27) results in

$$\zeta = -Fn^2\varphi'_x \tag{9.29}$$

$$Fn^2\varphi'_{xx} + \varphi'_z = 0 \tag{9.30}$$

or an identical condition for φ. This is the well-known *Kelvin free-surface condition*, which long has been the basis for all theoretical considerations of wave making. It is consistent to impose it at the undisturbed free surface $z = 0$ since all transfer terms are of higher order. A very similar time-dependent form has been derived in Section 5.3.1.

The original nonlinear free-surface problem has now been reduced to a linear problem in a fixed domain, bounded by the ship hull and the undisturbed water surface. Therefore, simple source panel methods can be applied again. To enforce the free-surface boundary condition, panels and collocation points on the undisturbed water surface are then needed, in addition to those on the hull surface.

It is actually quite possible to solve this problem in that way. However, the simplicity of the Kelvin condition (specifically, the fact that it has constant coefficients) admits a particular solution method which has played a principal role in early ship wave-making research. An elementary potential field can be constructed that not only satisfies the Laplace equation in the flow domain, but also the Kelvin condition at the undisturbed free surface and the radiation condition, regardless of the location of the singular point $\vec{x} = \vec{x}_0$ (provided that $z_0 < 0$). The potential fields induced by a distribution of such *Kelvin sources* (or *Havelock sources*) then only need to be superimposed in such a way that the hull boundary condition is satisfied.

The potential field of a Kelvin source with unit strength located at $\vec{x} = (x_0, y_0, z_0)$ is derived in, e.g., Wehausen (1973) and can be written as

$$\begin{aligned}&\phi(x,y,z) = -\frac{1}{4\pi R}+\frac{1}{4\pi R_1}+\\&\frac{K_0}{\pi^2}\int_0^{\frac{\pi}{2}}d\theta\sec^2\theta\int_0^{\infty}dk\,\frac{e^{k(z+z_0)}}{k-K_0\sec^2\theta}\times\\&\cos[k(x-x_0)\cos\theta]\cdot\cos[k(y-y_0)\sin\theta]+\\&\frac{K_0}{\pi}\int_0^{\frac{\pi}{2}}d\theta\sec^2\theta\, e^{K_0(z+z_0)\sec^2\theta}\times\\&\sin[K_0(x-x_0)\sec\theta]\cos[K_0(z-z_0)\sin\theta\, sec^2\theta]\end{aligned}\tag{9.31}$$

in which $K_0 = g/U_\infty^2$, $R = \sqrt{(x-x_0)^2+(y-y_0)^2+(z-z_0)^2}$, and $R_1 = \sqrt{(x-x_0)^2+(y-y_0)^2+(z+z_0)^2}$.

Using this Kelvin source potential, or its generalization to a Kelvin source distribution, the linearized free-surface potential flow problem can be solved in a way quite similar to the approach described before: the underwater part of the ship hull is covered with Kelvin source panels; the velocities induced by all panels at all hull collocation points are computed; and the hull boundary condition at the collocation points is expressed in these velocities. This yields an equation of the form (9.10), which is solved to find the source strengths. The velocity field along the hull and the wave pattern can then be found.

These methods are generally denoted *Neumann-Kelvin* methods, as they solve the *Neumann-Kelvin* problem: the potential-flow problem defined by a Neumann boundary condition on the hull (i.e., given $\partial\phi/\partial n$) and the Kelvin condition on the water surface (Brard, 1972). Quite reasonable predictions of the wave resistance curves for some cases were shown in, e.g., Baar and Price (1988). Although the approach is apparently straightforward, the automatic satisfaction of the Kelvin free-surface boundary condition comes at a price. Evaluating the Kelvin source potential at a large number of points, as is needed in a panel method, is a computationally demanding operation, although several approximations for this expression have been published (Noblesse, 1977, 1978). In the past, however, the possibility to satisfy the free-surface conditions without necessarily using thousands of sources on the water surface and solving large systems of equations has been a significant advantage.

Thin-Ship Theory Thin-ship theory was first proposed by J. H. Michell in 1898 already (Michell, 1898; Tuck, 1989). It is a further simplification of the uniform-flow linearization, valid for ships with a small beam/length ratio. The idea is to linearize also the hull boundary condition, and to impose it in the centerplane rather than at the hull surface.

Suppose we have a slender ship hull form defined by $y/L = \pm F(x,z)/L = \mathcal{O}(\varepsilon)$. A vector normal to the hull surface is $\left(-\frac{\partial F}{\partial x}\; 1\; -\frac{\partial F}{\partial z}\right)^T$. As we still assume that $\phi(x,y,z) = x + \varphi'(x, y, z)$, the hull boundary condition can be linearized to

$$\frac{\partial\phi}{\partial n} = -\partial F/\partial x + \partial\phi/\partial y + \mathcal{O}(\varepsilon^2) = 0$$

so

$$\partial\phi/\partial y = \partial F/\partial x \tag{9.32}$$

If the left-hand side is now expressed in the values at $y = 0+$ by a Taylor expansion, it appears that this adds just more terms of $\mathcal{O}(\varepsilon^2)$ or higher, and no change is needed. Consequently, $\partial\phi/\partial y$ in the centerplane is explicitly given by equation (9.32); and it has a jump there from $-\partial F/\partial x$ to $+\partial F/\partial x$.

A Kelvin source distribution is now positioned in the centerplane within the hull. This is a plane surface, and at any point in the centerplane the normal velocity has a contribution from the local source panel only, not from any other panel. Therefore, the local source density is given explicitly in terms of the waterline slope at the corresponding location on the hull:

$$\sigma(x, z) = 2\,\frac{\partial F(x, z)}{\partial x}$$

The wave pattern can be evaluated directly from this source distribution. This linearization of the hull boundary condition therefore not only reduces the number of panels needed, but also eliminates the need to solve a system of equations.

The wave resistance according to the thin-ship theory can be expressed directly in the hull form, without any explicit calculation of a pressure distribution or wave pattern, by the so-called *Michell integral*, which can be written in various forms, among which

$$R_W = \frac{4g^2\rho}{\pi U_\infty^2}\int_0^{\frac{\pi}{2}} \sec^3\theta\,[P^2(\theta) + Q^2(\theta)]\,d\theta \tag{9.33}$$

in which

$$P = \iint_{S_0} \frac{\partial F(x,z)}{\partial x}\, e^{K_0 z\cdot\sec^2\theta} \cos\,(K_0 x \sec\theta)\,dxdz$$

$$Q = \iint_{S_0} \frac{\partial F(x,z)}{\partial x}\, e^{K_0 z\cdot\sec^2\theta} \sin\,(K_0 x \sec\theta)\,dxdz$$

in which S_0 is the ship's centerplane area.

Thin-ship theory has taken a most prominent place in the research on ship waves. Although initially Michell's work stayed unnoticed, it was taken up again in the 1930s by Havelock (1932, 1934) who has studied the wave patterns found from this approximation, has analyzed many properties, and has applied it to several bodies. All this work, and that by other researchers, has contributed much to the understanding of the physics of ship waves.

On the other hand, the results found from thin-ship theory for practical vessels are generally inaccurate. At somewhat lower Froude numbers in particular, the resistance curve thus found usually displays large humps and hollows because of an exaggeration of interference effects. This can be understood if we realize that strictly the validity of thin-ship theory is confined not only by the requirement $B << L$ but also by $B << \lambda$; the latter permitting the transfer of the boundary condition to the centerplane. At lower Froude numbers this cannot be satisfied. In general, the thin-ship linearization has been found to be limited to very thin vessels only, or to multihull vessels which have narrow hulls in most cases. (This requires the use of Kelvin source distributions in multiple centerplanes, and permits inclusion of the wave interference effect. For incorporating induced resistance or dealing with asymmetric sidehulls, Kelvin dipole distributions are needed in addition.)

While today other methods are used for most practical applications, thin-ship linearization still finds some application in the context of automatic optimization, in which the small computation time needed is of interest; and in computing far-field wave patterns of high-speed craft, in which the analytical expressions have the advantage of having no numerical damping and admitting high resolution (Doctors & Day, 2000; Tuck, Scullen, & Lazauskas, 2002).

Various alternative simplifications of the hull form have been studied, such as slender-body theory and flat-ship theory. None of these has a sufficiently large range of application to still find frequent application. Subsequent research in the period from 1960 to 1975 focused on various ways to extend the linear thin-ship theory to second order. However, this met many difficulties and questions. Alternative approaches were inspired by good results shown for a method proposed by Guilloton (1964), who applied a coordinate transformation to the source distribution in the centerplane of a thin-ship method. This coordinate transformation was based on the first-order result and could be shown to lead to the satisfaction of second-order boundary conditions on hull and water surface. Alternative formulations of the coordinate straining were then proposed (Dagan, 1975; Noblesse, 1975; Noblesse & Dagan, 1976). However, further research on this topic seems to have been interrupted by the demonstrated success of slow-ship theories.

9.6.4 Slow-Ship Linearization. After extensive research had been done on the thin-ship and Neumann-Kelvin formulations, around 1974 several authors derived an alternative linearization of the free-surface boundary conditions. Early research on this was done by Ogilvie (1968) and Dagan (1972). In the same period, important studies on the physics of ship waves and the adequacy of linearizations were done by Inui and Kajitani (1977), who pointed out the importance of the curved flow field around the hull on the propagation of ship waves and thereby on wave pattern and wave resistance. One of the first implementations of a slow-ship method was that of Baba and Takekuma (1975), and results for ships were shown in Baba and Hara (1977).

The idea behind this so-called *slow-ship linearization* is that, in order to improve the validity of the wave resistance computations for fuller hull forms, we cannot assume that the perturbation of a uniform flow is small. Whatever the significance of wave making, the flow at least needs to go around the hull. A more refined linearization then is based on the assumption that the flow around the hull with waves is a small perturbation of the flow around the hull without waves. We refer to the statement made in Section 9.5.5: for $Fn \rightarrow 0$, the flow field approaches the double-body flow, except for short waves superimposed on it. Therefore, if we decompose the velocity field as

$$\nabla\phi = \nabla\Phi + \nabla\varphi' \tag{9.34}$$

where $\nabla\Phi$ is the double-body flow velocity, for a sufficiently low Froude number the perturbation should be small enough to admit linearization. An appropriate perturbation parameter for the linearization then is $\varepsilon = Fn^2$, and we assume that the perturbation velocity $\nabla\varphi' = \mathcal{O}(Fn^2) << 1$.

For the wave elevation, the corresponding decomposition follows from the linearized dynamic free-surface condition (9.26)

$$\begin{aligned} \zeta(x,y) &= \frac{1}{2}Fn^2\,(1 - \nabla\Phi \cdot \nabla\Phi) - \frac{1}{2}Fn^2(2\,\nabla\Phi \cdot \nabla\varphi') \\ &= \zeta_r(x,y) + \zeta' \end{aligned} \tag{9.35}$$

in which the nonlinear terms

$$-\frac{1}{2}Fn^2\,(\nabla\varphi' \cdot \nabla\varphi') = \mathcal{O}(Fn^6)$$

have been neglected. ζ_r is the "double-body wave height." The linearized combined free-surface boundary condition is simply (9.27) with $H = \zeta_r$.

The final step is the transfer of the boundary condition from the unknown wave surface to a known approximate surface, by means of a Taylor expansion. It would seem rational to choose the surface $z = \zeta_r$ for this. However, evaluating the double-body flow velocities $\nabla\Phi$ at points above the still water surface may not be a good idea. Instead, most slow-ship linearized methods apply the linearized boundary condition on the still water surface $z = 0$. In principle, this simply requires transfer over a distance ζ in the same way. However, a difficulty arises here. We expect that the perturbation will have a wave-like character, with a wave number approximately proportional to Fn^{-2}. Each differentiation of the perturbation potential φ' then reduces its order by a factor Fn^2. Because $\zeta = \mathcal{O}(Fn^2)$, each term in the Taylor expansion is formally of the same order in Fn^2 and the expansion cannot be consistently truncated.

Because of this problem, different assumptions on the order of the terms have been made by different authors, leading to a variety of slow-ship free-surface conditions, such as those of Baba and Takekuma (1975), Newman (1976), Eggers (1981), and Brandsma and Hermans (1985). However, by far the most common form of the slow-ship condition simply omitted the transfer terms altogether, which yields

$$\begin{aligned} &Fn^2(\Phi_x^2\varphi'_{xx} + 2\Phi_x\Phi_y\varphi'_{xy} + \Phi_y^2\varphi'_{yy}) - \\ &2\varphi'_x\zeta_{r_x} - 2\,\varphi'_y\zeta_{r_y} + \varphi'_z = \Phi_x\zeta_{r_x} + \Phi_y\zeta_{r_y} \end{aligned} \tag{9.36}$$

at $z = 0$. This was proposed by Dawson (1977), although in his method he used an even simpler form based on streamline coordinates, in which further approximations were hidden.

The popularity of this condition had more to do with the practical solution method proposed in the same paper than with mathematical correctness. Nevertheless, in a comparative study of several slow-ship formulations (Raven, 1996), Dawson's formulation appeared to be a fairly reliable choice for most practical hull forms, whereas the more consistent formulation of Eggers (1981) could lead to problems for blunt hull forms.

Dawson's Method The slow-ship linearization again reduces the original nonlinear free-surface problem to a linear problem in a fixed domain, bounded by the ship hull and the undisturbed water surface. Unlike the Kelvin boundary condition, slow-ship conditions have spatially varying coefficients depending on the double-body flow field, and an elementary potential field satisfying the free-surface condition cannot be constructed. Therefore, an alternative solution method had to be devised. We here describe essentially the method proposed by Dawson (1977), which has been widely used for some time, mostly in the period from 1985 to 1995.

The method uses the principles of the source panel methods described in Section 9.5.3, and like those, uses the simple Rankine source potential field (9.3), not the Kelvin source potential. Therefore, the elementary flow field does not satisfy the free-surface boundary conditions or the radiation condition. The free-surface boundary conditions are explicitly enforced by a free-surface source distribution on a part of the undisturbed water surface around the hull. As Dawson found, this free-surface panel domain could be relatively small, of the order of half a ship length to all sides, and he used only some hundreds of panels on each side of the free surface. Of course, much finer panelings could be used later.

The first step to be made is to compute the double-body flow as described before, using a panel method. Then, a panel distribution is constructed on the still water plane around the hull, usually by algebraic methods. Next, at the free-surface collocation points, usually the panel centers, the double-body flow velocity components are evaluated, and thereby the coefficients in Φ_x, Φ_y, ζ_r, etc., that occur in the free-surface boundary condition (9.36).

The next step is to express the φ' terms in the free-surface condition in the induction of all panels: both the panels on the water surface and those on the hull. It is noted that the boundary condition now not only contains unknown velocities, but also their derivatives along the water surface, φ'_{xx} and φ'_{yy}. An original contribution from Dawson was to express these in the velocities at collocation points, using finite difference schemes. For example, if we have a row of collocation points ... $i-2, i-1, i, i+1$, ... in the x-direction, a term ϕ_{xx} can be approximated as

$$(\phi_{xx})_i \approx a_0(\phi_x)_i + a_1(\phi_x)_{i-1} + a_2(\phi_x)_{i-2} + a_3(\phi_x)_{i-3}$$

Each of the ϕ_x-terms is a sum of contributions from all panels. Collecting the contributions from each panel to all four terms, we obtain a form $(\phi_{xx})_i \approx \Sigma_{j=1}^{N} C_{ij} \cdot \sigma_j$. The final matrix entries (influence coefficients) are then composed from contributions from the various terms in the free-surface boundary condition. In this way, a system of equations of the form

$$A_{ij}\vec{\sigma} = \overrightarrow{RHS} \qquad (9.37)$$

is again obtained. The number of equations and unknowns is the sum of the number of hull and free-surface panels. Solving the system provides the source strengths on hull and water surface. The velocity field is then easily obtained from equation (9.8), in which the summation is over all hull and free-surface panels. The wave pattern follows from evaluating the dynamic free-surface condition, either in linearized form [equation (9.35)] or in the nonlinear form (9.19). The pressure is found from the Bernoulli equation, and the wave resistance is found from integrating the longitudinal component of the pressure forces acting on all hull panels.

An important detail is the consideration that formally, the solution of the problem is still nonunique because the radiation condition has not been imposed yet, and solutions with waves upstream of the bow could still be found. But Dawson found that it is possible to enforce this condition indirectly by using an *upstream* differencing for the longitudinal derivatives of the velocities in the free-surface condition, together with the proper conditions at the upstream edge of the free-surface domain. This usually provides the right bias in the solution procedure to ensure satisfaction of the radiation condition. A variety of upstream difference schemes have this property, but following Dawson four-point upwind schemes are mostly used.

An alternative to the use of difference schemes is to compute the velocity derivatives analytically as a sum of contributions from all panels. This removes numerical errors arising from the difference schemes, but requires a different treatment of the radiation condition, proposed in Jensen (1987). It consists of adding an additional row of collocation points at the upstream edge of the free-surface domain and an additional row of source panels downstream. Such a "staggered" free-surface panel arrangement is actually used successfully in some methods.

Dawson's method contained several original ideas, while of course making use of earlier research by others; such as the development of slow-ship linearizations, by Baba and Takekuma (1975) and Newman (1976), an earlier method using Rankine sources to model surface waves by Bai and Yeung (1974), and a similar but earlier method for the wave resistance problem by Gadd (1976). However, the simplicity and promising results of Dawson's paper attracted much interest and initiated a sort of breakthrough in wave pattern calculation capabilities. Whereas the great majority of earlier methods used Kelvin sources, since about 1980 most work on wave resistance prediction concerned this new class of "Rankine-source methods." The drawback of the much larger number of panels due to the necessity of a free-surface paneling is largely offset by the far simpler arithmetic operations and by the flexibility in imposing different free-surface boundary conditions and dealing with various geometric configurations.

In its original form Dawson's method contained significant numerical errors, leading to, for example, incorrect wave lengths. Moreover, for dense free-surface panelings, oscillations in the velocity field occurred. These drawbacks could be removed by using higher-order panels, improved numerical schemes, or explicit dispersion corrections. An important theoretical analysis of the numerical properties of this class of methods was published by Sclavounos and Nakos (1988), based on earlier work by Piers (1983). This was later applied to select suitable difference schemes by Strobel and Cheng (1992), and by Raven (1996) for a nonlinear method. The research on these methods (Nakos, 1990; Nakos and Sclavounos, 1994; Raven, 1988) has given the method a stronger foundation and has provided alternatives and improvements.

In general, the wave pattern as predicted by these methods was far more realistic than that found from previous methods, in particular for fuller hull forms. But the "slow-ship" methods actually were found also to work well for faster, more slender ships: for increasing slenderness of the hull, the free-surface condition reduces to the normal Kelvin condition, which is not limited to low Froude numbers. Transverse wave components, and the wave profile along the hull, were in general well predicted. On the other hand, the bow wave crest is systematically too low (sometimes by 50%) for all linearized methods, and diverging wave components from the bow are also often far underestimated. Predicted wave amplitudes at a distance from the hull are often much too low. An explanation has been given in Raven (1997). The predicted stern waves are often too high and rather unrealistic, so slow-ship linearized methods were mainly used for optimizing the forebody.

Wave resistance predictions from Dawson's method were usually fairly good for slender ships at relatively high Froude numbers, such as frigates and sailing yachts, but not for most merchant vessels. The fuller the hull form and the lower the Froude number, the more the predicted wave resistance was usually underestimated; for cases such as tankers, the predicted wave resistance was often negative, a paradoxical result that could be explained by certain properties of the linearization (Raven, 1996).

On the other hand, differences in wave pattern between hull form variations were usually qualitatively well predicted, making the method practically useful for design. Dawson's method and its developments were used intensively in ship hull form design in the period until 1995 approximately; after which they were quickly replaced by nonlinear methods. With their shortcomings, they have proven to be most useful tools for ship design, provided the predictions were considered with care (van den Berg, Raven, & Valkhof, 1990).

9.6.5 Solution Methods for the Nonlinear Wave Resistance Problem. While linearization on the one hand makes the solution much easier and has been a necessity in the past, it introduces certain errors that are responsible for the shortcomings mentioned in the previous section. There are many nonlinear contributions omitted in such methods, which for completeness and accuracy need to be taken into account:

- All nonlinear terms in the free-surface boundary conditions need to be included. Among others, these include effects of wave propagation over the curved and uneven flow field around the hull, found to be essential for good prediction of diverging bow waves in particular (Raven, 1997).
- The boundary conditions need to be imposed on the actual wave surface, not on any approximate surface or the still waterplane; this is a requirement for an accurate prediction of bow wave height and is also essential where the flow field has large vertical variations, such as around a bulbous bow.
- The actual flow domain extends up to the wavy free surface, and a part of the hull form above the design waterline plays a role; but in linearized calculations, the domain is bounded by the undisturbed free surface and anything above that is not felt. This can be particularly important in case of, for example, a large bow flare, a bulbous bow extending above the still water surface, or a flat stern above the still water surface.
- Linearized methods usually disregarded the dynamic trim and sinkage, and also these can be important nonlinear contributions.

Therefore, solution of the complete, nonlinear problem without any linearization is preferred. As a matter of fact, when fully nonlinear methods became available, they produced a surprisingly large improvement of the predictions in many cases. Fig. 9.7 (Raven, 1996) illustrates an early result for a containership, showing the difference in bow wave height and diverging bow wave system. The nonlinear result here closely agreed with the experimental data.

To some extent, a nonlinear method can be set up as an extension of a linearized method. Linearization starts with selecting an estimated free-surface shape and free-surface velocity field. The unknowns are defined to be a perturbation of the estimates; and the better the estimates are, the smaller the errors introduced by the linearization. A crude estimate such as double-body flow thus produces a fairly realistic slow-ship solution. If we reuse this solution as an improved estimate for a next step, the next result should be even closer to reality. This process can be repeated, leading to an iterative solution procedure. If this procedure is properly formulated and it *converges* (i.e., the change between successive iterations decreases below a small tolerance), the terms neglected in the linearization vanish and the result is a solution of the exact nonlinear inviscid problem without any approximation, except for discretization and other numerical errors.

However, there is no guarantee that it will converge to a final solution. Actually, in the first years of the developments, converged solutions were hard to achieve for all cases having substantial nonlinear effects. Important convergence difficulties were the rule, and no distinct improvement compared to linearized predictions had been obtained until about 1990. Numerical details appear to be crucial for the convergence, and success hinges on a correct and careful treatment of many modeling and implementation issues.

One of the earliest relevant attempts was made by Gadd (1976), even preceding Dawson's paper! The nonlinear free-surface boundary conditions were solved iteratively, but were imposed at the still waterplane. His method was very original, using distributions of Rankine sources over the hull and the still water surface and several numerical tricks to improve stability and accuracy. But the hardware then available forced to use excessively coarse discretizations, and the results could not be any better than those of later slow-ship linearized methods.

Another very early nonlinear method, which was based on Dawson's ideas, was proposed by Daube and

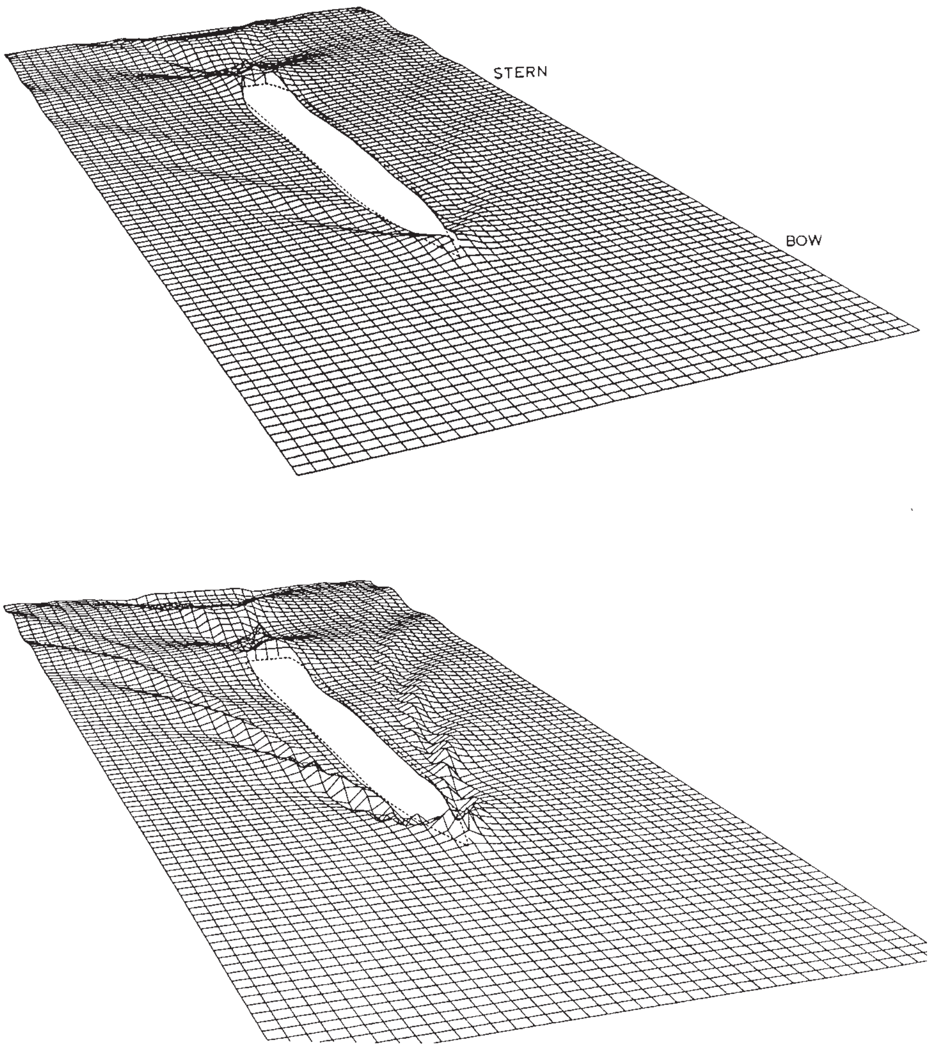

Figure 9.7 Wave pattern for a containership, predicted by Dawson's method (code DAWSON) and a fully nonlinear method (RAPID). Wave heights magnified 5 times.

Dulieu in 1981. The exact combined free-surface condition was cast in a form containing derivatives along free-surface streamlines, which were approximated by the streamlines of the double-body flow. Other nonlinear effects were included and, on convergence, the free-surface condition was imposed on the actual free surface. After publication of some first results, the development seems not to have been pursued. Some other methods using an incomplete nonlinear free-surface condition were published in those years, mostly imposing that condition on the still water surface.

A complete nonlinear free-surface condition in a 3D flow was imposed by Xia (1986) in Gothenburg, who studied some prototype iterative methods, with somewhat limited success. This development was continued more successfully by Ni (1987), Kim (1989), and Janson (1997), resulting in the SHIPFLOW code.

Another development was initiated around 1986 at Institut für Schiffbau in Hamburg, Germany, by Jensen et al. (Jensen, 1988; Jensen, Bertram, & Söding, 1989; Jensen, Mi, & Söding, 1986). This method is based on the use of simple point sources at a distance above the wave surface, an approach that subsequently has widely been adopted, with modifications, in other solution methods. Satisfaction of the radiation condition was accomplished by shifting the free-surface sources back over one source spacing relative to the collocation points. The resulting code was called SHALLO, its current successor v– SHALLO (Gatchell et al., 2000).

A development started in 1990 by Raven (1992, 1996) at MARIN led to an alternative method based on raised source panels and using difference schemes for the free-surface condition. This was implemented in the code RAPID.

Besides these three codes, which are probably those with the widest distribution and most frequent use, some others have been developed subsequently, mostly along similar lines but often differing in numerics, solution methods, or modeling details. We mention here the codes SPLASH, ODYSSEE, VSAERO-FSWAVE (Hughes, 1997), and DASBOOT (Wyatt, 2000) as examples. Today, the principal methods deal with a wide variety of practical cases without convergence difficulties and are routinely applied in ship design.

Basic Formulation The basics of the main methods are now rather similar, though they still differ in several numerical issues. In general, the iterative procedure consists of the following steps:

1. Choose an initial approximation of the free surface, $H(x, y)$, and an initial velocity distribution $\nabla\Phi(x, y, H)$ on that surface.
2. Define a panel distribution on the hull and (on or above) the free surface. Choose collocation points on the free surface $H(x, y)$.
3. At the free-surface collocation points, impose the combined free-surface condition (9.27) or a similar form, linearized in perturbations of the estimated velocity distribution and wave elevation. Impose the hull boundary condition at the hull collocation points. Solve the resulting set of linear equations for the source strengths.
4. Compute the velocity and pressure field. Calculate a new estimate of the wave elevation $\zeta(x, y)$ from the dynamic free-surface condition. Compute a new free-surface velocity field $\nabla\phi(x, y, \zeta)$.
5. Determine the resistance, vertical force, and trimming moment by integrating pressure forces over the hull. Determine the imbalance of the ship's weight distribution and the forces, and estimate the new dynamic trim and sinkage from hydrostatics.
6. Calculate the residual errors in the nonlinear free-surface conditions (i.e., the normal velocity through the free surface and the deviation from atmospheric pressure). If these or the trim and sinkage change exceed the specified tolerances: Adjust the attitude of the hull for trim and sinkage changes; update the estimated wave surface $H(x, y)$ and free-surface velocity field $\nabla\Phi(x, y, H)$ using the latest result; and return to step 2. Otherwise, stop.

Implementation Some of the details are now described.

In step 1, the initial approximation is usually a flat water surface and a uniform flow, as there is no need to bother about something better. The final solution does not depend on the initial approximation.

In step 2, the free-surface panel generation is usually algebraic, and is not Cartesian or flow-aligned. Therefore, the derivatives in x- and y-direction occurring in the free-surface condition need to be transformed to derivatives along the local panel coordinates.

As in Dawson's method and its variations, in the nonlinear methods the radiation condition is also imposed "numerically," using either of the same two basic approaches: one is the use of an upwind finite difference scheme applied to the dominant terms in the combined free-surface condition and the other is a forward shift of the collocation points relative to the panels over one panel length, a method introduced in Jensen, Mi and Söding (1986) and Jensen (1987). Both approaches are combined with suitable zero-perturbation conditions at the upstream edge of the free-surface domain.

The entire system again takes a form as equation (9.37). As opposed to the system obtained for just a body boundary condition, the matrix A is not diagonally dominant, as a result of the form and implementation of the free-surface boundary condition. Although the system has long been considered unsuited to iterative solution, a fast iterative solution is possible by using modern preconditioners and iterative solvers.

Once the source strengths are known, the velocity field again follows from equation (9.8), summation going over all hull and free-surface panels. This is typically evaluated only at the collocation points, but is possible just as well for any other point in the flow domain, provided such a point is not close to a panel edge or outside the area covered with free-surface panels. The pressure field again is found from the Bernoulli equation.

In step 6, one could just choose $H(x, y)$ and $\nabla\Phi(x, y, H)$ identical to the last results from step 4 (ζ and $\nabla\phi$). However, to improve the stability and convergence of the iterative procedure, underrelaxation is often used; i.e., the new estimates of the wave surface and velocity field are defined as weighted averages of the old estimates and the latest solutions.

The number of iterations needed (for rather strict convergence criteria) depends strongly on the case and on the panel density chosen, but usually lies between 5 and 20.

Desingularization A noteworthy common feature of several of the principal methods is the use of "raised panels" or "desingularization" for the free surface. This means that the singularities are at a certain distance above the free surface. The collocation points (where the free-surface condition is satisfied) must still be on the free surface itself. This is theoretically permissible; the derivation of the source panel method is still just as valid, except that in equation (9.16), we must set $T = 1$ in evaluating the boundary conditions. There are, however, limits on the distance of the panels from the boundary.

Such raised-singularity methods have some advantages in the present context:

- Because of the distance between the panels and the free surface, the velocity field induced in the fluid domain is smoother than with a usual method.
- Since the distance from the panels to the free surface is arbitrary within certain limits, it is no longer necessary to adapt the source panels to the new free surface in each iteration. We only have to move the free-surface collocation points up or down to the new approximation of the free surface.

- As shown theoretically in Raven (1996) and found in practice, the raised-panel formulation admits a large reduction of numerical dispersion errors and elimination of point-to-point oscillations that were found in earlier methods such as Dawson's. This is partly achieved by exploiting the liberty in choosing the position of the collocation points relative to the panels.
- The iterative solution procedure for the nonlinear problems has been found to have better convergence and stability properties if raised-singularity methods are used.

Raised-singularity methods were first used in ship wave pattern calculations by Xia (1986) and by Jensen et al. (1986). In the form of raised source panels, this has now been adopted in most methods for the nonlinear ship wave-making problem. In all methods, the singularities are at around one typical panel dimension (or source spacing) above the wave surface. In most methods, they are adjusted from time to time during the iteration process in order to keep the distance more or less constant, which is important for accuracy and stability. Theoretical analyses of the numerical dispersion and damping for various choices of discretization are found in Raven (1996) and Janson (1997).

Transom Sterns The flow off a transom stern has some particular properties that require a separate treatment in these methods. It is important to note that only a flow regime in which the free surface detaches smoothly from the transom edge (dry-transom flow) can be adequately modeled in inviscid methods; cases in which the transom is wetted are strongly affected by viscosity and their modeling in an inviscid method is only approximate.

For dry-transom flows, the proper model is one in which the water surface detaches from the transom edge, and the free-surface conditions are satisfied everywhere. Just aft of the transom, the flow is governed by the requirement of tangential flow off the hull and of atmospheric pressure at the transom edge. Different implementations are used; free-surface panel strips aft of the transom are normally added and no body boundary condition $\partial\phi/\partial n = 0$ should be imposed on the transom.

Validations have shown that the resulting wave pattern is reasonably accurate for cases in which the transom is really dry, although deviations are somewhat larger than elsewhere because of the effect of the boundary layer that detaches from the hull (Raven, 1998). Unfortunately, for a range of transom immersions it is possible to obtain a dry-transom flow prediction from a potential-flow code, while in reality the transom would be wetted; therefore, assessment is needed. For transom immersions larger than $0.4(V^2/2g)$, a converged inviscid dry-transom solution is unlikely to be found.

Practical Aspects As these nonlinear methods today are the principal tools to compute a ship's wave making, we shall pay some attention to the practical aspects of such calculations.

The first step is the generation of a panel distribution on the hull surface. The most practical way is a panel generation tool which is based on the CAD system used or is able to read a general hull shape description written by a CAD system. Panel generation then proceeds largely automatically, but should admit control of panel density, local refinements, etc., by the user.

Choosing a suitable hull panel distribution is important. The panel size must be small enough to resolve all essential aspects of both the hull geometry and the flow field. For example, local refinement of the paneling is often needed on a bulbous bow to resolve the strong curvature and large pressure gradients there. What density is required for an acceptable accuracy is basically a matter of experience. A too coarse hull paneling primarily affects the accuracy of the wave resistance evaluation by pressure integration over the hull, while the wave pattern is somewhat less sensitive. Today, a few thousand panels for each symmetric half of the hull is usual.

The free-surface paneling is generated either fully automatically or based on user input of its density and extent. Typically, the paneling is generated algebraically. Free-surface panels must be small enough to resolve the principal waves, and as a rule their length should be no more than 5% of the transverse wave length $\lambda_0 = 2\pi Fn^2 L$. The free-surface paneling is usually cut off at a few transverse wave lengths aft of the stern, and should be wide enough to cover the Kelvin wedge over that length. In practice, 5000–10,000 panels for half the water surface are often used, dependent on Fn. Fig. 9.8 illustrates the hull and free-surface paneling (2300 + 5200 panels per symmetric half, in this case) used for a case at $Fn = 0.26$.

In the course of the iterative solution process, both panelings will usually need to be adjusted. Raised singularity distributions normally are adjusted in order to stay at a more or less constant distance from the wave surface. Therefore, the intersection of the free-surface panels and the hull changes during the solution process, and as far as the panelings match that intersection, they need to be adjusted automatically as well.

Once the converged solution has been obtained, the results are inspected using visualization tools: the wave pattern, the hull pressure distribution, the (inviscid) streamline direction along the hull, a hull wave profile, longitudinal wave cuts, and integral quantities: the wave resistance, dynamic trim, and sinkage. In case lifting surfaces have been modeled (hydrofoils, keels, rudders) by special methods not discussed here, the lift force and induced resistance can also be computed. It has been found useful to compute the wave resistance not only from pressure integration, but also from a wave pattern analysis approach, based on a number of transverse or longitudinal wave cuts through the computed wave pattern (Heimann, 2000; Raven and Prins, 1998). This quantity is less sensitive to the hull panel density than the resistance from hull pressure integration. More on the use of the results in ship design is discussed in Section 11.5.

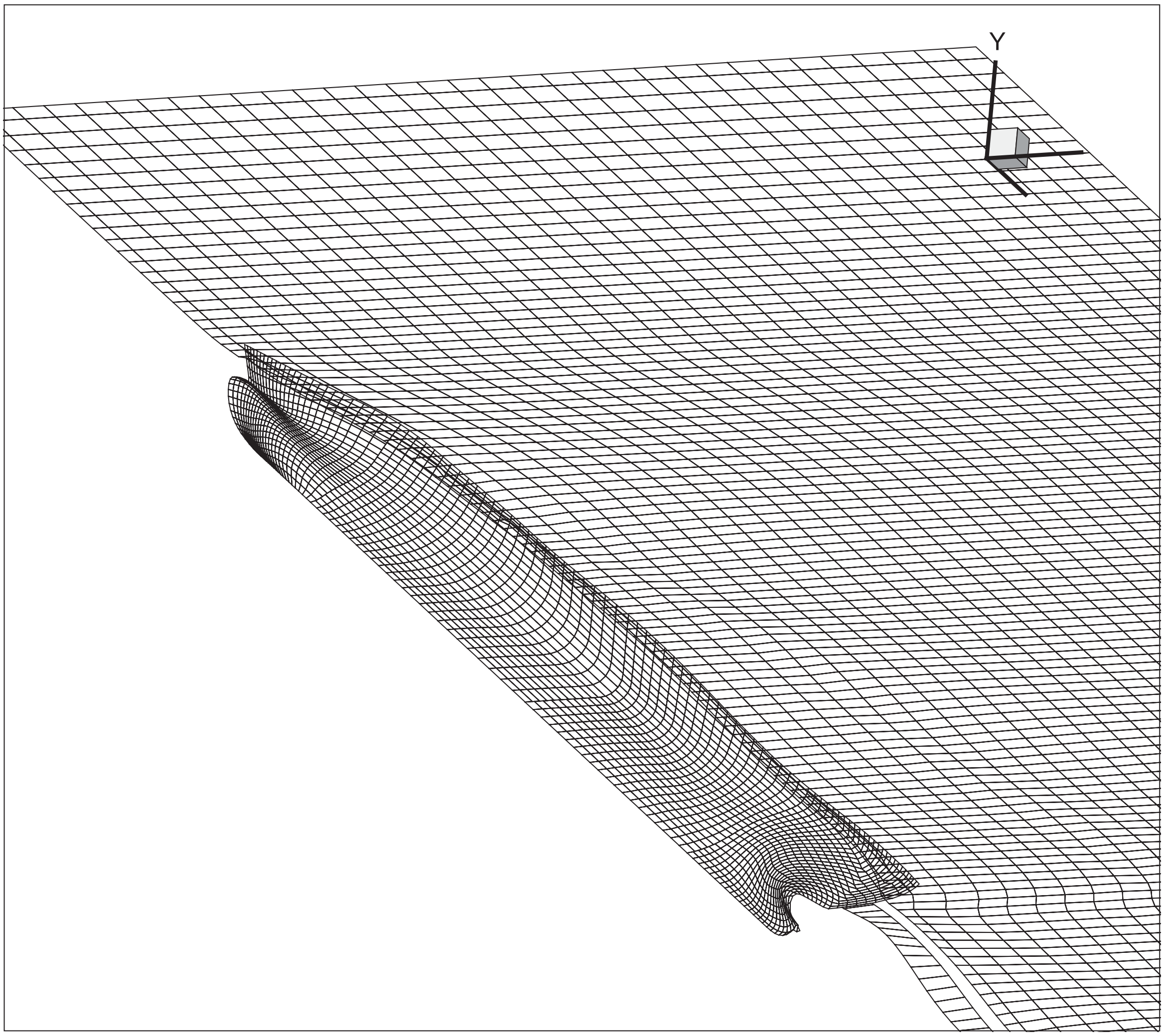

Figure 9.8 Example of hull and free-surface paneling.

Besides the results on the hull and wave surface, the velocity and pressure in field points can also be computed using postprocessors. This can be useful for appendage alignment. Here, however, one has to realize that the velocity field computed is that in inviscid flow, and inside the boundary layer and wake the velocity magnitude will be much different in reality, and the velocity direction deviates as well due to the cross-flow. The computed velocities on the hull are actually close to those at the edge of the boundary layer in reality. For bilge keel alignment, these methods will normally be adequate, for shaft support struts rarely.

A complete nonlinear computation for a usual case with 8000–12,000 panels may take 2–5 minutes of computer processing unit (CPU) time on a single 3GHz processor if the fastest codes are used. Therefore, whereas only 10 years ago solving the nonlinear free-surface potential flow problem meant quite an effort, today it forms a small computational task. Nonlinear free-surface potential flow tools are thus suitable for incorporation in a systematic hull form variation or optimization procedure (Heimann, 2006; Hoekstra and Raven, 2003; Valdenazzi et al., 2003).

Validations The general experience is that nonlinear free-surface potential flow codes can provide very good predictions of the wave pattern for a large class of cases. For somewhat more slender ships in particular, the predictions are often quite accurate. As an example, Fig. 9.9 compares the predicted and measured wave pattern for the Kriso Container Ship (KCS) at $Fn = 0.26$, a benchmark case for which measurements have been made in Korea and Japan (Kume, Ukon, & Takeshi, 2000; Van et al., 1998b). The prediction captures most wave-making features, but overestimates the wave system originating aft of the transom. The latter is due to the effect of the boundary layer on the transom flow, but in addition the transom might not have been entirely dry in the experiment.

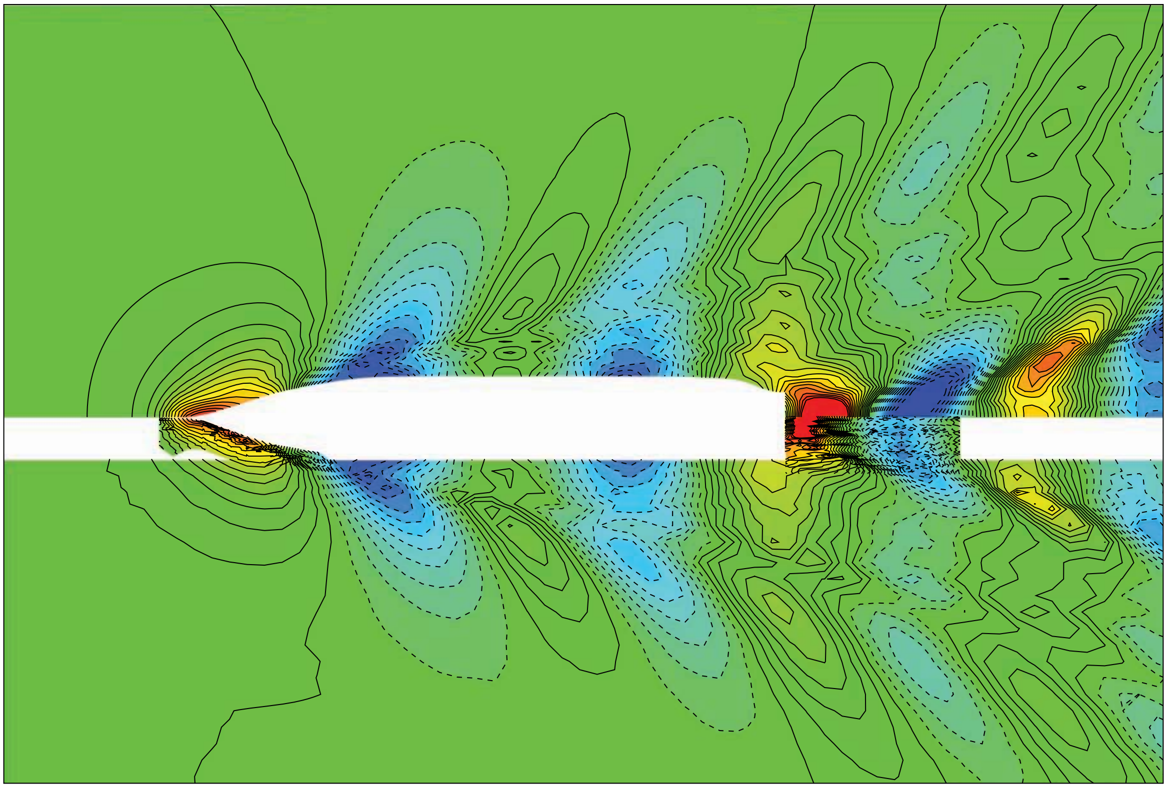

Figure 9.9 Wave pattern of *KRISO* containership (KCS). *Top*: prediction (using RAPID); *bottom*: experiment.

Compared with previous linearized methods there is a big improvement in the prediction of the bow wave height; the systematic underestimation has been removed, although thin sheets of water rising along a sharp bow cannot be predicted. Also the previous severe underestimation of the diverging bow wave system has been eliminated; this feature is studied in Raven (1997).

The resistance estimates are far better than with linearized methods, at least for somewhat fuller hull forms such as containerships and ferries. However, in absolute values the accuracy of the predicted wave resistance is still not very high. This is due to the fact that this resistance is often a small difference between large contributions (pressure forces on different parts of the hull) which almost cancel each other, making the result very sensitive to small numerical errors. The resistance may be used for comparisons between different designs, provided the Froude number is not too small or too large. At low Froude numbers, below 0.15 say, the wave resistance is so small that it may be of the same order as the discretization error.

The recommended way to use these panel methods is to study the wave pattern and pressure distribution and draw conclusions on possible hull form improvements from those, as discussed in Section 11.5. For this, it is of primary importance that differences in wave pattern between models are well predicted. Fig. 9.10 compares longitudinal wave cuts for two variations of a RoRo vessel, as measured in the towing tank and as predicted. The agreement is quite favorable (Valdenazzi et al., 2003).

Some more validation can be found in Raven (1996, 1998, 2000), Janson (1997), Gatchell et al. (2000), and others. In general, it appears that for most practical cases, good results are obtained if sufficient care is given to the paneling and numerics. Applicability is by no means restricted to the forebody only. Although limitations result from the neglect of viscous effects (see the restrictions mentioned later), this usually affects the stern wave system only, and free-surface potential-flow codes can still be most adequate for aft-shoulder waves, for example. For slender vessels with dry-transom flow, they can also be helpful for stern design, as shown by an example of a duck tail optimization in Raven (1998), but one needs to be much more careful here.

Restrictions Based on experience with nonlinear free-surface potential flow codes, and based on the assumptions made in their derivation, the following assessment of their restrictions and limitations can be made:

- Evidently, these potential-flow methods provide no information on the viscous flow. The velocity field computed contains no boundary layer or wake. Therefore, locally close to the wall and in the wake it is incorrect; the pressure field is less affected. Also, flow separation is not indicated.

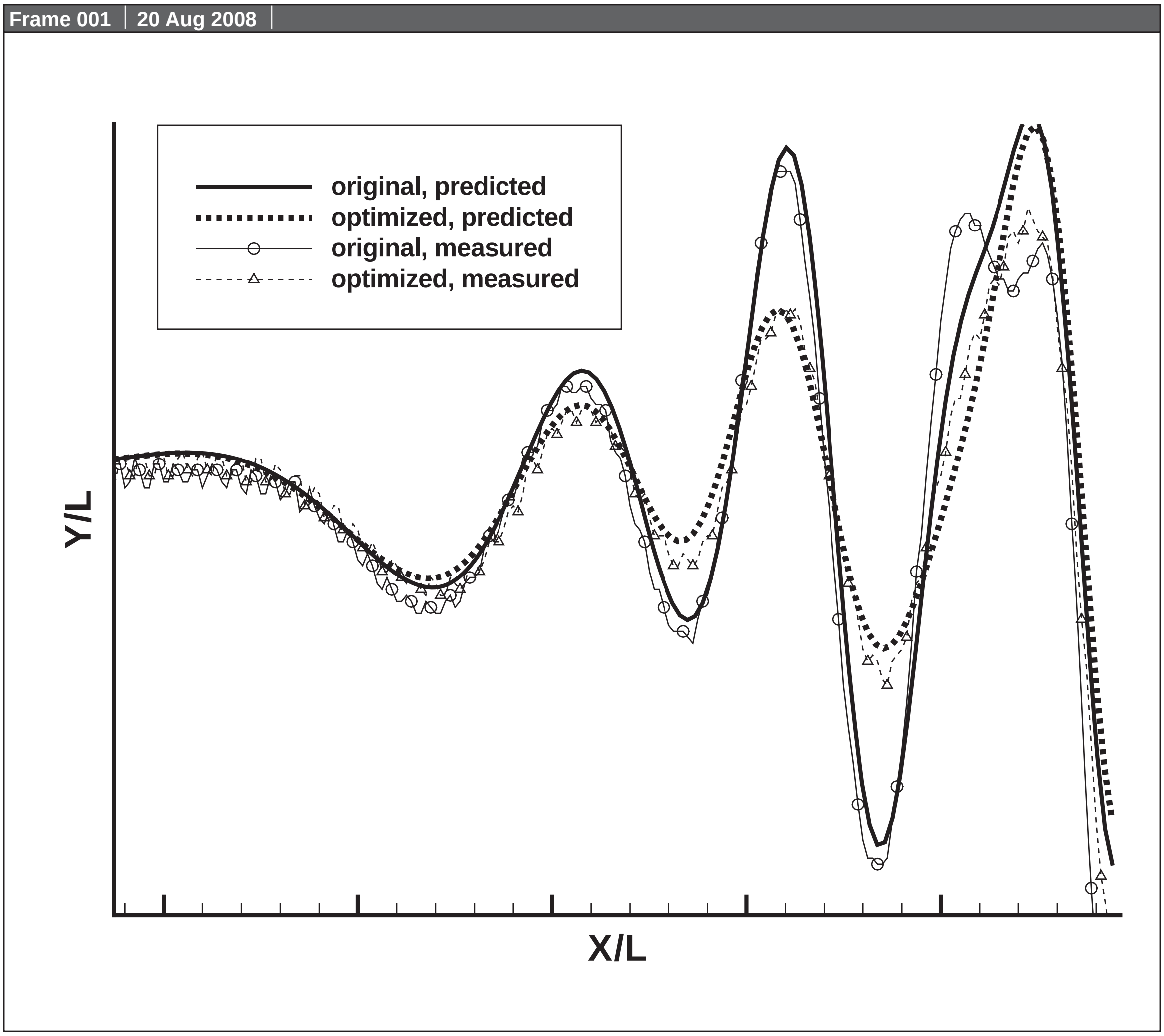

Figure 9.10 Comparison of predicted and measured wave cuts for two variations of a RoRo vessel.

- In Section 5.7 we briefly considered some viscous effects on ship wave patterns. Physically, the presence of a thick boundary layer reduces the pressure level at the stern, and sharp pressure rises at the stern are unlikely to occur in a viscous flow. These effects are disregarded in potential flow codes, which gives restrictions on their applicability. Specifically, it prevents making a quantitatively accurate prediction of the stern wave system for all but the most slender vessels. In general, the amplitude of the stern wave system is overestimated by inviscid codes; very little for slender transom-stern ships such as frigates or fast ferries, but substantially for fuller vessels such as container ships. Fig. 9.11 gives an example. Larger disagreement occurs if the transom in reality is not cleared while in the computations that is assumed. In general, the disagreement is smaller for full scale than for model scale.
- It is also not possible to make a quantitatively accurate prediction of the wave resistance for cases in which the stern wave system is substantially affected by viscous effects.
- The numerical accuracy of the predicted wave resistance is limited, in particular for full hull forms at low Froude number.
- Differences in resistance between design variations can be fairly well predicted using the best codes with a sufficiently dense paneling, as long as no hull form changes are allowed at the stern. If the viscous effects on the stern wave system vary significantly between design variations, inviscid codes may not give the right result (Janson & Larsson, 1996).
- Based on these computations, it cannot be predicted (but can sometimes be assessed) whether the flow off a transom stern will be a dry-transom or wetted-transom flow. This is a rather unstable process dependent on factors not included in the potential flow model used. For deeply immersed transoms, the dry-transom model that is consistent with inviscid flow may have no solution at all.

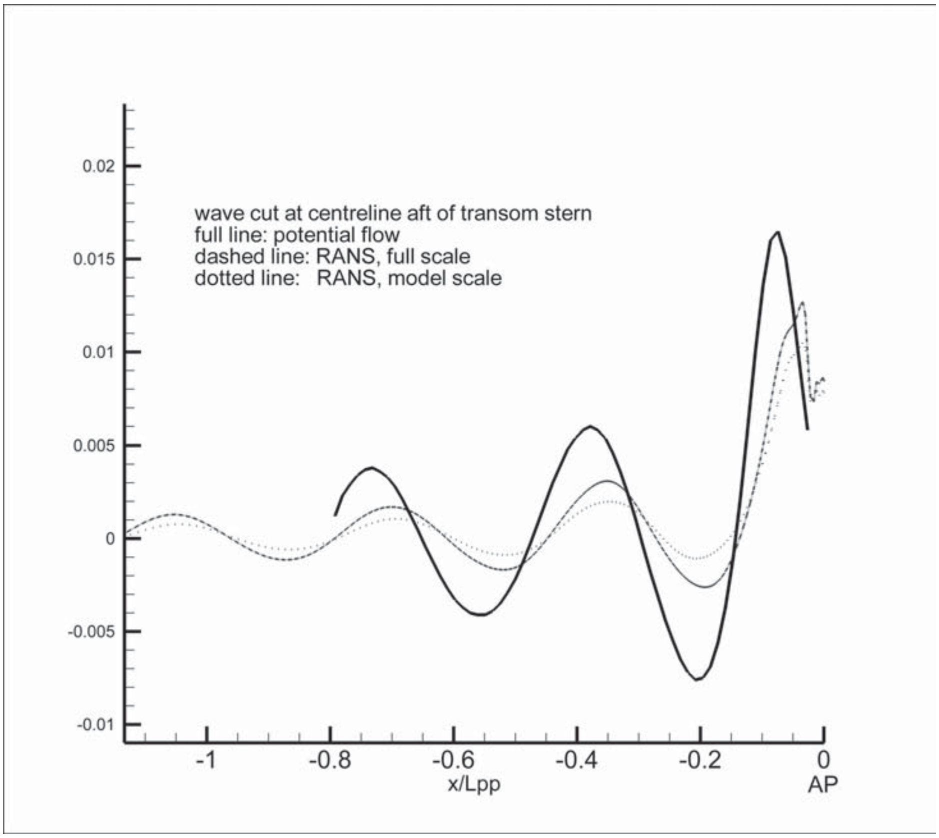

Figure 9.11 Effect of viscosity on stern wave system. Computed longitudinal wave cuts at centerline aft of transom stern for the "Hamburg Test Case" containership; for model scale, full scale, and according to inviscid approximation. From Raven et al. (2008).

- The neglect of wave breaking in potential-flow computations seems no serious omission in most practical cases and still mostly admits a good prediction of the wave pattern. Deviations should occur for cases in which wave breaking occurs close to the hull and dissipates a substantial part of the wave energy. It may even be impossible to produce a converged inviscid solution for cases displaying heavy wave breaking in reality. Otherwise, the computations provide no direct indication on whether or not waves will break, except based on semi-empirical wave steepness criteria.
- Unless planing effects are explicitly modeled, they will probably not be represented accurately.
- In addition, deviations may occur as a result of numerical errors. Insufficient panel densities on the hull cause a poor resistance estimate and a lack of resolution of the pressure distribution. A too coarse free-surface paneling smoothes the wave system, reduces the wave amplitude at a distance from the vessel, and may modify the wave lengths and directions due to the effect called "numerical dispersion." For comparing different variations of a design, the use of similar panel distributions is recommended.

Predicting the inviscid flow past the hull is now a quick and efficient procedure and provides a comprehensive view of the flow properties, but it appears that some aspects are just useful in a comparative sense rather than for performance prediction, for example. As indicated, this is largely fundamental to the basic flow model. Removing the limitations listed primarily requires modeling the viscous effects on the flow and wave making, a topic discussed in Section 9.8. However, provided that the restrictions are duly taken into account and the results are sensibly considered, analyzed, and interpreted, nonlinear free-surface potential flow codes can be very powerful and practical tools in ship design. The use of their predictions will be further discussed in Section 11.5.

9.7 Prediction of the Viscous Flow Around a Body. Having introduced the numerical methods most commonly used for inviscid flow, we will now turn to the viscous flow methods. Referring to Section 9.4, we will first make use of the zonal approach (i.e., to consider the viscous flow independent of the free-surface flow). In Section 9.7, we will thus assume that the free surface is flat, or more precisely a symmetry plane, as in Section 9.5.5. The double-model approach is thus employed in the present section. Then, in Section 9.8, the free surface will be introduced.

9.7.1 Classification of Methods Based on the Navier-Stokes Equations. As explained in Section 2, incompressible fluid flows with constant viscosity are governed by the Navier-Stokes equations (2.13a) to (2.13c) and the continuity equation (2.1), together with relevant boundary conditions (2.14) to (2.21).

In principle, these equations may be solved numerically, but the problem is the required computational effort. To understand the formidable task of solving the Navier-Stokes equations for a full-scale ship, consider the size of the smallest eddies in the flow around the hull and compare their size with the total domain of the flow in which we need to solve the equation (the computational domain). The smallest eddies in the turbulent ship boundary layer are of the order of 0.1 mm; to be able to compute an eddy, it has to be resolved by several grid points in each direction. The step size of the grid must thus be of the order of 0.01 mm. On the other hand, the computational domain needs to be a few ship lengths long and about one ship length wide and deep. To get an order of magnitude estimate, assume that all three dimensions are 100 m. With the resolution just described, this means 10^7 steps in each direction and a total number of grid points of the order of 10^{21}! At present, the achieveable number of grid points is of the order of 10^9. So, with a linear increase in computational effort with number of grid points (the best possible scalability), computers would need to be 10^{12} times faster than today. Now, the resolution does not need to be that high in the entire computational domain, so the requirements are somewhat lower. On the other hand, the number of time steps required will increase one or two orders of magnitude relative to today's computations. Therefore, the estimate is in no way exact, but it reveals the enormous computational power required to solve the Navier-Stokes equations for a ship flow. The same reasoning may also be used for showing that the computational effort for a ship model case is considerably smaller, but still out of reach at present. It is smaller because the absolute size (not relative to the hull size) of the smallest eddies in a ship model boundary layer are of the same order as those of the ship. The computational domain is, however, one to two orders of magnitude (depending on the scale factor) smaller than for the ship in each direction. Solution techniques based on the Navier-Stokes equations without modifications are known as *DNS methods* (see Fig. 9.12).

To obtain manageable computational times, techniques have been developed where the details of the flow are neglected. Obviously, it is not of great interest to know the development of each small eddy (of the order of 0.1 mm) in a ship boundary layer. The larger eddies may however play a more important role, for instance in the prediction of pressure fluctuations, vibrations, and noise. Moreover, the larger eddies are often anisotropic and therefore more difficult to model than the smaller ones, which may be assumed isotropic. Methods where the mean flow and the larger eddies are

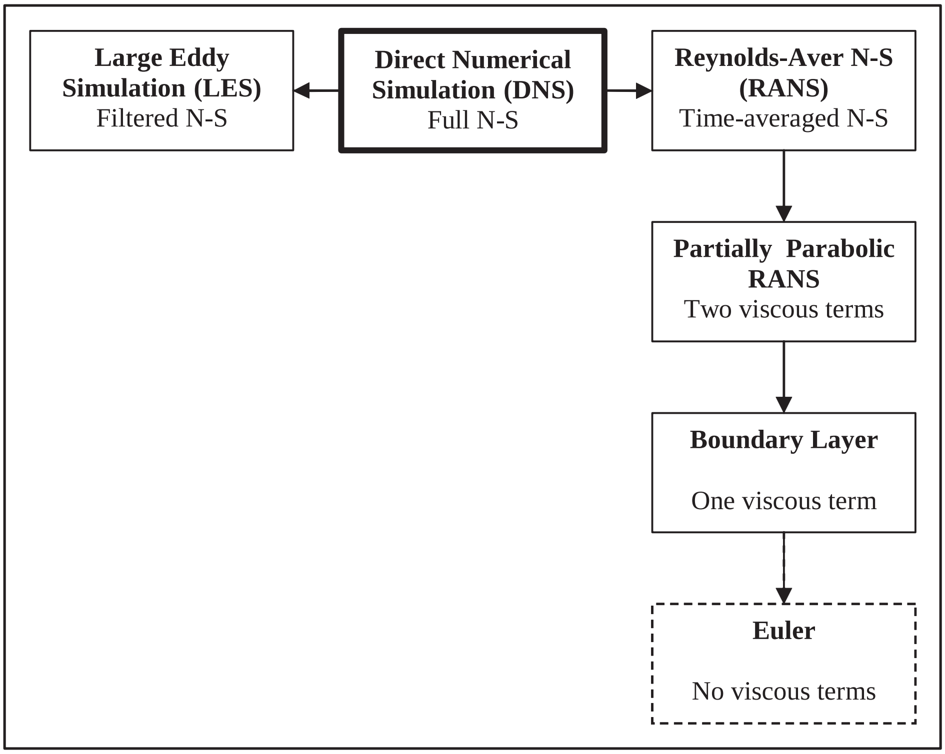

Figure 9.12 Classification of methods used in viscous computational hydrodynamics.

computed, whereas the smaller ones are modeled, are known as *LES methods*. The Navier-Stokes equations now have to be somewhat modified through a filtering process, where eddies smaller than a certain size, the filter width, are removed. When applying the filter to the equations, the nonlinear terms will give rise to additional unknowns, which have to be modeled in some way, so separate equations have to be derived and solved for these quantities. The equations are referred to as *subgrid scale models*.

In general fluid mechanics, there is a strong interest in LES methods and subgrid scale models of increasing complexity are being developed. However, the problem with computations in hydrodynamics is the high Reynolds number, even at model-scale. It is not feasible today to carry out a complete LES calculation for a ship model, and certainly not for a full-scale ship. To accomplish this, the flow close to the hull surface must be treated in a different way. One possibility is to apply wall functions, based on the similarity properties of the flow in this region, as explained in Section 6.3.3. Another possibility is to compute the flow using a RANS method (see later discussion) near the hull and to match this solution to a LES solution further out. The most well known of these *hybrid methods* was proposed by Spalart and Allmaras (1992) and is known as *Detached Eddy Simulation*. In any case, the computational effort is too large for routine applications. For ships, the required effort is of the order of 10^5 CPU-hours. A good survey of LES for high Reynolds number flows is found in Fureby et al. (2003), and an overview of ship hydrodynamic applications is given in Fureby (2008).

To make the equations really useful for practical purposes, one step further has to be taken. All turbulent fluctuations have to be removed and the Navier-Stokes equations solved only for the mean flow. This is achieved through a process where the equations are averaged over a time larger than the largest turbulent scale (but smaller than the scale for mean flow variations). The resulting equations are known as the *RANS equations*. As in the LES equations, additional unknowns, here called the *Reynolds stresses*, appear, and separate equations, the *turbulence model*, are required for these quantities. RANS methods have been the subject of intense research (see Section 1.2.3) over the past 30 years, not least in hydrodynamics, and methods based on this technique are just making their way into the design offices.

In all methods discussed so far, the full Navier-Stokes equations are used, sometimes with additional terms including new unknowns. There are, however, several classes of methods available where terms in the original equations have been dropped. The three second derivatives in the viscous part of the equations may be interpreted as representing the diffusion of momentum in the three different directions. If a typical length scale of the flow is small in one direction, derivatives in this direction are large and the diffusion may be assumed important. The full RANS equations are required if the mean flow scales are small in all three directions, as in a region of 3D separation. However, in a typical 3D attached boundary layer, the scale is small only in the direction normal to the surface. Momentum diffusion may then be neglected in the two directions along the surface, but is important in the third direction. Only one of the viscous terms then has to be retained (in the y-direction). This gives rise to the *boundary layer approximation* of the Navier-Stokes equations. As mentioned in Section 6.2.2, another result of the boundary layer approximation is that the equation in the normal direction degenerates to the simple statement that the normal derivative of the pressure is zero. The pressure is thus constant through the boundary layer.

Because the RANS equations maintain all three viscous terms in the Navier-Stokes equations and the boundary equations retain only one, there are two other possibilities, mentioned here for completeness (see Fig. 9.12). If two terms are maintained, in the normal and girthwise directions, the *partially parabolic approximation* is obtained. This was used in some of the first hydrodynamic Navier-Stokes methods and simplified the solution of the RANS equations because a marching procedure could be applied in the solution. The other possibility is to drop all the viscous terms, which results in the *Euler equations*. These are used both in fluid machinery calculations and in aircraft aerodynamics and are an alternative to the potential flow methods described, which are based on the continuity equation. The problem with both methods is that boundary layers cannot be represented, so some matching to boundary layer solutions is needed close to the boundaries. Euler methods are hardly used at all in hydrodynamics.

By far, the most important technique for viscous flow computations today is the RANS approach. It is relatively accurate, can account for complex flow situations like massive separation and propeller effects, and it can be used for unsteady problems such as cavitation, manoeuvring, and even seakeeping. It is still on the verge of being too computer demanding, at least for unsteady problems, but it is rapidly gaining popularity as a design tool. In the following, we will give brief introduction to the theory of RANS methods. For obvious reasons, this introduction has to be brief. More comprehensive descriptions may be found in textbooks on the subject, like the classical introductory book by Patankar (1980), the very similar but updated one by Versteeg and Malalasekera (1995), or the excellent, more comprehensive one by Ferziger and Peric (1999).

The purpose of the present text is to familiarize the reader with the main concepts related to RANS computations. Whenever a computer code based on the RANS equations is to be applied, the user has a number of choices, which require some background knowledge of these concepts. In the following, they will be introduced under the headings:

- The Reynolds-Averaged Navier Stokes equations
- Turbulence modeling
- Grid
- Discretization
- Boundary conditions

9.7.2 The Reynolds-Averaged Navier-Stokes Equations.

9.7.2.1 COORDINATE SYSTEM AND BASIS VECTORS. As will be seen in Section 9.7.4, the numerical grid used for discretizing the governing equations will be curvilinear, in general. This is so because it is easier to represent the hull boundary conditions in this type of grid than in a Cartesian grid.[*] The fact that the coordinates run along curved lines does not necessarily mean that the basis vectors, to which vector and tensor quantities are referred, have to be aligned with these lines. These basis vectors can be of several different forms: Cartesian, cylindrical, covariant, or contravariant. In the first two cases, the direction of the vectors is constant in space, but in the latter two cases the direction of the vector is determined by the grid. Covariant basis vectors are aligned with the grid lines, but contravariant vectors are at right angles to the coordinate surfaces. In any case, the governing equations have to be transformed, and they will become considerably more complex, involving geometrical quantities related to the curvature of the grid lines. The increase in complexity is particularly large if covariant or contravariant basis vectors are selected. For this reason, Cartesian or cylindrical basis vectors seem to be the most popular choice at present.

The increased complexity is related to the introduction of metrics, representing the stretching of the coordinates. Derivatives of these metrics (up to third order for covariant and contravariant basis vectors) appear in the equations. The basic features of the methods to be described later are however independent of these geometrical complications, so in the following we will assume Cartesian coordinates. Transformation to other systems is described, for instance, in Ferziger and Peric (1999).

9.7.2.2 TIME AVERAGING OF THE NAVIER-STOKES EQUATIONS. To make the Navier-Stokes equations and the continuity equation more compact, Cartesian tensors will be used in the following.[†] This means that vector components are denoted by one index and tensor components by two. Because we are interested in 3D cases the indices run from 1 to 3. The velocity components are represented by u_i, the three coordinate components by x_i and the stress tensor components by σ_{ij}. The most important rule, which makes the equations more compact, is Einstein's summation rule: if an index is repeated in a term, summation from 1 to 3 shall be made with respect to this index.

Now, the Navier-Stokes equations (2.13a) to (2.13c) may be written in a compact form as

$$\frac{\partial u_i}{\partial t} + u_j \frac{\partial u_i}{\partial x_j} = -\frac{1}{\rho}\frac{\partial p}{\partial x_i} + F_i + \nu \frac{\partial^2 u_i}{\partial x_j \partial x_j} \tag{9.38}$$

With the same notation, the continuity equation (2.1) reads

$$\frac{\partial u_i}{\partial x_i} = 0 \tag{9.39}$$

To obtain the final expression for the viscous term in the derivation of the Navier-Stokes equations, it was assumed in Section 2 that the viscous stresses σ_{ij} are proportional to the rate of strain tensor S_{ij}, in other words

$$\sigma_{ij} = \mu S_{ij} \tag{9.40}$$

where μ is the dynamic viscosity and

$$S_{ij} = \frac{\partial u_i}{\partial x_j} + \frac{\partial u_j}{\partial x_i} \tag{9.41}$$

As appears from the derivation in Section 2, this means that

$$\nu \frac{\partial^2 u_i}{\partial x_j \partial x_j} = \frac{1}{\rho}\frac{\partial \sigma_{ji}}{\partial x_j}$$

Using equation (9.39), the second term of equation (9.38) may be expressed as follows

$$u_j \frac{\partial u_i}{\partial x_j} = \frac{\partial}{\partial x_j}(u_j u_i) - u_i \frac{\partial u_j}{\partial x_j} = \frac{\partial}{\partial x_j}(u_j u_i)$$

Equation (9.38) may then be written

$$\frac{\partial u_i}{\partial t} + \frac{\partial}{\partial x_j}(u_j u_i) = -\frac{1}{\rho}\frac{\partial p}{\partial x_i} + F_i + \frac{1}{\rho}\frac{\partial \sigma_{ji}}{\partial x_i} \tag{9.42}$$

We want to rewrite the equations such that all fluctuations arising from turbulence are removed. This is done by averaging the equations over a time larger than the largest scale of the turbulence.[*] The mean values of velocity, pressure, and stress are denoted $\overline{u}_i$, $\overline{p}$, and $\overline{\sigma}_{ij}$, respectively, whereas the instantaneous deviations from the mean are u_i', p', and σ_{ij}'. F_i is assumed constant. Thus,

$$u_i = \overline{u}_i + u_i' \qquad p = \overline{p} + p' \qquad \sigma_{ij} = \overline{\sigma}_{ij} + \sigma_{ij}' \tag{9.43}$$

Introduce equation (9.43) in (9.42) and time-average the whole equation!

$$\begin{aligned} &\frac{\overline{\partial \overline{u}_i}}{\partial t} + \frac{\overline{\partial u_i'}}{\partial t} + \overline{\frac{\partial}{\partial x_j}(\overline{u}_j \overline{u}_i)} + \overline{\frac{\partial}{\partial x_j}(\overline{u}_j u_i')} + \\ &\overline{\frac{\partial}{\partial x_j}(u'_j \overline{u}_i)} + \overline{\frac{\partial}{\partial x_j}(u_j' u_i')} = \\ &-\frac{1}{\rho}\frac{\overline{\partial \overline{p}}}{\partial x_i} - \overline{\frac{1}{\rho}\frac{\partial p'}{\partial x_i}} + F_i + \frac{1}{\rho}\frac{\overline{\partial \overline{\sigma}_{ji}}}{\partial x_j} + \frac{1}{\rho}\frac{\overline{\partial \sigma_{ji}'}}{\partial x_j} \end{aligned} \tag{9.44}$$

---

[*] Cartesian, non–boundary-fitted grids are indeed used in some methods especially in aerodynamics, but their lack of ability to resolve the flow very close to a no-slip wall makes them unsuitable for viscous flow computations. They may work well, however, for Euler methods. Overlapping grid methods often use Cartesian background grids, in which the body-fitted grids are embedded.

[†] For a short introduction to Cartesian tensors, see Wilcox (1998).

[*] Note that this time-averaging is not unambiguous. By filtering out time variations arising from turbulence, variations of the mean flow may also disappear. This may render unsteady RANS computations uncertain, particularly for flows with rapid changes, such as cavitating flows. A more rigorous approach is to use ensemble averaging (see Wilcox, 1998).

Note that the time-average of the fluctuations u', p', and σ_{ij}' is zero by definition. This holds also for their derivatives. We thus have

$$\frac{\partial \overline{u}_i}{\partial t} + \frac{\partial}{\partial x_j}(\overline{u}_j\overline{u}_i) + \frac{\partial}{\partial x_j}(\overline{u_j'\,u_i'}) = -\frac{1}{\rho}\frac{\partial \overline{p}}{\partial x_i} + F_i + \frac{1}{\rho}\frac{\partial \sigma_{ji}}{\partial x_j} \tag{9.45}$$

Here we have used the fact that the average of the derivative of a quantity is equal to the derivative of its average.

Note that equation (9.45) is very similar to equation (9.42). Except that the instantaneous values of equation (9.42) have been replaced by the averaged values in equation (9.45), there is only one new term: the third term. The reason for the appearance of this term is nonlinearity. For all linear terms, the fluctuating contribution disappears in the averaging process, but the nonlinear term of equation (9.42) gives rise to a non-zero product of fluctuating contributions.

As the new term contains derivatives with respect to the same variable as the stress term, it is tempting to combine them. This yields

$$\frac{\partial \overline{u}_i}{\partial t} + \frac{\partial}{\partial x_j}(\overline{u}_j\overline{u}_i) = -\frac{1}{\rho}\frac{\partial \overline{p}}{\partial x_i} + F_i + \frac{1}{\rho}\frac{\partial}{\partial x_j}(\sigma_{ji} + R_{ji}) \tag{9.46}$$

where

$$R_{ji} = R_{ij} = -\rho\overline{u_i'u_j'} \tag{9.47}$$

Equation (9.46) is the basis for methods of the RANS type. We have removed the turbulent fluctuations from the equations, but we have introduced a new quantity R_{ij}, which is unknown and must be modelled. R_{ij} is a correlation between two fluctuating velocity components, but appears in the equations in the same way as σ_{ij}, and may therefore be interpreted as an additional stress, known as the Reynolds stress. Like σ_{ij}, R_{ij} is symmetric and contains six independent components. In order to compute these, a turbulence model is required.

Unlike the Navier-Stokes equations, no new terms are introduced when time-averaging the continuity equation (9.39). Because the equation is linear, all turbulent contributions will disappear and the equation looks as before, but with the instantaneous velocities replaced by the mean values.

$$\frac{\partial \overline{u}_i}{\partial x_i} = 0 \tag{9.48}$$

We will return to the question of boundary conditions for equations (9.46) and (9.48) in connection with the discretization.

9.7.3 Turbulence Modeling. Turbulence modeling has been one of the most important research areas of fluid mechanics in the past 40 years, and a large number of models have been proposed. An excellent overview is found in Wilcox (1998). All turbulence models include empirical constants and no model capable of generating accurate results for all possible conditions has been developed. The best models work well for certain classes of flows, but less well for others. To obtain the best possible accuracy, different turbulence models must be tested for the type of problem at hand. In ship hydrodynamics, this has been the topic of the series of international workshops held approximately every 5 years since 1990 (Hino, 2005; Kodama et al., 1994; Larsson, Patel, & Dyne, 1991; Larsson, Stern & Bertram, 2002, 2003).

In the following, we will give a brief introduction to five classes of turbulence models:

- Zero-equation models, in which no transport (differential) equation is used for turbulent quantities
- One-equation models, based on one transport equation for turbulence
- Two-equation models with two transport equations
- Algebraic stress models (ASM)
- Reynolds stress models (RSM)

The basis for the first three models is the classical *Boussinesq assumption* (Boussinesq, 1877).

9.7.3.1 THE BOUSSINESQ ASSUMPTION. The Boussinesq assumption is perhaps the most important approximation in turbulence theory. It is assumed that the Reynolds stresses R_{ij} can be computed from the rate of strain tensor S_{ij} in the same way as the viscous stresses, the only difference being that the molecular viscosity μ is now replaced by a turbulent equivalent μ_T. Because the viscous stresses arise from molecular mixing, it is thus inherently assumed that the turbulent mixing resembles the molecular mixing. However, whereas μ is a physical constant, the turbulent viscosity μ_T is unknown and must be computed at every point in the flow.

Because S_{ii} is zero according to the continuity equation, R_{ii} would be zero as well, without further assumptions. But according to equation (9.47)

$$R_{ii} = -\rho\overline{u_i'u_i'} \tag{9.49}$$

and $\overline{u_i'u_i'}$ may be interpreted as twice the turbulent kinetic energy k per unit of mass. Therefore,

$$R_{ii} = -2\rho k \tag{9.50}$$

so the Boussinesq assumption may be written

$$R_{ij} = \mu_T S_{ij} - \frac{2}{3}\rho k\delta_{ij} \tag{9.51}$$

where δ_{ij} is the Kronecker delta.*

$$\delta_{ij} = \begin{cases} 1 \text{ for } i = j \\ 0 \text{ for } i \neq j \end{cases} \tag{9.52}$$

To describe turbulence, one velocity scale, ϑ, and one length scale, l, must be known. Because, according to

---

*Note that $\delta_{ii} = \delta_{11} + \delta_{22} + \delta_{33} = 3$, which explains the factor 3 in the denominator of the second term of equation (9.51).

equation (9.51), μ_T shall have the dimension $[kg/(m \cdot s)]$, dimensional analysis shows that

$$\mu_T = const \cdot \rho \vartheta l \tag{9.53}$$

9.7.3.2 Zero-Equation Models. In the zero-equation models, turbulent quantities are computed using algebraic equations and they are therefore often referred to as algebraic models. The most common approach is the mixing length models, where the length scale is prescribed analytically (for instance as a function of the distance to the wall) and the velocity scale is computed as the length scale times the dominant velocity gradient. Mixing length models were developed for thin shear layers, notably boundary layers, where the only important derivative of the velocity vector is that in the direction normal to the surface. These models work well for thin attached boundary layers, and a special development, the Baldwin-Lomax model (Baldwin & Lomax, 1978), became very popular in aerodynamics for many years, particularly for predicting the flow around wings. The Baldwin-Lomax model was used to a considerable extent also in ship hydrodynamics in the first RANS methods, and at the CFD Workshop in Tokyo in 1994 (Kodama et al., 1994), some good results were presented. However, a closer analysis revealed that limiters used in the method actually helped predicting the wake for the test cases. More advanced models are needed to predict the complex flows around a ship stern.

9.7.3.3 One-Equation Models. Over the years, a number of turbulence models have been proposed where one transport equation is solved for k (Wilcox, 1998). The velocity scale ϑ may then be determined as $k^{1/2}$,which has the dimension $[m/s]$. The length scale l in these one-equation models is prescribed analytically, as in the zero-equation models. No method of this kind has become popular, most likely due to the requirement for prescribing l.

A different kind of one-equation model was proposed by Spalart and Allmaras (1992). Rather than computing the turbulent viscosity μ_T from the length and velocity scales, they devised a transport equation for a quantity ν, closely related to μ_T directly. This model has become rather popular in recent years, also for ship flows, and some notably good wake predictions have been made using the model (see the Workshop results in Hino, 2005; Larsson, Stern, & Bertram, 2002, 2003). The model does, however, contain eight empirical constants, and the good wake results were obtained by varying one of the constants. One way of doing so is to apply a correction for vortical flows, devised by Dacles-Mariani et al. (1995). An interesting feature of the Spalart-Allmaras model is that it can be used also in Detached Eddy Simulation methods, where RANS is used in the boundary layer and LES in the outer flow.

9.7.3.4 Two-Equation Models. The most common of all turbulence models in the past 30 years has been the two-equation $k - \varepsilon$ model (Jones & Launder, 1972) in which one transport equation for the turbulent kinetic energy per unit mass, k, and one for its rate of dissipation, ε, are solved. Because k has the dimension $[m^2/s^2]$, ε must have the dimension $[m^2/s^3]$. The length scale l may thus be defined as $k^{3/2}/\varepsilon$ and because the velocity scale ϑ may be set as $k^{1/2}$, equation (9.53) may be written

$$\mu_T = const \cdot \rho \frac{k^2}{\varepsilon} \tag{9.54}$$

The $k - \varepsilon$ model has been enhanced in several ways, for instance using Renormalization Group Theory (Yakhot et al., 1992). By remodeling some of the terms in the equations, the "realizable" $k - \varepsilon$ model was developed by NASA (Shih, Zhu, & Lumley, 1992). In ship hydrodynamics, the $k - \varepsilon$ model and its variants have always been a popular choice. At all workshops, there has been a number of methods employing this model. However, it has become increasingly clear that the detailed features of the ship wake cannot be obtained in this way. The wake contours, which are often quite irregular, are smoothed out. It is well known from other fluid mechanics applications that this model is not suitable for flows with strong streamwise vorticity, and as we have seen in Section 6.7.2, the ship wake is dominated by such vorticity, generated at the aft bilges, at least for full-bodied ships. Therefore, a somewhat different approach, the $k - \omega$ model, has gained in popularity. This will now be described.

Rather than solving for the dissipation rate ε directly, an equation for the specific dissipation rate $\omega = \varepsilon/k$ is solved. The physical significance of ω has been a matter for discussion for a long time and a good review is given in Wilcox (1998). We will not repeat this discussion here. It is sufficient to note that the $k - \omega$ model has shown superior performance when predicting ship flows, as compared to the $k - \varepsilon$ model. Replacing the dynamic viscosities μ and μ_T by their kinematic equivalents

$$\nu = \frac{\mu}{\rho} \qquad \nu_T = \frac{\mu_T}{\rho} \tag{9.55}$$

the equations in the $k - \omega$ model are as follows

$$\nu_T = \frac{\mathrm{k}}{\omega} \tag{9.56}$$

$$\begin{gathered}\frac{\partial k}{\partial t} + \overline{u}_j \frac{\partial k}{\partial x_j} = \frac{\tau_{ij}}{\rho} \frac{\partial \overline{u}_i}{\partial x_j} - \beta * k\omega + \\ \frac{\partial}{\partial x_j}\left[(\nu + \sigma * \nu_T) \frac{\partial k}{\partial x_j}\right]\end{gathered} \tag{9.57}$$

$$\begin{gathered}\frac{\partial \omega}{\partial t} + \overline{u}_j \frac{\partial \omega}{\partial x_j} = \alpha \frac{\omega}{k} \frac{\tau_{ij}}{\rho} \frac{\partial u_i}{\partial x_j} - \beta\omega^2 + \\ \frac{\partial}{\partial x_j}\left[(\nu + \sigma \nu_T) \frac{\partial \omega}{\partial x_j}\right]\end{gathered} \tag{9.58}$$

The empirical constants are as follows

$\alpha = 5/9 \quad \beta = 3/40 \quad \beta^* = 9/100 \quad \sigma = 1/2 \quad \sigma^* = 1/2$

Note that the structure of the two transport equations (9.57) and (9.58) is quite similar to that of the momentum equation (9.46).

One difficulty with the ω equation is that it is hard to define a robust boundary condition at the outer edge. On the hull surface, ω goes to infinity, but this problem can be handled in different ways, as will be seen in Section 9.7.6. Because ε has a well-defined value at the boundary layer edge, Menter (1993) proposed a blending of the two transport equations such that the resulting equation represents only ω at the surface and only ε outside of the boundary layer. This modification of the original method is referred to as the Baseline (BSL) $k - \omega$ model. Menter also suggested a further modification of the BSL model, by which an improved prediction of the principal shear stress is obtained in adverse pressure gradients. This is known as the Shear Stress Transport (SST) model.

9.7.3.5 ALGEBRAIC STRESS AND REYNOLDS STRESS MODELS. The Boussinesq assumption, which is the basis for all models described so far, has had a tremendous importance for turbulence modeling and most RANS calculations carried out rest on this approximation. However, the basic assumption that the stress tensor is proportional to the rate of strain tensor* is questionable. The relation is true for viscous stresses, created by molecular activity, but it is not generally true for turbulent stresses, which depend on turbulent fluctuations influenced, for instance, by history effects, presence of boundaries, and free-stream turbulence. Therefore, many attempts have been made to improve the assumption, and in the most advanced methods, it has been abandoned altogether.

A logical way of extending the Boussinesq assumption is to include nonlinear terms in the constitutive relation (9.51). Such terms may include not only the mean rate of strain tensor $\overline{S}_{ij}$, [see equation (9.41)], but also the mean rotation tensor Ω_{ij}, defined as

$$\overline{\Omega}_{ij} = \frac{\partial \overline{u}_i}{\partial x_j} - \frac{\partial \overline{u}_j}{\partial x_i} \tag{9.59}$$

A nonlinear $k - \varepsilon$ model attributed to Craft, Launder, and Suga (1996) was tested by Svennberg (2001) for ship stern flow and a considerable improvement was obtained, relative to the conventional model. This approach has not been much used in ship hydrodynamics, however.

One result of the effort to develop nonlinear models is the ASMs. These are based on transport equations for the individual Reynolds stresses and each partial derivative with respect to the stresses is modelled algebraically. A nonlinear set of algebraic equations then evolves, not necessarily including turbulent viscosity. The complexity of the equations depends on the modeling and the models normally include k and either ε or ω. The ASMs thus have to be used in connection with a two-equation model. A particularly successful ASM developed in recent years is that reported by Deng, Queutey and Visonneau (2005). At the Tokyo workshop in 2005 (Hino, 2005), this model performed almost as well as the full Reynolds stress model (Fig. 9.13). This ASM uses k and ω from the $k - \omega$ BSL model as described.

In the Reynolds stress (RSM) models, transport equations for each of the six Reynolds stress components are solved. Further equations are required because many of the terms in the equations have to be modeled. Most often, the modeled equations contain k and ε, which means that one additional equation (for ε) has to be included. k can be obtained directly from the normal Reynolds stresses. The most recent development of RSMs for ship flows is reported in Deng, Queutey and Visonneau (2005). Because these models represent the physics better than the other models described, they can be expected to be more accurate. Although the ASM are very close, this has indeed been the case in all investigations known to the authors, where these models have been compared with others (see, for instance, Hino, 2005; Larsson, Stern, & Bertram, 2002, 2003; Svennberg, 2001). The disadvantage of the RSMs is the increased computational effort caused not only by the need for solving more equations, but also by the loss in stability of the solution procedure. In many cases, it may be difficult to make the iterative solution procedure converge at all, and even if the iterations converge, the rate is normally slower than for other turbulence models.

Fig. 9.13 shows a comparison between predictions of the stern flow of a full-bodied tanker using three different turbulence models: a Reynolds stress model, an explicit ASM, and the $k - \omega$ SST model. Measured data are also shown at the top. The results are from the Tokyo workshop in 2005 (Hino, 2005) and were all obtained by the same group from Ecole Centrale de Nantes using the same numerical method and the same grid of about 3M cells. Of interest are the details of the flow in the central part of the wake (i.e., the propeller disk). Comparing the predicted wake contours with the measured ones, it is seen that the RSM results are most detailed and rather accurate. Some smoothing may be seen in the ASM results, which are still quite good. The SST results are less detailed.

The wake contours around the same hull were discussed in Section 6.7.2. Because the propeller operates in the region with the most "hooked" contours, the exact shape of the contours is important for the designer. In fact, an experienced ship designer can move the bilge vortex, creating the contours, to a position where the flow into the propeller is optimum (see Section 11.4.1). Today, numerical methods are often used for this purpose.

A discussion of the boundary conditions for the turbulence transport equations will be given in connection with the discretization scheme.

9.7.4 Grid. For the numerical solution of the momentum and continuity equations (9.46) and (9.48), as well as of turbulence equations such as (9.57) and (9.58), most numerical methods will require a grid on

---

*This means that the principal axes of one tensor coincide with the corresponding ones of the other tensor.

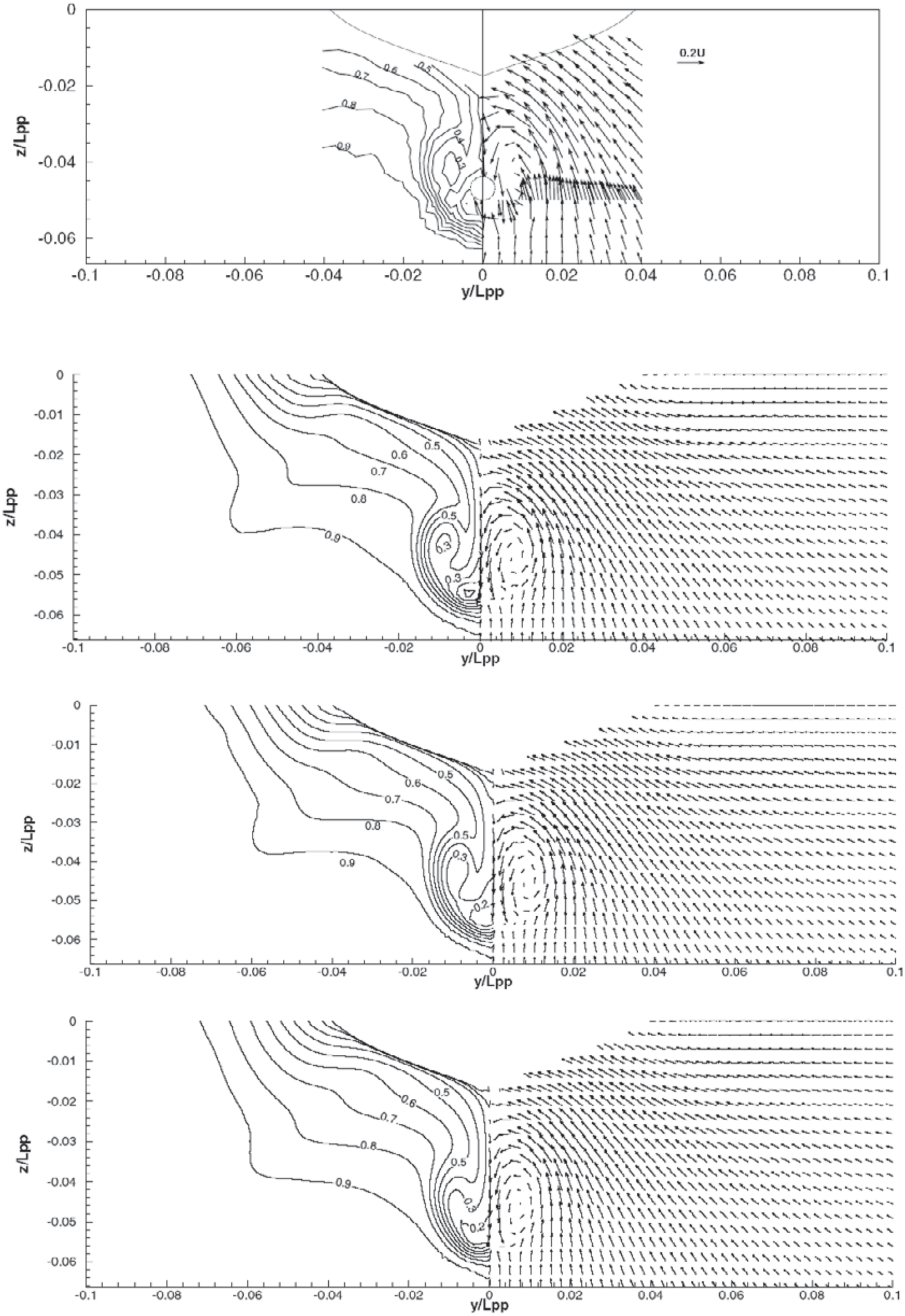

Figure 9.13 Wake contours (*left*) and cross-flow velocity vectors (*right*) in the propeller plane of a VLCC (Hino, 2005; courtesy of the author). *Top*: Experiments; *second from top*: Reynolds stress model; *second from bottom*: ASM; *bottom*: $k - \omega$ SST model.

which the continuous equations can be discretized. The whole computational domain must be covered by the grid and in the discretized equations, values of the dependent variables will be the computed at the grid nodes. There are two main types of grids: *structured* and *unstructured*. In both cases, the entire grid may consist of only one block—*single block grids*—or it may be divided into two or more grid blocks—*multiblock grids*. For the multiblock grids, combinations of structured and unstructured blocks may be used as well.

9.7.4.1 SINGLE-BLOCK STRUCTURED GRIDS. In a 3D structured grid, each grid point may be uniquely defined by a triplet of indices (i, j, k), where each index runs from 1 and upward along a grid line, defined by constant values of the two other indices. This logical structure of the points simplifies the programming and leads to a banded structure of the matrix in the numerical solution procedure, as will be seen. Because there are very efficient solution procedures for banded matrices, this is a great advantage.

Fig. 9.14 shows a single block structured grid of a VLCC. The grid is enclosed in a cylindrical domain with a radius of 1.5 hull lengths from the centerline. A symmetry plane represents the free surface, and the cylinder is truncated 0.8 hull lengths in front of and behind the hull. The inner surface of the grid is the hull itself. It is seen that the organization of the grid points, at the intersection between the grid lines, is very regular. There are three families of grid lines: in the longitudinal, radial, and girthwise directions, respectively, and in each one of them the lines run smoothly from one boundary to the opposite one without intersecting.

Note that the longitudinal grid lines are concentrated close to the hull and the radial lines near the bow and stern, where the variations in flow quantities are largest. Close to the hull the inner part of the boundary layer has to be resolved very accurately. The grid shown has been coarsened for clarity and contains only about 30,000 cells whereas real grids normally contain at least a million cells.

If i, j, k are the indices running along the lines in the longitudinal, radial, and girthwise directions, respectively, the grids in the i, j-planes will be of H-type (i.e., both families of lines will run from one boundary to the opposite one), together forming an H-pattern. However, the grids in the j, k-planes will be of the O-type. The k-lines are thus halves of deformed circles surrounding the hull (the free surface is a symmetry plane). Grids of the type shown Fig. 9.14 are called H-O grids and are the most common ones in ship hydrodynamics. Other types do exist, however. In O-O grids, the i-lines are closed loops around the hull; in C-O grids, the i-lines form a C-shape around the bow (i.e., they start at the downstream boundary, run upstream around the bow, and back to the exit plane). The advantage of the H-O grids is that the flow is more or less aligned with the i-lines, which may reduce numerical diffusion, as will be seen later. For O-O and C-O grids, the flow is more at right angles to the grid lines at the bow, and the same hold for the stern in case of the O-O grids. The disadvantage of the H-O grids is that they contain singularity points on lines downstream of the stern and upstream of the bow. At such points, the curvature of the j-lines is infinite, which may cause difficulties in the numerical solution.

9.7.4.2 MULTIBLOCK STRUCTURED GRIDS. The advantage of the structured grids is that they are computationally efficient. The disadvantage is that it is very difficult to represent complex boundaries. For instance, it is almost impossible to incorporate appendages on a hull, such as

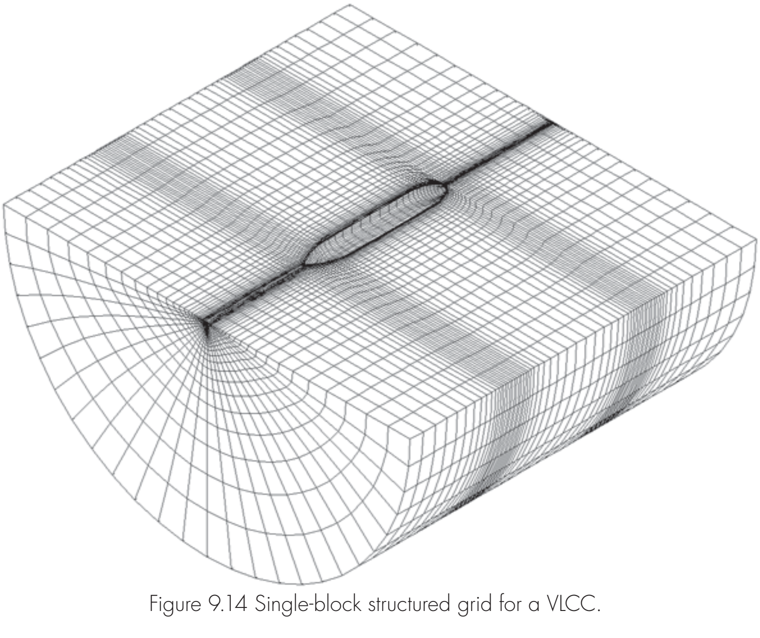

Figure 9.14 Single-block structured grid for a VLCC.

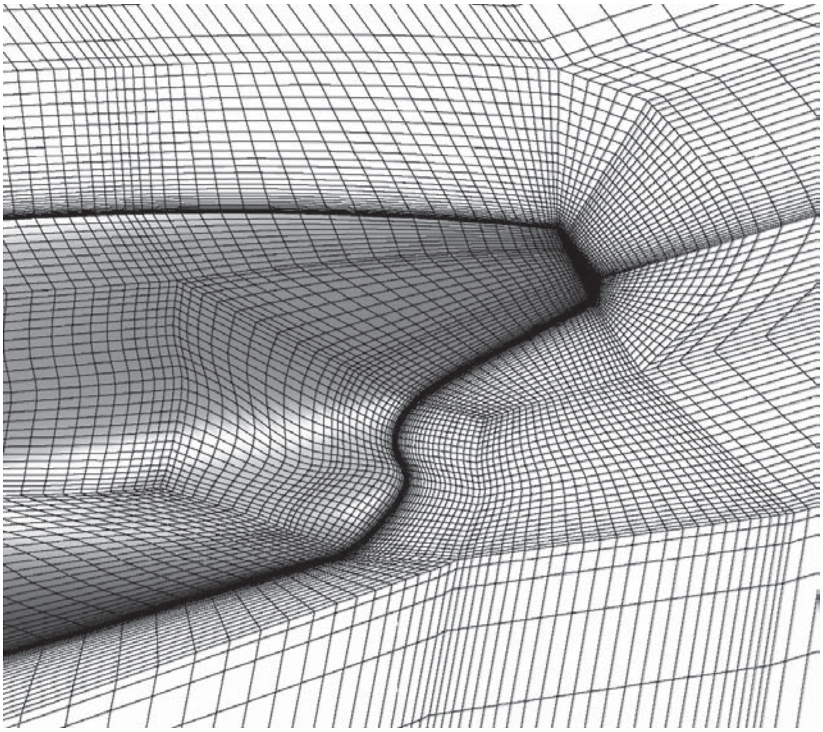

Figure 9.15 Multiblock structured grid for a VLCC (Bull, 2005; courtesy of the author).

fins, brackets, or shafts. Rudders, placed in the symmetry plane, may be somewhat easier to include, but even that is difficult. If the grid is divided into different blocks, the flexibility is increased. A typical example of a multiblock structured grid is shown in Fig. 9.15. It is the same hull as in Fig. 9.14, but only a close-up of the stern region is presented, and for clarity only the boundaries (hull and symmetry planes) are shown. At the block intersections, the grid density and the direction of the gridlines change abruptly. In the present grid, the lines from both sides of a common boundary match each other, but this condition may be relaxed. It is possible to develop techniques for conserving flow quantities, even without this match (Ferziger & Peric, 1999). To handle the multiblock grids, a more complex solution technique is required.

9.7.4.3 Overlapping Grids. Even larger flexibility is offered if the different blocks are allowed to overlap. Grid components may then be generated around each part of a complex boundary, for instance around a rudder, fin, bracket, or shaft outside a hull. Complex regions of the hull itself may also be covered by several overlapping grids. The body-fitted, curvilinear component grids may be immersed into one or more Cartesian background grids. Fig. 9.16 shows an overlapping grid around the stern of a tanker hull. As in Fig. 9.15, only the boundaries are shown. Several overlapping body-fitted grids are used to accurately represent the stern shape, and these grids are immersed into a background grid with several levels of refinement.

As for the "butt-joined" multiblock grids, the interaction between the grid components has to be taken care of by the solution algorithm. The demands are larger, however, on an overlapping grid. Another disadvantage is that it is difficult to ensure conservation across overlapping grid boundaries.

9.7.4.4 Unstructured Grids. In structural mechanics, unstructured grids are used almost exclusively, in

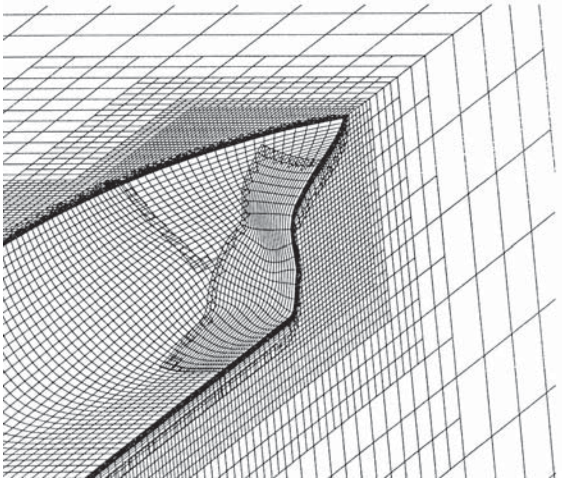

Figure 9.16 Overlapping grids around the stern of a tanker (Regnström, Broberg, & Larsson, 2000).

combination with finite element numerical solvers. So far, this technique has not reached the same popularity in fluid mechanics, and particularly not in hydrodynamics. Here single or multiblock structured grids dominate, but there is an increasing interest in unstructured techniques, mainly in connection with finite volume solvers. The major advantage of unstructured grids is flexibility. It is considerably easier to fit an unstructured grid to a complex boundary, and automatic grid generation techniques are well developed. Further, the waste of cells in bands where a large density is not required (see Fig. 9.14) is avoided. The disadvantage is the irregular data structure. The connectivity between the cells as well as their location has to be stored and the solution matrix loses its diagonal structure, which increases the computational effort. Another disadvantage is the larger numerical diffusion associated with this type of grid.

An example of an unstructured grid is shown in Fig. 9.17. It shows one cross-section of a grid around a frigate. The hull is seen at the top right corner, and the undisturbed free surface is in the middle of the dense spacing of the horizontal lines. Computations are to be carried out using the free-surface capturing method, to be explained later, and the grid extends above the undisturbed surface. Note that close to the boundaries, where a very high resolution in the normal direction is required, a structured grid is used. A high enough resolution in this region can hardly be achieved with a completely unstructured grid, but other techniques based on prisms in the normal direction are also used. The grid shown is based on planes of constant x, even for the unstructured part. Grid cells in this plane are triangles. In a completely unstructured grid, the cells are most often tetrahedra, and are not aligned with cross-sections.

9.7.5 Discretization.

9.7.5.1 THE GENERAL TRANSPORT EQUATION. The RANS equations (9.46) and the two turbulence equations (9.57) and (9.58) may be written in a common format

$$\frac{\partial \phi}{\partial t} + \frac{\partial}{\partial x_i}(u_i \phi) = \frac{\partial}{\partial x_i}\left(\Gamma \frac{\partial \phi}{\partial x_i}\right) + S \qquad (9.60)$$

where ϕ is the general dependent variable (i.e., u_i, k, or ε), Γ is a generalized diffusion coefficient, and S* is a source term. The definitions of Γ and S are linked to the dependent variable and differ considerably between the RANS equations and the turbulence equations. Subsequently, the overbar is dropped for mean quantities.

Equation (9.60) is a general transport equation for the quantity ϕ. Referring to an infinitesimal fluid element, it may be interpreted as

Rate of increase of ϕ + Net rate of flow of ϕ out = Rate of increase of ϕ due to diffusion + Rate of increase of ϕ due to sources

The first term is only relevant for unsteady problems, and most flows in ship hydrodynamics are indeed unsteady. However, when computing the calm water resistance of a ship, the flow may be considered steady,

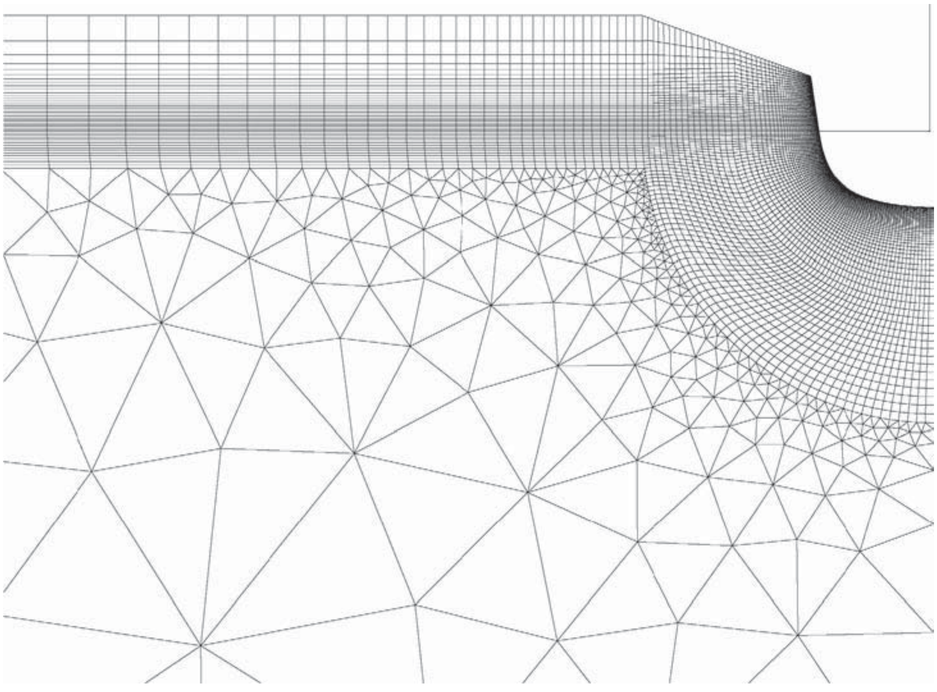

Figure 9.17 Unstructured grid around a frigate (Deng, Guilmineau, Queutey, & Visonneau, 2005; courtesy of the authors).

---

*This scalar is not to be mixed up with the rate of strain rate tensor S_{ij} defined in equation (9.41)!

as has been seen in connection with the potential flow methods. Then the first term is zero. The second term represents the effect of *convection* of the fluid quantity of interest (i.e., the transport of the quantity by the velocity of the fluid).

On the right-hand side, the first term expresses the effect of *diffusion* of the quantity. In theory, this diffusion is only because of molecular motions, but as we have introduced the Reynolds stresses in previous equations, the diffusion by the macroscopic turbulent motions should be included as well. The convection is thus, in our approximation, only due to the mean velocities. Sources in the fluid element represent mechanisms for producing the quantity in question. A negative sign means that the quantity is destroyed.

In the following, we shall look at the numerical solution of equation (9.60), which has several important properties.

First, equation (9.60) is *nonlinear*. In the convective term, the transported quantity ϕ is multiplied by the unknown velocity u_i.* To resolve this problem, iterations are required. By far, the most common technique is *Picard linearization*, where the required velocity is taken from a previous iteration.† This technique will be adopted in the following.

Second, convection and diffusion are two very different physical processes, and the numerical approximation has to reflect these differences. Although information can only be transported in the flow direction by convection, it is transported in all directions, even upstream, by diffusion. As we will see, the relative importance of these two transport mechanisms will have an impact on the discretization scheme.

Third, in the RANS equations, the source terms include the pressure gradient, which causes a problem because there is no explicit equation for the pressure. If the continuity equation is introduced, there are indeed as many equations (six) as there are unknowns (u_1, u_2, u_3, p, k, ε), so the system of equations is closed, but the fact that the continuity equation does not include pressure causes a major problem in the numerical solution. Different means for overcoming this problem will be discussed in Section 9.7.5.3, but first we will discuss the discretization of the linearized equations.

9.7.5.2 DISCRETIZATION OF THE CONVECTION-DIFFUSION EQUATION. The problems associated with the numerical solution of convection-diffusion problems may be explained by considering a simple 1D case. Because the time derivative and the source term do not influence the particular behavior of interest, they may be dropped as well. Here, we will start with this simplified problem, thereafter generalizing to the fully 3D case.

After introducing the simplifications, equation (9.60) reads

$$\frac{d}{dx}(u\phi) = \frac{d}{dx}\left(\Gamma\frac{d\phi}{dx}\right) \tag{9.61}$$

This has to be solved together with the continuity equation

$$\frac{du}{dx} = 0 \tag{9.62}$$

The notation used in the following is defined in Fig. 9.18. P represents the node point in the control volume where the equation is to be discretized and W and E the west and east neighboring nodes. w and e represent the west and east faces of the control volume and the δs stand for distances, as seen in Fig. 9.18. A is the cross-section of the control volume. The task is to derive a formula relating ϕ at P, ϕ_P, to ϕ at W and E, ϕ_W and ϕ_E, respectively.

Two different techniques dominate in hydrodynamic CFD to link the nodal values. In the *finite difference* techniques, the derivatives in the governing equations are replaced by finite difference approximations derived from Taylor expansions of the unknown function [see the derivation of the order of accuracy below, equations (9.77) and (9.78)]. In the *finite volume* methods, on the other hand, the nodes are linked through integration of the equations over each grid cell (control volume). At the most recent hydrodynamics CFD workshop (Hino, 2005), approximately two-thirds of the methods belonged to the second category, and this is also the most common technique in commercial CFD software, so it will be adopted here. It is interesting to note that the *finite element* technique, which completely dominates in structural mechanics, is very little used in CFD, particularly in hydrodynamics. No finite element method has been used in any of the four hydrodynamic CFD workshops since 1990.

Integrating equation (9.61) over the 1D control volume yields

$$(uA\phi)_e - (uA\phi)_w = \left(\Gamma A\frac{d\phi}{dx}\right)_e + \left(\Gamma A\frac{d\phi}{dx}\right)_w \tag{9.63}$$

and equation (9.62) gives

$$(uA)_e - (uA)_w = 0 \tag{9.64}$$

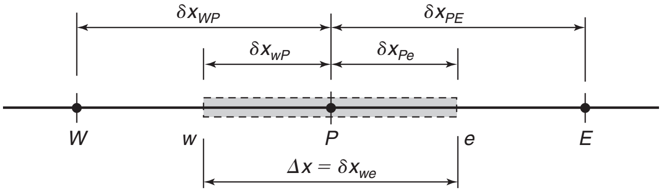

Figure 9.18 Notation for 1D convection-diffusion problem.

---

*Under some circumstances, the flow may be assumed uninfluenced by the transported quantity ϕ. This may hold, for instance, for chemical species in a pollution problem. Then the flow may be computed first and the known velocities introduced in the transport equation for ϕ. This equation is then linear.

†More rapid convergence is obtained using Newton linearization (Ferziger & Peric, 1999), but the equations become considerably more complex.

Now, define two quantities representing the volume flux per unit area, F, and the diffusion conductance, D, respectively

$$F = u \qquad D = \frac{\Gamma}{\delta x} \tag{9.65}$$

Because the governing equations (9.46) and (9.48) are written in Cartesian coordinates, the cross-sectional area A is inherently assumed constant along the control volume.* Equations (9.63) and (9.64) may now be written

$$F_e\phi_e - F_w\phi_w = D_e(\phi_E - \phi_P) - D_w(\phi_P - \phi_W) \tag{9.66}$$

and

$$F_e - F_w = 0 \tag{9.67}$$

where the x-derivatives in the diffusion terms of equation (9.63) have been obtained by a central finite difference approximation (see later) of the values at two neighboring node points. F_e and F_w are assumed known, normally from a previous iteration.

In order to link ϕ_P to ϕ_W and ϕ_E, the values of ϕ at the west and east boundaries, ϕ_w and ϕ_e, must be calculated. Several different schemes for this interpolation have been proposed. Here, we will take a look at the three most common ones.

Central differencing means that the function is approximated as a straight line between two points, one on each side of the point where the function is to be evaluated. This approach was used for approximating the derivative in the diffusion terms. It seems natural to apply the same approximation for obtaining ϕ_w and ϕ_e, in the convective terms. For constant grid spacing, we get

$$\phi_w = (\phi_W + \phi_P)/2 \tag{9.68}$$

and

$$\phi_e = (\phi_P + \phi_E)/2 \tag{9.69}$$

If this is inserted into equation (9.66), the following expression is obtained

$$\begin{aligned} F_e(\phi_P + \phi_E)/2 - F_w(\phi_W + \phi_P)/2 \\ = D_e(\phi_E - \phi_P) - D_w(\phi_P - \phi_W) \end{aligned} \tag{9.70}$$

Collecting the coefficients in front of ϕ_P, ϕ_W, and ϕ_E, this relation may be written

$$a_P\phi_P = a_W\phi_W + a_E\phi_E \tag{9.71}$$

where

$$a_W = D_w + \frac{F_w}{2} \tag{9.72}$$

$$a_E = D_e - \frac{F_e}{2} \tag{9.73}$$

$$a_P = a_W + a_E + (F_e - F_w) \tag{9.74}$$

or, using equation (9.67),

$$a_P = a_W + a_E \tag{9.75}$$

To solve equation (9.61), the expression (9.71) is used for all grid nodes. This yields a system of equations in the unknown ϕ at all nodes. Note that the boundary conditions have to be considered as well.

Central differencing seems a natural choice, but it is easy to show an example where it fails completely. For instance, assume the following

$$D_w = D_e = 1 \qquad F_w = F_e = 4 \qquad \phi_W = 100 \qquad \phi_E = 200$$

The result is $\phi_P = 50$. Now, for a convection-diffusion problem in the absence of sources, it is physically impossible for the value to fall outside the range defined by the values at the neighbors, so the result is wrong!

In order to ensure a physical behavior of a discretization scheme, it must possess three basic properties. The first one is *boundedness*, which states that in the absence of internal sources, the value of any quantity ϕ shall be bounded by its boundary values. To ensure this, all coefficients in the discretization scheme must have the same sign. This means physically that an increase in ϕ at one point shall imply an increase also in the neighboring points.

According to the definition of a_E in equation (9.73), its sign depends on the relative magnitude of F_e and D_e. Defining a local Peclet number as

$$Pe = \frac{F}{D} \tag{9.76}$$

its value at the east face, Pe_e, will determine the sign of a_E. The requirement for a_E to be positive is that $Pe_e < 2$. On the other hand, a_W will be negative for $Pe_w < -2$, so the same sign of all coefficients is ensured only if $|Pe| < 2$.

This constraint on Pe is satisfied for sufficiently small F (i.e., sufficiently low velocity), according to the definition in equation (9.65). However, according to the definition of D in the same formula, this quantity is inversely proportional to the grid step size, so the smaller the step the larger the value of D, and the larger the permissible velocity. High velocities thus require fine grids. In our example, $Pe = 4$, so the requirement on boundedness is not satisfied.

The second requirement of the discretization scheme is *transportiveness*. As the Peclet number increases, the influence of convection on the transportation becomes more and more pronounced, relative to that of diffusion. This means that the higher the Peclet number, the more important the upstream influence of the transportation. For high Peclet numbers, the discretization scheme therefore must be adapted to the direction of the flow. Obviously, the central differencing scheme does not satisfy this requirement because it puts an equal weight upstream and downstream.

---

*For A to be variable, the equations must be written in curvilinear coordinates. Metrics and their derivatives are then introduced, and they would have been retained also in the 1D equations (9.61) and (9.62). Note that the present approach yields $u = const$, which means that equation (9.61) is linear.

A third requirement is *conservativeness*. This means that no flux shall be lost or generated at boundaries between grid cells. The flow that enters a cell through a face shall be exactly equal to that leaving the adjacent cell. This is accomplished by applying the same expression for the flux at both sides of the face. As we have seen, this is indeed the case for central differencing, but we may envisage a scheme where different expressions are used. For instance, if a higher order (i.e., higher order than linear) interpolation is used for obtaining the values at a cell face, more grid points than those next to the cell face are included in the approximation. These "extra" points may well be different, depending on whether the face is considered an east boundary in a cell or a west boundary of the adjacent cell. The approximation of the fluxes may then be different. Note that not all higher order discretization schemes suffer from this problem.

Having discussed the three fundamental requirements of a discretization scheme, it may be of interest also to discuss its accuracy. In the derivation of the discretization formula (9.71), two approximations were made. The first one was related to the x-derivatives in the diffusion terms of equation (9.63). These were to be evaluated at the cell faces e and w. In equation (9.66), the derivatives were computed by central differencing using the values at the two adjacent nodes (i.e., E,P and P,W, respectively). The second approximation was made in the computation of the ϕ-values at the cell faces, required in the convective terms of equation (9.63). According to equation (9.68) and (9.69), ϕ_e and ϕ_w were approximated by linear interpolation between the adjacent grid points. We will analyze both approximations.

To compute the error of the derivative approximation, use Taylor expansion forward and backward from a point x

$$\phi(x + \Delta x) = \phi(x) + \left(\frac{\partial \phi}{\partial x}\right)_x \Delta x + \left(\frac{\partial^2 \phi}{\partial x^2}\right)_x \frac{\Delta x^2}{2} + HOT \quad (9.77)$$

$$\phi(x - \Delta x) = \phi(x) - \left(\frac{\partial \phi}{\partial x}\right)_x \Delta x + \left(\frac{\partial^2 \phi}{\partial x^2}\right)_x \frac{\Delta x^2}{2} + HOT \quad (9.78)$$

where *HOT* stands for higher order terms.

Subtracting the two equations and dividing by twice the step size gives

$$\frac{\phi(x + \Delta x) - \phi(x - \Delta x)}{2\Delta x} = \left(\frac{\partial \phi}{\partial x}\right)_x + \mathcal{O}(\Delta x^2) \quad (9.79)$$

where the last term means terms of order Δx^2 (higher order terms are also included).

Equation (9.79) shows that the approximate derivative on the left-hand side differs from the exact derivative on the right-hand side only by the last term of order Δx^2. The error is thus proportional to the step size squared and the method is said to be of second order. When Δx is reduced, for instance, in a grid refinement study, the error is reduced as Δx^2.

Applying equation (9.79) to the east face of the control volume, x defines position e, $x + \Delta x$ position E and $x - \Delta x$ position P. If Δx is set equal to $\delta_x/2$,* the following expression is obtained for the derivative at e

$$\left(\frac{\partial \phi}{\partial x}\right)_e = \frac{\phi_E - \phi_P}{\delta x} - \mathcal{O}(\Delta x^2) \quad (9.80)$$

that is, the approximation is second order accurate. The same conclusion holds for the derivative at the west face.

The approximation of the face values in the convective terms may be analyzed easily by adding equation (9.77) and (9.78). Dividing by two, this yields

$$\frac{\phi(x + \Delta x) + \phi(x - \Delta x)}{2} = \phi(x) + \mathcal{O}(\Delta x^2) \quad (9.81)$$

that is, the approximate value of ϕ at x differs from the exact value by terms of order Δx^2. This approximation is then also of second order. Defining the position of e, E, and P as previously shown, we see that

$$\phi_e = \frac{\phi_E + \phi_P}{2} - \mathcal{O}(\Delta x^2) \quad (9.82)$$

similarly for ϕ_w. We have now shown that the central differencing approximations related to both diffusion and convection are of second order.

It may now be of interest to look at another differencing scheme, where the drawbacks related to boundedness and transportiveness are removed. Such a scheme is obtained by upwind differencing. Note, however, that we only need to modify the approximation related to convection. Central differencing is very suitable for diffusion, and it is used in most CFD methods.

The simple approach in upwind differencing is to set the face value equal to the value at the closest upstream node point. Thus for $u_w > 0$ and $u_e > 0$, $\phi_w = \phi_W$ and $\phi_e = \phi_P$, whereas for $u_w < 0$ and $u_e < 0$, $\phi_w = \phi_P$ and $\phi_e = \phi_E$. In the first case (i.e., flow in the positive direction), the equivalent of equation (9.70) reads

$$F_e \phi_P - F_w \phi_W = D_e(\phi_E - \phi_P) - D_w(\phi_P - \phi_W) \quad (9.83)$$

Using the discrete continuity equation (9.67), $F_e = F_w$ and equation (9.83) may be rewritten as

$$a_P \phi_P = a_W \phi_W + a_E \phi_E \quad (9.84)$$

that is, the same equation as (9.71). The difference lies in the coefficients, which now are

$$a_W = D_w + F_w \quad (9.85)$$

and

$$a_E = D_e \quad (9.86)$$

As before [equation (9.75)]

$$a_P = a_W + a_E \quad (9.87)$$

---

*Note that for the derivation to be exact, the cell face has to be midway between E and P. This may not be the case for stretched grids, and then the order of magnitude analysis will only be approximate.

For flow in the negative direction

$$a_W = D_w \tag{9.88}$$

and

$$a_E = D_e - F_e \tag{9.89}$$

and equations (9.84) and (9.87) are unchanged. Short forms of a_W and a_E, valid for both flow directions, are

$$a_W = D_w + max(F_w, 0) \tag{9.90}$$

$$a_E = D_e + max(0, -F_e) \tag{9.91}$$

In the upwind scheme, all coefficients are guaranteed to be positive. The boundedness criterion is thus satisfied. Further, the scheme obviously adapts to the direction of the flow and is thus transportive. Consistent expressions are used in and out at a cell face so the scheme is also conservative. It therefore looks to be an ideal scheme, but as we will see, it is not as accurate as the central differencing scheme.

Apply equation (9.78) at the west boundary w. With Δx as the distance between the node point W and w

$$\phi_W = \phi_w - \left(\frac{\partial \phi}{\partial x}\right)_w \Delta x + HOT \tag{9.92}$$

or

$$\phi_w = \phi_W + \mathcal{O}(\Delta x) \tag{9.93}$$

The approximation is thus of first order in Δx, and the same holds for the east boundary. This means that the solution converges slower toward the continuous solution when the grid is refined, as compared to the second order central difference scheme. At least for coarse grids, the upwind difference solution is therefore too smooth; particularly if the grid lines in a 2D or 3D case are not aligned with the flow, considerable errors may occur. In fact, second order accuracy is considered the minimum for good CFD methods, and some journals refuse to accept results from first order methods.

We have now seen one discretization method which has good accuracy, but which turns unstable for Peclet numbers larger than 2. In addition, we have seen one method that is stable, but with poor accuracy. There are, however, a large number of other methods available, all of which attempt to optimize both accuracy and stability.

An early attempt by Spalding (1972) was to combine central and upwind differencing in such a way that central differencing is used for all terms if $|Pe| < 2$, whereas upwind differencing for convection terms and a total neglect of diffusion terms is used otherwise. This discretization is called the *hybrid scheme.*

A more accurate representation of the flux through the cell faces is obtained by the *power law* scheme proposed by Patankar (1979). Here, diffusion is neglected for $|Pe| > 10$ and upstream differencing is used for convection. For $|Pe| \leq 10$, the flux through a cell face exhibits a smoother dependence of Pe than for the hybrid method, where the approximation is rather unsatisfactory near $|Pe| = 2$. In the power law, the flux depends on a fifth power expression in Pe.

Another popular scheme is *quadratic upstream interpolation for convective kinetics* (*QUICK*) proposed by Leonard (1979). Note that this is only used for the convective terms. Here, three node points are used for a quadratic interpolation of the values at the cell faces. The three points are the closest ones on each side of the face plus another one upstream.

Both the hybrid and the power law schemes satisfy the requirements on boundedness, transportiveness, and conservativeness, but they deteriorate to first order for high Peclet numbers. They are thus stable, but not highly accurate under all circumstances. This problem is avoided in the QUICK scheme, which may be shown to be third order accurate, again at the expense of less stability because boundedness cannot be assured for all flow conditions. QUICK does satisfy the transportiveness and conservativeness criteria, and the problems with unboundedness are often restricted to small overshoots in the solution.

It should be mentioned that there is also a large number of more modern schemes, which avoid the oscillations often seen in the QUICK solutions. This holds particularly for the so-called *Total Variation Diminishing* schemes developed for capturing shocks in aerodynamic computations (see Chakravarthy & Osher, 1985).

The numerical accuracy may be increased without increasing the computational effort significantly using the *deferred correction* approach (Khosla & Rubin, 1974). The formal accuracy of the discretization depends on the degree of the polynomial used for interpolating values to the cell faces. The higher the degree of the polynomial, the higher the possible accuracy. However, a higher degree of the polynomial requires more node points to determine its coefficients, which means that the discretization stencil (i.e., the node points involved in the discretization of the governing equation at one point) becomes large. This calls for a larger computational effort when solving the resulting system of equations. In the deferred correction approach, the values at points other than the closest ones are taken from a previous iteration. Only the values at the closest points are then considered as unknowns, which reduces the solution efforts. If the method converges, the difference between the previous and the new values tend to zero and the converged solution is the same as for the higher order method.

Based on the simple equation (9.61), we have been able to derive a number of important properties of discretized convection-diffusion equations. These properties are common to the complete equation (9.60). As shown, for instance, in Patankar (1980), Versteeg and Malalasekera (1995), and Ferziger and Peric (1999), it is relatively straightforward* to generalize the derivation to the general case and the result is as follows.

With N, S, T, and B representing the north, south, top, and bottom neighbors of the point P and n, s, t, and b the cell faces with normals in these directions, the discretized equation (9.60) reads

$$a_P\phi_P = a_E\phi_E + a_W\phi_W + a_N\phi_N + a_S\phi_S + a_T\phi_T + a_B\phi_B + b \tag{9.94}$$

which can be compared with the discretized equation (9.61) in equation (9.71). A compact notation is

$$a_P\phi_P = \sum a_{nb}\phi_{nb} + b \tag{9.95}$$

where the index nb stands for a value at a neighboring point. Note that equations (9.94) and (9.95) do not accommodate higher order techniques, where more nodes than the neighboring ones are involved. The generalization is rather straightforward, however.

The coefficients of equations (9.94) and (9.95) are as follows

$$a_E = D_eA(|Pe_e|) + \max(-F_e, 0) \tag{9.96}$$

$$a_W = D_wA(|Pe_w|) + \max(F_w, 0) \tag{9.97}$$

$$a_N = D_nA(|Pe_n|) + \max(-F_n, 0) \tag{9.98}$$

$$a_S = D_sA(|Pe_s|) + \max(F_s, 0) \tag{9.99}$$

$$a_T = D_tA(|Pe_t|) + \max(-F_t, 0) \tag{9.100}$$

$$a_B = D_bA(|Pe_b|) + \max(F_b, 0) \tag{9.101}$$

$$a_P = a_E + a_W + a_N + a_S + a_T + a_B + a_P^0 + S_p\Delta V \tag{9.102}$$

$$b = S_c\Delta V + a_P^0\,\phi_P^0 \tag{9.103}$$

The convective flow rate, F, and the diffusion conductance, D, may be defined as in equation (9.65), except that they now have to include the area of the cell face where they are to be evaluated

$$F = uA_{\text{face}} \qquad D_i = \frac{\Gamma}{\delta x_i}A_{face} \tag{9.104}$$

In the 1D derivation the area of the inlet cell face area was assumed to be the same as that of the outlet face, which meant that this area disappeared from the equation. For Cartesian coordinates in 3D, opposing cell faces will have the same area, but this area may differ in the three coordinate directions, so it needs to be retained. Note that the step size used for defining D may differ between the three directions. The Peclet number, Pe, is defined as in equation (9.76)

$$Pe_i = \frac{F}{D_i} \tag{9.105}$$

a_P^0 is a coefficient arising from the time derivative

$$a_P^0 = \rho_P^0\frac{\Delta V}{\Delta t} \tag{9.106}$$

The index^0 refers to a known value from a previous time step.

S_P and S_C in the previous equations arise from a linearization of the source term, which is expressed as

$$\overline{S} = S_C + S_P\phi_P \tag{9.107}$$

where $\overline{S}$ is the mean value of S in the cell. The function $A(Pe)$ differs between the different discretization schemes. For the central, upwind hybrid and power law schemes, it is given in Table 9.1 (Patankar, 1980).

The discretized form of the continuity equation reads

$$F_e - F_w + F_n - F_s + F_t - F_b = 0 \tag{9.108}$$

9.7.5.3 PRESSURE-VELOCITY COUPLING. The governing equations in a RANS method are the momentum equations (9.46), the continuity equation (9.48), and a set of equations for turbulent quantities, such as equations (9.57) and (9.58). There is no explicit equation for pressure, but the pressure gradient in equation (9.46) drives the velocity and the velocity has to satisfy the continuity equation (9.48), so there is an indirect coupling between the pressure distribution and the continuity equation. In a large class of CFD methods, this link is used to derive an equation for the pressure or for the pressure correction. These kinds of *pressure-based methods* will be discussed, followed by a brief description of other alternatives.

Before we start the discussion of the pressure-based methods, we need to take a look at the discretization of the pressure gradient in equation (9.46). In the previous discussion, this gradient was assumed included in the source term of the general transport equation (9.60), but at this stage it has to be taken out of the source term and considered separately. A natural way to obtain the pressure gradient, for instance in the x-direction at the node point P, would be to use the pressure difference between the two opposing faces and divide by the cell length in this direction, in other words

$$\left(\frac{\partial p}{\partial x}\right)_P \approx \frac{p_e - p_w}{\delta x} \tag{9.109}$$

Table 9.1 The Function $A(P)$ for Different Discretization Schemes

Scheme	$A(P)$
Central difference	$1 - \frac{1}{2}\lvert Pe\rvert$
Upwind	1
Hybrid	$\max\left(0, 1 - \frac{1}{2}\lvert Pe\rvert\right)$
Power law	$\max\left(0, 1 - \frac{1}{10}\lvert Pe\rvert^5\right)$

---

*Integrating equation (9.60) over a control volume in 3D involves evaluations of both surface and volume integrals. Normally, these are approximated to second order by the function's value at the cell face center times the face area, respectively the value at the cell center times the cell volume (Ferziger & Peric, 1999).

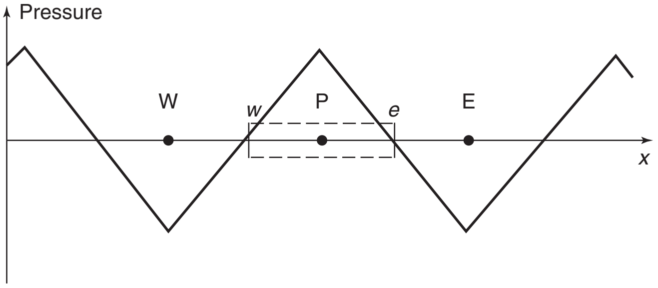

Figure 9.19 Point-to-point oscillations in pressure.

The problem with this approach is that p is not known at the cell faces. Let us assume that it is obtained by linear interpolation between the closest node points. This gives*

$$p_e = \frac{p_E - p_P}{2} \qquad p_w = \frac{p_P - p_W}{2} \tag{9.110}$$

and, after introduction in equation (9.109)

$$\left(\frac{\partial p}{\partial x}\right)_P \approx \frac{p_E - p_W}{2\delta x} \tag{9.111}$$

The pressure gradient is thus obtained from the pressures at the two node points adjacent to P, but the value at P is not included. This sparse discretization stencil may give rise to point-to-point oscillations in the pressure. See, for instance, the 1D pressure distribution shown in Fig. 9.19.

Using the discretization formula (9.111), the pressure gradient obtained at all node points will be zero, in spite of the fact that the pressure fluctuates heavily. Similar problems may occur in all three directions of a 3D problem. This is not an acceptable feature of the numerical method.

The classical remedy to the point-to-point oscillation problem (checker-board oscillations in 2D) is to shift the location of the cells for discretizing the velocity components. Thus, only the scalar values, like pressure or turbulence quantities, are computed at the regular grid points, whereas velocity components are computed at the cell faces. The u-velocity is thus obtained at the center of the east cell face, and a new cell is constructed around this point. Similarly, a new cell for the v-velocity is defined around the center of the north face and cell for the w-velocity around the top face center. We now have a *staggered grid*. It is messy to display in 3D, but a 2D example is shown in Fig. 9.20.

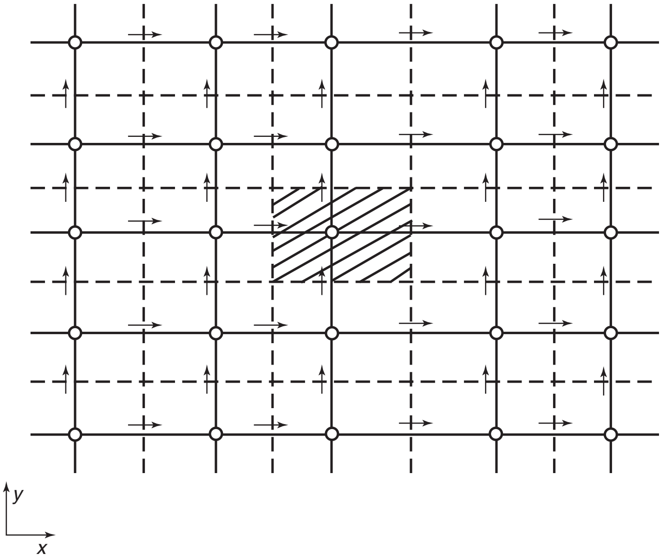

Figure 9.20 A 2D staggered grid. Pressure and turbulence quantities are computed at the grid nodes, marked as circles. u-velocities are obtained at the location of the horizontal arrows, and v-velocities are obtained at the vertical arrows. For u and v, new cells are constructed around the arrow.

Using the staggered grid, the computation of the pressure gradient becomes very simple and the point-to-point oscillation problem is removed. See, for instance, the computation of the pressure gradient in the u-cell shown in Fig. 9.21 . The cell is centered around the point e, and the pressure gradient is naturally obtained from the values at E and P

$$\left(\frac{\partial p}{\partial x}\right)_e \approx \frac{p_E - p_P}{\delta x} \tag{9.112}$$

The discretization stencil for the pressure gradient is now compact and contains values at two adjacent node points. Similar discretization can be done in the other two coordinate directions.

Because staggered grids solved the pressure oscillation problem, they were very popular during the 1970s and 1980s, but during the 1990s the interest in these grids decreased, mainly because of the increased complexity in storing unknowns at different locations, especially in 3D. In the following, we will derive the most common equations for pressure-velocity coupling in staggered

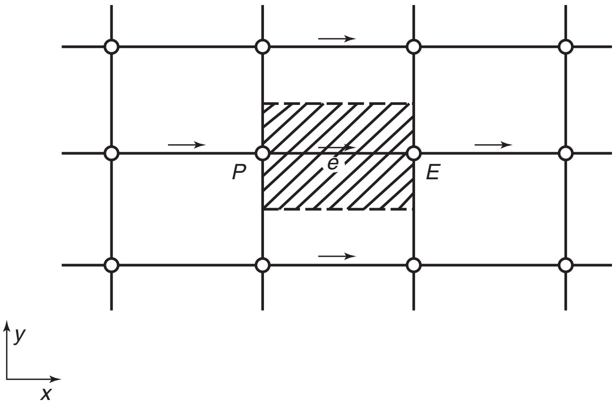

Figure 9.21 A cell for discretization of the u-velocity.

---

*Assuming constant grid spacing. The problem to be discussed is present also for varying spacing, but in a less clear way.

grids, thereafter explaining their use also in nonstaggered (colocated) grids.

Let us first write equation (9.95) for a u-cell with the pressure gradient removed from the constant b (which is thus redefined).

$$a_e u_e = \sum a_{nb} u_{nb} + b - \frac{p_E - p_P}{\delta x} \Delta V_u \qquad (9.113)$$

where ΔV_u is the volume of the u-cell (ΔV_u comes from the integration over the cell). The equation may be written

$$a_e u_e = \sum a_{nb} u_{nb} + b + (p_P - p_E) A_e \qquad (9.114)$$

The fact that the cell is now centered around e rather than P does not change the expressions for the constants, but the flow rate, F, and diffusion conductance, D, must now be evaluated at E and P, rather than e and w. Equations corresponding to equation (9.114) may be set up for v and w.

The basis for pressure-based methods is the semi-implicit method for pressure-linked equations (SIMPLE) algorithm proposed by Patankar and Spalding (1972). In SIMPLE, an equation for the pressure correction is used. It will now be derived.

Assume that an estimate, p^*, of the pressure field is known. Inserting this into equation (9.114) yields a velocity field, u^*, from the following equation

$$a_e u^*_e = \sum a_{nb} u^*_{nb} + b + (p^*_P - p^*_E) A_e \qquad (9.115)$$

Because the pressure is not likely to be correct, there is an error also in the velocities. To obtain the right values, corrections have to be added. If these are denoted by primes, the following relations hold

$$p = p^* + p' \qquad (9.116)$$

$$u = u^* + u' \qquad (9.117)$$

If equation (9.115) is subtracted from equation (9.114), an equation for the velocity correction is obtained

$$a_e u_e' = \sum a_{nb} u_{nb}' + (p_P' - p_E') A_e \qquad (9.118)$$

In the SIMPLE algorithm, it is assumed that $\Sigma a_{nb} u_{nb}'$ is negligible relative to the pressure term. This is not well substantiated and may be a reason why the method converges slowly, but it should be noted that on convergence, all u' shall be negligible, so there is no error introduced in the final solution. We thus have, approximately

$$a_e u_e' = (p_{\mathrm{P}}' - p_E') A_e \qquad (9.119)$$

Introducing $d_e = A_e / a_e$, the correct velocity u_e may be written using equation (9.117)

$$u_e = u^*_e + d_e (p_P' - p_E') \qquad (9.120)$$

This is a velocity correction formula, and similar expressions can be derived for the two other velocity components. To obtain a pressure correction formula, equation (9.120) and its counterparts are introduced into the discretized continuity equation (9.108). The result may be written

$$a_P p_P' = a_E p_E' + a_W p_W' + a_N p_N' + a_S p_S' + a_T p_T' + a_B p_B' + b' \qquad (9.121)$$

where

$$a_E = (Ad)_e \qquad a_W = (Ad)_w \qquad a_N = (Ad)_n \qquad (9.122)$$

$$a_S = (Ad)_s \qquad a_T = (Ad)_t \qquad a_B = (Ad)_b \qquad (9.123)$$

$$a_P = a_E + a_W + a_N + a_S + a_T + a_B \qquad (9.124)$$

and

$$b' = (u^*A)_w - (u^*A)_e + (v^*A)_s - (v^*A)_n + (w^*A)_b - (w^*A)_t \qquad (9.125)$$

Note that $-b'$ corresponds to the left-hand side of the continuity equation (9.108) if u^* rather than u is used for defining the flow rate F. Thus, when the iterations converge and u^* approaches u, b' will tend to zero. As long as b' is non-zero, it will act as a source term to force the pressure correction to yield a flow field satisfying the continuity equation. Note that if the guessed pressure p^* is far from the correct one, the pressure correction will be so large that the iterative process diverges. To resolve this problem, underrelaxation is used. In every new iteration, only part of the newly computed corrections for pressure and velocities are included.

We are now in a position to describe the iterative scheme in SIMPLE:

1. Start with a guessed pressure field p^*. This could come from, for instance, a potential flow solution. Even assuming a constant pressure will work with suitable underrelaxation.
2. Use p^* and solve equation (9.115) and its counterparts in the other two directions. This yields u^*, v^*, and w^*.
3. Compute p' from equation (9.121).
4. Calculate p from equation (9.116) using p^* and p'.
5. Calculate u, v, and w from equation (9.120) and its counterparts in the other two directions.
6. Solve the transport equation (9.95) for turbulence quantities using the just computed velocity field.
7. Return to step 2 and use the calculated p from step 4 as the new guessed pressure p^*. Continue the process until convergence.

The weakest point of SIMPLE is the neglect of the neighboring correction velocities $\Sigma a_{nb} u_{nb}'$ in equation (9.119). This makes the burden of the pressure correction rather heavy and considerable underrelaxation will be required. However, as shown by Patankar (1980), the velocity field often converges much more rapidly than the pressure field, so a more efficient algorithm could be constructed if the pressure correction was used only to update the velocities, and the pressure itself was computed by another procedure. This is done in SIMPLE Revised (SIMPLER; Patankar, 1979). Here a separate equation for the pressure, p, is used. This equation turns out to look the same as the one for the pressure correction p', equation (9.121), and the only difference lies in the computation of the source term b', which can now be computed from a known velocity field. SIMPLER therefore starts with a guessed velocity field used to obtain a pressure, which can be set as the initial guess, p^*, needed in the SIMPLE algorithm. The rest of the iteration sweep is unchanged, but the pressure is never updated by the pressure correction; it is always computed from the pressure equation at the beginning of each sweep.

Another variant of SIMPLE is SIMPLE Consistent (SIMPLEC; van Doormal & Raithby, 1984), which includes a modification of the velocity correction equation (9.119), such that the approximation is less severe. Otherwise, the procedure is the same as that of SIMPLE.

Of the three pressure-velocity coupling techniques described so far, SIMPLER is by far most widely used. It is known to converge considerably faster than both SIMPLE and SIMPLEC. However, another technique, known as Pressure Implicit with Splitting of Operators, or PISO (Issa, 1986), has gained in popularity in recent years. Here, a second pressure correction step is introduced, where a second pressure correction equation is solved to yield an updated pressure from which the velocity field is obtained. Otherwise, the procedure is the same as for SIMPLE.

Staggered grids solve the problem with point-to-point oscillations, but they are not convenient in 3D problems, particularly if the grid is curvilinear. Therefore, a technique proposed by Rhie and Chow (1983) has become popular in recent years. Using this approach, SIMPLE and its variants can be used also on colocated grids.

Checking the SIMPLE procedure described, it is seen that it can be used together with a central differencing scheme for obtaining the starred velocities u^*, v^*, and w^*, if only the source term b' in the pressure correction equation can be estimated. b' is obtained from equation (9.125), where the starred velocities are required at the cell faces.

It seems natural to just interpolate these velocities linearly to a cell face using the values computed at the adjacent nodes. However, this would lead to the same problem with point-to-point oscillations as we have seen for p previously. A simple 1D example will show this.

In 1D, assuming a constant face area, equation (9.125) may be written

$$b' = u^*_w - u^*_e \tag{9.126}$$

Linear interpolation* yields

$$b' = \frac{u^*_P + u^*_W}{2} - \frac{u^*_E + u^*_P}{2} = \frac{u^*_W + u^*_E}{2} \tag{9.127}$$

The discretization point P is thus not involved in the computation of the source term b'. In a point-to-point oscillation, where the values at W and E are the same, but different from that at P, the source term in the p'-equation (9.121) would be zero, and no pressure correction would be computed, in spite of the fluctuating pressure field.

To resolve the problem, Rhie and Chow (1983) proposed adding a damping term to the computation of b'. The task of the damping term should be to reduce oscillations, and its order should be higher than that of the basic discretization scheme, so that the formal order of accuracy of the method would not change due to the inclusion of this artificial term. A suitable form of the damping term was also derived. It was shown to be of fourth order in Δx and thus formally smaller than the second or third order errors obtained in most discretization schemes. Using this damping, point-to-point oscillations are effectively damped.

The pressure-based procedures described so far are all based on iterations, where the transport equations are solved sequentially (*segregated* solutions) in each sweep of the solution process. This takes care of the nonlinearity as well as the coupling between the equations. In the CFD vocabulary, these iterations are often referred to as *outer* iterations, and the *inner* iterations are related to the solution of the system of equations. For time dependent problems, there is also a *time-stepping* loop outside of the two iteration loops. Convergence of the latter is required before a new time step can be taken. However, in many cases, time-stepping methods are used also for steady state computations. In this case, the solution converges in time toward the steady state, but the iterations in each time step do not have to be fully converged.

Although the pressure-based methods dominate hydrodynamic CFD, there are other methods in use. In a compressible flow, the continuity equation contains a time derivative of the density, and pressure is linked to density through an equation of state. There is thus a direct coupling between pressure and velocities. This is not so for incompressible flows, where density is independent of pressure, but one idea proposed by Chorin (1967) is to include an artificial time derivative of the pressure in the continuity equation for steady state incompressible flows. If the steady state is reached through time stepping, this extra term will tend to zero as the solution converges. The continuity equation may then be written

$$\frac{1}{\beta}\frac{\partial p}{\partial t} + \frac{\partial}{\partial x_i}(\rho U_i) = 0 \tag{9.128}$$

where β is a parameter, whose value has to be chosen by experience. Values of β that are too large make the system of equations difficult to solve (i.e., an iterative equation solver will converge slowly). On the other hand, values that are too small will put strong requirements on the convergence of the global time-stepping scheme. Techniques based on this approach are known as artificial compressibility methods.

Techniques that have gained in popularity in recent years are the *direct solution methods* where no

---

*Constant spacing.

explicit pressure equation is used. An early method of this kind was proposed by Rubin (1984). The system of equations is solved directly with at least the momentum and continuity equations coupled. Methods based on this technique are those by Hoekstra (1999), and Regnström et al. (2005). Present experience from the methods is that they are more robust than the traditional segregated methods and converge faster, particularly for the very stretched grids used in full-scale computations.

9.7.6 Boundary Conditions. Boundary conditions for velocities and pressure have been discussed in Section 2.4 in connection with the derivation of the Navier-Stokes equations. These are the mathematical conditions needed for a the solution of the continuous differential equations. In the numerical solution of the RANS equations, some boundary conditions have to be modified because we now have a finite computational domain with artificial external boundaries. Here we will treat conditions for the following boundaries:

1. Inlet
2. Outlet
3. Symmetry (centerplane and water surface)
4. External
5. Wall

9.7.6.1 INLET. In most CFD methods for the flow around the hull, the inlet plane is located well in front of the hull, so in principle undisturbed conditions may be applied. The axial velocity is then set equal to the ship speed and the other two components are set to zero. Different ways of setting the pressure are used. Dirichlet conditions (i.e., fixed values) are specified in some cases. In double-model solutions, the pressure is then set to a constant; in a free-surface case, the effect of the hydrostatic pressure has to be added. Neumann conditions (i.e., zero derivative normal to the inlet plane) are used in some methods and in others the pressure is extrapolated from interior nodes. Even if turbulence should be negligible at this position, inlet values of transported quantities such as k and ε or ω must be specified. These are computed based on estimated length and velocity (or turbulence intensity) scales.

9.7.6.2 OUTLET. At the outlet plane the flow is not known, even if it is placed far downstream, because the wake from the hull has to pass the plane. Therefore, velocities or turbulence quantities cannot be specified. The usual choice is to specify a Neumann condition for these quantities. Zero variation of the quantities normal to the plane is thus assumed. Alternatively, zero diffusion may be assumed, which means zero second derivative normal to the plane of these variables. As to the pressure, the Neumann condition could be specified as well, but if this condition has also been applied upstream, the pressure must be given at one point at least. Otherwise, the magnitude of the pressure in the computational domain would be undetermined; only the gradients could be computed. If the plane is far away, say at least half a ship length, the pressure may be assumed undisturbed. Some methods apply this condition for all outlet points.

9.7.6.3 SYMMETRY. Symmetry conditions are normally applied at the centerplane outside the hull and (in the double-model approximation) at the water surface. At the centerplane, this is a true condition only if the (symmetric) hull is moving straight ahead and there is no propeller action. The propeller induces rotation in the slipstream, which is not accounted for if symmetry is assumed. Most ship flow calculations are, however, without a propeller, and even if the propeller is included, the slipstream rotation is often neglected. This assumption reduces the computational effort considerably because the grid then has to cover only one side of the hull. Symmetry conditions for tangential velocities, pressure, and turbulence quantities are zero gradient normal to the surface (i.e., a Neumann condition). For the velocity component normal to the surface, a Dirichlet condition applies: this velocity component is zero.

9.7.6.4 EXTERNAL. At the external (or *far-field*) boundary of the computational domain symmetry conditions are often applied. This means that there is no flow through the boundary and the normal derivative of the tangential velocity is zero, implying no shear stress at the surface. Therefore, symmetry conditions are also called slip conditions. Great care should be exercised when applying this condition at the external boundary because the flow is then constrained by the "tube" defined by the boundary. If this is far away, say at least a ship length, this is acceptable, but if the boundary is closer, there must be a way for the flow to pass the boundary. This can be accomplished by applying Dirichlet conditions for all variables except the normal velocity. The latter may be determined by applying the continuity equation at cells adjacent to the boundary. Values for the Dirichlet condition may be set the same as at the inlet (i.e., undisturbed flow), or they may be obtained from a matching potential flow solution at the boundary.

9.7.6.5 WALL. Two types of *wall* boundary conditions are used. The most straightforward one is the no-slip condition, where all velocity components are zero. With zero tangential velocity, the pressure gradient normal to the wall is also zero according to the relation between streamline curvature and pressure gradients in Section 5.2.2.* A Neumann condition can thus be applied on the surface.

The no-slip condition implies that the fluctuating part of the velocity is also zero, which means that k is zero on the surface.

As shown by Wilcox (1998), ω tends to infinity as y approaches zero. A finite value can be determined,

---

*In Section 5.2, the effect of the viscous stresses is neglected, but because the normal velocity is identically zero on the surface, and so is its derivative in the normal direction (due to continuity), there will be no viscous stresses in the normal direction generated.

however, if the surface is assumed to have a roughness. This value may be obtained from

$$\omega = \frac{u_\tau^2}{\nu} S_R \tag{9.129}$$

where S_R is defined as

$$S_R = \begin{cases} \dfrac{50}{k_S{}^+} & k_S{}^+ < 25 \\ \dfrac{100}{k_S{}^+} & k_S{}^+ \geq 25 \end{cases} \tag{9.130}$$

and $k_S{}^+$ is the nondimensional equivalent sand roughness (see Section 6.8.2) defined by

$$k_S{}^+ = \frac{u_\tau k_S}{\nu} \tag{9.131}$$

In practice, a small value ($k_S{}^+ \leq 5$) is set for a hydraulically smooth surface.

The surface boundary condition for ε is more difficult to express in a simple way because the ε equation cannot be directly integrated through the viscous sublayer. A large number of so-called low Reynolds number corrections to the equation have been proposed. These yield different boundary conditions, the simplest one being a Neumann condition. For a review, see Wilcox (1998).

To resolve the boundary layer close to the wall, the grid has to be extremely fine in this region. With y_1 defining the distance from the wall to the first discretization point, a corresponding $y^+{}_1$ may be obtained according to the definition (6.23)

$$y^+{}_1 = \frac{u_\tau y_1}{\nu} \tag{9.132}$$

$y^+{}_1$ should be no larger than 1 for the no-slip conditions to be applied, so the point has to be well within the viscous sublayer (see Section 6.3.3). Note that $y^+{}_1 = 1$ corresponds to a distance of about three microns for a full-scale ship.

A large number of points may be saved if the flow closest to the wall is modeled by empirical relations such as the wall law, equation (6.27). In this *wall function* approach, $y^+{}_1$ is typically in the range $30 \leq y^+{}_1 \leq 100$. Boundary conditions for the velocity are then set at y_1. Because the wall law requires a value of u_τ, the skin friction has to be estimated. One way of doing this is to fit the wall law to u_2 (i.e., the value at the second point) in the previous iteration. v_1 is obtained by setting v_1/u_1 equal to v_2/u_2 in the previous iteration and w_2 is set to zero.

Boundary conditions for k, ω, and ε may be obtained in a straightforward way by assuming that the effects of convection, pressure gradient, and molecular diffusion may be neglected in the wall law region (the wall law itself may be derived from the momentum equations in the same way). The result for the $k - \omega$ model is

$$k = \frac{u_\tau^2}{\sqrt{\beta^*}} \qquad \omega = \frac{u_\tau}{\sqrt{\beta^*}\kappa y_1} \tag{9.133}$$

where κ is the von Kármán constant (see Section 6.3.3) and β^* is defined in connection with the model (9.58). For the $k - \varepsilon$ model, the following relations hold

$$k = \frac{u_\tau^2}{\sqrt{C_\mu}} \qquad \varepsilon = \frac{u_\tau^3}{\kappa y_1} \tag{9.134}$$

where C_μ is a constant in the $k - \varepsilon$ model (= 0.09).

The disadvantage of the wall law is that the assumptions on the near wall flow might deteriorate under certain conditions, such as close to separation. Experience shows that bubble-type separation is delayed and that vortex-type separation is reduced. Wall laws are therefore avoided as boundary conditions in modern hydrodynamics CFD.

9.8 Prediction of Viscous Flow with a Free Surface. In Section 9.7, the free surface was assumed to be a symmetry plane (i.e., the double model approximation was applied), and no waves were considered. In the present section, we will introduce the free-surface waves. Note that this is just another boundary condition; the main solution procedure for the RANS equations, as described in Section 9.7, is still applicable.

Before we go into the fully viscous approach, we will introduce a hybrid method employing both potential flow and RANS methods.

9.8.1 The Hybrid Approach. Because the introduction of the free-surface boundary conditions in the RANS method will call for a considerably increased computer effort, at least if the waves away from the hull are to be computed without too much damping, it is tempting to try to combine potential flow and RANS methods. Then the free-surface waves could be computed first using the potential flow method and thereafter the viscous flow could be calculated with a fixed wavy free surface. The computational effort required for the RANS solution would then be approximately the same as for the double-body approach of Section 9.7. This hybrid approach was first presented by Raven and Starke (2002), who fitted their viscous flow grid to their precomputed wavy surface and applied free-slip conditions (zero shear stress and zero normal velocity) in the RANS solution. Another application of the same technique is found in Regnström and Bathfield (2006). The wave effect on the viscous flow is thus taken into account, but not the viscous flow effects on the waves. Because the latter is important mainly in the wake behind the hull, the solution is good everywhere, except in this region, where the waves in the potential flow solution are exaggerated because of the neglect of the boundary layer displacement effect.

9.8.2 Fully Viscous Solutions. To obtain the full free-surface/viscous flow interaction, the boundary conditions presented in Section 2.4 need to be considered in the viscous flow method. Equation (2.20) represents the kinematic condition, which ensures that there is no flow through the surface, and equations (2.16) and (2.17) express the dynamic conditions in the tangential and normal directions, respectively. Very few methods use the complete dynamic equations, but an exception was presented by Alessandrini and Delhommeau (1996). Often, the effect of the viscous stresses is neglected, as well as the surface tension.

There are two principally different ways of treating the free surface in RANS methods. In the *interface tracking* methods, the numerical grid is fitted to the surface (another name is surface-fitting methods) and updated in each iteration or time step when the surface changes its shape. The kinematic and dynamic boundary conditions are applied on the surface and the flow is computed only in the water. In the *interface capturing* methods, on the other hand, the grid is fixed, and the location of the free surface in the grid is computed in every iteration/time step. The flow may be computed in both air and water, in which case the surface is just an internal boundary where viscosity and density change in a region as thin as possible, but where no boundary conditions are applied. Alternatively, the flow may be computed only in the water, in which case the boundary conditions may be used.

Comparing the two types of methods, it is obvious that the tracking techniques will have problems with complex surface shapes, such as overturning waves, and they will not at all be able to handle plunging breakers, drops, and enclosed air bubbles. In principle, these restrictions do not apply to interface capturing methods, which have therefore gained in popularity in recent years. However, the resolution required to predict details like drops and smaller air cavities is not high enough with affordable grids, so the advantage of the interface capturing methods is not very large in this respect. Also, there is a problem with these methods in keeping the interface sharp. The numerical damping may be very large in the free-surface region, which smears out the interface. Compressive discretization schemes (Orych et al, 2010) alleviate this problem, as does an approach by the same authors, where a component grid of high density is located at the surface in a overlapping grid method.

9.8.2.1 INTERFACE TRACKING METHODS. Practically all interface tracking methods use a time stepping approach where the dynamic-free surface boundary condition is applied to compute the flow below the free surface obtained in the previous time step. At the end of each new step, the free surface is updated using the kinematic boundary condition. The only exception known to the authors is the method by Raven, van der Ploeg, and Starke (2004), where the problem is solved by iterations without time stepping in very much the same way as in free-surface potential flow methods. Thus, a combined kinematic and dynamic boundary condition is applied at a surface obtained in the previous iteration, after which the surface is updated using the dynamic condition.

A typical finite volume time stepping method using SIMPLE is described by Ferziger and Peric (1999). One time step is thus as follows.

1. Set p^* as the hydrodynamic pressure (equal to the hydrostatic pressure, but with the opposite sign) at the current location of the free surface. Compute the starred velocities u_i^* obtained from equation (9.115) and the corresponding equations in the other two directions.
2. Solve the pressure correction equation (9.121) for p' with a Dirichlet boundary condition, $p' = 0$ on the free surface.
3. Calculate u_i from equation (9.120) and its counterparts in the other two directions. Because p' was set to zero on the surface, this step will produce a velocity through the surface (as long as p^* is not the converged value).
4. Move the free surface in every surface cell such that the volume flux due to the movement is the same as that through the surface in step 3.
5. Iterate between steps 2 and 4 until convergence.
6. Take the next time step.

The largest problem is the vertical movement of the surface in step 4. Since the procedure only specifies the additional *volume* required at each step, while the unknowns are the cell *corners* (usually four) on the surface, all nodes have to be considered as unknowns and solved via a system of equations, each one expressing the required additional volume for one cell in terms of its corner displacements. A simplified procedure is however proposed by Muzaferija, Peric, and Yoo (1996).

9.8.2.2 INTERFACE CAPTURING METHODS. At present, two techniques dominate among the interface capturing methods. The Volume of Fluid (VOF) method, originally proposed by Hirt and Nichols (1981), is the most well-known one and is standard for general free-surface flow problems. However, in recent years the other alternative, the Level Set method proposed by Osher and Sethian (1988), has become very popular in hydromechanics. At the 2005 Tokyo Workshop (Hino, 2005), there were twice as many Level Set methods as VOF methods. One reason for this may be the excellent performance of one of the two Level Set methods at the previous workshop in Gothenburg (Cura Hochbaum & Vogt, 2002). Recently, a combination of the two methods has also been used (Wang et al, 2009).

In the VOF method, a transport equation is solved for the void fraction, c (i.e., the fraction of a cell containing water). $c = 1$ means that the cell is completely filled with water, and $c = 0$ means that it is filled with air. The transport equation for c is

$$\frac{\partial c}{\partial t} + \frac{\partial}{\partial x_i}(u_i c) = 0 \qquad (9.135)$$

c is initialized at time $t = 0$ and computed at every time step in connection with the other transport equations. The free surface at every step is located within a domain in which $0 < c < 1$. Unfortunately, this domain is not very thin because numerical diffusion tends to spread the c-values within the critical range to several cell widths. Therefore, $c = 0.5$ is often taken as the surface.

Most VOF methods compute the flow in air and water simultaneously, and the value of the physical constants is defined by the void fraction as

$$\rho = \rho_w c + \rho_a(1 - c) \qquad \mu = \mu_w c + \mu_a(1 - c) \qquad (9.136)$$

Techniques for one-phase computations are also available.

In the Level Set method, a scalar function ϕ is initialized in the computational domain at $t = 0$ and its transport is thereafter computed from the equation

$$\frac{\partial \phi}{\partial t} + \frac{\partial}{\partial x_i}(u_i \phi) = 0 \qquad (9.137)$$

which (using the continuity equation) can be written as

$$\frac{\partial \phi}{\partial t} + u_i \frac{\partial \phi}{\partial x_i} = 0 \qquad (9.138)$$

With $u_i = \frac{\partial x_i}{\partial t}$, this relation may be interpreted as the total derivative of ϕ with respect to time. ϕ will thus change in time and space as if every water particle was marked with a fixed value of ϕ. Because the kinematic boundary condition states that there is no flow through the surface, every particle originally on the surface must stay there at all times. Thus, if these particles initially could be marked with a distinguishing value of ϕ, the surface at all later times could be found by looking for that value. The approach chosen is to initially set ϕ equal to the distance from the surface, positive in one direction and negative in the other. A linear distribution with zero at the surface is thus obtained. After every time step, the surface can be found at $\phi = 0$.

To integrate equation (9.138), flow velocities are required around the interface; in most Level Set methods, the flow is computed simultaneously in the water and the air. Because the numerics cannot handle discontinuous variations in the physical quantities ρ and μ, smoothing is applied near the surface. The smoothing function is normally a function of ϕ. Parametric investigations of the required thickness of the smoothing layer and the number of cells within this layer are reported by Vogt and Larsson (1999). Here also a technique is proposed where the flow solution is restricted to the water region, obtaining the necessary flow velocities around the interface by extrapolation employing the dynamic boundary condition. The advantage of the latter approach, apart from the obvious saving in grid cells, is that ρ and μ are constant in the entire computational domain. This stabilizes the solution and keeps the interface sharp, but the extrapolation can be cumbersome in regions with a complex surface shape (such as overturning waves). The latter approach is often referred to as the single-phase Level Set technique, as opposed to the two-phase technique normally applied.

Experience shows that the level set function gets rather complicated after several time steps, so a procedure for reinitialization was proposed by Sussman et al. (1994). A separate differential equation (Hamilton-Jacobi) was proposed, which produces a new ϕ field of the same sign and with the same zero level as the original one, but with a smoother distribution. This separate equation has to be solved once at every nth time step, where the optimum number of n can be found by experience (see, for instance, Vogt & Larsson, 1999).

Note that the sharpness of the free surface, both in Level Set and VOF methods, depends to a large extent on the discretization scheme for solving the governing equations (9.135) and (9.138), respectively. First order upwind differences are bound to fail because they will introduce too much numerical diffusion. Higher order schemes are required, and special compressive schemes for maintaining discontinuities have been developed (see Ubbink, 1997, & Orych et al., 2010).

Free surface RANS computations have been in use in hydrodynamics since the early 1990s. In general, the wave profile along the hull is very well predicted, but the waves away from the hull are often damped because of numerical viscosity. Grid densities required for accurate wave predictions at some distance from the hull are often hard to afford, and there is in general a considerable increase in computer effort associated with the introduction of the free surface. Obviously, these problems will be alleviated with the expected future increase in computer power. In any case there is much progress in this field, and the possibility for computational prediction of viscous and scale effects on wave patterns, wave resistance, transom flow regimes, etc. starts being used in research and in practical ship design.

9.9 Practical Aspects of Ship Viscous Flow Computations. After the discussion of solution methods for ship viscous flow, we shall now summarize some practical aspects. This may help to set up a computation with an existing flow code for a ship viscous flow computation. In addition we aim at providing a background that may help a naval architect, confronted with CFD results for a certain vessel, to assess their quality and reliability. We give some general guidelines based on what is customary today, as, e.g., observed in workshops such as the Gothenburg 2000 workshop (Larsson et al. 2002, 2003) and the CFD Workshop Tokyo 2005 (Hino, 2005). Clearly, with the expanding use of RANS computations in ship design these guidelines will change over time.

9.9.1 Modeling. There are some modeling aspects to be considered when setting up a computation. A first question is whether a computation with free surface is needed, or a double-body flow computation is sufficient, or perhaps a "hybrid" computation (Section 9.8.1). Generally, free-surface RANS methods are still somewhat less established, ask longer computation times, and more care is needed to reach the same numerical accuracy. While they are of course in principle more complete, they are not in all cases the best choice yet. This depends on the objective, for example:

- For predicting the wake field in the propeller plane, incorporating the free surface is not essential for most merchant ships at moderate Froude numbers. Its main effect is a slightly different vertical velocity in the propeller plane, but usually it gives little qualitative change in the wake field. However, for rather full hull forms that generate large waves, larger effects may occur, as a result of a change of the location of flow separation.
- For predicting viscous and scale effects on wave making and wave resistance, wave-induced flow separations, or detailed viscous flow phenomena close to the water surface, free-surface RANS computations are required.

- For aligning appendages and scoops, the effect of the wave profile on the local flow direction can be important, and a hybrid or free-surface viscous flow computation is often desired.

Another modeling aspect is the choice of turbulence model. This has been discussed in Section 9.7.3. Entirely algebraic turbulence models are now obsolete, some one-equation models perform well, two-equation models from the k - ω class are most common, and EASM methods are also used successfully.

The domain in which the computation is carried out differs between methods. One example was shown in Fig. 9.3. Required domain size depends on the objective (e.g., viscous pressure resistance for a full hull form is very sensitive) and on the type of outer boundary conditions. Typical extensions are: the inflow plane at about 1 ship length (L) upstream of the bow, the outflow plane at 1.5 L or more downstream of the stern, and lateral boundaries again at 1 L distance or even more, dependent on the boundary conditions imposed. For free-surface computations using an unsteady formulation, larger domains are frequently chosen to limit wave reflections.

A final modeling aspect is whether or not to use wall functions. Using wall functions saves many grid points, and for very large and complicated problems can be desired for that reason; but it does introduce deviations for strongly three-dimensional flows, thick boundary layers and flow separations, thus possibly affecting the wake field. For many codes, using wall functions is still the only way to compute flows at full scale, due to numerical aspects. Therefore, in general the use of wall functions is not desirable but not uncommon either.

9.9.2 Discretization. Section 9.7.5 described discretization schemes and their properties. Methods used differ mainly in the discretization of the convective terms in the momentum equations, which has a profound influence on the accuracy for our applications. The robust and simple first-order upwind schemes are too inaccurate and should be considered substandard, but also the blended or hybrid upwind schemes which mix first-order upwind and central schemes are to be avoided. Higher-order upwind schemes, the QUICK scheme, or so-called high-resolution schemes should be used in practical calculations. On the other hand, for the turbulence model transport equations, low-order schemes are widely used and are considered acceptable.

The grid could have a large influence on the computed results. It must be of a good quality and must be dense enough. Grid quality is not easy to define and differs between the grid categories described in Section 9.7.4, but if possible, in general there should be a smooth and gradual variation of cell sizes and direction of grid lines, even for unstructured grids; cells should have a limited deviation from orthogonality because too skewed cells reduce accuracy and convergence; and it can be beneficial for accuracy if one set of grid lines is more or less flow-aligned. In unstructured grid methods, tetrahedral cells can be used but these cause a larger numerical diffusion; hexahedral cells have better properties. In high-*Rn* boundary layers, tetrahedral cells cannot be used at all and normally a structured-grid layer along walls is used, with hexahedral or prismatic cells.

Required grid density depends on the method and the objective. The grid must be dense enough to resolve all significant variations of flow variables. This means:

- a strong grid contraction towards the wall, to resolve the large velocity gradients in high-*Rn* turbulent flows. This requires $y^+ < 1$ if no wall functions are used, or the right y^+-range for wall functions (dependent on the Reynolds number);
- typically, at least some 30 cells across the boundary layer, if no wall functions are used;
- increased grid density near bow and stern;
- for free-surface RANS computations, dense enough to resolve the relevant ship waves. This often requires some 50 cells per wave length, which leads to severe requirements for low Fn and diverging waves.
- for free-surface capturing methods, dense enough in the area of the wave surface, with small cell sizes normal to the surface in particular; to limit numerical errors in the free surface treatment (e.g., interface smearing, wave damping).

In practice, typically 1.5 to 5 million cells are used today, with the larger numbers applying to free-surface computations; but these are for relatively simple, symmetric, unappended single-screw cases without propeller modeling. Other cases require larger cell numbers.

As was pointed out in Section 9.3, grid dependence checks are desired for each new method and each new class of applications, whether or not accompanied by a formal numerical uncertainty analysis. In particular if detailed quantities need to be predicted, e.g., scale effects, the grid dependence on the result needs to be established. Probably the most grid-dependent aspects in the results are the wake field in the propeller plane, in particular the effect of longitudinal vorticity; and the wave pattern at a distance from the hull.

9.9.3 The Computation. As was pointed out, several iterative procedures are used in the solution of the RANS equations: outer loops in pressure correction methods; the corresponding pseudo-time integration in artificial-compressibility methods; time-stepping in time-dependent computations for steady problems; and inner loops or iterative equation solvers. The latter are usually of little concern, but the convergence of the pressure-velocity coupling procedure is an issue. Few methods are able to reach machine accuracy in this iteration, in practice convergence often stagnates at a certain residual* level. Sound convergence criteria need to be imposed and satisfied, based on the level of residuals

---

*The residual is the difference between the left and right sides of an equation and is thus a measure of the (lack of) convergence in an iteration.

and/or related with the maximum change between iterations, not only based on inspection of integral quantities such as the computed resistance; see Section 9.2. It is not unusual to express the convergence criterion as a certain reduction of a norm of the residuals compared to that in the first iteration, but clearly that depends on the initial solution chosen; a bad initial guess thus could lead to an inaccurate final solution. Also, if the maximum difference between consecutive iterations is below a certain convergence level, the local error can still be much higher than that level, in particular if convergence is slow. Therefore convergence criteria should be rather strict.

If the convergence criteria have not been met and the maximum norm of the residuals still exceeds the desirable level, it can be an option to identify the location of the larger residuals. If these are at a relatively harmless location, e.g., far from the ship, the computed results may still be qualitatively useful, although there are no guarantees.

In time-dependent formulations for steady problems, the time integration performs the same role as an iterative procedure. The result should converge to a steady solution in which all transients vanish. If that is not the case, in most cases one should consider the result as "unconverged." Only in particular cases a physical time-dependence can be assumed, e.g., blunt-body flows, ships at large leeway angles, with small keel clearance or close to a side bank of the waterway, or vortex shedding from cylindrical structures; but usually not for the type of flows considered in this book. A rather typical remaining time-dependence is in RANS/FS computations, caused by sloshing between domain boundaries or due to slowly decaying transient waves. A graph of the computed time history of, e.g., the resistance often clearly reveals this.

9.9.4 Assessment of Accuracy. It is not easy to assess the accuracy of a CFD result provided, unless insight in several of the aspects mentioned above is given. In any case, generally plausible results and attractive visualizations are no guarantee for practical usability.

The smoothness of the flow fields obtained can give some indication. If contours show traces of the grid resolution, this often means that the resolution is insufficient. If there are wiggles in the solution, or the solution is not smooth towards the boundaries, there are numerical problems; not always invalidating the result but asking some attention. As opposed to this, low-order discretization leads to too smooth flow fields with possibly large errors. For free-surface computations, if a Kelvin wedge with a sequence of crests and troughs is not visible, probably the grid is too coarse or the discretization is of a too low order.

From validations of state-of-the-art computations we can deduce the following indications of accuracy now to be expected:

- Wake fields are sensitive to the turbulence model used and to grid density, but can be predicted fairly accurately using today's preferred turbulence models (such as SST) and a grid of a few million grid points for a bare-hull case.
- Limiting streamlines, and streamline patterns in general, for most of the hull are probably accurate, but with larger variations at separation (due to grid density, or wall functions).
- Frictional resistance is sensitive to the turbulence model but less so to the grid density.
- Viscous pressure resistance, for full hull forms at least, is sensitive to grid density, domain size, and boundary conditions at the outer and outflow boundaries.
- For free-surface RANS computations, the wave profile along the hull is generally well predicted, but waves at a distance are often too much damped.
- For the resistance at model scale, with much care for the numerics and modeling an accuracy of a few percent is possible for the usual benchmark cases. At the Tokyo workshop 2005 (Hino, 2005) the standard deviation of all predictions for total resistance varied from 4% to 7% for the cases considered, while the mean values for the different hulls were within the experimental accuracy of around 2%. However, geometric complications, such as appendages, probably increase the errors.
- Full-scale resistance predictions are helpful for studying scale effects, but not yet for direct power predictions, as long as no roughness effects are incorporated and no correlation allowances have been established.

We hope that the general statements made above will help to make an educated and fruitful use of RANS computations in practical naval architecture. There are great benefits of doing so, but attention to quality and accuracy is needed.

10
Empirical Resistance Prediction

At an early stage in the ship design process, the designer often wants to make a selection between several possible alternatives and may then benefit from methods which are not as accurate as models tests or numerical predictions, but which are good enough for a ranking of various alternatives, often differing considerably even in the main parameters. Such methods may be very rapid, enabling the designer to investigate a large number of alternatives in a short time. Many CAD packages for ship design include methods of this kind. In this section, an overview will be given of rapid methods based on empirical data.

As discussed in Section 1.2.2, there are two principally different approaches: systematic series and statistical evaluation of unsystematic data. In a systematic series, variations in main parameters have been made in a large test program and the results presented in the form of diagrams and tables in which the resistance of a new design can be obtained by interpolation. More modern series, such as the Delft series of sailing yachts (see Keuning & Sonnenberg, 1998), are presented in the form of formulas containing hull parameters, where the coefficients have been obtained through regression analysis of the systematic data. This principle is borrowed from methods based on the analysis of unsystematic data, first proposed by Doust and O'Brien (1959).

10.1 Systematic Series

10.1.1 Parameters Varied. In a systematic series, one or more parent models known to have good resistance properties are used to develop other hulls through a systematic variation of main dimensions and form parameters. The developed hull forms are assumed to, in some sense, inherit the main shape of the parents.

Examples of parameters systematically varied are:

- The block coefficient C_B or the prismatic coefficient C_P
- The slenderness ratio $L/\nabla^{1/3}$, where ∇ is the volume displacement
- The length/beam ratio L/B
- The beam/draft ratio B/T
- The longitudinal position of the center of buoyancy (LCB)
- The bottom loading coefficient for planing hulls $A_P/\nabla^{2/3}$, where A_P is the vertical projection of the wetted area.

Results are presented in different ways. For displacement hulls, the residuary resistance coefficient C_R is often, at least in more modern series, presented as a function of Froude number for different form parameters. By simply adding the ITTC-57 friction, the total resistance can be obtained at any scale. Note that this procedure is based on the Froude scaling described earlier, with the limitations stated.

In older literature, the speed is often given as the speed/length ratio

$$\frac{V}{\sqrt{L}}$$

where V is given in knots and L in feet, or the "circular K," defined as

$$Ⓚ = \sqrt{4\pi \frac{L}{\nabla^{1/3}} Fn_L} \tag{10.1}$$

The total resistance is sometimes given as "circular C" for a "standard" ship length of 400 feet, or 122 m

$$Ⓒ = \frac{125}{\pi} \frac{S}{\nabla^{2/3}} C_T \tag{10.2}$$

Note that this coefficient depends on the size of the ship. It may be converted to other scales by computing the total resistance for $L = 122m$, subtracting the viscous resistance for this scale and adding this resistance at the scale of interest. For best accuracy, the form factor should be included in this procedure. [It has to be estimated, for instance from equation (8.18).]

For planing and semiplaning hulls, the weight is very important and the Froude number is defined using the third root of the volume displacement rather than the length

$$Fn_\nabla = \frac{V}{\sqrt{g\nabla^{1/3}}} \tag{10.3}$$

There is thus a simple relation between K and Fn_∇

$$Ⓚ = \sqrt{4\pi} Fn_\nabla \tag{10.4}$$

The beam may also be used to represent the length

$$Fn_B = \frac{V}{\sqrt{gB}} \tag{10.5}$$

The resistance is in some cases presented for a given weight, and conversions, as indicated previously, must be done to other weights (i.e., scales).

10.1.2 Summary of Systematic Series. In Table 10.1, the parameter range is presented for three different types of series:

1. Displacement hulls
2. Semiplaning hulls
3. Planing hulls.

References are given to all series. It is seen that all of them are decades old except for the sailing yacht series from Delft, which is in fact still expanding. The reason why so few series are more recent is the very large cost in building and testing the models. In the past, these expenses were affordable, but this is not so any longer. On the other hand, CFD may be expected to take over the role of empirical methods in the future.

Table 10.1 Parameter Variation in Some Systematic Series

DISPLACEMENT SHIPS

Series	C_B	$L/\nabla^{1/3}$	L/B	B/T	Fn_L
Taylor (1933)	0.48–0.86	5–11		2.25 and 3.75	0.09–0.6
Series 60 (Todd, 1963)	0.6–0.8	5.1–6.1	6.5–8.5	2.5–3.5	0.1–0.32
Lindblad (1946, 1948, 1950)	0.535–0.7		7.4	2.4	0.18–0.32
SSPA fast cargo liners (Nordström, 1948–1949)	0.625	5.5–6.8	6.3–8.7	2.2–2.8	0.21–0.31
SSPA cargo liners (Williams, 1969)	0.525–0.725	5.1–6.9	6.2–8.4	2.4	0.18–0.32
SSPA tankers (Edstrand, Freimanis, & Lindgren (1953–1956)	0.725–0.8		7.2–8.1	2.3–2.5	0.14–0.22
SSPA coastal ships (Warholm, 1953–1955)	0.60–0.75	4.5–6.1	5.5–7.5	2.0–2.8	0.16–0.36
BSRA (Lackenby & Parker, 1966)	0.65–0.80	4.2–5.8	5–8	2.1–3.9	0.14–0.28
MARAD (Roseman, 1987)	0.80–0.875		4.5–6.5	3.0–4.5	0.10–0.20
Delft sailing yachts (Keuning & Sonnenberg, 1998)	C_p = 0.52–0.60	4.34–8.5	2.73–5	2.46–19.4	0.1–0.6

SEMIDISPLACEMENT SHIPS

Series	C_B	$L/\nabla^{1/3}$	L/B	B/T	Fn_L
Taylor, extended (Graff, Kracht, & Weinblum, 1964)	0.48–0.86	5–11		2.25–3.75	0.09–0.9
KTH/NSMB Series (Nordström, 1951)	0.35–0.55	5.8–7.8		3.2–4.4	> 0.9
Series 63 (Beys, 1963)			2.5–6.0		
Series 64 (Yeh, 1965)	0.35–0.55	8–12	8.5–18	2–4	0–1.5
SSPA small, fast displacement ships (Lindgren, 1969)	0.40–0.55	6–8		3–4	0.35–1.3
NPL (Bailey, 1976)	0.40		3.3–7.5	1.7–10.2	0.3–1.2

PLANING HULLS

Series	C_B	$L/\nabla^{1/3}$	L/B	$A_p/\nabla^{2/3}$	Fn_∇
EMB Series 50 (Davidson & Suarez, 1949)	0.35–0.42	5.5–9			< 4
Series 62 (Clement, 1963)	0.44–0.50	4.1–7.7	2–7	4.3–8.5	0.5–6
Series 65 (Hadler, Hubble, & Holling, 1974)		4–10.4	2.4–9.4	5–8.5	0–3

BSRA,British Ship Research Association; EMB, Experimental Model Basin (at the Washington Navy Yard); KTH, Royal Institute of Technology (Stockholm); NSMB, Netherlands Ship Model Basin (presently MARIN); MARAD, Maritime Administration (USA); NPL, National Physical Laboratory (London).

10.1.3 Series 60. It is out of the scope of this text to present all the series listed in Table 10.1, but one example will be given. Although many years old, the Series 60 is by far the most well-known series, and it is still used to some extent; a short presentation will be given.

The models of most methodical series have been derived from a single parent form by changes in the area curve and proportional geometrical changes. When used for very different proportions and for fullness coefficients suitable to very different values of the Froude number, such changes led to unrealistic forms, regardless of how good the parent lines may have been for the original design conditions. In Series 60, another approach was used. Five parent forms of $C_B = 0.60$, 0.65, 0.70, 0.75, and 0.80 were developed, each incorporating the features considered necessary for good resistance qualities at its appropriate value of C_B, as deduced from results for successful ships. The sectional area and waterline curves for these parents were plotted and faired to a base of the prismatic coefficients of entrance and run and cross-faired with the area curves and body plans. Auxiliary curves showed the lengths of parallel middle body for each value of C_B, and the necessary lengths of entrance and run to be associated with these to give any desired position of LCB. The sectional area curves for the five parent models are shown in Fig. 10.1.

A number of models were then run to determine the optimum location of LCB for each block coefficient, their lines being derived from the design charts just described. The results of these tests are summarized in Fig. 10.2. This shows the optimum LCB locations and the corresponding minimum circular C values. For a given value of C_B, the optimum LCB location moves aft as the value of circular K is increased. When C_B and circular K are known, this figure will give the optimum LCB position and the corresponding minimum circular C value if the proportions and lines of the ship conform with those of the Series 60 parents. Thus, for a $C_B = 0.65$ and a circular $K = 2.1$, the best position of LCB is 1.45% of L, aft of midships, the corresponding minimum circular C value for a length of 122 m (400 ft) being 0.73 and $Fn = 0.244$. A point of considerable

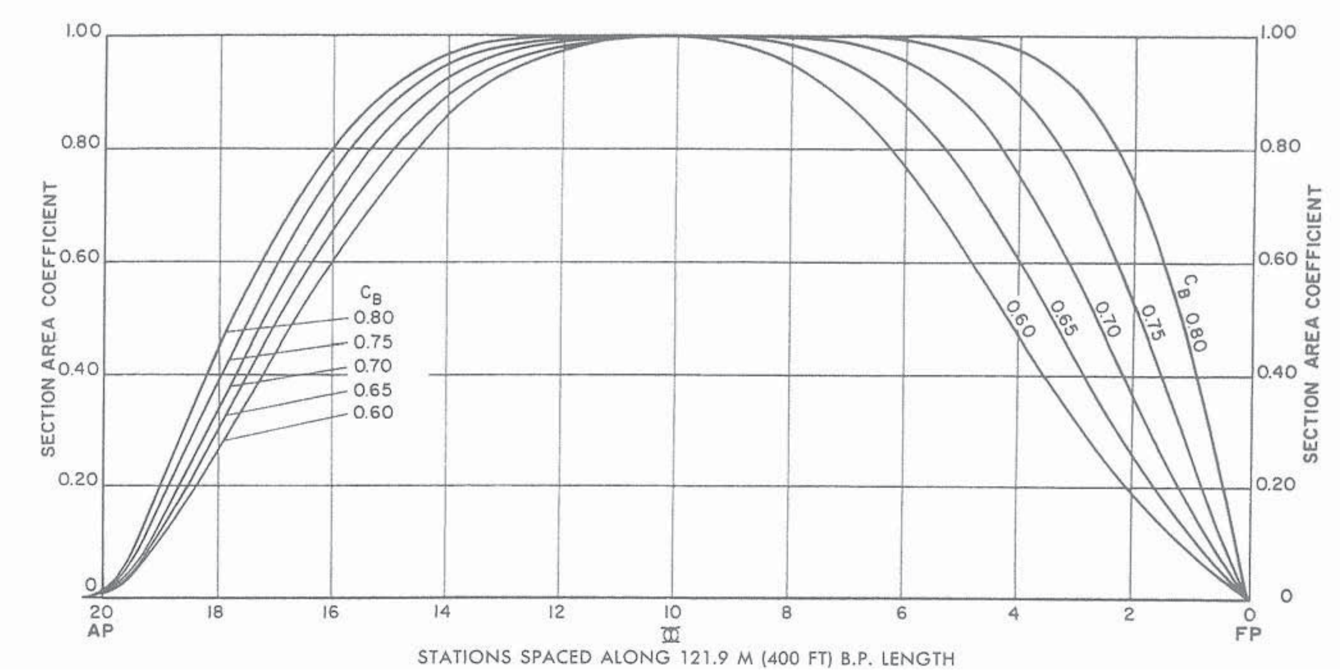

Figure 10.1 Series 60. Sectional area curves of parent models.

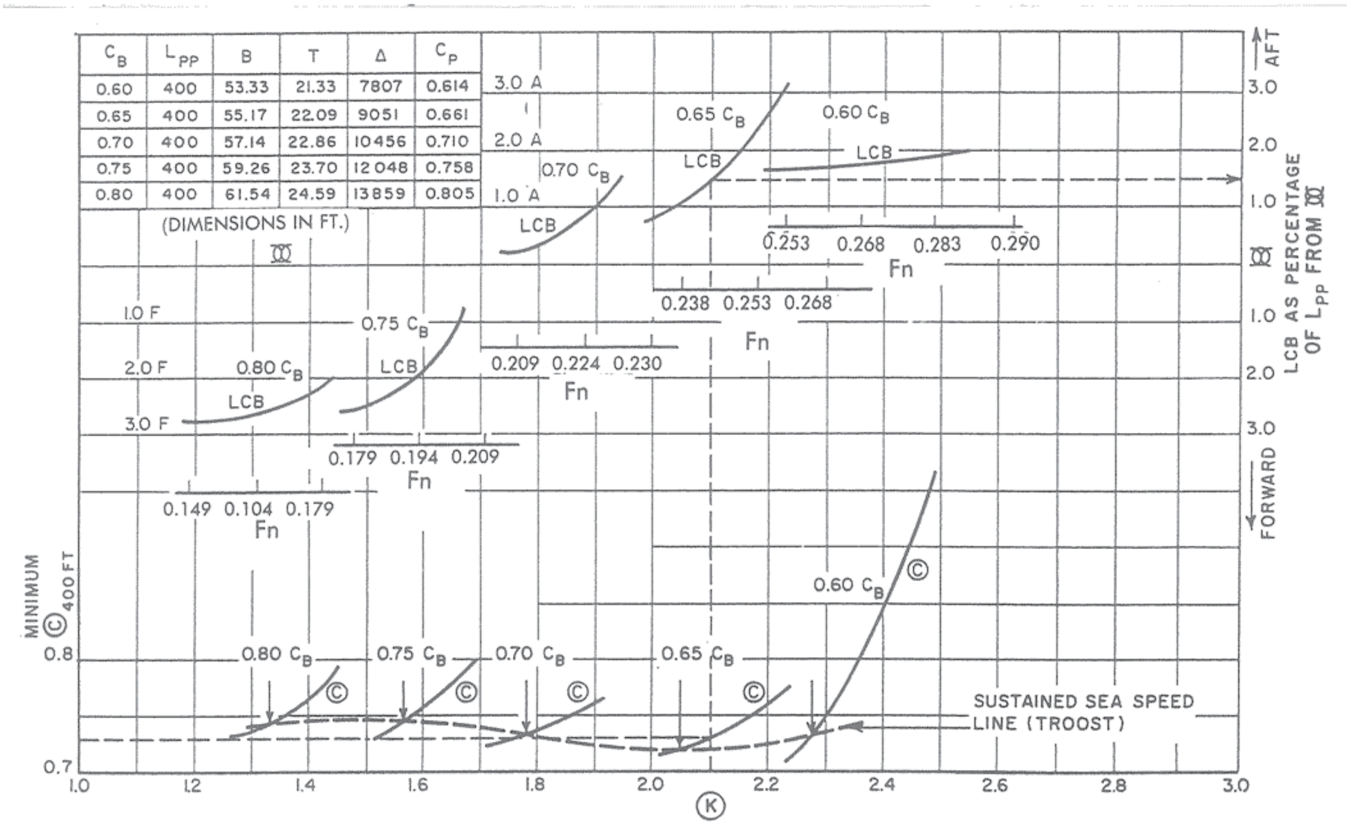

C_B	L_{PP}	B	T	Δ	C_P
0.60	400	53.33	21.33	7807	0.614
0.65	400	55.17	22.09	9051	0.661
0.70	400	57.14	22.86	10456	0.710
0.75	400	59.26	23.70	12048	0.758
0.80	400	61.54	24.59	13859	0.805

(DIMENSIONS IN FT.)

Figure 10.2 Series 60 minimum circular *C* values (for a 122 m ship) and optimum *LCB* positions.

interest is the remarkable constancy of the minimum circular C value at the Troost sustained sea speeds, which varies only between 0.72 and 0.74 over the full range of block coefficients.

The optimum location of LCB was then assumed to apply to all models of a given block coefficient, regardless of L/B and B/T, and these ratios were varied on a number of models to cover the range of values shown in Table 10.1. The results of all tests were presented in two ways:

1. Residuary resistance contours R_R/W in lbs per long ton (2240 lb) of displacement, against C_B, and L/B, each chart being for given values of B/T and $V/(\sqrt{L})$.
2. Contours of circular C for a length of 122 m against C_B, and L/B, each chart being for given values of B/T and circular K. The circular C-values included a model ship roughness allowance of 0.0004.

For design use, assuming that L, B, T, and ∇ are known, these charts enable the resistance and effective power to be estimated over a range of speeds for a ship having Series 60 lines and an LCB in the position chosen for the parent forms. For any other position of LCB dictated by design needs, the change in R_{Ts} and P_E can be estimated from the results of the auxiliary LCB variation series.

Using presented contours of sectional area and load waterline coefficients, a body plan may be produced quickly which will fulfill all the foregoing design conditions.

The data may also be used to explore the effects on power of changes in principal dimensions and coefficients during feasibility studies, so as to ensure the best results within the design conditions or to determine the penalties involved in such changes.

Further, the contours can be used for comparative purposes. If a new design has secondary characteristics which differ from those of its Series 60 equivalent, but model results are available for some other ship which more closely resembles it in these respects, the latter may be used as a "basic ship." Calculations of P_E can then be made from the contours for the Series 60 equivalents of both the new design and the basic ship. Then approximately

$$P_{Enew} = P_{ES60new}\frac{P_{Ebasic}}{P_{ES60basic}} \qquad (10.6)$$

Fig. 10.3 shows the predicted P_E for a bulk carrier with $C_B = 0.78$ derived in this way, using a tanker as the basis ship, compared with the P_E derived from actual model tests.

Finally, the models of Series 60 were all run self-propelled, and Todd (1963) includes contours of wake fractions, thrust deduction fractions, and propulsive efficiencies for a number of propeller diameters and power characteristics. These data, together with the P_E values, enable close estimates to be made of the delivered horsepower, P_D, at the propeller.

10.2 Statistical Methods. Apart from the results of the systematic series, there is a huge data bank of unsystematic material available at all towing tanks. A natural way to exploit this would be to statistically evaluate this material to find empirical relations between the resistance and the form parameters. This technique was pioneered by Doust and O'Brien (1959) who used the results from towing tests with 150 fishing vessels and tried to express the total resistance as a function of six different form parameters. The coefficients of a large polynomial up to second order in the form parameters were determined by regression analysis of the empirical data for each speed of interest. A very important result of including the second degree terms in the equation was that optimization with respect to the form parameters could be carried out.

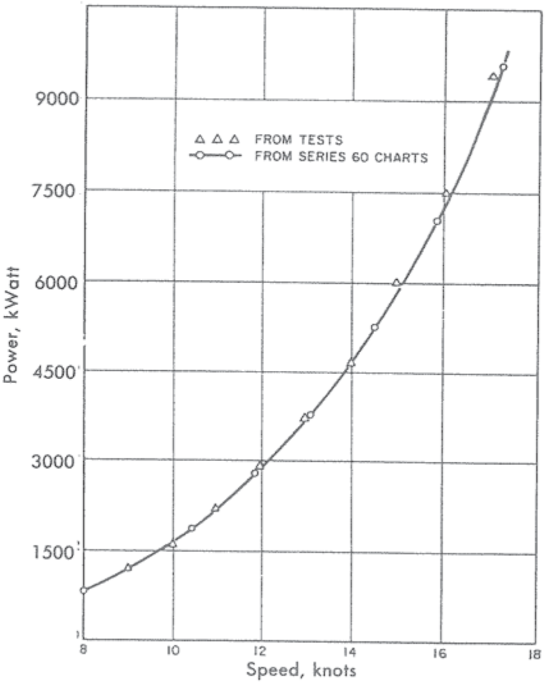

Figure 10.3 Comparison of *effective power* from model tests of a bulk carrier with estimate from Series 60 charts.

10.2.1 The Holtrop-Mennen Method. The Doust and O'Brien method is interesting in a historical perspective, but it is not in much use today. Instead, a more modern method attributed to Holtrop and Mennen (1978) has acquired widespread recognition. One disadvantage of the first statistical methods was that the formulas were entirely numerical, without any consideration of the physics. Holtrop and Mennen tried to include physical aspects in their formulas, but used the experimental data for determining the coefficients. A summary of their method which is based on test results from 334 models of tankers, cargo ships, trawlers, ferries, etc., will now be given.

The resistance is split into viscous and wave resistance. For the viscous resistance, the standard formula is used

$$C_V = (1 + k)C_F \qquad (10.7)$$

where C_F is obtained from the ITTC-57 formula. The form factor k is determined from a formula obtained statistically as $k = f(B/L, T/L, L/L_R, L^3/\nabla, C_P, c)$. c is a coefficient dependent on the shape of the afterbody and L_R is the length of the afterbody. If L_R or S are unknown, they may be obtained from other statistically derived formulas.

The appendage resistance is considered as a correction to the form factor.

For the wave resistance, Holtrop and Mennen use a theoretical expression attributed to Havelock (1913), obtained by replacing the hull by two pressure disturbances separated by the wave making length of the hull. The original expression is, however, somewhat elaborate and a simplification is made. This leads to the following equation

$$\frac{R_R}{W} = C_1 C_2 C_3 e^{mFn^d} + m_2 \cos(\lambda Fn^{-2}) \qquad (10.8)$$

where W is the weight of the ship and C_1, C_2, C_3, m, and m_2 are coefficients, which are functions of the form parameters of the hull. Different coefficients are used for $Fn < 0.40$ and $\mathrm{Fn} > 0.55$. In the intermediate range, the residuary resistance is obtained by an interpolation formula between the two limits.

Holtrop and Mennen also suggest a formula for the roughness allowance ΔC_F and compute the total resistance as

$$R_T = \frac{1}{2}\rho V^2 S[C_F(1 + k) + \Delta C_F] + \frac{R_W}{W}W \qquad (10.9)$$

10.2.2 Savitsky's Method for Planing Hulls. Although the Holtrop-Mennen method is by far the most widely used for displacement hulls, the method attributed to Savitsky (1964) and Hadler (1966) is still in very frequent use for planing hulls. It is based on systematic tests with planing prisms, where the trim angle, deadrise angle, wetted length, and wetted length/beam ratio were systematically varied.

Given the values of the speed V, the weight W, the deadrise angle β, and the maximum beam b, measured between the chines, Savitsky's formulas give the wetted length L_m, the trim angle τ, and the relation between the dynamic lift and the buoyancy. When planing, the resistance of the hull may be computed from

$$R = W \tan\tau + \frac{\frac{1}{2}\rho V^2 L_m b C_F}{\cos\tau \cos\beta} \qquad (10.10)$$

where C_F is obtained from a Reynolds number based on the wetted length L_m and a velocity which is lower than the free speed because the pressure is higher on the bottom of the hull than in the free stream. The first term in the equation is the wave resistance, which is thus easily calculated for the planing hull as the horizontal component of the pressure force acting on the bottom. The second term is the friction. Form effects are very small for planing hulls.

11

Hull Design

Although the considerations of the present section may be of guidance to naval architects in the choice of hull shape and dimensions, they must meet many other demands and will be influenced to a large extent by the knowledge of the particulars of existing successful ships. The process of design is essentially an iterative one, in which the various elements are changed until a proper balance is attained. In order to do this, parametric surveys have to be made on the effects of changes in dimensions, hull form, machinery types, and so on. Thanks to the rapid development in computer technology, the designer may now consider a far greater number of possible solutions than could ever be made in the past.

We will start this section with general discussions on the choice of main dimensions and form parameters. These topics will be discussed in Sections 11.1 and 11.2, respectively. Because the minimization of propulsive power also involves the hull/propeller interaction, a short note on the relation between resistance and delivered power is presented in Section 11.3, followed by a discussion of design principles for four different ship types in Section 11.4. The possibilities of locally improving the hull shape have increased considerably during the past years, particularly due to the development of the numerical methods descibed in Section 9, but also due to the more advanced experimental techniques of Section 8. In Sections 11.5 and 11.6 the application of these modern tools for local hull refinement will be presented.

11.1 Main Dimensions. The length of the ship is mainly determined from considerations which are not of a hydrodynamic nature. Such considerations are building cost, scantlings, equipment, and geometrical restrictions because of the slipway, building dock, locks or harbors. Schneekluth and Bertram (1998) give a formula for the optimum length considering production cost

$$L_{pp} = 3.2\,\Delta^{0.3} V^{0.3} \frac{C_B + 0.5}{0.145/Fn + 0.5} \qquad (11.1)$$

The formula is applicable for bulbous bow ships with $\Delta \geq 1000t$ and $0.16 \leq Fn \leq 0.32$. Ships optimized for yield are about 10% longer than those optimized using equation (11.1).

statistically as $k = f(B/L, T/L, L/L_R, L^3/\nabla, C_P, c)$. c is a coefficient dependent on the shape of the afterbody and L_R is the length of the afterbody. If L_R or S are unknown, they may be obtained from other statistically derived formulas.

The appendage resistance is considered as a correction to the form factor.

For the wave resistance, Holtrop and Mennen use a theoretical expression attributed to Havelock (1913), obtained by replacing the hull by two pressure disturbances separated by the wave making length of the hull. The original expression is, however, somewhat elaborate and a simplification is made. This leads to the following equation

$$\frac{R_R}{W} = C_1 C_2 C_3 e^{mFn^d} + m_2 \cos(\lambda Fn^{-2}) \qquad (10.8)$$

where W is the weight of the ship and C_1, C_2, C_3, m, and m_2 are coefficients, which are functions of the form parameters of the hull. Different coefficients are used for $Fn < 0.40$ and $\mathrm{Fn} > 0.55$. In the intermediate range, the residuary resistance is obtained by an interpolation formula between the two limits.

Holtrop and Mennen also suggest a formula for the roughness allowance ΔC_F and compute the total resistance as

$$R_T = \frac{1}{2}\rho V^2 S[C_F(1+k) + \Delta C_F] + \frac{R_W}{W}W \qquad (10.9)$$

10.2.2 Savitsky's Method for Planing Hulls. Although the Holtrop-Mennen method is by far the most widely used for displacement hulls, the method attributed to Savitsky (1964) and Hadler (1966) is still in very frequent use for planing hulls. It is based on systematic tests with planing prisms, where the trim angle, deadrise angle, wetted length, and wetted length/beam ratio were systematically varied.

Given the values of the speed V, the weight W, the deadrise angle β, and the maximum beam b, measured between the chines, Savitsky's formulas give the wetted length L_m, the trim angle τ, and the relation between the dynamic lift and the buoyancy. When planing, the resistance of the hull may be computed from

$$R = W \tan\tau + \frac{\frac{1}{2}\rho V^2 L_m b C_F}{\cos\tau\cos\beta} \qquad (10.10)$$

where C_F is obtained from a Reynolds number based on the wetted length L_m and a velocity which is lower than the free speed because the pressure is higher on the bottom of the hull than in the free stream. The first term in the equation is the wave resistance, which is thus easily calculated for the planing hull as the horizontal component of the pressure force acting on the bottom. The second term is the friction. Form effects are very small for planing hulls.

11

Hull Design

Although the considerations of the present section may be of guidance to naval architects in the choice of hull shape and dimensions, they must meet many other demands and will be influenced to a large extent by the knowledge of the particulars of existing successful ships. The process of design is essentially an iterative one, in which the various elements are changed until a proper balance is attained. In order to do this, parametric surveys have to be made on the effects of changes in dimensions, hull form, machinery types, and so on. Thanks to the rapid development in computer technology, the designer may now consider a far greater number of possible solutions than could ever be made in the past.

We will start this section with general discussions on the choice of main dimensions and form parameters. These topics will be discussed in Sections 11.1 and 11.2, respectively. Because the minimization of propulsive power also involves the hull/propeller interaction, a short note on the relation between resistance and delivered power is presented in Section 11.3, followed by a discussion of design principles for four different ship types in Section 11.4. The possibilities of locally improving the hull shape have increased considerably during the past years, particularly due to the development of the numerical methods descibed in Section 9, but also due to the more advanced experimental techniques of Section 8. In Sections 11.5 and 11.6 the application of these modern tools for local hull refinement will be presented.

11.1 Main Dimensions. The length of the ship is mainly determined from considerations which are not of a hydrodynamic nature. Such considerations are building cost, scantlings, equipment, and geometrical restrictions because of the slipway, building dock, locks or harbors. Schneekluth and Bertram (1998) give a formula for the optimum length considering production cost

$$L_{pp} = 3.2\,\Delta^{0.3} V^{0.3}\,\frac{C_B + 0.5}{0.145/Fn + 0.5} \qquad (11.1)$$

The formula is applicable for bulbous bow ships with $\Delta \geq 1000t$ and $0.16 \leq Fn \leq 0.32$. Ships optimized for yield are about 10% longer than those optimized using equation (11.1).

Hydrodynamically, a longer ship will normally perform better in a seaway. As to the resistance, a longer ship at a given speed will operate at a lower Froude number than a shorter one, which will reduce the wave resistance, as explained in Section 5. As this resistance component increases very rapidly at higher speeds, this effect can be significant. On the other hand, it has to be balanced against the increased wetted surface which will cause an increased viscous resistance. Because the ratio of the two resistance components (i.e., R_W/R_V) increases with speed, a high-speed ship should be longer than a low-speed ship at a given displacement. A classical formula based on statistics from actual ships is attributed to Ayre (see Schneekluth & Bertram (1998)

$$\frac{L_{pp}}{\nabla^{\frac{1}{3}}} = 3.33 + 10.2Fn \tag{11.2}$$

Here the original speed/length ratio has been replaced by the Froude number, assuming an acceleration of gravity of 9.81 m/s^2. This formula is for ships without a bulbous bow. A bulb should reduce the L_{pp} by 75% of the bulb length in front of the forward perpendicular. Other formulas are also given in Schneekluth and Bertram (1998).

The length should be chosen such that a hollow in the wave resistance curve occurs at the design speed of the ship. If this is not possible, at the very least humps should be avoided. As explained in Section 5, humps and hollows arise from interference effects between the wave systems around the hull. This interference is complex and can only be accurately evaluated through experiments or numerical predictions using methods described in Section 9. An approximate evaluation of the interference might be made using the Baker and Kent theory mentioned in Section 5.5 but it must be stressed that this theory is too simple to account for large differences in hull shape. In Table 11.1, empirical values for the Froude number of different ships are given. The speed of a displacement hull is normally restricted by the last hump and it is often hard to achieve higher Froude numbers than about 0.45.

Having determined displacement and length, the next step is often to fix the block coefficient C_B. This will be dealt with in the Section 11.2. The product $B \cdot T$ can then be obtained from the definition of the block coefficient

$$C_B = \frac{\nabla}{L \cdot B \cdot T} \tag{11.3}$$

Table 11.1 Approximate Froude Numbers for Humps and Hollows

Fn	Hump/Hollow	Typical Hull
0.19	Hollow	Medium size tankers
0.23	Hump	
0.25	Hollow	Containerships, dry cargo ships, ferries
0.29–0.31	Hump	Fishing vessels
0.33–0.36	Hollow	Reefers, sailing yachts upwind in a breeze
0.45–0.50	Hump (last)	Frigates, destroyers

It remains to determine the B/T ratio.

The beam, B, is one of the governing factors in ensuring adequate stability, and a minimum value of B/T is generally necessary on this account. An increase in B/T will increase the resistance because volume is moved closer to the surface, which will increase the wave resistance. In cases of low-speed ships, however, a small reduction in length and a compensating increase in beam, because of the resulting decrease in wetted surface, may result in little or no increase in resistance. This results in a cheaper ship and also meets the need for increased stability for ships with large superstructures. This idea has been exploited in a number of large tankers.

The minimum wetted surface for a given displacement is also sensitive to the B/T ratio, the optimum value of which is about 2.25 for a block coefficient of 0.80 and about 3.0 for $C_B = 0.50$. However, the penalty for normal departures from these values is not very great. The effects of changes in B/T on wave-making resistance can be studied from model-experiment results. Generally, stability considerations and draft limits usually preclude values of B/T below 2.25 for full ships and 2.5 or even more, for fine, higher speed ships. It should be noted that a larger draft normally gives more space for the propeller, whose diameter may be increased and the propulsive efficiency improved.

11.2 Fullness and Displacement Distribution. The fullness of a ship and its longitudinal distribution of displacement is determined by the sectional area curve, which is an important output from all CAD programs for ship design. It is often desirable to start with a good sectional area curve and try to keep this more or less unchanged while optimizing the detailed hull shape. As will be seen, particularly critical regions are the fore and aft shoulders, where a too large normal curvature of the hull in the flow direction will cause unnecessarily deep wave troughs. Such curvatures may be avoided with a suitable shape of the sectional area curve. Examples of good sectional area curves will be given in the more detailed description of several classes of ships in Section 11.4.

The two main parameters derived from the sectional area curve are the prismatic coefficient C_P and the *LCB*. Optimum values of these parameters are strongly Froude number dependent, and the sectional area curve should be designed such that optimum values of the parameters are achieved. In this section, the reasons for the different optima will be explained. Five different Froude number ranges will be discussed, as defined in Fig. 11.1. It should be mentioned that the optimum is also dependent to some extent on the specific form of the fore and afterbody lines. For instance, a barge-type stern should have a more aftward *LCB* than a V-type stern.

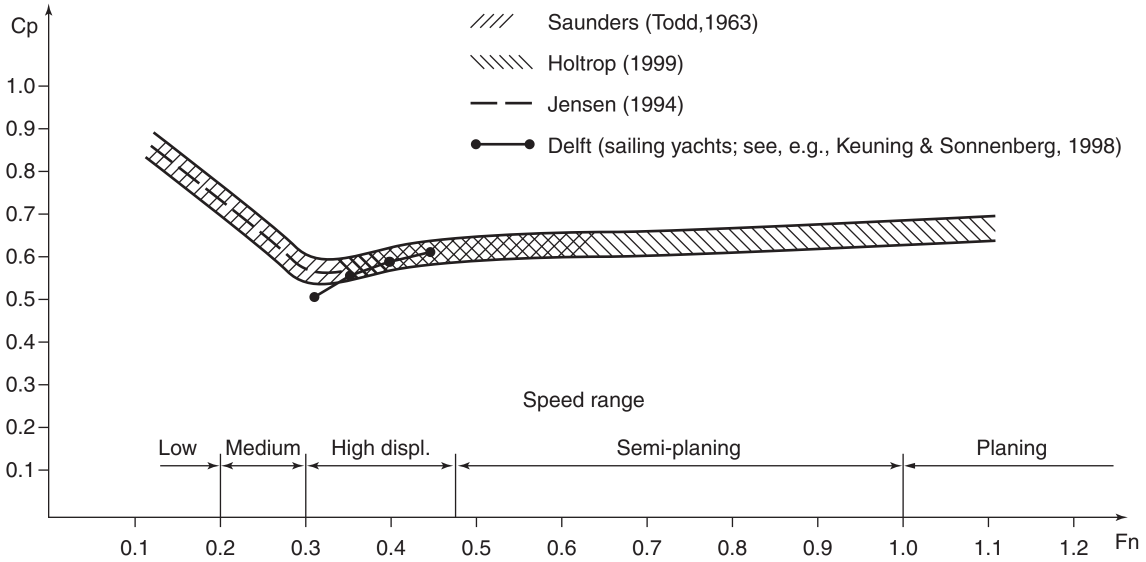

Figure 11.1 Optimum prismatic coefficient versus Froude number.

Fig. 11.1 is based on results from four different sources and shows the optimum* prismatic coefficient for all Froude numbers from low speed to planing. It is seen that at the lowest speeds, the optimum hull is very full and prismatic coefficients as high as 0.85 or even higher are the best. Increasing the Froude number, the optimum C_P is rapidly reduced to a minimum of 0.55–0.60 in the region $Fn = 0.30$–0.35, thereafter increasing relatively rapidly to 0.60–0.65 around the main hump. In the semi-planing range, C_P increases slowly to 0.65–0.70, and this increase continues in the planing range.

The prismatic coefficient may be converted into the block coefficient using the midship section coefficient C_M as follows

$$C_B = C_M \cdot C_P \tag{11.4}$$

C_M varies with fullness. For the most full-bodied slow ships, it may be as high as 0.995. As the fullness decreases and the length of the parallel middle body becomes shorter, it is necessary to ease the midship section area somewhat to avoid too pronounced shoulders in the lower waterlines. Typical relations among C_B, C_P, and C_M for displacement ships are shown in Table 11.2.

The variation of *LCB* is shown in Fig. 11.2, where the optimum position relative to midship is presented. The distance is made dimensionless by the L_{pp} and is positive forward. There is a very rapid shift aftward of the *LCB*, from about +3% to about −2% in the Froude number range 0.15–0.25. Thereafter, the shift is more gradual, reaching −6% at a Froude number of 1.0.

The reason for the changes in C_P and *LCB* is the relative weight of the two main resistance components: viscous and wave resistance. At low speed, the viscous resistance is dominant, but its importance is reduced as the speed is increased. How this affects the fullness and displacement distribution will now be explained.

11.2.1 Low Speed ($Fn \leq 0.2$). As was seen in Fig. 4.1, the viscous resistance is by far the largest resistance component for a tanker. This means that emphasis should be placed on minimizing the wetted surface and that the stern should be fine enough for the boundary layer to develop slowly. Separation, particularly of the bubble type, should be avoided and the boundary layer should be as thin as possible to minimize the momentum losses. A reasonably fine stern is also necessary to obtain a good wake field. Fig. 11.3 shows a principal sketch of the design waterline of a ship optimized for this low speed range.

An elongated, pointed bow will have a relatively large wetted surface, so it is better to make the bow more bluff, particularly as the forward shoulder may then be made

Table 11.2 Typical Relations among Block, Prismatic, and Midship Section Area Coefficients for Displacement Ships

C_B	0.80	0.75	0.70	0.65	0.60	0.55	0.54–0.52
C_P	0.805	0.758	0.710	0.661	0.614	0.59	0.59–0.575
C_M	0.994	0.990	0.986	0.982	0.978	0.93	0.915–0.905

Source: Lewis, E. (Ed.). (1988). *Principles of Naval Architecture* (2nd rev., Vol. II). Jersey City, NJ: SNAME.

---

*Strictly speaking, the data from Saunders (1957), Marin (Holtrop, 1999), and Jensen (1994) indicate a design lane (i.e., a range within which most existing ships are designed). Other aspects than pure resistance are thus considered. The resistance is however the major parameter, and in the case of the Delft series this is the only parameter considered.

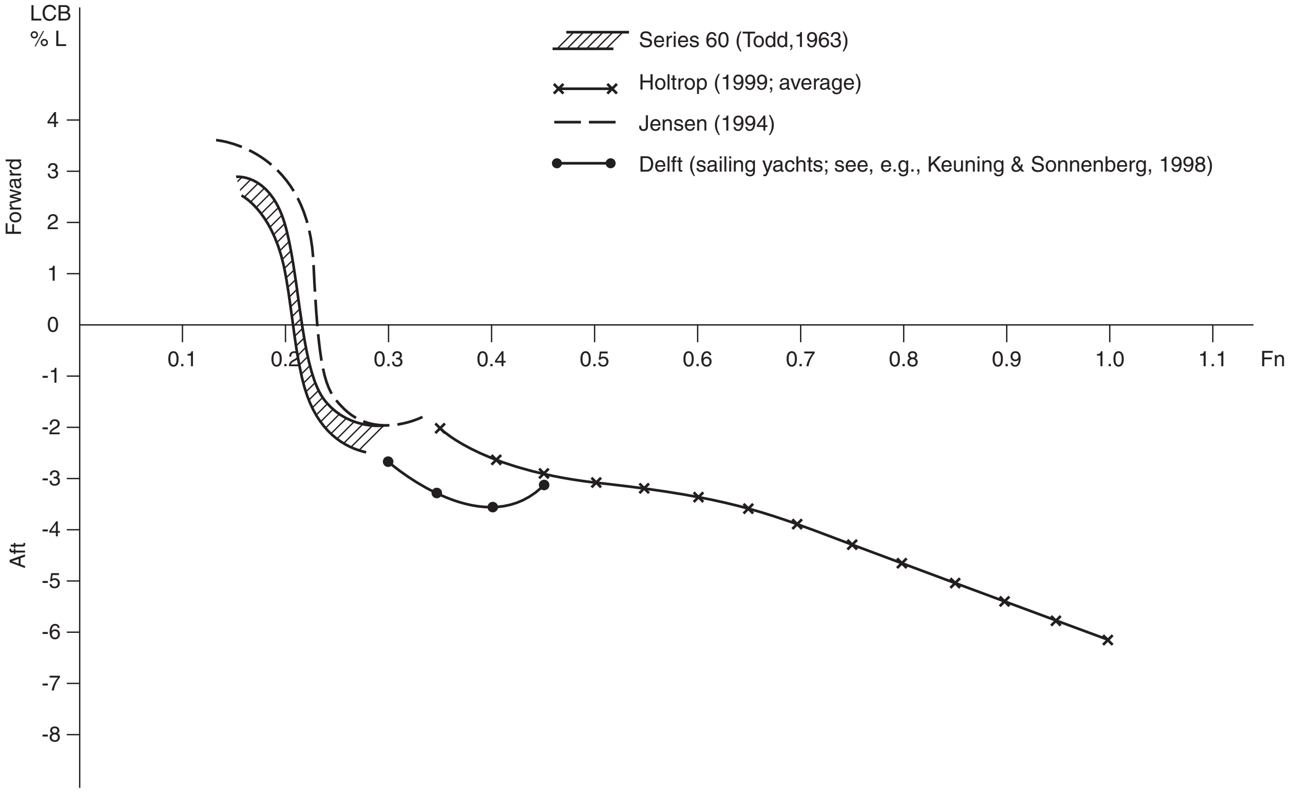

Figure 11.2 Optimum location of center of buoyancy versus Froude number.

softer (i.e., with a larger radius). Although the wave resistance is very small (7.5% of the total in Fig. 4.1), a reduction by making the shoulder wave trough less deep is noticeable.

Because the stern has to be more slender than the bow, the *LCB* is forward of midship. The large fullness of the bow causes C_P and C_B to be high.

11.2.2 Medium Displacement Speed ($0.2 < Fn \leq 0.3$). The wave resistance is now more important (17.5% of the total in the example shown in Fig. 4.1), and the bow needs to be shaped to reduce the large peak in pressure caused by a bluff bow. A much thinner and elongated pointed bow is thus required, as seen in Fig. 11.4. Otherwise, the bow wave would be very large.

Because the bow is now much thinner, the *LCB* is moved aft and C_P and C_B are reduced considerably to the minimum value presented in Fig. 11.1.

11.2.3 High Displacement Speeds ($0.3 < Fn \leq 0.5$). We are now in a speed range typical of the fishing vessel in Fig. 4.1, and the wave resistance is the largest component (62.5% in the example). There are reasons not to make the ends too fine in this case. With fine ends, the pressure disturbance is reduced, but the peak of the pressure is moved toward midship at both ends (i.e., the wave-making length is reduced). This effect is shown for the forebody in Fig. 11.5.

Also, with the ends too fine, a large part of the volume is concentrated near midship, which may cause the

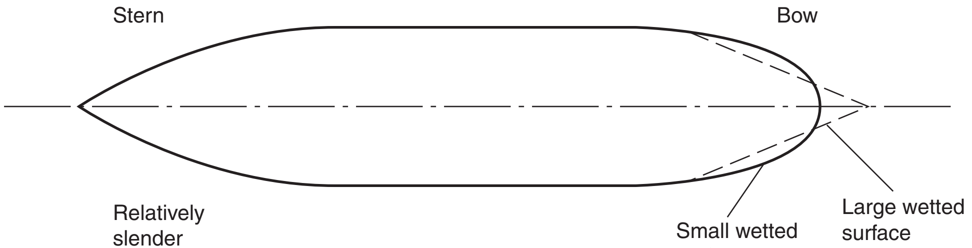

Figure 11.3 Low speed shape (principle).

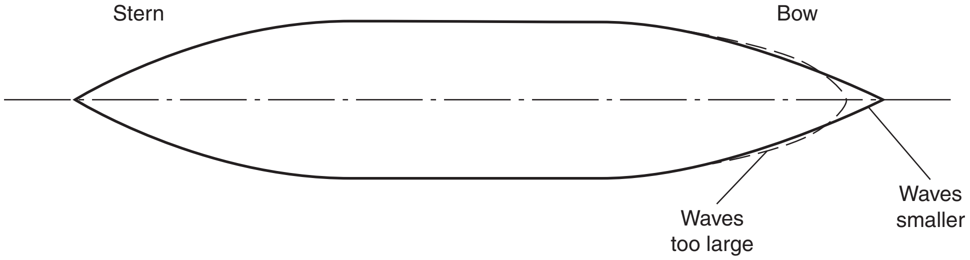

Figure 11.4 Medium displacement speed shape (principle).

normal curvature of the waterlines in this area to be unnecessarily large, resulting in a deep wave trough being generated. This so-called "diamond effect" gives rise to a too large wave resistance.

At the afterbody, there is an additional advantage of a somewhat fuller stern. As was shown in Fig. 6.9, the pressure is reduced because of the displacement effect of the boundary layer, particularly if the flow separates (bubble type). Unfortunately, this gives rise to the viscous pressure resistance, but it also gives rise to a reduction in the stern waves. Further, the hull is elongated, as seen in Fig. 11.5, and this increases the wave-making length. A full stern means a thick boundary layer, possibly even with some bubble-type separation, and is thus advantageous from a wave resistance point of view. Great care should be exercised, however, not to increase the viscous pressure resistance too much.

A final reason for having a relatively full stern at these Froude numbers is to reduce the trim, which can be excessive approaching the last hump.

The not-too-thin bow and the relatively full stern means a higher C_P than at medium speed and the LCB continues to move backward.

11.2.4 Semiplaning ($0.5 < Fn \leq 1.0$) and Planing ($Fn > 1.0$) Speeds. Around the main hump in the resistance curve ($Fn \approx 0.5$), the wave resistance is the dominating component. Higher up, both the wave and the viscous resistance are important. Typical of hulls at these high speeds is the submerged transom.* The flow leaves the bottom tangentially backward at the transom edge where the hydrodynamic pressure is low and the wave has a trough. The first crest (rooster tail wave) is formed behind the hull (Fig. 11.6). Of course, this is provided the water clears the transom. At a certain critical Froude number, the rooster tail wave will become

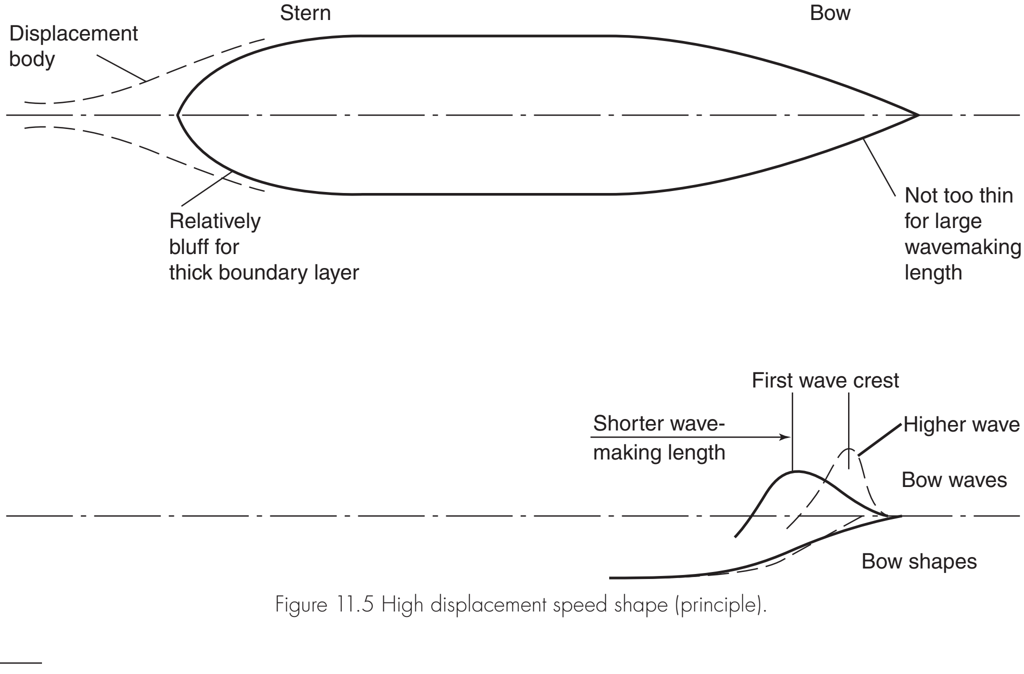

Figure 11.5 High displacement speed shape (principle).

---

*Transom sterns are also used at lower speeds. In fact, even the slowest ships may have a small submerged transom, but that is not dry. This is to make the ship as short as possible. An alternative would have been to steepen the slope of the buttocks aft, but that may cause even more recirculating flow and resistance than the small transom. Dry transoms may occur in the upper high displacement speed range to lengthen the effective waterline length. A more comprehensive discussion of transom sterns will be given in Section 11.5.11.1.

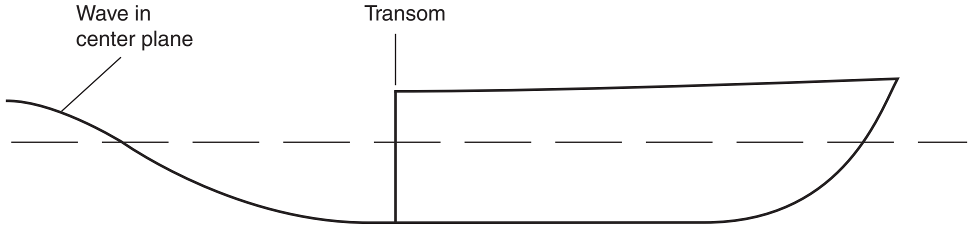

Figure 11.6 Transom stern hull and rooster tail wave (cut through centerplane).

very steep just behind the transom and start breaking, with breakers rolling forward. At speeds lower than the critical value, the transom will become fully wetted. In Section 11.5.11, considerations for estimating the critical Froude number are given and guidelines are presented for optimizing the transom stern hull.

The disadvantage of dry transoms is that the hydrostatic pressure $-\rho g z$ is lost in this area. Because there is no water, the pressure must be atmospheric. In a linearized sense (see Section 9.6.2), the hydrostatic pressure for a ship without a transom does not give rise to any force in the horizontal plane. Integrating this pressure component around the hull up to the undisturbed waterline $z = 0$ should give a zero net force horizontally. (As opposed to vertically, where the buoyancy force is obtained.) For a dry transom, the loss of the force pointing forward gives rise to a resulting hydrostatic pressure force of equal magnitude pointing backward (i.e., a resistance component). In coefficient form, this may be computed as

$$C_{tr} = \frac{-\rho g \int_{z_{tr}}^{0} z b dz}{\frac{1}{2}\rho V^2 S} = \frac{-\rho g \bar{z}_{tr} A_{tr}}{\frac{1}{2}\rho V^2 S} = -2\frac{A_{tr}}{S}\frac{\bar{z}_{tr}}{L}\frac{gL}{V^2}$$

$$= -\frac{A_{tr}}{S}\frac{\bar{z}_{tr}}{L}\frac{2}{Fn^2} \qquad (11.5)$$

Here, b is the local width of the transom and $\bar{z}_{tr}$ and A_{tr} the z-coordinate of the centroid and the area of the submerged part of the transom, respectively (Fig. 11.7). Note that $\bar{z}_{tr}$ is negative.

The previous discussion is for the linearized case where the integration of the pressure is made only up to the undisturbed water level (see Section 9.6.2). In reality, the integration must be made up to the wavy surface (Section 9.6.5). If this is done all around the hull, the hydrostatic part of the pressure force is then generally non-zero, even for hulls without a transom. This is however a higher order effect and the estimated pressure force in equation (11.5) is a good approximation. The transom resistance coefficient is thus inversely proportional to the Froude number squared. At speeds slightly above the critical value, where the transom is dry, C_{tr} is often considerably larger than the resistance associated with the hydrodynamic pressure. The transom area must therefore be kept rather small at these speeds, normally considerably smaller than the area of the midship section. As the speed increases, the convex curvature of the buttocks aft of midship tends to suck the hull into the water and should therefore be straightened out, with a larger transom as a consequence. There is thus a balance between the lift generating full afterbody and the transom resistance. The larger the speed, the more important the full afterbody, so the prismatic coefficient goes up steadily and the *LCB* moves aft with speed.

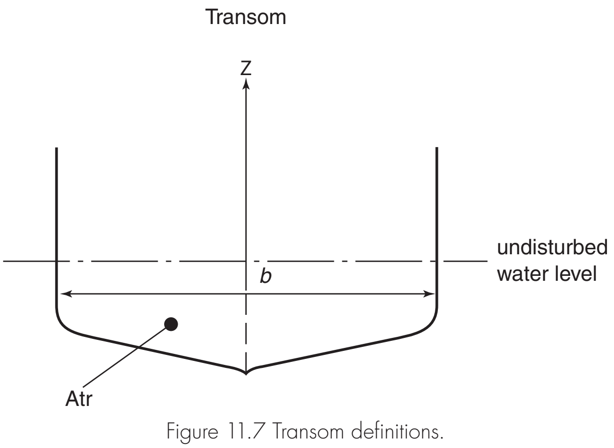

Figure 11.7 Transom definitions.

11.3 Resistance and Delivered Power. Before entering into a discussion of the more detailed design of some common ship types, the relationship between resistance and delivered power must be clarified. Focusing entirely on the resistance aspects will lead to a suboptimization which might very well produce a nonoptimum shape from the point of view of overall propulsive power. To minimize the power consumption, the interaction between the hull and the propeller must be taken into account and this is strongly dependent on the shape of the afterbody.

The power useful for moving the ship is called the effective power, P_E. This is related to the total resistance, R_T, through the equation

$$P_E = R_T V \qquad (11.6)$$

The power delivered to the propeller by the shaft is the delivered power, P_D. A propulsive efficiency η_D may thus be defined as

$$\eta_D = \frac{P_E}{P_D} \qquad (11.7)$$

In the Propulsion volume of the *Principles of Naval Architecture*, it is shown that η_D may be subdivided as follows

$$\eta_D = \eta_H \eta_R \eta_0 \qquad (11.8)$$

where η_0 represents the efficiency of the propeller operating in an undisturbed flow and η_R accounts for the change in propeller efficiency when operating in the highly turbulent flow behind the hull. The parameter of interest in the present context is η_H, the hull efficiency. This takes into account both the suction effect from the propeller on the flow around the stern and the reduction in inflow velocity to the propeller due to the boundary layer/wake from the hull. It turns out that η_H is larger than 1 for many ships, which may seem impossible for an efficiency factor, but it is related to the fact that the momentum loss in the boundary layer/wake may be utilized to increase the propulsive efficiency. The basic principle may be explained with reference to Fig. 11.8.

Seen by an observer onboard the ship, the wake of the hull generally exhibits smaller velocities than in the undisturbed flow further out. However, in the slipstream behind the propeller, the velocity is higher than the undisturbed velocity. A rather uneven distribution of velocity is therefore often left behind the hull. If the excess velocities in the slipstream could be designed to exactly compensate for the velocity deficit in the entire wake, an undisturbed flow would be left behind the hull. This is the optimum case, and it cannot be achieved in practice. But the mere fact that there is some compensation gives rise to an increase in the total propulsive efficiency, manifested through a hull efficiency larger than 1. In the optimization process, the designer has to consider this effect as well as the resistance.

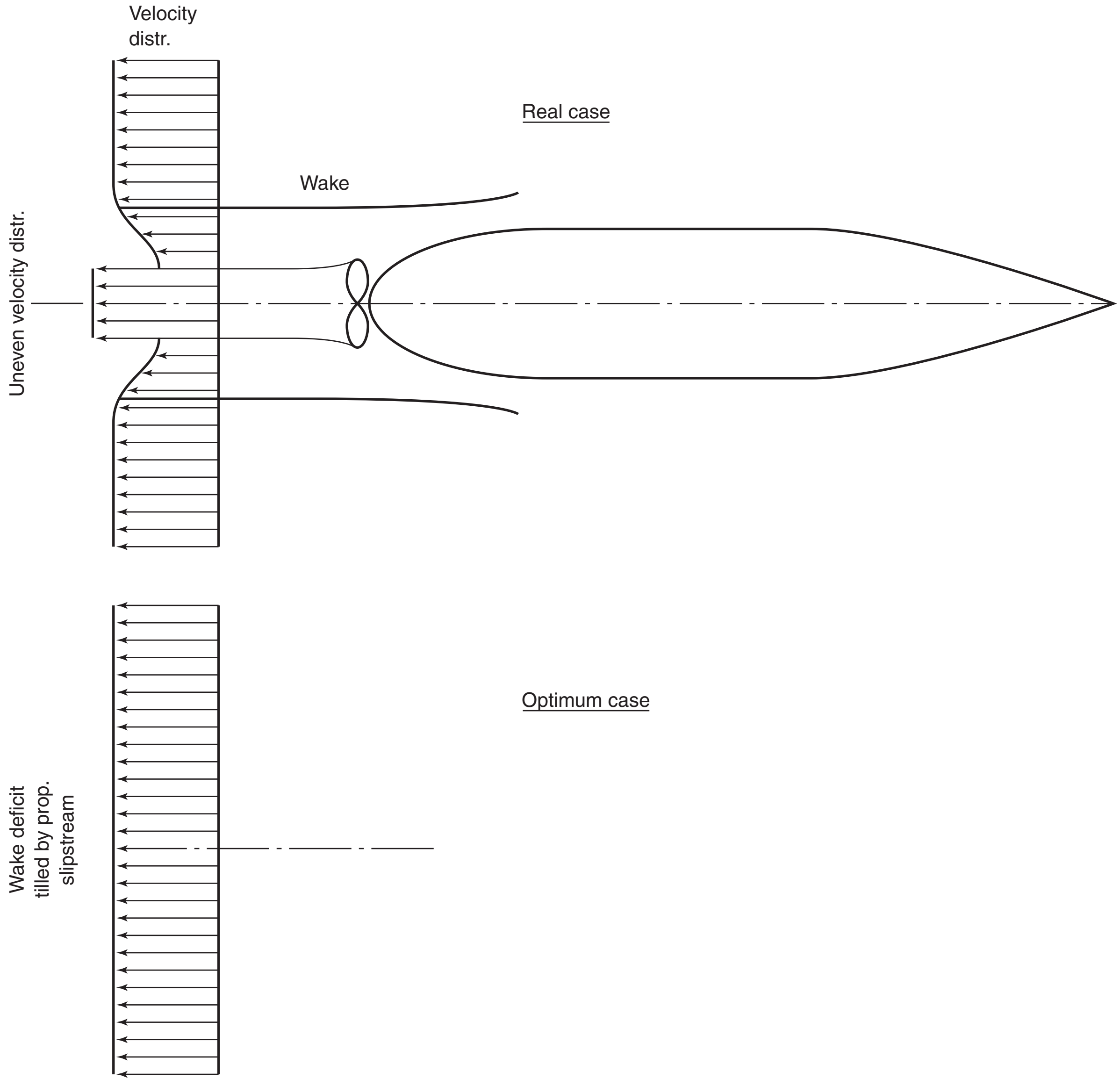

Figure 11.8 Nonoptimum and optimum velocity distribution in the far field behind a propelled ship (principle).

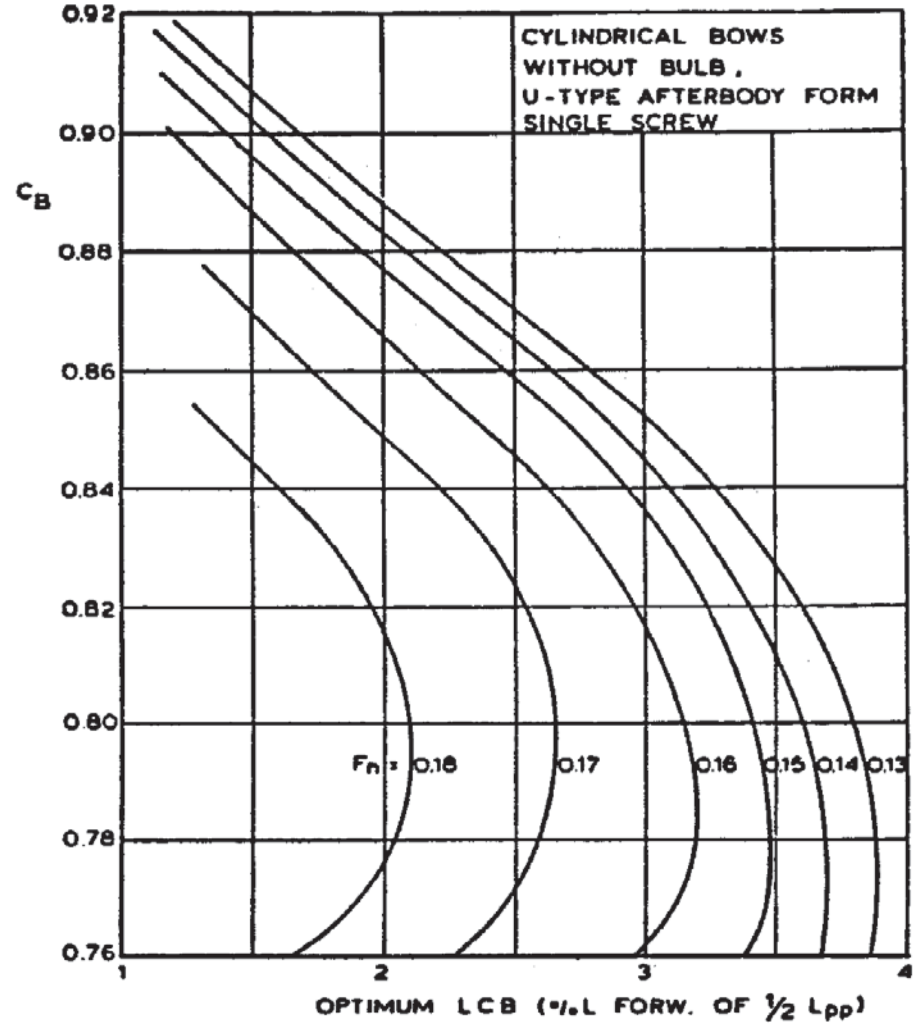

Figure 11.9 Optimum *LCB* for high-block ships (MARIN).

11.4 Typical Design Features of Four Classes of Ships.* In this section, typical features of four classes of ships will be described. The classes are:

1. Full ship forms
2. Slender hull forms
3. Ferries and cruise liners
4. High-speed ships

General guidelines will be given for the main parameters and for the forebody and afterbody design. Note that further discussions on the design of the forebody and afterbody will be presented in Sections 11.5 and 11.6.

11.4.1 Full Ship Forms

11.4.1.1 Fullness and Displacement Distribution. Ships covered here have block coefficients in the range of 0.76–0.90. They operate at low Froude numbers in the range 0.13–0.19. A rough estimate of *LCB* may be made using Fig. 11.2, but a better optimization can be obtained using the diagram presented in Fig. 11.9. The diagram is for cylindrical bows with a U-type single screw afterbody. For deviations from this shape, the recommendations of Table 11.3 are given. A typical sectional area curve for

Table 11.3 Corrections to the Optimum *LCB* from Figure 11.9

Form Deviation	Shift of Optimum *LCB*
Bulb	Forward
Noncylindrical bow	Aft
Barge-type afterbody	Aft
Twin screw	Aft
Increase *B*/*T*	Aft

---

*Most of the material in Section 11.4 is based on a course synopsis by Jan Holtrop, MARIN, Holland (Holtrop, 1999). Some parts of these are due to older material composed by E. Vossnack and others. The authors are indebted for the permission to use this synopsis. Many comments and discussions are added, however.

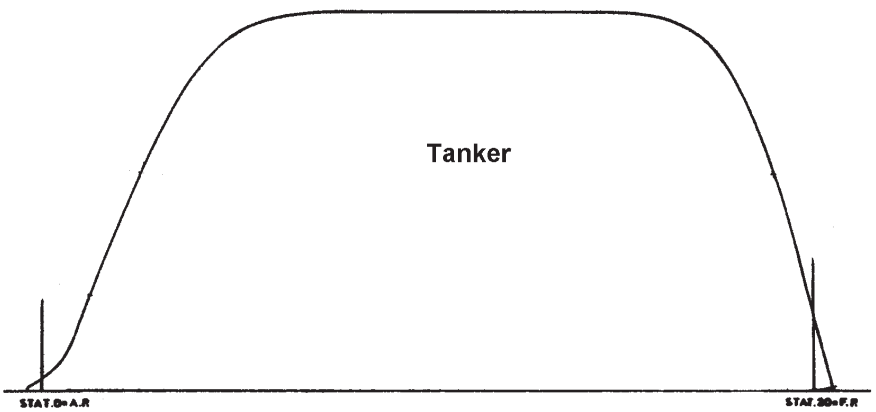

Figure 11.10 A typical sectional area curve for a conventional tanker (Valkhof, 1999).

a conventional tanker with a bulbous bow is shown in Fig. 11.10.

11.4.1.2 Forebody Design. Designing the forebody of these full ship forms is a subtle balance between the bluntness of the bow and the sharpness of the forward shoulder. The only wave interaction of importance for this ship type is that between the bow and the forward shoulder wave. If the bow is made too blunt, the wave gets very steep and considerable breaking may occur. On the other hand, if the bow is made more sharp, volume is moved aft and the shoulder will be more pronounced. This may cause the wave trough to be very deep.

One way to remove volume from the shoulder area is to move it to the aftbody and a successful change in this direction is presented in Fig. 11.11. For the two hulls, experiments indicated a reduction in ship resistance of 12% to 15% by this modification. In this case, the hull was run at a relatively high Froude number, so the wave resistance was considerably larger than the normal circa 10% for a tanker.

Considerable improvements in resistance are also obtained by fitting a suitable bulb to the bow. In fact, in this case reductions larger than the wave resistance are also obtained. There is thus also an effect on the viscous flow and this may be explained with reference to Fig. 11.12. As shown in Fig. 6.17, the flow on a full forebody without a bulb has a considerable downward component. Fig. 6.17 shows potential flow streamlines, which essentially represent the flow at the edge of the boundary layer. But, as explained in the text, the flow close to the surface points even more downward in the region above the inflexion point in the potential flow streamlines. Below this point, the innermost flow moves upward and the convergence of the limiting streamlines

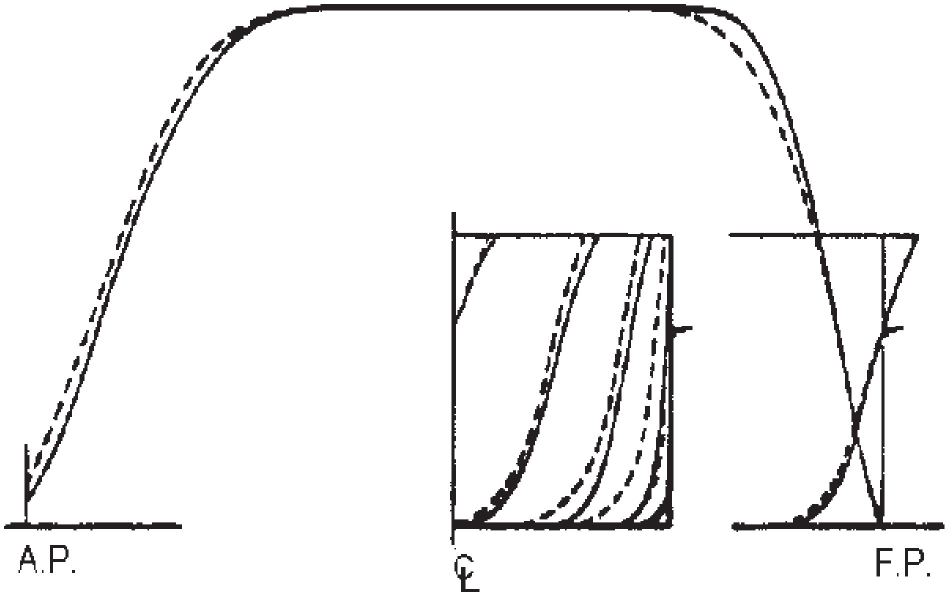

Figure 11.11 Smoothing the forward shoulder.

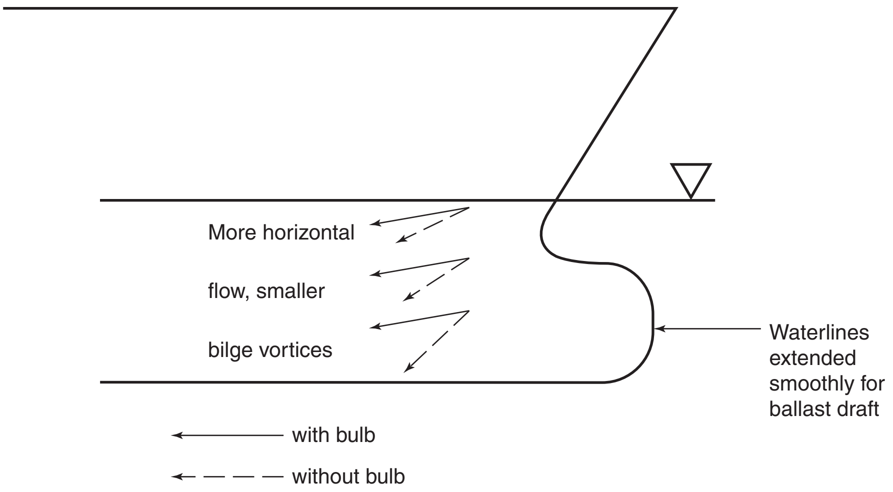

Figure 11.12 Reduction in downward flow at the bow due to the bulb.

creates a vortex-type separation (see Fig. 6.14). A bilge vortex is thus created on the forebody, and this increases resistance. If a bulb is fitted to the forebody the flow becomes more horizontal, and thereby the bilge vortex gets weaker or may disappear completely.

Modern bulbs for this class of ships may be designed to operate at two different drafts. At full load, the bulb works as described but, at ballast draft, the bulb works as an extension of the hull. Thus, the bulb has a very large cross-section at the forward perpendicular FP (up to 15% of the midship section). The lower part, submerged also at ballast draft, is created by extending the waterlines without knuckles from the forebody to the more or less sharp forward end of the bulb. A quite slender forebody is then created. Fig. 11.13 shows an example of a modern bulb for a tanker/bulk carrier.

Cylindrical forebodies have been used relatively successfully for many years, but they have now become obsolete. The general idea is to move volume forward to reduce the sharpness of the forward shoulder and this may work for the fullest forms, at full load. In ballast conditions, the results of measurements indicate zero or even negative effects, relative to a conventional bow. The transition from the vertical stem to the horizontal bottom is critical. If not properly designed, vortex separation may occur in this region. The cylindrical bow has a disadvantage relative to the conventional bow in short waves of encounter, where the added resistance may increase considerably.

11.4.1.3 AFTERBODY DESIGN. Three types of conventional sterns are shown in Fig. 11.14 and the corresponding wake distributions in Fig. 11.15. The wake fraction w presented as contour lines in Fig. 11.15 is defined as

$$w = 1 - \frac{V_A}{V} \tag{11.9}$$

where V_A is the local axial velocity.

The most traditional stern is the V-shape, which has the lowest resistance. However, it also has some undesired features when it comes to the wake distribution. As appears from Fig. 11.15, the high wake (i.e., the low speed) is concentrated to a V-shaped region around the propeller center. From a hull efficiency point of view, this is not optimal because the excess velocities in the cylindrical propeller slipstream can hardly balance the velocity deficit in an area of such different shape. Further, the propeller blades will encounter rapidly varying axial flow velocities during rotation. This means a rapidly varying angle of attack and a pulsating load, which will give rise to vibrations.

The U-shaped stern has a considerably more axisymmetric distribution of the wake, and a further improvement is obtained with the bulb shape. Both are thus more desirable from a hull efficiency and vibration point of view. The mechanism behind the improvement may be explained with reference again to Section 6.7, where the generation of the stern bilge vortex was described in some detail. It is seen in Fig. 6.19 that the vortex hits the propeller plane and redistributes the velocity contours. In fact, there is a considerable reshuffling of the contours by the vortex. This is utilized by ship designers to move contours out from the central and lower parts of the propeller disk and to squeeze them together at the top of the disk, as seen in Fig. 11.16. The trick is thus to generate a suitably strong vortex and to position it correctly. By going from the V-shape, via the U-shape to the bulb shape, the vortex becomes stronger and stronger because the bilge radius gets smaller and smaller in the region in front of the propeller. This is a well known and safe way to optimize the stern from a hull efficiency and vibration point of view. To find the optimum solution, the positioning of the vortex is important, however, and this may call for considerable experimentation either in laboratories or in CFD. Note that there may be significant scale effects in the model tests, as explained in Section 6.7.

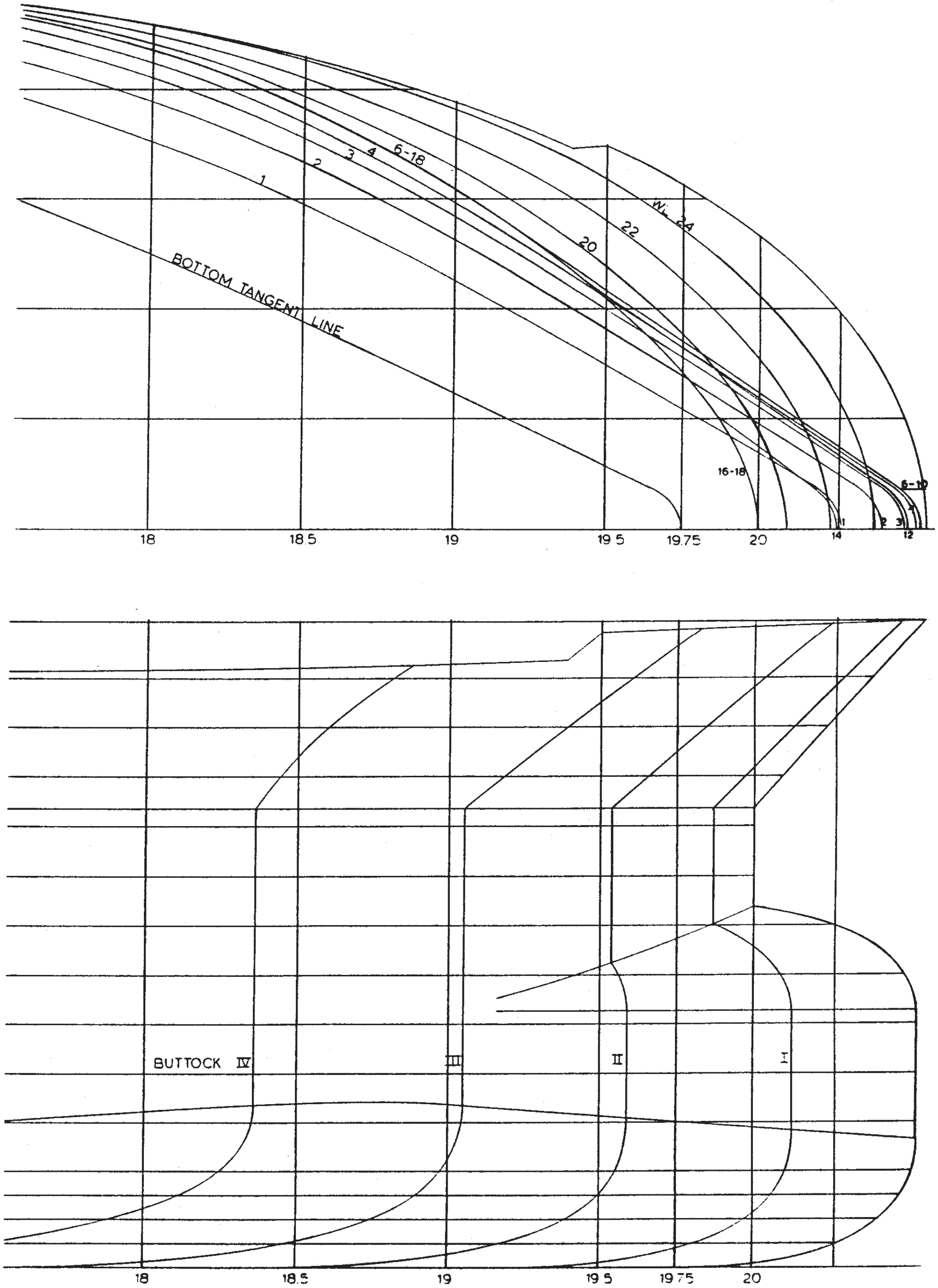

Figure 11.13 A modern bulb for a tanker/bulk carrier (Valkhof, 1999).

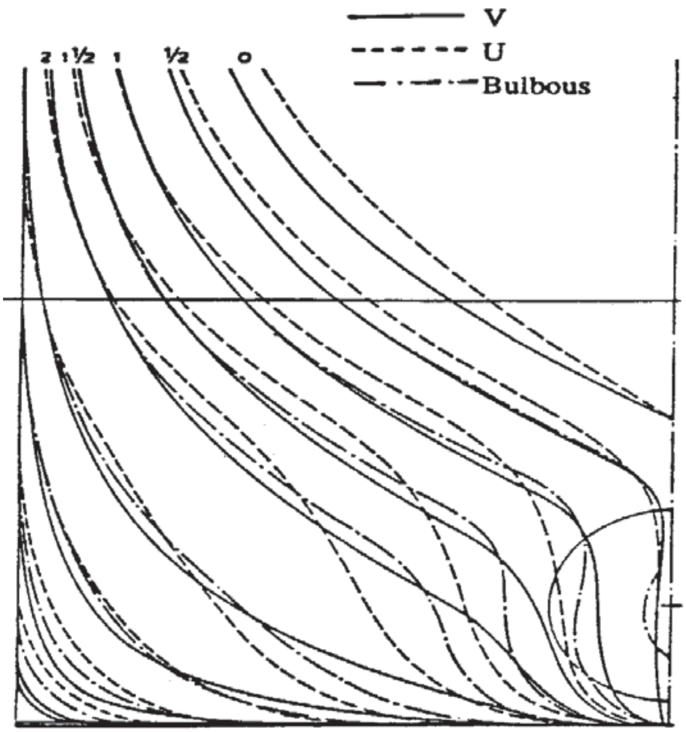

Figure 11.14 Three conventional full-body stern forms.

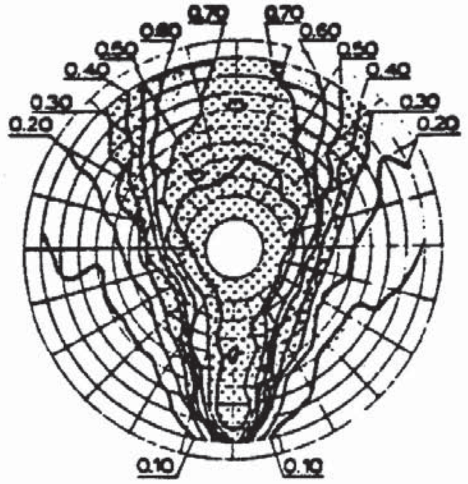

V - STERN

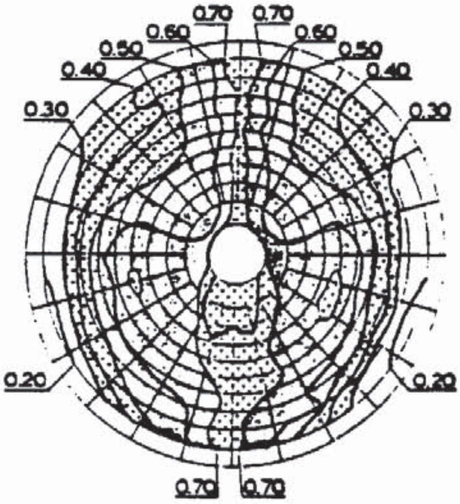

U - STERN

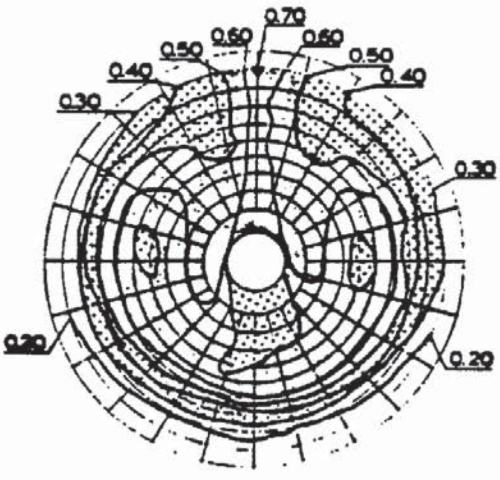

BULBOUS STERN

Figure 11.15 Wake distributions for the three sterns of Figure 11.14.

The disadvantage of the U- and bulb-shaped sterns is that the vortex requires energy. The resistance is increased and this increase is often large enough to just cancel the advantage of the higher hull efficiency. From a propulsive power point of view, the stern type is thus not too important; the real advantage of the vortex generating sterns is the reduced variation in propeller loading and the resulting smaller vibrations.

In Fig. 11.17, two full-body sterns of the barge type are shown. This type is characterized by straight and flat buttocks and a central gondola in which the machinery is located. Such hulls have proven to have a very low resistance and vortices can be avoided entirely by careful design of the bilge region. As seen Fig. 11.17, hard chines may be utilized as well, often with little or no increase in resistance. It should be stressed, however, that if the bilges are not well designed, so that vortices are created, the positive effect described does not materialize because they will pass the propeller plane far outside of the propeller disk.

Because the hull boundary layer will be spread over the large girth of the stern sections, there will be no concentration in the propeller disk, which will only collect the much thinner boundary layer from the gondola. The hull efficiency is therefore much lower than for a conventional stern, and there is also a tendency for a larger suction effect of the propeller at the stern (larger thrust deduction) so the advantage of the small resistance is lost.

The reason why the barge shape is still of interest is that the flat stern sections are less prone to separation,

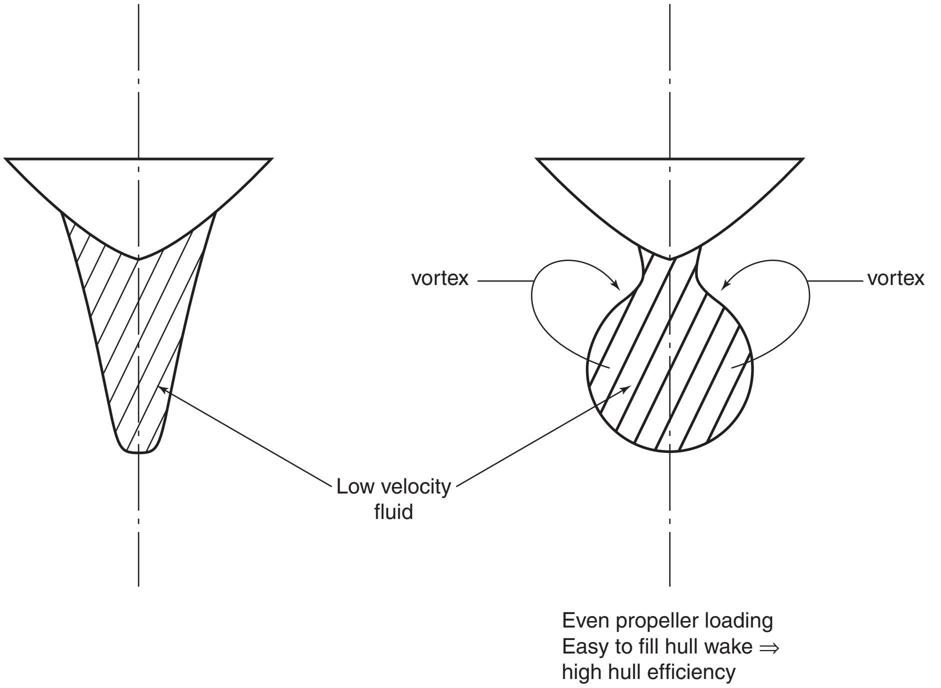

Figure 11.16 Utilizing the bilge vortex for creating a circular wake.

so the stern may be made fuller than for a conventional shape. In fact, this shape is only of interest for $C_B > 0.8$. Larger deck areas are also possible in many cases.

A third possibility for the stern shape is the twin skeg, shown in Fig. 11.18. This type of stern for full ships is particularly advocated by SSPA in Sweden. Savings in delivered power of 10% to 20% are reported by van Berlekom (1985), but more recent data indicate that the gain ranges from a few percent up to around 10% compared with conventional sterns. The shape is particularly advantageous for beamy and shallow hulls, especially if the block coefficient is large. A careful design of the gondolas is however required because the upper part has to follow the inviscid streamlines, whereas the lower part necessarily must be aligned with the shafts in the axial direction. This calls for tilted gondola sections, as seen in Fig. 11.18.

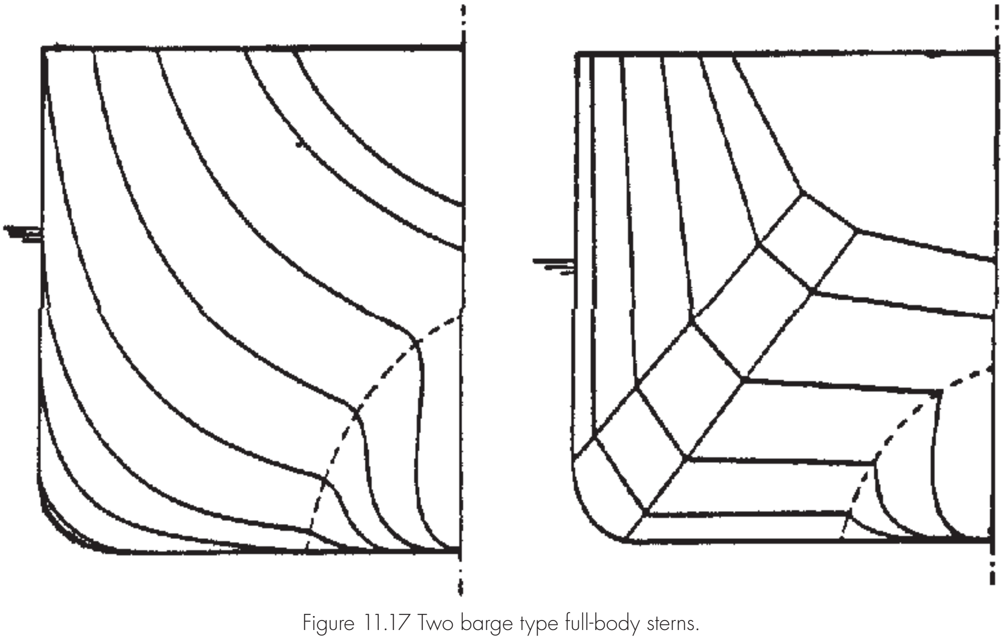

Figure 11.17 Two barge type full-body sterns.

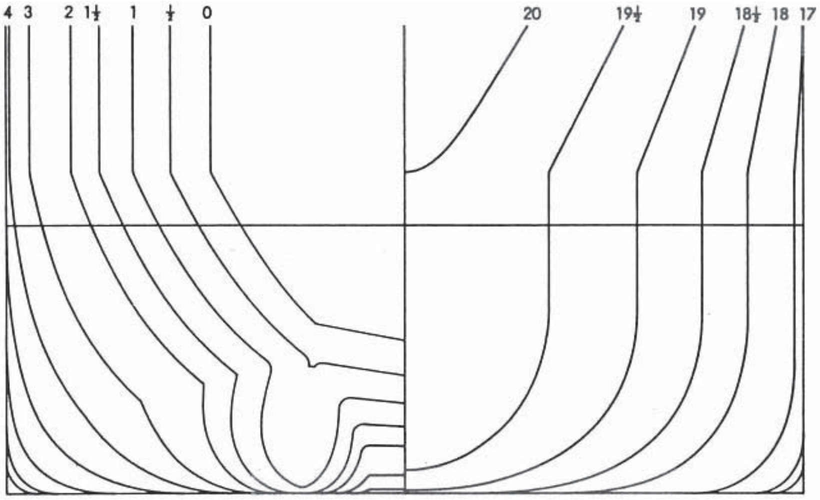

Figure 11.18 A twin skeg tanker (van Berlekom, 1985; courtesy of SSPA).

As pointed out before, most modern full ships have transoms which are somewhat submerged. This is seen in the body plans of Figs. 11.14, 11.17, and 11.18.

11.4.2 Slender Hull Forms. In this section, we will consider slender hull forms operating at Froude numbers around 0.25. Typical ships of this kind are containerships, reefers, and various Ro-Ro ships (Ro-Ro, Ropax, and car carriers).

The most spectacular designs of this class are the very large single screw containerships with a capacity of over 7000 TEU and propeller powers approaching 100 MW on a single shaft. Because the wake peak may be rather deep, and the clearance between the tip of the propeller and the hull must be kept at a minimum to give space for the propeller, there is a risk of excessive cavitation and the associated vibrations and propeller erosion. The design of this class of ships is thus a challenge.

11.4.2.1 FULLNESS AND DISPLACEMENT DISTRIBUTION. A typical sectional area curve is shown in Fig. 11.19.

11.4.2.2 FOREBODY DESIGN. The forebody of these ships is often optimized by potential flow methods. In recent years, the bulb shape has evolved toward a gooseneck shape, shown later for a ferry or a cruise liner in Fig. 11.26. It is characterized by a maximum cross-section ahead of the FP and with lines sloping down aftward. It is very well integrated with the hull lines. The downslope of the upper surface and the convex curvature preceding it will help to draw the flow down, thus reducing the wave height. Further, the longitudinal inclination of the lines may reduce the viscous resistance. As pointed out previously, the streamlines in the bow region point downward, and with this bulb shape, the flow will experience a smaller curvature of the surface when passing along the bulb and the forebody. This minimizes the boundary layer growth and the risk of vortex separation.

The forebody sections should be V-shaped and the design waterline straight. In this case, it is imperative to keep the shoulder as smooth as possible. As will be seen later, the position of the shoulder is also important.

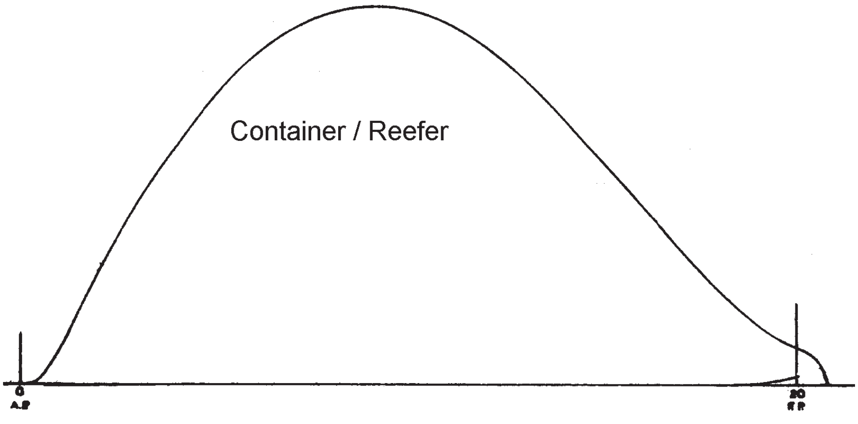

Figure 11.19. A typical sectional area curve for a containership/reefer (Valkhof, 1999).

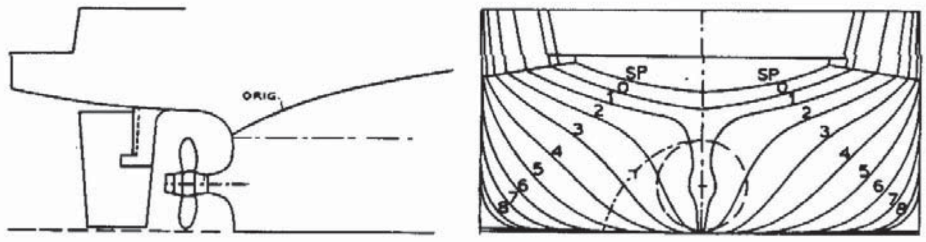

V-shape

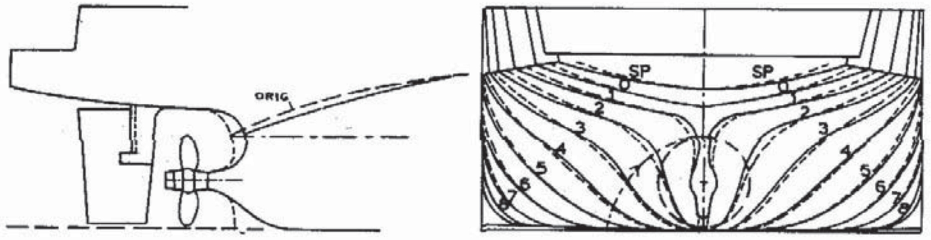

—— Moderate U
----- V-shape original

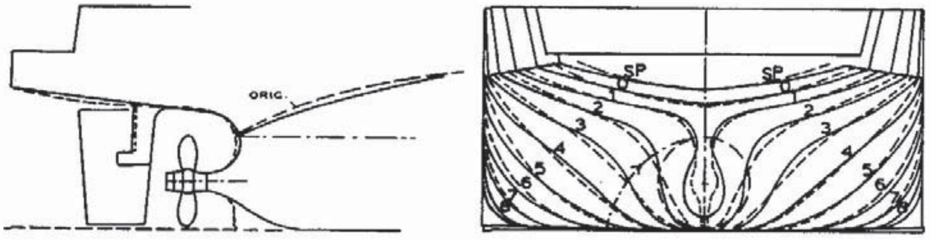

—— Extreme U
----- V-shape original

Figure 11.20 Three different sterns of a Ro-Ro containership.

11.4.2.3 Afterbody Design. The wake of a slender single screw afterbody is considerably less homogenous than that of full forms, although the mean value of the velocity in the propeller plane is higher (the mean wake is lower). Great emphasis must therefore be placed on the optimization of the stern lines. Figs. 11.20 and 11.21 show the systematic improvement of the wake of a Ro-Ro containership (Vossnack et al., 1977). The hull sections are gradually changed from a typical V-form to a bulb-like form and this has two positive effects, clearly visible in the wake distributions shown in Fig. 11.22. As before, the larger curvature of the bilge causes the vortex to be stronger, which redistributes the velocity contours in a favorable way. Further, the lines above the propeller shaft become more slender, as seen in Fig. 11.21, which reduces the deep wake peak at the top of the propeller disk. The resulting wake pattern, shown at the bottom of Fig. 11.22, is considerably better than the top one, both from a vibration and a hull efficiency point of view.

Barge-type forms are used also for slender hulls. In Fig. 11.23, the body plan of a containership is shown. Here, the main engine is located in the gondola, which should be kept as slender as possible, both from a resistance and a propulsion point of view. The wake distribution is shown in Fig. 11.24.

Because of the extreme power required for the very large containerships, it would be tempting to use a twin screw arrangement either with open shafts or with twin-skegs. However, the disadvantage of large appendage drag makes the first alternative less attractive, and the advantages of the twin-skeg design are much smaller for these slender hulls than for the full and more beamy ones described previously. Therefore,

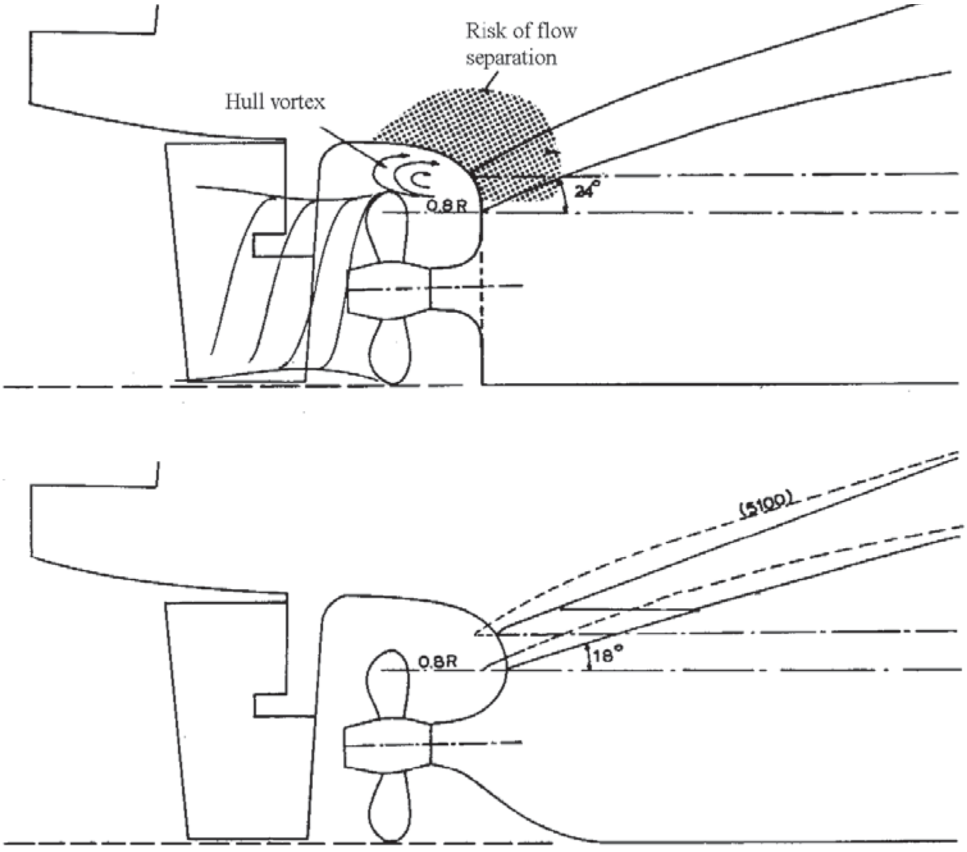

Figure 11.21 Straightening the diagonals to avoid separation.

it is questionable whether a twin screw concept is feasible today.

For ships operating at Froude numbers around 0.25, the transom should be designed to be above the still waterline.

11.4.3 Ferries and Cruise Liners

11.4.3.1 Fullness and Displacement Distribution. The block coefficient of these ships is in the range 0.60–0.65, but values as high as 0.69 have been seen. They operate at Froude numbers around 0.25. The center of buoyancy is relatively far aft, in several designs as far back as 4%–5% aft of midship. However, more optimum designs have their *LCB* around −3.5%. Even this is far aft at this moderate Froude number, as appears from Fig. 11.2.

A typical sectional area curve for a ferry is shown in Fig. 11.25.

11.4.3.2 Forebody Design. As for slender cargo ships, goose-neck bulbs are used for ferries and cruise liners. An example is shown in Fig. 11.26.

To minimize resistance, the waterlines are mostly straight, at least if an optimum bulb can be designed. If certain restrictions must be applied on the bulb design, slightly concave lines may be preferable. As in the other cases discussed previously, it is very important to smooth the forward shoulder.

11.4.3.3 Afterbody Design. Ferries and cruise liners are mostly twin screw ships, either with open shafts or with twin-skegs. Four principally different stern shapes are used for this class of ships (see Tikka & van der Baan, 1985).

The conventional stern shape is used for unsheltered waters, where seakeeping performance is important. Particularly for stern seas, this shape is better than the others, which may experience broaching and slamming on the flat afterbody.

Twin-skeg sterns are developed mainly for increasing the space for the propeller. As can be seen in Fig. 11.27, the lines are optimized for that purpose. However, quite a sharp wake peak is often encountered just behind the skeg and this may cause vibrations, which are very critical for this type of ship. The solution is to use highly skewed propellers which even out the pressure loads on the blades when passing the wake peak.

The mixed and barge shapes have open shafts and rather undisturbed flow into the propeller, which is good from a vibration point of view. By proper shaping of the bilges, the hull resistance can be made very small, but there is a considerable appendage drag. The hull efficiency is low because the boundary layer on the hull

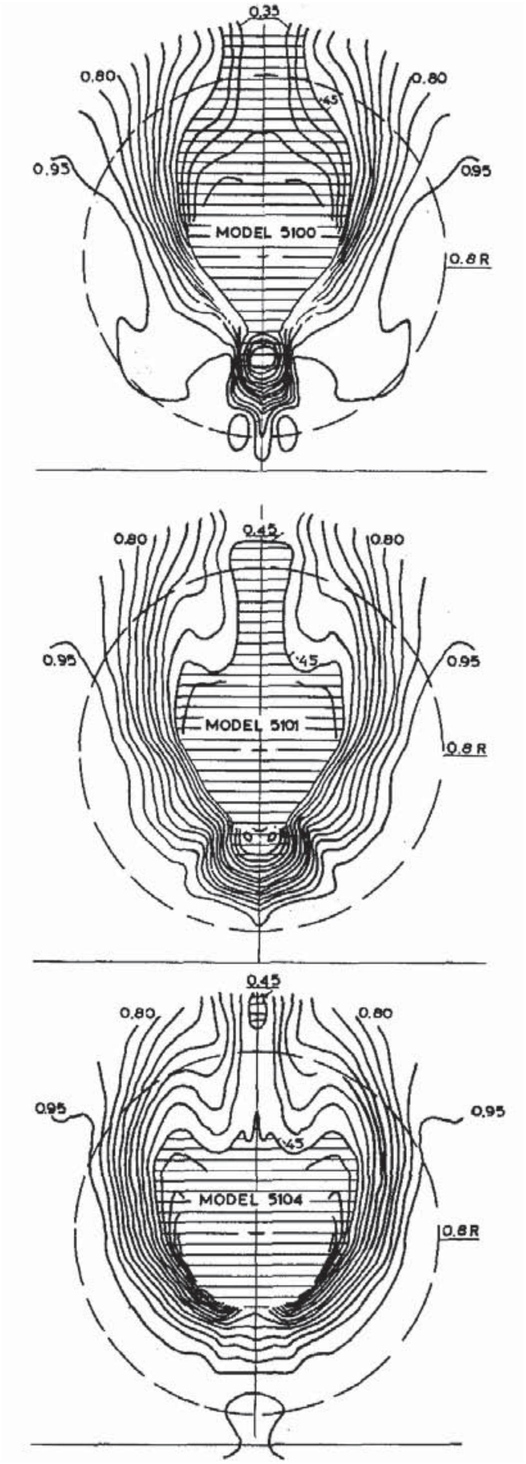

Figure 11.22 The wakes of the hulls in Figure 11.20.

will only partly pass through the propeller disk. Most of the velocity deficit passes above the disk. The mixed shape is a mix between the conventional and the barge-type stern. To increase the propeller diameter, tunnels at the bottom of the hull are sometimes used, and in the body plan for the mixed shape a tendency for a tunnel shape is seen.

All afterbody shapes in Fig. 11.27 are quite flat with wide transoms. The buttock shape is then very important, not least for the wave generation, as explained in Section 11.5.11. In this case, the transom should be designed to be above the still waterline.

The flat sterns offer the possibility of using podded propulsors. This possibility is often utilized, particularly for cruising ships. Using rotatable pods, rudders, and tunnel thrusters at the stern may be dispensed with and the drag is smaller than for open shaft solutions. Further, if the propeller is in front of the pod, the approaching flow is undisturbed, which minimizes the risk of vibrations, a very important advantage for a cruising ship. Because the electrical power equipment may be placed much more freely on the ship than a conventional engine, the general arrangement of the ship is simplified.

11.4.4 High-Speed Ships. Considerable research has been carried out during the past decades on the resistance of various types of high-speed craft and advanced marine vehicles (see Faltinsen [2005] for an overview). Such craft can be distinguished by the means adopted to support their weight: through buoyancy, through hydrodynamic lift, through aerostatic lift, or through combinations of these. Fig. 11.28 displays the subdivision that can be made in this way (Lewis, 1988). The first category is composed of round-bilge and hard chine monohulls, and the second is composed of catamarans and small waterplane area twin hulls (SWATH) ships. The third category includes surface piercing and submerged hydrofoil craft, and the fourth category contains air cushion vehicles (ACVs) and surface effect ships (SESs).

In the following, we will discuss monohull ships. The reader interested in multihulls, with or without hydrofoil support, is referred to the very comprehensive book *Multi-Hull Ships* by Dubrovsky and Lyakhovitsky (2001).

11.4.4.1 HYDROSTATIC AND HYDRODYNAMIC LIFT. Fig. 11.29 shows in principle how the hydrostatic (buoyancy) forces are replaced by hydrodynamic forces for increasing Froude numbers. Even at very low speeds, the vertical component of the generated hydrodynamic pressure on the hull surface will cause the hull to change its attitude from that at zero speed. Although not shown in Fig. 11.29, the generated lift may well be negative. Increasing the speed, the effect of the hydrodynamic pressure becomes more and more important because it increases with speed squared, while the hydrostatic pressure is constant. The relation between the forces (rather than the pressures) is however much more complicated because the attitude of the hull and the wetted surface also change with speed.

In the displacement speed region, the hydrostatic forces dominate; in the fully planing region, the hydrodynamic forces take over the major part of the lift required to support the hull. In an intermediate region, both hydrostatics and hydrodynamic forces are

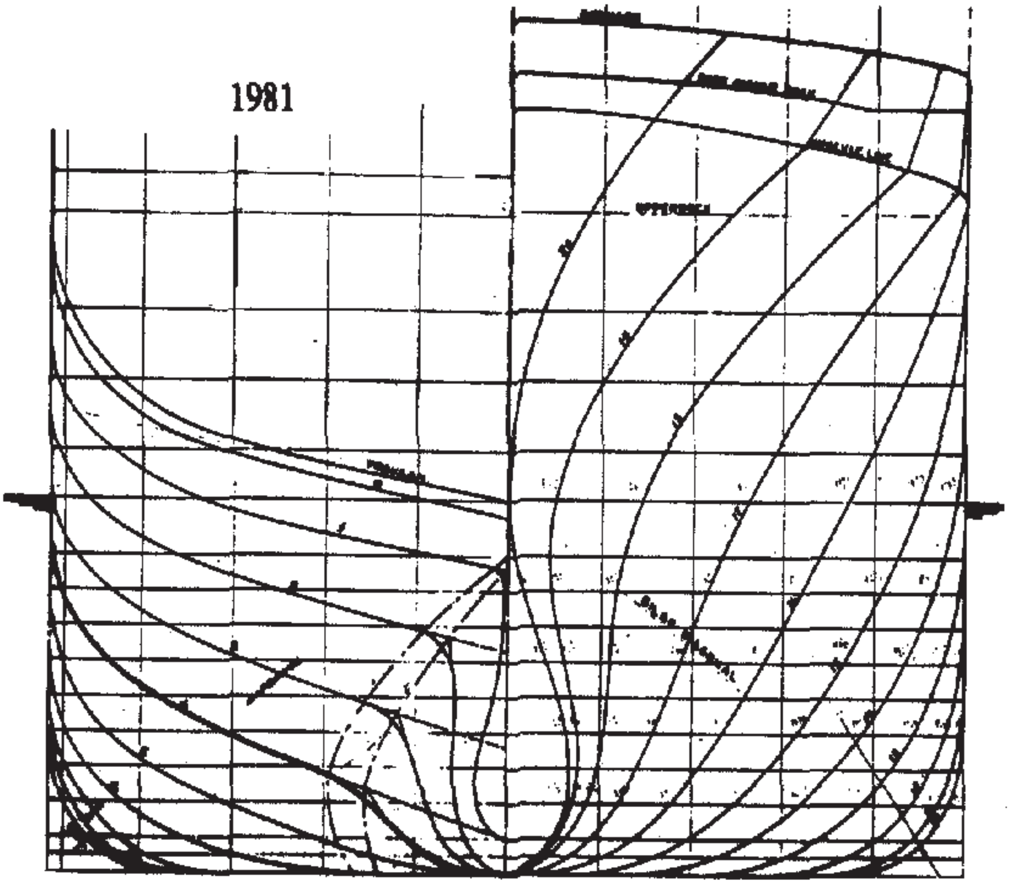

Figure 11.23 A containership with a barge-type stern.

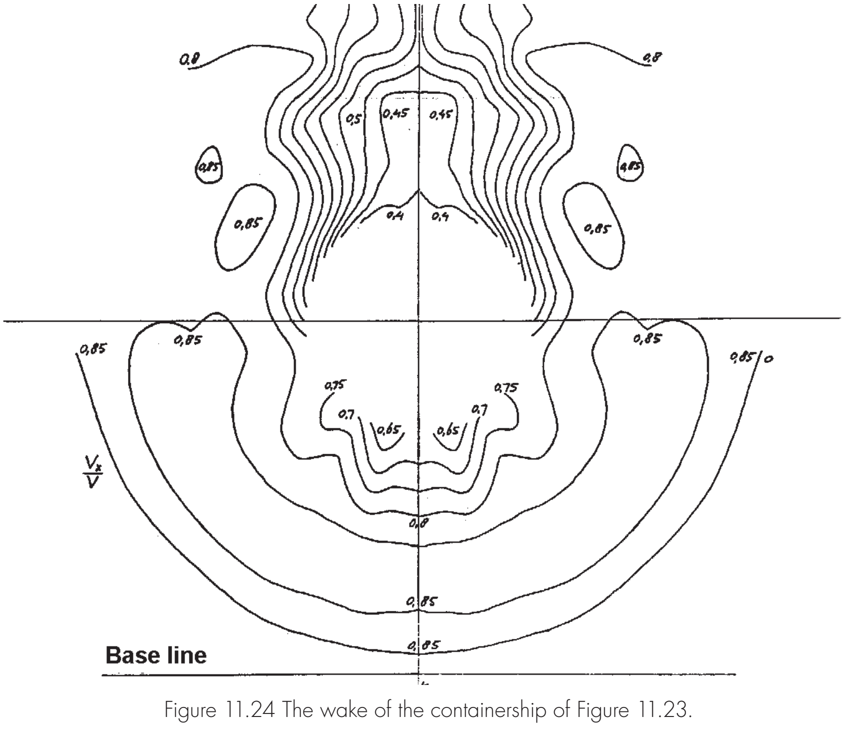

Figure 11.24 The wake of the containership of Figure 11.23.

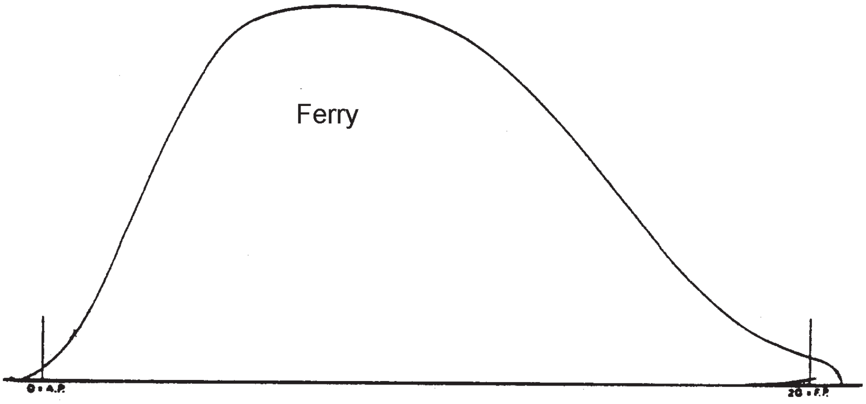

Figure 11.25 A typical sectional area curve for a ferry (Valkhof, 1999).

important. Somewhat arbitrarily, the upper limit for displacement speeds is usually set at $Fn = 0.5$, whereas the lower limit for planing is defined as $Fn = 1.0$. The intermediate region is called the semiplaning or semidisplacement speed range.

As has been obvious from the previous discussion, the normal curvature of the hull surface is very important for a displacement speed ship. The hull needs to be smooth, and sharp edges must be avoided, at least if not aligned with the flow. This is to avoid a thick boundary layer and separation and the associated large viscous resistance. On the other hand, if the hull is to be supported by hydrodynamic lift forces, the convex curvatures required at lower speed will be detrimental because they tend to generate low pressures. In the high-speed case, flat or concave surfaces are better, and this calls for sharp edges on the surface. Hulls with hard chines are more efficient. In practice, it has turned out that the Froude number limit where the hard chine hulls become preferable is around 1.0 (i.e., the limit for planing). In the semiplaning range, the round bottom hulls are more efficient, but in both cases submerged transom sterns are required.

11.4.4.2 Fullness and Displacement Distribution. While the Froude number ranges of interest for the three types of

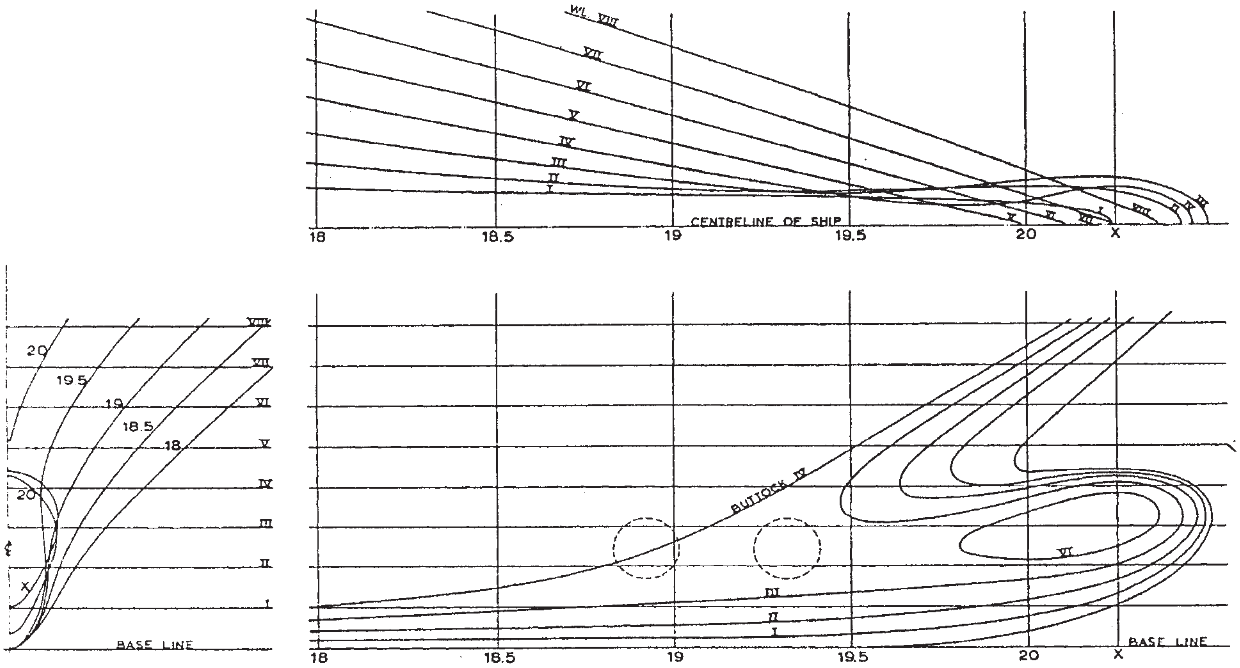

Figure 11.26 A goose-neck bulb for a ferry or a cruise liner.

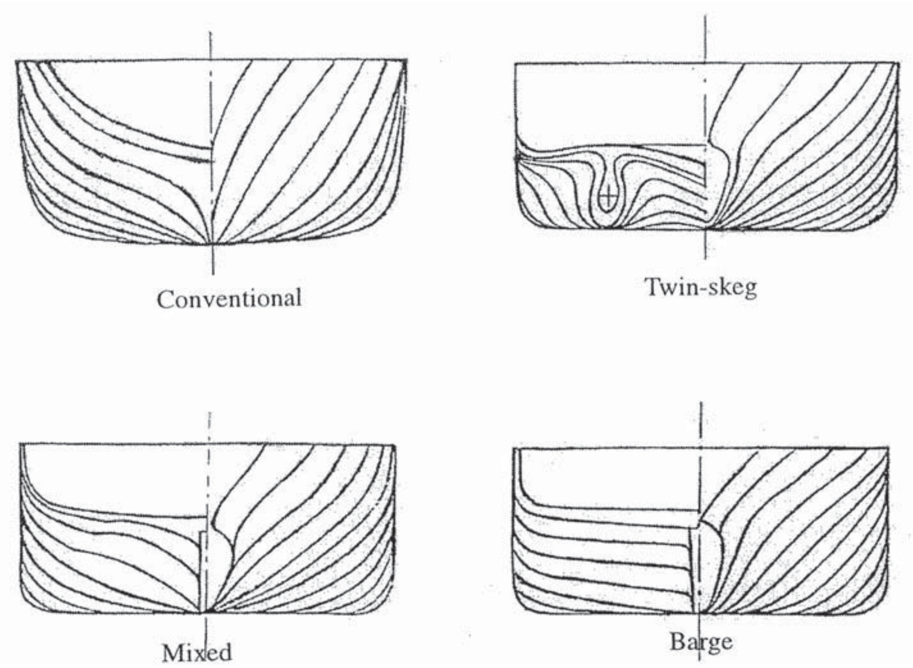

Figure 11.27 Four stern shapes.

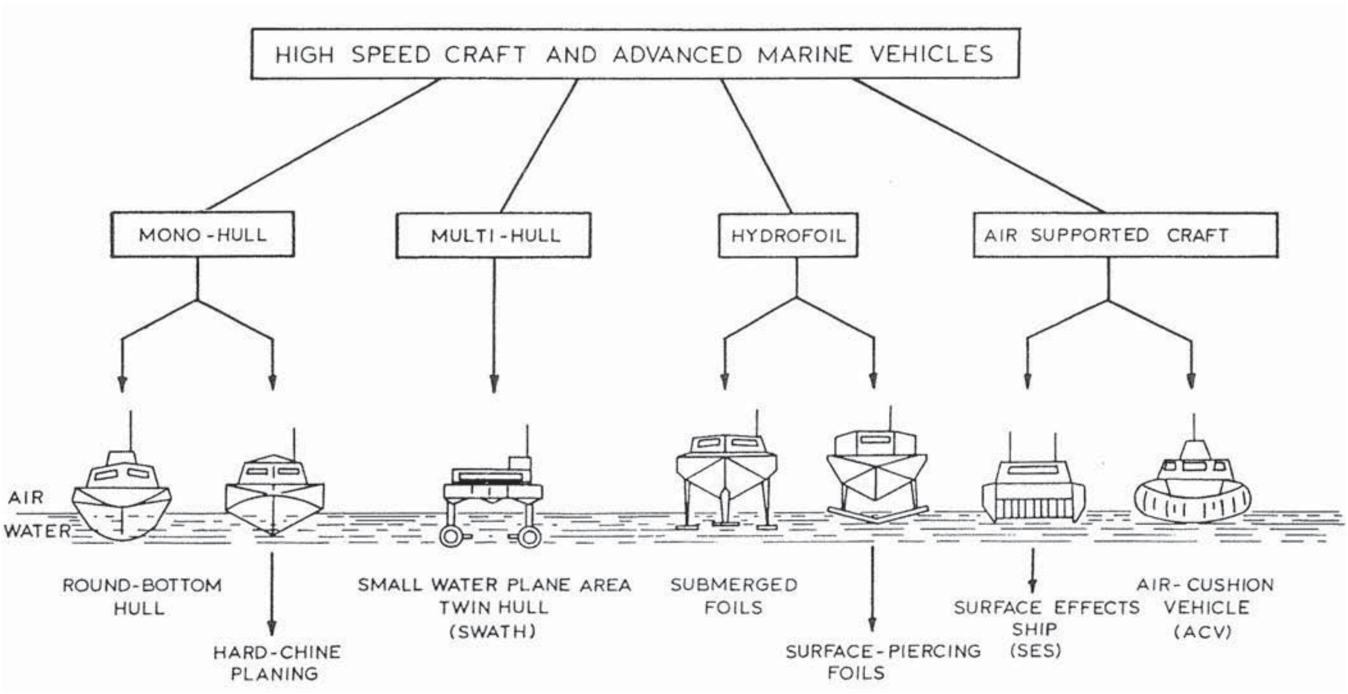

Figure 11.28 Main types of high-speed craft and advanced marine vehicles.

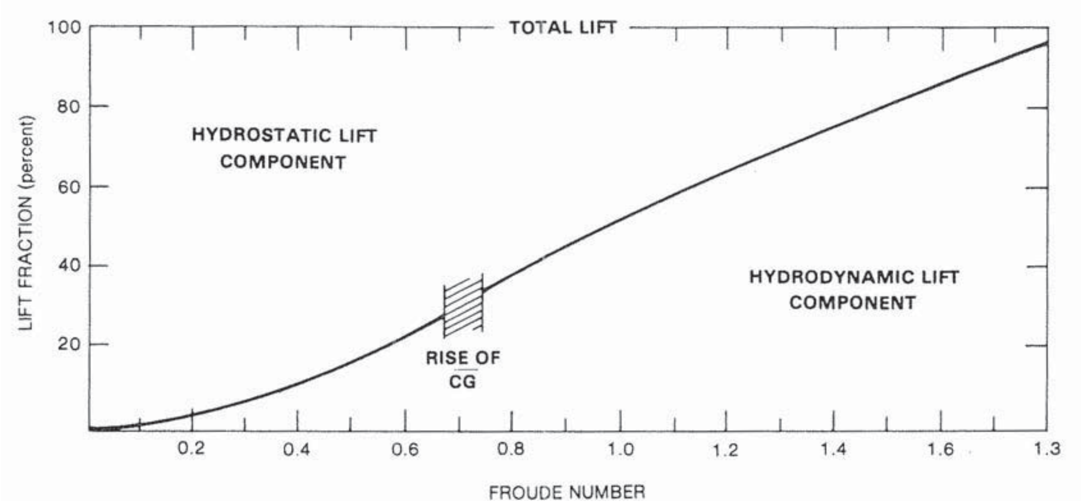

Figure 11.29 Distribution of hydrostatic and hydrodynamic lift.

displacement hulls discussed above were quite restricted, the range covered by the high-speed hulls is very large, in principle all Froude numbers above 0.5. There is thus a considerable variation in the optimum sectional area curves as well as in the associated prismatic coefficients and *LCB*s. As a general rule, the size of the optimum transom increases with speed and the corresponding optimum afterbodies therefore become fuller and fuller as the speed increases. This means an increase in prismatic coefficient and an aftward shift in *LCB*. Table 11.4 indicates optimum values of C_p, *LCB* (% L_{WL} from midship) and the size of the submerged part of the transom when the ship is at rest, A_{tr} (A_M is the maximum sectional area) for different Froude numbers. The values given for the first two quantities correspond to those of Figs. 11.1 and 11.2.

11.4.4.3 Hull Shape. Because the hull of a high-speed ship is supported by the dynamic lift from the high pressure on the bottom, the most efficient bottom from a resistance point of view has zero deadrise. Most of the water hitting the bottom of the hull will then be deflected downward, with a resulting large lifting force. For a hull with finite beam, some water will however always be deflected sideward as spray. At non-zero deadrise, more deflected water will have a component of velocity sideward, so the generated force will be directed inward. In fact, neglecting friction, the force is always at right angles to the surface.

Table 11.4 Optimum Values of C_p, *LCB*, and A_{tr} for High-Speed Ships

Fn	C_p	*LCB* (negative aft)	A_{tr}/A_M
0.35	0.6	−1.5 to −2.5	0.0
0.4	0.58–0.62	−2.0 to −3.5	0.0–0.09
0.5	0.62	−3.0	0.14
0.6	0.63	−3.3	0.18
0.8	0.64–0.68	−4.7	0.28
1.0	0.64–0.70	−4.5 to −7.0	0.4–0.5
>1	0.70–0.82	Approximately −10	0.7–0.95

Although the zero deadrise bottom (with a large beam) is the most efficient one, it cannot be used for seakeeping reasons. A hull with this shape would experience very uncomfortable motions in a seaway, so some deadrise (and a reasonably small beam) is always required. It turns out that a good compromise is the warped bottom, where the relatively large deadrise on the forebody is gradually reduced to a much smaller value at the stern. Typical stern values are 10–15 degrees, whereas the forebody values may be more than twice that. Of course, these numbers are mainly relevant for hard-chine hulls, but the principle also applies to round bottoms.

A way to reduce the lateral deflection of water (i.e., to minimize the spray) is to fit spray rails along the bottom. These are longitudinal strips of triangular cross-section that deflect the spray downward, thereby generating lift (Fig. 11.30). It is important to keep the outer edge of the rail sharp; the bottom side may be inclined downward up to 10 degrees to maximize the lift. Normally, the width of the rail is 1.5%–2% of the hull beam. Because the flow separates on the rail, the wetted surface of the hull gets narrower than when separation occurs at the sharp bilge. The wetted part thus often becomes somewhat longer. This is an advantage because the longitudinal stability of the hull is then improved.

The bottom of a modern hard-chine craft operating at two different speeds is seen in Fig. 11.31. The inner rails are shortened, and the outer ones extend all the way to the transom. Because the flow is directed more outward on the forebody, the rails are most efficient there.

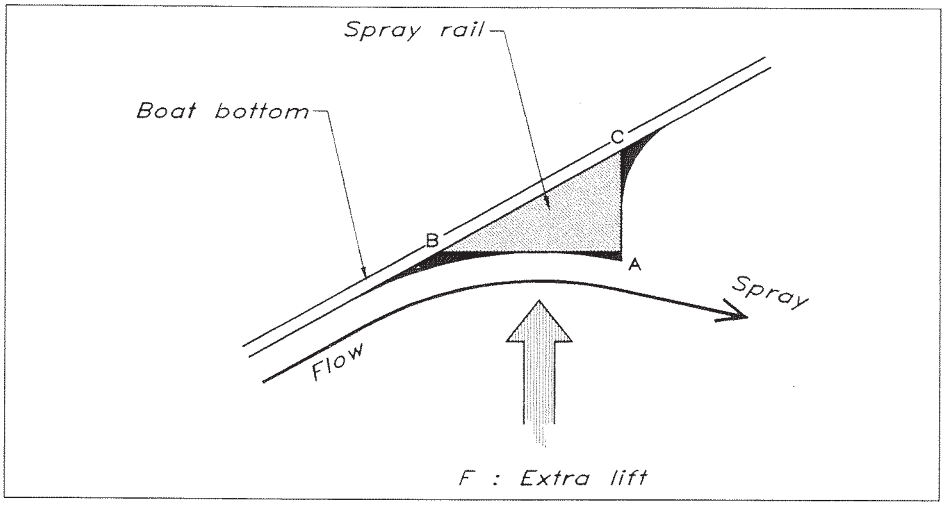

Figure 11.30 Cross-section of a spray rail.

Close to the stern where the flow is more or less straight back, they might even increase the resistance. This is why the inner ones are cut short. The reason for keeping the outer rails all the way is that the wetted surface at the higher speed is short. Had there been no rail close to the stern, the flow would have separated at the bilge and the wetted surface would have been wider and shorter.

Another design feature of high-speed hulls is the trim wedge. This is fitted to the aftbody (Fig. 11.32). The purpose is to generate concave buttocks with an associated high pressure close to the stern, which increases the lift

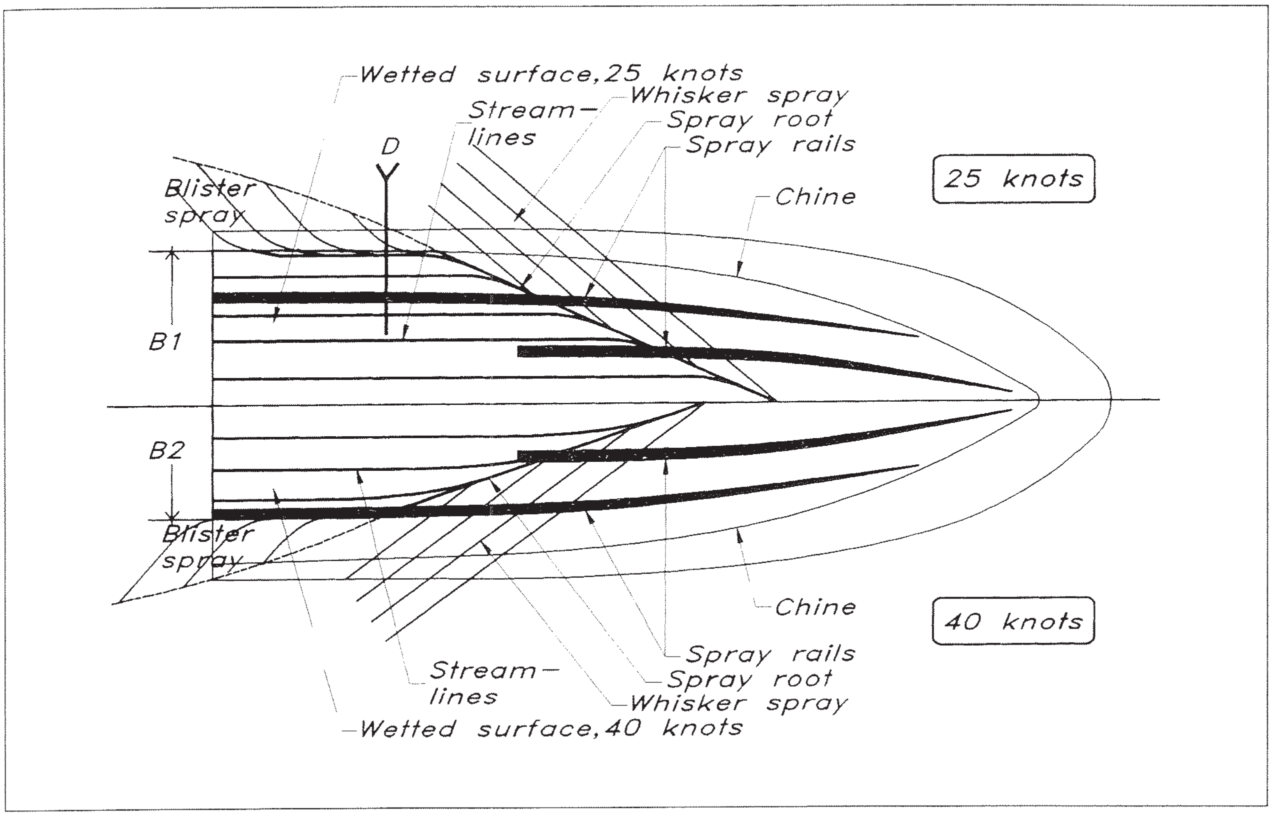

Figure 11.31 A bottom with spray rails.

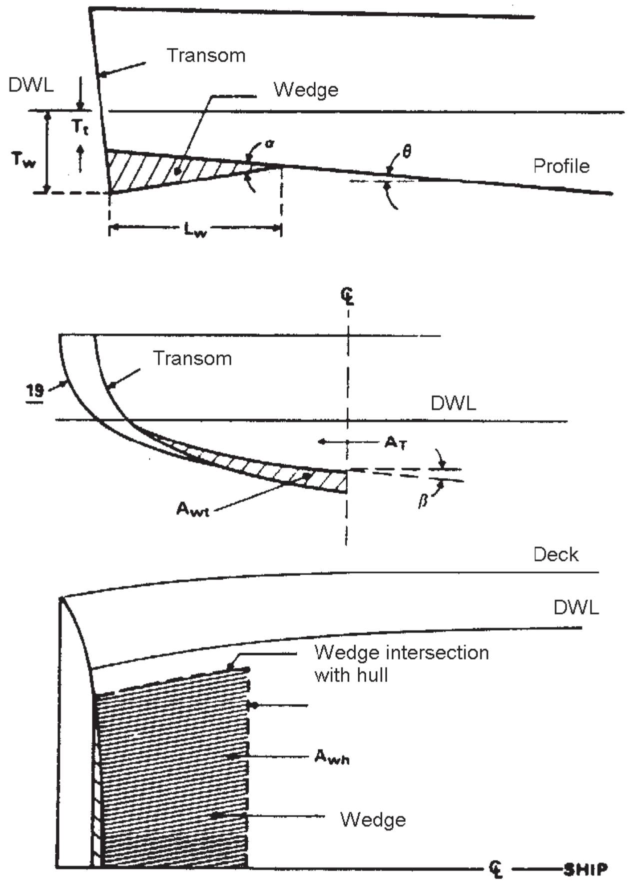

Figure 11.32 A trim wedge.

and reduces the trim of the hull. In a Froude number range of approximately 0.3–1.2, this may cause a reduction in resistance. Normally, a trim wedge occupies 1.5% to 2% of the length at waterline. The optimum angle depends on the speed and on the transom immersion. Angles as large as 15 degrees, or even higher, are found around the hump speed, but the optimum angle is reduced gradually to zero at the upper and lower speeds where they are effective. If the transom is larger than normal (see Table 11.4), the wedge angle should be reduced and vice versa.

Less common today is the stepped hull, where one or more steps in the buttocks are used to reduce resistance (Fig. 11.33). The idea is to suck in air behind each step such that the wetted surface is reduced. When the flow passes over the edge of the step, a low pressure is generated. If no air was supplied, a massive separation zone would be generated behind the step and the pressure resistance would be huge. However, the low pressure may be used to suck air, either from the sides of the hull or through tubes from the deck. If this is permitted, the pressure is increased, the pressure resistance reduced, and, thanks to the reduced friction, the total resistance may be reduced. Stepped hulls have been used, particularly for racing boats, since the 1930s and have shown good performance. However, some notable accidents have occurred for hulls with air suction through tubes when the inlet has been blocked for some reason, for instance by water from a wave. The resistance then increases abruptly resulting in a very sudden deceleration.

11.4.4.4 Appendages. As shown in Fig. 4.1, the appendage drag of a high-speed hull may be considerable. This is so because the hull will be lifted more and more out of the water as the speed increases. The wetted surface of the hull is thus reduced, and so is its viscous resistance. Appendages, on the other hand, such as shafts, brackets, fins, etc., rarely get out of the water, which means that their proportion of the viscous resistance is increased. For very high speeds (racing hulls), the wetted hull surface is practically zero, which would mean that almost all viscous resistance would come from the appendages. To reduce resistance, appendages must therefore be avoided, through waterjet propulsion or surface piercing propellers, where the shaft goes out through the transom. In recent years, the interest in waterjet propulsion has increased considerably and is now considered a most important alternative to the open shaft propeller for speeds above 30 knots.

If shafts are required, they should be aligned with the flow to the largest possible extent (i.e., they should be as horizontal as possible considering the diameter, tip clearance, and the arrangement of engine and gearboxes inside the hull). Brackets should be designed to avoid cavitation. In Zondervan and Holtrop (2000), a series of sections designed to delay the onset of cavitation and suitable for brackets is presented.

11.5 Detailed Hull Form Improvement—Wave-Making Aspects

11.5.1 Introduction. After the general guidelines on main parameters and hull lines discussed in the previous subsections, here we shall consider several aspects of the more detailed hull form design. First, we address ship wave making and how it affects the design.

The wave pattern and wave resistance of a ship are most sensitive to details of the hull form design. This makes the design a critical issue, but also provides the opportunity to make substantial improvements without violating any practical constraints. In this section, we will provide some specific guidelines on hull form aspects, but first we propose and demonstrate a methodology for minimizing wave making that can be applied more generally. This methodology has emerged from the practical application of free-surface potential flow calculations in ship design at MARIN since 1987 (Hoekstra & Raven, 2003; Raven & Valkhof, 1995; Raven et al., 1998; vanden Berg, Raven & Valkhof, 1990). It provides general, qualitative insights based on the theory of ship waves described in Section 5, and an understanding of the relation between hull form and wave pattern. This usually permits a directed hull form improvement rather

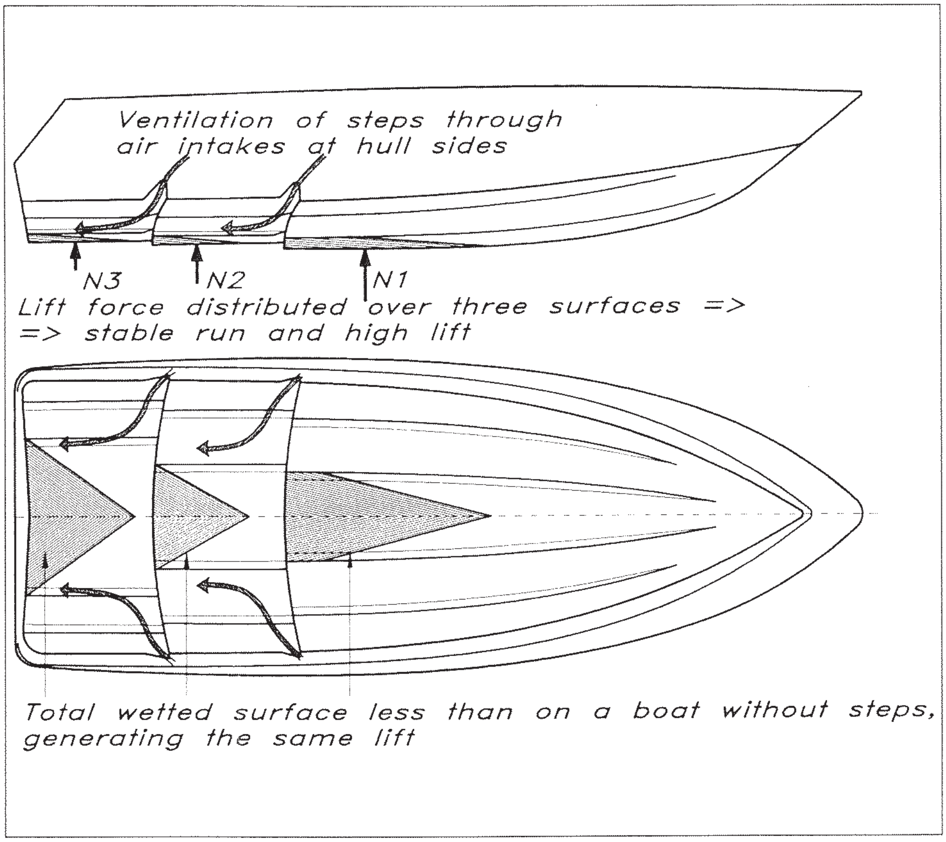

Figure 11.33 A stepped hull.

than just a trial-and-error approach. Even for systematic hull form variation or optimization, such understanding is very effective to decide on the design variations to be investigated and to assess the computed trends (Hunt & Zondervan, 2007). The resulting procedure has proven to be successful and to lead frequently to substantial reductions of the wave making.

The procedure starts with a given wave pattern for an initial hull form and provides guidelines to analyze that wave pattern and decide on possible improvements of the hull form from a wave-making point of view. This initial wave pattern may have been observed or measured or it can be a computed pattern, for example from one of the methods discussed in Sections 9.6 [free-surface potential flow] or 9.8 [free-surface viscous flow]. As will appear, availability of the hydrodynamic pressure distribution, usually only available from computations, is of great help in the analysis.

In the examples given, we use free-surface potential flow calculations. As argued in Section 9.6, these give a generally accurate prediction of the wave pattern, except usually for stern waves, but they do not always provide accurate wave resistance predictions. Using such codes in a process to minimize wave resistance may seem risky. On the other hand, with sufficient care such computations give good predictions of the effect of hull form changes on the flow field and wave pattern. The analysis procedure we propose is based on this predicted flow field and wave pattern rather than just on the predicted resistance, and thus avoids the result to be significantly affected by shortcomings in the prediction method used. Moreover, flow field and wave pattern provide much clearer indications on how to improve a hull form.

Using the predicted flow field and wave pattern to decide on possible modifications of the hull form is an approach that requires some guidelines or insights and experience. The guidelines and insights we use are based on the theoretical observations on ship wave making in Section 5, but simplifications are applied. This leads to an understanding of the main trends, but finding the right measure and the right compromise depends much on experience. What is discussed here addresses just a number of aspects, but it demonstrates the approach and possibilities.

11.5.2 The Basic Procedure. Suppose one has available a computed wave pattern and flow field for an initial design at a given speed, and the question is whether and how the wave resistance can be reduced by adjustments of the hull form.

From a free-surface potential flow computation, the wave resistance can be found by integrating the pressure forces over the hull. One might suppose that the hull pressure distribution would already indicate how to reduce the wave resistance (e.g., by reducing the pressure at the forebody, increasing it at the afterbody). However, the relationship between pressure distribution and wave resistance is subtle. The hull pressure distribution in a potential flow without free surface often looks very similar but actually yields zero resistance (d'Alembert's paradox). Therefore, reducing resistance by simple manipulation of the pressure distribution is rarely feasible.

Therefore, instead we base our approach on the relation between the wave pattern and the wave resistance. Section 5 demonstrated that at a sufficient distance from the ship hull, the wave pattern can be regarded as a superposition of linear wave components, originating from different parts of the hull, propagating in various directions and interfering. This simplification is based on the linearity of the system (Laplace equation + linearized free-surface boundary conditions) that is satisfied for small wave amplitudes. For larger wave amplitudes, the validity of the approximation will be somewhat less, but still it provides essentially the right answers. A somewhat bolder step is to use a similar analysis relatively close to the ship hull, where a near-field disturbance is present that sometimes affects the analysis. The possible deviations arising from this should kept in mind.

In Section 5.5, an expression has been given for the wave resistance in terms of the amplitudes of wave components in the far field:

$$R_w = \frac{1}{2}\pi\rho V^2 \int_{-\frac{\pi}{2}}^{+\frac{\pi}{2}} [A(\theta)^2 + B(\theta)^2]\cos^3\theta d\theta \quad (11.10)$$

in which $[A(\theta)^2 + B(\theta)^2]$ is the amplitude squared of a wave component propagating in a direction making an angle θ with the ship's course. The far-field wave components result from the waves generated by different parts of the hull (bow, shoulders, etc.) that propagate away from the hull and interfere. Therefore, to reduce the wave resistance one needs to reduce the amplitudes of the waves where they are generated, and to improve the interference between wave systems generated by different parts of the hull, in order to minimize their amplitude in the far field.

Accordingly, the principal aspect to be considered is the far-field wave pattern, which is directly related to the wave resistance. This can be in the form of, for example, a visual representation of the wave pattern, one or more longitudinal wave cuts, and/or a wave spectrum that indicates the distribution of wave energy over the wave propagation directions. "Far field" does not necessarily mean a large distance here, but far enough to discern separate wave components, their directions and amplitudes, outside the immediate neighborhood of the hull (so in practice, perhaps 0.2 to 0.5*Lpp* away from the centerline). This consideration also demands that a computational method predicts the wave pattern at some distance from the hull with reasonable accuracy.

The analysis should in general not be based only on the wave profile along the hull: there is no direct relation between the wave profile along the waterline and a far-field wave amplitude or the wave resistance, and the hull wave profile is strongly affected by the near-field disturbance that is meaningless for the wave resistance. The main use of the hull wave profile is that it may help to identify the location where waves that are observed in the far field are being generated.

The approach to be followed to analyze and improve a wave pattern using calculations is:

- Study a visualization of the wave pattern and assess which components are dominant for the resistance. One should take into account here the fact that transverse waves contribute more to the wave resistance than diverging waves of the same amplitude. Therefore, wave steepness is not the critical aspect, but amplitude and direction (or wave length) are.
- Identify the hull form features that generate these waves, and adjust these features in order to reduce the wave amplitudes and to improve their interference.
- Carry out a wave pattern calculation for the modified hull, and check what has been achieved. If necessary, repeat the procedure for a further fine-tuning or for other hull form aspects.

The second stage requires insight into the complicated connection between hull form and wave making. That connection is not easy to grasp in general. In practical applications it has been found useful to apply a two-step analysis to get that insight:

1. Consider the relation of the hull form to the hydrodynamic pressure distribution.
2. Consider the relation of the pressure distribution to wave making.

[We note here that, if one would consider this as strictly separate and consecutive computational steps, the first step would require computation of the pressure distribution at the still water surface in double-body flow; and the second step would require computation of the wave pattern generated by that pressure distribution. However, we follow such a procedure only loosely, just to provide an understanding of the mechanisms, and we shall often use pressure distributions from free-surface potential flow computations also in step 1. Section 11.5.6 provides some further discussion.]

This gives rise to the general procedure, which is a formalization of the approach developed at MARIN based on many practical hull form development projects using free-surface potential flow computations. The procedure will be further explained now. The next two subsections address the two steps, then we discuss the simplifications and limitations of the approach.

11.5.3 Step 1: Relation of Hull Form and Pressure Distribution. The quantity to be considered is the hydrodynamic pressure coefficient

$$c_{Phd} = \frac{p + \rho g z}{\frac{1}{2}\rho U_\infty^2} = 1 - \frac{u^2 + v^2 + w^2}{U_\infty^2}$$

simply denoted as c_P in the later text. We shall inspect the c_P distribution over the hull surface and, as a result of that, over the still water surface. This pressure distribution is determined by the hull form and conditions such as ship speed, water depth, etc. To a large extent it can be approximated by the pressure in a potential flow around the hull, but at the stern, deviations occur caused by the boundary layer and wake.

In Sections 5.2.2 and 5.2.3, some characteristics of potential flows around bodies have already been discussed. In general, the relation between hull form and pressure distribution can be summarized by the following guidelines:

High pressures occur:

Near stagnation points: Exactly at a stagnation point, such as occurs at the bow of a ship, the pressure coefficient is $c_P = 1$, which is the maximum value in steady flow. In an area around that point the pressure will be relatively high. Normally there is also a pressure rise towards the stern, although this depends on the stern type and is reduced by viscous effects.

At concave streamwise curvatures: Where the flow goes over a part of the hull surface that is concave in the direction of the streamlines, the centrifugal acceleration acting on fluid particles must be balanced by a pressure increase toward the wall (see Fig. 5.2). Consequently, the pressure is higher at the hull surface.

At large streamwise slopes: A large angle of the wall streamlines relative to the longitudinal direction (outward on the forebody or inward on the aftbody) will often have a somewhat elevated pressure (due to the streamwise curvature further away from the hull).

Under a wave crest: If a wave system is generated at some point, the wave trailing aft will cause alternating high and low pressures on the hull near the water surface. Therefore, such pressures are the result of waves, not the cause of waves, and they are not related to a local hull form aspect. In double-body flow results this does not occur.

Low pressures occur:

At convex streamwise curvatures: Caused by the same mechanism as described above. The centrifugal acceleration is directed outward, and the pressure decreases toward the hull.

Due to displacement effect: The presence of the hull causes a speedup of the flow next to it, leading to a slight underpressure. (In Section 5.2.2 this was explained from the slight streamline curvature at a distance from the hull.) In unrestricted water this is a weak effect; in restricted water it is much stronger.

Under a wave trough: Again as a result of waves generated somewhere upstream.

Except for the stagnation point effect, the effect of streamwise curvature is by far the strongest in most practical cases for ship hulls.

Fig. 11.34 illustrates some of these aspects. The pressure distribution shown is for double-body flow, so there is no effect of waves visible in the graph. The resulting more direct relation between hull form and pressure distribution is a merit of this type of result. The following features are noticeable (the numbers refer to locations indicated in Fig. 11.34):

1. There is a small high-pressure area on the tip of the bulbous bow, where the stagnation point is located.

2. There is another area of elevated pressure near the waterline aft of the bow ($c_P = +0.22$), which is partly caused by the concave waterline curvature here.

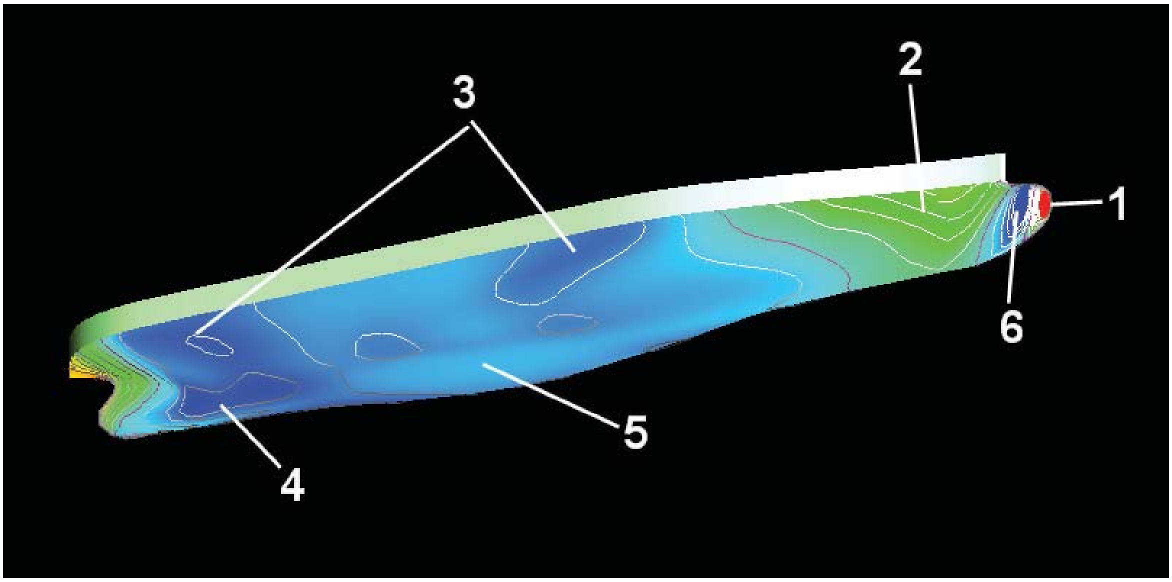

Figure 11.34 Double-body pressure distribution. Colors indicate c_p distribution: red is high and blue is low. (The numbers indicate features discussed in the text.)

3. Low-pressure areas are observed at the fore and aft shoulder ($c_P = -0.13$), caused by the convex curvature of the waterlines.

4. There is a low-pressure area at the stern bulb and bottom of the stern sections ($c_P = -0.19$), where again the curvature is convex for the streamlines coming from under the bottom and going in an upward direction.

5. Along the midbody, the pressure is around $c_P = -0.08$ as a result of the displacement effect.

6. Large pressure variations are present on the bulbous bow, with a pronounced underpressure ($c_P = -0.30$) at its sides; again this is caused by the strong convex curvature of the bulb waterlines.

Clearly, using the guidelines given, the pressure distribution is easily understandable in qualitative terms, and it is evident how details of the hull form could be modified to change that distribution: if desired, the underpressures at locations 3, 4, and 6 could be reduced by reducing the local convex curvature in the streamline direction; the overpressure at the bow (location 2) could be reduced (or moved forward) by avoiding the concave curvature; but nothing could be done on the stagnation pressure (location 1), or the reduced pressure due to displacement effect (location 5) which depends on the main hull dimensions rather than on the detailed hull form.

Fig. 11.35 shows the pressure distribution on the same hull form but now including the effect of the ship wave pattern, from a free-surface potential flow computation. The distribution corresponds in general with the double-body flow case, but the underpressures (location 3 in Fig. 11.34) near the water surface at the fore and aft shoulder are lower (–0.20 to –0.25) and are somewhat shifted aft; the overpressure on the forebody near the waterline (location 2) is higher (0.35). For the stern bulb region there is a rather small change. Along the aft midbody, an area of increased pressure is now visible (location 7), which is a result of a wave crest of the wave system generated by bow and forebody.

Therefore, there is a qualitative agreement of Figs. 11.34 and 11.35, although there are differences mainly closer to the water surface. Also for situations with free-surface waves, many features of the hull pressure distribution are still directly related to the local hull form; and the guidelines given still hold, at least for moderate Froude numbers (0.28 in this case), which gives support to the applicability of our procedure.

The aspect of this pressure field that generates waves is the pressure distribution at the still water surface. If the pressure at the still water surface deviates from zero in the vicinity of the ship, it will set the water surface into motion, in a way addressed in step 2.

We thus have to relate the hull pressure distribution to the resulting pressure distribution on the still water surface. Clearly, pressure variations on the hull close to the water surface have a larger effect than those further beneath the water surface. To illustrate how a pressure variation caused by a hull form feature at some point is felt at a distance, Fig. 11.36 shows the pressure field of a single submerged point source in a uniform flow, on the still water surface, for three different submergence distances of the source. The amplitude of the pressure variation induced at the still water surface decreases quickly with distance (inversely proportional to distance squared, for this case), whereas the length scale of that pressure variation increases with distance to the source. In general:

- A short, local pressure variation caused by a hull form feature far beneath the water surface hardly contributes to the pressure at the still water surface.
- A longer scale pressure variation at the same depth, however, has less decrease of its amplitude and is felt more strongly at the still water surface.
- Therefore, the pressure distribution on the still water surface is caused by all hull pressure variations close to the waterline, and by the larger-scale pressure variations farther beneath the water surface. Pressure variations at the water surface with small length scales can only be generated by form features close to the water surface.

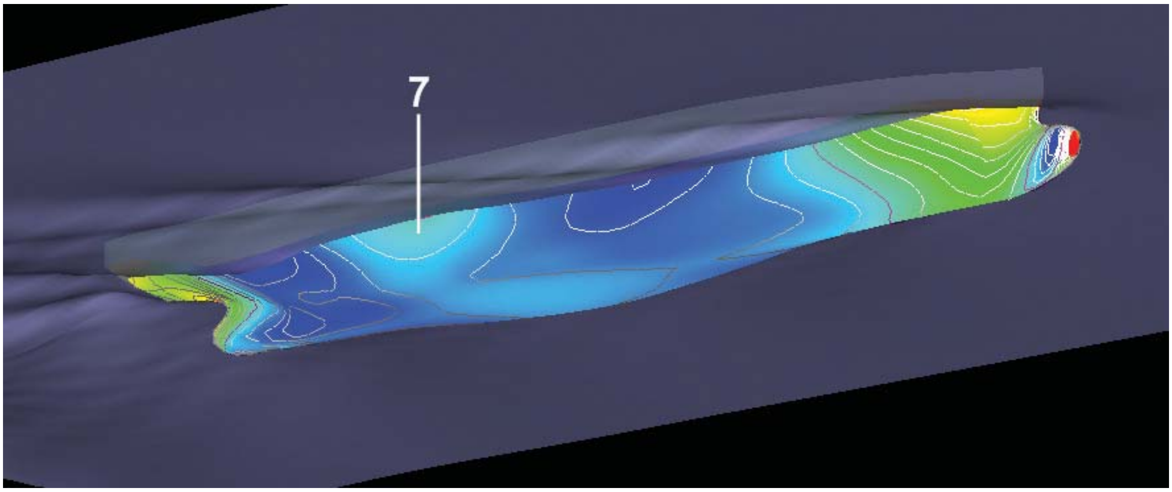

Figure 11.35 Pressure distribution for same hull with free surface, at $Fn = 0.28$.

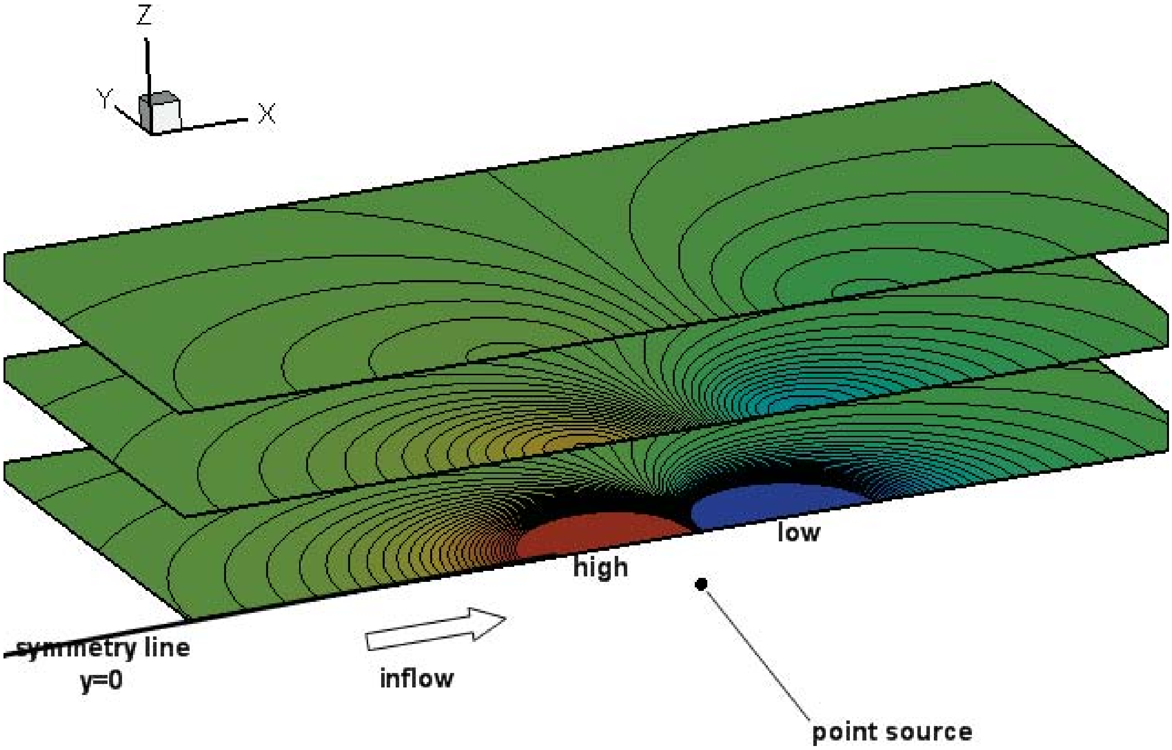

Figure 11.36 Pressure field at the still water surface induced by a submerged source (indicated by the dot) for different submergence distances.

Raven (2010) provides some more illustration of these guidelines.

Fig. 11.37 shows an example of the double-body flow pressure field of a Series 60 parent hull ($C_B = 0.60$). Evidently, the pressure field is continuous from hull to still water surface. On the still water surface, we observe an overall pressure variation with a length comparable to the ship length, with an area of elevated pressure around the bow and stern, and a reduced pressure next to the hull. The lower pressures near the shoulders, being of smaller extent but located adjacent to the waterline, are also visible on the water surface. On the other

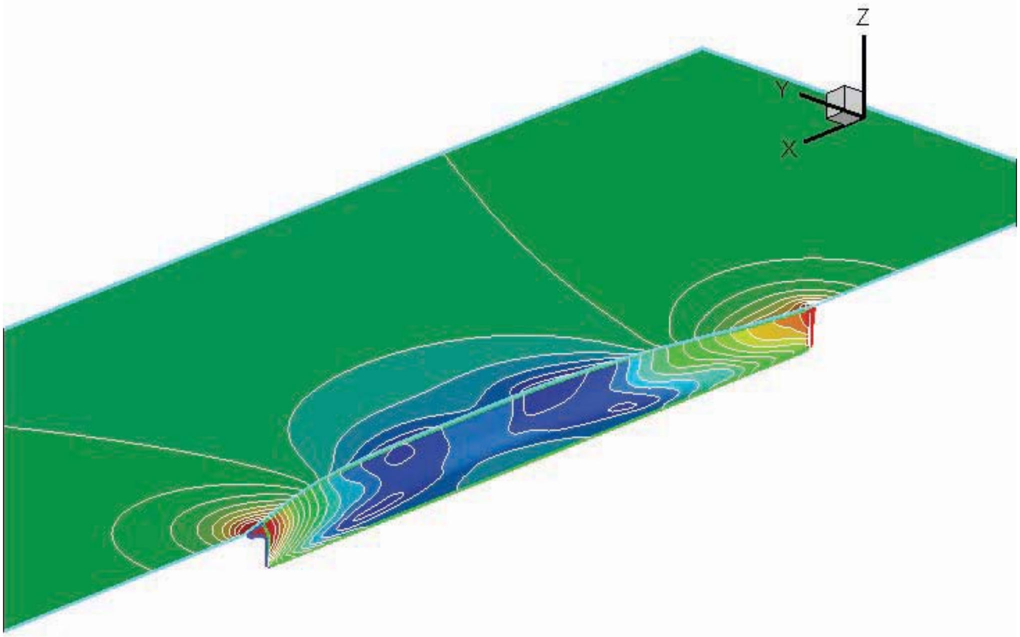

Figure 11.37 Pressure distribution for Series 60 parent hull in double-body flow.

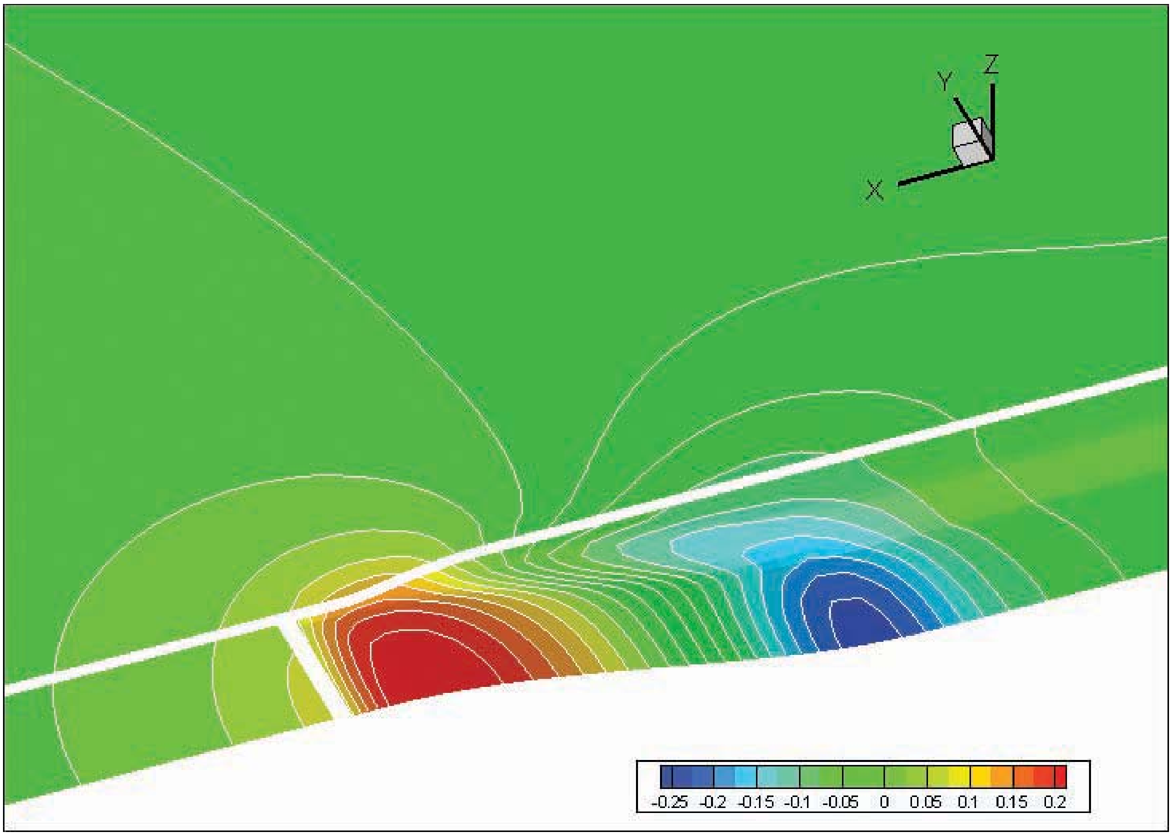

Figure 11.38 Pressure distribution for a barge-type stern in double-body flow.

hand, the low pressure at the bilge in the afterbody is a localized disturbance far beneath the water surface and is not noticeable at the water surface. Instead, Fig. 11.38 shows an example of a barge-type stern that has a low-pressure area of larger size at the bottom caused by the convex curvature of the buttocks. As a result of its greater length scale, this underpressure is visible at the water surface, albeit with reduced amplitude.

11.5.4 Step 2: Relation of Pressure Distribution and Wave Making. It is the pressure distribution on the still water surface (or rather, its derivative in the streamwise direction) in double-body flow that is regarded as the cause of the generation of waves. The challenge of the second step is to understand qualitatively the connection between this pressure distribution and the height, length, and direction of the waves generated. For simplicity we here consider the effect of the pressure distribution in isolation (i.e., in absence of the ship), an approximation briefly addressed in Section 11.5.6.

The dynamic free-surface boundary condition given in Section 9.6.1 leads to an expression for the wave elevation

$$\zeta = \frac{1}{2} Fn^2 L \cdot c_P$$

using again the hydrodynamic pressure coefficient. Thus, if c_P is high on a part of the hull just below the water surface, this will generate a local wave crest plus a trailing wave system. Similarly, a low pressure will generate a local wave trough plus a trailing wave system.

An isolated local pressure at the still water surface (e.g., at the tip of the bow or at a sharp convex corner of the waterline) in principle would generate a complete Kelvin wave system made up of wave components propagating in all directions. However, a smooth hull form causes a smooth pressure distribution as well; and an almost equal pressure in the vicinity would cancel some of those wave components and amplify some others. Therefore, a smooth pressure distribution does not generate the same complete Kelvin pattern but generates some preferred components, and much less of the others. So, which wave components will be significant and which will not?

The answer can be formulated as the following guideline: **A wave of a certain length is most effectively generated by a pressure variation of comparable length and shape.** To illustrate this, suppose the pressure on a part of the hull surface has a more or less sinusoidal variation with a length L_P. One example, illustrated in Fig. 11.39, is the usual overall pressure pattern on a ship hull, with a high pressure at the bow, a lower pressure beside the hull, and often a higher pressure again at the stern. This overall pressure pattern has a typical length $L_P \approx L$.

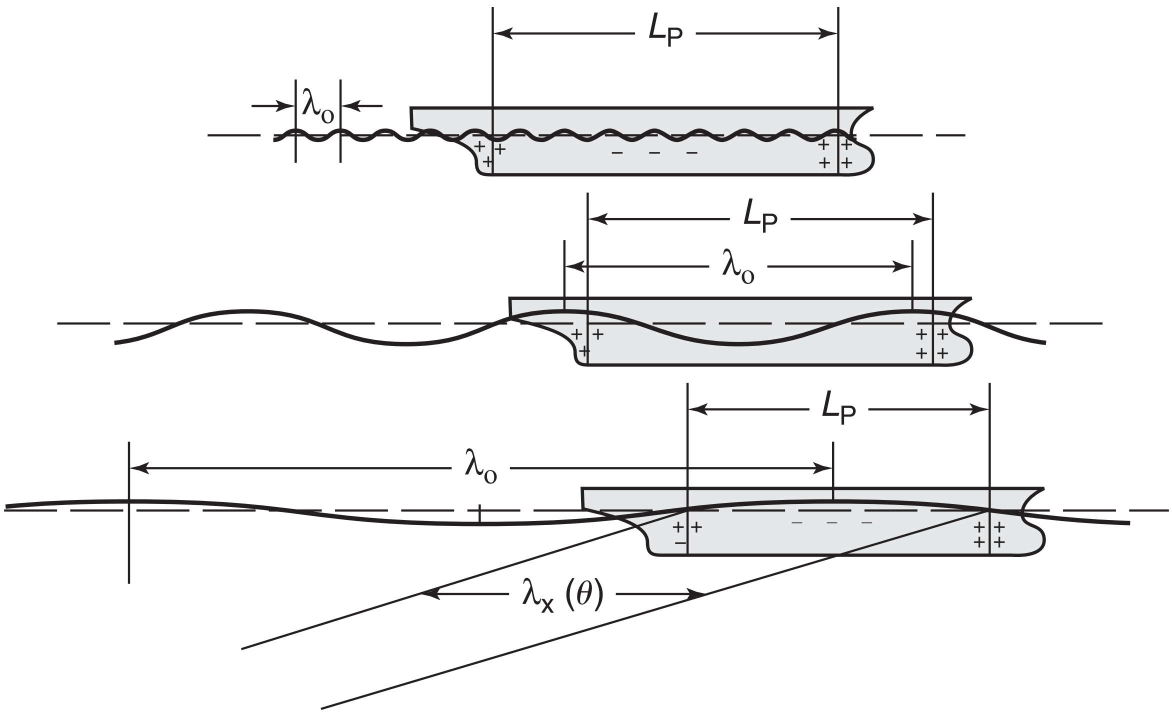

Figure 11.39 Pressure distribution and wave making. *Top*: low Froude number; *middle*: *Fn* ≈ 0.4; *bottom*: high Froude number.

As we have seen in Section 5.4.2, for a ship speed *V* the length of wave components in the steady wave pattern is

$$\lambda = 2\pi \frac{V^2}{g} \cos^2\theta = \lambda_0 \cos^2\theta$$

and the wave length measured in the longitudinal direction is

$$\lambda_x = 2\pi \frac{V^2}{g} \cos\theta = \lambda_0 \cos\theta$$

Therefore, wave lengths vary between 0 and λ_0 dependent on the divergence angle θ.

The top sketch in Fig. 11.39 shows the case of a rather low Froude number, at which $\lambda_0 << L_P$. The length scale of the pressure distribution is much larger than the length of any wave (regardless of θ), so any high- or low-pressure region would act on crests and troughs alike and is ineffective to generate a wave. Therefore, the ship-scale pressure distribution will not generate waves at this low *Fn*—but local pressure variations (e.g., around the bow and forebody) may well be better matched with the possible waves and are more important at low *Fn*.

The middle sketch of Fig. 11.39 illustrates the situation in which the transverse wave length $\lambda_0 \approx L_P$. The higher pressure at the bow, the lower pressure next to the hull, and the higher pressure at the stern all cooperate to generate a substantial transverse wave.

Finally, at high Froude numbers when $\lambda_0 >> L_P$, the pressure variation occurs over just a small fraction of the length of the transverse wave. Positive and negative pressures effectively cancel on the length scale of the transverse wave, and as a result this pressure variation will not generate a transverse wave: it does not have a comparable length. However, there is a value of θ for which $\lambda_x(\theta) \approx L_P$, and waves with that divergence angle are quite effectively generated by this pressure variation.

A similar reasoning applies to other, more local pressure variations. The guideline provides a general understanding of wave making that is helpful to anticipate and explain ship wave patterns.

We note that this guideline on the relationship between a free-surface pressure distribution and its wave pattern, is an interpretation of the theoretical expression according to linear theory (Wehausen & Laitone, 1960). This indicates that the amplitude of waves in direction θ generated is proportional to the 2D Fourier transform of the distribution of the longitudinal pressure derivative at the wave frequency,

$$\sec^3\theta \iint_{FS} \frac{\partial p}{\partial x} \exp\left[i \frac{g(x\cos\theta + y\sin\theta)}{V^2\cos^2\theta}\right] dxdy$$

and comparison with equation (5.30) confirms our guideline.

11.5.5 Some Consequences. The general insights explained help in understanding a variety of well-known physical phenomena:

- As remarked, transverse waves are most effectively generated by the ship-scale pressure distribution if $\lambda_0 \approx L$ (the middle sketch of Fig. 11.39), which is the case at $Fn = 0.4$. As a matter of fact, transverse waves are strongly amplified in this speed range. Since transverse waves contribute most to the wave resistance, this leads to the primary resistance hump which occurs at $Fn \approx 0.5$.

Figure 11.40 Wave pattern at high Froude number. Transverse waves nearly absent; no Kelvin angle visible; only sharply diverging waves.

- The guideline applies not only to the longitudinal but also to the transverse direction: a pressure disturbance over a substantial width tends to generate transverse waves. Much care is therefore needed in designing wide flat transom sterns.
- Except at low Froude number, local pressure disturbances of small extent generate shorter, diverging waves, not transverse waves. Around the bow stagnation point, the pressure is high; on a sharp bow, it decreases quickly with distance from the stagnation point, so the pressure distribution has a small length scale, and sharp bows thus generate primarily diverging waves. On a blunt bow, the high-pressure region is more extensive and of greater lateral extent, and it will tend to generate transverse waves as well (in particular at low Froude numbers).
- Similarly, local features such as the corners of a transom stern will generate diverging waves.
- For very high Froude numbers, all pressure variations present on the hull surface are short relative to most of the possible waves (e.g., at $Fn = 1$, $\lambda_0 = 6.25L$), and only diverging waves for $\theta \approx 80$ degrees have $\lambda_x \approx L$. Consequently, for Fn increasing above the primary resistance hump, transverse waves are gradually disappearing, and any wave energy goes into diverging waves of larger and larger angles. This explains the observation that the whole wave pattern gets narrower. Fig. 11.40 shows an example. There is, however, no change of the Kelvin angle: the theoretical envelope is still at the same angle, but the outer waves are too weak to be noticeable.
- At low Froude numbers, all waves are short relative to the dimensions of the ship. These waves are generated by shorter components of the free-surface pressure distribution. Those components can only be caused by hull form features close to the water surface, whereas a pressure disturbance or hull form feature at greater depth has no effect. Therefore, at low Froude numbers, it is the waterline shape that dominates the wave making.
- At higher Froude numbers, however, waves are longer and thus respond to longer components of the free-surface pressure distribution, which are determined by the entire hull shape. The shape of the sectional area curve thus becomes more important at higher Froude numbers.
- Pressure variations over a short length far beneath the water surface are normally insignificant for the wave making (but of course can be detrimental for viscous flow).

11.5.6 Discussion of the Procedure—Simplifications and Limitations. The two-step procedure to relate the wave pattern to the hull form is a substantial simplification of the entire problem. This makes it easier to understand,

Next Page

but one may question the validity. We shall address that here. A more complete discussion and validation is provided in Raven (2010).

A first approximation is that we try to explain the hull pressure distribution from the local hull form only. But the pressure distribution we use is normally the one found in a free-surface potential flow calculation, and the wave making changes the distribution to some extent. As demonstrated, the effect of the wave making on the pressure distribution is rather limited for usual merchant-ship speeds. In the analysis, we keep in mind that the free surface increases the pressure extremes, shifts them slightly aft, and contains pressure variations caused by waves generated upstream (see Fig. 11.35). To clarify the analysis one could use a double-body pressure distribution, but that would introduce other deviations in certain cases.

A second approximation is that the analysis of the waves generated by the pressure distribution entirely disregards the boundary condition on the hull surface; and ignores the fact that the waves propagate over the curved flow field with variable velocity around the hull, which slightly affects the wave amplitudes and locations. However, these approximations are justified as long as we aim only at a qualitative understanding and use a more complete method for quantitative prediction of the wave pattern.

In Raven (2010) it is demonstrated that the decomposition into two steps and the simplifications applied in each correspond closely with the earliest slow-ship linearized methods (see Section 9.6.4), such as that of Baba and Takekuma (1975). Also, to illustrate the validity of the procedure, some computations are shown by a strict computational equivalent of it: first the pressure distribution $p(x, y)$ on the still water surface in a double-body flow around the hull is determined, then the wave pattern generated by $-p(x, y)$ acting on the water surface (omitting the hull) is computed. It is shown that this wave pattern often agrees closely with that of the ship itself. Fig. 11.41 shows an example from Raven (2010), comparing the wave pattern of the free-surface pressure distribution with that of the ship, for the Series 60 parent hull at $Fn = 0.316$. The agreement is just remarkable. For other cases, in particular with pronounced differences between the double-body and free-surface pressure fields, larger differences occur, but the usefulness of the procedure for general understanding is supported.

The approach outlined above and the simple guidelines given enable us to foresee what sort of pressure distribution a given hull form will have, which aspects of that pressure distribution will generate waves at certain speeds, and conversely, how the dominant waves

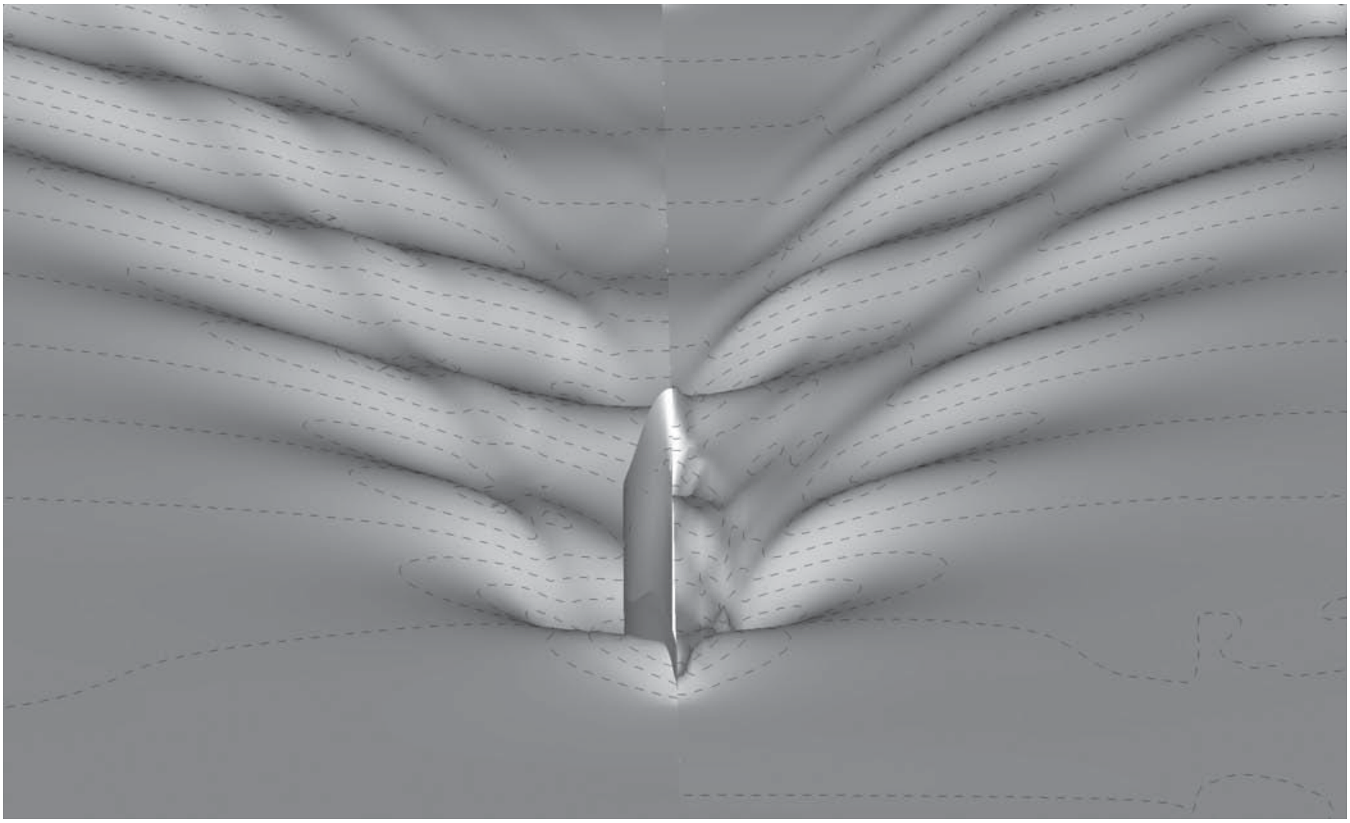

Figure 11.41 Computed wave patterns of Series 60 $C_B = 0.60$ at $Fn = 0.316$ (*left*), and of its double-body pressure field moving at the same speed over the still water surface (*right*).

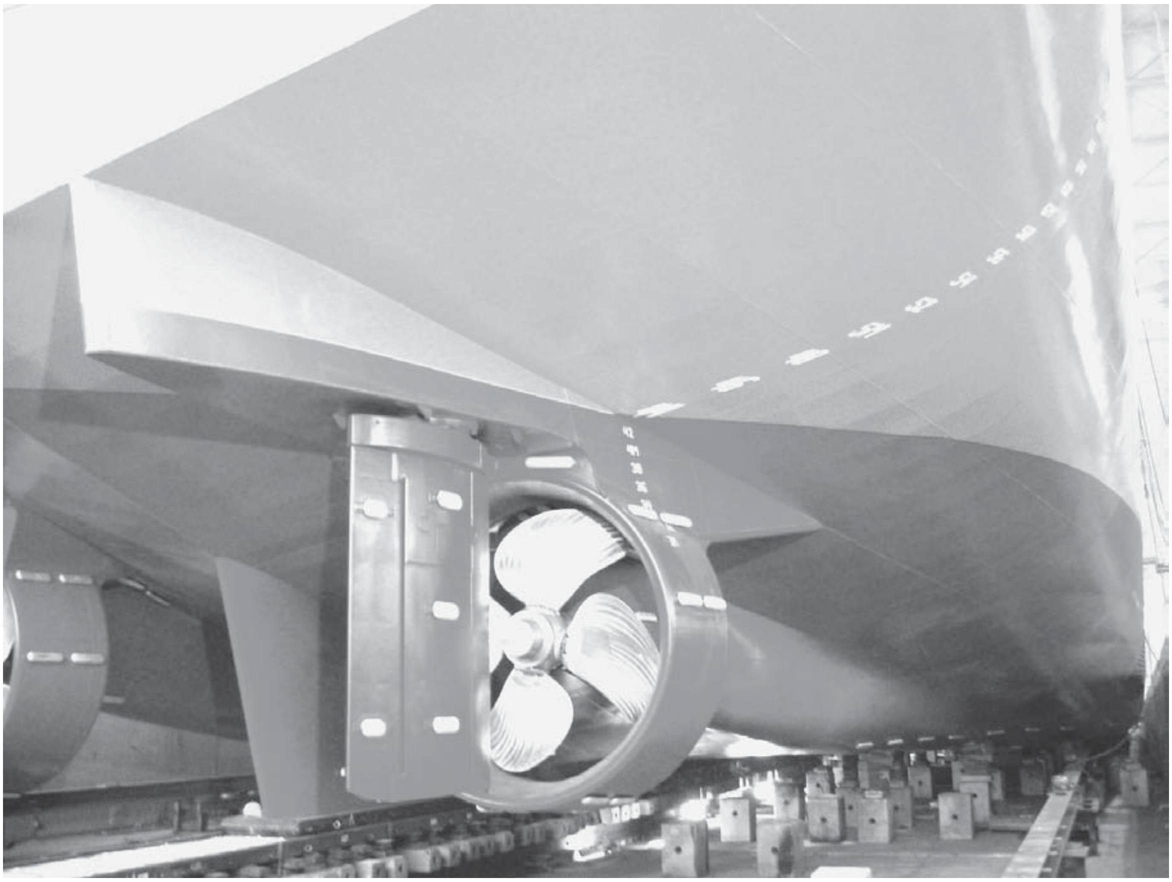

Figure 11.62 Afterbody of a twin-screw dredger, with twin gondolas, ducted propellers, tunnels, headboxes, and central skeg. (Courtesy of IHC Dredgers B.V., The Netherlands.)

In summary, the detailed hull form design to achieve a good viscous flow is complicated by having to consider different, partly opposing objectives regarding resistance and wake field; by the sensitivity of the viscous flow to hull form changes; and by the substantial scale effects. The aim of the present section has been to provide basic insight in trends that will be useful, for example, in improving a design based on available experimental or computational information on the viscous flow around the hull.

References

Abbot, I. H., & von Doenhoff, A. E. (1949). *Theory of wing sections*. New York, NY: McGraw-Hill.

Abdel-Maksoud, M., Rieck, K., & Menter, F. R. (2002). Unsteady numerical investigation of the turbulent flow around the container ship model (KCS) with and without propeller. In Larsson, L., Stern, F., & Bertram, V. (Eds.). *Gothenburg 2000. A workshop on numerical hydrodynamics. Proceedings*. Report No. CHA/NAV/R-02/0073. Gothenburg: Chalmers Univ. of Techn.

Abdelmeguid, A. M., Markatos, N. C. G., Spalding, D. B., & Muraoka, K. (1978). A method for predicting three-dimensional turbulent flows around ship hulls. *Proc. Int. Symp. Ship Viscous Flow, SSPA, Gothenburg, 3* (1–3),24

Acheson, D. J. (1990) *Elementary fluid dynamics*. Oxford, UK: Oxford Applied Mathematics and Computing Science Series.

af Chapman, F. H. (1795). Physical findings on the resistance experienced by bodies moving on a straight course in water. *Swedish Royal Academy of Sciences, Transactions*.

Alessandrini, B., & Delhommeau, G. (1996). A multi-grid velocity-pressure-free surface elevation fully coupled solver for calculation of turbulent incompressible flow around a hull. *21st Symposium on Naval Hydrodynamics* (328–345), Washington, DC: National Academy of Sciences, 328–345.

Alessandrini, B., & Delhommeau, G. (1999). A fully coupled Navier-Stokes solver for calculations of turbulent free surface flow past a ship hull. *International Journal for Numerical Methods in Fluids*, *29* (2), 125–142.

Almeida, E., Diamantino, T. C., & de Sousa, O. (2007). Marine paints: The particular case of antifouling paints. *Progress in Organic Coatings*, *59* (1), 2–20.

American Society of Mechanical Engineers, Committee PTC 61. (2008). *ASME V & V 20-2008: Standard for verification and validation in computational fluid dynamics*. Alexandria, VA: ASME.

Anderson, J. D., Jr. (1991). *Fundamentals of aerodynamics* (2nd ed.). New York, NY: McGraw-Hill.

Baar, J. J. M., & Price, W. G. (1988). Developments in the calculation of the wavemaking resistance of ships. *Proceedings of the Royal Society of London*, *416*, 115–147.

Baba, E. (1969). A new component of viscous resistance. *Journal of the Society of Naval Architects of Japan*, *125*, 23–34.

Baba, E., & Hara, M. (1977). Numerical evaluation of a wave-resistance theory for slow ships. *2nd International Conference on Numerical Ship Hydrodynamics*, Berkeley, CA, 17–29.

Baba, E., & Takekuma, K. (1975). A study on free-surface flow around bow of slowly moving full forms. *Journal of the Society of Naval Architects of Japan*, *137*, 1–10.

Bai, K. J., & Yeung, R. W. (1974). Numerical solutions to free-surface problems. *10th Symposium on Naval Hydrodynamics*, Cambridge, MA, 609–633.

Bailey, D. (1976). The NPL high-speed round-bilge displacement hull series. Resistance, propulsion, manoeuvring and seakeeping data. *RINA Maritime Technology Monograph*, *4*.

Baker, G. S. (1937). Development of hull form of merchant vessels. *NECI Transactions*, *54*.

Baker, G. S., & Kent, J. L. (1919). Speed, dimensions and form of cargo vessels. *Journal of the American Society for Naval Engineers*, *31* (2) , 494–508.

Baldwin, B. S., & Lomax, H. (1978). *Thin-layer approximation and algebraic model for separated turbulent flows*. AIAA Paper 78-257. Huntsville, AL: AIAA.

Beaufoy, M. G. (1834). *Nautical and hydraulic experiments*. London: H. Beaufoy.

Bechert, D. W., Bartenwerfer, M., Hoppe, G., & Reif, W.-E. (1986). Drag reduction mechanisms derived from shark skin. *15th Congress of the International Council of the Aeronautical Science*, London, United Kingdom.

Berntsson, K. M., Andreasson, H., Jonsson, P. R., Larsson, L., Ring, K., Petronis, S., et al. (2000). Reduction of barnacle recruitment on micro-textured surfaces: Analysis of effective topographic characteristics and evaluation of skin friction. *Biofouling*, *16* (2–4), 245–261.

Beys, P. M. (1963). *Series 63—Round bottom boats*. Report No. 949. Hoboken, NJ: Stevens Inst. of Techn., Davidson Lab.

Birk, L., & Harries, S. (Eds.). (2003). OPTIMISTIC—optimization in marine design. *39th WEGEMT Summer School*, Berlin, May 19–23.

Blendermann, W. (1990). External forces, wind forces. In J. Brix (Ed.), *Manoeuvring technical manual* (Nos. 2 and 3). Hamburg, Germany: Schiff und Hafen/ Kommandobrücke.

Bolt, E. (2001). *Fast ferry wash measurement and criteria*. FAST 2001 Symposium, Southampton, England.

Boussinesq, J. (1877). Théorie de l'ecoulement tourbillant. *Mem. Présentés par Divers Savants Acad. Sci. Inst. Fr.*, *23*, 46–50.

Brandsma, F. J., & Hermans, A. J. (1985). A quasi-linear free surface condition in slow ship theory. *Schiffstechnik*, *32*, 25–41.

Brard, R. (1972). The representation of a given ship form by singularity distributions when the boundary condition on the free surface is linearized. *Journal of Ship Research*, *16*, 79–92.

Buckingham, E. (1914). On physically similar systems; Illustrations on the use of dimensional equations. *Physical Rev*iew, *4* (4), 345–376.

Bull, P. (2005). Verification and validation of KVLCC2M tanker flow. In T. Hino (Ed.), *CFD Workshop Tokyo 2005*. Tokyo, Japan: National Maritime Research Institute, 581–586.

Bushnell, D. M., Hefner, J. N., & Ash, R. L. (1977). Effect of compliant wall motion on turbulent boundary layers. *Physics of Fluids*, *10*, 31–48.

Chakravarthy, S. R., & Osher, S. (1985). *A new class of high-accuracy TVD schemes for hyperbolic conservation laws*. AIAA Paper 85-0363. Huntsville, AL: AIAA.

Chorin, A. J. (1967). A numerical method for solving incompressible viscous flow problems. *Journal of Computational Physics*, *135* (2), 118–125.

Clement, E. P., & Blount, D. L. (1963). Resistance tests of a systematic series of planing hull forms. *Transactions of the Society of Naval Architects and Marine Engineers*, *71*, 491–579.

Cointe, R., & Tulin, M. P. (1994). A theory of steady breakers. *Journal of Fluid Mechanics*, *209*, 405–433.

Comstock, J. P., & Hancock, C. H. (1942). The effect of size of towing tank on model resistance. *Transactions of the Society of Naval Architects and Marine Engineers*, *50*, 149.

Craft, T. J., Launder, B. E., & Suga, K. (1996). Development and application of a cubic eddy-viscosity model of turbulence. *International Journal of Heat and Fluid Flow*, *17* (2), 108–115.

Cura Hochbaum, A., & Vogt, M. (2002). Flow and resistance prediction for a container ship. In L. Larsson, F. Stern, & V. Bertram (Eds.), *Gothenburg 2000. A workshop on numerical hydrodynamics. Proceedings*. Report No. CHA/NAV/ R-02/0073. Gothenburg: Chalmers Univ. of Techn.

Dacles-Mariani, G. G., Zilliac, J. S., Chow, P., & Bradshaw, P. (1995). Numerical/experimental study of a wingtip vortex in the near field. *AIAA Journal*, *33* (9), 1561–1568.

Dagan, G. (1972). *Small Froude number paradoxes and wave resistance at low speeds*. Tech. Rep. 7103-4, Hydronautics Inc., Laurel, MD, USA.

Dagan, G. (1975). A method of computing nonlinear wave resistance of thin ships by coordinate straining. *Journal of Ship Research*, *19* (3), 149–154.

Dahlström, M., Mårtensson, L. G. E., Jonsson, P. R., Arnebrant, T., & Elwing, H. (2000). Surface active adrenoceptor compound prevents the settling of cyprid larvae of balanus improvises. *Biofouling*, *16* (2–4), 191–203.

Daube, O., & Dulieu, A. (1981). A numerical approach of the nonlinear wave resistance problem. *3rd International Conference on Numerical Ship Hydrodynamics* (73–80). Paris, France.

Davidson, K. S. M., & Suarez, A. (1949). *Test of twenty related models of V-bottom motor boats, EMB Series 50*. DTMB Report No. R-47. Hoboken, NJ: Stevens Inst. of Tech.

Dawson, C. (1977). A practical computer method for solving ship wave problems. *2nd International Conference. on Numerical Hydrodynamics* (30–38). Berkeley, CA.

Deng, G. B., Guilmineau, E., Queutey, P., & Visonneau, M. (2005). Ship flow simulations with the ISIS CFD code. In T. Hino (Ed.), *CFD Workshop Tokyo 2005*. Tokyo, Japan: National Maritime Research Institute, 530–538.

Deng, G. B., Queutey, M., & Visonneau, M. (2005). Three-dimensional flow computation with Reynolds stress and algebraic stress models. In W. Rodi (Ed.), *Engineering Turbulence Modelling and Experiments 6*. Atlanta, GA: Elsevier.

Doctors, L., & Day, A. (2000). Steady-state hydrodynamics of high-speed vessels with a transom stern. *23rd Symposium on Naval Hydrodynamics*. Val de Reuil, France.

Doctors, L. J., & Day, A. H. (2001). The generation and decay of waves behind high-speed vessels. *Proceedings of the 16th International Workshop on Water Waves and Floating Bodies* (33–36). Hiroshima, Japan.

Doust, D. J., & O'Brien, T. P. (1959). Resistance and propulsion of trawlers. *Trans. NECI Transactions*, *75*.

Doyle, R., Whittaker, T. J. T., & Elsaesser, B. (2001). *A study of fast ferry wash in shallow water*. FAST 2001 Symposium, Southampton, England.

Doyle, R., Whittaker, T. J. T., & Elsaesser, B. (2001a). Wake wash characteristics of high-speed ferries in shallow water. *Ship Technology Research*, *48*, 181–196.

Dubrovsky, V., & Lyakhovitsky, A. (2001). *Multi-Hull ships*. Fair Lawn, NJ: Backbone Publishing Co.

Eça, L., & Hoekstra, M. (2006). Discretization uncertainty estimation based on a least-squares version of the Grid Convergence Index. *2nd Workshop on CFD Uncertainty Analysis*. Instituto Superior Tecnico, Lisbon, Portugal.

Eca, L., & Hoekstra, M. (2008). The numerical friction line. *Journal of Marine Science and Technology*, *13-4*, 328–345.

Eça, L., & Hoekstra, M. (Eds.). (2008a). *Third workshop on CFD uncertainty analysis*. Instituto Superior Tecnico, Lisbon, Portugal.

Edstrand, H., Freimanis, E., & Lindgren, H. (1953–1956). *Experiments with Tanker Models I–V*. SSPA Reports No. 23, 26, 29, 36 och 37. Gothenburg: Swedish State Shipbuilding Experiment Tank (SSPA).

Eggers, K. (1981). Non-Kelvin dispersive waves around non-slender ships. *Schiffstechnik*, *28*, 223–252.

Eggers, K., Sharma, S., & Ward, L. (1967). An assessment of some experimental methods for determining the wavemaking characteristics of a ship form. *Transactions of the Society of Naval Architects and Marine Engineers*, *75*, 112–157.

Emerson, A. (1959). Ship model size and tank boundary correction. *NECI Transactions*, *76*.

Faltinsen, O. M. (2005). *Hydrodynamics of high-speed marine vehicles*. Cambridge, UK: Cambridge University Press.

Ferrante, A., & Elghobashi, S. (2004). On the physical mechanisms of drag reduction in a spatially developing turbulent boundary layer laden with microbubbles. *Journal of Fluid Mechanics*, *503*, 345–355.

Ferziger, J. H., & Peric, M. (1999). *Computational methods for fluid dynamics* (2nd ed.). Berlin, Germany: Springer-Verlag.

Froude, R. E. (1881). On the leading phenomena of the wave-making resistance of ships *Transactions of the Institute of Naval Architects*, *22*, 220–245.

Froude, R.E. (1888). On the "constant" system of notation of results of experiments on models used at the Admiralty Experiments Works. *Transactions of the Institute of Naval Architects*, *29*.

Froude, W. (1872, 1874), Experiments on surface friction. *British Association Reports*.

Froude, W. (1877). On experiments upon the effect produced on the wave-making resistance of ships by length of parallel middle body. *Transactions of the Institute of Naval Architects*, *18*.

Froude, W. (1955). Observations and suggestions on the subject of determining by experiment the resistance of ships. In *The Papers of William Froude, 1810–1879*. London, UK: Royal Institution of Naval Architects.

Fureby, C. (2008). Large eddy simulation of ship hydrodynamics. *27th Symposium on Naval Hydrodynamics* (389–408). Seoul, Korea.

Fureby, C., Alin, N., Wikström, N., Menon, S., Svanstedt, N., & Persson, L. (2003). *On large eddy simulations of high Reynolds number wall bounded flows*. AIAA Paper No. 2003-0066. Huntsville, AL: AIAA.

Gadd, G. E. (1976). A method for computing the flow and surface wave pattern around full forms. *Transactions of the Royal Institute of Naval Architects*, *118*, 207–220.

Gatchell, S., Hafermann, D., Jensen, G., Marzi, J., & Vogt, M. (2000). Wave resistance computations—A comparison of different approaches. *23rd Symposium of Naval Hydrodynamic* (792–804)*s*. Val de Reuil, France.

Gertler, M. (1954). *A re-analysis of the original test data for the Taylor standard series*. TMB Report 806 DTRC.

Graff, W., Kracht, A., & Weinblum, G. (1964). Some extensions of the D. W. Taylor's standard series. *Transactions of the Society of Naval Architects and Marine Engineers*, *72*, 374.

Gray, J. (1936). Studies in animal locomotion. VI. The propulsive powers of the dolphin. *Journal of Experimental Biology*, *13*, 192–199.

Grigson, C. W. B. (1993). A planar friction algorithm and its use in analysing hull resistance. *Transactions of the Royal Institute of Naval Architects*, 76–115.

Guilloton, R. (1964). L'etude theorique du bateau en fluide parfait. *Bulletin de l'Association Technique Maritime et Aeronautique*, *64*, 537.

Hadler, J. B. (1966). The prediction of power performance on planing craft. *Transactions of the Society of Naval Architects and Marine Engineers*, *74*.

Hadler, J. B., Hubble, E. N., & Holling, H. D. (1974). Resistance characteristics of a systematic series of planing hull forms—Series 65. *SNAME Chesapeake Section.*

Hamalainen, R., & Van Heerd, J. (1998). Hydrodynamic development for a large fast monohull passenger ferry. *Transactions of the Society of Naval Architects and Marine Engineers*, *106*, 413–441.

Han, K. (2008). Numerical optimization of hull/propeller/rudder interaction (Doctoralthesis, Shipping and Marine Technology, Chalmers University of Technology, Gothenburg).

Hansen, H. (2007). *Enhanced wind tunnel techniques and aerodynamic force models for yacht sails* (Doctoral thesis, Mechanical Engineering, University of Auckland, Auckland).

Havelock, T. H. (1908). The propagation of groups of waves in dispersive media, with application to waves on water produced by a travelling disturbance. *Proceedings of the Royal Society*, *London*, *81* (549), 398–430.

Havelock, T. H. (1913). Ship resistance, the wavemaking properties of certain travelling pressure disturbances. *Proceedings of the Royal Society*, *London*, *89* (613), 489–499.

Havelock, T. H. (1932). The theory of wave resistance. *Proceedings of the Royal Society A*, *138*, 339–348.

Havelock, T. H. (1934). Wave patterns and wave resistance. *Transactions of the Institute of Naval Architects*, *76*, 430–446.

Havelock, T. H. (1951). Wave resistance theory and its application to ship problems. *Transactions of the Society of Naval Architects and Marine Engineers*, *59*, 13–24.

Heimann, J. (2000). Application of wave pattern analysis in a CFD-based hull design process. *Proceedings of the 3rd Numerical Towing Tank Symposium.* Tjarno, Sweden.

Heimann, J. (2006). CFD-based optimization of the wavemaking characteristics of ship hulls. *Proceedings STG*, *Hamburg*, *100.*

Hess, J. L. (1990). Panel methods in computational fluid dynamics. *Annual Review of Fluid Mechanics*, *22*, 255–274.

Hess, J. L., & Smith, A. M. O. (1962). *Calculation of non-lifting potential flow about arbitrary three-dimensional bodies.* Douglas Aircraft Report No ES 40622. Long Beach, CA: Douglas Aircraft.

Hino, T. (Ed.). (2005). *CFD Workshop Tokyo 2005.* Tokyo, Japan: National Maritime Research Institute.

Hirt, C. W., & Nichols, B. D. (1981). Volume of fluid (VOF) method for dynamics of free boundaries. *Journal of Computational Physics*, *39* (1), 201–225.

Hoekstra, M. (1975). Prediction of full-scale wake characteristics based on model wake survey. *International Shipbuilding Progress*, *22–250.*

Hoekstra, M. (1999). Numerical simulation of ship stern flows with a space-marching Navier-Stokes method (Doctoral thesis, Delft University).

Hoekstra, M., & Raven, H. (2003). A practical approach to constrained hydrodynamic optimization of ships. *NAV 2003 Symposium*, Palermo, Italy.

Hoerner, S.F. (1965). *Fluid dynamic drag.* Hoerner Fluid Dynamics: Bricktown, New Jersey.

Holtrop, J. (1999), Ship hydrodynamics and hull forms—an introduction (lecture notes). *MARIN Training Course on Hydrodynamics in Ship Design*, Wageningen, Netherlands.

Holtrop, J., & Mennen, G. G. J. (1978). A statistical power prediction method. *International Shipbuilding Progress*, *25*, 253.

Hughes, G. (1952). Frictional resistance of smooth plane surfaces in turbulent flow. *Transactions of the Institute of Naval Architects*, *94.*

Hughes, G. (1954). Friction and form resistance in turbulent flow and a proposed formulation for use in model and ship correlation. *Transactions of the Institute of Naval Architects*, *96.*

Hughes, G. (1957). The effect of model and tank size in two series of resistance tests. *Transactions of the Institute of Naval Architects*, *99.*

Hughes, G. (1961). Tank boundary effects on model resistance. *Transactions of the Royal Institute of Naval Architects*, *103.*

Hughes, M. J. (1997). Application of CFD to the prediction of wave height and energy from high-speed ferries. *International Conference on Computational Fluid Dynamics*, Ulsteinvik, Norway.

Hunt, B. (1980). The mathematical basis and numerical principles of the boundary integral method for incompressible flow over 3-D aerodynamic configurations. In B. Hunt (Ed.), *Numerical methods in applied fluid dynamics* (pp. 49–135). London, UK: Academic Press.

Hunt, S., & Zondervan, G. J. D. (2007). Use of CFD in the optimisation of a naval support ship. 13th International Conference on Computer Applications in Shipbuilding, Portsmouth, UK.

Inui, T. (1980). *From bulbous bow to free surface shock wave-Trend of twenty years research on ship waves at the Tokyo University Tank*. 3rd George Weinblum Memorial Lecture. *Journal of Ship Research*, *25*, 147–180.

Inui, T., & Kajitani, H. (1977). A study on local nonlinear free-surface effects in ship waves and wave resistance. *Schiffstechnik*, *24*.

Issa, R. I. (1986). Solution of the implicitly discretised fluid flow equations by operator splitting. *Journal of Computational Physics*, *62*, 40–65.

ITTC (1978). *Proceedings of the 15th ITTC, The Hague, The Netherlands*. Netherlands Ship Model Basin (MARIN): Wageningen, Netherlands.

Janson, C.-E. (1997). *Potential* flow panel methods for the calculation of free surface flows with lift (Doctoral thesis, Chalmers University of Technology).

Janson, C.-E., & Larsson, L. (1996). A method for the optimization of ship hull forms from a resistance point of view. *21st Symposium on Naval Hydrodynamics* (pp. 680–696). Trondheim, Norway.

Jensen, G. (1988). *Berechnungen der stationären Potentialströmung um ein Schiff unter Berücksichtigung der nichtlinearen Randbedingung an der Wasseroberfläche* (Doctoral thesis, University of Hamburg).

Jensen, G. (1994). Moderne Schiffslinien (in German). *Handbuch der Werften*, *22*, Hansa, 93–110.

Jensen, G., Bertram, V., & Söding, H. (1989). Ship wave-resistance computations. *5th International Conference on Numerical Ship Hydrodynamics* (pp. 593–606). Hiroshima, Japan.

Jensen, G., Mi, Z.-X., & Söding, H. (1986). Rankine source methods for numerical solutions of the steady wave resistance problem. *16th Symposium on Naval Hydrodynamics* (pp. 575–582). Berkeley, CA.

Jensen, P. S. (1987). On the numerical radiation condition in the steady-state ship wave problem. *Journal of Ship Research*, *31* (1), 14–22.

Jiang, T. (2001). A new method for resistance and propulsion prediction of the ship performance in shallow water. *8th International Symposium on Practical Design of Ships and Other Floating Structures* (pp. 509–515). Shanghai, China.

Johansson, L.-E. (1984). The local effect of hull roughness on skin friction. Calculations based on floating element data and three-dimensional boundary layer theory. *Transactions of the Royal Institute of Naval Architects*, *92*, 187–201.

Jones, W. P., & Launder, B.E. (1972). The predicition of laminarization with a two-equation model of turbulence. *International Journal of Heat and Mass Transfer*, *15*, 301–315.

Karafiath, G., Cusanelli, D., & Lin, C. W. (1999). Stern wedges and stern flaps for improved powering—US Navy experience. SNAME Annual Meeting, Baltimore, MD.

Karafiath, G., & Fisher, S. C. (1987). The effect of stern wedges on ship powering performance. *Naval Engineers Journal*, *99* (3), 27–38.

Katsui, T., Asai, H., Himeno, Y., & Tahara, Y. (2005). The proposal of a new friction line. *Proceedings of the 5th Osaka Colloquium on Advanced CFD Applications to Ship Flow and Hull Form Design* (pp. 76–83*)*. Osaka, Japan.

Kempf, G. (1929). Results obtained in measuring frictional resistance. *Transactions of the Institute of Naval Architects*, *71*.

Keuning, J. A., & Sonnenberg, U. B. (1998). Approximation of the hydrodynamic forces on sailing yacht hulls based on the Delft systematic yacht hull series. *15th International HISWA Symposium on Yacht Design and Yacht Construction* (pp. 99–152). Amsterdam, Netherlands.

Khosla, P. K., & Rubin, S. G. (1974). A diagonally dominant second order accurate implicit scheme. *Computers and Fluids*, *2*, 207–209.

Kim, H. C. (1962). *Blockage correction in ship model testing*. Ann Arbor, MI: University of Michigan.

Kim, K. J. (1989). Ship flow calculations and resistance minimization (Dissertation thesis, Chalmers University, Göteborg, Sweden).

Kim, W. J., Van, S. H., & Kim, D. H. (2001). Measurement of flows around modern commercial ship models. *Experiments in Fluids*, *31*, 567–578.

Kirkman, K.L. & Kloetzli, J. W. (1980). *Scaling problem of model appendages*. American Towing Tank Conference, University of Michigan, Ann Arbor.

Kline, S. J., Coles, D. E., & Hirst, E. A. (Eds.). (1968). Computation of turbulent boundary layers. *Proceedings of the 1968 AFOSR-IFP-Stanford Conference*.

Kodama, Y., Takheshi, H., Hinatsu, M., Hino, T., & Uto, S. (Eds.). (1994). *Proceedings CFD Workshop Tokyo 1994*. Tokyo, Japan: Ship Research Institute.

Kracht, A. M. (1978). Design of bulbous bows. *Transactions of the Society of Naval Architects and Marine Engineers*, *86*, 197–217.

Kramer, M. O. (1961). The dolphin's secret. *Journal of the American Society of Naval Engineers*, *73*, 103–107.

Kreitner, J. (1934). Ueber den Schiffswiderstand auf beschraenktem Wasser. *Werft, Reederei, Hafen*, *15-7*, 77–82.

Kuethe, A. M., & Chow, C.-Y. (1986). *Foundations of aerodynamics*. New York, NY: John Wiley & Sons.

Kume, K., Ukon, Y., & Takeshi, H. (2000). Measurements of surface pressure and local velocity field around a KCS model and uncertainty analysis. *Proceedings of the Gothenburg 2000 Workshop*, Chalmers University, Sweden.

Lackenby, H. (1963). The effect of shallow water on ship speed. *Shipbuilder and Marine Engine Builder*, 446–450.

Lackenby, H., & Parker, M. (1966). The BSRA methodical series—An overall presentation. *Transactions of the Royal Institute of Naval Architects*.

Landweber, L. (1939). *Tests of a model in restricted channels*. EMB Report 460, David Taylor Research Center, Annapolis, MD.

Larsson, L. (1975). Boundary layers of ships (three-dimensional effects) (Doctoralthesis, Dept. Applied Thermo and Fluid Dynamics, Chalmers University of Technology, Gothenburg).

Larsson, L. (1981). *Proceedings of the 1980 SSPA-ITTC Workshop on Ship Boundary Layers*. SSPA Publication No. 90. Gothenburg: Swedish State Shipbuilding Experiment Tank, SSPA.

Larsson, L., & Eliasson, R. E. (2007). *Principles of yacht design* (3rd ed.). London, UK: Adlard Coles Ltd.

Larsson, L., Hammar, L., Nilsson, L. U., Berndtsson, A., Knutson, K., & Danielson, H. (1989). *A Study of Ground Simulation - Correlation between Wind-Tunnel and Water-Basin Tests of a Full-Scale Car*. SAE Technical Paper Series, 890368. Warrendale, PA: SAE International.

Larsson, L., Kim, K. J., & Zhang, D. H. (1989). New viscous and inviscid CFD-techniques for ship flows. *5th International Conference on Numerical Ship Hydrodynamics*. Hiroshima, Japan.

Larsson, L., Patel, V. C., & Dyne, G. (Eds.). (1991). *SSPA-CTH-IIHR Workshop on Ship Viscous Flow*. Report No. 2. Gothenburg: FLOWTECH International AB.

Larsson, L., Stern, F., & Bertram, V. (Eds.). (2002). *Gothenburg 2000. A Workshop on Numerical Hydrodynamics. Proceedings*. Report No. CHA/NAV/R-02/0073. Gothenburg: Chalmers Univ. of Techn.

Larsson, L., Stern, F., & Bertram, V. (2003). Benchmarking of computational fluid dynamics for ship flows: The Gothenburg 2000 workshop. *Journal of Ship Research*, *47* (1), 63–81.

Launder, B. E., & Spalding, D. B. (1974). The numerical computation of turbulent flows. *Computer Methods in Applied Mechanics and Engineering*, *3*, 269.

Lee, S.-J., Kim, H.-R., Kim, W.-J., & Van, S.-H. (2003). Wind tunnel tests on flow characteristics of the KRISO 3,600 TEU containership and 300K VLCC double-deck ship models. *Journal of Ship Research*, *47* (1), 24–38.

Leer-Andersen, M., & Larsson, L. (2003). An experimental/numerical approach for evaluating skin friction on full-scale ships with surface roughness. *Journal of Marine Science and Technology*, *8*, 26–36.

Leonard, B. P. (1979). A stable and accurate convective modelling procedure based on quadratic upstream interpolation. *Computer Methods in Applied Mechanics and Engineering*, *19*, 59–98.

Lewis, E. (Ed.). (1988). *Principles of Naval Architecture* (2nd rev., Vol. II). Jersey City, NJ: SNAME.

Lighthill, J. (1980). *Waves in fluids*. Cambridge, UK: Cambridge University Press.

Lighthill, M. J. (1958). On displacement thickness. *Journal of Fluid Mechanics*, *4*, (4), 383–392.

Lindblad, A. (1946, 1948, 1950). *Experiments with models of cargo liners*. London, UK: Royal Institution of Naval Architects.

Lindgren, H. (1969). *Systematic tests with small, fast displacement vessels, including a study of spray strips*. SSPA Report No. 65. Gothenburg: Swedish State Shipbuilding Experiment Tank, SSPA.

Löfdahl, L., & Larsson, L. (1984). Turbulence measurements near the stern of a ship model. *Journal of Ship Research*, *28* (3), 186–201.

Marchaj, C. A. (1979). *Aero-hydrodynamics of sailing*. London, UK: Granada Publishing Ltd.

Marzi, J. (2008). VIRTUE—*A European approach to developing the numerical towing tank*. RINA Marine CFD Conference, March 26-27, 2008, Southampton, UK.

Maskell, E. C. (1955). *Flow separation in three dimensions*. RAE Aero. Rep. 2565. London, UK: Ministry of Supply.

Menter, F. R. (1993). Zonal two-equation k-ω turbulence models for aerodynamic flows. *Proceedings of the 24th Fluid Dynamics Conference*. Orlando, FL. AIAA Paper 93-2906.

Merkle, C. L., & Deutsch, S. (1989). Microbubble drag reduction. In M. Gad-el-Hak (Ed.), *Frontiers in experimental fluid mechanics* (pp. 291–335). Berlin, Germany: Springer.

Michell, J. H. (1898). The wave resistance of a ship. *Philosophical Magazine*, *5*, 45.

Muzaferija, S., Peric, M., & Yoo, S. D. (1996). Numerical calculation of the flow around a wing below a free surface [in German]. *Jahrb. Schiffbaut. Gesellschaft*, *89*.

Nakos, D. E. (1990). Ship wave patterns and motions by a three-dimensional rankine panel method (Thesis, MIT, Boston, MA).

Nakos, D. E., & Sclavounos, P. D. (1994). Kelvin wakes and wave resistance of cruiser- and transom-stern ships. *Journal of Ship Research*, *38*, 9–29.

Nash, J.F. & Patel, V.C. (1972). *Three-dimensional turbulent boundary layers*. SBC Technical Books, Atlanta, Georgia.

Newman, J. N. (1976). Linearized wave resistance theory. *Proceedings of the International Seminar on Wave Resistance* (pp. 31–43). Tokyo/Osaka, Japan.

Newman, J. N. (1977). *Marine hydrodynamics*. Cambridge, MA: MIT Press.

Newton, I. (1687). *Philosophiæ Naturalis Principia Mathematica (Principia)*. London.

Ni, S.-Y. (1987). Higher-order panel methods for potential flows with linear or nonlinear free-surface boundary conditions (Doctoral thesis, Chalmers University, Gothenburg, Sweden).

Noblesse, F. (1975). A perturbation analysis of the wave making of a ship, with an interpretation of Guilloton's method. *Journal of Ship Research*, *19* (3).

Noblesse, F. (1977). The fundamental solution in the theory of steady motion of a ship. *Journal of Ship Research*, *21* (2), 82–88.

Noblesse, F. (1978). The steady wave potential of a unit source, at the centreplane. *Journal of Ship Research, 22* (2), 80–88.

Noblesse, F., & Dagan, G. (1976). Nonlinear ship-wave theories by continuous mapping. *Journal of Fluid Mechanics, 75*, 347–371.

Nordström, H. F. (1948–1949). *Some systematic tests with models of fast cargo vessels.* SSPA Report No. 10 and 14. Gothenburg: Swedish State Shipbuilding Experiment Tank, SSPA.

Nordström, H. F. (1951). *Some tests with models of small vessels.* SSPA Report No. 19. Gothenburg: Swedish Maritime Research Centre.

Ogilvie, T. F. (1968). *Wave resistance: The low-speed limit.* Report No. 002. Ann Arbor, MI: Univ. Michigan, Dept. Nav. Arch. Mar. Eng.

Orych, M., Regnström, B., & Larsson, L. (2010). Adaptive overlapping grid techniques and spatial discretization schemes for increasing surface sharpness and numerical accuracy in free surface capturing methods. *28th Symposim on Naval Hydrodynamics.* Pasadena, California.

Osher, S., & Sethian, J. A. (1988). Fronts propagating with curvature-dependent speed: Algorithms based on Hamilton-Jacobi formulations. *Journal of Computational Physics, 79*, 12–49.

Panton, R. L. (1984). *Incompressible flow.* New York, NY: John Wiley & Sons.

Park, D. W., Kim, M. G., Chung, S. H., & Chung, Y. K. (2007). Stern flow analysis and design practice for the improvement of self-propulsion performance of twin-skeg ships. *10th International Symposium on the Practical Design of Ships and Other Floating Structures.* Houston, Texas.

Park, H. G., Paik, K. J., & Noble, P. G. (2005). A study on hydrodynamics for high-speed LNGC with high block coefficient. *Society of Naval Architects & Marine Engineers Annual Meeting*, Paper D44.

Patankar, S. V. (1979). A calculation procedure for two-dimensional elliptic situations. *Numerical Heat Transfer, 4*, 409–425.

Patankar, S. V. (1980). *Numerical heat transfer and fluid flow.* New York, NY: Hemisphere Publishing Corp.

Paterson, R. W., & Abernathy, F. H. (1970). Turbulent flow drag reduction and degradation with dilute polymer solutions. *Journal of Fluid Mechanics, 43*, 689–710.

Piers, W. J. (1983). *Discretization schemes for the modelling of free water surface effects in first-order panel methods for hydrodynamic applications.* Report No. NLR TR 83093 L. Amsterdam, The Netherlands: National Aerospace Laboratory.

Prandtl, L. (1904). On fluid flow of very small friction [in German]. *Proceedings of the 3rd International Congress on Mathematics.* Heidelberg, Germany.

Prandtl, L., & Tietjens, O. G. (1957). *Fundamentals of hydro- and aeromechanics.* Mineola, NY: Dover Publications.

Raven, H. C. (1988). Variations on a theme by Dawson. *17th SympOsium on Naval Hydrodynamics* (pp. 151–171). The Hague, Netherlands.

Raven, H. C. (1992). A practical nonlinear method for calculating ship wavemaking and wave resistance. *19th Symposium on Naval Hydrodynamics* (pp. 349–370). Seoul, South Korea.

Raven, H. C. (1996). A solution method for the nonlinear ship wave resistance problem (Doctoral thesis, Technical University of Delft, MARIN, Holland).

Raven, H. C. (1997). The nature of nonlinear effects in ship wavemaking. *Ship Technology Research, 44* (1).

Raven, H. C. (1998). Inviscid calculations of ship wavemaking—Capabilities, limitations and prospects. *22nd Symposium on Naval Hydrodynamics* (pp. 738–754). Washington, DC..

Raven, H. C. (2000). Numerical wash prediction using a free-surface panel code. *International Conference on Hydrodynamics of High-Speed Craft: Wake Wash and Motion Control* (Paper 10*)*. London, UK.

Raven, H. C. (2010). Validation of an approach to analyse and understand ship wave making. *Journal of Marine Science and Technology*, to be published.

Raven, H. C., & Prins, H. J. (1998). Wave pattern analysis applied to nonlinear ship wave calculations. *13th International Workshop Water Waves and Floating Bodies.* Alphen a/d Rijn, Netherlands.

Raven, H. C., & Starke, A. R. (2002). Efficient methods to compute ship viscous flow with a free surface. *24th Symposium on Naval Hydrodynamics.* Fukuoka, Japan.

Raven, H. C., & Valkhof, H. H. (1995). Application of nonlinear ship wave calculations in design. *International Symposium on Practical Design of Ships and Mobile Units.* Seoul, Korea.

Raven, H. C, van der Ploeg, A., & Starke, A. R. (2004). Computation of free-surface viscous flow at model and full scale by a steady iterative approach. *25th Symposium on Naval Hydrodynamics.* St. Johns, Newfoundland.

Raven, H. C., Van der Ploeg, A., Starke, A. R., & Eça, L. (2008). Towards a CFD-based prediction of ship performance—Progress in predicting full-scale resistance and scale effects. *International Journal of Maritime Engineering (RINA Transactions Part A), 150*, (A4), 31–42.

Raven, H. C., Van Hees, M., Miranda, S., & Pensa, C. (1998). A new hull form for a Venice urban transport waterbus: Design, experimental and computational optimization. *7th Int. Symp. Practical Design of Ships and Mobile Units* (pp. 395–404). The Hague, Netherlands.

Reech, F. (1844). Lecture notes on mechanics. Ecole d'Application du Génie Maritime, Laurient. In O. Darrigol (Ed.) (2005), *Worlds of flow: a history of hydrodynamics from the Bernoullis to Prandtl.* Oxford, UK: Oxford University Press.

Regnström, B., & Bathfield, N. (2006). Drag and wake prediction for ships with appendages using an overlapping grid method. *26th Symposium on Naval Hydrodynamics* (pp. 243–258). Rome,Italy.

Regnström, B., Broberg, L., & Larsson, L. (2000). Ship stern flow calculations on overlapping composite grids. *23rd Symposium Naval Hydrodynamics*. Val de Reuil, France.

Regnström, B., Broberg, L., Östberg, M., Bathfield, N., & Larsson, L. (2005). Drag prediction for the KVLCC2M hull. In T. Hino (Ed.), *CFD Workshop Tokyo 2005* (pp. 564–568). Tokyo, Japan: National Maritime Research Institute.

Reynolds, O. (1883). An experimental investigation of the circumstances which determine whether the motion of water shall be direct or sinuous, and the law of resistance in parallel channels. *Philosophical Transactions of the Royal Society*, *174*, 935–982.

Rhie, C. M., & Chow, W. L. (1983). A numerical study of the turbulent flow past an isolated airfoil with trailing edge separation. *AIAA Journal*, *21*, 170–183.

Roache, P. J. (1998). *Verification and validation in computational science and engineering.* Albuquerque, NM: Hermosa Publishers.

Roache, P. J. (2009). *Fundamentals of verification and validation.* Albuquerque, NM: Hermosa Publishers.

Roseman, D. P. (1987). *The MARAD systematic series of full form ship models*. Jersey City, NJ: SNAME.

Rota, G. (1900). On the influence of depth of water on the resistance of ships. *Transactions of the Institute of Naval Architects*, *42*.

Rubin, S. G. (1984). Incompressible Navier-Stokes and parabolized Navier-Stokes formulations and computational techniques (pp. 51-99). In W. G. Habashi (Ed.), *Computational methods in viscous flows: Recent advances in numerical methods in fluids* (Vol. 3). Swansea, UK: Pineridge Press.

Rumble, H. P. (1955). The admiralty experiment works, Haslar. *Transactions of the Institute of Naval Architects*, *97*.

Sasajima, H., & Tanaka, I. (1966). On the estimation of the wake of ships. *Proceedings of the 11th ITTC* (pp. 140–143). Tokyo,Japan.

Saunders, H. E. (1957). *Hydrodynamics in ship design* (Vol. I). Jersey City, NJ: SNAME.

Savitsky, D. (1964). Hydrodynamic design of planing hulls. *Marine Technology*, *1* (1), 71–95.

Savitsky, D., DeLorme, M. F., & Datia, R. (2007). Inclusion of whisker spray drag in performance prediction method for high-speed planing hulls. *Marine Technology*, *44*, 35–56.

Schrenk, O. (1940). *Simple approximation method for obtaining spanwise lift distribution.* NACA TM 948, Vol. 7, Issue 4.

Schlichting, H. (1987). *Boundary layer theory* (7th ed.). New York, NY: McGraw-Hill.

Schlichting, O. (1934). Ship resistance in water of limited depth-resistance of sea-going vessels in shallow water. *Jahrbuch der STG*, *35*, 127–138.

Schneekluth, H., & Bertram, V. (1998). *Ship design for efficiency and economy* (2nd ed.). Oxford, UK: Butterworth Heinemann.

Schoenherr, K. E. (1932). Resistance of flat surfaces moving through a fluid. *Transactions of the Society of Naval Architects and Marine Engineers*, *40*, 279–313.

Sclavounos, P. D., & Nakos, D. E. (1988). Stability analysis of panel methods for free-surface flows with forward speed. *17th Symposium on Naval Hydrodynamics* (pp. 173–194). Den Haag, Netherlands.

Shih, T. H., Zhu, J., & Lumley, J. L. (1992). *A realizable Reynolds stress algebraic equation model.* NASA TM 105993.

Spalart, P. R., & Allmaras, S. R. (1992). *A one-equation turbulence model for aerodynamic flows.* AIAA Paper 92-439. Reno, NV.

Spalding, D. B. (1972). A novel finite-difference formulation for differential expressions involving both first and second derivatives. *International Journal for Numerical Methods in Engineering*, *4* (4), 551–559.

Starke, A. R., Raven, H. C., & van der Ploeg, A. (2007). Computation of transom-stern flows using a steady free-surface fitting RANS method. *9th International Conference Numerical Ship Hydrodynamics.* Ann Arbor, MI.

Starke, B., & Windt, J. (2003). Two examples of hull-form optimization using viscous-flow computations. *CFD 2003: RINA Conference on Computational Fluid Dynamics Technology in Ship Hydrodynamics.* London, UK.

Starke, A. R., Windt, J., & Raven, H. C. (2006). Validation of viscous flow and wake field predictions for ships at full scale. *26th Symposium on Naval Hydrodynamics.* Rome, Italy.

Stern, F., Wilson, R. V., Coleman, H. W., & Paterson, E. G. (2001). Comprehensive approach to verification and validation of CFD simulations—Part I: Methodology and procedures. *ASME Journal of Fluids Engineering*, *123*, 793–802.

Strobel, K. H., & Cheng, B. H. (1992). Finite-difference operators for the Rankine source method. *Proceedings of the 11th Offshore Mechanics and Arctic Engineering Conference*. Calgary, Canada.

Stumbo, S., Elliott, L., & Fox, K. (2000). An assessment of wake wash reduction of fat ferries at supercritical Froude numbers and at optimized trim. *RINA Conference on Hydrodynamics of High-Speed Craft*. London, UK.

Sussman, M., Smereka, P., & Osher, S.J. (1994). A level set approach for computing solutions to incompressible two-phase flow. *Journal of Computational Physics*, *114*, 146–159.

Svennberg, S. U. (2001). On turbulence modeling for bilge vortices: A test of eight models for three cases (Doctoral thesis, Chalmers University of Technology, Gothenburg).

Taylor, D. W. (1933). *Speed and power of ships.* Washington, DC: Press of Ransdell.

Telfer, E. X. (1953). Ship model correlation and tank wall effect. *NECI Transactions*, *70*.

Thompson, W. (Lord Kelvin). (1887). On ship waves. *Transactions IME*, *3*, 409–433.

Thompson, W. (Lord Kelvin). (1904). On deep water two-dimensional waves produced by any given initiating disturbance. *Proceedings of the Royal Society of Edinburgh, 25* (1), 185–196.

Tikka, J., & van der Baan, J. (1985). *On the design of modern ferry hull forms.* Workshop on Hull Form Design. Wageningen, The Netherlands: MARIN.

Todd, F. H. (1951). The fundamentals of ship model testing. *Society of Naval Architects & Marine Engineers Transactions, 59.*

Todd, F. H. (1963). *Series 60-Methodical experiments with models of single-screw merchant ships.* DTMB Report 1712. Hoboken, NJ: Stevens Inst. of Tech.

Toms, B. A. (1948). Some observations on the flow of linear polymer solutions through straight tubes at large Reynolds numbers. *Proceedings of the 1st International Congress on Rheology, 2,* 135–141.

Towsin, R. L., & Byrne, D. (1980). Speed, power and roughness: The economics of outer bottom maintenance. . *Transactions of the Royal Institute of Naval Architects, 122,* 459–483.

Tuck, E. O. (1989). The wave resistance formula of J.H. Michell (1898) and its significance to recent research in ship hydrodynamics. *Journal of the Australian Mathematical Society, Series B, 30,* 365–377.

Tuck, E. O., Scullen, D. C., & Lazauskas, L. (2002). Wave patterns and minimum wave resistance for high-speed vessels. *24th Symposium on Naval Hydrodynamics.* Fukuoka, Japan.

Tulin, M. P., & Landrini, M. (2000). Breaking waves in the ocean and around ships. *23rd Symposium on Naval Hydrodynamics* (pp. 713–745). Val de Reuil, France.

Tursini, L. (1953). Leonardo da Vinci and the problems of navigation and naval design. *Transactions of the Institute of Naval Architects, 95,* 97–102.

Ubbink, O. (1997). Numerical prediction of two-fluid systems with sharp interfaces (Doctoral thesis, University of London).

Valdenazzi, F., Harries, S., Janson, C. E., Leer-Andersen, M., Maisonneuve, J. J., Marzi, J., et al. (2003). The FANTASTIC RoRo: CFD optimisation of the forebody and its experimental verification. *Proceedings of the NAV2003 Conference.* Palermo, Italy.

Valkof, H.H. (1999). Hull form design strategy. Course synopsis, MARIN Training Course on Hydrodynamics in Ship Design. Wageningen, Netherlands.

Valkhof, H. H., Minguito, E., & Kooiker, K. (2005). New promising generation of twin-gondola LNG carriers optimized with the aid of CFD calculations. *SNAME Annual Meeting,* Paper D33.

van Berlekom, W. B. (1981). Wind forces on modern ship forms—Effects on performance. *North East Coast Institution of Engineers and Shipbuilder Transactions, 97,* 123–134.

van Berlekom, W. B. (1985). *Twin skeg afterbodies can save fuel.* Workshop on Hull Form Design. Wageningen, The Netherlands: MARIN.

van den Berg, W., Raven, H. C., & Valkhof, H. H. (1990). Free-surface potential flow calculations for merchant vessels. *Symposium on CFD and CAD in Ship Design* (pp. 165–181). Wageningen, Netherlands.

van Doormal, J. P., & Raithby, G. D. (1984). Enhancement of the SIMPLE method for predicting incompressible fluid flows. *Numerical Heat Transfer, 7,* 147–163.

Van, S.-H., Kim, D.-H., Son, B.-R., Lee, J.-K., Cha, D.-Y., & Huh, J.-K. (1996). Experimental study on resistance and propulsion characteristics for Ro-Ro passenger ship of twin propellers. *Symposium on Practical Design of Ships and Mobile Units* (pp. 439–446).

Van, S. H., Kim, W. J., Yim, D. H., Kim, G. T., Lee, C. J., & Eom, J. Y. (1998a). Flow measurement around a 300K VLCC model. *Proceedings of the Annual Spring Meeting, SNAK* (pp. 185–188) Ulsan,.

Van, S. H., Kim, W. J., Yim, G. T., Kim, D. H., & Lee, C. J. (1998b). Experimental investigation of the flow characteristics around practical hull forms. *Proceedings of the 3rd Osaka Colloquium on Advanced CFD Applications to Ship Flow and Hull Form Design* (pp. 215–227). Osaka, Japan.

Versteeg, H. K., & Malalasekera, W. (1995). *An introduction to computational fluid dynamics.* London, UK: Prentice Hall.

Visonneau, M., Deng, G. B., & Queutey, P. (2006). Computation of model and full scale flows around fully appended ships with an unstructured RANSE solver. *26th Symposium on Naval Hydrodynamics.* Rome, Italy.

Vogt, M., & Larsson, L. (1999). Level set methods for predicting viscous free-surface flows. *7th International Conference on Numerical Hydrodynamics.* Nantes, France.

Vossnack, E., Buys, C. T., Jonk, A., Kamps, J., & van de Beek, J. (1977). Ontwikkeling van het achterschip voor container-en RoRo-Schepen. 1971-1977 *Symposium Trillingshinder bij schepen.* Tech. Univ. Delft. (in Dutch).

Walsh, M. J., & Anders, J. B. (1989). Riblet/LEBU research at NASA Langley. *Applied Scientific Research, 46,* 255–262.

Walsh, M. J., & Lindemann, A. M. (1984). *Optimization and application of riblets for turbulent drag reduction.* AIAA Paper No. 84-0347. Huntsville, AL: AIAA.

Wang, Z., Yang, J., & Stern, F. (2009). A coupled level set and volume of fluid method for 3D sharp interface simulation of plunging breaking waves. *International Journal of Multiphase Flow, 35,* 227–246.

Warholm, A. O. (1953–1955). *Tests with models of coasters.* SSPA Reports No. 24 and 25. Gothenburg: Swedish State Shipbuilding Experiment Tank, SSPA.

Watanabe, K., Udagawa, Y., & Udagawa, H. (1999). Drag reduction of Newtonian fluid in a circular pipe with a highly water-repellent wall. *Journal of Fluid Mechanics, 381,* 225–238.

Wehausen, J. V. (1973). The wave resistance of ships. In C.–S. Yih (Ed.), *Advances in applied mechanics* (Vol. 13, pp. 93–245). Washington, DC: Academic Press.

Wehausen, J. V., & Laitone, E. V. (1960). Surface waves. In *Encyclopedia of Physics* (Vol. IX, pp. 446–778). Berlin, Germany: Springer Verlag.

White, F. M. (2005). *Fluid mechanics* (5th ed.). New York, NY:McGraw-Hill.

Whittaker, T. J. T., Doyle, R., & Elsaesser, B. (2001). *An experimental investigation of the physical characteristics of fast ferry wash.* HIPER 2001 Conference, Hamburg, Germany, May 2001.

Wigley, C. (1931). Ship wave resistance. *NECI Transactions*, *47.*

Wigley, C. (1934). A comparison of experiment and calculated wave profiles and wave resistance for a form having parabolic waterlines. *Proceedings of the Royal Society*, *144* (851), 144–159.

Wigley, C. (1942). Calculated and measured wave-making resistance for a series of forms defined algebraically, the prismatic coefficient and angle of entrance being varied independently. *Transactions of the Institute of Naval Architects*, *86*, 41–56.

Wilcox, D. C. (1998). *Turbulence modeling for CFD* (2nd ed.). La Canada, CA: DCW Industries, Inc.

Williams, Å. (1969). *The SSPA cargo liner series. Resistance.* SSPA Report No. 66. Gothenburg: Swedish State Shipbuilding Experiment Tank, SSPA.

Wyatt, D. C. (2000). Development and assessment of a nonlinear wave prediction methodology for surface vessels. *Journal Ship Research*, *44* (2), 96–107.

Xia, F. (1986). Numerical calculations of ship flows, with special emphasis on the free-surface potential flow (Doctoral thesis, Chalmers University, Göteborg, Sweden).

Yakhot, V., Orzag, S. A., Thangam, S., Gatski, T. B., & Speziale, C. G. (1992). Development of turbulence models for shear flows by a double expansion technique. *Physics of Fluids A*, *4* (7), 1510–1520.

Yeh, H. Y. H. (1965). Series 64. Resistance experiments on high-speed displacement forms. *Marine Technology*, *2* (3).

Zondervan, G.-J. D., & Holtrop, J. (2000). Application of advanced section profiles in the design of propulsors and ship appendages. *SNAME Propeller and Shafting Symposium.* Virginia Beach, VA.

INDEX